PACIFIC EARTHQUAKE ENGINEERING RESEARCH CENTER

Effect of Vertical Acceleration on Shear Strength of Reinforced Concrete Columns

Hyerin Lee

Khalid M. Mosalam

Department of Civil and Environmental Engineering
University of California, Berkeley

PEER 2014/04
APRIL 2014

Effect of Vertical Acceleration on Shear Strength of Reinforced Concrete Columns

Hyerin Lee

Khalid M. Mosalam

Department of Civil and Environmental Engineering
University of California, Berkeley

PEER Report 2014/04
Pacific Earthquake Engineering Research Center
Headquarters at the University of California, Berkeley

April 2014

ABSTRACT

The effect of vertical excitation on shear strength of reinforced concrete (RC) columns has been investigated by various researchers. Field evidence, analytical studies, and static or hybrid simulations suggested that excessive tension or tensile strain of the column may lead to shear degradation, and that vertical excitation can be one of the causes of shear failure. Due to limitations of testing facilities, published literature has not reported the results of dynamic experiments to investigate the effect of vertical excitation on the shear strength of RC columns. Considering that current seismic codes do not have a consensus on the effect of vertical acceleration on the shear demand and capacity, the presented dynamic tests and accompanying analytical investigation contribute to better understanding of the effect of vertical excitation on shear failure, one of the most critical brittle failure mechanisms.

This report provides both experimental and computational results, which confirm that vertical acceleration can induce shear strength degradation of RC columns. Dynamic tests of two reduced geometrical scale specimens were conducted on the University of California, Berkeley shaking table at Richmond Field Station. The two specimens had different transverse reinforcement ratio. As a result of an analytical investigation and preliminary fidelity tests, the 1994 Northridge earthquake acceleration recorded at the Pacoima Dam was selected as an input motion among the 3551 earthquake acceleration records in the PEER NGA database. The chosen ground motion was applied to the test specimens at various levels ranging from 5% to 125%. The specimens were subjected to combinations of vertical component and the larger of the two horizontal components of the selected ground motion record. For the 125%-scale, not only was the combined vertical and horizontal motion applied but also a single horizontal component was considered for direct evaluation of the effect of the vertical excitation.

The experimental results imply that vertical acceleration has the potential to degrade the shear capacity of RC columns. The peak shear force in the 125%-scale run with only the horizontal component was larger than that in the 125%-scale runs with the horizontal and vertical components for each specimen, where the peak force was determined by the shear strength at these high-level tests. For these runs, considerable tensile forces were induced on the tested columns due to the vertical excitation. Tension in the columns resulted in degradation of the shear strength, which is mainly due to the degradation of the concrete contribution to the shear strength. Flexural damage at the top of the column took place before the flexural damage at the base since the bending moment at the top was larger. This was a result of the large mass moment of inertia and rigid body rotation of the mass blocks at the top of the column. In addition, comparison of the bending moment histories at the base and top of the two test specimens indicated that they were opposite in sign during the strong part of the excitation of all the intensity levels, suggesting that the columns were in double-curvature. As a result of flexural yielding at the top and base of the column when bending in double curvature, the shear force reached its shear capacity, which would not take place if yielding occurred only at the base. Consequently, shear cracks occurred and extended over the entire column height as the intensity increased, especially when subjected to significant axial tension.

The analytical investigation also revealed that considerable axial tension forces can be induced in RC columns, which resulted in degradation in the shear strength. Two types of computational models were utilized in the computational platform OpenSees. Models A and B had a beam with hinges element and a nonlinear beam-column element, respectively. In addition, a new shear spring element was implemented in the same computational platform to employ code-based shear strength estimation. The element incorporates the shear strength estimations based on ACI or Caltrans SDC equations, addressing the effect of column axial load and displacement ductility. Both Models A and B were developed without and with the newly-developed shear spring element. Upon improved modeling, results from the analysis of the tested specimens were examined in terms of shear strength variation. Accordingly, current code equations and the corresponding computational models were evaluated. The models without the shear springs did not capture the shear strength degradation accurately, whereas those including the ACI and Caltrans SDC shear springs captured the shear strength degradation due to the axial tension. Both of the ACI and Caltrans SDC springs provided results on the conservative side, where the ACI shear spring predictions were closer to the experimental results than those of the Caltrans SDC shear spring. Elimination of the concrete contribution to the shear strength under any tension was the main reason for the highly conservative predictions of the Caltrans SDC shear strength equation, where the strength reduction caused by ductility was not as significant as that caused by axial tension force.

ACKNOWLEDGMENTS

This work was supported by the California Department of Transportation (Caltrans) under Master Agreement No. 22A0486 (Award Number 07-003895-UCB) for the project entitled "Effect of Vertical Ground Motions on Shear Demand and Capacity in Bridge Columns." It is gratefully acknowledged. The authors would like to thank Professor Sashi K. Kunnath at the University of California, Davis, for his valuable suggestions, and Dr. Selim Günay, for his intellectually stimulating exchanges.

The help provided by staff at the Pacific Earthquake Engineering Research Center (PEER), University of California, Berkeley, is gratefully appreciated. In particular, the experimental phase of this research, conducted in the research laboratories of PEER, benefited considerably from the advice and hard work of Mr. Don Clyde, Dr. Shakhzod Takhirov, and Mr. Wesley Neighbour. Without Dr. Frank McKenna, the analysis presented herein would not have been possible.

CONTENTS

LIST OF FIGURES

LIST OF TABLES

1 Introduction

1.1 MOTIVATION

1.1.1 Statement of the Problem

Bridges constitute a major component of the transportation network. Partial or total collapse of bridges after earthquakes may lead to considerable interruption of emergency and recovery services. Reinforced concrete (RC) and prestressed concrete (PC) bridges, a vital component in transportation systems, were observed to have substandard performance during earthquakes, due to the inherent lack of redundancy of the structural system [Priestley et al. 1996]. Bridges and other parts of the transportation network have been constructed prior to recent advances in earthquake engineering in many parts of the world. In addition, bridges designed according to the modern codes have been severely damaged or collapsed in the earthquakes that have occurred within the last two decades in various parts of the world, including the United States, Japan, Taiwan, and others. Since bridge structures are not designed with enough redundancy and columns are the most critical part of the bridge structural system, their brittle failure should be prevented.

Shear failure is one of the most critical brittle failure mechanisms and involves rapid strength degradation due to a complex shear mechanism related to increasing flexure-shear crack width. It is known that axial force or strain affects the shear capacity. As an example, near-fault vertical ground motions may lead to tensile forces on the bridge columns during short time intervals, leading to negligible contribution of concrete to shear capacity after cracking. Although the effect of axial force on shear capacity is an accepted fact, current seismic codes do not have a consensus on this effect, and different code equations might lead to different shear capacity estimations. On the demand side, axial forces that are not taken into consideration, such as those due to vertical excitation, may lead to an increase in the moment capacities, resulting in greater shear forces than expected.

1.1.2 Objectives and Scope of Research

The main objective of this study is to investigate the effect of axial force produced by the vertical component of the ground motion on the behavior of bridge columns, especially on shear strength degradation. An outline of the research program is presented in Figure 1.1.

This study consisted of three parts. First, a bridge prototype is described, with the stated assumption that its shear demand changed under the existence of vertical acceleration. Also, a parametric study was conducted on a single column model, which is based on a representative bridge prototype. Using a sub-set of ground motions from the Pacific Earthquake Engineering Research (PEER) Center's Next Generation Attenuation (NGA) ground motion database[1] [2013], with strong influence of the vertical acceleration, the shear demand was compared to capacity suggested in current codes. The outline of specimen design and input candidates were determined based on the parametric study results.

Second, dynamic tests were designed and test results reported. The specimens, which were one-quarter-scale models of the prototype columns, were designed based on the Caltrans[2] Seismic Design Criteria [2013][3]. Corresponding mass and mass moment of inertia were determined from the prototype. Fidelity tests were used to choose the most suitable motion that could be replicated by the shaking table at the Richmond Field Station, University of California, Berkeley (UCB). Dynamic tests of two specimens were conducted and the results imply that vertical acceleration has the potential to degrade the shear capacity of an RC bridge column.

Third, a new OpenSees[4] shear spring element was developed because existing elements do not reflect the ductility-axial-shear coupled behavior. Upon improved modeling, results from the specimen analysis were examined scrupulously, especially in terms of shear strength variation. Current code equations were evaluated and compared to the analysis results.

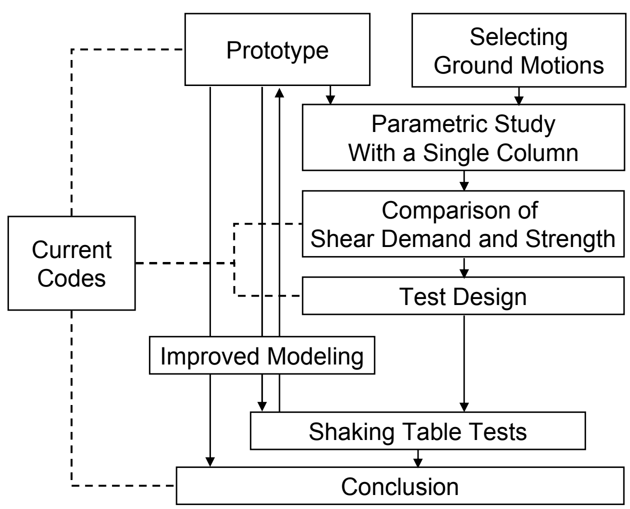

Figure 1.1 Outline of the research.

[1] PEER NGA is an update and extension to PEER Strong Motion Database, http://peer.berkeley.edu/nga/.
[2] Caltrans is California Department of Transportation.
[3] Seismic Design Criteria, http://www.dot.ca.gov/hq/esc/earthquake_engineering/SDC_site/.
[4] OpenSees is the Open System for Earthquake Engineering Simulation, http://opensees.berkeley.edu/.

1.2 OVERVIEW OF SHEAR STRENGTH ASSESSMENT

Estimating the shear strength of RC members is still controversial, and there is a wide divergence of opinions, design approaches, and code equations. In particular, the influences of axial load, flexural ductility, and size of members and aggregates are not well agreed upon within different codes. The following code equations and an analytical approach are widely used methods to estimate the shear strength of RC members, e.g., columns.

1.2.1 ACI 318-11 [2011]

According to ACI[5] 318-11 [2011], the nominal shear strength is computed by:

$$V_n = V_c + V_s \tag{1.1}$$

where V_c and V_s are the nominal shear strength provided by concrete and shear reinforcement, respectively. When shear reinforcement perpendicular to the axis of the member is used, one can use

$$V_s = \frac{A_v f_y d}{s} = \frac{A_v f_y (0.8D)}{s} \tag{1.2}$$

where A_v is the cross-sectional area of the spiral reinforcement within spacing s, and D is the diameter of the concrete section. For circular members with circular ties, hoops, or spirals used as shear reinforcement, it is permitted to take the effective depth, d, as 0.80 times the diameter of the concrete section, and A_v can be taken as two times the area of the bar cross section used as the spiral. Finally, f_y is the specified yield strength of the spiral reinforcement.

For members subjected to axial compression,

$$V_c = 2\left(1 + \frac{N_u}{2000A_g}\right)\sqrt{f_c'}\, b_w d \tag{1.3}$$

For members subjected to axial tension,

$$V_c = 2\left(1 + \frac{N_u}{500A_g}\right)\sqrt{f_c'}\, b_w d \tag{1.4}$$

but not less than zero, where N_u is positive for compression and negative for tension. In the above two equations, N_u/A_g and the concrete compressive strength of the standard specimen f_c' have psi units, and A_g is the gross cross-sectional area with web width b_w and effective depth d.

For circular members, the area used to compute V_c can be taken as the product of the diameter and effective depth of the concrete section. Hence, the following V_c can be used,

[5] ACI is American Concrete Institute.

$$V_c = 2\left(1+\frac{N_u}{2000A_g}\right)\sqrt{f_c^{'}}\left(0.8D^2\right) \text{ for members subjected to axial compression} \quad (1.5)$$

$$V_c = 2\left(1+\frac{N_u}{500A_g}\right)\sqrt{f_c^{'}}\left(0.8D^2\right) \text{ for members subjected to axial tension} \quad (1.6)$$

where $A_g = \dfrac{\pi D^2}{4}$.

1.2.2 A Note about Size Effect

Unfortunately, 'size effect' is not considered in Equations (1.3) to (1.6) for V_c. Size effect is the phenomenon whereby the failure shear stress for members without web reinforcement decreases as the member depth increases. Equations (1.3) to (1.6) were obtained from specimens with an average height of 340 mm (13.4 in.). As a result, the ACI expressions offer a continuous and linear increase in the contribution of concrete to shear capacity as the member depth increases. This means that these expressions are not suitable for deeper members without web reinforcement.

The Modified Compression Field Theory (MCFT) [Vecchio and Collins 1986] provides an analytical model that is capable of predicting the load-deformation response of RC elements subjected to in-plane shear and normal stresses. It is developed from the compression-field theory for RC members subjected to torsion and shear. While the compression-field theory did not take into account tension in the cracked concrete, the MCFT reflects tensile stresses between cracks. Also, in the MCFT, the size effect is related to the crack spacing in the web and the crack width.

Cracking usually occurs along the interface between the cement paste and the aggregate particles, and the rough cracks can transfer shear by aggregate interlocking. Walraven's experimental study [1981] derived the relationship between the shear transfer across the crack and the crack width. Roughly, the larger crack width that occurs in a larger member reduces aggregate interlocking and accordingly reduces the shear transfer. In other words, the shear stress decreases as the crack width increases and as the relative maximum aggregate size (compared to the member size) decreases. Therefore, the shear stress limit of a large member is lower than that of a small member. The crack width is the average crack width over the crack surface; it can be taken as the product of the principal tensile strain and the crack spacing. Therefore, crack widths increase linearly with both the tensile strain in the reinforcement and the spacing between cracks.

The AASHTO[6] LRFD[7] [2012] and the CSA[8] Standards [2004] are based on the Simplified Modified Compression Field Theory (SMCFT) [Bentz et al. 2006], but have been considerably simplified. Simple expressions have been developed for the factor determining the

[6] AASHTO is the American Association of State Highway and Transportation Officials.
[7] LRFD is the Load and Resistance Factor design.
[8] CSA is the Canadian Standards Association.

ability of diagonally-cracked concrete to transmit tension, β, the crack angle, θ, and the longitudinal strain in the web, ε_x, thereby eliminating the need to iterate to solve for these values.

1.2.3 AASHTO [2012]

The AASHTO LRFD Bridge Design Specification [2012] defines the shear resistance of a concrete member as the sum of resistance due to shear stress of concrete, V_c, tensile stress in the transverse reinforcement, V_s, and the vertical component of prestressing force, if any, V_p, as follows:

$$V_n = V_c + V_s + V_p \tag{1.7}$$

The contribution of concrete is determined in N-mm units as follows:

$$V_c = 0.083\beta\sqrt{f_c'}b_v d_v \tag{1.8}$$

where b_v is the effective web width taken as the minimum web width with the depth d_v. For a circular section, $b_v = D$, $d_v = 0.9d_e$ can be used, where $d_e = \dfrac{D}{2} + \dfrac{D_r}{\pi}$, as shown in Figure 1.2. The value of β, the factor to determine the ability of diagonally-cracked concrete to transmit tension, is defined as follows:

$$\beta = \frac{4.8}{1 + 750\varepsilon_s} \tag{1.9a}$$

$$\beta = \left(\frac{4.8}{1 + 750\varepsilon_s}\right)\left(\frac{51}{39 + s_{xe}}\right) \tag{1.9b}$$

Equation (1.9a) is for sections containing at least the minimum amount of transverse reinforcement, and Equation (1.9b) is for the rest. The minimum amount of transverse reinforcement is defined as $A_v \geq 0.05 b_w s / f_y$, where b_w is the width of web. In addition, the crack spacing parameter is calculated as follows:

$$s_{xe} = s_x \frac{1.38}{a_g + 0.63} \tag{1.10}$$

where a_g is the maximum aggregate size in mm, and s_x is the lesser of either d_v or the maximum distance between layers of longitudinal crack control reinforcement. s_{xe} should be between 12 in. (305 mm) and 80 in. (2032 mm). If there is no prestressing tendon, the net longitudinal tensile strain in the section at the centroid of the tension reinforcement, ε_s, is defined as follows:

$$\varepsilon_s = \frac{\left(\dfrac{|M_u|}{d_v} + 0.5N_u + |V_u|\right)}{E_s A_s} \tag{1.11}$$

where N_u , M_u , and V_u are the factored axial force, bending moment, and shear force, respectively, and A_s and E_s are the cross-sectional area and modulus of elasticity for the longitudinal tension reinforcement.

The contribution of transverse reinforcement is determined as follows:

$$V_s = \frac{A_v f_y d_v \left(\cot\theta + \cot\alpha\right)\sin\alpha}{s} \tag{1.12}$$

$$\theta = 29^o + 3500\varepsilon_s \tag{1.13}$$

The parameter α is the angle of inclination of transverse reinforcement (with cross-sectional area, A_v, yield stress, f_y, and spacing, s) to the longitudinal axis of the member, and θ is the angle of inclination of the diagonal compressive stress. The factors β [Equation (1.9)] and θ [Equation (1.13)] depend on the applied loading and the properties of the cross-section.

Prior to the 2008 interim revisions, AASHTO provided the procedure for shear design, which was iterative and required the use of tables for the evaluation of β and θ. With the 2008 revisions, this design procedure was modified to be non-iterative, and algebraic equations were introduced for the evaluation of β and θ. These equations are functionally equivalent to those used in the Canadian code [CSA 2004], which were also derived from the SMCFT [Bentz et al. 2006]. Because Equations (1.8) and (1.16) are equivalent, only CSA equations will be used in Chapter 2.

The longitudinal strain, ε_s, is affected by diagonal compressive stresses. After diagonal cracks have formed in the web, the shear force applied to the web concrete, V_u, is primarily carried by diagonal compressive stresses in the web concrete. These stresses result in a longitudinal compressive force in the web concrete of $V_u \cot\theta$; see Figure 1.3. Equilibrium requires that this longitudinal compressive force in the web needs to be balanced by tensile forces in the two flanges, with half the force, that is, $0.5V_u \cot\theta$, being taken by each flange. For simplicity, the longitudinal demand due to shear in the longitudinal tension reinforcement may be taken as V_u without significant loss of accuracy. After the required axial forces in the two flanges are calculated, the resulting axial strains in the steel reinforcement and concrete, ε_s and ε_c, respectively, can be calculated based on the axial force-axial strain relationships.

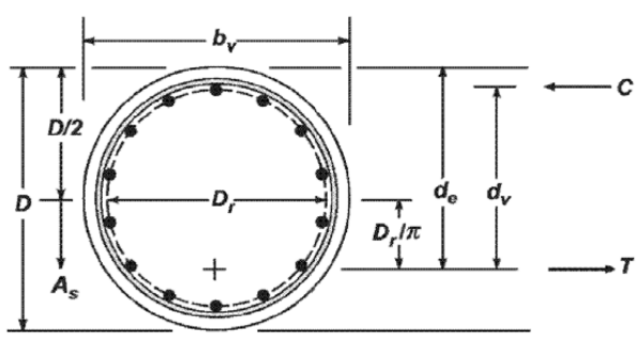

Figure 1.2 Parameters b_v, d_v and d_e for a circular column, AASHTO [2012].

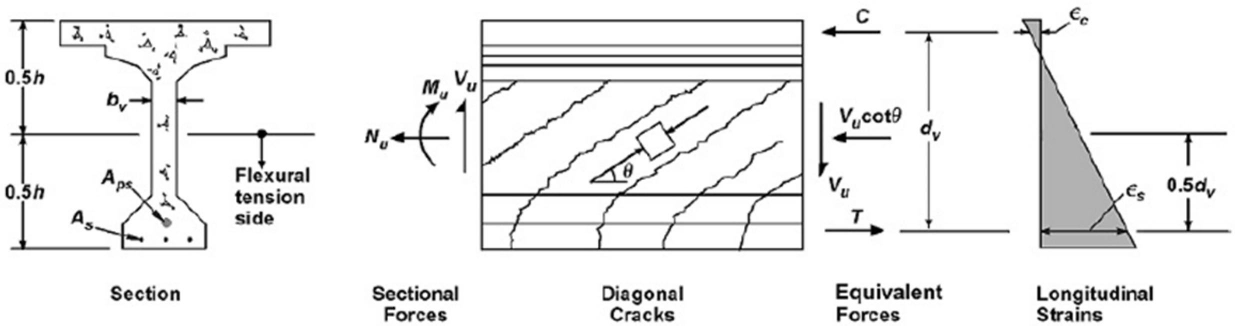

Figure 1.3 Shear parameters, AASHTO [2012].

1.2.4 Canadian Code [2004]

The CSA A23.3 [2004] shear provisions for RC are based on the MCFT like the AASHTO [2012]. In CSA, the shear strength in assumed to be the sum of V_c, V_s, and V_p [Equation (1.7)]. As in other codes V_c is the shear resistance from concrete, which is due to the shear stress transfer across the crack itself, usually called aggregate interlocking stresses, V_s is from the transverse reinforcement, specifically due to the yielding stirrup legs that cross the diagonal crack, and V_p is the vertical component of the prestressing force, if any. Since the vertical force from dowel action is ignored in the MCFT, it is ignored in the CSA as well.

The aggregate interlocking resistance of the complex crack geometry may be estimated at only one depth in the member, e.g., mid-height, which can represent the entire crack surface. Because the shear stress resistance of the flexural compression region is larger than that of the cracked region, the ability of the cracks to resist shear stresses controls the member strength for members without stirrups.

The shear resistance from transverse reinforcement is defined as follows:

$$V_s = \frac{A_v f_y d_v \cot\theta}{s} \tag{1.14}$$

$$\theta = 29^o + 7000\varepsilon_x \tag{1.15}$$

$$V_c = \beta\sqrt{f_c^{'}}b_v d_v \tag{1.16}$$

$$\beta = \left(\frac{0.4}{1+1500\varepsilon_x}\right)\left(\frac{1300}{1000+s_{ze}}\right) \tag{1.17}$$

where A_v is the cross-sectional area of the spiral reinforcement, f_y is the yield strength of the spiral reinforcement material, s is the spacing of the spiral reinforcement, and $f_c^{'}$ is the compressive strength of concrete (its unit is MPa). The parameters that define β and θ for the determination of V_c and V_s, respectively, are similar to the case of AASHTO, except for the longitudinal strain. In CSA, the longitudinal strain at the centroid, ε_x, is used rather than the longitudinal strain at the centroid of the tension reinforcement, ε_s.

Since the aggregate interlocking relationship directly depends on the crack width, the calculation of such crack width is needed to determine V_c. Approximately, the crack width can be estimated as the product of average crack strain perpendicular to the crack and the average crack spacing in this direction. Previous studies demonstrated that the crack patterns are consistent from one size to another, and the crack spacing increases as the RC member (without shear reinforcement) is scaled to a larger size. Since wider cracks carry less shear stresses, a larger member's shear stress related to V_c cannot exceed that of a smaller member. However, members with transverse reinforcement do not follow this trend because transverse reinforcement controls the crack spacing. Therefore, such RC members (with shear reinforcement) do not show a significant size effect. Hence, the basic crack spacing s_z is taken as 300 mm (11.8 in.) for the members with stirrups or transverse reinforcement, rather than $s_z = d_v = 0.9D$ (where D is the diameter of the column), which is used by CSA 2004 for the members without stirrups.

The effective crack spacing parameter, s_{ze}, reflects the effect of different coarse aggregate sizes in mm, a_g, and it is calculated as follows:

$$s_{ze} = \frac{35 s_z}{15 + a_g} \geq 0.85 s_z \tag{1.18}$$

In case of a member with transverse reinforcement and 19 mm (0.75 in.) coarse aggregate, $s_{ze} = 308.8$ mm (12.2 in.). For a circular section, $d_v = 0.72D$ in CSA 2004. Also, nominal shear strength should not be taken larger than the following:

$$V_{n,\max} = 0.25 f_c^{'} b_v d_v \tag{1.19}$$

1.2.5 Eurocode [CEN 1992]

Eurocode 2 [CEN 1992] suggests the following equations. Using the standard method with Equation (1.1), the resistance of shear reinforcement is as follows:

$$V_s = \frac{A_v z f_y}{s} = \frac{A_v f_y \left(0.72D\right)}{s} \tag{1.20}$$

where z is the lever arm. It may be taken to be 0.6 for $f_c^{'} \leq 60\text{MPa}$, and $0.9 - f_c^{'}/200 > 0.5$ for high-strength RC members.

$$V_c = \frac{\pi D_c^{\,2}}{4}\left[\tau_{rd} k \left(1.2 + 40\rho_l\right) + 0.15\sigma_{cp}\right] \tag{1.21}$$

$$D_c = D - 2c_c - 2d_{bw} \tag{1.22}$$

where d_{bw} is the diameter of the spiral reinforcement, and c_c is the concrete cover outside the spiral.

$$\tau_{rd} = 0.25\left(0.7\sqrt{f_c^{'}}\right) \tag{1.23}$$

$$k = 1 \tag{1.24}$$

$$\sigma_{cp} = \frac{N}{A_c} \tag{1.25}$$

where N is the axial load and $A_c = \pi D_c^2/4$.

The nominal shear strength should not be taken larger than the following:

$$V_{n,\max} = \frac{b_w z \nu f_c'}{2} \tag{1.26}$$

Or using the variable strut inclination method,

$$V_n = \min\left(\frac{A_v z f_y \cot\theta}{s}, \frac{b_w z \nu f_c^{'}}{\cot\theta + \tan\theta}\right) \tag{1.27}$$

where θ is the angle of the inclined struts. The recommended limiting values are: $0.4 \le \cot\theta \le 2.5$. In this study, $\cot\theta = 1$, i.e., $\theta = 45°$, is used unless otherwise noted. The parameter ν is a coefficient that takes into account the increase of fragility and the reduction of shear transfer by aggregate interlocking with the increase of the compressive concrete strength. It is noted that the standard method is applied in this report.

1.2.6 Priestley et al. [1996]

Priestley et al. [1996] suggested the following equations to calculate the nominal shear strength of RC columns. In this approach, V_c is calculated for the plastic hinge zone considering the effect of displacement ductility, and V_s is calculated based on the truss model for circular columns. The shear strength enhancement resulting from axial compression, V_p, is considered as an independent compression strut. Accordingly, Equation (1.7) is used in this model.

The contribution of transverse reinforcement to the shear strength is based on the truss mechanism, using θ as the angle of inclination between the shear cracks and the vertical column axis. Accordingly, one obtains,

$$V_s = \frac{\pi}{2}\frac{A_v f_y D^{'}}{s}\cot\theta \tag{1.28}$$

where A_v is the total transverse reinforcement cross-sectional area, and $D^{'}$ is the distance between centers of the peripheral hoop in the direction parallel to the applied shear force. The angle of the critical inclined flexure shear cracking to the column axis is taken as $\theta = 30°$ unless limited to larger angles by the potential corner-to-corner crack. The contribution of concrete is given as follows:

$$V_c = k\sqrt{f_c^{'}}A_e \tag{1.29}$$

where $A_e = 0.8A_g$ is the effective shear area and k depends on the instantaneous displacement or ductility. In case of displacement ductility and when subjected to biaxial ductility demand, μ_Δ, k is defined as follows when the concrete strength and the effective shear area are respectively in MPa and mm^2 units:

$$\begin{pmatrix} \mu_\Delta \le 1 : k = 0.29 \\ 1 < \mu_\Delta \le 3 : k = 0.10 + 0.19(3 - \mu_\Delta)/2 \\ 3 < \mu_\Delta \le 7 : k = 0.05 + 0.05(7 - \mu_\Delta)/4 \\ 7 < \mu_\Delta : k = 0.05 \end{pmatrix} \tag{1.30}$$

The shear strength increase by axial force is calculated as a result of an inclined compression strut given as follows:

$$V_p = P \tan\alpha = \frac{D - c}{2a} P \tag{1.31}$$

where D is cross-section height or diameter, c is the compression zone depth determined from flexural analysis. The parameter a is the shear span, which is $L/2$ for a column in double curvature and L for a column in single curvature; see Figure 1.4.

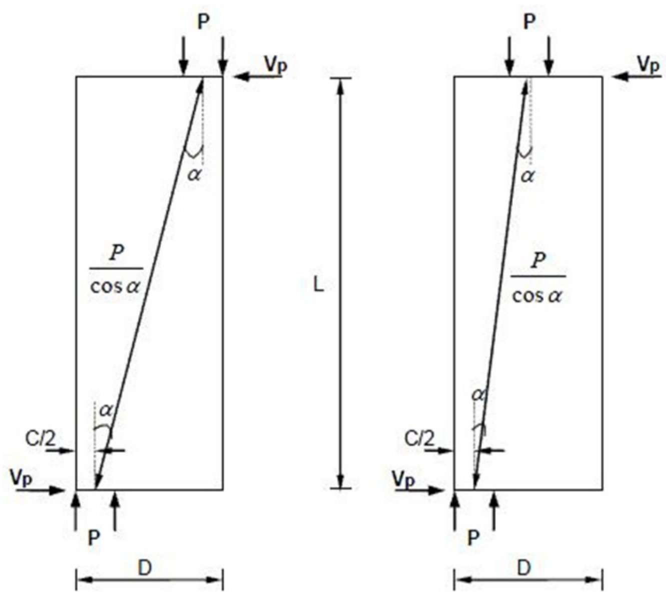

Figure 1.4 Contribution of axial forces to shear strength [Priestley et al. 1996].

1.2.7 Caltrans SDC [2013]

The Caltrans Seismic Design Criteria (SDC) [2013] suggests the use of Equation (1.1) with following definitions for the shear strength of ductile concrete circular members.

$$V_s = \frac{A_v f_y D'}{s} \tag{1.32}$$

$$A_v = n\left(\frac{\pi}{2}\right)A_b \tag{1.33}$$

$$V_c = v_c A_e \tag{1.34}$$

where n is the number of branches of the transverse reinforcement crossed by the diagonal shear cracks, A_b is the cross-sectional area of the bar used as transverse reinforcement, $A_e = 0.8A_g$ is the effective shear area, and v_c is determined by the location of the cross section, transverse reinforcement, and ductility demand ratio as follows:

Inside the plastic hinge zone, 'Factor1' is included in calculating v_c

$$v_c = \text{Factor1} \times \text{Factor2} \times \sqrt{f_c^{'}} \leq 0.33\sqrt{f_c^{'}} \tag{1.35}$$

Outside the plastic hinge zone, the constant, 0.25, is used instead of 'Factor1'.

$$v_c = 0.25 \times \text{Factor2} \times \sqrt{f_c^{'}} \leq 0.33\sqrt{f_c^{'}} \tag{1.36}$$

It should be noted that $f_c^{'}$ is the concrete strength in MPa.

The factors in the above equations are defined as follows:

$$0.025 \leq \text{Factor1} = \frac{\rho_s f_{yh}}{12.5} + 0.305 - 0.083\mu_d \leq 0.25 \tag{1.37}$$

where f_{yh} is transverse reinforcement (e.g., hoop) yield strength in MPa units, and $\rho_s f_{yh}$ (where ρ_s is the volumetric ratio of the transverse reinforcement) is limited to 0.35 ksi (2.413 MPa).

$$\text{Factor2} = 1 + \frac{P_c}{13.8A_g} < 1.5 \tag{1.38}$$

where P_c is the axial load in N, and A_g is in mm^2. As defined above, 'Factor1' is affected by the transverse reinforcement and lateral displacement ductility, μ_d, and 'Factor2' is affected by the axial pressure. Note that $v_c = 0$ for members whose net axial load is in tension.

Except that it takes account of displacement ductility instead of curvature ductility in the estimation of the shear strength, Caltrans SDC [2013] adopts the approach of Priestley et al. [1996] (Section 1.2.6) for ductility and combines it with the approach of ACI Committee 318 [2011] and Eurocode [CEN 2004] for axial pressure. Another unique feature of the SDC approach is that it provides different estimation along the member. 'Factor1', which is determined by the transverse reinforcement and displacement ductility, is only effective inside the plastic hinge zone and it ranges from 0.025 to 0.25. Since 0.25 is applied instead of 'Factor1,' V_c of the cross-section outside the plastic hinge zone is equal or larger than that inside the plastic hinge zone.

1.3 STUDIES ON VERTICAL TO HORIZONTAL GROUND ACCELERATIONS

One of the sources of axial load on bridge columns is attributed to the effect of the vertical component of the earthquake acceleration. Vertical excitation has been neglected in most design provisions for several decades. However, as confirmed in Papazoglou and Elnashai [1996] and other field observations, the effect of vertical ground motion can be destructive. In addition, the ratio of peak vertical-to-horizontal ground accelerations (V/H) may exceed two-thirds, which is the value usually considered in current design codes in near-source regions. For the 1994 Northridge, California, the vertical peak ground acceleration (PGA) at Rinaldi receiving station was 0.83*g* and the horizontal one was 0.63*g* according to PEER NGA database [2013], for which the ratio of vertical PGA to the horizontal PGA (V/H) is 1.31. Table 1.1 presents the V/H ratios from various earthquakes that are greater than two-thirds.

In many codes, vertical earthquake motion is represented by scaling a single design spectrum that is derived for horizontal components; this procedure was devised by Newmark et al. [1973] and has been widely used. Generally, the scaling factor, i.e., the vertical-to-horizontal ratio, has been taken as two-thirds. The weakness of this procedure is that horizontal and vertical components have the same frequency content, which does not reflect the actual structural responses of bridge systems.

Current provisions in the Caltrans SDC [2013] specify the requirements on demand due to vertical ground motion. As specified in Section 2.1.3 of SDC [2013], the current provisions do not provide guidelines considering the adverse consequences of vertical accelerations in seismic design of ordinary bridges where the site peak rock acceleration is smaller than 0.6*g*. Also, when this acceleration is 0.6*g* or greater, only equivalent static methods are required. In other words, current provisions in the SDC do not provide adequate guidelines for the effect of vertical accelerations in ordinary bridges. This deficiency is demonstrated by the following review of previously published research.

Table 1.1 V/H ratios from several earthquakes.

Earthquake	Station	PGA (g)		V/H
		Horizontal	Vertical	
Nahanni 1985	Site 1	1.06	2.09	1.98
Gazli 1976	Karakyr	0.644	1.26	1.96
Kobe 1995	Port Island	0.315	0.562	1.78
Kobe 1995	Kobe University	0.310	0.380	1.23
Landers 1992	Lucerne	0.721	0.819	1.14
Loma Prieta 1989	LGPC	0.784	0.886	1.13
Northridge 1994	Jensen Filter Plant	0.764	0.825	1.08

1.3.1 Vertical Component of Ground Motion

As widely known, the vertical component of ground motion is associated with the P-waves, while the horizontal components are mainly caused by the S-waves. The wavelength of the P-waves is shorter than that of the S-waves, which means that the former is associated with higher frequencies. In the near-source region, ground motion is characterized mainly by source spectra. The P-wave spectrum has a higher corner frequency than that of the S-wave. P and S corner frequencies gradually move to lower frequencies as waves propagate away from the source and, as a result, the vertical motion is modified at a faster rate. The relative characteristics of these two components of ground motion are often represented by the V/H PGA ratio.

The dependence of V/H on distance and local site conditions is explained from a seismological point of view and it is related to S-to-P conversion. Silva [1997] explains the S-to-P conversion mechanism at near-source soil and rock sites. At near-source soil sites, as the waves propagate through rock/soil boundary, the large contrast in S-waves at the interface induces inclined SV-waves to be converted to P-waves. These are amplified and refracted into a more vertical angle of incident by a shallow P-wave velocity gradient. This has the effect of significantly increasing the amplitude of the vertical component of ground motion over that caused by direct P-waves only. This effect is diminished at near-source rock sites because of less S-to-P converted energy due to the smaller S-wave and P-wave velocity gradients, and a subsequently smaller value of V/H. In case of larger distances, the SV-wave is beyond its critical angle of incidence and does not propagate to the surface effectively [Silva 1997; Kawase and Aki 1990]. Hence, the lower amplitude direct P-waves will be dominant in the vertical component and cause relatively smaller values of V/H. Similarly, Amirbekian and Bolt [1998] concluded that the high-amplitude, high-frequency vertical accelerations observed on near-source accelerograms are most likely generated by the S-to-P conversion within the transition zone between the underlying bedrock and the overlying softer sedimentary layers.

1.3.2 Vertical Design Spectra

To consider the effect of vertical ground motion appropriately, some recent studies have focused on constructing vertical design spectra. In particular, Elnashai [1997], Elnashai and Papazoglou [1997], and Collier and Elnashai [2001] proposed a vertical design acceleration spectrum that consists of a flat portion at short periods (0.05 to 0.15 sec) and a decaying spectral acceleration for $T \geq 0.15$ sec. Collier and Elnashai [2001] suggested procedures for assessing the significance of vertical ground motion, indicating when it should be included in the determination of seismic forcess on buildings. These procedures included the calculation of elastic and inelastic vertical periods of vibration that incorporate the effects of vertical and horizontal motion amplitude and the cross-coupling between the two vibration periods. Also, a procedure was suggested for combining vertical and horizontal seismic action effects that accounts for the likelihood of coincidence or otherwise of peak responses in the two directions.

Elgamal and He [2003] studied the characteristics of vertical ground motion with 111 free-field records and down-hole array records. They found that significant high frequency (about 8 Hz or higher) prevailed in all vertical records, and site distance from source affects the spectral shape. They also discovered that the spectra proposed by Elnashai and Papazoglou [1997]—that the corner periods of 0.05 sec and 0.15 sec—are quite representative for near-field sites. From the scarce available down-hole array records, they found little variation with depth in spectral shape and concluded that using the surface spectral shape for a spectrum at any depth may be acceptable, but the values should be gradually reduced by one-half to two-thirds as the depth reaches the range of 20 m.

Niazi and Bozorgnia [1992] investigated the behavior of the vertical and horizontal peak and spectral ground motion in the near-source region. The results from the ground motions recorded in Taiwan showed that the shape of response spectra for both vertical and horizontal components depends on magnitude and distance. They found that the 2/3 ratio of vertical and horizontal components is unconservative in the near-field for high frequency ground motion. Niazi and Bozorgnia [1993] also developed the attenuations of the vertical and horizontal response spectra of the 1989 Loma Prieta earthquake. Using the ground motions recorded at 53 sites, they confirmed that the conclusion of the previous study, especially the shape of V/H, is valid. Bozorgnia et al. [1998] analyzed the recorded vertical response of twelve instrumented structures during the Northridge earthquake. They concluded that the identified lowest vertical frequencies are between 3.9 and 13.3 Hz, and that the range may correspond to high vertical spectral accelerations, especially in the near-source region. Based on the observation of the Northridge earthquake, they pointed out that the vertical component needs to be considered, especially in the near-source region and for sensitive nonstructural elements. Bozorgnia and Campbell [2004] studied the characteristics of vertical ground motion extensively and proposed a ground motion model for the vertical-to-horizontal ratio (V/H) of the peak ground accelerations. From over 400 near-source accelerations with large M_w (i.e., $4.7 \leq M_w \leq 7.7$), they found no bias in the V/H estimates from independent analyses of vertical and horizontal response spectra.

In addition, V/H was found to be a strong function of natural period, local site conditions, and source-to-site distance, and a relatively weaker function of magnitude, faulting mechanism, and sediment depth. V/H exhibits its greatest differences at long periods on firm rock (NEHRP: BC), where it has relatively low amplitudes, and at short periods on firm soil (NEHRP: D), where it has amplitudes that approach 1.8 at large magnitudes and short distances. Bozorgnia and Campbell [2004] suggested a 5%-damped acceleration design spectrum, as shown in Figure 1.5. Even if the vertical spectral ordinate at $T = 0.1$ sec is not available, the design spectrum can be obtained using their V/H model [Bozorgnia and Campbell, 2004]. Note that FEMA P-750 [2009], which explains the development of vertical spectra in Chapter 23 of the NEHRP Provisions, is based on Bozorgnia and Campbell [2004].

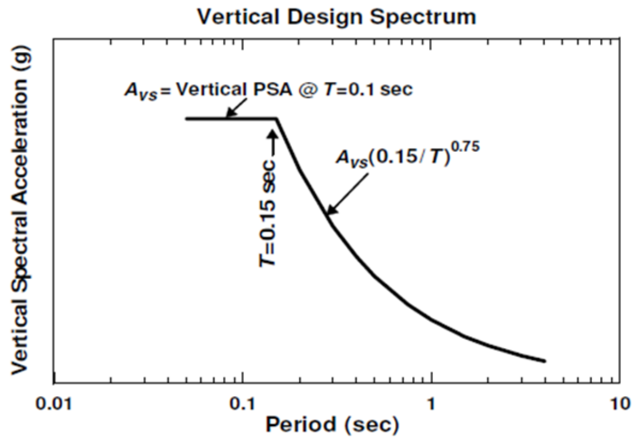

Figure 1.5 Suggested vertical design spectrum by Bozorgnia and Campbell [2004].

1.3.3 Arrival Time Interval

As discussed in Collier and Elnashai [2001] and Kim and Elnashai [2008], the arrival time interval is an important parameter that affects the interaction between horizontal and vertical responses. These studies use the interval between the peak acceleration of horizontal component and that of vertical one as the arrival time interval. According to the results, arrival time interval was shown to be zero, i.e., coincident, within a radius of 5 km of an earthquake source, and the interaction was significant within a radius of 25 km. In addition, this turned out to be magnitude-dependent similar to the V/H ratio. Collier and Elnashai [2001] pointed out that a maximum interaction effect between the horizontal and vertical motions occurs when the arrival time interval is less than 0.5 sec. They also showed that there is no interaction effect when the arrival time is longer than 4.0 sec.

1.4 STUDIES ON BRIDGE COLUMNS SUBJECTED TO COMBINED VERTICAL AND HORIZONTAL EXCITATION

1.4.1 PWRI Study

Sakai and Unjoh [2007] conducted shaking table experiments with combined horizontal and vertical excitations. The specimen was a 1/4-scale circular column, 3 m high and 600 mm in diameter, corresponding to an effective aspect ratio (AR) of 5; see Figure 1.6. The inertia mass was 27,000 kg, and the axial force and stress were 280 kN and 0.99 MPa at the bottom cross section. The longitudinal reinforcement ratio was 1.01% (40-D10 bars), and the hoop reinforcement ratio was 0.31% (D6 bars at 75-mm spacing). Yield strengths of the D6 and D10 bars were 340 MPa and 351 MPa, respectively. Ultimate strengths were 514 MPa and 496 MPa for the D6 and D10 bars, respectively. The standard cylinder strength of concrete was 41.7 MPa.

The test had two phases, one for dynamic response in elastic range and the other for nonlinear response. The amplitudes in all the three directions were scaled by 20% and 400% for each phase. The lateral period was 0.3 sec and the vertical period was 0.08 sec. Note that the vertical period was much smaller than those of real bridge systems, implying that the experiment may not represent the real behavior of bridge columns. Figure 1.7 shows the displacements at the center of gravity (C.G. in Figure 1.6) in 20% and 400% tests. After repeating the test four times with 40% to 75% larger displacements than the ultimate displacement based on the Japanese design code, slight spalling of cover concrete was observed. As the displacement increased up to twice of the ultimate displacement, the cover concrete spalled and the longitudinal bars buckled. Because the predominant natural period in the vertical direction was 25% of that in the lateral directions, the lateral response and axial force rarely reached their maximum values simultaneously. Hence, the lateral response was not significantly affected by the fluctuation of the axial force.

Figure 1.8 compares the responses obtained from analytical simulations for three-dimensional (3D) excitation (XYZ), two-dimensional (2D) excitations (XY and XZ), and one-dimensional (1D) excitation in X. Two horizontal motions (XY) produced 15% larger displacement than the 1D ground motion due to the bidirectional bending effects; however, the vertical ground motion did not have a significant effect on the lateral displacement response.

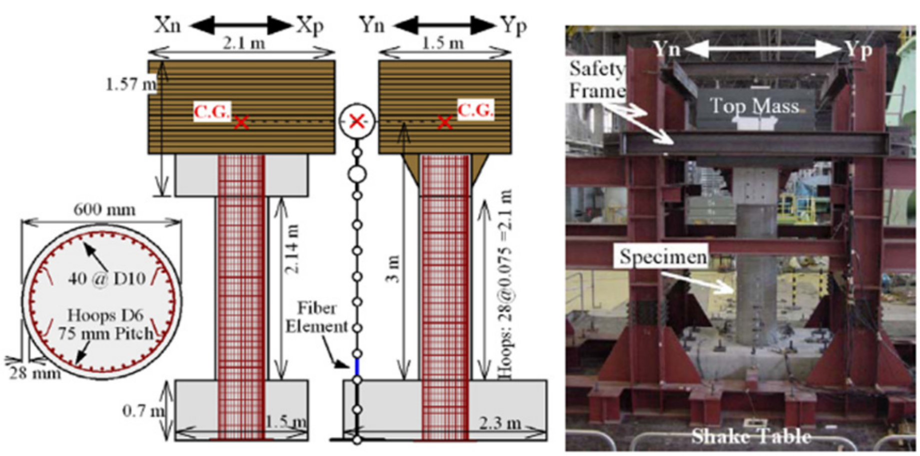

Figure 1.6 Specimen and shaking table set-up of Sakai and Unjoh [2007].

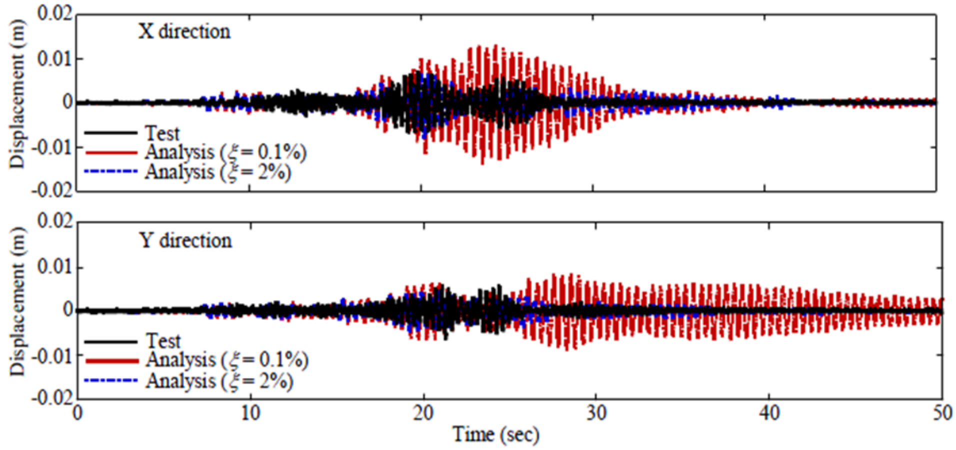

(a) 20% of 1983 Nihonkai Chubu earthquake (Tsugaru bridge record)

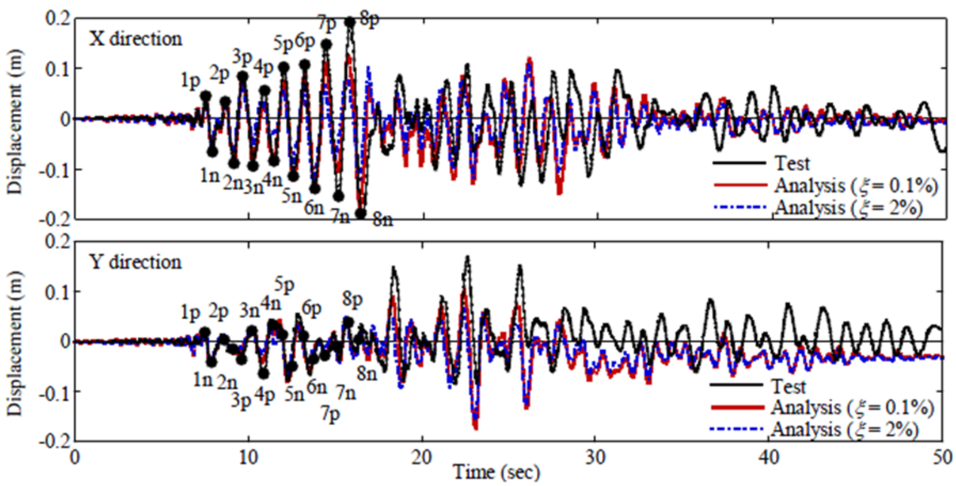

(b) 400% of 1983 Nihonkai Chubu earthquake (Tsugaru bridge record)

Figure 1.7 Displacement at the C.G. [Sakai and Unjoh 2007].

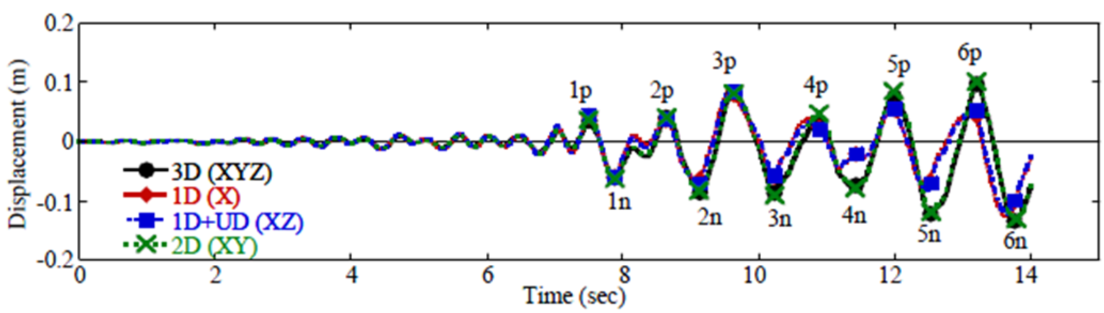

Figure 1.8 Analytical study on the effect of multidirectional loading ($\xi = 0.1\%$) [Sakai and Unjoh 2007].

1.4.2 Multi-Axial Full-Scale Substructure Testing and Simulation Study

To investigate the effect of vertical ground motion on RC bridges and buildings, Kim and Elnashai [2008] performed extensive analytical and experimental investigations. For RC bridges, they assessed the effect of various peak vertical-to-horizontal acceleration ratios and studied the effect of time intervals between the arrival of vertical and horizontal peaks of given earthquake records. In addition, they investigated the effect of vertical ground motion on RC bridge piers by employing sub-structured pseudo-dynamic (SPSD) tests with combined horizontal and vertical excitations of earthquake ground motion. They evaluated the effect of axial load on bridge piers by employing cyclic static tests with different constant axial load levels.

1.4.2.1 Analytical Investigation

The Kim and Elnashai [2008] investigation evaluated the effect of vertical ground motion on RC bridge columns with two prototypes: Santa Monica Bridge (Figure 1.9) and FHWA Bridge #4 (Figure 1.10). Some observations gleaned from their analytical study are as follows:

- The ratio of vertical seismic force to gravity load of pier was higher for the bridge with a shorter span because the fundamental period of short-span bridge was close to the dominant period of vertical motion.
- The shear capacity decreased due to vertical excitation.
- The contribution of vertical ground motion to axial force variation increased as the span ratio (i.e., the ratio between the two adjacent span lengths) increased since increased span ratio was associated with a shorter vertical period. Therefore, the shear capacity was reduced as well, but the effect of vertical ground motion on shear demand varied irregularly.
- The shear capacity of shorter column height was significantly reduced with vertical excitation, while shear demand decreased as the height increased.

They also assessed the effect of vertical-horizontal interaction on the inelastic periods of RC columns and on axial force amplitude and direction. They concluded that lateral inelastic periods were significantly affected by vertical ground motion in case of Santa Monica Bridge but were not significantly in case of FHWA Bridge #4; the vertical period increased in both cases. As vertical amplitude increased, the lateral displacement increased or decreased in both bridges. The ranges were -34% to 24% for the Santa Monica Bridge and -7% to 11% for the FHWA Bridge #4). Including vertical ground motion significantly affected the moment demand as well as the axial force variation of the pier when the V/H ratio increased. They noted that increased axial force variation led to significant reduction of shear capacity, which may cause brittle shear failure. The analysis of Santa Monica Bridge and FHWA Bridge #4 noted that reduction of shear capacity occurred up to 30% and 24%, respectively.

Kim and Elnashai [2008] concluded that the effect of arrival time was insignificant on the periods of vibration, axial force variation, and moment and shear demands. On the other hand, the time interval did have an effect on the shear capacity, which changed by -18% to 23% (Santa Monica Bridge) and -7% to 22% (FHWA Bridge #4) compared to the response with coincident horizontal and vertical peaks. In summary, Kim and Elnashai [2008] stated that vertical ground motion should be considered in assessing the shear capacity and the demand assessment when V/H is likely to be high and the arrival time interval is near zero or very short.

1.4.2.2 Experimental Study

In this investigation, Kim and Elnashai (2008) conducted SPSD tests and cyclic static tests with different axial loads using the Multi-Axial Full-Scale Sub-Structured Testing and Simulation (MUST-SIM) facility at the University of Illinois at Urbana-Champaign. The prototype was the FHWA Bridge #4 (see Figure 1.10), and the sub-structure was selected as an experiment module. Note that the pinned connection at the base was modified to a fixed connection; this increased the shear demand on the column. Due to the capacity limitations of the MUST-SIM facility, a 1/2-scale model was constructed. Two SPSD tests were conducted to investigate the effect of vertical ground motion: one under horizontal ground motion only (IPH) and the other under horizontal and vertical ground motions (IPV). To investigate the effect of axial force, two specimens were used for static cyclic tests: one subjected to tension (ICT) and the other subjected to compression (ICC). Their properties are listed in Table 1.2; the axial forces were based on the analytical predictions of the bridge system.

In specimen IPH, significant flexural, vertical and inclined shear cracks were observed at the top and bottom of the pier. Spalling of the concrete cover was observed on the left face at the top and on the right face at the bottom of the pier.

In specimen IPV, significant diagonal cracks occurred in the middle of the pier while the simulation was approaching the second peak. Inclined cracks on the front of the pier along the height as well as significant flexural and vertical cracks at the top and bottom of the pier were observed. Spalling of concrete cover was observed at the top left and bottom right of the pier.

Table 1.2 Aspect ratios and expected axial levels of test specimens [Kim and Elnashai 2008].

Specimen	Height (mm)	Aspect ratio	Axial load (kN)	$P/A_g f'_c$ (%)
IPH	3048	2.5	-1348 to -613	-10.63 to -4.84
IPV	3048	2.5	-2652 to 450	-20.92 to 3.55
ICT	2590.8	2.125	222	1.75
ICC	2590.8	2.125	-1112	-8.77

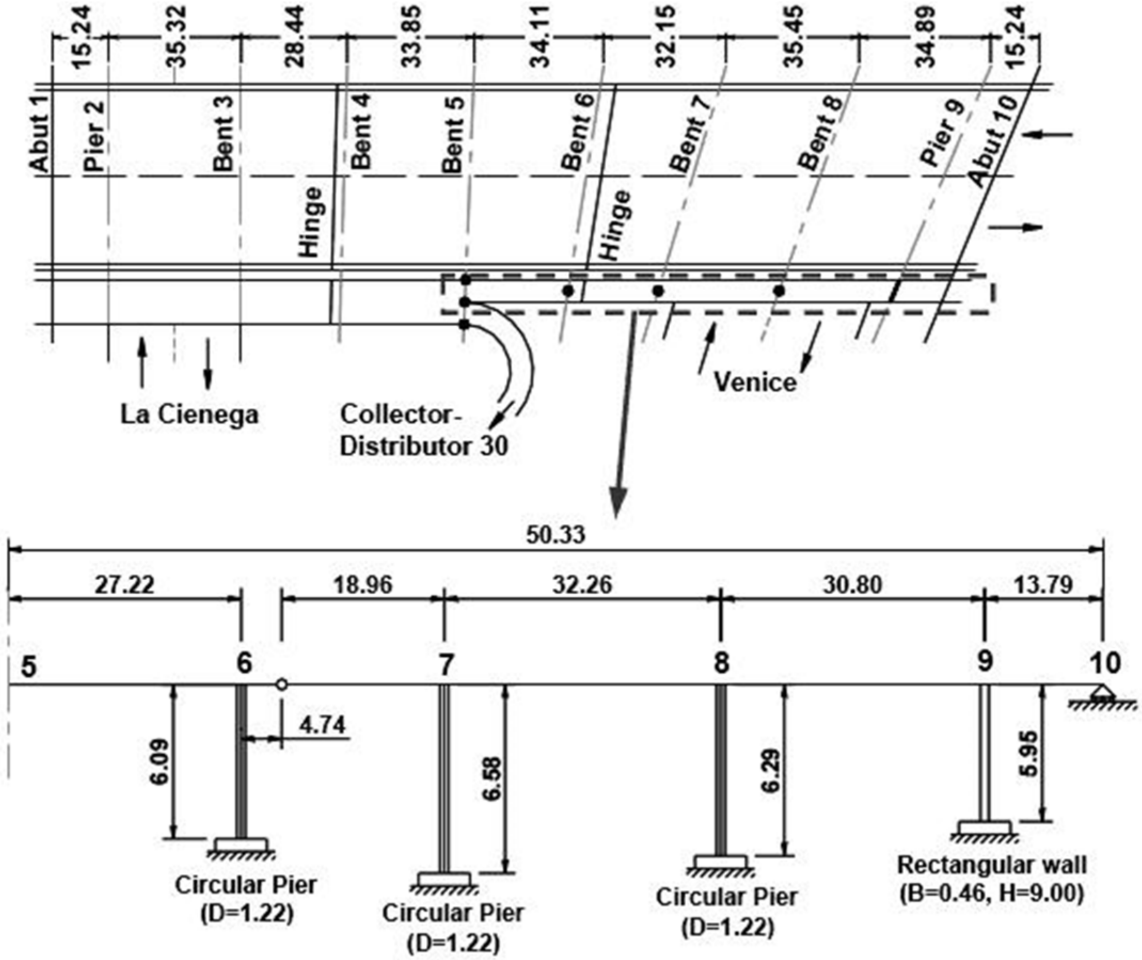

(a) layout (unit: m)

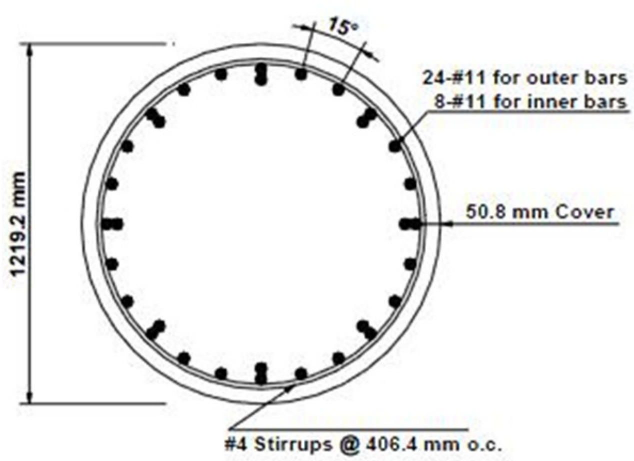

(b) pier reinforcement

Figure 1.9 Santa Monica Bridge [Kim and Elnashai 2008].

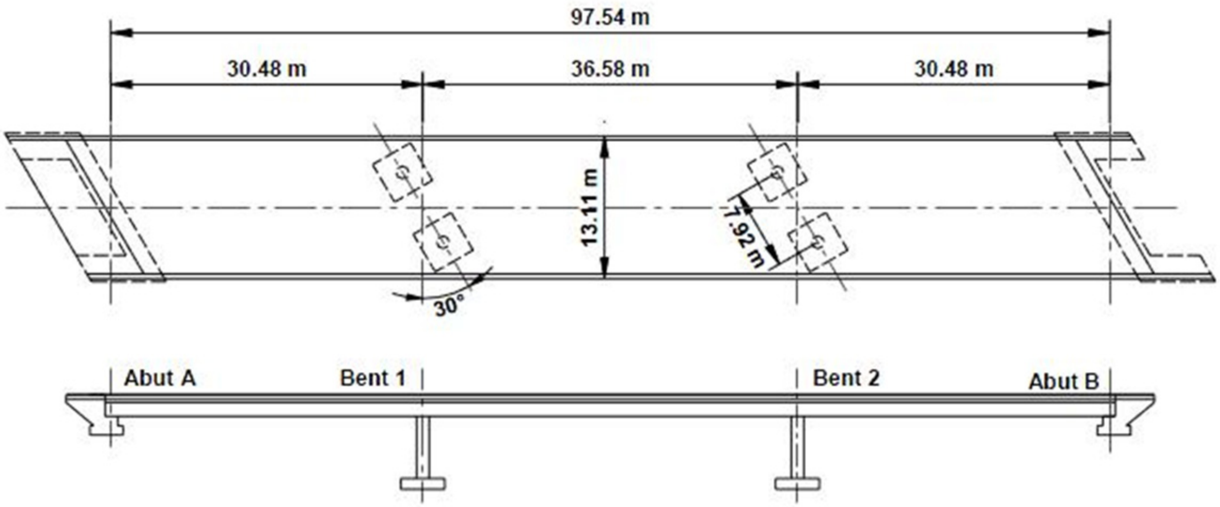

(a) plan view and elevation

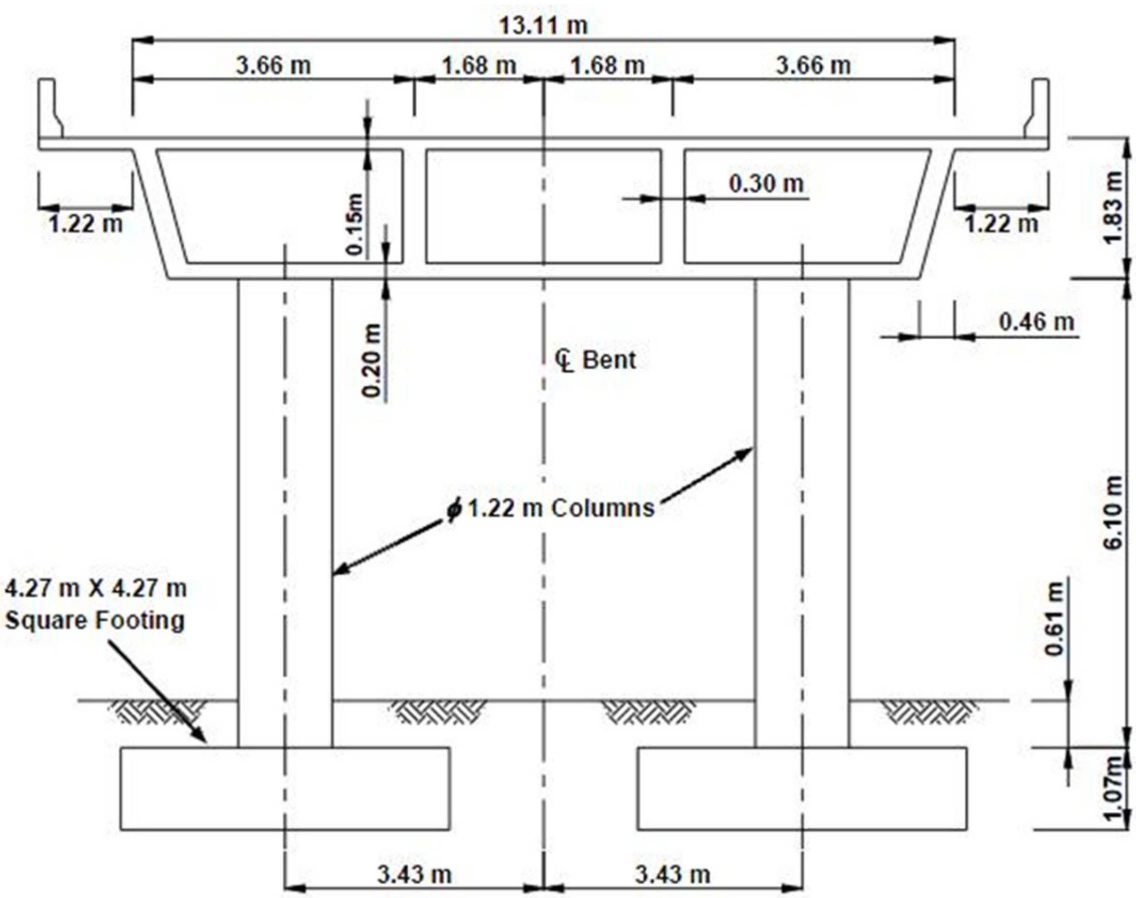

(b) cross section

Figure 1.10 FHWA Bridge #4 [Kim and Elnashai 2008]

1.4.3 E-Defense Tests

In most dynamic tests, substantially reduced scale specimens were used. Considering many critical behavior issues that are sensitive to scale, full-scale testing is optimum. In addition, test methods such as quasi-static and pseudo-dynamic tests affect the measured behavior due to changing the strain rate. Hence, full-scale shaking table tests are considered the most ideal approach in earthquake engineering, and the E-Defense shaking table in Japan is an excellent venue for such tests. Based on the NEES and E-Defense collaboration, large-scale shaking table tests on bridge structures have been conducted on E-Defense, the world's largest shaking table in Miki City, Japan, based on the testing plan agreed by Japanese and U.S. researchers in August 2005 [Kawashima et al. 2007].

The C1 tests component models, had the following objectives: (1) clarifying the failure mechanism of RC columns that failed during the Kobe earthquake; (2) determining the effectiveness of the current standard seismic retrofit methods for existing RC columns; (3) estimating the seismic performance of RC columns based on the current design codes in Japan and the U.S.; and (4) evaluating the effect of damper technology. The U.S. C1 models, designed in accordance with the Caltrans SDC, were large-scale RC columns designed to have as large cross sections as possible. The C2 tests on system models had the following objectives: (1) clarifying progressive failure mechanisms of a bridge system under various loading conditions; and (2) determining the effectiveness of advanced technology such as damper and unseating prevention devices.

The test of the first specimen of the Japanese C1 column was conducted in December 2007. It was a full-scale bridge column connected to horizontal members. Seven full-scale RC bridge columns that represent past and current Japanese design and construction practices (see Figure 1.11) were planned to be conducted in 2008 and 2009. Although the U.S. full-scale column specimen was designed after testing the first specimen of the Japanese C1 column on the E-Defense shaking table, it has not been tested yet. The C2 tests were planned to be conducted in 2009, but they have been postponed indefinitely. A unique feature of the test set-up is its mass support conditions. As shown in Figure 1.12, each girder is supported by the top of the specimen at one end and by a steel pier at the other end. Figure 1.13 shows the configuration of the support bearings under the 10-m-long steel girders. As shown, three different types of bearings were used on the column: pin, movable pin, and sliding bearings. All bearings were free to rotate. Pin bearings were fixed in the longitudinal, transverse, and vertical directions. Movable pin bearings were fixed in the transverse and vertical directions only. Thus, the girder could move in the longitudinal direction. Sliding bearings were fixed only in compression in the vertical direction. As a result, the bending moment at the top of the specimen was negligible.

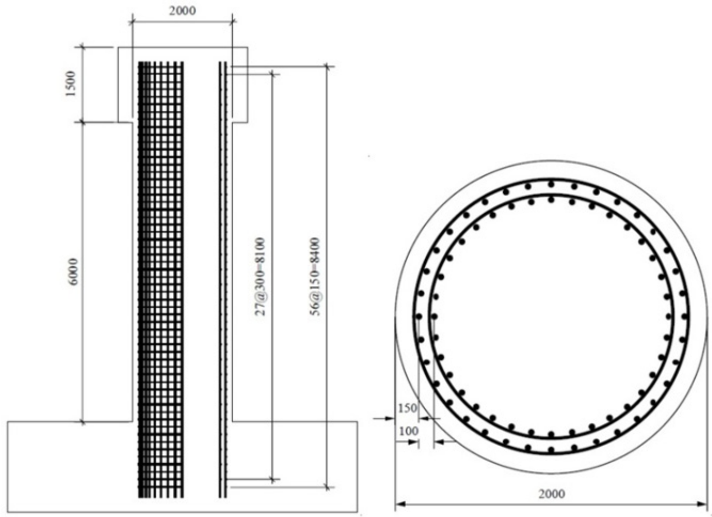

Figure 1.11 E-Defense C1 model designed based on Japanese current design criteria (unit: mm) [Jeong et al. 2008].

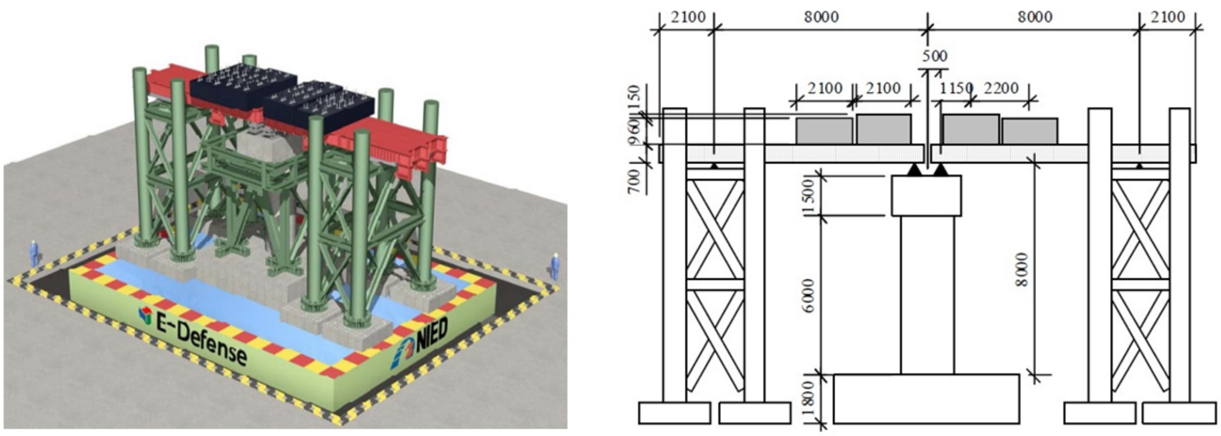

Figure 1.12 E-Defense C1 test set-up (unit: mm) [Jeong et al. 2008].

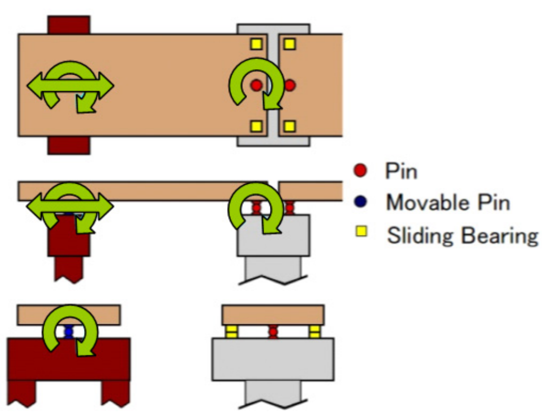

Figure 1.13 Conditions of support bearing [Jeong et al. 2008].

1.5 ORGANIZATION OF REPORT

Chapter 2 presents the development of dynamic test program. First, the number of ground motion candidates is narrowed down from 3551 in PEER NGA database. Based on three criteria, the ground motions with high shear demand and noticeable vertical acceleration were selected. Second, a parametric study was performed to choose the AR, test set-up, number of components, and ground motions with significant shear strength degradation by current codes.

Chapter 3 discusses the design of dynamic tests. Based on the fidelity test results, the input motion and the geometric scale of the specimen were determined. The specimens corresponding to the 1/4-scale prototype were designed. Subsequently, the test set-up, instrumentation, and test sequence were finalized.

Chapter 4 presents the global responses of dynamic tests. From the stiffness tests, free vibration tests, and low-level tests, the period and the damping values of each specimen were estimated. As the scale of input became larger, the inelastic behavior was observed more clearly. In addition, the shear cracks spread over the east and west sides of the columns. Based on the test data, the responses under the existence of vertical acceleration are examined thoroughly and are compared to those without vertical excitation. Force and displacement histories are presented.

Chapter 5 presents the local responses of dynamic tests. Curvature and strain histories are presented. In particular, the responses under the strongest excitation with and without the vertical component are compared.

Chapter 6 describes the development and evaluation of a new analytical model. OpenSees, a computational platform for developing applications to simulate the performance of structural systems, provides several material models and beam-column elements for various analyses. However, because existing material models and elements in OpenSees do not represent the shear strength change due to axial force or ductility variation, a shear spring material was developed to reflect code-based shear strength estimation. The responses of column models with and without this new shear spring are compared to each other, and the validity of each analytical model is discussed.

Chapter 7 presents the conclusions gleaned from this research project. In addition, the suggestions for future research are proposed.

2 Development of Dynamic Tests

This chapter presents the analyses conducted prior to the planned shaking table tests on the PEER earthquake simulator of University of California, Berkeley (UCB). Results of these analyses were utilized as a guidance to select the ground motions, column geometry, and reinforcement, and the set-up of the shaking table tests. First, the method used for selecting a smaller number of critical ground motions from a larger set is presented. Subsequently, the possible representative bridge prototypes are described. Finally, a parametric study conducted for a single column based on one of the prototypes is described, and the results of this parametric study are presented.

2.1 SELECTION OF GROUND MOTION

The PEER NGA database [2013] provides 3551 earthquake acceleration records and their meta-data. Among them, 3466 ground motions, with all three components available, were selected from the database. Three criteria were utilized to select the ground motions from these 3466 recorded motions to be used in the parametric study. According to the first criterion, ground motions with a PGA of one or two horizontal components less than 0.25*g* were eliminated, reducing the possible ground motion set to only 293 ground motions. The second criterion was based on the ratio of the pseudo-spectral acceleration corresponding to the vertical component (PSa_v) to those corresponding to the horizontal components (PSa_{h1}, PSa_{h2}). For each of the 293 ground motions, pseudo-spectral accelerations of the vertical component were calculated corresponding to the vertical periods (T_v) of 0.05, 0.1, 0.15, and 0.2 sec; pseudo-spectral accelerations of the horizontal components were calculated corresponding to the horizontal periods (T_h) of 0.4, 0.5, 0.6, 0.7, and 0.8 sec. The chosen T_v and T_h values resulted in 20 T_v, T_h pairs. Since each ground motion has two horizontal components, there are two spectral ratios for each pair: namely, PSa_v/PSa_{h1} and PSa_v/PSa_{h2}. Figures 2.1 and 2.2 present the relationships of the ratios PSa_v/PSa_{h1} versus the ratios PGA_v/PGA_{h1}, PGA_{h1}, and PGA_v for T_h=0.4 sec and T_h=0.7 sec, respectively, for different values of T_v. The following observations were deducted from Figures 2.1 and 2.2.

1. As T_v increases, the ratio PSa_v/PSa_{h1} tends to decrease.
2. As T_h increases, the ratio PSa_v / PSa_{h1} tends to increase.

3. There are many ground motions that have small PGA_{h1}, PGA_v, and PGA_v / PGA_{h1}, but large ratios of PSa_v/PSa_{h1}. Among them, ground motions with small PGA_{h1} are not useful since they will not lead to inelastic behavior.
4. In the plots of PSa_v/PSa_{h1} versus PGA_v/PGA_{h1}, the dispersion angle around the origin becomes narrower as T_v increases.

If PSa_v/PSa_{h1} or PSa_v/PSa_{h2} is larger than 1.0 in at least 15 pairs among the 20 pairs defined above, it is selected as one of the ground motions to be applied in the parametric study. The number of the considered ground motions is reduced from 293 to 80, according to this second criterion.

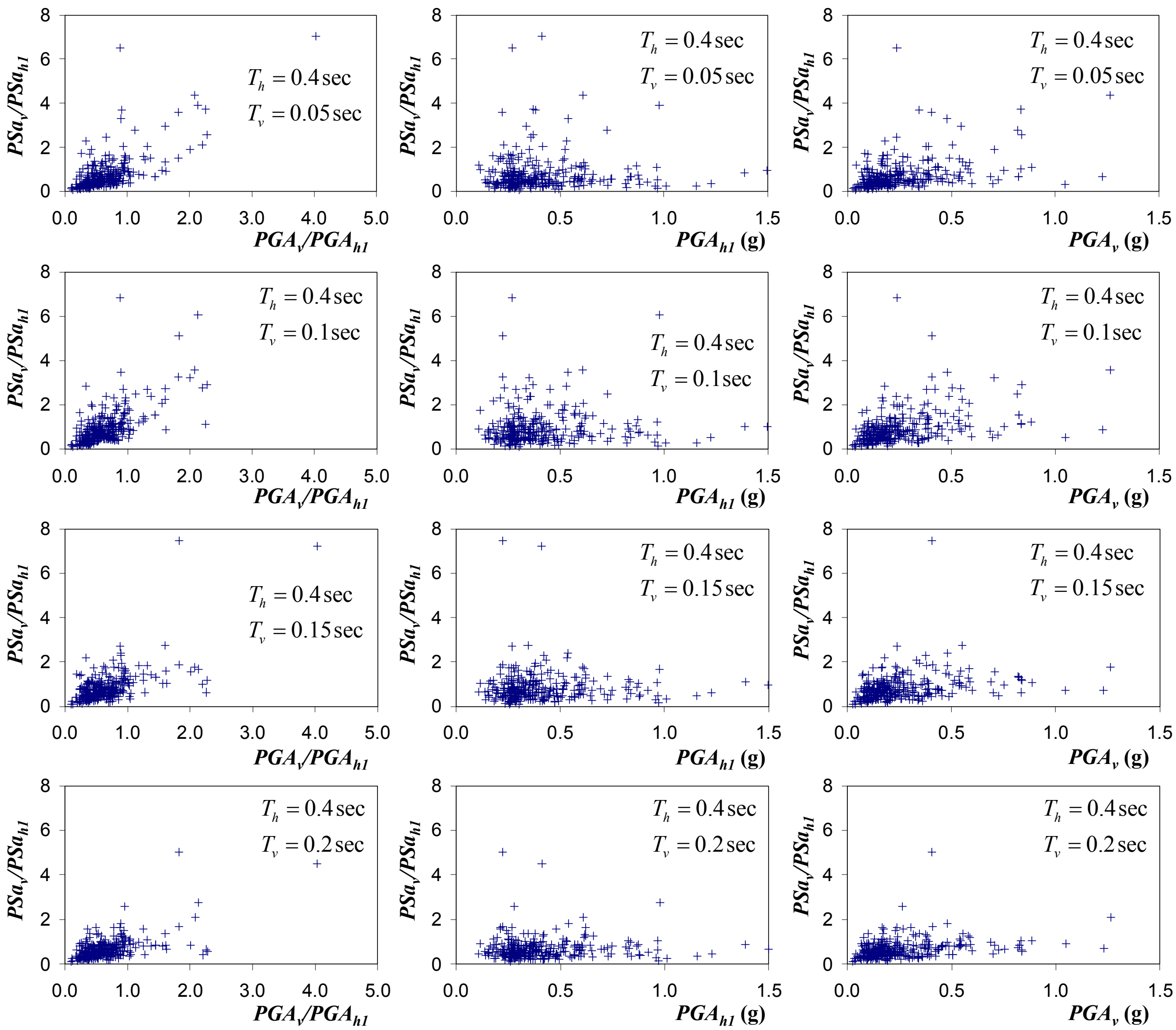

Figure 2.1 Variation of PSa_v/PSa_{h1} with peak ground accelerations and their ratio for T_h = 0.4 sec.

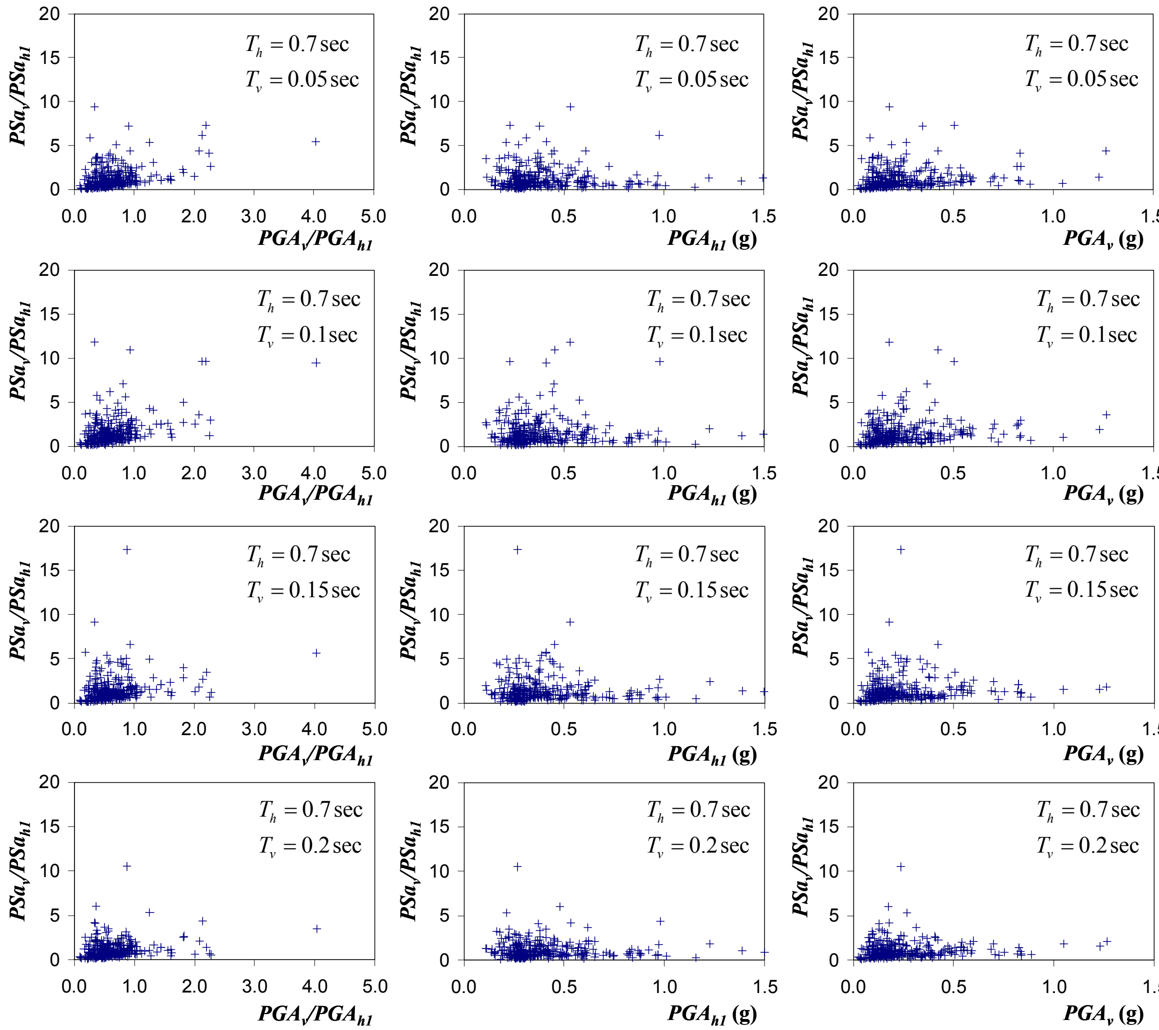

Figure 2.2 **Variation of PSa_v/PSa_{h1} with peak ground accelerations and their ratio for T_h = 0.7 sec.**

Arrival time is utilized as the third criterion. As discussed in Collier and Elnashai [2001], and Kim and Elnashai [2008], because the interval between the horizontal and the vertical peak accelerations affects the interaction of the horizontal and the vertical responses, it can be considered as an indicator. Among the 80 chosen ground motions after application of the second criterion, there were some motions that have significant arrival time intervals. Anza-02 earthquake recorded at Idyllwild-Kenworthy Fire Station (record sequence number (RSN) 1944 in PEER NGA database [2013] is shown in Figure 2.3 as an example). The interval between the peaks is longer than 3 sec, i.e., 3.160 sec for H1 versus V and 3.345 sec for H2 versus V. In this case, the PGA of the vertical component took place more than 3 sec before the horizontal components reached their PGA values. With this perspective, 14 additional ground motions were eliminated from the 80 ground motions. In addition, four ground motions were removed since they had only low-frequency content. One ground motion was removed because it was almost identical to another ground motion. Finally, based on the above three criteria and after removing the ground motions with only low-frequency content, 61 ground motions were selected from the existing 3551 ground motions in PEER NGA database [2013], which are listed in Appendix A.

Selection of ground motions based on the ratio PSa_v/PSa_h being greater than 1.0 discussed above might lead to the exclusion of some important ground motions in the cases where PSa_h is large and PSa_v is large enough to produce a significant difference between the two cases with and without vertical excitation (even if PSa_v/PSa_h is not larger than 1.0). This issue is discussed further at the end of the chapter.

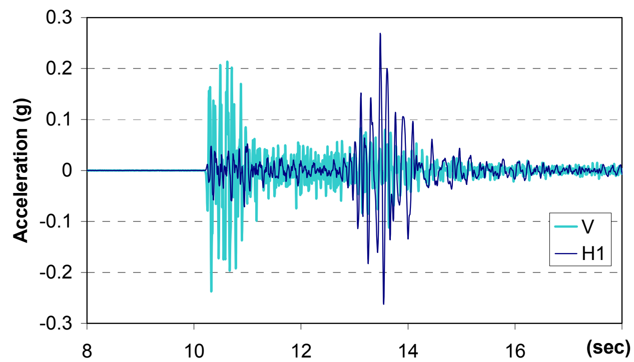

(a) H1 and V components

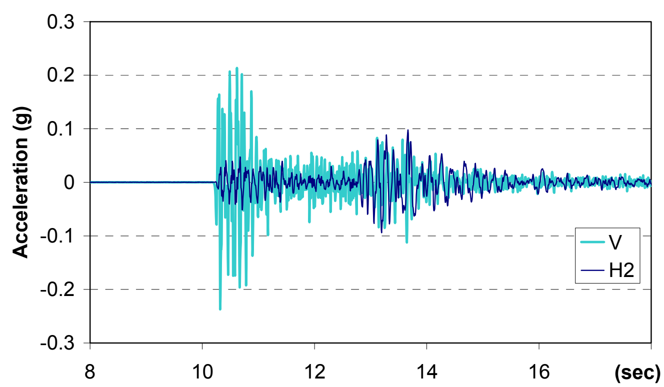

(b) H2 and V components

Figure 2.3 **Horizontal and vertical components of Anza-02 earthquake at Idyllwild-Kenworthy Fire Station.**

2.2 PROTOTYPE

Kunnath et al. [2008] considered two types of bridges: a single bent, two-span overpass and a single-column bent, multi-span bridge. For the overpass system, a segment of El Camino Del Norte Bridge was selected as the prototype bridge, whereas the Amador Creek Bridge (ACB) was used as the prototype bridge for the multi-span system. The selected overpass represents short-span RC bridges, whereas the multi-span system represents long-span PC bridges.

According to the analyses in Kunnath et al. [2008], the effect of the vertical acceleration was more significant in El Camino Del Norte Bridge, which has a multi-column bridge bent. However, even though the effect of axial force might be more significant in multi-column bridge bents, it is not practical to represent this effect in shaking table testing. Moreover, the complexity of the behavior of multi-column bridge bents due to other factors beyond the effect of vertical acceleration makes shaking table testing of single-column bridge bents for understanding the effect of vertical acceleration more realistic. Hence, the columns of single-column bridge bents are investigated herein. Note that only ACB was used as the prototype for the parametric study in Section 2.3.

2.2.1 Prototype 1: Amador Creek Bridge

Amador Creek Bridge is a 685 ft (207.6 m) long, three-bent, four-span RC bridge. The spans are 133.0 ft (40.5 m), 177.1 ft (53.7 m), 177.1 ft (53.7 m), and 133.0 ft (40.5 m). The bents of the bridge consist of single double-spiral columns. Figure 2.4 shows the elevation view and cross-sectional details of the columns. The column heights are 64.8 ft (19.75 m), 91.9 ft (28.0 m), and 83.7 ft (25.25 m). Based on the height of the third bent, H3 in Figure 2.5(a), the column ARs (ratio of height to cross-section dimension in the loading direction) considering the weak (X) and strong (Y) axes are 13.95 and 9.30, respectively.

The bridge was assumed to have an elastic superstructure based on the SDC capacity design approach [Caltrans 2013] and modeled as an elastic superstructure supported on nonlinear columns founded on elastic foundation using OpenSees [2000]. The superstructure cross-section properties of the ACB are presented in Table 2.1, where area is A, moment of inertia is I_x, I_y, and the polar moment of inertia is J.

The compressive strength of unconfined concrete and the yield strength of longitudinal reinforcement are specified to be 4 ksi (27.6 MPa) and 60 ksi (413.7 MPa), respectively, as designated on the design drawings. The compressive strength and ultimate strain of confined concrete were computed to be 5.83 kips (25.9 kN) and 0.0157 using per Mander [Mander et al. 1988]. *Concrete01* material in OpenSees was used for both the confined and unconfined concrete. A bilinear model with a post-yield stiffness of 1% of the initial stiffness was used to model the reinforcing steel. Because the bridge columns rest on shallow foundations, six elastic springs in three translational and three rotational directions were used to model the soil−foundation system for each column. The approximate expressions in FEMA-356 [FEMA 2000] were used to compute the properties of the corresponding springs. Table 2.2 lists the values of the spring stiffness representing the foundation system resting on a soil with a shear wave velocity of 1181 ft/sec (360.0 m/sec).

Seat-type abutments are used at both ends of the bridge. Spring systems were used to model the stiffness of the abutments. In the transverse direction, shear keys are designed to break off during a strong ground motion. Hence, the seat-type abutments do not possess stiffness in the transverse direction. In the vertical direction, the movement of the bridge is prevented at the abutments in both upward and downward directions. Thus, the abutments were modeled as restraining supports in the vertical direction. In the longitudinal direction, the bridge is free to move in the opposite direction of the abutment at each end. Towards the abutment, there is a certain amount of gap before the deck makes contact with the abutment. When the deck and the abutment are in contact, the stiffness of the abutment was computed as $K_{abut} = K_i w(h/5.5)$ [Caltrans 2013], where K_i is the initial stiffness of the abutment and is taken as 20.0 k/in. per ft of abutment width (11.49 kN/mm per m), and w and h are the projected width and height (in feet) of the abutment taken as 22.8 ft and 82.0 ft, respectively. Accordingly, a spring that has no stiffness in tension and elastic in compression with spring stiffness of 6785 kip/ft (99,019.6 kN/m) and with a 4-in. (101.6-mm) gap was used to model the abutment behavior in the longitudinal direction.

In single-column bridge bents, the superstructure is expected to be more vulnerable to torsional effects [rotation about X-axis defined in Figure 2.5(a)] than multi-column bridge bents. To ensure the proper modeling of the torsional properties of the deck, a 3D shell model of the bridge was created in SAP2000 [Computers and Engineering, Inc. 2006]; see Figure 2.5(b). The inertia properties of the OpenSees model, see Table 2.1, were adjusted later to match the periods of vibration of the SAP2000 model.

Table 2.1 Section properties of the Amador Creek Bridge superstructure.

Parameter	Value
A	6.73 m^2
I_x	4.56 m^4
I_y	73.75 m^4
J	78.31 m^4

Table 2.2 Elastic properties of springs used to model the soil-foundation system for the Amador Creek Bridge.

Parameter	Value
Translation, X	5.18×10^6 kN/m
Translation, Y	6.01×10^6 kN/m
Translation, Z	4.99×10^6 kN/m
Rotation, X	1.05×10^8 kN-m/rad
Rotation, Y	1.16×10^8 kN-m/rad
Rotation, Z	5.30×10^7 kN-m/rad

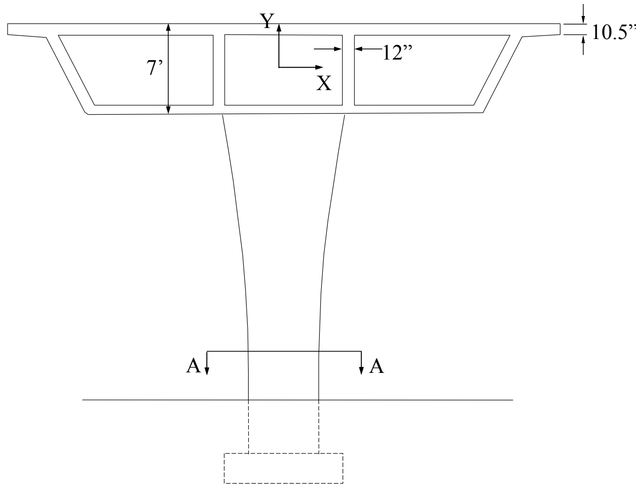

(a) elevation

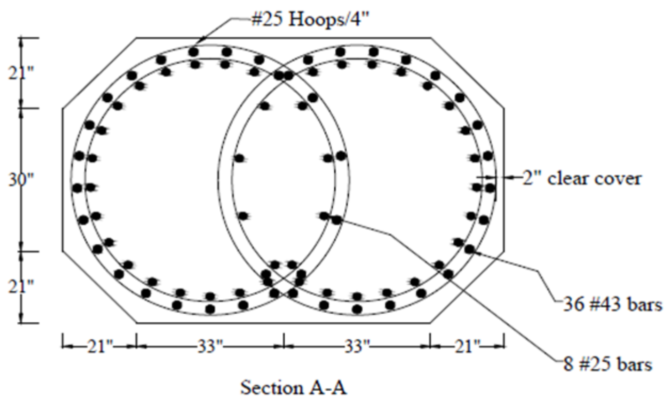

(b) interlocking spiral section (original section, units: inches)

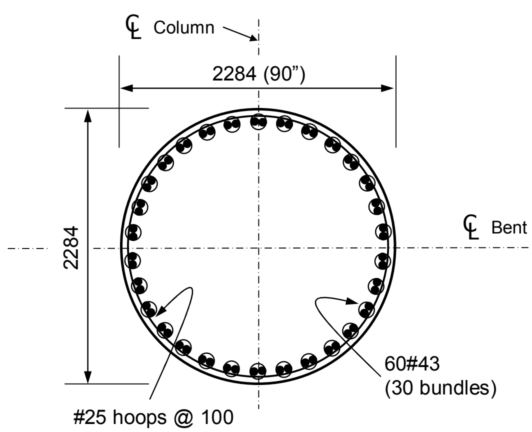

(c) Effective circular section (units: mm)

Figure 2.4 Bent elevation and column cross-section of the Amador Creek Bridge.

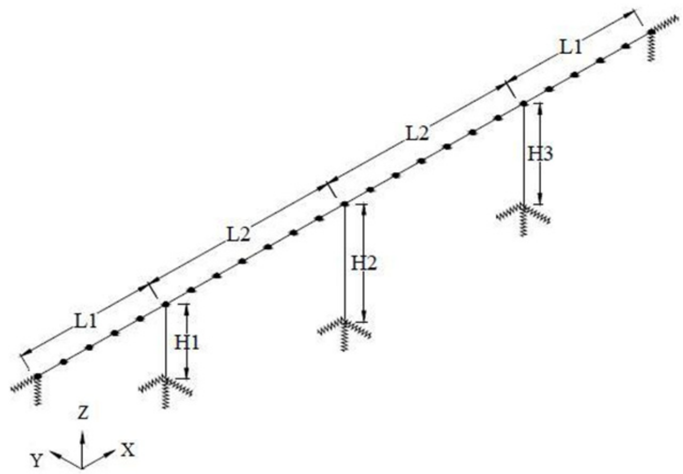

(a) line model in OpenSees

(b) 3D shell model in SAP2000

Figure 2.5 OpenSees and SAP2000 models of the Amador Creek Bridge.

2.2.1.1 Interlocking Spiral Section and Effective Circular Section

As mentioned previously, the objective of the parametric study is to provide guidance about the ground motion, column geometry and reinforcement, and set-up of the shaking table tests. Since the objective of the tests is to observe the effect of vertical excitation, a symmetric circular cross section is more suitable than an asymmetric interlocking spiral cross section. In this way, an unnecessary complication affecting the result—the effect of the difference of the cross-section moment of inertia and capacity in the two main orthogonal directions—is avoided. In addition, a circular section is more suitable from a practical point of view for test specimen detailing and construction. Due to the shaking table limitations, the test specimen should at most be a 1/4-scale of the prototype dimensions. Under these conditions, the interlocking spiral reinforcement should be installed in a small cross section with unknown influence of this reduced scale on the role of the interlocking spiral. Considering these reasons, the interlocking spiral section, which has different properties in each direction, was replaced by an effective circular cross section.

To determine the size and number of longitudinal reinforcing bars and size (i.e., radius) of the effective circular column, flexural and axial capacities were considered. Since the original (interlocking spiral) cross section had different moment capacities in each direction, the weak axis properties were chosen as the properties to be matched. Resulting area and moment of inertia values for the effective cross section in comparison with the original interlocking spiral cross-section are listed in Table 2.3. The spacing and diameter of the spiral reinforcement used in the interlocking spiral column were directly employed for the effective circular cross section.

A series of elastic modal analyses were carried out on both systems (with interlocking spiral and with effective circular cross sections) to calibrate the inertial properties of the superstructure of the OpenSees model. Figure 2.6 presents the fundamental elastic mode shapes in longitudinal, transverse, vertical, and torsional directions, along with the corresponding periods for OpenSees models. Also, Table 2.4 clearly shows that the line model created in OpenSees is capable of reasonably capturing the eigenvalues of the ACB in all directions compared to the more detailed finite element shell model developed in SAP2000.

Table 2.3 Column cross-section properties of the Amador Creek Bridge.

Parameter	Interlocking Spiral Section	Effective Circular Section
A	5.03 m^2	4.10 m^2
I_x	1.40 m^4	1.40 m^4
I_y	3.13 m^4	1.40 m^4
J	4.53 m^4	2.80 m^4

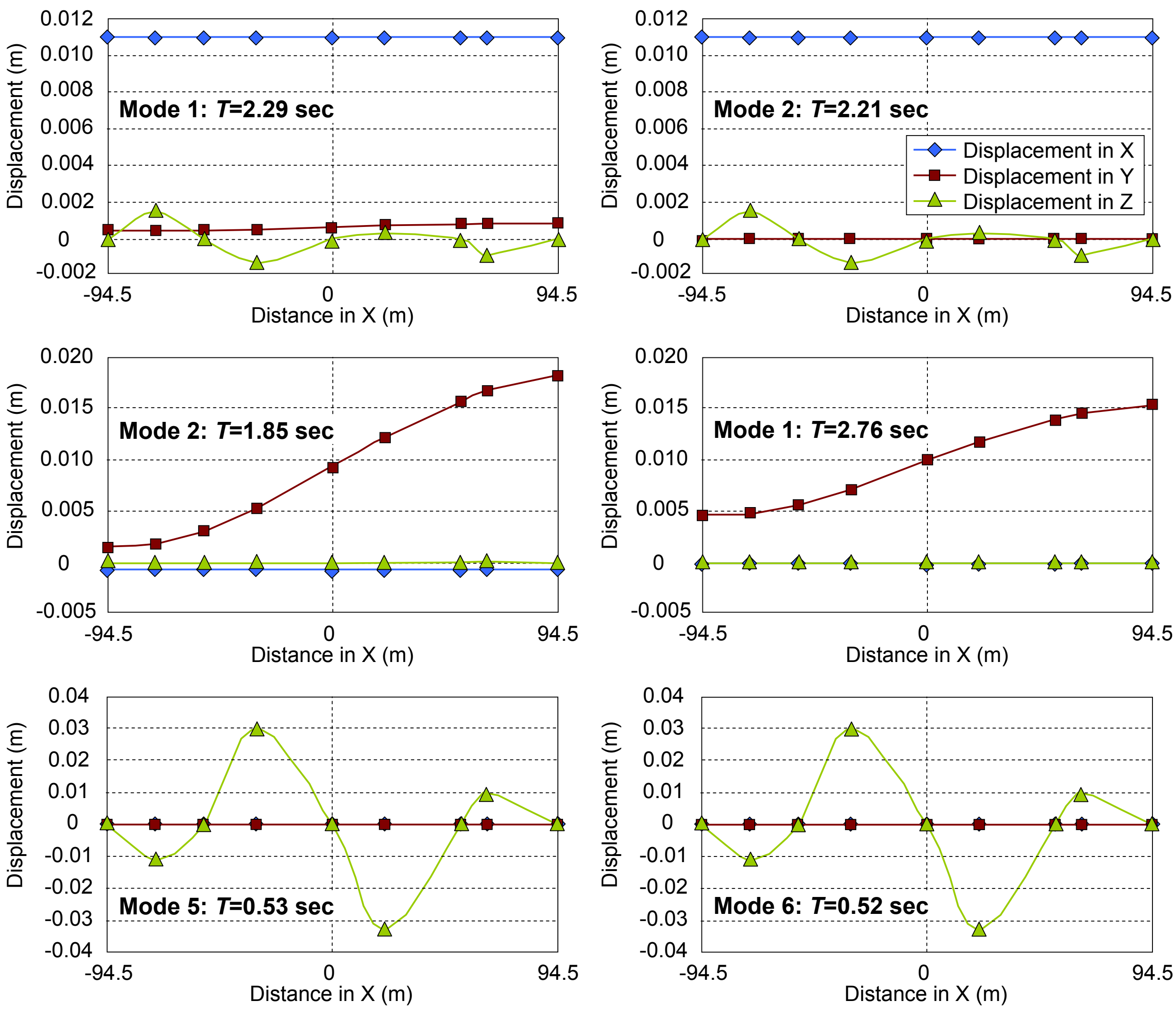

(a) Interlocking spiral column

(b) Effective circular column

Figure 2.6 Eigenvectors of the Amador Creek Bridge.

Table 2.4 Modal properties of the Amador Creek Bridge.

Cross Section	Mode number	SAP2000 [Figure 2.5 (b)] Period (sec)	OpenSees (a) [Figure 2.5(a)] Period (sec)
Interlocking spiral	1	2.12 (X)	2.29 (X)
	2	1.81 (Y)	1.85 (Y)
	3	1.28 (mixed)	1.35 (mixed)
	4	1.04 (mixed)	0.80 (mixed)
	5	0.52 (Z)	0.53 (Z)
	6	0.41 (mixed)	0.40 (mixed)
Circular	1	2.51 (Y)	2.76 (Y)
	2	2.15 (X)	2.21 (X)
	3	1.78 (mixed)	1.86 (mixed)
	4	1.08 (mixed)	0.83 (mixed)
	5	0.53 (Z)	0.68 (mixed)
	6	0.42 (mixed)	0.52 (Z)

2.2.1.2 Comparison of Responses of the Bridge Systems with the Interlocking and the Effective Circular Cross Sections

Figure 2.7 compares responses at the second column of the ACB [Column H2 in Figure 2.5(a)] with the interlocking cross section and the corresponding effective circular cross section as described above. These results are provided for the bridge response under the three components of the ground motion #40 in Appendix A (RSN 1063 in PEER NGA database [2013], Rinaldi receiving station, Northridge earthquake).

Figure 2.7(a), (b), and (c) compares moment at the base, M_x, base shear force, F_y, and axial force, F_z, respectively, for column H2 [Figure 2.5 (a)] of the ACB using the OpenSees line model shown in Figure 2.5(a). Although the interlocking spiral and the circular cross sections do not have the same response, the discrepancy is less than 20% when considering the maximum values. Therefore, using the effective circular cross section instead of the interlocking spiral cross section is an efficient option, thereby reducing the complexity of this study and the planned shaking table experiments.

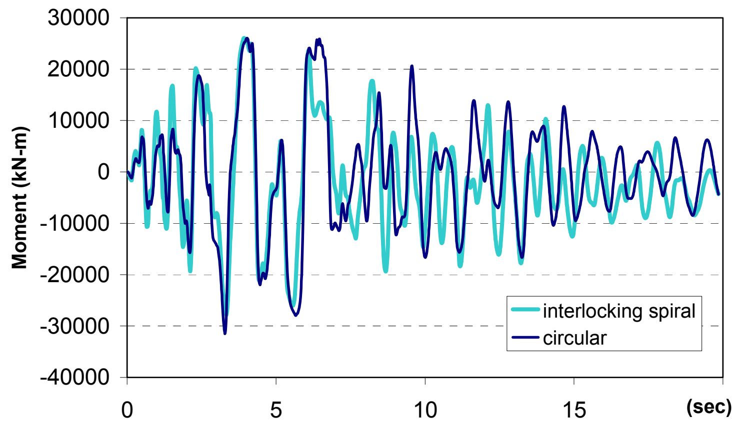

(a) moment, M_x

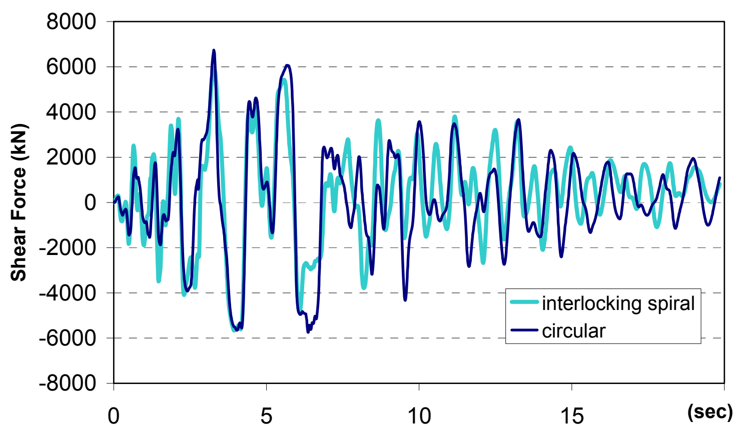

(b) shear force, F_y

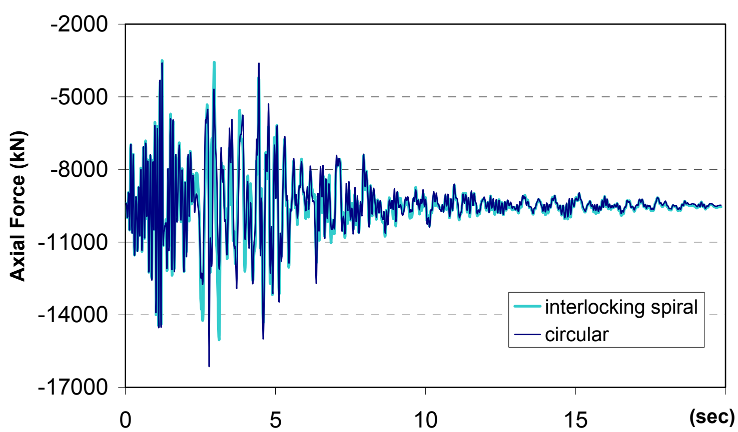

(c) axial force, F_z

Figure 2.7 Responses of the Amador Creek Bridge at column H2 [Figure 2.5(a)] with interlocking spiral and effective circular cross sections.

2.2.2 Prototype 2: Plumas-Arboga Overhead Bridge

The Plumas-Arboga Overhead Bridge (PAOB) is a 456 ft (139 m) long, two-bent, three-span RC bridge. Like the ACB, it was designed by Caltrans according to post-Northridge design practice. The spans connected to abutments are about 133 ft (40.5 m) each and the span between columns is about 190 ft (58.0 m). The heights of the two bents shown in Figure 2.8(a) were modeled as 29.7 ft (9.0 m). The AR along the 'Bent center line' (weak axis) is 3.58 and that along the 'Bridge center line' (strong axis) is 5.37. Table 2.5 presents area and moment of inertia properties of the elastic superstructure of the PAOB. Table 2.6 lists properties of its original interlocking spiral column cross section and the modified effective circular cross section. This latter cross section was used to design the shaking table test specimens. Column properties related to mass and mass moment of inertia are discussed in Chapter 3, since its AR is closer to the desired value than that of ACB.

Table 2.5 Cross-section properties of the Plumas-Arboga Overhead Bridge superstructure.

Parameter	Value
A	6.73 m^2
I_x	5.28 m^4
I_y	70.09 m^4
J	75.37 m^4

Table 2.6 Column cross-section properties of the Plumas-Arboga Overhead Bridge.

Parameter	Interlocking Spiral Cross Section	Modified Effective Circular Cross Section
A	3.61 m^2	3.14 m^2
I_x	0.715 m^4	0.788 m^4
I_y	1.247 m^4	0.788 m^4
J	1.962 m^4	1.575 m^4

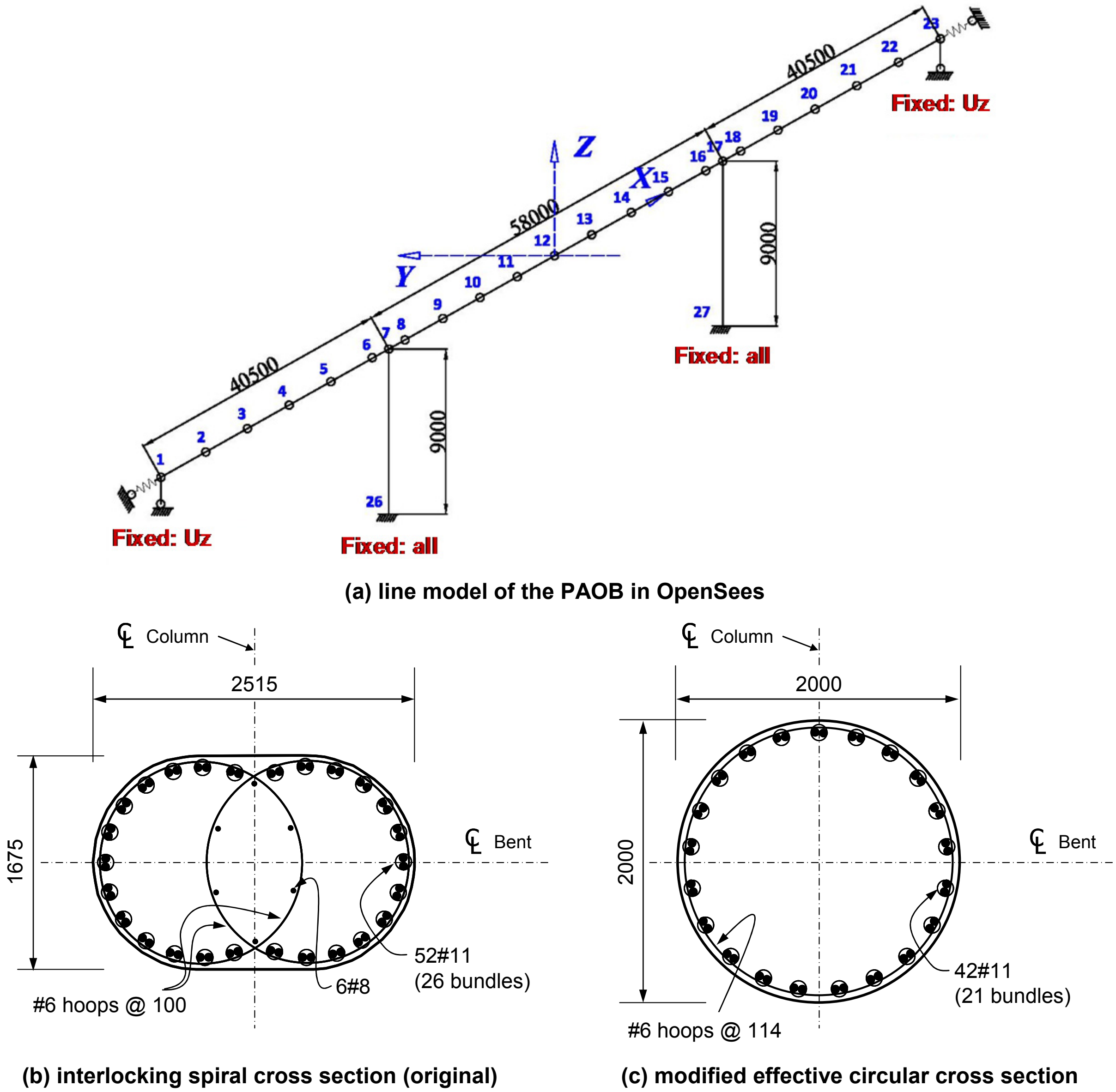

Figure 2.8 OpenSees line model and column cross sections of the Plumas-Arboga Overhead Bridge (unit: mm).

2.3 DESCRIPTION OF PARAMETRIC STUDY

Using a single column model with effective circular cross-section from the ACB, the following parametric study is conducted. Considered parameters were ground motions, number of components of ground motions, ARs, and existence of mass moment of inertia. The chosen values of these parameters are described in the following next.

2.3.1 Parameters

2.3.1.1 Ground Motions

As stated in Section 2.1, 61 ground motions are selected in this study from the PEER NGA database [2013]. To confirm the effectiveness of the selected ground motions, 293 ground motions with PGA larger than 0.25*g* were applied in this parametric study and the results were compared.

2.3.1.2 Ground Motion Components

To study the effect of vertical motions, the responses with and without vertical ground motion were compared. In this comparison, three cases were utilized:

- X, Y, and Z components versus X and Y components (effect of vertical excitation when both horizontal components are present)
- X and Z components versus X component (effect of vertical excitation when one of the horizontal components only is present)
- Y and Z components versus Y component (effect of vertical excitation when the other horizontal component is present only)

2.3.1.3 Mass Moment of Inertia

To represent a bridge system that is idealized with free rotation at the connection between the column and the bridge deck, a model with no mass moment of inertia on top of the column was adopted. However, mass moment of inertia can be added on top of the column corresponding to the more realistic connection in the bridge system. Note that the value of the mass moment of inertia was calibrated to obtain the same periods, mainly the period in the bridge transverse direction, T_T , for both the bridge system (with the bridge deck modeled) and the single column cases.

2.3.1.4 Aspect Ratio

As the AR, i.e., height to diameter ratio, of a column, i.e., H/D, increases, the column becomes less likely to experience shear failure. To study this important parameter, six ARs of values 2.5, 3.0, 3.5, 4.0, 4.5, 5.0, were considered. Note that H is taken as the height of the column itself, which does not include the rigid end zone lengths due to the physical size of the added mass on top of the column, as discussed below, or due to the footing size.

2.3.2 Computational Models

To represent the full-scale single column, the following models were used: Type 1 and Type 2 represented the cases without and with mass moment of inertia, respectively (Figure 2.9). For both models, the suggested equivalent circular cross section was considered, and the column was modeled using the '*beam with hinges'* (*BWH*) element in OpenSees. For Type 1, mass blocks were installed below the column top to lower the center-of-mass to the pin location. Since the system can become unstable during shaking, a catching system needed to be used for safety purposes, but it is not included in the analytical model. For Type 2, regular mass blocks were employed, as shown in Figure 2.9. In addition, a third model, designated as Type 2-1, was used, which was derived from Type 2 model by employing the mass blocks of the Type 1 model to lower the center-of-mass. Line representations of the three types are presented in Figure 2.10.

Mass was determined from the gravity load of the full-scale prototype bridge system, and mass moment of inertia was determined to match the periods of the bridge system.. However, it was not possible to match the vertical period of the single column to that of the bridge system, mainly because of the lack of the additional flexibility introduced by the bridge deck in the single-column model. Instead, the vertical response of the single column model was matched to that of the corresponding column, which is a part of the whole bridge system model. The horizontal and vertical periods of the models Types 1 and 2 are shown in Table 2.7. The periods of Type 2 are larger than those of Type 1, which is due to the added mass moment of inertia and the difference in height. The differences between the periods of models Type 2-1 and Type 1 are smaller than the differences between the periods of models Type 2 and Type 1 since models Type 1 and Type 2-1 have the same heights, as shown in Figure 2.10.

Table 2.8 presents the vertical periods of the bridge system, which can be compared to those of Type 2 or Type 2-1 single column model listed in Table 2.7. Vertical periods of the bridge system can be as high as 8.5 times of those of the single column model. The difference is basically due to the effect of the flexibility of the deck in the bridge system, which, as noted above, was not considered in the single column model. Note that the vertical periods do not significantly change due to the properties of the springs at the column base that represent the flexible foundation. Since the vertical response is expected to have an influence on the shear strength and is closely related to the vertical period, these differences cannot be neglected.

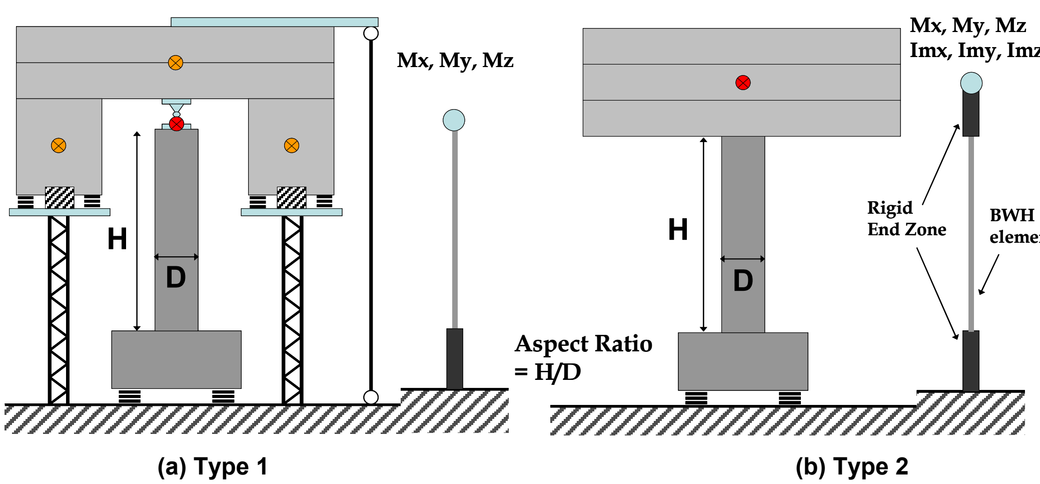

Figure 2.9 Models for the parametric study.

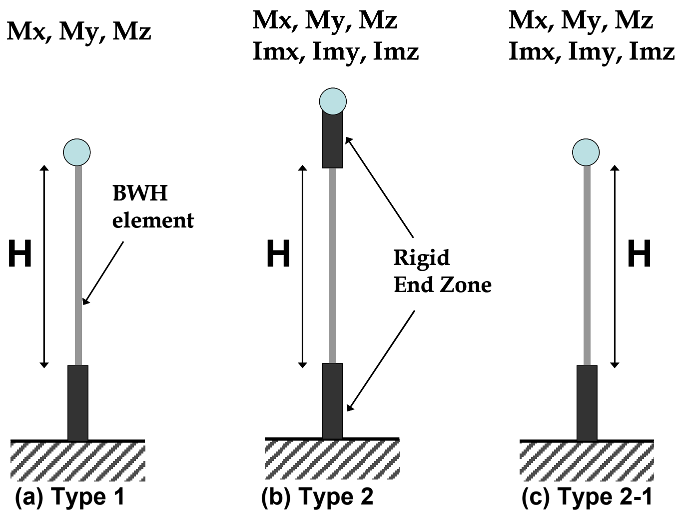

Figure 2.10 Line representations of the considered models.

Table 2.7 Modal properties of the single column models.

AR	Type 1		Type 2		Type 2-1	
	T_h (sec)	T_v (sec)	T_h (sec)	T_v (sec)	T_h (sec)	T_v (sec)
2.5	0.320	0.046	0.469	0.054	0.372	0.046
3.0	0.429	0.051	0.584	0.058	0.475	0.051
3.5	0.549	0.055	0.716	0.062	0.597	0.055
4.0	0.687	0.059	0.860	0.066	0.731	0.059
4.5	0.835	0.063	1.014	0.069	0.876	0.063
5.0	0.993	0.067	1.179	0.073	1.032	0.067

Table 2.8 Vertical periods of the bridge system model with the effective circular cross section.

AR	T_v (sec)	
	Fixed	With Springs at the Base
2.5	0.385	0.392
3.0	0.386	0.393
3.5	0.389	0.395
4.0	0.392	0.397
4.5	0.395	0.400
5.0	0.397	0.402

2.3.3 Comparison of Responses of the Bridge System and the Single Column Models

Ideally, the response of the single column model should be identical to that of the bridge system, but for practical purposes, differences within ±20% are considered to be acceptable. Figure 2.11 presents the bending moment and axial force of the single column model, specifically Type 2 with AR = 4.0, and those of the corresponding system model using all three components of ground motions #60 (Whittier Narrows earthquake record at LA Obregon Park) and #7 (Northridge earthquake record at Rinaldi Receiving Station) (see Appendix A for further details about these records). In case of ground motion #60, the bending moment history was similar in the two models, and the amplitude of axial force was also similar, even though the frequency was quite different from each other; this is because the vertical period of the bridge system is longer than that of the single column. However, ground motion #7 produced very different results. Although the bending moment history is similar in the two models for ground motion #7 as in the case of ground motion #60, the amplitude of the axial force of the bridge system was less than 40% of that of the single column. Therefore, in this case the axial response of the single column will not represent the real axial response of the bridge system in shaking table tests. Since the axial force and accordingly the axial strain are considered the main parameters in estimating the shear strength (refer to Section 1.2), underestimation of the shear strength and, as a result, overestimation of the effect of the vertical component of the ground motion may occur.

Due to the limitations of the shaking table, it was not possible to construct the complete bridge system. Even though the discrepancy was related to the properties of ground motion, modifying input excitations may not be an effective way to resolve this discrepancy within the limits of the shaking table. In that regard, the experimental effort on a single column model, even taking into account his discrepancy in comparison with the bridge system model, can be viewed as a means to generate benchmark experimental data sets for developing and calibrating accurate analytical shear strength models for further use in computational modeling of the full bridge system. Finally, it is expected that the effect of the vertical excitation on the seismic response of the bridge system can be computationally assessed using these accurate analytical shear strength models of the RC bridge columns.

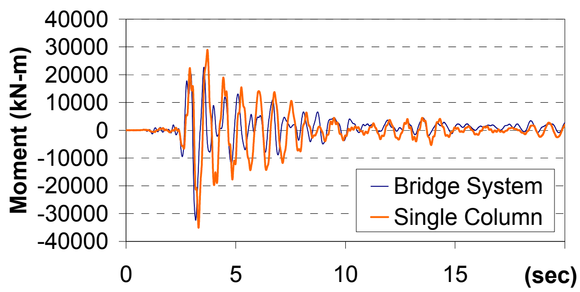

(a) bending moments at the base due to #60 ground motion

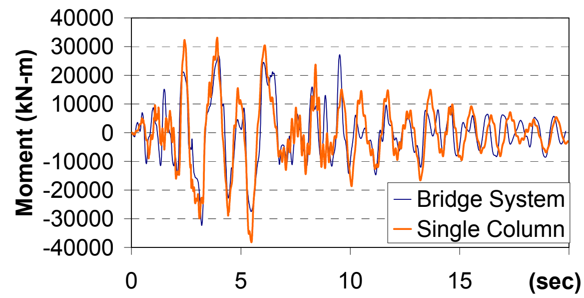

(b) bending moments at the base due to #7 ground motion

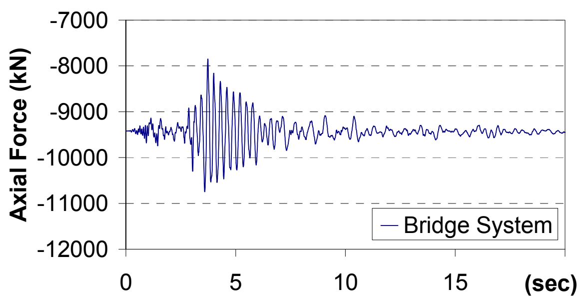

(c) axial force in the bridge system due to #60 ground motion

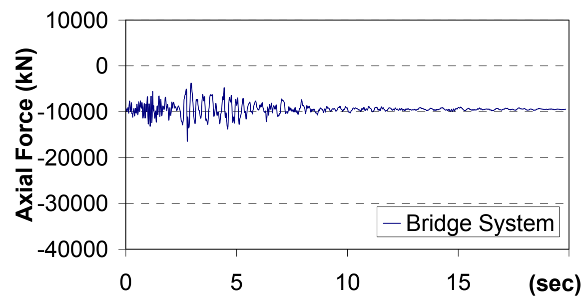

(d) axial force in the bridge system due to #7 ground motion

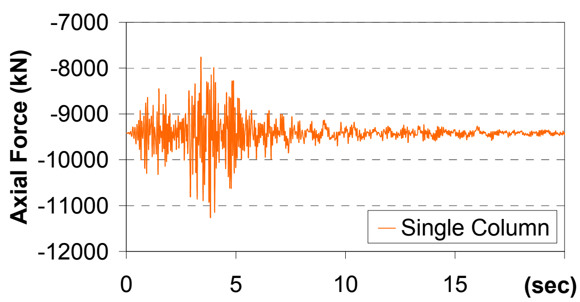

(e) axial force in the single column due to #60 ground motion

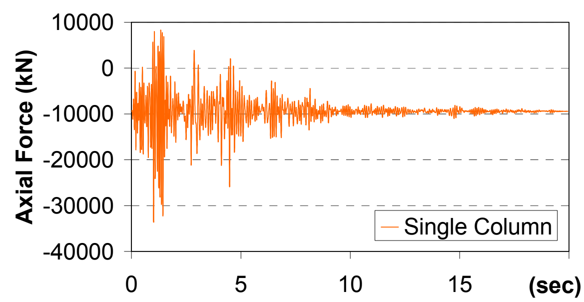

(f) axial force in the single column due to #7 ground motion

Figure 2.11 Responses of the bridge system and the single column models.

2.4 RESULTS OF PARAMETRIC STUDY

Given there were three cases of ground motion components (Section 2.3.1.2), 2 models (Types 1 and 2 only) and six aspect ratios, a total of 36 cases were analyzed. For each case, 61 ground motions were applied, and maximum values of translational displacements at the top of the column, and maximum forces and bending moments at the bottom of the column were calculated. The difference ratio due to the vertical component (*VDR*) was computed using Equation (2.1).

$$VDR = \frac{\max\left(\text{response with vertical component}\right)}{\max\left(\text{response without vertical component}\right)} - 1 \tag{2.1}$$

The ratios using the X+Y+Z and X+Y (effect of vertical excitation when both horizontal components are present) that were applied to Type 2 model are shown in Figure 2.12. Values on the horizontal axis are the ground motion numbers, and those on the vertical axis are the difference ratios (*VDR*), as defined in Equation (2.1). Although the ratios are not narrowly-distributed, most of them are concentrated near zero and mostly located in the range of -0.1 to 0.1, except for the case of the maximum displacement in the Z-direction, D_z, and the maximum force in the Z-direction, F_z; the *VDR*s for D_z and F_z are all positive. Note that the ground motion numbers on the horizontal axis in Figure 2.12 are sorted in a descending order of the peak vertical acceleration (PGA_v). Therefore, it can be concluded that the motions with relatively larger vertical acceleration result in larger *VDRs* in most responses.

The average values of the absolute *VDR*s for a constant AR are shown in Figure 2.13. The values on the horizontal axis are ARs, and those on the vertical axis are absolute *VDR*s. Since X+Z versus X and Y+Z versus Y do not have significant responses in the Y-direction and X-direction, respectively, the values corresponding to these cases are not presented in the corresponding figures.

Except the maximum displacement and force in the Z-direction, D_z and F_z, respectively, the effect of the vertical ground motion is not significant. The averages for the maximum displacement in the X-direction, D_x, are less than 1.5% for all cases, and those for the maximum displacement in the Y-direction, D_y, are less than 1.4%. In case of forces in the X- and Y-directions, F_x and F_y, respectively, average values are less than 3%, and they are less than 2.5% for moments about the X- and Y-directions, M_x and M_y, respectively. However, the average values for D_z are between 28% and 75%, and those for F_z are between 50% and 85%. As the AR becomes larger, the different ratios tend to increase. This means that in general the effect of vertical motion becomes more significant as the column becomes taller.

As shown in Figures 2.12 and 2.13, the change in the response quantities other than the axial force and axial displacement is not important. Accordingly, it can be stated that the shear demand change due to the vertical ground motion is a minor importance compared to the change in shear capacity. However, the change in the axial force due to vertical ground motion is noteworthy, resulting in a decrease of the shear strength when axial tensile forces occur. Since Figures 2.12 and 2.13 plot the maximum responses, the effect of the occurrence of the axial tensile forces or the decrease in the axial compressive forces is not explicitly identifiable from these figures. However, the drastic change in the axial forces due to the vertical excitation can be clearly observed. The effect of axial force in the reduction of shear force capacity is examined in more details in the following section. The difference due to the number of applied horizontal components is not significant on the effect of the vertical excitation on the axial force F_z. In Figure 2.13(f), note that the difference between the average *VDR* in the presence of two and one horizontal component is less than 10%.

The difference ratio due to the employed model (Type 1 versus Type 2) was calculated using Equation (2.2), which defines the type difference ratio. The results using this ratio are presented in Figures 2.14 and 2.15.

$$TDR = \frac{\max\left(\text{response in Type 1}\right)}{\max\left(\text{response in Type 2 or Type 2 - 1}\right)} - 1 \qquad (2.2)$$

Figure 2.14 presents the *TDR* values under the presence of all three components of ground motion. As before, the ground motions were sorted in a descending order of the peak vertical acceleration (PVA). The motions with large PVA tend to have smaller *TDR* values, except for D_z and F_z. The ratios are more widely distributed than the *VDR* values obtained by Equation (2.1), mainly due to the different dynamic properties of the two types and the presence of the top moment in Type 2 model Most of these values were in the range of -1.0 to 1.0. However, having observed that the axial force is one of the response parameters that is affected by the vertical ground motion (see Figures 2.12 and 2.13), it can be concluded that the effect of the model type for axial force F_z is not important considering that the *TDR* values are within the range -0.2 and 0.2, and mainly concentrated around zero. This same observation can be deduced from Figure 2.15, which presents the average for the absolute values of the *TDR* for different ARs with and without vertical excitation cases. Here, the average absolute values for the axial force are mostly below 10% and between 15% and 38% for the other response parameters. For all the response parameters, the *TDRs* tend to be larger as the AR becomes smaller.

Figure 2.16 compares the average absolute *TDR* values for different response parameters Type 1 and Type 2-1 models, i.e., the average of the absolute *TDR*s between Type 1 and Type 2-1, instead of Type 1 and Type 2 as shown in Figure 2.15. The mean of *TDR* between Type 1 and Type 2-1 decreased compared to that between Type 1 and Type 2. This can be explained by the reduced discrepancy of periods, which are shown in Table 2.7. This is especially true for the average values of *TDR* for D_y, D_z, F_y, and M_x, which decreased significantly when compared to the results in Figure 2.16, i.e., the average absolute *TDR* values for different response parameters comparing Type 1 and Type 2-1 models to those in Figure 2.15.

In addition, the average absolute values of *TDR* for D_z and F_z have different patterns. Comparing Figure 2.15(c) to Figure 2.16(c) and Figure 2.15(f) to Figure 2.16(f), the values under the presence of vertical excitation (designated as 'With Z') decreased noticeably when Type 2-1 was used instead of Type 2; this is because Type 1 and Type 2-1 have smaller differences in T_h and the same T_v. When vertical excitation is applied, the vertical responses are more dependent more on the vertical periods compared to the horizontal periods. Hence, compared to Type 2, Type 2-1 is closer to Type 1 in terms of the responses D_z and F_z.

The results discussed above can be summarized as follows:

- The presence of one or both of the horizontal components does not produce significant differences.

- Except for the axial displacement and force (D_z and F_z), the difference in other response quantities due to vertical excitation is not significant, less than 5%, in general.
- For both models Types 1 and 2, the effect of vertical excitation is significant in F_z, with the potential to affect their shear strength.
- The difference in D_z or F_z in Type 1 and Type 2 is relatively small. For other response parameters, the difference between Type 1 and Type 2 cannot be ignored, and becomes larger as the AR of column becomes smaller. However, since the axial force is the only important parameter that is significantly affected by vertical excitation, it can be concluded that the differences between models Types 1 and 2 are not important for the purposes of this study. These differences are even less important between Types 1 and 2-1.

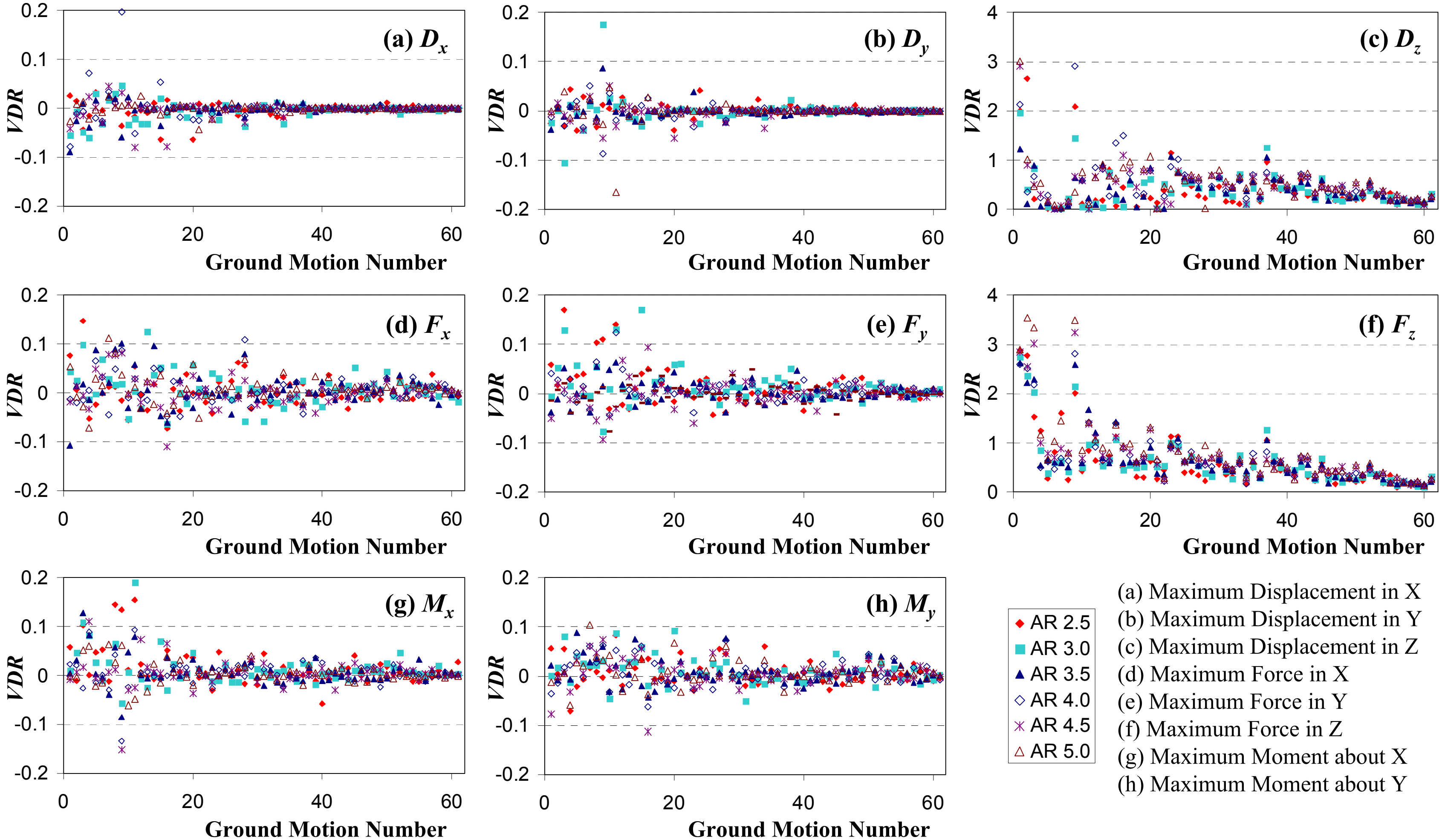

Figure 2.12 ***VDR* values for different response parameters for model Type 2, both horizontal components present.**

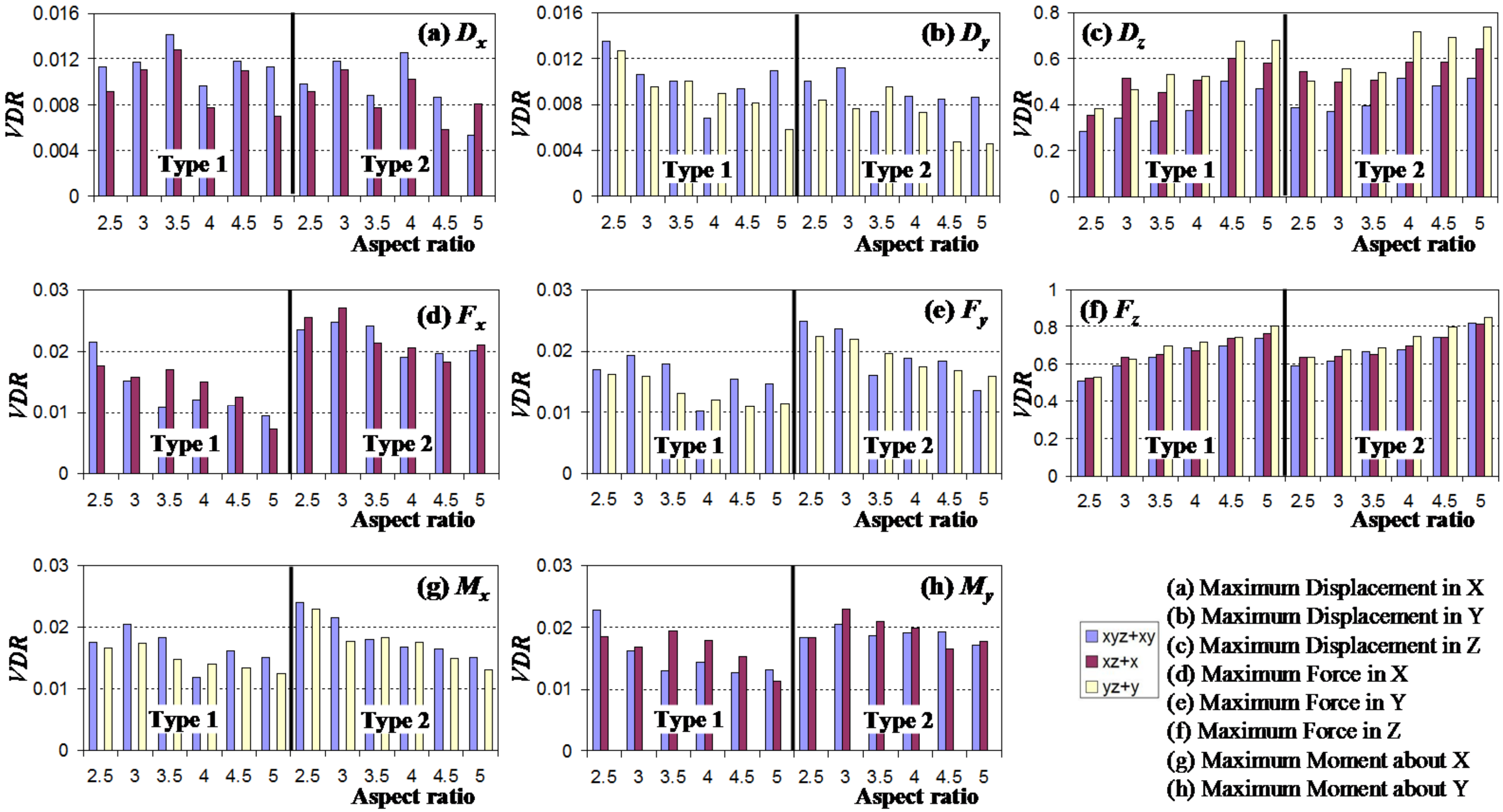

Figure 2.13 Average absolute *VDR* values for different response parameters.

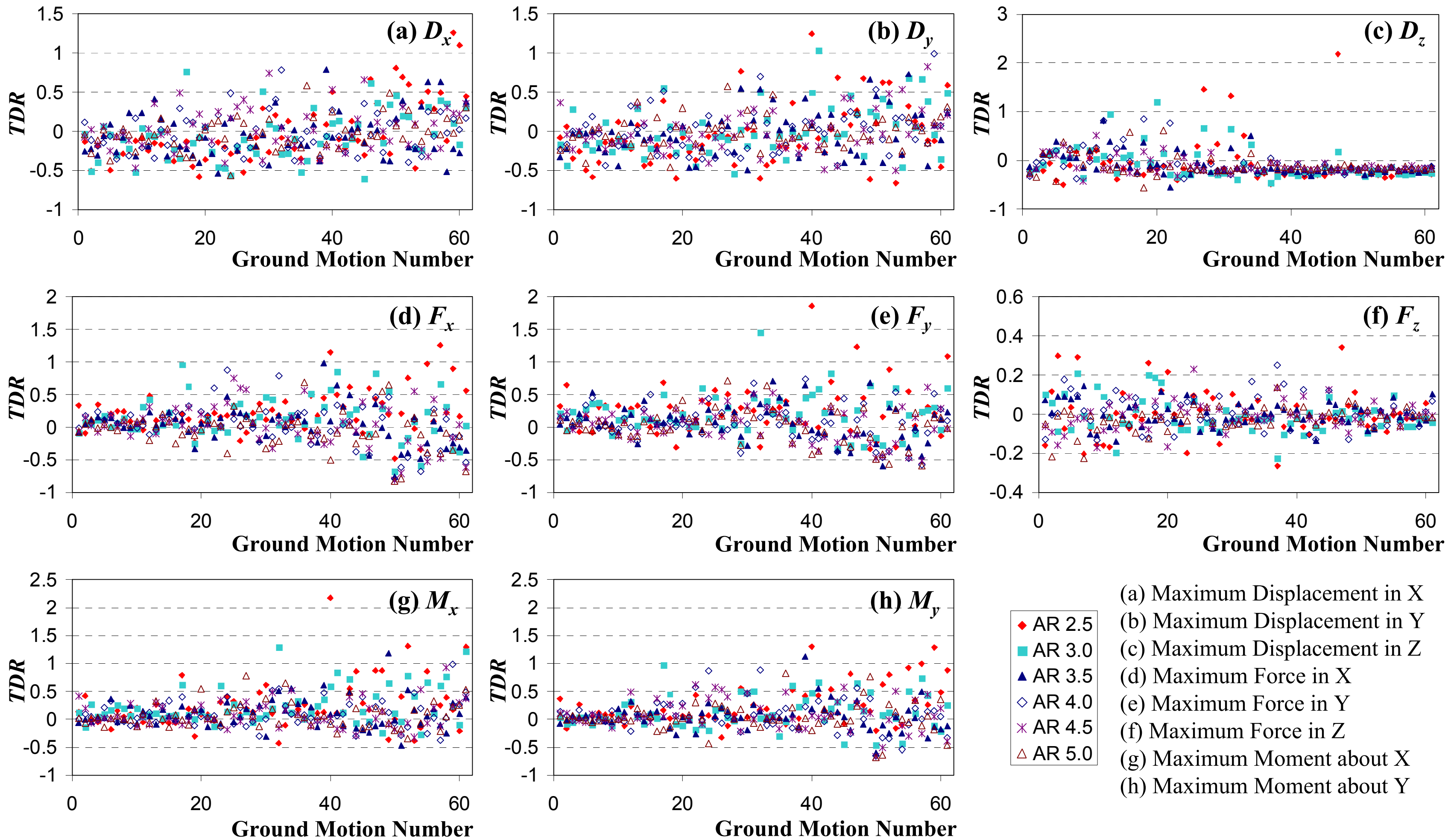

Figure 2.14 *TDR* values for different response parameters comparing models Type 1 and Type 2, both horizontal components present.

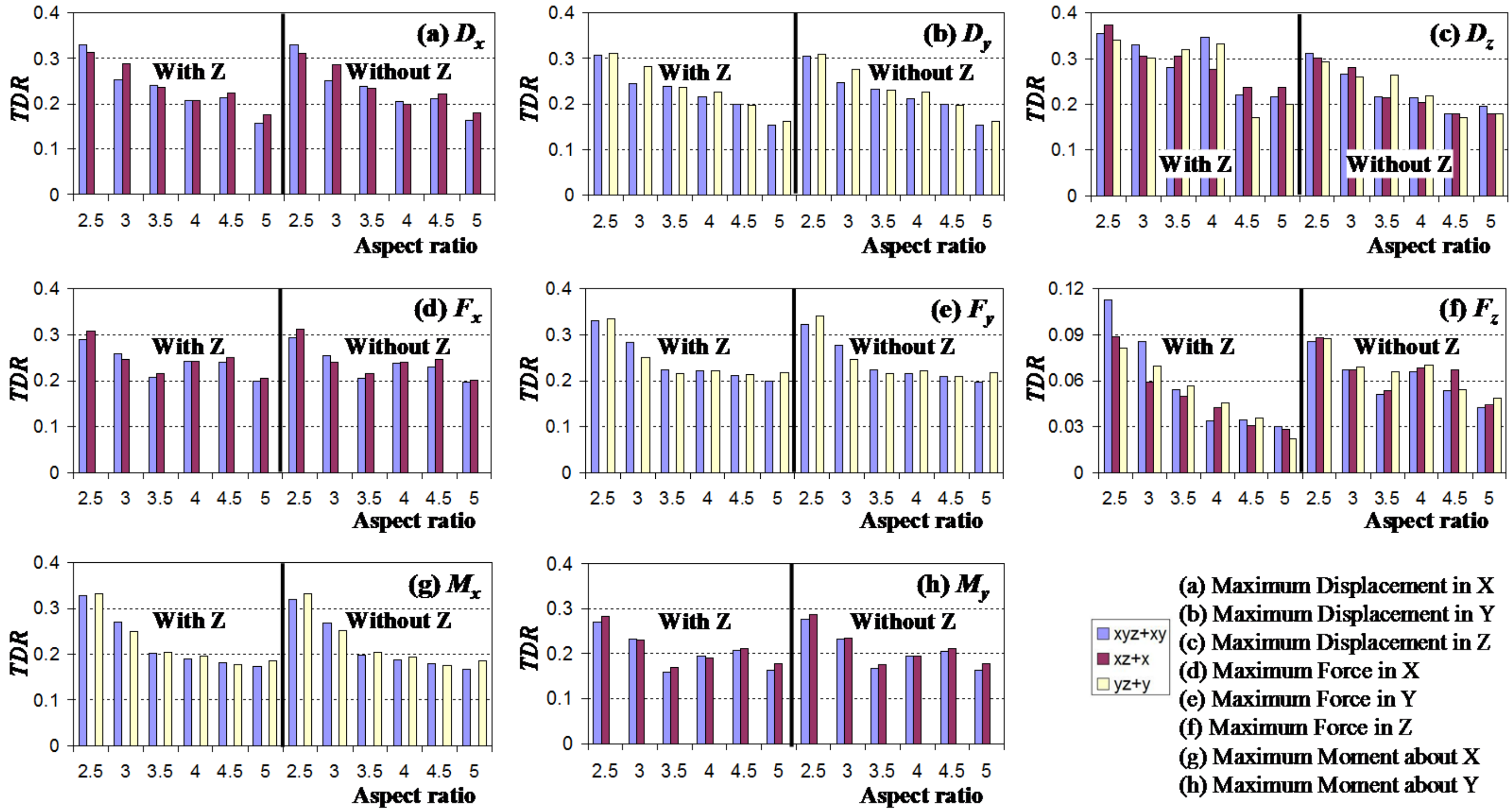

Figure 2.15 Average absolute *TDR* values for different response parameters comparing models Type 1 and Type 2.

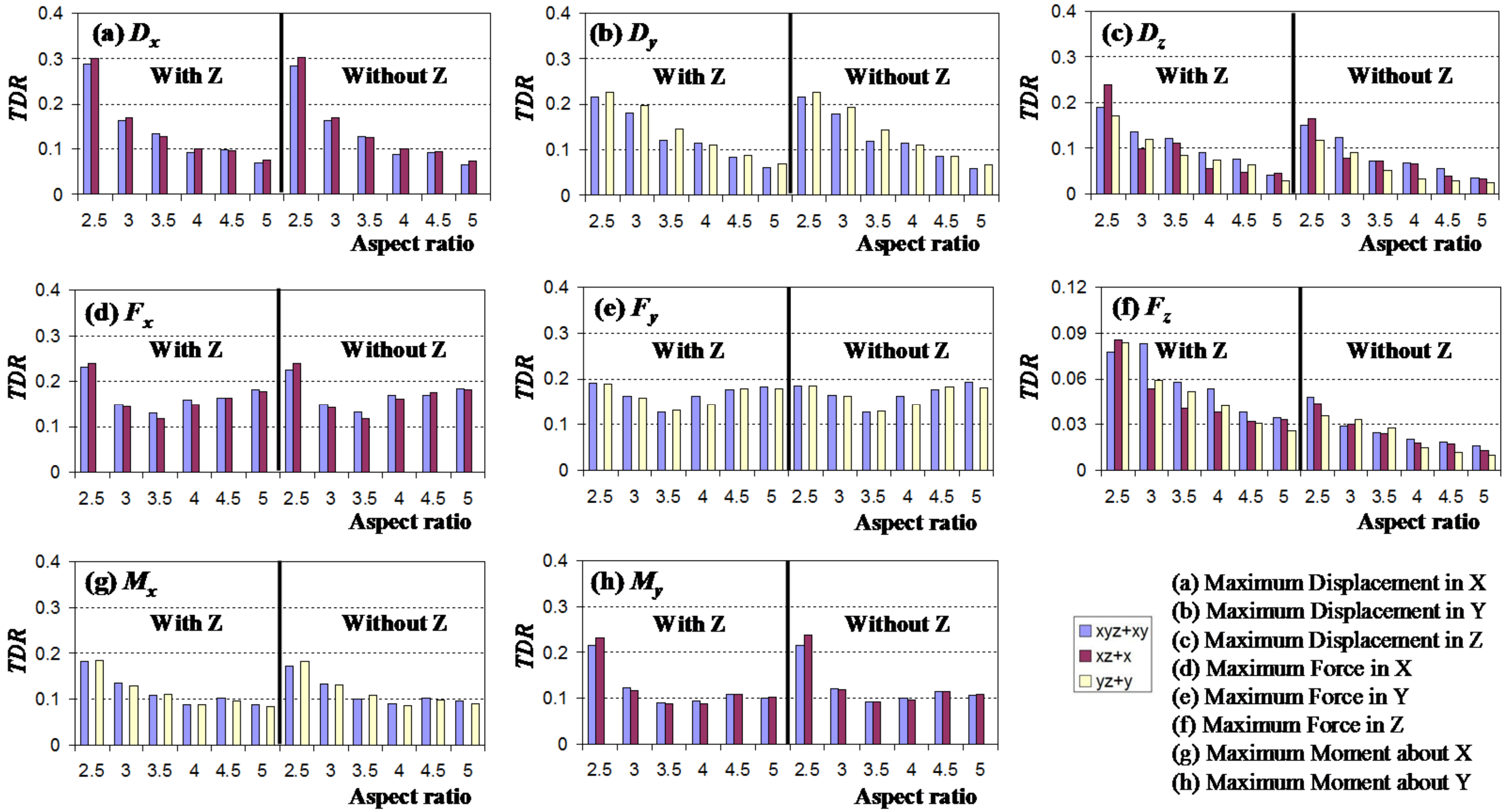

Figure 2.16 Average absolute *TDR* values for different response parameters comparing models Type 1 and Type 2-1.

2.5 DETAILED INVESTIGATION OF THE EFFECT OF AXIAL FORCE ON SHEAR CAPACITY

2.5.1 Comparison of Shear Demand and Capacity

Section 2.4 discussed the change of demand due to vertical excitation using three different modeling types, several ARs, and various ground motions. It was determined that axial force is the only force parameter affected by the presence of vertical excitation. In this section, the effect of axial force on the shear strength is investigated in detail, using the different shear strength equations presented in Chapter 1. In addition, the shear demand is compared with the shear capacity.

Figure 2.17 compares the shear strength calculated using equations given in ACI-318-11 (Section 1.2.1), CSA (Section 1.2.4), Eurocode (Section 1.2.5) and Caltrans SDC (Section 1.2.7) and the shear demand using ground motion #9 (Landers earthquake recorded at Lucerne station) (see Appendix A for further details) with one of the horizontal components and with and without the vertical component (designated as ‘xz’ and ‘x’, respectively); Figure 2.17(c) and (d) are for model Type 2. Note that ACI, CSA, Eurocode, and SDC documents are not consistent results in estimating the shear strength. Before the ground motion is applied (i.e., under the presence of only gravity loading), ACI offers the most conservative estimation, but once the dynamic excitation is included, the estimates change significantly for all methods. In general, CSA’s prediction changes during dynamic excitation more dramatically than the ACI, Eurocode, or SDC documents. Another observation from Figure 2.17 is that the possibility of shear failure increases when vertical excitation is present. For example, including the Z-component produces a shear strength that is much closer to the shear demand compared to the shear strength without the Z-component. Worth noting is that the SDC has a minimum value of 5681.9 kips whenever tensile axial force is applied, as shown in Figure 2.17(b) and (d).

The maximum ratio of the shear demand and shear strength, *Maxdcr*, and the reduction of the shear strength due to the earthquake excitation, *Red*, are calculated using Equation (2.3) and Equation (2.4), respectively. *Maxdcr* and *Red* using ACI are shown in Figure 2.18. All ARs are considered for all the 61 ground motions. Only the results of the case ‘X+Y+Z and X+Y’ (the effect of vertical excitation when both horizontal components are present) applied to Type 2 are shown. Almost all of the *Maxdcr* values are between 0.1 and 0.6; as expected, small ARs have large values of *Maxdcr*. Although *Maxdcr* values do not significantly change by adding the vertical earthquake component, there are differences in some of the ground motions. For example, *Maxdcr* for AR = 2.5 increases from 0.564 to 0.617 under ground motion #3 (see Appendix A). As expected, the *Red* values change significantly with relatively large vertical acceleration (ground motion (GM) #1 to approximately #20),. In general, *Maxdcr* values decrease as the number of the ground motion increases. Note that, as before, the ground motion numbers on the horizontal axis of Figure 2.18 are sorted in a descending order of the peak vertical acceleration (PGA_v).

$$Maxdcr = \max\left(\frac{\text{shear demand at each time step}}{\text{shear strength at each time step}}\right) \tag{2.3}$$

$$Red = \frac{\min\ (\text{shear strength})}{\text{shear strength before excitation}} \tag{2.4}$$

The ACI and SDC documents provide similar *Maxdcr* and *Red* values with relatively small vertical acceleration (GM#20 or above). However, with the ground motions below #20, there is a greater disparity between *Maxdcr* and *Red* of SDC and those of ACI. Figure 2.19(a) and (b) shows the *Maxdcr* values based on SDC without and with the Z-component, respectively. Both cases have the values between 0.1 and 1.0 with the ground motions below #20, but it is noticeable that more points are between 0.6 and 1.0 in Figure 2.19(b) than those in Figure 2.19(a). Figure 2.19(c) and (d) shown *Red* values based on SDC without and with Z-component, respectively. There are four ground motions that have significant reduction caused by lateral displacement ductility even without Z-component. Worth noting is that there are more than 20 ground motions causing the same *Red* around 0.53 with the Z-component included. Since the shear strength contribution of concrete, V_c, from SDC is zero under tension, only the shear strength of transverse reinforcement remains. Note that under the SDC, V_c is zero regardless of how large the tension is. That is why for all the ground motions that result in tension, *Red* becomes equal to V_c divided by the sum of V_c and V_s, which is equal to 0.53. In the SDC, zeroing the concrete contribution to shear strength under tension makes a significant difference between ACI and SDC estimates. *Maxdcr* and the minimum of shear strength may not occur simultaneously in case of the ACI estimate. Therefore, *Maxdcr* may not increase significantly even if there is noticeable reduction in *Red* using ACI. In contrast,, *Red* using SDC may occur several times during the excitation and, in general, *Maxdcr* may occur during one of these times. Consequently, *Maxdcr* based on SDC equations increases significantly with the inclusion of the Z-component.

The average values of *Maxdcr* and *Red* for models Types 1 and 2 and all ARs are shown in Figure 2.10 using the ACI approach, Figure 2.21 using the SDC approach, Figure 2.22 using the Eurocode approach, and Figure 2.23 using the CSA approach. As shown, *Maxdcr* decreases as the AR increases, and *Red* increases as the AR increases even though it is a very small increase (almost constant) in the case of the ACI and Eurocode approaches. Moreover, the difference due to the number of horizontal components (one versus two) is less than 10% in *Maxdcr* for ACI, Eurocode, and SDC. In contrast, this difference is sometimes more than 10% in *Maxdcr* for CSA; this difference tends to increase as the AR decreases. However, all approaches are similar in producing larger *Maxdcr* with two horizontal components included compared to only one horizontal component. Finally, the effect of the vertical component is much more noticeable in *Red* where it decreases to 0.6 for some ground motions.

For all four codes, *Red* decreases when the vertical component is included, i.e., the capacity decreases with the inclusion of the vertical excitation. This is expected because the ACI, SDC, and Eurocode documents have an axial force term and CSA has an axial strain term. With vertical excitation, these terms fluctuate significantly, and the shear strength also goes up and down. Due to the discrepancy of the variation of the axial force of the cross section and that of the axial strain at the centroid (which is affected not only by the cross-section axial force but also by the cross-section bending moment), the shear strength estimate by CSA code is quite different from ACI, SDC, and Eurocode documents.

Figure 2.24 presents *Maxdcr* and *Red* for all 293 ground motions whose horizontal PGA's are larger than 0.25*g*. Similar to Figure 2.18, Figure 2.24 shows the results for model Type 2 including the X+Y+Z and X+Y components. To avoid excluding ground motions that may have significant vertical excitation, all 293 motions (discussed in Section 2.1) were applied and analyzed. As observed in Figure 2.18, GM #1, #2, #3, #4, #7, and #10 in Appendix A have a significant decrease in *Red* with the inclusion of the vertical (Z) excitation.

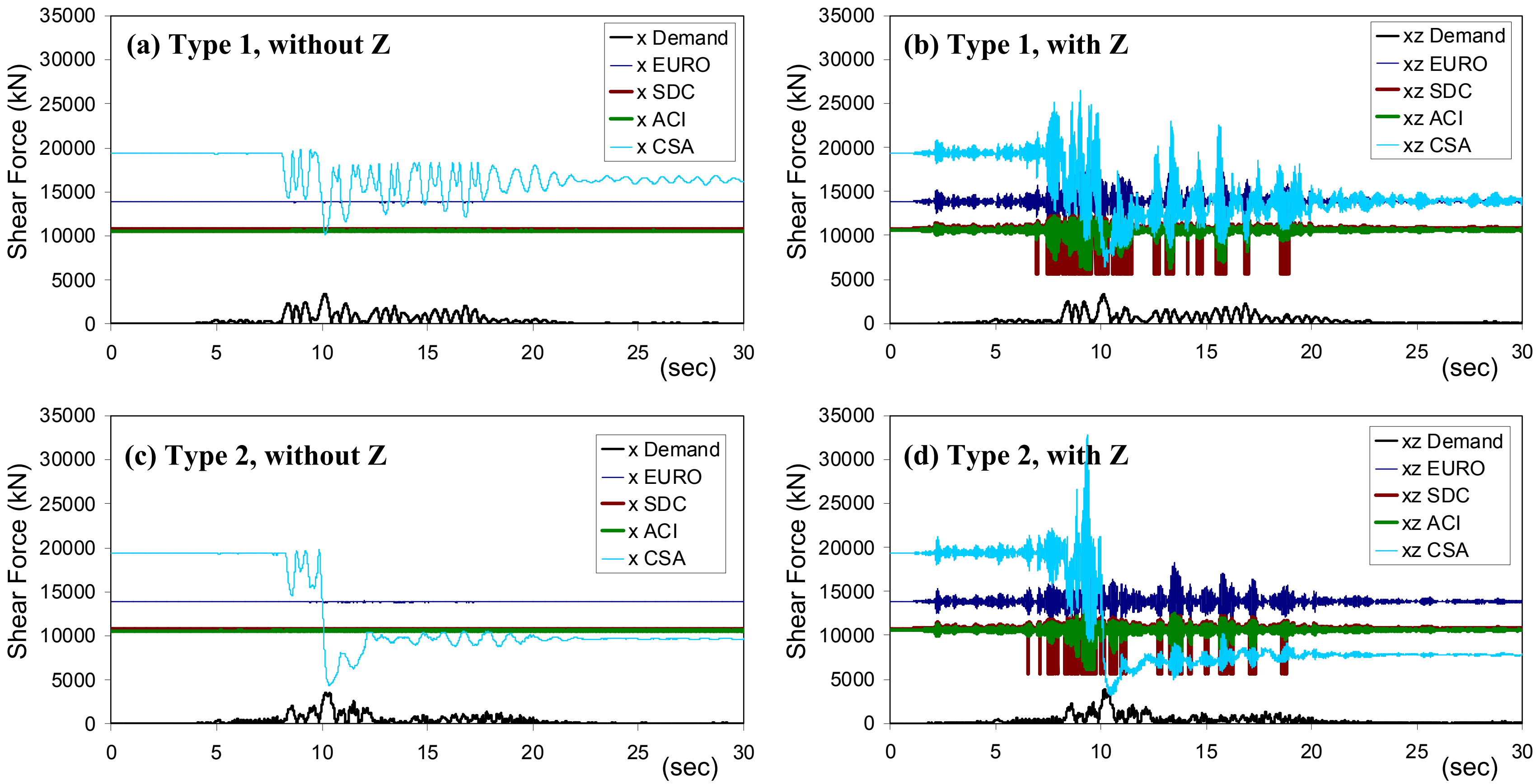

Figure 2.17 Shear demand and capacity with ground motion #9.

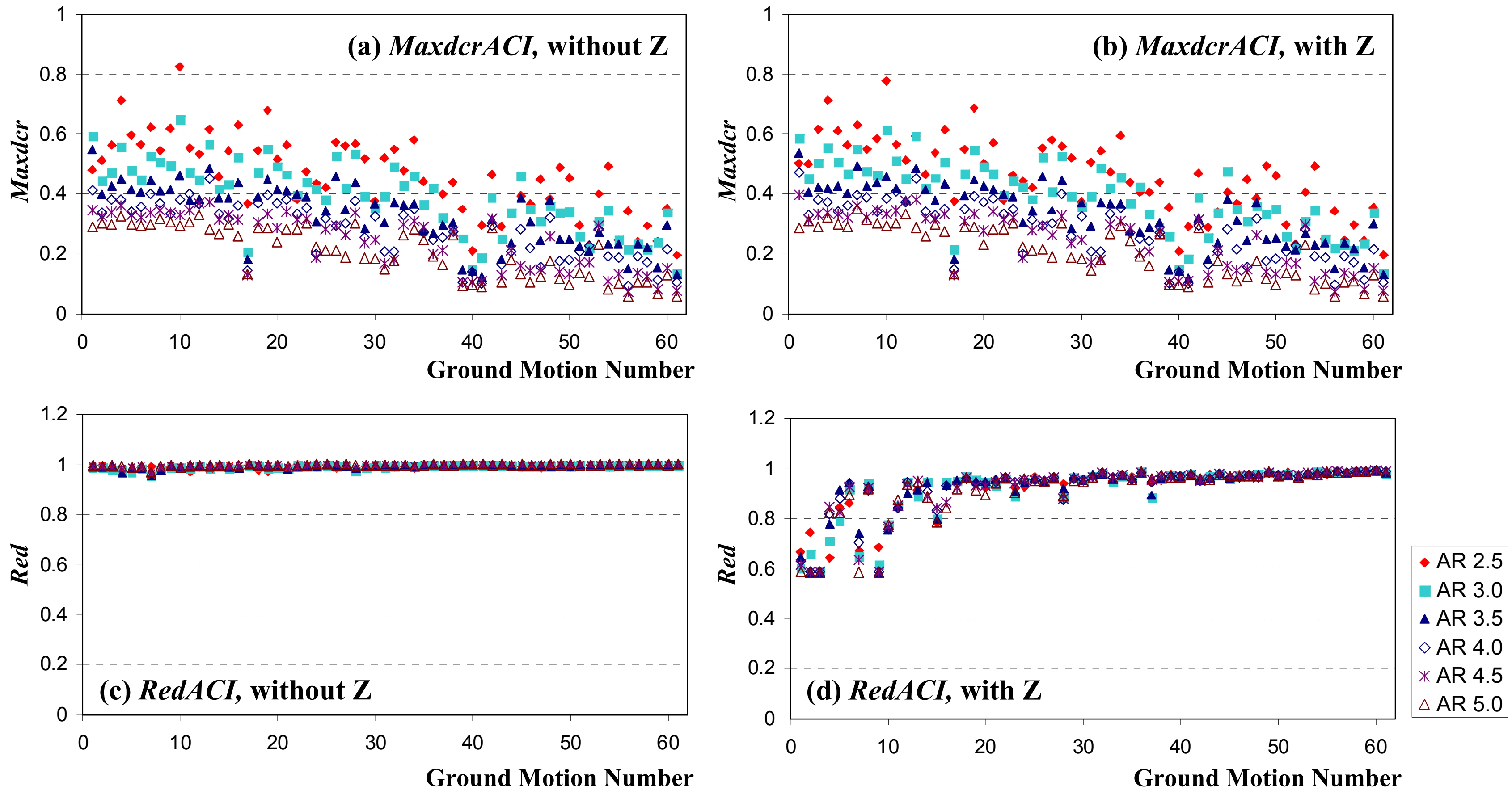

Figure 2.18 Demand to capacity ratio (*Maxdcr*) and reduction in shear strength (*Red*) considering ACI equation for Type 2 and selected 61 ground motions.

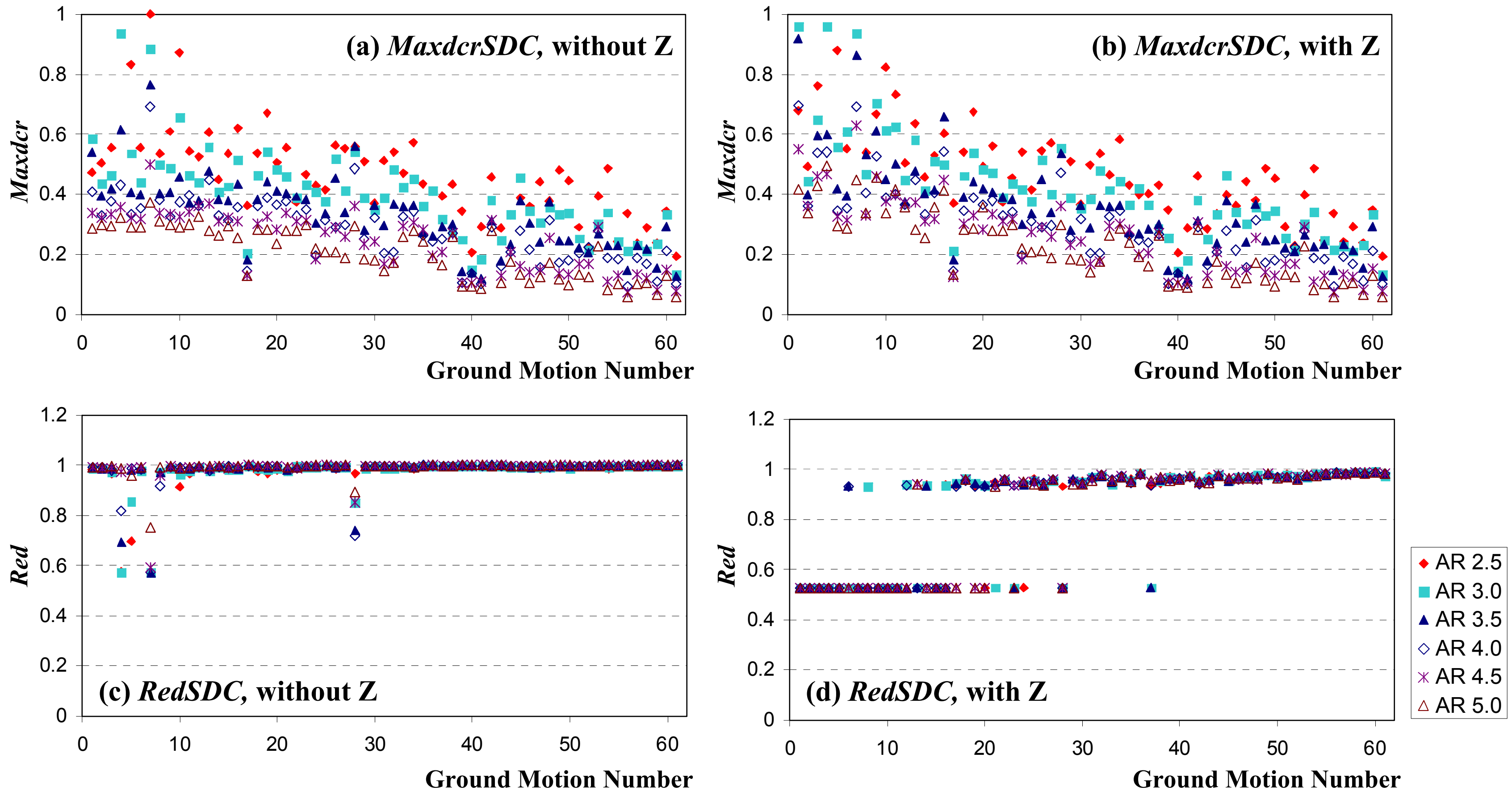

Figure 2.19 Demand to capacity ratio (*Maxdcr*) and reduction in shear strength (*Red*) considering SDC equation for Type 2 and selected 61 ground motions.

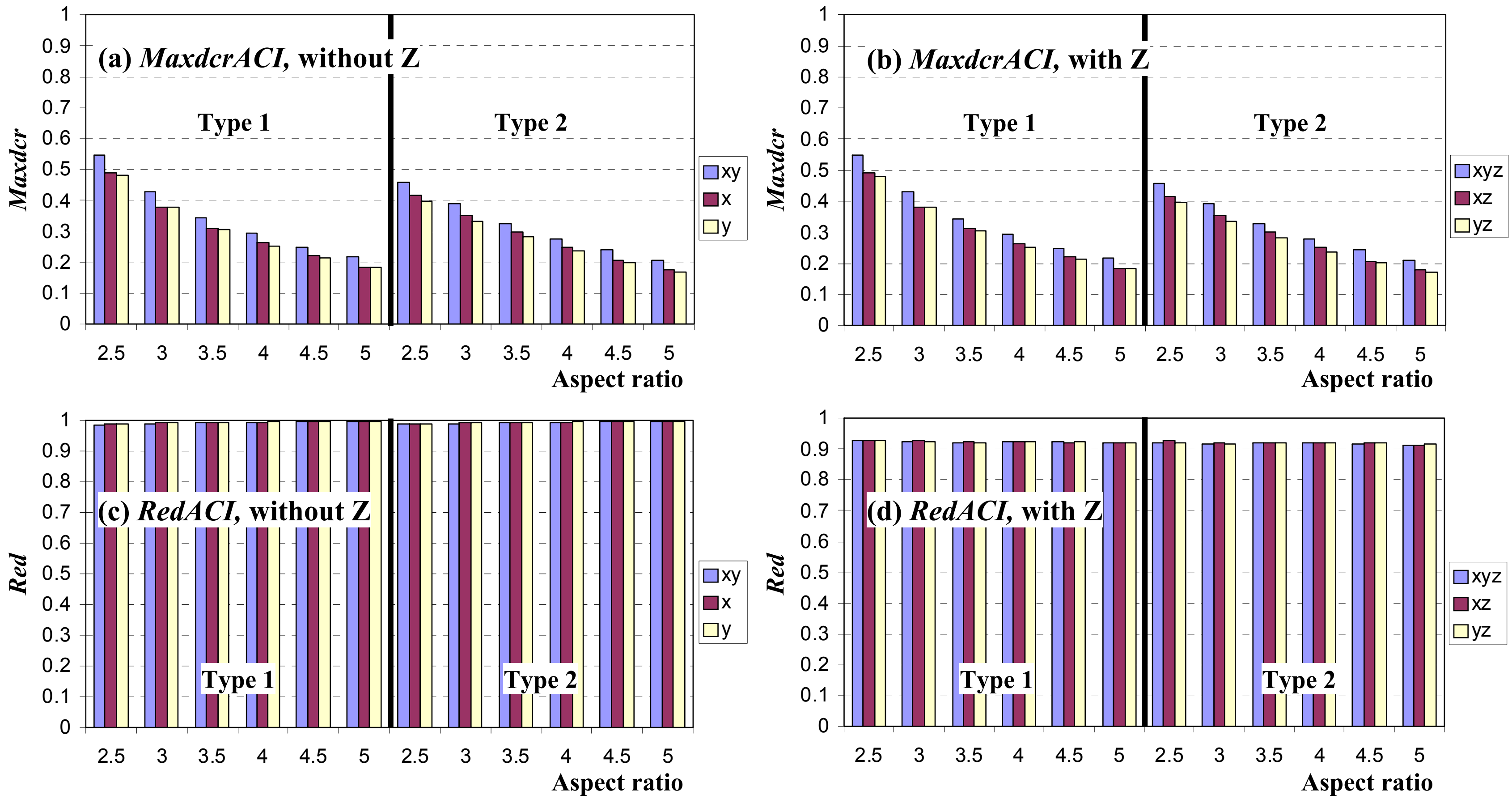

Figure 2.20 **Mean of demand to capacity ratios (*Maxdcr*) and mean of reduction in shear strength (*Red*) considering the ACI approach.**

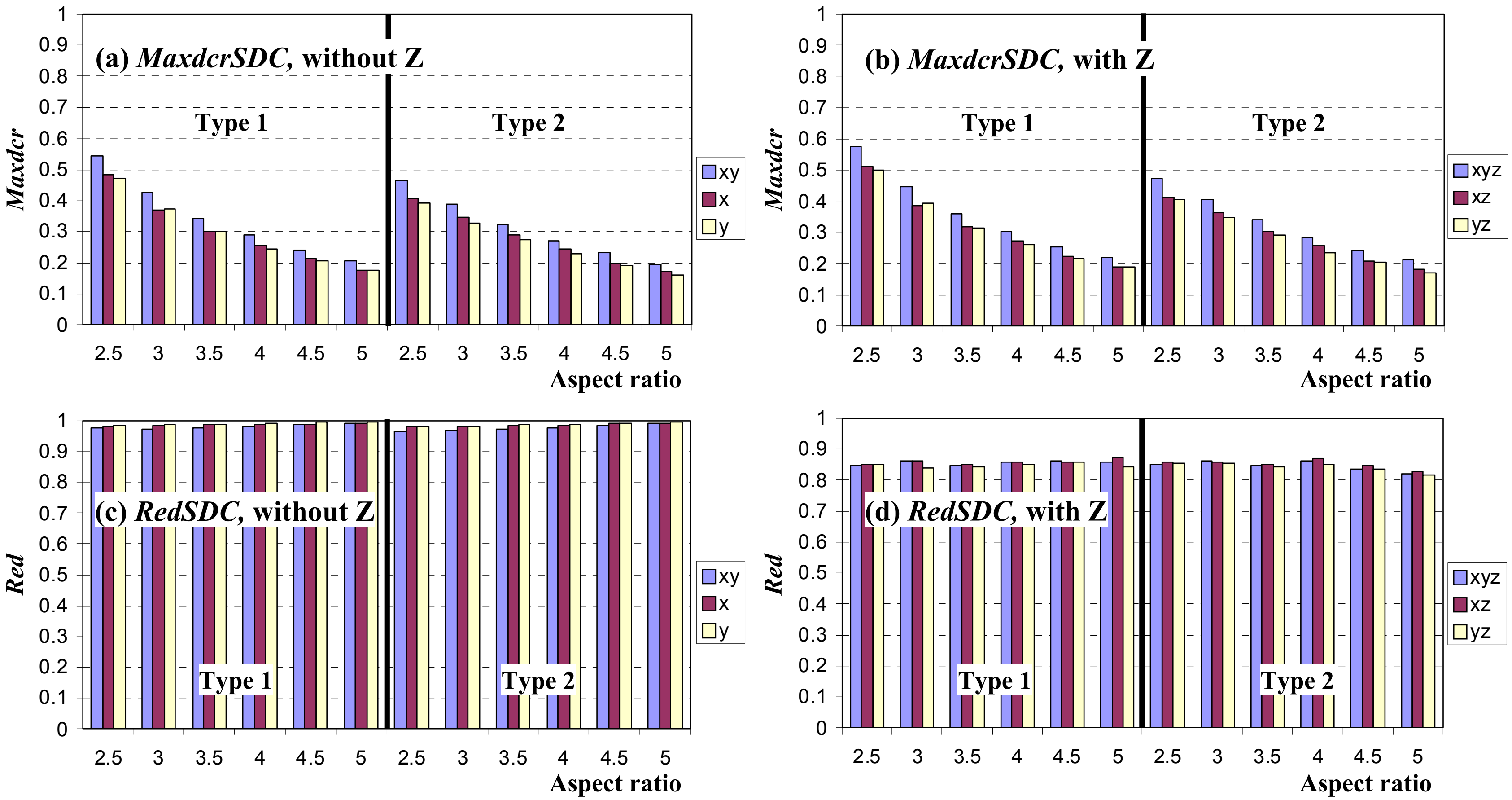

Figure 2.21 Mean of demand to capacity ratios (*Maxdcr*) and mean of reduction in shear strength (*Red*) considering the SDC approach.

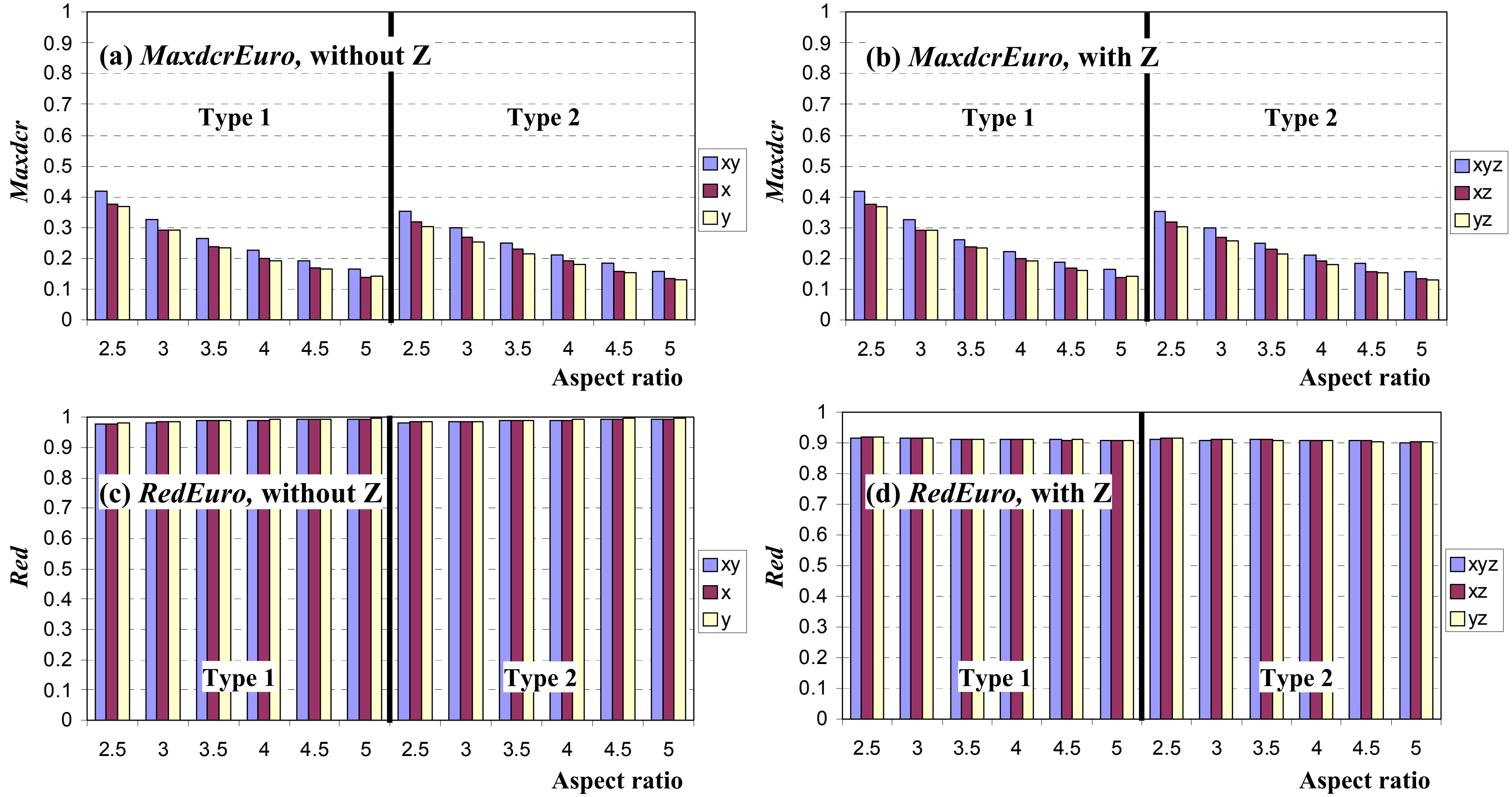

Figure 2.22 Mean of demand to capacity ratios (*Maxdcr*) and mean of reduction in shear strength (*Red*) considering the Eurocode approach.

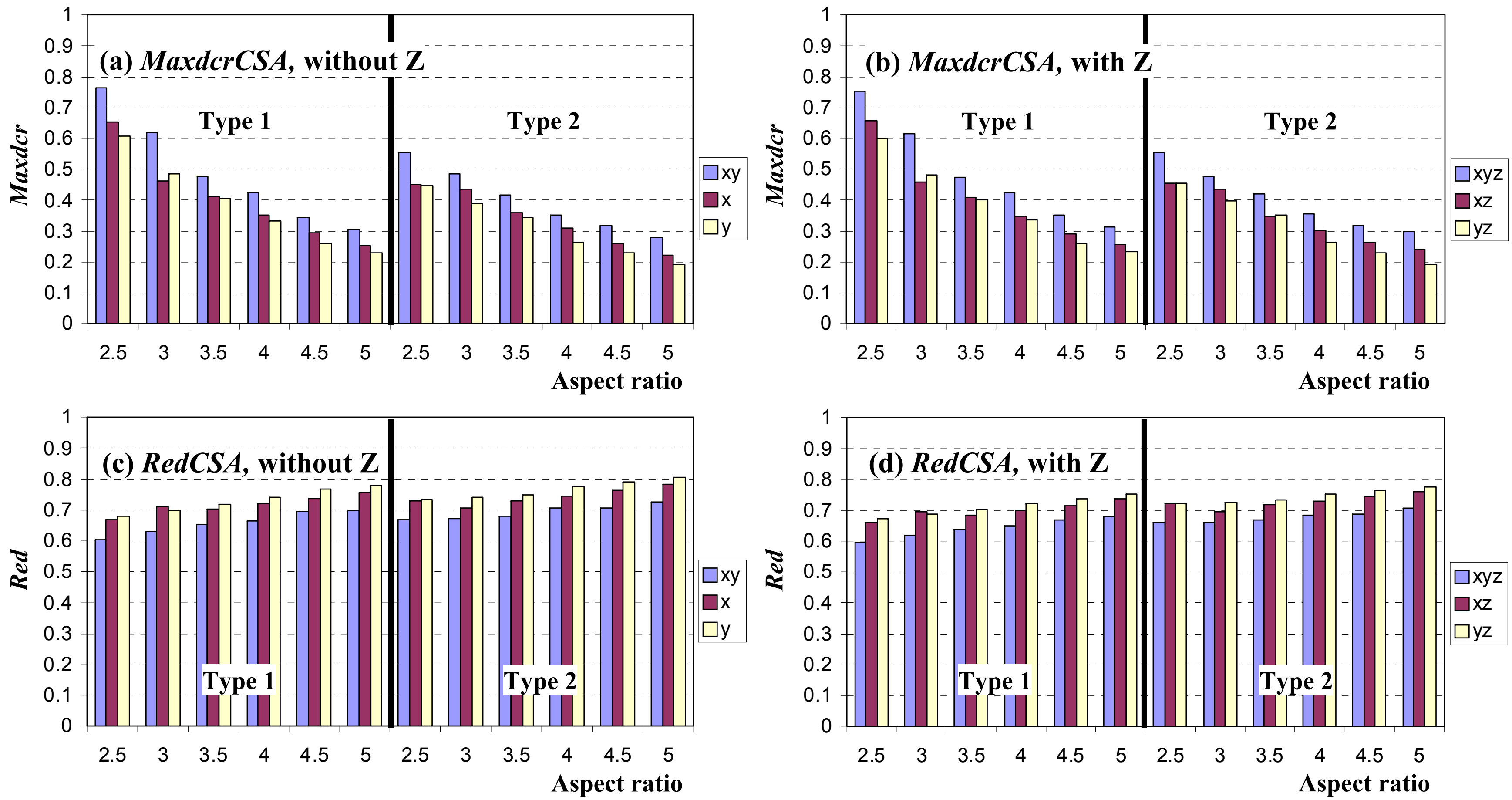

Figure 2.23 Mean of demand to capacity ratios (*Maxdcr*) and mean of reduction in shear strength (*Red*) considering the CSA approach.

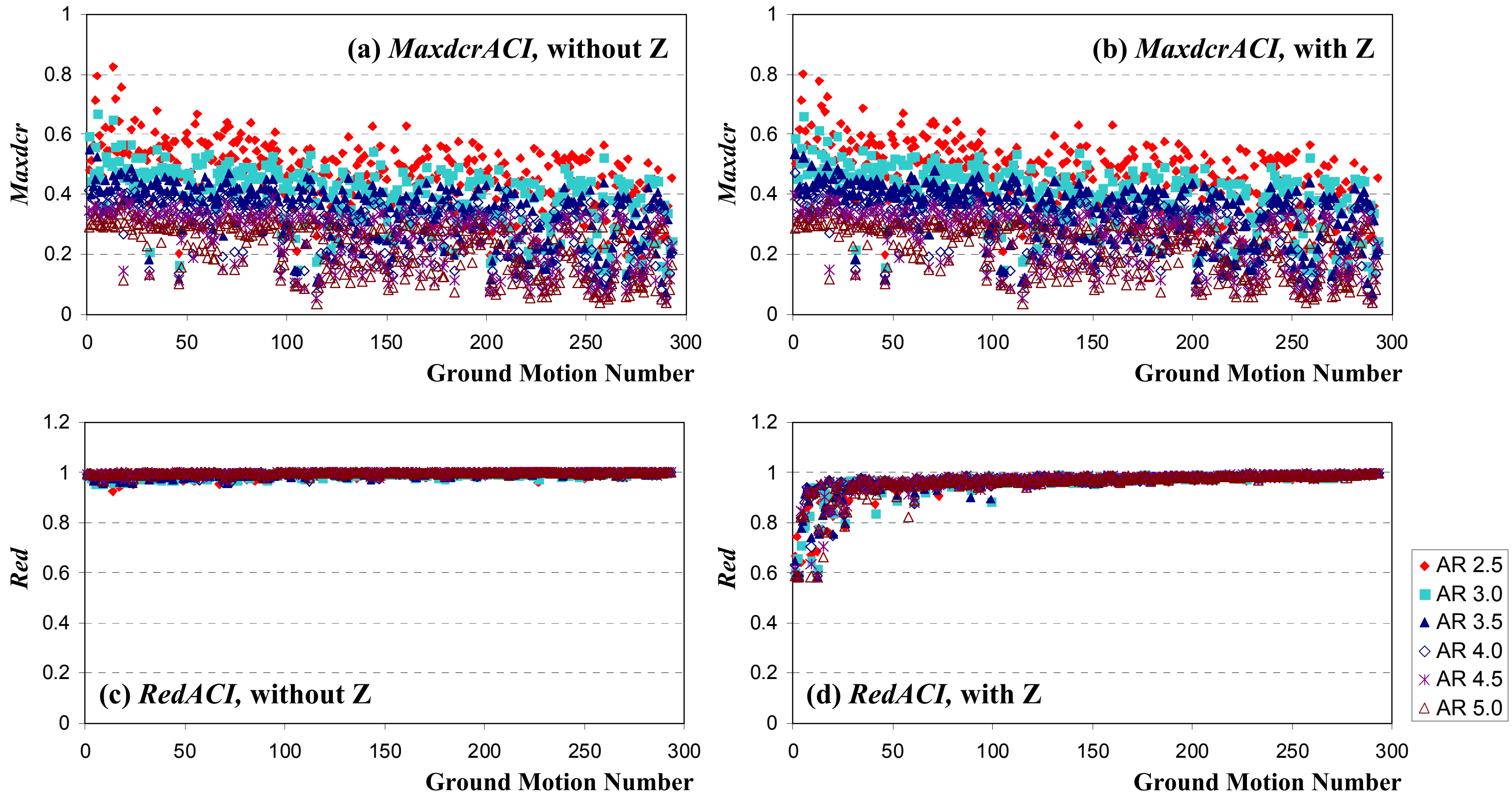

Figure 2.24 Demand to capacity ratio (***Maxdcr***) and reduction in shear strength (***Red***) considering the ACI equation for model Type 2 and the 293 ground motions with PGA_h > 0.25g.

2.5.2 Concluding Remarks

Based on the results and discussions above, the main observations from the parametric study can be summarized as follows:

- Due to considering both horizontal components, *Maxdcr* of the column subjected to X+Y+Z (or X+Y) is larger than that subjected to X+Z, Y+Z (or X, or Y).
- Reduction of shear strength (*Red*) due to application of X+Y+Z (or X+Y) is smaller than that due to application of X+Z, Y+Z (or X, Y).
- For shear strength demand to capacity ratio (*Maxdcr*) values, the order in estimates of different codes is Eurocode < ACI ≤ SDC < CSA, on average. The inequality between ACI and SDC holds when tension is present.
- For shear strength reduction (*Red*) values, the order in estimates of different codes is CSA < SDC < ACI ≈ Eurocode, on average.
- A smaller AR tends to have a larger *Maxdcr*, and a larger AR tends to have a slightly larger *Red* factor (i.e., it is reduced less).
- The pattern of reduction factors found in the ACI, SDC, and Eurocode documents depends moderately on the vertical excitation. In cases of ACI-318-11 and the Eurocode, the reduction factors of several ground motions are less than 0.85. The ground motions that cause noticeable changes are #1, #2, #3, #4, #7, and #10 (descending order of PGA_v, see Appendix A). The SDC has a unique pattern because its V_c is zero under tension regardless of the value of the tension.
- The reduction factors in CSA do not depend on the vertical excitation as much as ACI-318-11, the SDC and the Eurocode. Their reduction pattern does not change significantly with or without the vertical component.
- ACI-318-11, the SDC, and the Eurocode explicitly consider the axial force. Therefore, in the case without vertical excitation, their capacity predictions do not differ from ground motion to ground motion or from AR to AR compared to those from CSA.
- CSA takes the effect of axial force into consideration by using axial strain at the centroid of the section, resulting in differences in the shear capacity predictions for different ground motions and different ARs in cases without vertical excitation, since the axial strain at the centroid of the section is not only affected by the axial force but also by the bending moment.

2.6 SUMMARY

Among 3551 earthquake acceleration records in the PEER NGA database and discarding those records with only low-frequency content, 61 ground motions were selected as input candidates based on three criteria: (1) at least one of the horizontal components should have the PGA larger than 0.25*g*; (2) For the 20 pairs of periods T_h-T_v (T_v=0.05, 0.1, 0.15, and 0.2 sec and T_h=0.4, 0.5, 0.6, 0.7, and 0.8 sec), the PSa_v/PSa_{h1} or PSa_v/PSa_{h2} were calculated based on the ratio of the pseudo-spectral acceleration corresponding to the vertical component (PSa_v) to those corresponding to the horizontal components (PSa_{h1}, PSa_{h2}), where if one of these two ratios is larger than 1.0 in at least 15 pairs, the ground motion is selected as one of candidates; and (3) the arrival time interval between horizontal and vertical peak accelerations is considered, which affects the interaction of the horizontal and the vertical responses. The interval should be shorter than the cut-off of 1 sec.

A parametric study was conducted on columns designed with the modified effective circular section of Prototype 1 (ACB) and subjected to ground motions to evaluate the effect of vertical excitation. The following parameters were varied: ground motion, number of components, mass moment of inertia, and AR. First, 61 motions were applied. Second, three cases were considered, all three components versus two horizontal components, X and Z components versus X component, Y and Z components versus Y component. Third, the existence of the mass moment of inertia was considered, and its effect on the response examined. The mass moment of inertia of Prototype 1 (ACB) was applied to Type 2. Since Type 2-1 has no rigid end zone, it is identical to Type 1 except for the inclusion of mass moment inertia, and its lateral and rotational periods were obtained. Fourth, six ARs from 2.5 to 5.0 were taken into account.

The parametric study determined that: (1) the presence of two or one of the horizontal components does not produce significant differences; (2) except for D_z and F_z, the difference in other responses due to vertical excitation was not significant; (3) the effect of vertical excitation was significant in F_z, which could affect the shear strength for models Types 1 and 2; and (4) the difference in D_z or F_z between models Types 1 and 2 is relatively small. For other response parameters, the discrepancy between Types 1 and 2 becomes larger as the AR decreases. However, since the axial force is the only parameter that was significantly affected by the vertical excitation, it can be concluded that the differences between Types 1 and 2 (especially Type 2-1) may not be important for the purpose of this study.

The effect of axial force on the shear strength was investigated using different shear strength code approaches. Comparing the shear demand to the shear strength, the maximum ratio of shear demand and shear strength, *Maxdcr*, and the reduction of the shear strength due to the earthquake vertical excitation, *Red*, were calculated. *Maxdcr* of the column subjected to X+Y+Z (or X+Y) was larger than that subjected to X+Z, Y+Z (or X, or Y). For *Maxdcr*, Eurocode < ACI ≤ SDC < CSA, regarding the general order in estimates. *Red* due to application of X+Y+Z (or X+Y) was smaller than that due to application of X+Z, Y+Z (or X, or Y). For *Red*, CSA < SDC < ACI ≈ Eurocode, regarding the general order in estimates. Moreover, a smaller AR tends to have a larger *Maxdcr*, and a larger AR tends to have a slightly larger *Red*, i.e., it is reduced less. Note that ACI, SDC, and Eurocode documents explicitly consider axial force. CSA, however, takes the effect of axial force into consideration by using axial strain at the centroid of the cross section, resulting in differences in the shear capacity predictions for different ground motions and different ARs, even cases without vertical excitation. This is because the axial strain at the centroid of the cross-section is not only affected by the axial force but also by the bending moment.

3 Design of Dynamic Tests

3.1 INTRODUCTION

Dynamic testing is the optimum method to replicate earthquake input motions. Due to limitation of facilities, to date only a few shaking table tests have been conducted to examine the effect of vertical acceleration on bridge columns. To perform tests on the UC Berkeley shaking table at the Richmond Field Station (RFS), 1/4-scale bridge column specimens, instrumentation, and input sequence were prepared to investigate the response of a bridge column subjected to the horizontal and vertical dynamic excitations.

3.2 DESCRIPTION OF SHAKING TABLE

In 1969, Professors J. Penzien and Ray Clough led the design of the world's first shaking table at the RFS. After several upgrades over the decades, it is now has six degrees-of-freedom (6 DOFs), with three translational and three rotational components of motions. Operated by the Pacific Earthquake Engineering Research (PEER) Center, it is now the largest 6 DOFs shaking table in the U.S.

The shaking table is stiffened by heavy transverse ribs, and the eight horizontal hydraulic actuators (four in each direction) are attached to the ribs. The four vertical actuators are attached to the table by post-tensioning rods at points located 1.5 ft×1.5 ft (305 mm× 05 mm) from each corner. All 12 actuators are 75 kips (334 kN) capacity hydraulic actuators and connected to a 1580-kips (7028-kN) reaction block. As a result, about 3*g* can be achieved when the table is empty, which weighs about 100 kips (445 kN). Decoupling of components is accomplished by the length of the actuators and the control system. A unique feature of the UC-Berkeley shaking table is that a 1.5-psi air pressure supports the total weight of the table and specimen while the table is in operation. This feature allows the hydraulic actuators to operate more efficiently during dynamic loading. Table 3.1 summarizes the characteristics of the UC-Berkeley shaking table. As discussed in next section, fidelity tests were performed before the actual RC bridge column tests to confirm the performance of the shaking table.

Table 3.1 Characteristics of the UC-Berkeley shaking table.

Property	Value
Table dimensions	20 ft×20 ft (6.1 m×6.1 m)
Table weight	About 100 kips (445 kN)
Components of motion	6 DOFs
Displacement limits	horizontal limits are ±5 in (±127 mm) vertical limit is ±2 in (±50.8 mm)
Velocity limits	30 in./sec (0.76 m/sec) in all axes with an unloaded table
Acceleration limits	About 3*g* in all axes with an unloaded table

3.3 SELECTION OF INPUT MOTION: FIDELITY TESTS

In the presence of vertical excitation, the shaking table is governed by its own frequency, and it is not possible to reproduce all frequencies of the input motion exactly. Therefore, it may not be possible to reproduce some motions. Performing fidelity tests is the considered approach to select suitable motions for the intended dynamic tests. On March 19, 29, and April 2, 2010, a total of 30 trials were conducted to check the table's performance and the feasibility of inputting four different ground motions selected from the PEER NGA database [2013]; see Section 2.1.

3.3.1 Fidelity Test Set-Up

To verify the shaking table performance, it is important to ensure that the fidelity test set- up similar to the intended dynamic test specimen. Even though it is not feasible to achieve the exact horizontal and vertical periods comparable to those of the real specimen, the over-turning moment due to the height of the center of gravity (C.G.)—which is one of the main factors affecting the table performance—under vertical and horizontal excitation inputs can be controlled by stacking mass blocks and supporting steel beams.

The geometrical scale of the set-up corresponds to the 1/4-scaled prototype. The total weight is 118 kips (525 kN) and the C.G. is 9 ft (2.74 m) above the table (see Figures. 3.1 and 3.2). Locations of the instruments placed on the shaking table and the mass blocks are shown in Figure 3.3. Since the specimen is a 1/4 scale (length scale= S_L = prototype length/model length = 4), each ground motion is compressed in time using a factor of $\sqrt{S_L}$ =2.

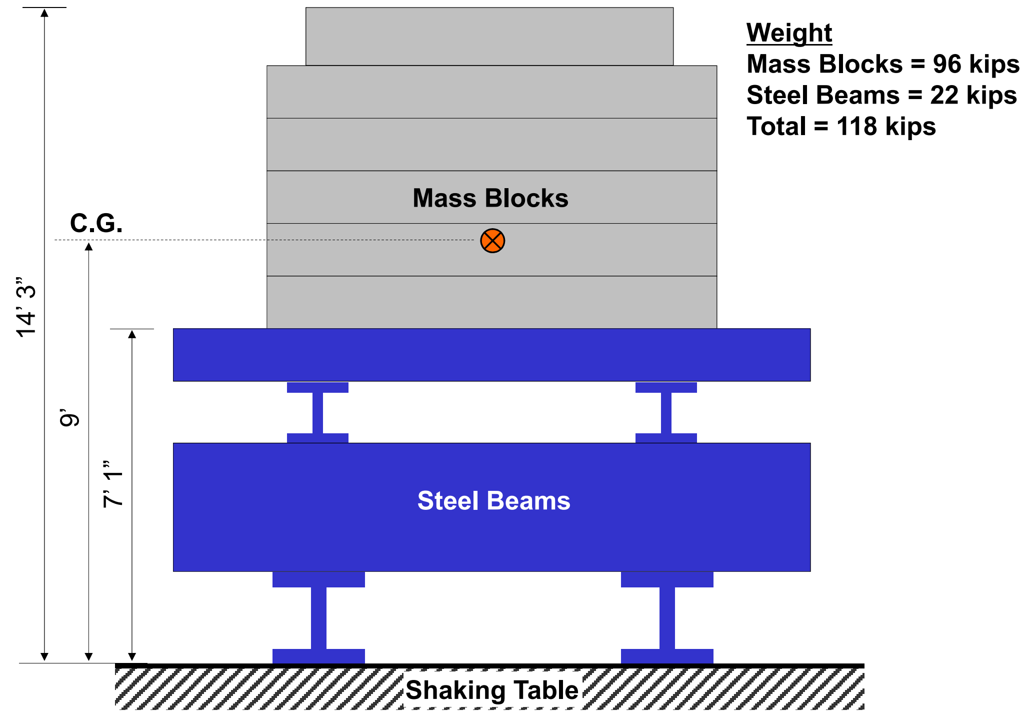

Figure 3.1 Schematic of the fidelity test set-up (1 ft = 305 mm, 1 in.=25.4 mm).

Figure 3.2 Photograph of the fidelity test set-up.

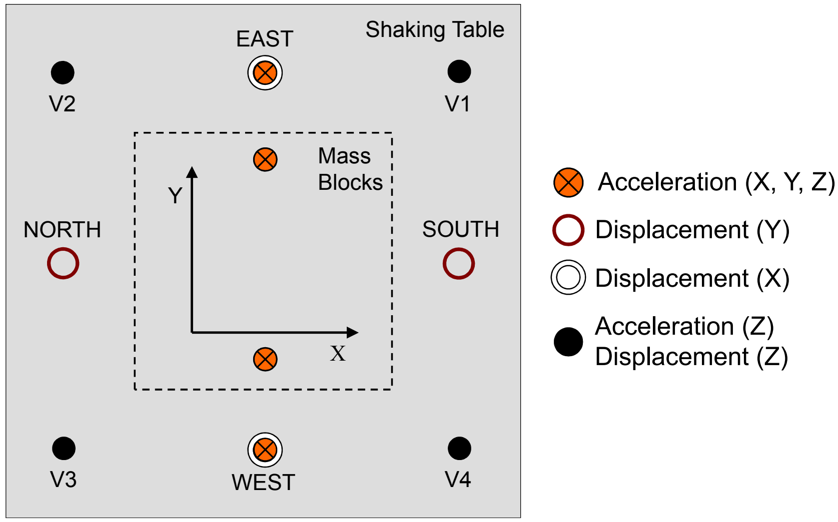

Figure 3.3 Shaking table plan, axes, and instrumentation for the fidelity tests.

3.3.2 Input Ground Motion Candidates and Scale Factors

The ground motions listed in Table 3.2 were selected based on the analysis using a full-scale single-column model with an AR of 3.5 (see Chapter 2). Ground motions 1, 2, 3, 5, 7, and 9 (earthquake records #3, 1, 15, 9, 4, and 7, respectively, see Table A.1) were selected from the 80 ground motions. This satisfies the first and second criteria listed in Section 2.1, based on the capacity reduction calculated using the ACI equation (*RedACI* <0.8) and a comparison of demand and capacity history. Ground motions 4, 6, 8, and 10 (earthquake records #10, 8, N/A (because it belongs to the 80 records not the 61 records listed), and 28 in Table A.1) were added because the ductility demand is high (even though they are not selected based on the *Red* and *Maxdcr* values). Note that X-component produced a more significant effect on *Red, Maxdcr*, and displacement ductility, rather than Y-component. Therefore, only *PGA* for X-component was specified in Table 3.2.

Table 3.2 Ten selected ground motions for the fidelity tests.

GM	RSN	EQ Name	YYMMDD	Station	*PGA* (*g*) (unfiltered)	
					X	Z
1	126	Gazli, USSR	760517	Karakyr	0.61	1.26
2	495	Nahanni, Canada	851223	Site 1	0.98	2.09
3	752	Loma Prieta	891018	Capitola	0.53	0.54
4	825	Cape Mendocino	920425	Cape Mendocino	1.50	0.75
5	879	Landers	920628	Lucerne	0.73	0.82
6	982	Northridge-01	940117	Jensen Filter Plant	0.57	0.82
7	1051	Northridge-01	940117	Pacoima Dam (upper left)	1.58	1.23
8	1054	Northridge-01	940117	Pardee-SCE	0.66	0.38
9	1063	Northridge-01	940117	Rinaldi Receiving Station	0.83	0.83
10	1085	Northridge-01	940117	Sylmar-Converter Sta. East	0.83	0.38

Because the performance of the shaking table needs to be verified for the entire intensity level range which will be applied in the dynamic tests, magnitude scales for different intensity levels should be determined. Based on the results from the parametric study in Chapter 2, these scales were calculated as follows:

- Nonlinear time history analyses of the full-scale single-column were conducted using the full-scale ground motions with the larger of the two horizontal components (referred to as X component) and the vertical (Z) component. The force reduction factor (R) was calculated from the obtained ductility values, μ, based on the equal energy assumption by Newmark and Hall [1982], i.e., $R = \sqrt{2\mu - 1}$. The scale factor for 'Yield Level' was subsequently calculated as $1/R$.
- Because significant strain hardening is expected, the maximum considered earthquake (MCE) level is assumed to correspond to ductility = 2, hence the force reduction factor corresponding to MCE level (R_{MCE}) was calculated as $\sqrt{2 \times 2 - 1} = 1.73$.
- The scale factor for MCE was calculated as R_{MCE} multiplied by the scale of the yield level, which is equal to $1.73/R$.
- For simplicity and to preserve the basis of the selection criteria mentioned in Section 2.1, the scale factors determined for the horizontal components using the above procedure were utilized for the vertical components as well.

Note that the MCE level was not determined from the USGS maps (using the typical method of site-specific pseudo-acceleration, S_a, at low and high periods and then finding S_a at the specific period) because the site of the prototype bridge resulted in small S_a values. Instead of choosing another site, the MCE level was determined based on the response. In addition, although the maximum ductility achieved in the tests with the actual specimen were about five in the dynamic tests (see Table 4.1), the scales determined using the assumption of ductility = 2 (as mentioned in item 2 above) was sufficient to evaluate the table performance since the scales determined in this manner resulted in accelerations close to the table limits.

After further elimination based on the demand and capacity histories, ground motions 1, 5, 7, and 9 were utilized in the fidelity tests with the determined scales (in terms of the target PGA after filtering, as mentioned below) and are listed in Table 3.3. As mentioned before, all ground motions were compressed in time using a factor of two. The ground motions were filtered using a filter range of 0.6~30 Hz for the X components and 2~60 Hz for Z components to accommodate the displacement limits of the shaking table.

Table 3.3 Properties of the ground motions selected for the fidelity tests.

GM	RSN	EQ Name	Station	Target PGA (g) (filtered)			
				Yield Level		MCE Level	
				X	Z	X	Z
1	126	Gazli, USSR	Karakyr	0.48	0.96	0.83	1.66
5	879	Landers	Lucerne	0.41	0.64	0.71	1.11
7	1051	Northridge-01	Pacoima Dam (upper left)	0.98	0.78	1.70	1.35
9	1063	Northridge-01	Rinaldi Receiving Station	0.25	0.26	0.44	0.44

3.3.3 Fidelity Test Results

Among the four ground motions shown in Figures 3.4 to 3.14, GM7 seems to be the most suitable input given the shaking table performance. In these figures, the expected natural period range of the test specimens and its elongation due to damage is identified in terms of the important frequency range (in this study) using double headed horizontal arrows. In addition, In addition, the legend "f-measured" in these figures stands for the filtered measured data. As discussed, the shaking table does not reproduce frequencies over the entire range in the vertical direction. For example, for each ground motion, the response spectrum of the measured vertical acceleration has a sharp peak at 5~15 Hz, a valley at 15~30 Hz, and another peak around 45 Hz. Therefore, ground motions with spectra like GM1 (Figures 3.4 and 3.5), GM5 (Figures 3.6 and 3.7), or to a lesser extent GM9 (Figures 3.11 to 3.14) are not suitable to be replicated on the UC-Berkeley shaking table. In most cases, the measured horizontal acceleration spectra are much more similar to the target spectra compared to the case of the vertical spectra.

Results of GM7 0.5-yield, yield, and MCE levels are shown in Figures 3.8, 3.9, and 3.10, respectively. The corresponding scale factors are 0.33, 0.66, and 1.14 compared to the originally recorded motion. In the important frequency range defined by the horizontal double headed arrow, the shaking table has an acceptable performance in matching the target spectra for yield and MCE levels of GM7 for both of the horizontal and vertical components. Basic information on GM7 is available in PEER NGA database [2013]; Table 3.4 shows the record and station information. The Northridge earthquake occurred on January 17, 1994, in Los Angeles, California. The epicenter was in Reseda and the hypocenter latitude and longitude were 34.2057 and -118.554, respectively.

The strong-motion response of Pacoima Dam was recorded by a network of California Division of Mines and Geology (CDMG) accelerometers. Pacoima Dam is a 365 ft (111.25 m) high concrete arch dam, with a thickness at the crown cross section that varies from 10.4 ft (3.17 m) at the crest to 99 ft (30.18 m) at the base. GM7 was recorded at the station on the left abutment, and its peak acceleration was 1.5g. Considering the peak acceleration at a downstream location was 0.44g and that at 80% of the height was 2.3g, frequency-dependent topological amplification affected the ground motion significantly; see Fenves and Mojtahedi [1995] and Alves [2005]. The motion of the dam had higher frequency components than those at the base or downstream. Moreover, Alves [2005] points out that the ground motion delays are consistent with the seismic waves traveling upward along the canyon, and that the waves appear to be dispersive because the delays are frequency-dependent. Fenves and Mojtahedi [1995] presumed that higher frequency components were possibly caused by higher mode contributions of the dam or impact due to pounding of contraction joints.

The GM7 obtained from the PEER NGA database [2013] does not have a higher frequency content compared to the other ground motions, i.e., GM1, GM5, or GM9, as shown in Figures 3.4 to 3.14. In particular, the frequency content of the vertical component of GM7 mostly leans towards lower frequency range compared to the other three ground motions (refer to Figures 3.8 to 3.10). It makes GM7 the most suitable motion to be reproduced by the table amongst four ground motions.

Table 3.4 GM7 Information.

Earthquake		Northridge-01 19940117 12:31
Moment magnitude		6.69
Seismic moment		1.2162+E26 dyne-cm
Mechanism		Reverse Fault Rupture
Hypocenter depth		17.5 km
Fault rupture length/width		18.0 km / 24.0 km
Average fault displacement		78.6 cm
Fault name		Northridge Blind Thrust
Slip rate		1.5 mm/yr
Station		CDMG 24207 Pacoima Dam (upper left abutment)
Instrument housing		Earth dam (abutment)
Mapped local geology		Granitic
Geotechnical subsurface characteristics		Rock
Preferred Vs30		2016.10 m/s
Epicentral distance		20.36 km
Hypocentral distance		26.85 km
Joyner-Boore distance		4.92 km
Campbell R distance		7.01 km
RMS distance		18.60 km
Closest distance		7.01 km

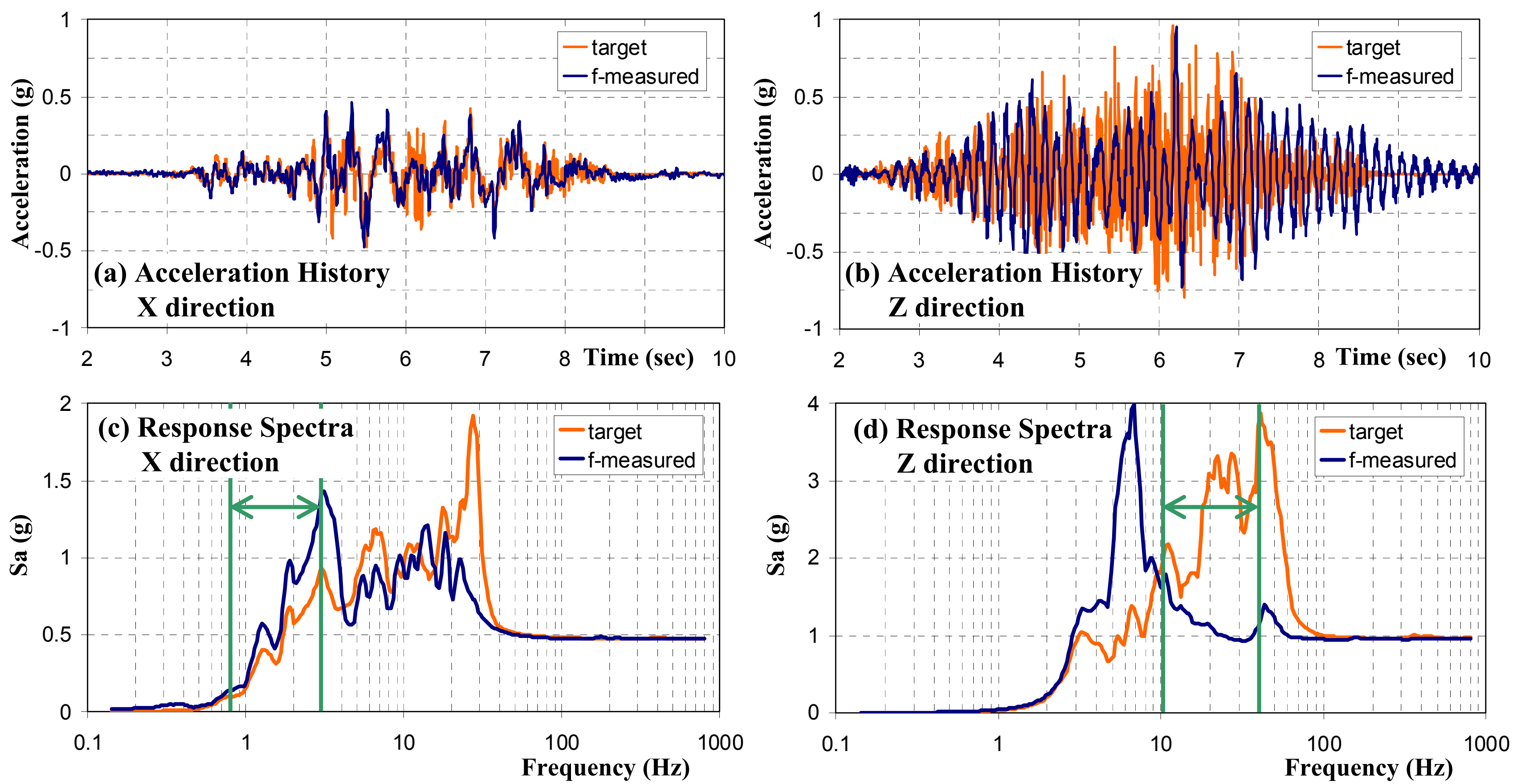

Figure 3.4 GM1 yield level.

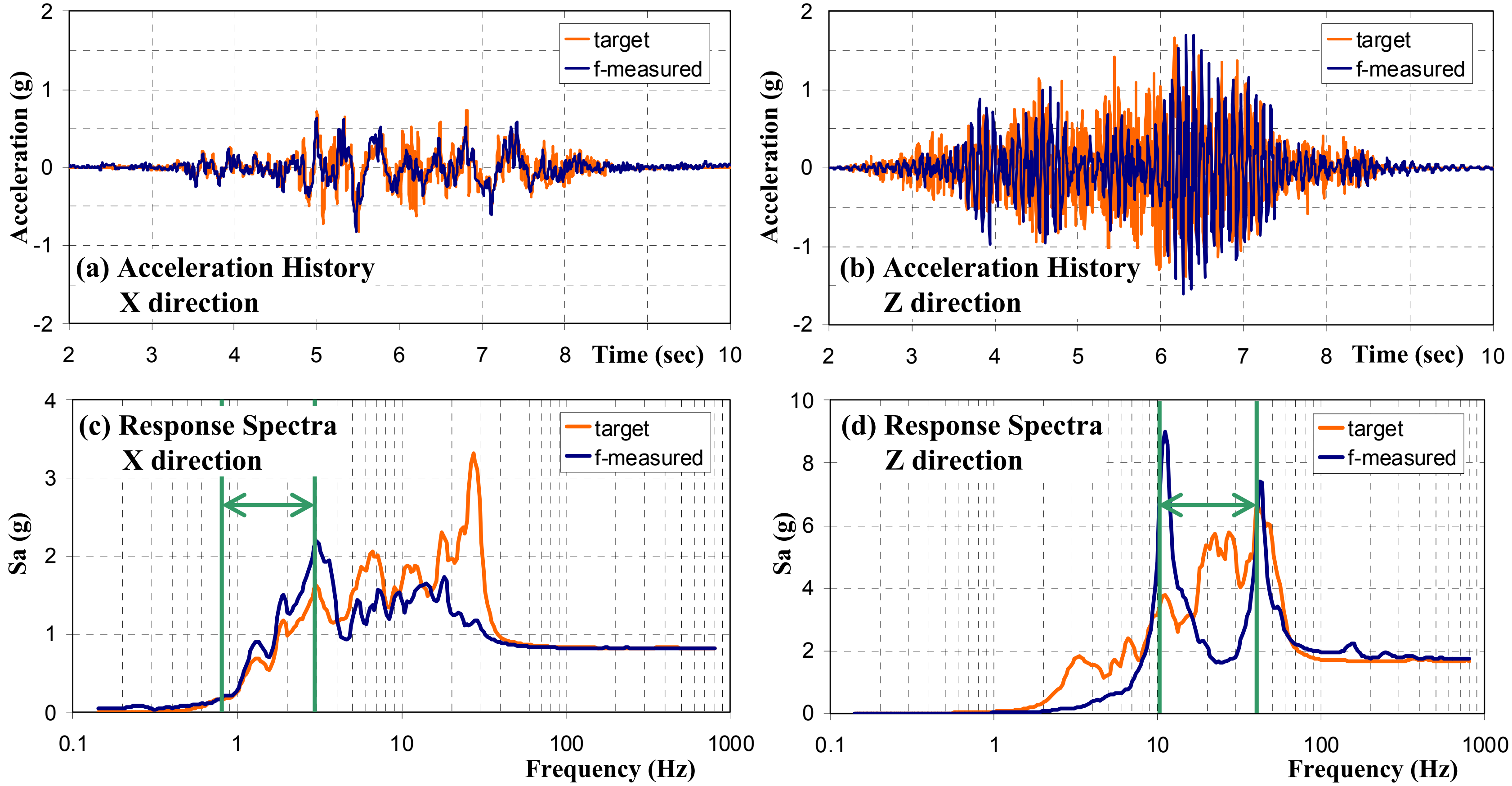

Figure 3.5 GM1 MCE level.

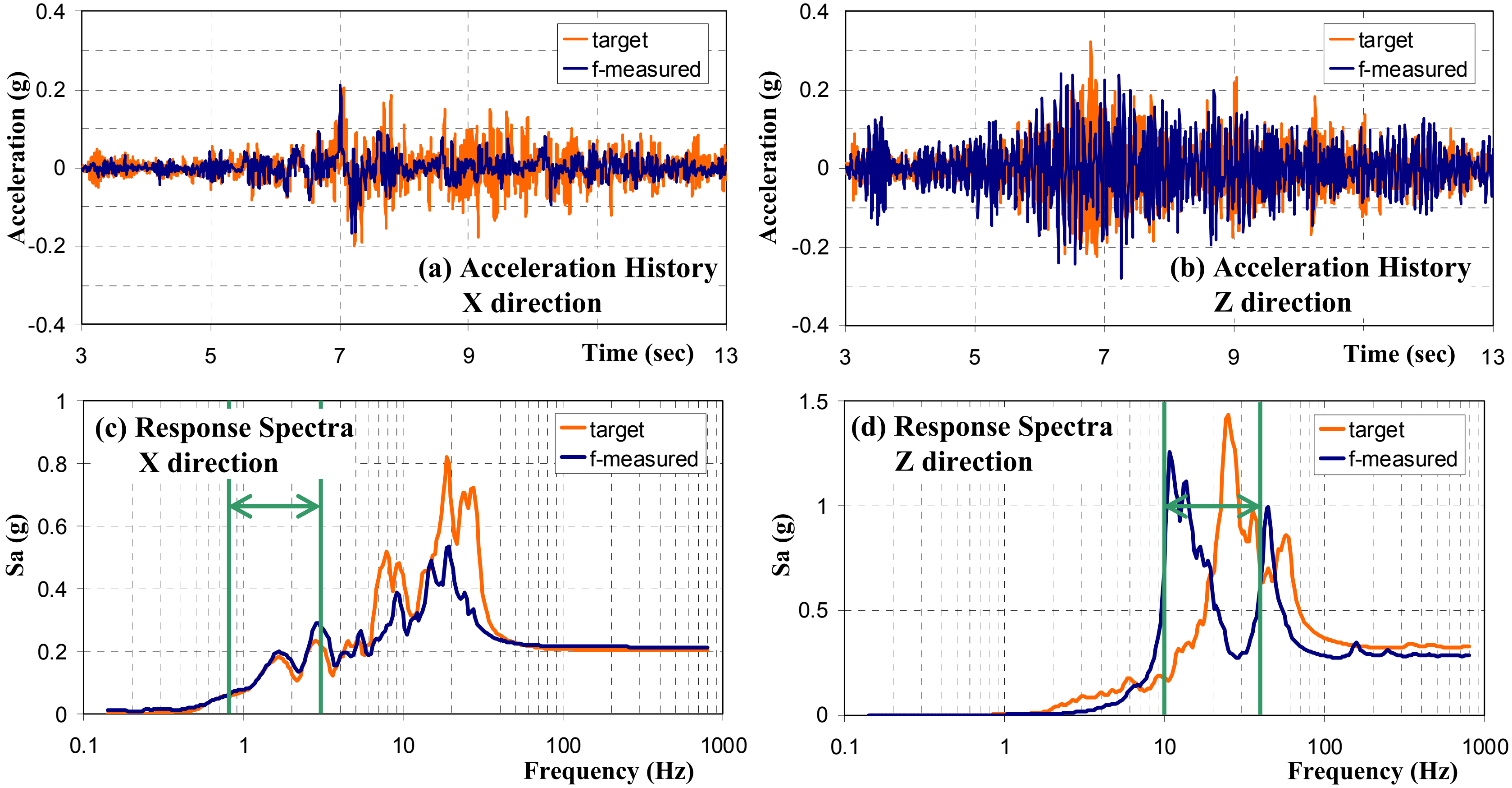

Figure 3.6 GM5 0.5-yield level.

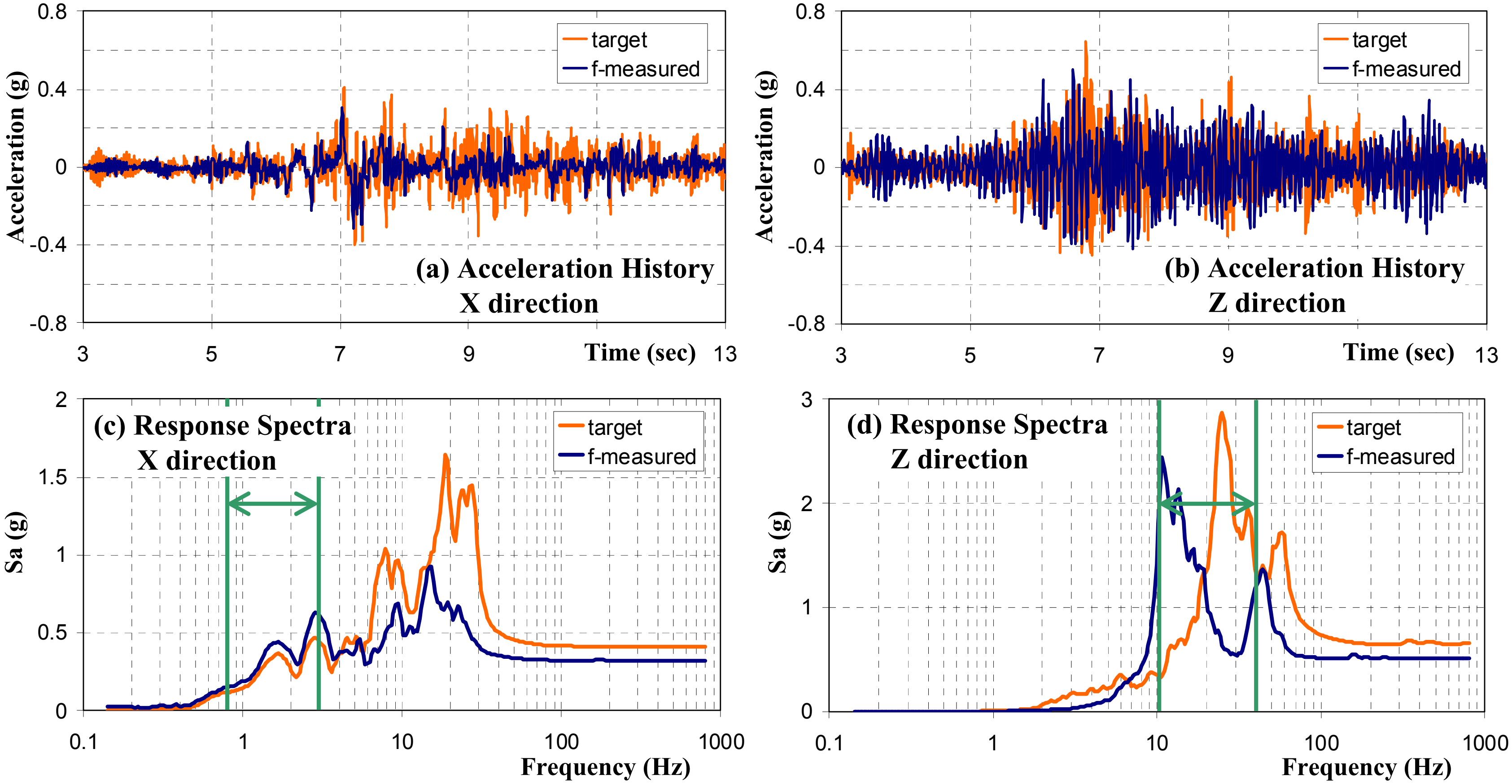

Figure 3.7 GM5 yield level.

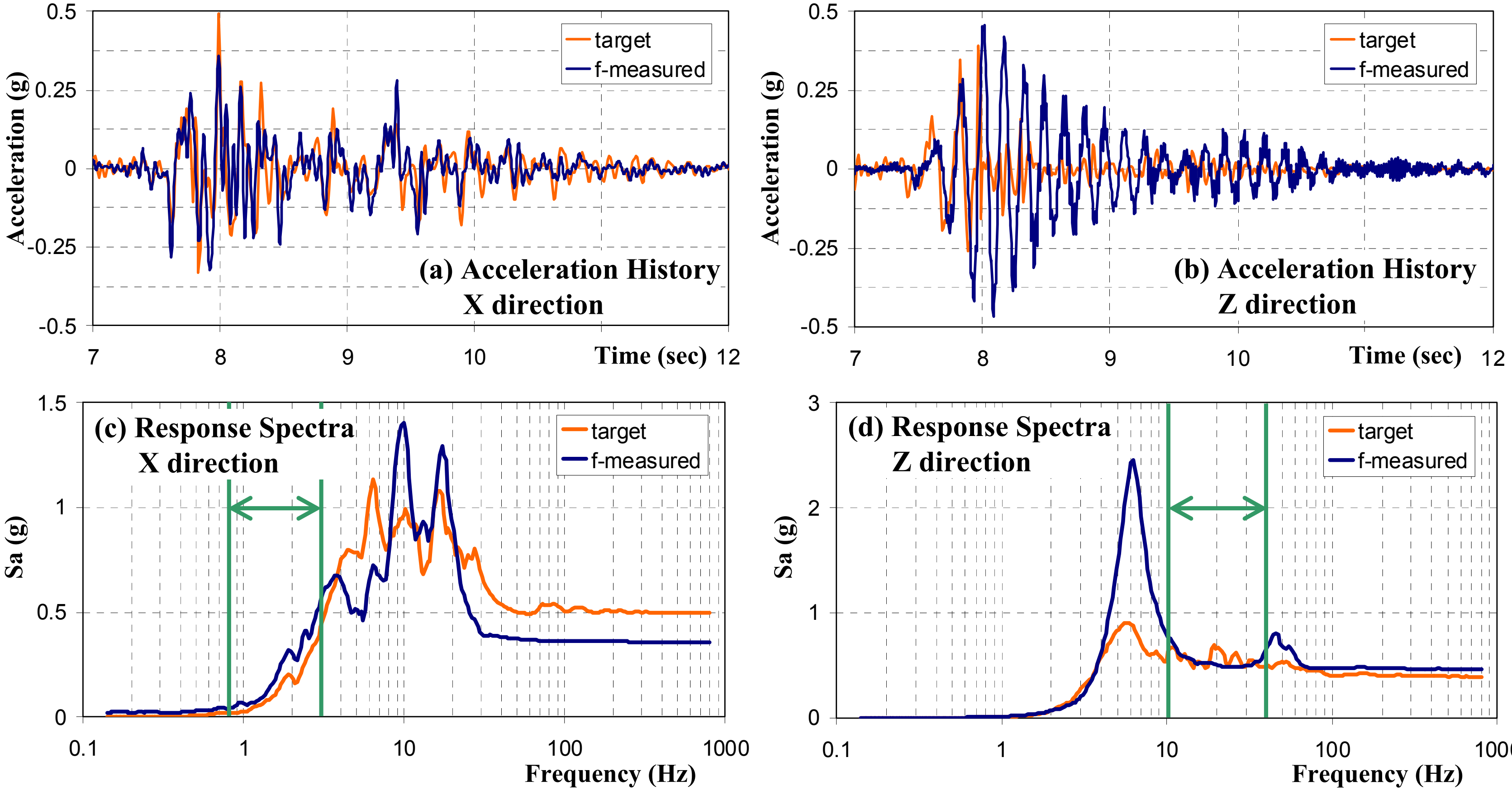

Figure 3.8 GM7 0.5-yield level.

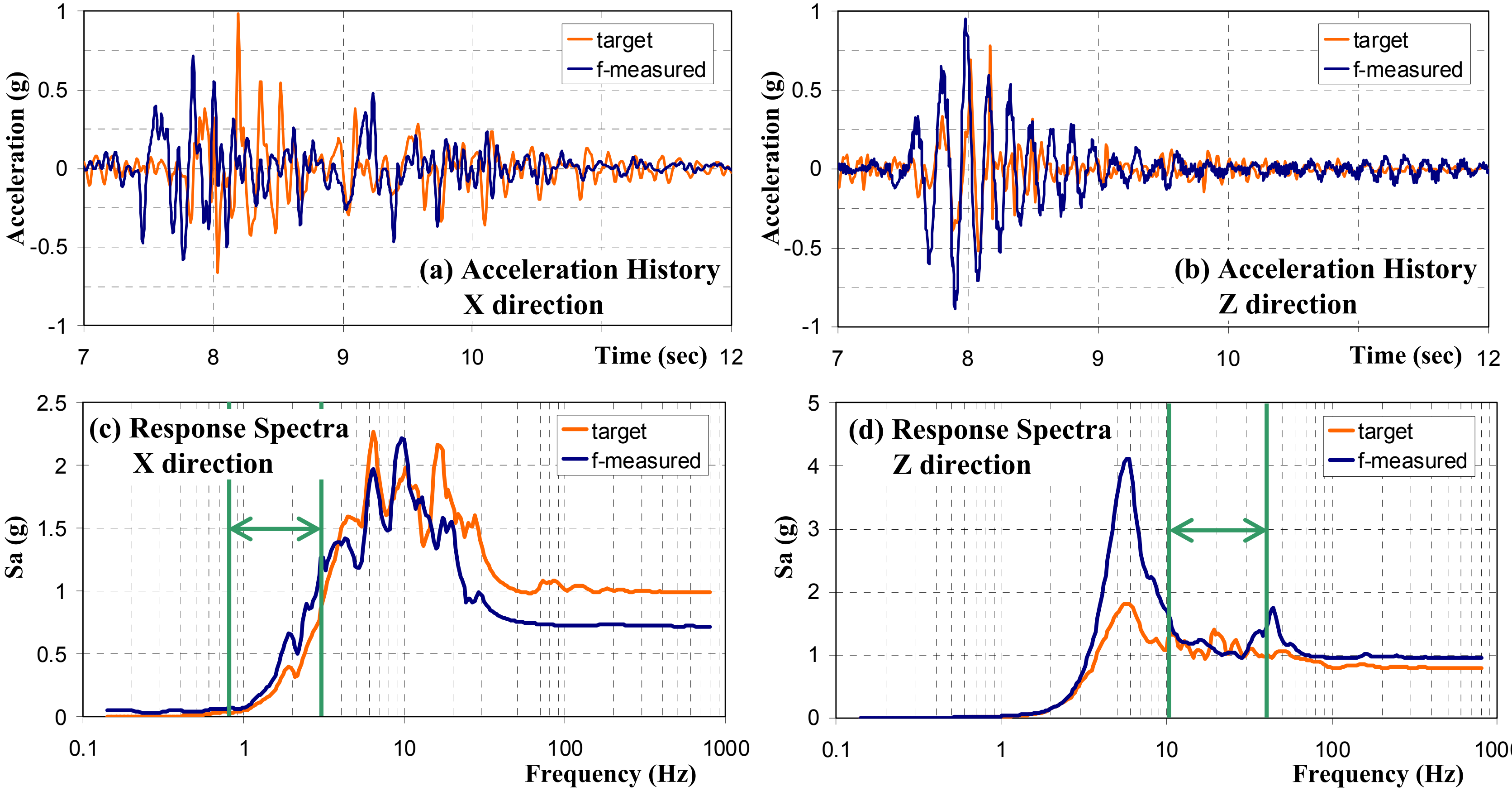

Figure 3.9 GM7 yield level.

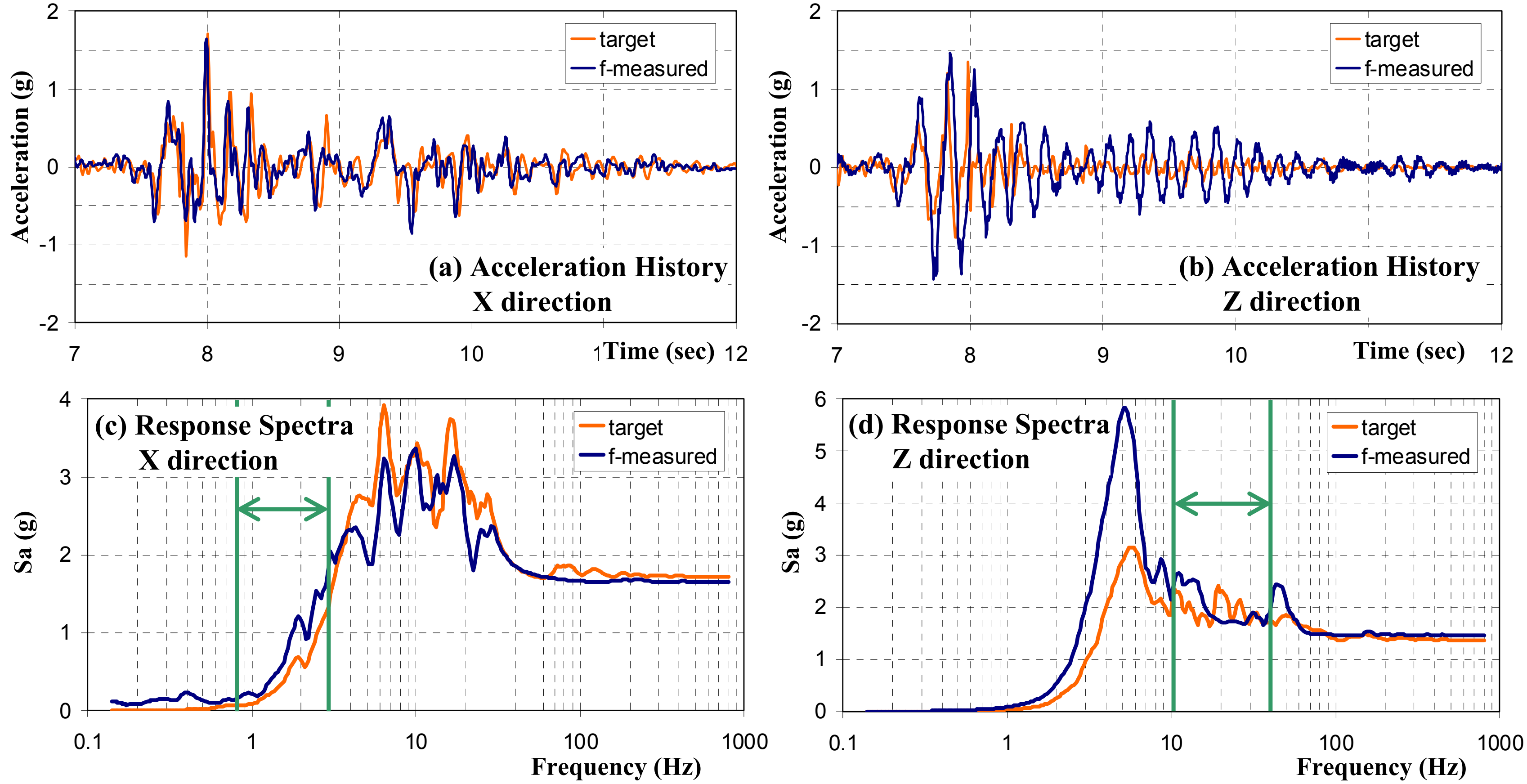

Figure 3.10 GM7 MCE level.

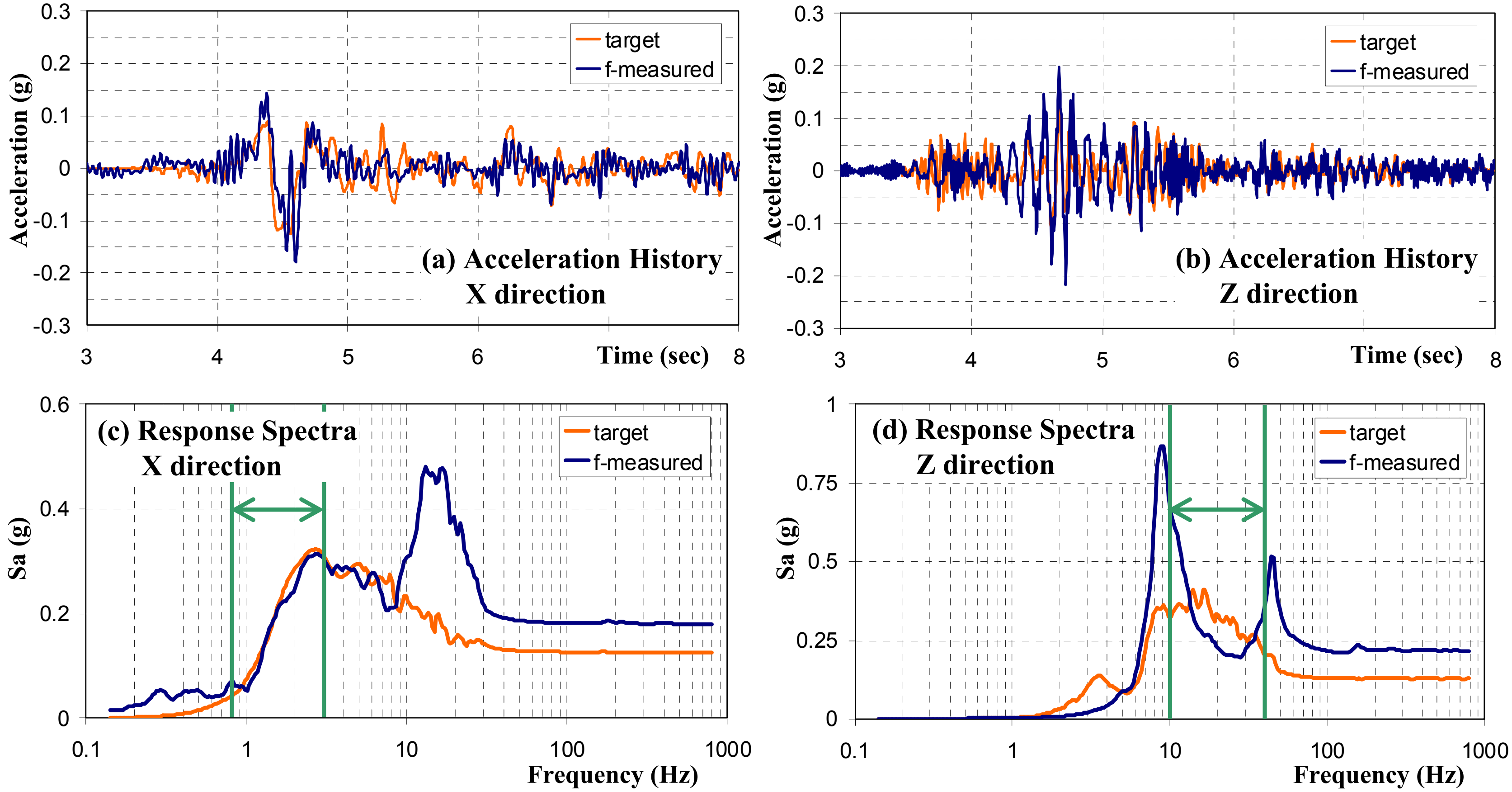

Figure 3.11 GM9 0.5-yield level.

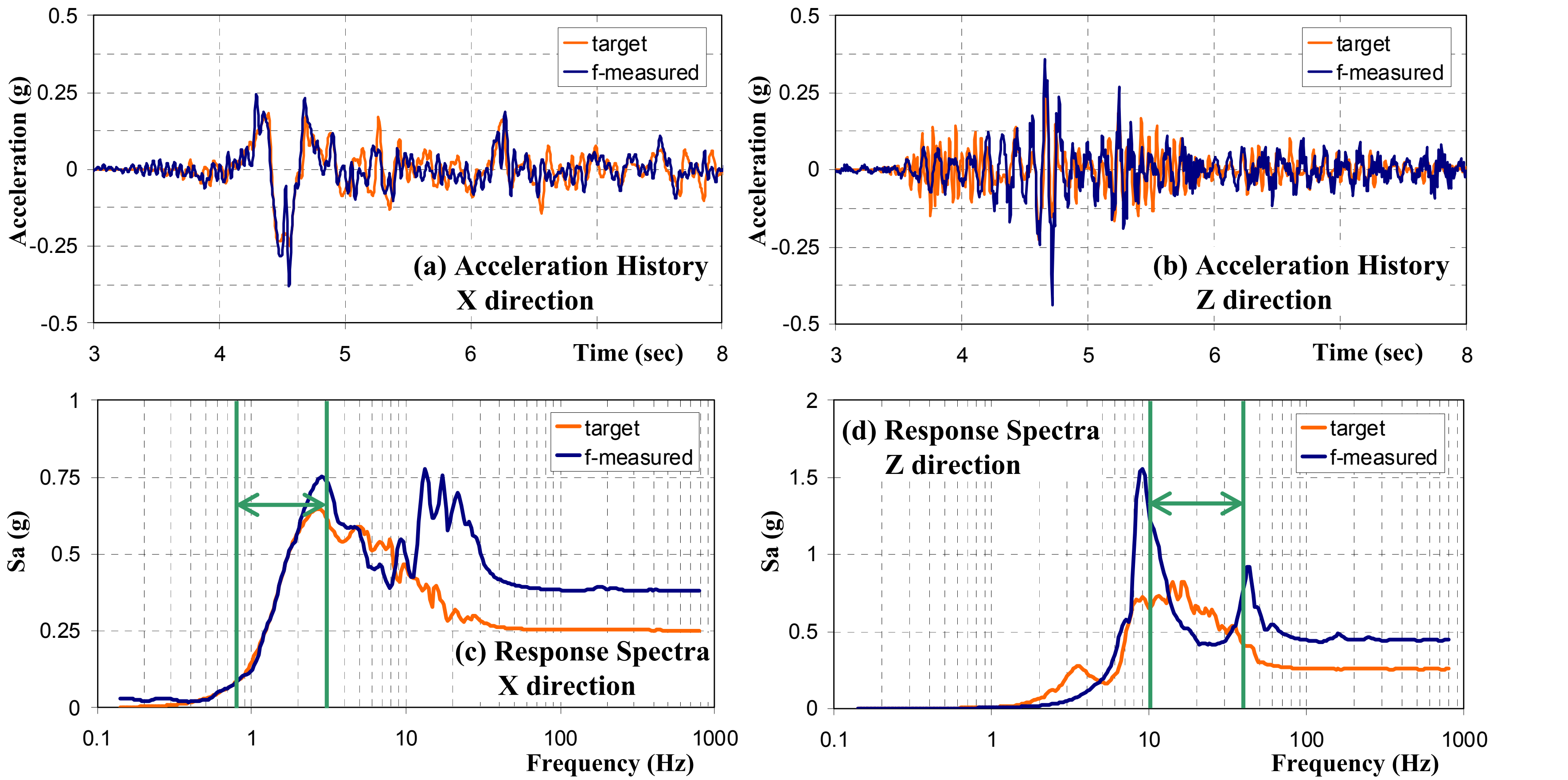

Figure 3.12 GM9 yield level.

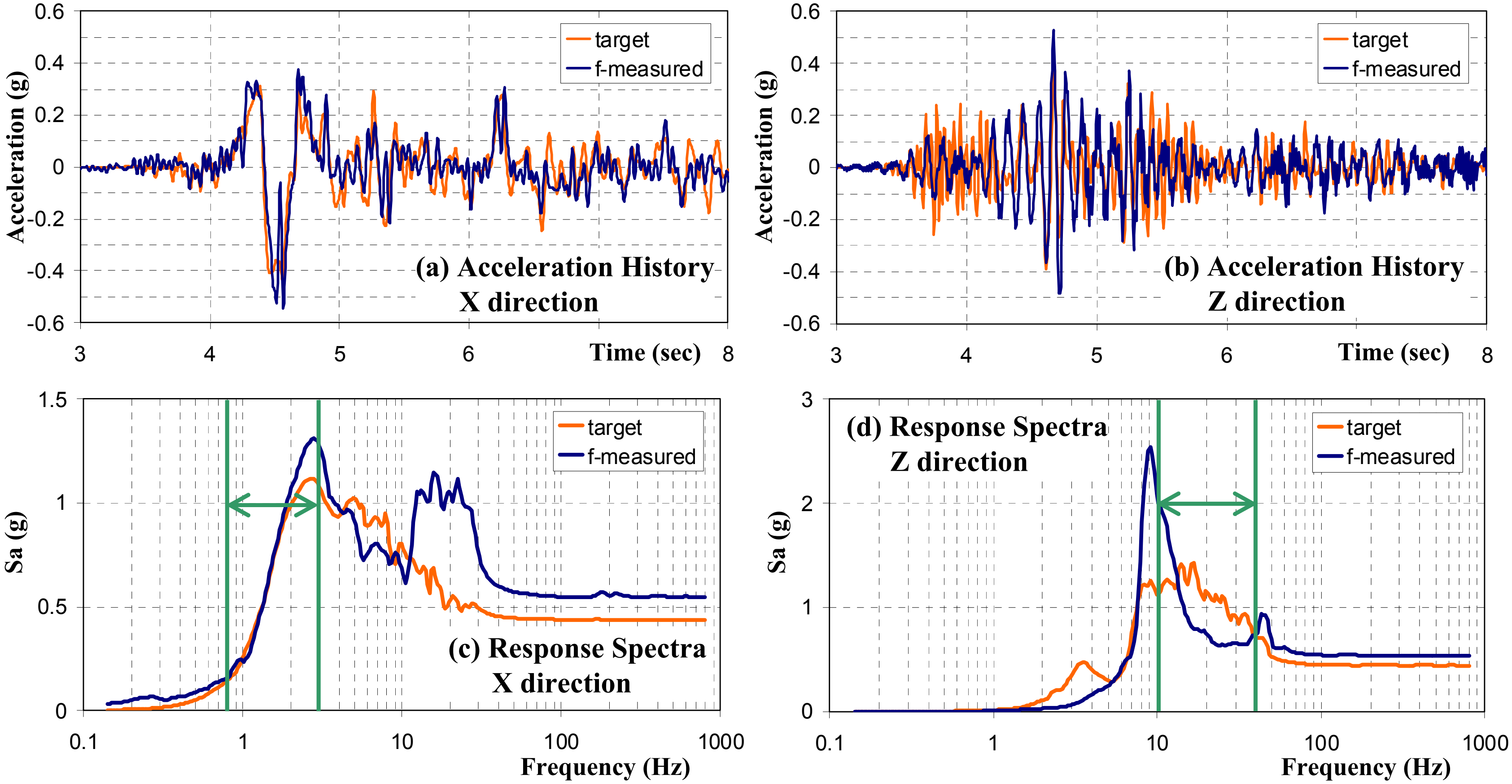

Figure 3.13 GM9 MCE level.

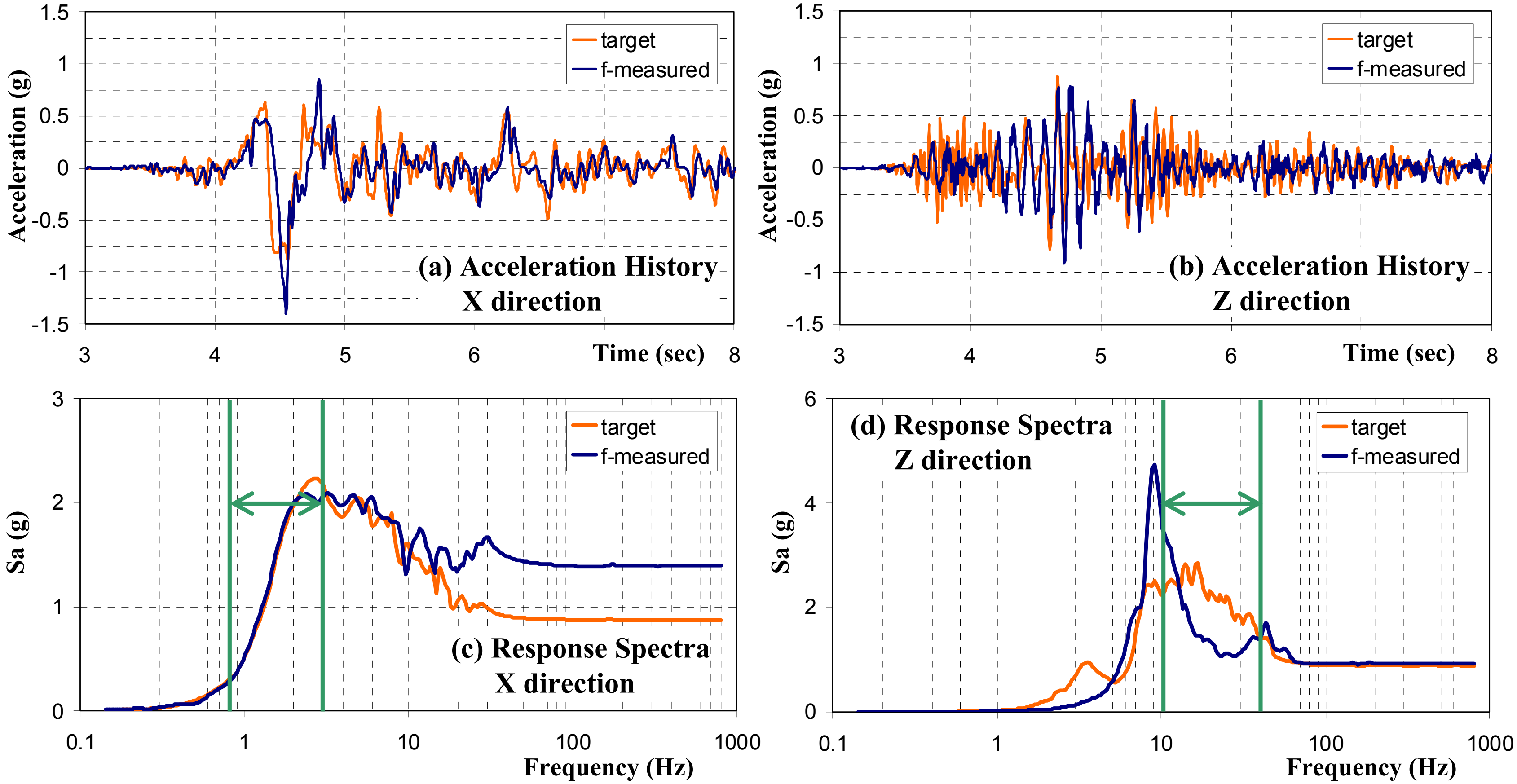

Figure 3.14 GM9 2-MCE level.

3.3.4 Further Discussion about GM7

After the completion of the fidelity tests, MCE level was determined to be the highest intensity level that could be applied with acceptable shaking table performance. This determination was based on the following calculations. The capacity of a vertical actuator is given as 77 kips (342.5 kN). There are four vertical actuators that should be able to resist (a) the vertical force due to vertical acceleration applied on the shaking table and test set-up and (b) the vertical force due to horizontal acceleration of the test set-up. It is noted that the damping force has been ignored for simplicity. The vertical force mentioned in (a) above is expressed as $(m_t a_t + m_s a_s)$, where m_t, m_s, a_t, and a_s are the shaking table mass, test set-up mass, vertical acceleration measured on the shaking table, and vertical acceleration measured on the mass blocks, respectively. This vertical force in (a) can be approximately expressed as $(m_t + m_s)a_t$ for all four vertical actuators because $a_t \approx a_s$ in most cases. On the other hand, the vertical force mentioned in (b) above is expressed as $\pm m_s a_s h/2l$, where h and l are the height of the C.G. [9 ft (2.74 m)] and the arm length between the opposite two pairs of the vertical actuators [17 ft (5.18 m)]. Therefore, two different equations can be used to determine the axial force demand of each vertical actuator.

$$P = (m_t + m_s)a_t/4 + m_s a_s h/2l \tag{3.1a}$$

$$P = (m_t + m_s)a_t/4 - m_s a_s h/2l \tag{3.1b}$$

Figure 3.15 shows the history of the axial forces calculated using these equations; note that both equations exceed the actuator force limit of 77 kips (342.5 kN) during short durations.

Since the forces are not obtained as a result of direct measurements but through calculations, the exceedance of the actuator force limits is further validated through an alternative calculation. Considering the shaking table weight is about 100 kips (445 kN), it is reasonable to accept that the acceleration limit of the empty shaking table (i.e., without any test specimen) is about 3*g* (precisely, $77\times 4/100 = 3.08g$). The total fidelity test set-up and shaking table weight is 218 kips (970 kN). Therefore, the maximum achievable vertical acceleration is $77\times 4/218 = 1.41g$. Figure 3.16 shows this limit and the acceleration history of each vertical actuator. Note that the actuators on the north side (V2 and V3) tend to have larger acceleration values than those on the south (V1 and V4), but both pairs exceed the average limit of 1.41*g*.

Although the calculated forces and measured accelerations of the individual actuators are slightly higher than the indicated limits for very short durations of time, the average measured accelerations of all four vertical actuators are below the limit. Figure 3.17 compares the average vertical acceleration history of the four actuators below the table and that measured on the east and west sides on the shaking table (accelerometers in Figure 3.3). The plotted time histories are slightly below the shaking table limits by a small margin. Hence, for good performance of the shaking table in this study, the MCE of GM7 for the specified mass and C.G. height of the test specimen is considered as the maximum excitation level that can be applied. Note that all the vertical acceleration data used in Figures 3.15 to 3.17 were filtered; the filter range was [0.01, 40] Hz.

Based on the results of the fidelity tests:

- The performance of the UC-Berkeley shaking table is acceptable to test the proposed mass and C.G. height of the 1/4-scale test specimen. Therefore, the proposed testing regimen is feasible unless bigger mass or higher C.G is utilized.
- Among the four ground motions that were selected based on the analytical study, GM7 is the most suitable for dynamic tests with vertical excitation considering the shaking table characteristics.
- The GM7-MCE level is the highest level that was applied in the fidelity tests; the response spectra suggest that the shaking table performance is still acceptable. However, based on the measured vertical accelerations this intensity level was found to be near the limits of the shaking table. Hence, sufficient performance is not expected if a stronger excitation is applied, or if a bigger mass or higher C.G is utilized. Therefore, the GM7-MCE level and the fidelity set-up mass and C.G height are considered as defining the upper limit for the excitation and specimen configuration in this study.

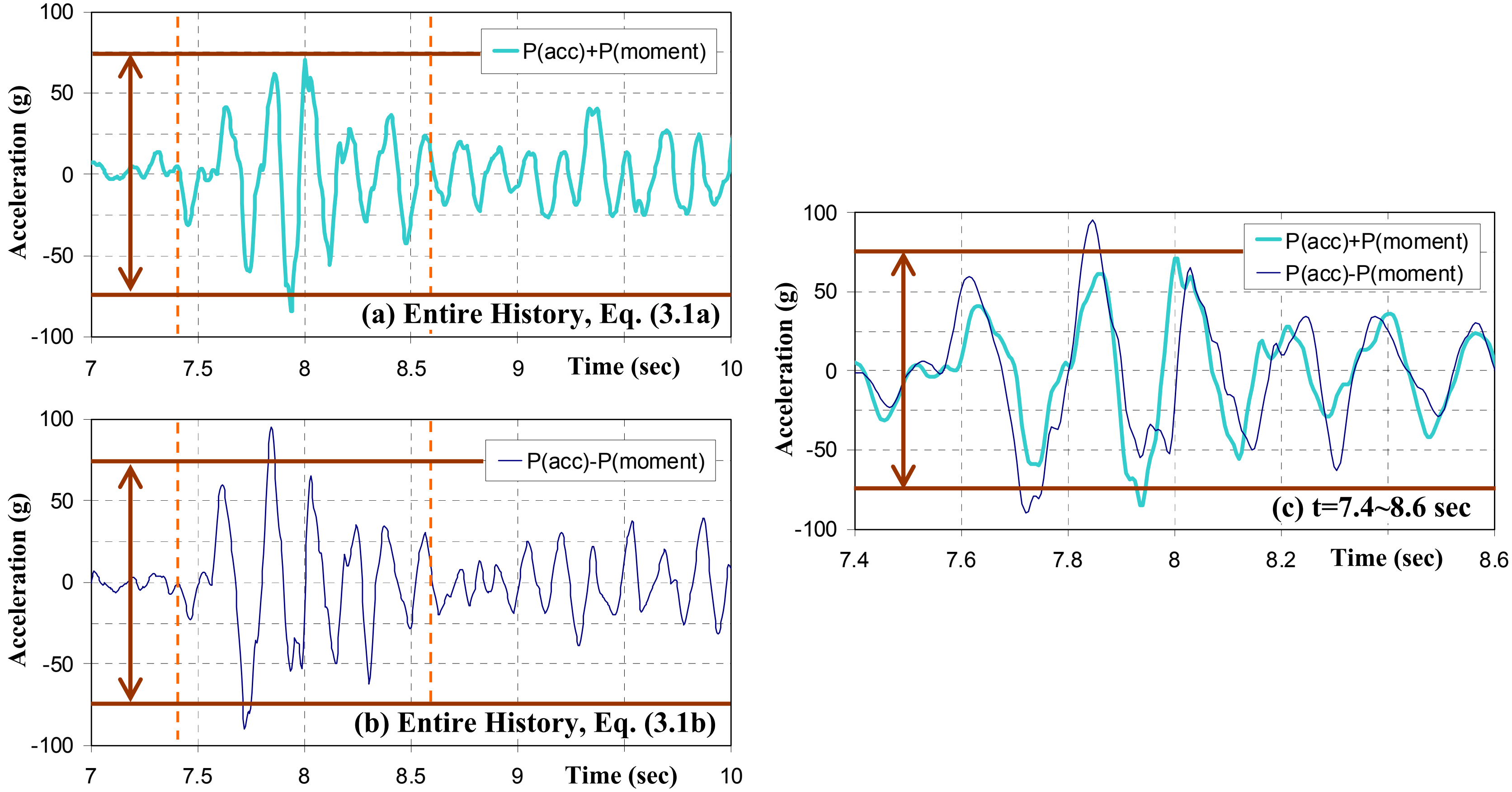

Figure 3.15 Axial force of a vertical actuator (GM7-MCE level).

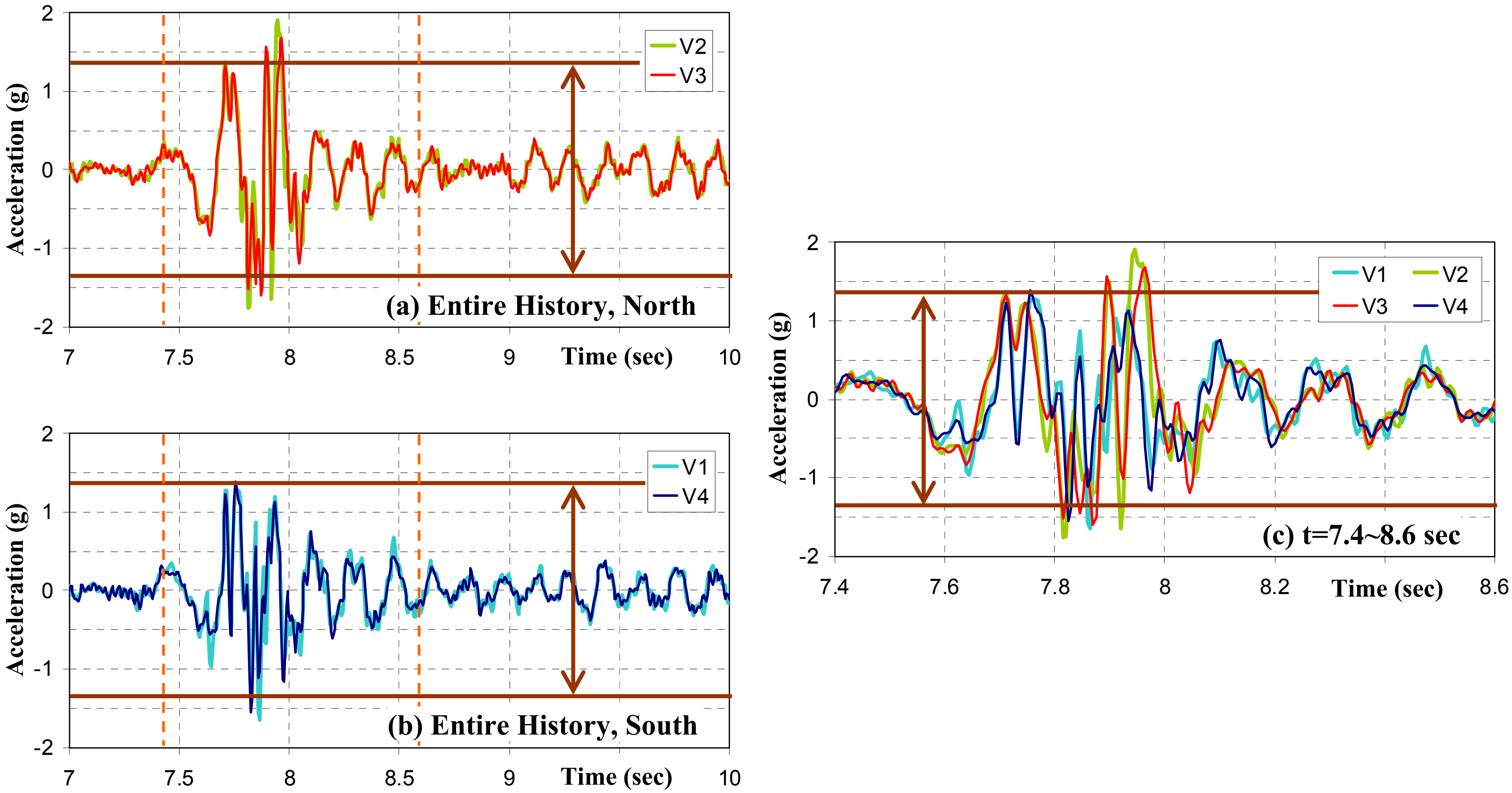

Figure 3.16 Vertical acceleration of all vertical actuators (GM7-MCE level).

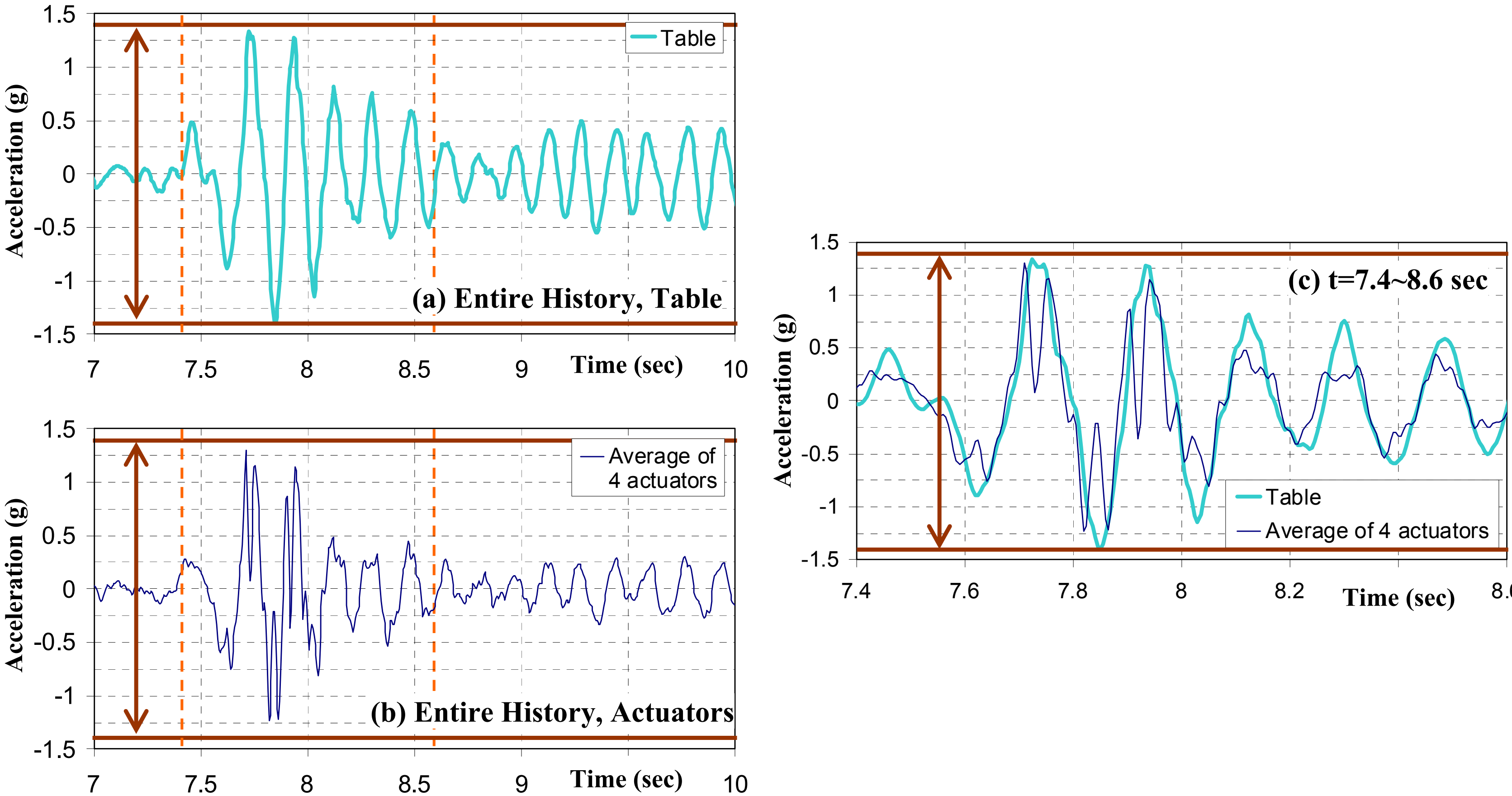

Figure 3.17 Average vertical acceleration measured (GM7-MCE level).

3.4 SPECIMEN DESIGN AND CONSTRUCTION

3.4.1 Design of Specimens

The Plumas-Arboga Overhead Bridge (PAOB) was selected as the prototype for designing the test specimens since its AR was closer to the desired value than that of ACB. Note that ACB was the prototype for the parametric study in Chapter 2 and not for the test specimen. In Section 2.2.2, the superstructure, original column cross section, and modified effective circular column cross section of the prototype were described. The circular cross-section was scaled down using a scale of 1/4 for the test specimen.

A column with a low AR (H/D) is expected to show shear or flexure-shear behavior. As discussed in Section 2.5.1, *Maxdcr* tends to increase as the AR decreases. To represent real bridge columns constructed in California, the test specimen was designed to have an AR of 3.5 for the dynamic tests.

3.4.1.1 Cross-Section Properties

The two specimens were identical in design except for the transverse reinforcement ratio. The comparisons of cross-section properties are summarized in Table 3.5. Section A is the cross section of the PAOB. Sections B and C are the cross sections of the first and second specimens (SP1 and SP2), respectively. These cross sections are illustrated in Figure 3.18

Confined concrete properties (peak stress and strain, $f'_{cc}, \varepsilon_{cco}$, respectively, and ultimate stress and strain, $f'_{ccu}, \varepsilon_{ccu}$, respectively) for each cross section were calculated based on Mander [Mander et al., 1988]. The M_{max} of each cross section was calculated assuming the yield strength of the longitudinal and transverse reinforcing bars f_y, f_{yt}, respectively, of 60 ksi (413.7 MPa); an AR of 3.5. V_s and V_c were calculated based on the ACI equations defined in Chapter 2.

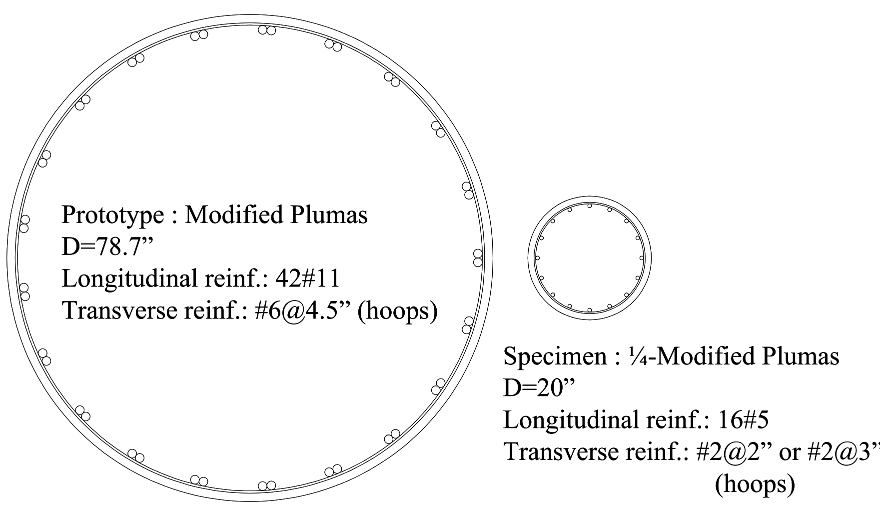

Figure 3.18 Prototype and test specimen column cross-sections (1 in. = 25.4 mm).

Table 3.5 specified the concrete contribution to the shear capacity, V_c, for the 'maximum tension' and 'gravity only.' The maximum tension was estimated as 1.98*g*, assuming the pseudo-acceleration of GM7-MCE level (corresponding to 114% of the original record) at 0.03 sec with 2% damping The vertical period, 0.03 sec, was calculated from the mass configuration in determined in Section 3.4.1.2 and from axial stiffness *EA/L*.

3.4.1.2 Mass and Mass Moment of Inertia

Mass at the top of the test specimen was determined to match 6.5% axial load ratio (ALR) as listed in Table 3.6. The mass moment of inertia (MMI) was calculated as 64.0 t-m^2 (47.2×10^3 slug-ft^2) by scaling MMI of the prototype column using similitude relationships; see Section 3.5.1.1. The MMI of the prototype column was determined such that the lateral period of the column matched the lateral period of the full-scale bridge system. Mass corresponding to 6.5% ALR was used in both of the single column and bridge system models. By using the same mass and matching the modal properties, the best resemblance between the prototype column in the bridge system model and that in the single-column model was achieved. Finally, the calculated MMI for the prototype column and the test specimen were 12.084×10^6 slug-ft^2 (16384 t-m^2) and 47.2×10^3 slug-ft^2 (64.0 t-m^2), respectively. A proper combination of concrete blocks, lead blocks, and steel beams on the test specimen ensured the desired weight for the intended ALR, MMI, and height of C.G.

Table 3.5 Cross-section properties.

Parameter	Unit	A. PAOB	B. SP1	C. SP2	A/B	A/C
Diameter, D	(in.) [(m)]	78.7 (2.0)	20 (0.508)	20 (0.508)	3.94	
Area, A	(in.^{2}) [(m^2)]	4869.5 (3.14)	314.2 (0.203)	314.2 (0.203)	15.50	
Height, H	(in.) [(m)]	275.6 (7.0)	70 (1.778)	70 (1.778)	3.94	
Longitudinal reinforcing bars		**42#11**	**16#5**	**16#5**	**-**	
Diameter, d_{sl}	(in.) [(mm)]	1.41 (35.8)	0.625 (15.875)	0.625 (15.875)	2.26	
Bar Area, A_{sl}	(in.^{2}) [(mm^2)]	1.56 (1007)	0.307 (197.9)	0.307 (197.9)	5.09	
Total Area, A_s	(in.^{2}) [(mm^2)]	65.52 (42310)	4.909 (3166.9)	4.909 (3166.9)	13.36	
Reinf. Ratio	[%]	1.348	1.563	1.563	0.862	
Transverse reinforcing bars		**#6@4.5 in.**	**#2@2 in.**	**#2@3 in.**	**-**	
Diameter, d_{sh}	(in.) [(mm)]	0.75 (19)	0.25 (6.35)	0.25 (6.35)	3.0	
Bar Area, A_{sh}	(in.^{2}) [(mm^2)]	0.44 (283.5)	0.0491 (31.68)	0.0491 (31.68)	9.0	
Spacing, s	(in.) [(mm)]	4.5 (114.3)	2 (50.8)	3 (76.2)	2.25	1.5
Vol. Reinf. Ratio	(%)	0.543	0.545	0.363	0.996	1.496
$A_v D/s, A_v = 2A_{sh}$	(in.^{2}) [(mm^2)]	15.39 (9929.2)	0.982 (623.4)	0.655 (415.6)	15.7	23.5
Confinement: f'_c = 4 ksi (27.58 MPa)						
f'_{cc}	(ksi)	4.98	5.02	4.68	0.992	1.064
f'_{ccu}	(ksi)	4.31	4.33	3.97	0.995	1.086
ε_{cco}	-	0.00446	0.00456	0.00371	0.978	1.202
ε_{ccu}	-	0.01187	0.01241	0.00961	0.956	1.235
Capacity (6.5% axial load)						
M_{max}	(k-ft) [(kN-m)]	15047.2 (20404)	233.0 (316.0)	230.3 (312.3)	64.57	65.33
V_s	(kip) [(kN)]	756.5 (3364.8)	46.5 (206.8)	31.0 (137.8)	16.27	24.42
$V_{c,\min}$ (max tension)	(kip) [(kN)]	307.7 (1368.8)	19.85 (88.29)	19.85 (88.29)	15.50	
$V_{c,\max}$ (gravity)	(kip) [(kN)]	709.0 (3153.4)	45.74 (203.45)	45.74 (203.45)	15.50	
$V_{n,\min} = V_s + V_{c,\min}$, $V_{n,\max} = V_s + V_{c,\max}$	(kip)	1064.2, 1465.5	66.35, 92.24	50.85, 76.74	16.04, 15.89	20.93, 19.10

Table 3.6 Mass of the one-quarter-scale test specimen.

Item	Unit	SP1 and SP2		
Diameter	(in.) [(m)]	20 (0.508)		
Area	(in.^{2}) [(m^2)]	314.2 (0.203)		
f_c'	(ksi) [(MPa)]	4.0 (27.58)		
$A_g f_c'$	(kip) [(kN)]	1256.8 (5590.0)		
Axial Load Ratio (ALR)	(%)	4.5	5.0	6.5
ALR× $A_g f_c'$	(kip) [(kN)]	56.6 (251.5)	62.8 (279.5)	81.7 (363.3)

3.4.2 Construction of Specimens

Two specimens were under construction from July 8 to July 28, 2010. The construction procedure included installing strain gages on the reinforcing steel bars, form-work, making reinforcing bar cages, placing the desired concrete mix, curing the cast concrete, stripping the forms, and finally transporting the specimen and attaching it to the shaking table. Detailed construction procedure and construction photographs are presented in Appendix B.

3.4.3 Material Properties

For reliable estimation of the capacity of test specimens, material properties were obtained by conducting material tests for standard concrete cylinders and samples of the reinforcing steel bars. These material tests were conducted in the material and structure laboratory, Davis Hall, UC-Berkeley.

3.4.3.1 Concrete

The concrete mix was specified as normal weight concrete with the 28th-day design strength of 4 ksi (27.58 MPa). Detailed concrete mix design specifications are presented in Table 3.7. A total of forty-eight 6 in.×12 in. concrete cylinders were prepared at the time the columns were cast. Three cylinders were tested on the 7th, 14th, 20th, and 28th days, the day of preliminary stiffness tests (72nd day), the days of tests (93rd and 111th days), and the 406th day, as specified in Table 3.8, where μ and σ represent the mean and standard deviation, respectively. Figure 3.19 presents the strength maturity curve based on these cylinder tests. The strength gradually increased until the 28th day, and the mean strength reached 85% of the design strength; however, the second and third cylinders on the 72nd day and all the cylinders on the 93rd days had relatively lower strength. The strength from these cylinders was significantly low even compared to expected values based on the linear interpolation between the mean values on the 28th and 111th days. Possible errors in concrete sampling and testing of these cylinders are suspected in causing this discrepancy.

Table 3.7 Concrete mix specifications.

28^{th} day strength (psi)		4.0 (27.58 MPa)
Cement		ASTM C-150 TYPE II
Fly ash		ASTM C-618 CLASS F 15%
Admixture (water reducer)		ASTM C-494 TYPE A
Cementitious sacks/yd^3		5.00
Maximum size aggregate (in.)		3/4 (19 mm)
Slump (in.)		4 (102 mm)
Water/cement ratio		0.602

Table 3.8 Strength properties of concrete.

Day	Compression strength (psi)	Tensile strength (psi)
7^{th} (Aug. 4, 2010)	1429, 1471, 1712	180, 154, 195
	μ=1537, σ=152.6	μ=177, σ=20.7
14^{th} (Aug. 11, 2010)	2009, 2447, 2104	258, 238, 242
	μ=2187, σ=230.6	μ=246, σ=10.3
20^{th} (Aug. 17, 2010)	2985, 3063, 2943	265, 265, 257
	μ=2997, σ=61.0	μ=262, σ=4.5
28^{th} (Aug. 25, 2010)	3572, 2978, 3657	361, 326, 347
	μ=3402, σ=370.0	μ=345, σ=17.3
72^{nd} (Oct. 8, 2010)	3897, 3057, 3196	N/A
	μ=3383, σ=450.6	
93^{rd} (Oct. 29, 2010)	2909, 3365, 3435	278, 307, 263
	μ=3236, σ=285.6	μ=283, σ=22.4
111^{th} (Nov. 16, 2010)	4108, 4144, 3759	336, 356, 368
	μ=4004, σ=212.5	μ=353, σ=16.1
406^{th} (Sep. 7, 2011)	4669, 4750, 4693	N/A
	μ=4704, σ=41.7	

The American Society for Testing and Materials (ASTM) (ASTM C31 [2010]) procedure for casting of concrete cylinders and testing was followed in this study. According to ASTM C172 [2010], it is important to obtain a sample of concrete that is representative of the concrete in the truck mixer and this sample should be obtained from the middle of the truck load. At least three portions of discharge are necessary to obtain a representative sample, since it is assumed that the first or last discharge portions from the load will not provide a representative sample. Using the last discharge might have caused the large deviations shown in Table 3.8 and Figure 3.19. In addition, the strength values on the 93^{rd} day are clustered between 2.9 and 3.5 ksi. Their standard deviation was not as large as those on the 28^{th} and 72^{nd} days. This implies that there is a high probability there was a mistake in testing the cylinders on the 93rd day. Of course, the possibility of choosing three low-strength cylinders cannot be ignored.

A sample stress-strain relationship that was obtained from one of the tested cylinders is shown in Figure 3.20. From this figure, the obtained compressive strength is 3.9 ksi (26.89 MPa), the corresponding peak strain is 0.35%, and the initial tangent modulus is 2500 ksi (17.24 GPa). The secant modulus, which connects the origin and the point of $0.4 f_c'$, is 2330 ksi (16.06 GPa), as specified in Figure 3.20.

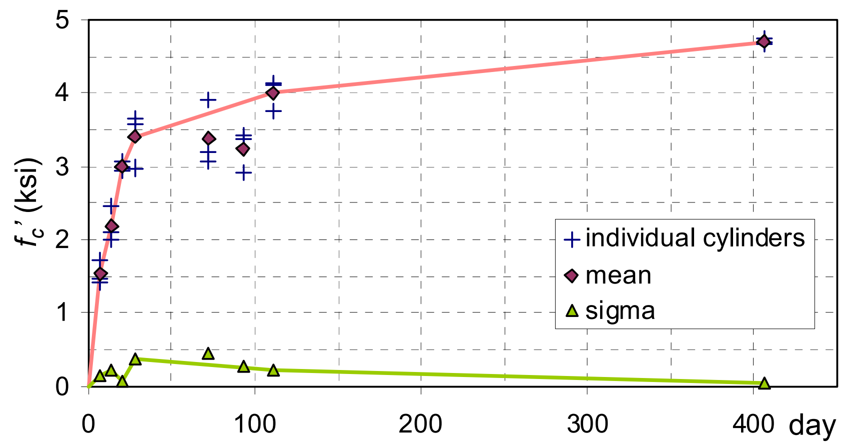

Figure 3.19 Concrete strength maturity curve.

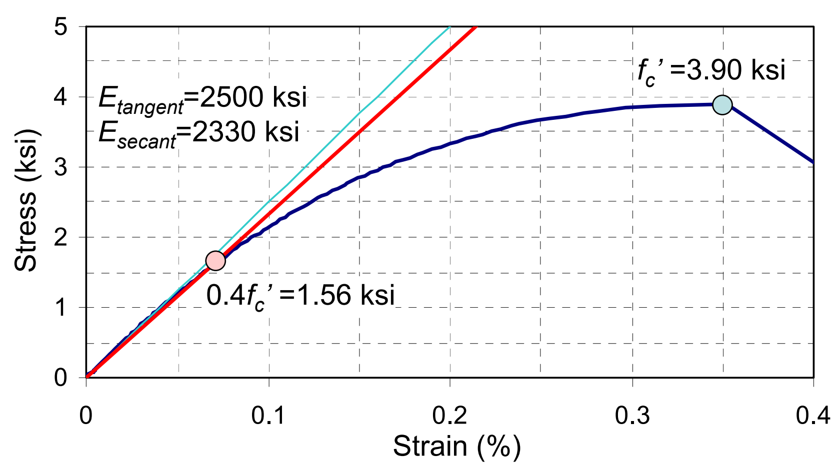

Figure 3.20 Example concrete stress-strain relationship on the 72nd day (1st cylinder).

3.4.3.2 Steel Reinforcing Bars

The strength and elastic modulus of reinforcing bars had to be tested to estimate the response of the test specimen. Both longitudinal and transverse (i.e., hoops) steel reinforcing bars of the columns are tested. Number 5 bars were used as longitudinal reinforcement. To check their properties, these bars were sampled from the test specimens after testing. Since the middle of the test specimen was not damaged, the portions of the longitudinal bars in the middle of the test specimen remained elastic, allowing them to be tested. A total of four tensile tests were conducted on September 28, 2011. In addition, four tensile tests were conducted on May 27, 2010, to confirm the properties of the #2 reinforcing bars used as hoops, as shown in the photograph of Figure 3.21(d). Figure 3.21(a) and (b) show the obtained stress-strain relationships of the longitudinal and transverse reinforcement, respectively. One linear variable differential transformer (LVDT) was used to measure the displacement between two points with 2 in. (51 mm) spacing. For the #2 bar, a strain gage was placed to measure strain at one point in the middle of the LVDT gage length. As shown in Figure 3.21(b), both stress-strain relationships are very similar. However, as shown in Figure 3.21(c), the strain from the LVDT had a slightly steeper slope and smaller strain after 5%-strain, which corresponds to 87 ksi (599.84 MPa) in stress. This is due to the difference in measuring the strain, i.e., the strain from the strain gage near the necking point is larger than that obtained by the LVDT averaging over its 2 in. (51 mm) gage length. Table 3.9 summarizes the properties of both reinforcing bars. The yield stress was calculated based on the 0.1% offset method [ASTM Standard E8/E8M, 2009].

Table 3.9 Average properties of the reinforcing bars.

Property	Longitudinal bars #5, from LVDT	Transverse bars #2, from LVDT
Yield stress, f_y (ksi)	77.54	63.13
Ultimate stress, f_u (ksi)	105.06	90.25
Yield strain, ε_y (%)	0.27	0.22
Ultimate strain, ε_u (%)	12.04	11.64

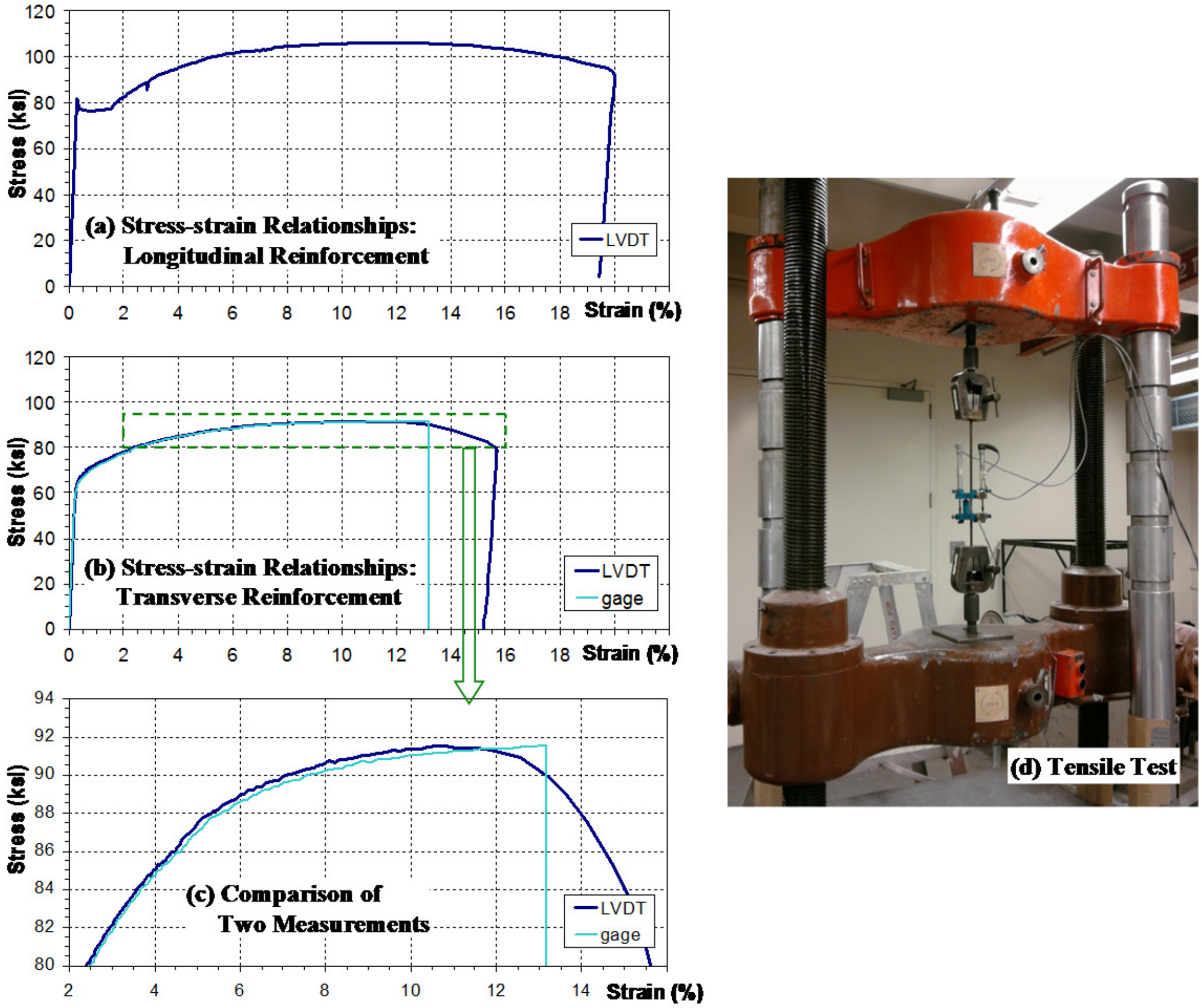

Figure 3.21 Testing longitudinal and transverse reinforcing bars (sample results and set-up).

3.5 EXPERIMENTAL SET-UP AND TEST PROGRAM

3.5.1 Test Set-Up

Two shaking table tests were conducted at the Richmond Field Station Earthquake Simulator, at Richmond Field Station of UC-Berkeley. As shown in Figure 3.22(a), the specimen was placed at the center of the shaking table using a thick large transition steel plate, 8 ft×8 ft×3.35 in. (2.44 m×2.44 m×85 mm), for better shaking table performance and control purposes, which was critical due to weight of the specimen. To prevent collapse and avoid sliding of the specimen during testing, steel chains shown in this figure were connected to the prestressing rods for the top concrete blocks.

3.5.1.1 Dimensional Analysis

As mentioned previously, the test specimens were scaled from the prototype column by using a length scale of 4. Keeping the accelerations and stresses the same for the prototype and the scaled columns led to the following scale factors for time, mass, and MMI.

Length: $L = 1/4$

Acceleration: $LT^{-2} = 1$, therefore, $T = 1/2$

Stress: $ML^{-1}T^{-2} = 1$, therefore, $M = 1/16$

MMI: $I = ML^2$, therefore, $I = 1/256$

where T and M are the scale factors for time and mass, respectively.

3.5.1.2 Column

The test columns were 20 in (508 mm) in diameter and 70 in (1778 mm) in height. For longitudinal reinforcement, 16#5 bars were used for both specimens, and the longitudinal reinforcement ratio was 1.563%. For transverse reinforcement, #2 hoops were used where the first specimen (SP1) had 2 in (51 mm) spacing; the second specimen (SP2) had 3 in. (76 mm) spacing. For both specimens, the spacing was uniform over the entire column height. The volumetric ratio of the transverse reinforcement was 0.545% for SP1 and 0.363% for SP2 as listed in Table 3.5. The LRFD Bridge Design Specifications (BDS) by AASHTO [2012] provide the required minimum volumetric ratio as 0.468%. Therefore, SP1 satisfied the BDS; SP2, however, did not satisfy the BDS in terms of the transverse reinforcement. Finally, the weight of the column, except for the footing, was about 3.9 kips (17.35 kN); see Appendix C for a complete set of drawings of the test specimens.

3.5.1.3 Base Plate, Footing, and Top Steel Beams

The 8 ft×8 ft×3.35 in. (2.44 m×2.44 m×85 mm), base steel plate was designed to place the test specimen at the center of the shaking table. Nine 2.5 in. (64 mm) holes were drilled to connect the plate to the shaking table, and 16 7/8 in. (22 mm) tap (threaded) holes were drilled to connect the load cells to the plate; see Appendix C for design details of the base plate.

The 60 in.×60 in.×18 in. (1524 mm×1524 mm×457 mm) footing was designed to fix the column to the shaking table and was reinforced with #6 deformed bars in both longitudinal directions and #3 ties in the transverse direction. The footing was set on four load cells, one at each corner. The footing weight was about 5.7 kips (25.35 kN); see Appendix C for footing details.

The top steel beams were designed to resist prestressing forces and to support inertia forces of the mass blocks (which consisted of two concrete blocks and 72 lead blocks). The four beam cross sections, HSS 20×12, were designed to have small deflection and enough flexural capacity to resist the bending moment produced in the tests. Figure 3.23 shows the layout of these four beams and the number of attached lead blocks; see Appendix C for more information on the design of steel beams. The lead blocks were hung by four prestressing rods fixed at the tip of smaller HSS pipes, which were welded to the top of the four steel beams; see Figure 3.24..

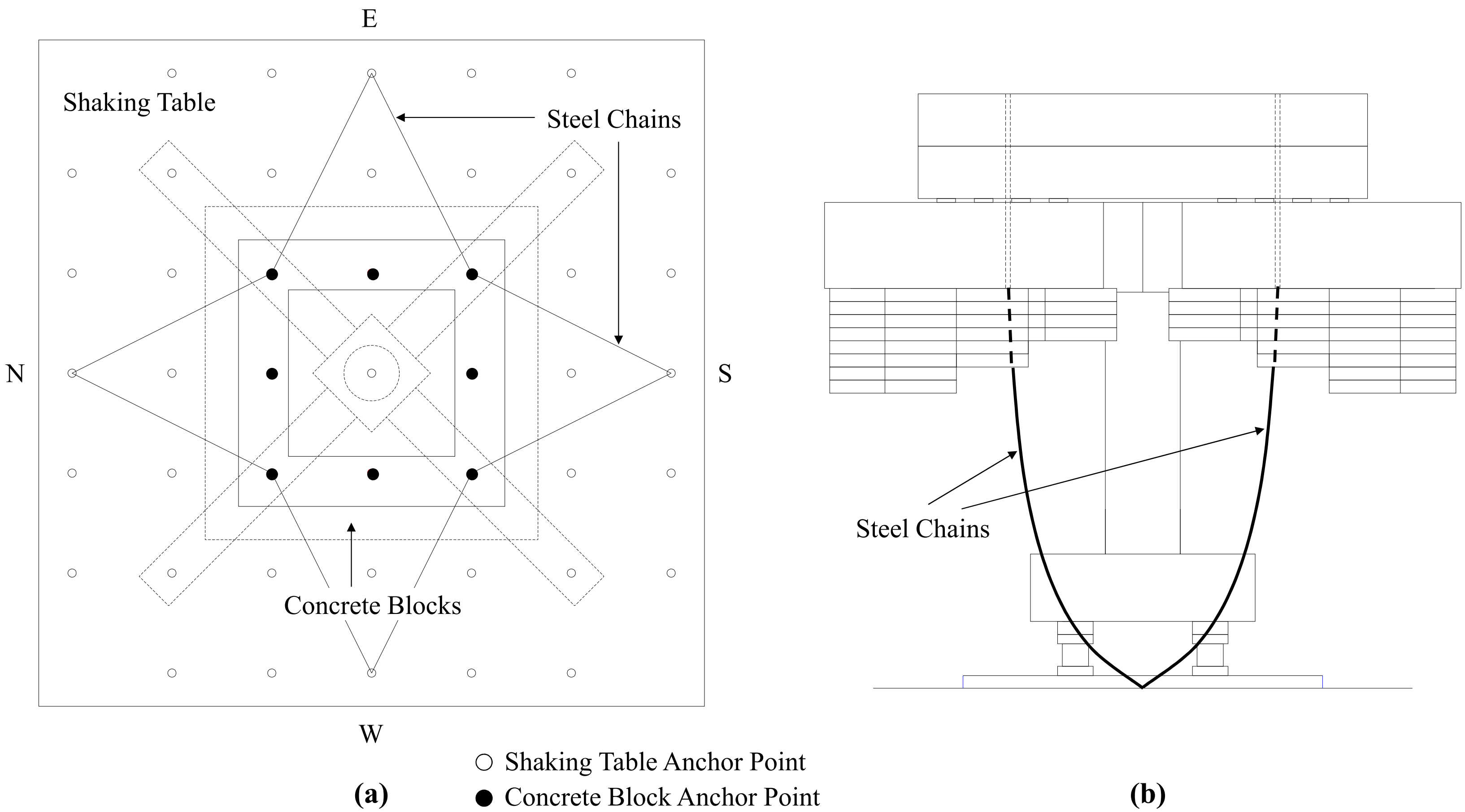

Figure 3.22 Specimen location on the shaking table and the catching safety system: (a) plan view, and (b) elevation view.

3.5.1.4 Mass Blocks

As explained in Section 3.4.1.2, the target ALR was 6.5%, but the additional weight of steel beams and miscellaneous items caused a slightly heavier gravity load on the column. Finally, 6.8% ALR, i.e., about 85.6 kips, was achieved by two concrete blocks and 72 lead blocks on the column (Figure 3.23), a monolithically case top block with the column, and the tie assembly. The concrete blocks were identical in dimension and weight: each block was 10 ft×10 ft×14 in. (3045 mm×3048 mm×356 mm) in dimensions and weighed about 16.5 kips (73.4 kN), i.e., the total of weight of the concrete blocks was 33 kips (146.8 kN). The lead blocks were also identical; each lead block was 27 in.×21 in.×3.5 in. (686 mm×533 mm×89 mm) in dimension and weighted 0.5 kips (2.22 kN), i.e., the total weight of the lead blocks was 36 kips (160.1 kN). As a result, the center of gravity (C.G.) was about 8.5 ft (2591 mm) above the shaking table, as dictated by the test set-up shown in Figure 3.24.

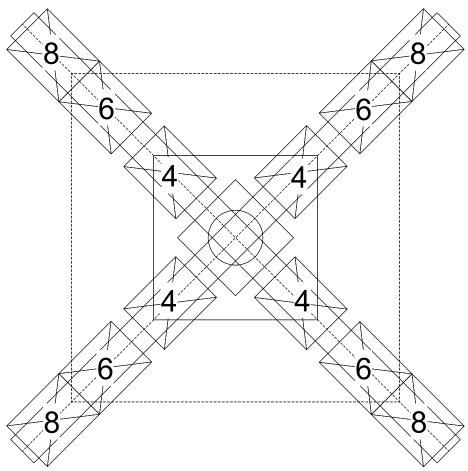

Figure 3.23 Final mass configuration.

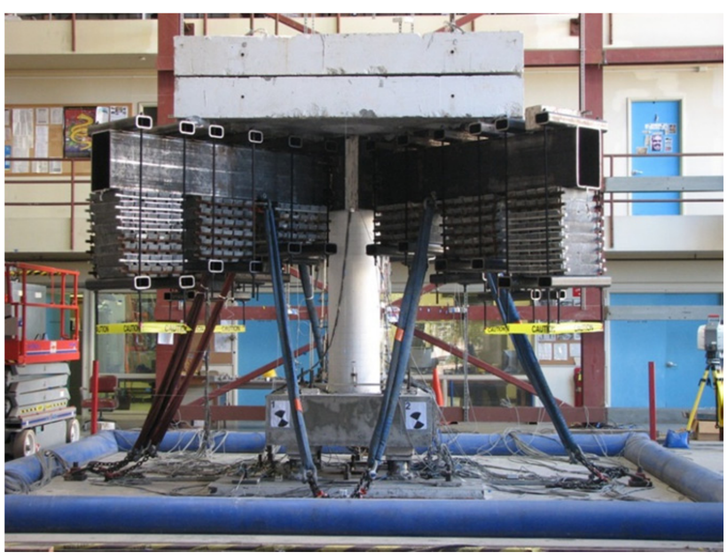

Figure 3.24 Final test set-up.

3.5.2 Instrumentation

A total of 137 channels were used for each shaking table test and were distributed as follows:

- 16 channels for monitoring accelerations and displacements of actuators under the table
- 12 channels for tri-axial load cells monitoring restoring force of the specimen
- 27 channels for nine 3D accelerometers and 9 channels for nine 1D accelerometers, monitoring the vertical acceleration at specific points of the test specimen
- 38 channels for strain gages on the longitudinal and transverse reinforcing bars
- 14 channels for Novotechniks (after the name of the manufacturer) and 2 channels for direct current differential transformers (DCDTs) monitoring local deformation of the test specimen
- 19 channels for wire potentiometers monitoring displacement at specific points of the test specimen

The channel list and instrumentation drawings are presented in Appendix D.

3.5.2.1 Internal Instrumentation

A total of 38 strain gages were installed on the reinforcing bars for each test specimen. Eighteen gages were installed on longitudinal bars (L) and 20 gages on transverse bars (H) at the following locations (defined by the column diameter, D, and the column height, H):

- at 3D/2 and 2D from the bottom and D/2 from the top as shown in Appendix D: 2 gages (L) and 2 gages (H)
- at D/2 from the bottom as shown in Appendix D: 2 gages (L) and 6 gages (H)
- at D from the bottom and also from the top as shown in Appendix D: 4 gages (L) and 2 gages (H)
- at mid-height (i.e., H/2) as shown in Appendix D: 2 gages (L) and 4 gages (H)

3.5.2.2 External Instrumentation

As shown in Appendix D, linear position transducers (Novotechnik), DCDTs, wire potentiometers, accelerometers, and load cells were installed to obtain local deformation, global displacement, acceleration, and restoring force, respectively. These instruments were installed in the following locations:

- **Novotechniks and DCDTs**
  - ❖ A total of 14 Novotechniks were installed to measure local deformation on the north and south sides of the column. They were mounted on threaded rods penetrating through the column in the horizontal loading direction, as shown in Appendix D. A total of six rods were kept unbonded from the surrounding concrete by a gap of 1/16 in. (1.6 mm) around the rod, except at the center of the

column. The bonded length was roughly 14 in. (356 mm). Each rod had a brace on each side to fix the Novotechnik and its wire. Locations of these measurements are given in Appendix D. From the Novotechnik data one can calculate the strain at D/2, D, 3D/2, and 2D from the bottom and at D/2 from the top. These strains obtained from the displacement measurements can be compared to the strains obtained directly from the reinforcing bar strain gages. In addition, section curvatures can also be obtained by using these computed strains on the north and south sides of the column. Moreover, two DCDTs were installed to capture the vertical displacement of the top concrete block. They were located 7 in. (178 mm) off from the east and west sides of the column.

- **Wire Potentiometers**
  - ❖ A total of 19 wire potentiometers were installed to measure displacement of the test specimen. They captured the displacement in the longitudinal (X), transverse (Y) and vertical (Z) directions. These measurements were arranged as follows:
    - o Column – 4 wire potentiometers in the X- and 4 wire potentiometers in Y-direction
    - o Footing – 2 wire potentiometers in X- and 1 wire potentiometer in Y-direction
    - o Mass – 2 wire potentiometers in X-, 2 wire potentiometers in Y- and 4 wire potentiometers in Z-direction
- **Accelerometers**
  - ❖ A total of 18 accelerometers were installed to measure acceleration at the following points. Four 3D accelerometers were located at each corner of the base plate, one below the top block, and four at each corner of the top of the concrete blocks. Eight 1D accelerometers were attached along the height on the north side of the column, and one at the center on the top concrete block to measure the vertical acceleration.
- **Load Cells**
  - ❖ Four tri-axial load cells support the specimen at the four corners below its footing to measure axial load and shear forces in the X- and Y-directions.

3.6 SUMMARY

The dynamic tests to examine the effect of vertical excitation on shear strength of RC bridge columns were designed within capacity of the UC-Berkeley shaking table located at the Richmond Field Station. The 1/4-geometric scale for the test specimens as selected. To confirm shaking table performance, fidelity tests were conducted with steel beams and concrete blocks stacked on the shaking table. Even though the periods were not comparable to those of the scaled prototype, the mass of the shaking table—which weighed 118 kips, and the center of gravity 9 ft —were comparable to those of the test specimens. Four ground motions were selected from 80 ground motions, satisfying the first and second and criteria determined in Section 2.1. They were chosen based on capacity reduction (parameter *Ted* defined in Chapter 2) calculated using the ACI-318-11 equation and on comparison of demand and capacity history. A total of 30 trials were conducted and the input motion was finalized. The intensity limit of the applied motion was also identified.

Each RC column—SP1 and SP2—was designed as a 1/4-scaled prototype. Both SP1 and SP2 had a longitudinal reinforcement ratio of 1.563%, which is close to the prototype value. The transverse reinforcement ratio of SP1 was close to that of the prototype, but SP2 had 2/3 of that of SP1, achieved by adjustment the hoop spacing. The mass on the column was identical in both specimens. Assuming f_c' =4 ksi (27.58 MPa) and 6.5% axial load ratio and including miscellaneous weight, a 85.6 kip-weight (38.83 ton) was placed on each column. The total weight on the table was slightly over 100 kips (45.36 ton). The center of gravity of each specimen was about 8.5 ft (2591 mm) above the table. A base plate and prestressing rods were placed to hold the specimen at the center of the shaking table. Steel chains held the mass blocks to avoid unexpected movement that might cause safety concerns.

A total of 38 strain gages were installed on the reinforcing bars of each specimen. Eighteen gages were attached to the longitudinal bars and 20 gages were attached to the hoops. For external instrumentation, nine 3D accelerometers, nine 1D accelerometers, 4 load cells, 14 Novotechniks, 2 DCDT, and 19 wire potentiometers were used.

The 1994 Northridge earthquake recorded at the upper abutment of Pacoima Dam was selected to be applied to the test specimens with increasing intensity, from 5% to 125%-scale. The 2D excitation in X and Z was planned in most cases, but the 1D excitation in X was also planned to be applied in some cases as these 1D runs are helpful in observing differences in response due to the effect of the vertical excitation. The detailed test sequence will be discussed in Section 4.1.

4 Results of Dynamic Tests: Global Responses

4.1 INTRODUCTION

A series of tests was conducted on the UC-Berkeley shaking table located at Richmond Field Station (RFS). The first specimen, SP1, was tested from October 22-November 2, 2010, and the second specimen, SP2, was tested from November 16-November 18, 2010; see Table 4.1. The ground motion recorded at the Pacoima Dam station of 1994 Northridge earthquake (RSN 1051) was applied. One of the horizontal [X, Figure 4.1(a)] and vertical [Z, Figure 4.1(b)] components were utilized in most cases. The X-component was selected because it produces bigger shear strength reduction than the other component does. Since the geometrical scale of the specimen corresponds to the 1/4-scale modified Plumas-Arboga Overhead Bridge (PAOB), each component of the ground motion was time-compressed by a factor of 2, as shown in Figure 4.1. Note that the acceleration history in Figure 4.1 is a 100% unfiltered input ground motion obtained from the PEER NGA database [2013].

The ground motion was applied in increasing intensity levels, and each intensity level was related to the curvature ductility at the top of the column, as shown in Table 4.1. It is also shown that the two specimens followed an identical test sequence. All excitations were scaled from 5% to 125% with the upper limit determined by the shaking table limits. Since each specimen would be subjected to irreversible inelasticity in medium or high-level tests, the intensity of excitation was increased gradually. The maximum curvature at the top of the column observed in the analysis was used as the basis for determining each intensity level. While conducting tests of SP1, the longitudinal strain near the base and the top of the column was checked. For SP2, the sequence of testing was almost the same as that for SP1. All tests were conducted with one of the horizontal and vertical components, except the ones noted with 'X only' in Table 4.1. The low-level tests, from 5% to 25%-scale excitations, did not result in yielding of the cross-section at height h = 60 in. (1524 mm) above the top of the footing, which corresponds to the mid-point of the plastic hinge at the top of the column, assuming a plastic hinge length equal to the diameter of the column, $L_p = D = 20''$ (508 mm). The yielding at h = 60 in. (1524 mm) occurred when 50%-scale motion was applied. Even though the maximum curvature of SP1 was larger than that of SP2 during the 50%-scale run, this can be considered as 'yield-level' for both specimens. After this yield-level, 70%, 95%, and 125%-scale motions were applied.

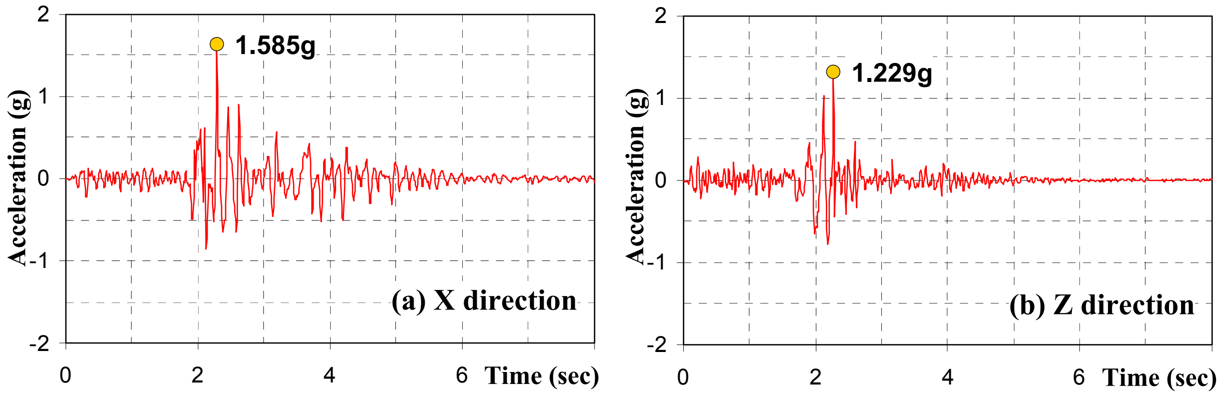

Figure 4.1 **Horizontal (X) and vertical components (Z) of 100% Northridge earthquake.**

Table 4.1 **Test sequence.**

SP	Run	Scale (%)	Ductility			Date	Notes
			Curvature		Displacement		
			ϕ/ϕ_{ys} @60 in.	ϕ/ϕ_y @60 in.	Δ/Δ_y @70 in.		
1	1-1	5.0	-	-	-	Oct. 22	-
	1-2	12.5	-	-	-	Oct. 22	-
	1-3	12.5	-	-	-	Oct. 26	50% increased Z
	1-4	12.5	-	-	-	Oct. 26	Repetition of 1-2
	1-5	25.0	0.41	0.35	0.93	Oct. 26	Half-yield
	1-6	50.0	1.11	0.96	1.73	Oct. 27	Yield
	1-7	70.0	1.57	1.36	1.93	Nov. 1	Onset of shear cracks
	1-8	95.0	4.62	4.00	2.33	Nov. 1	Onset of cover spalling
	1-9	125.0	6.15	5.33	4.27	Nov. 1	-
	1-10	125.0	6.54	5.67	4.77	Nov. 2	X only
	1-11	125.0	7.31	6.33	5.47	Nov. 2	Repetition of 1-9
2	2-1	5.0	-	-	-	Nov. 16	-
	2-2	12.5	-	-	-	Nov. 16	-
	2-3	25.0	0.40	0.35	1.05	Nov. 16	Half-yield
	2-4	25.0	0.41	0.36	0.84	Nov. 16	Half-yield, X only
	2-5	50.0	0.92	0.80	1.43	Nov. 16	Yield
	2-6	50.0	0.99	0.86	1.27	Nov. 16	Yield, X only
	2-7	70.0	1.23	1.07	1.97	Nov. 18	Onset of shear cracks
	2-8	95.0	5.00	4.33	2.47	Nov. 18	Onset of cover spalling
	2-9	125.0	5.38	4.67	4.60	Nov. 18	-
	2-10	125.0	5.00	4.33	4.50	Nov. 18	X only
	2-11	125.0	4.23	3.67	4.77	Nov. 18	Repetition of 2-9

As shown in Table 4.1, tests without the vertical component were conducted for 125%-scale (run 1-10) for SP1 and 25%, 50%, and 125%-scales (runs 2-4, 2-6, and 2-10, respectively) for SP2 to examine the effect of vertical excitation. In Table 4.1, the curvature ductility, $\varphi_y = 3.0 \times 10^{-4}$ in^{-1} (1.2×10^{-5} mm^{-1}), was obtained from the test data, and $\varphi_{ys} = 2.6 \times 10^{-4}$ in^{-1} (1.0×10^{-5} mm^{-1}) was obtained from the cross-section analysis. The curvature ductility at h = 60 in. (1524 mm) can be considered as an adequate global response parameter. At h = 70 in. (1778 mm), the yield displacement, Δ_y = 0.3 in (7.62 mm) for both SP1 and SP2, was estimated based on the shear force-lateral displacement relation shown in Figure 4.23. Note that only Imperial units (U.S. customary units) are used in this chapter.

4.2 STIFFNESS, NATURAL FREQUENCY, AND VISCOUS DAMPING

Before the main runs specified in Table 4.1, pullback and free vibration tests were conducted to obtain the stiffness and lateral and rotational vibration periods of each specimen. The period and damping values obtained were confirmed in part with the low-level tests, i.e., up to 12.5%-scale tests.

4.2.1 Pullback Tests

For SP1, a total of five pullback tests were conducted, as shown in Figure 4.2. Relative lateral displacement between the top of the footing and the column top (just below the monolithically cast RC block above the column) was measured in three tests; absolute displacement (i.e., displacement between the column top and the top of the table) was measured in two tests. The difference between the absolute and relative displacements resulted from the rotation of the footing due to the axial flexibility of the load cells. For SP2, three pullback tests were conducted. Relative displacement and absolute displacement were measured in one and two tests, respectively. The lateral stiffness obtained in each case is shown in Table 4.2. As specified, SP1 and SP2 had different stiffness values, and the stiffness of SP2 is almost 0.7 that of SP1, regardless of the displacement measurements. Lateral force-absolute displacement relationship in one case for each specimen is shown in Figure 4.3.

Table 4.2 Stiffness from pullback tests.

Displacement measurements	Stiffness of SP1 (k/in.)	Stiffness of SP2 (k/in.)	Stiffness Ratio (SP2/SP1)
Relative	148.0, 150.0, 148.2	102.1	0.687
	Mean: 148.7		
Absolute	121.8, 116.3	82.1, 82.8	0.693
	Mean: 119.0	Mean: 82.5	

Figure 4.2 Photographs of the pullback tests without (left) and with (right) total.

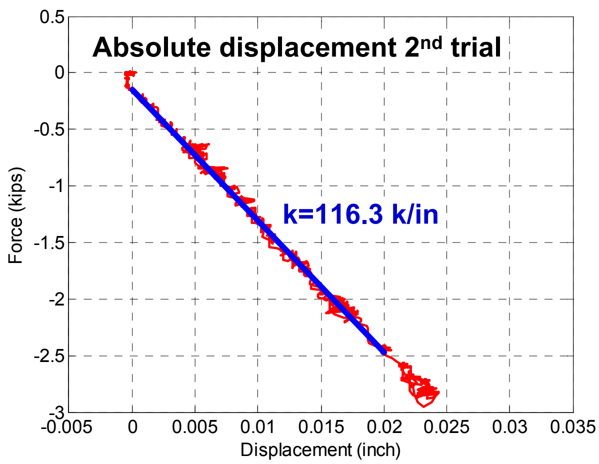

(a) Specimen 1

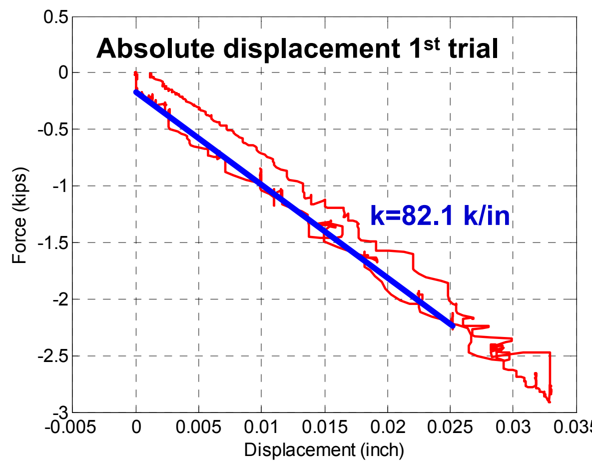

(b) Specimen 2

Figure 4.3 Estimation of lateral stiffness.

4.2.2 Free Vibration Tests

After pullback tests, the lateral and rotational vibration periods of each specimen were estimated based on free vibration tests. Two tests were conducted for SP1 and three tests for SP2. Lateral periods of SP1 and SP2 were 0.43 and 0.47 sec, respectively. Note that if the mass moment of inertia provided by the mass assembly did not exist, the ratio of lateral periods would be expected to be the square root of the lateral stiffness, namely 0.83. However, for the investigated columns, this ratio is 0.91, which is due to the coupling of the lateral and rotational modes. Lateral periods of the two specimens neared each other in the 12.5% scale runs (Table 4.3). Considering that cracks started to open and close during these excitations, it can be speculated that SP2 had experienced some cracking before the tests. During the 12.5% scale run, cracks initiated for SP1 and increased slightly for SP2, bringing the periods of the two specimens closer. Using Equation (4.1), the lateral damping of SP1 and SP2 were calculated as 1.9% and 2.9%,

Figure 4.4 shows the absolute lateral displacement measured at the top of the column and the theoretical displacement calculated by using the mentioned vibration period and damping values using an equivalent single degree of freedom (SDOF) system.

$$\zeta = \left(\ln\left(u_1 / u_{j+1}\right)\right) / \left(2 j \pi\right) \tag{4.1}$$

In Equation (4.1), u_1 is the displacement at the first cycle peak, and u_{j+1} is the displacement peak after a number of cycles equals j.

From the Fast Fourier Transform (FFT) amplitudes, damping values were calculated as 2.2~2.5% (SP1) and 2.5~3.0% (SP2), respectively, using half-power bandwidth method [Chopra, 2006]. In addition, the two specimens had the same rotational period of vibration, namely 0.096 sec as shown in Figure 4.5. This value was obtained from FFT amplitudes of the vertical acceleration at the top of the mass blocks and from the response spectra using the vertical acceleration measured on the shaking table with 3% damping. As specified in Figure 4.5, FFT and response spectra point to the same period. Another peak observed in the response spectra of the shaking table, namely 0.027 sec, was the vertical period of vibration of the test specimen, as discussed in the next section.

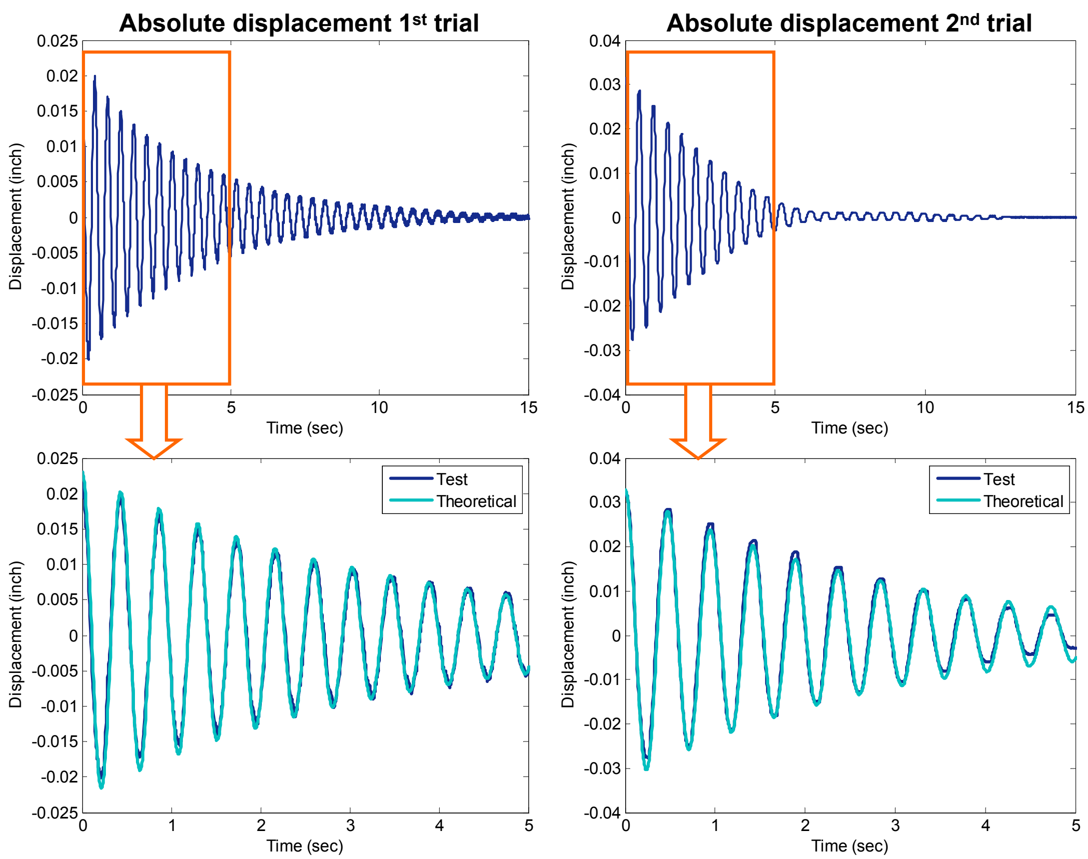

(a) Specimen 1

(b) Specimen 2

Figure 4.4 Absolute displacement measured in the free vibration tests.

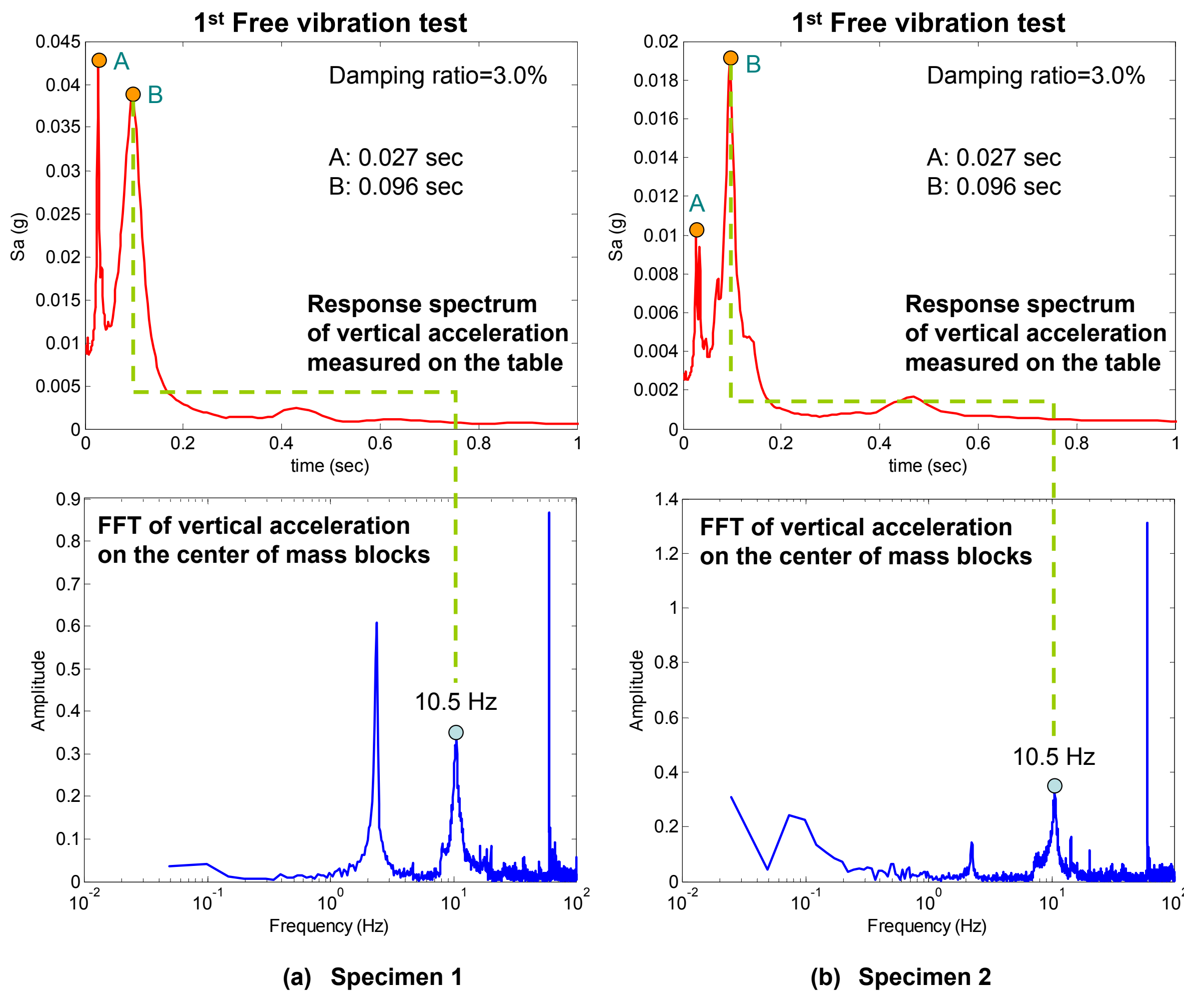

Figure 4.5 Dominant frequencies of vertical acceleration measurements.

4.2.3 Estimation of the Vertical Period

Up to the 12.5%-scale runs, the vibration periods did not change significantly. Hence, the periods obtained from FFT of the specimen response can be considered as a reasonable estimate of the initial periods of vibration. Note that the FFT peaks come from the response of the whole system, including the shaking table. This is clearly observed in Figure 4.6, which shows the FFT of the measured vertical accelerations at various locations where the main peaks are at 6.0~6.6 Hz, i.e., 0.15~0.17 sec. The same peaks were obtained from the vertical accelerometers placed along the heights of the columns for SP1 and SP2. Because the shaking table was flexing due to the interaction of the vertical actuators with each other and the table itself, which resulted in a vertical degree of freedom at the table level with large mass, a peak consistently appeared at the frequency of 6.47 Hz that does not reflect the vertical period of the test specimen.

Figure 4.6 shows the peaks for the vertical frequency of the test specimens, which are between 30 and 38 Hz. Although not clearly identified in the FFT plots, the response spectra are more effective in distinguishing these high vertical frequencies. Figure 4.7 shows the response spectra using the vertical acceleration obtained with 4.8% damping at different locations of SP1 under 5%- and 12.5%-scale motions. Except for the vibration period corresponding to peak A in Figure 4.7(a-2), which is 20% shorter than the others, the observed vertical period values are similar along the column under various intensity levels. The vibration period at peak B is the bending period of the shaking table, corresponding to the dominant frequency in Figure 4.6. Note that similar periods are observed for SP2.

The shaking table effect appears in the case of the rotational period of vibration of the test specimen. When the table flexes, it results in a rotational degree of freedom with relatively large mass moment of inertia, which increases the rotational period of the test specimen. In case of applying table motion, the vertical actuators are bending the table when they are trying to hold the table in the commanded vertical displacement. Therefore, the mass moment of inertia of the shaking table affects the rotational period of vibration. This does not occur in the free vibration test because the table is not flexing as the actuators are inactive and vertical restraint is provided by the large damping coefficient of the actuators. In this case, the boundary conditions of the test specimen are almost like four simple supports at the used four load cells. Therefore, the rotational periods obtained from free vibration tests shown in Figure 4.5 and listed in Table 4.3 can be considered as the rotational period of the specimen itself, excluding the shaking table effect. For both specimens, the rotational period was approximately 0.1 sec.

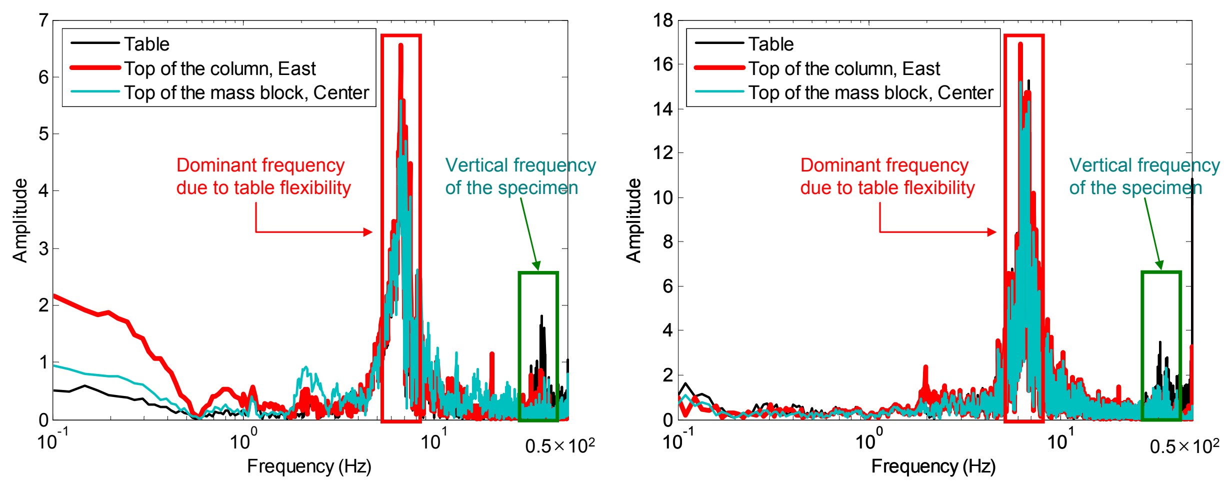

(a) SP1 @ 12.5% **(b) SP2 @ 12.5%**

Figure 4.6 FFT of vertical accelerations measured at various locations.

Table 4.3 **Estimation of the periods of vibration of the test specimens.**

SP	Test type	Horizontal (sec)	Rotation (sec)	Vertical (sec)
1	Free Vibration 1	0.43	0.10	0.027
	Free Vibration 2	0.43	0.10	0.027
	5% scale GM	0.43	0.15	0.028
	12.5% scale GM	0.49	0.15	0.029
2	Free Vibration 1	0.47	0.09	0.027
	Free Vibration 2	0.47	0.09	0.027
	Free Vibration 3	0.47	0.10	0.028
	5% scale GM	0.49	0.15	0.028
	12.5% scale GM	0.51	0.16	0.029

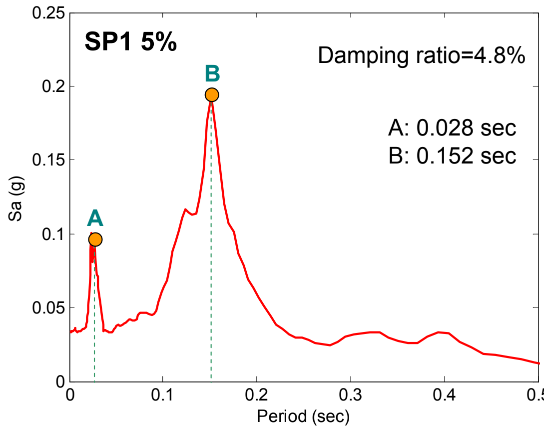

(a-1) Table

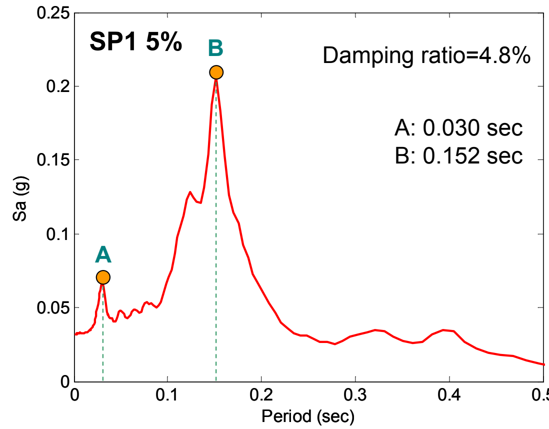

(a-2) Top of the column, East

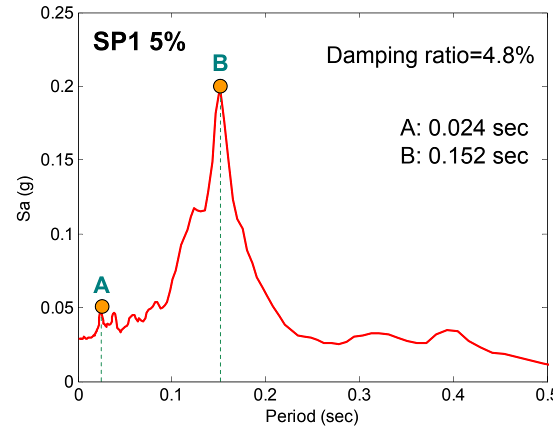

(a-3) Top of the mass blocks

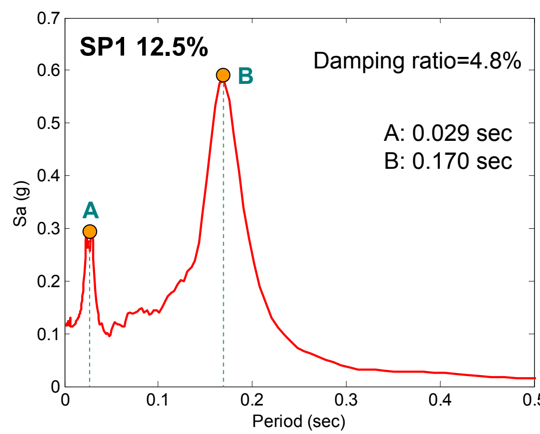

(b-1) Table

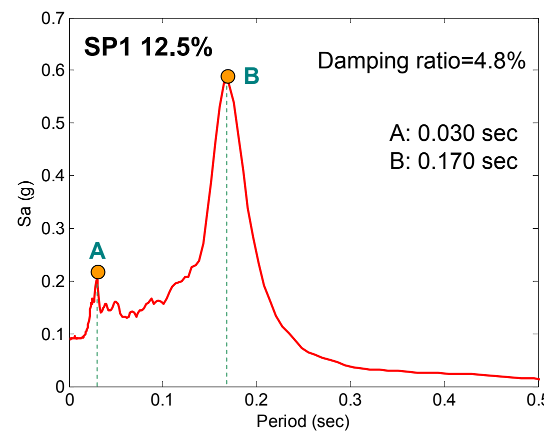

(b-2) Top of the column, East

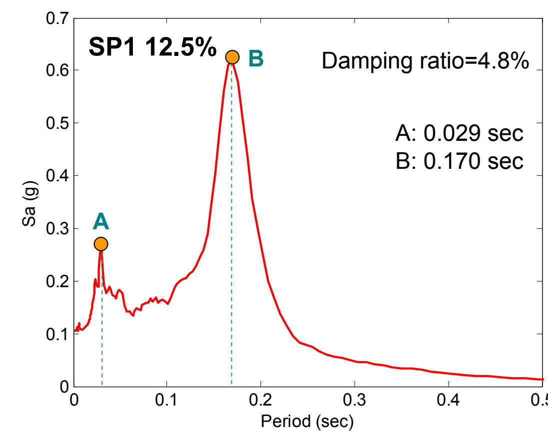

(b-3) Top of the mass blocks

Figure 4.7 Response spectra using the measured vertical accelerations.

4.3 STIFFNESS, NATURAL FREQUENCY, AND VISCOUS DAMPING

The acceleration response of the test specimen is closely related to the eigenvalues and inertia force of the system. The acceleration history is obtained directly from the accelerometers placed on the shaking table, specimen, and concrete blocks. First, the shaking table acceleration is discussed and compared to the target acceleration. Second, the acceleration responses at the top of the column and on the concrete blocks are compared to the shaking table acceleration. Finally, a discussion about the acceleration differences at each location is presented.

4.3.1 Shaking Table Acceleration

Figures 4.8 and 4.9 show the comparison of the time histories of the measured shaking table acceleration and the target acceleration, i.e., the original motion that must be reproduced using the shaking table. The table acceleration is the mean of acceleration values obtained from four accelerometers, one at each corner.

In Figure 4.8(a), (b), and (c), horizontal and vertical components of the shaking table motion in 50%-, 70%-, 95%-scale tests for SP1 are presented, respectively. The table replicates the horizontal (X) component with high precision in all three runs. Compared to the X-component, the time history of the vertical (Z) component has discrepancies. Although the obtained peak acceleration is similar to that of the target, the acceleration history after the peak does not resemble the target acceleration. This is observed in all three runs in Figure 4.8(a), (b), and (c). In spite of these differences, after the peak in the acceleration history the response spectra of both components obtained from the shaking table are comparable to those of the target, as already discussed in Section 3.3.3.

Another observation is the delayed excitation in the Z-direction. In particular, the 70%- and 95%-scale Z-components were delayed about 0.2 sec and 0.3 sec, respectively. This is also observed in the first 125%-scale test, shown in Figure 4.8(d), where the time lag was about 0.4 sec.

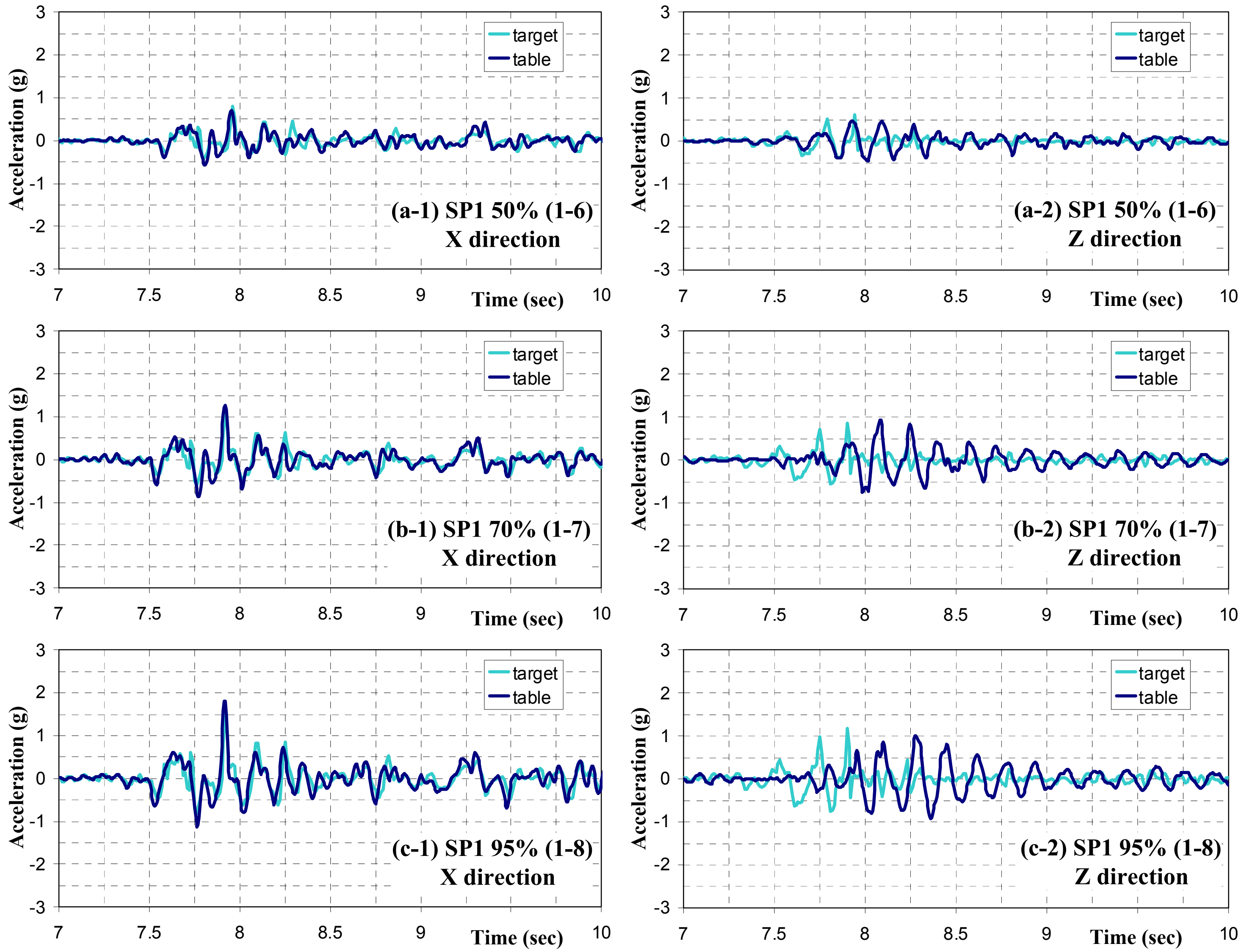

Figure 4.8 Shaking table acceleration history in SP1 tests.

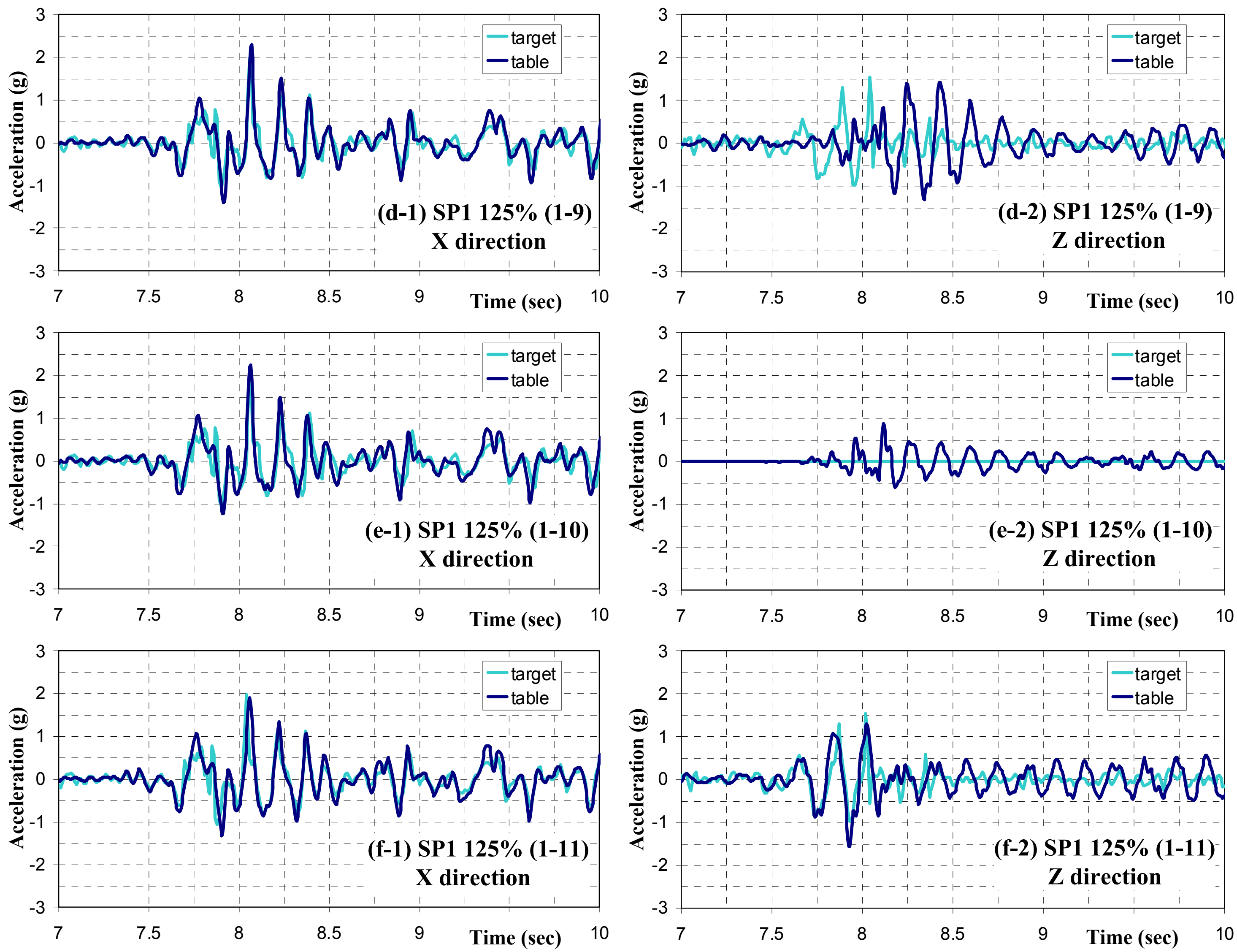

Figure 4.8 Continued.

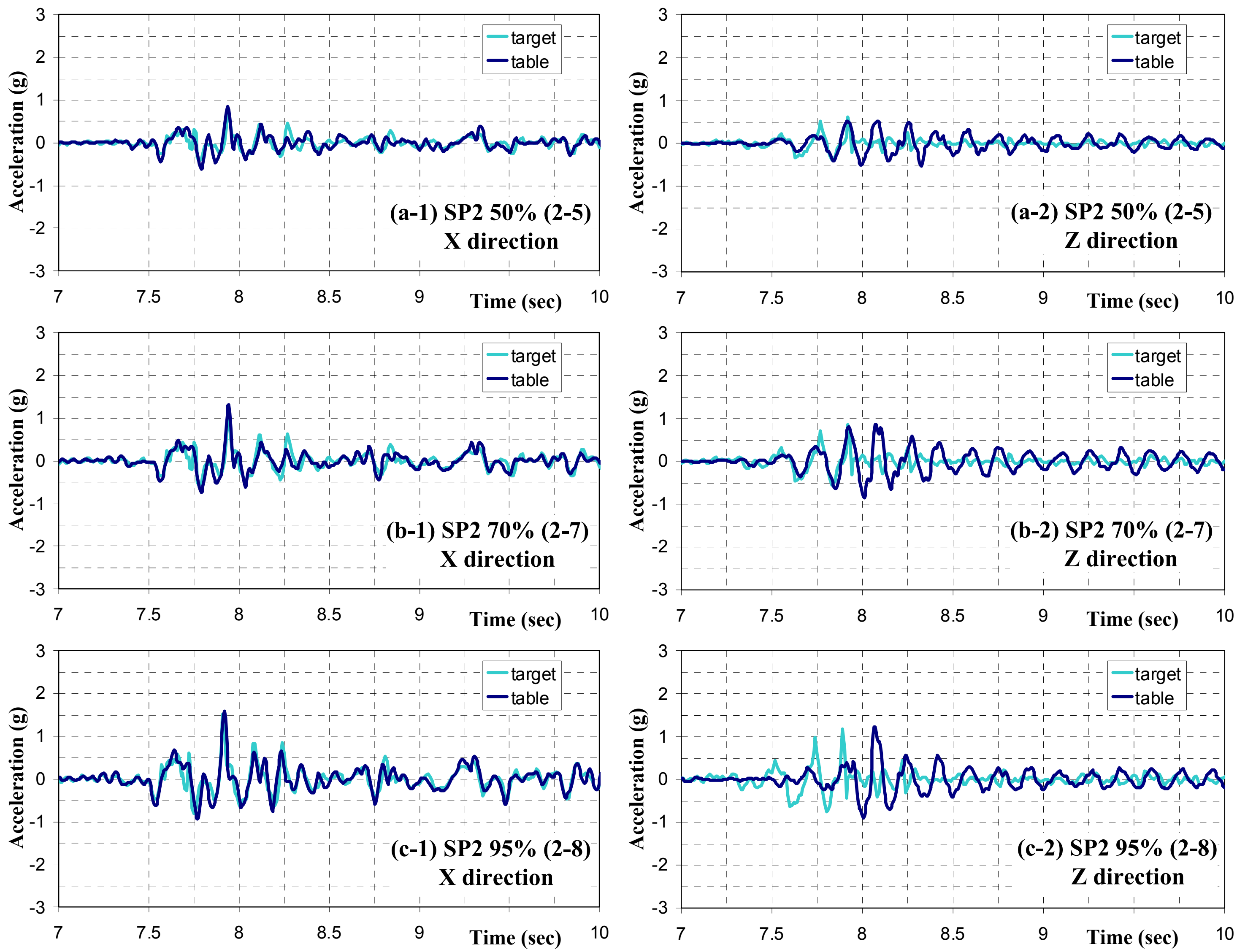

Figure 4.9 Shaking table acceleration history in SP2 tests.

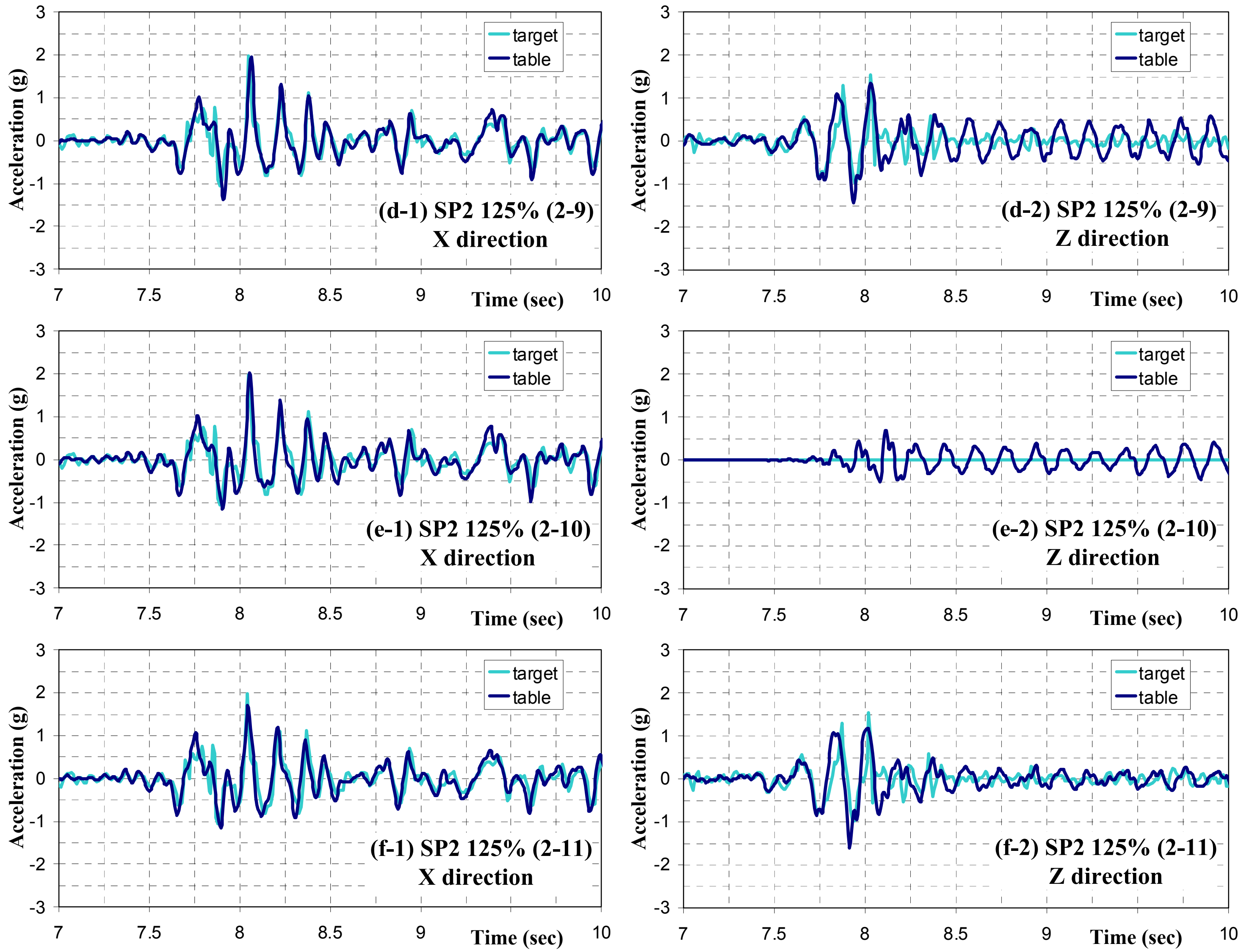

Figure 4.9 Continued

In Figure 4.8(d), (e), and (f), presents the horizontal and vertical components of the shaking table motion in 125%-scale tests for SP1. As mentioned in Table 4.1, the second 125%-scale run was for the X-component only. Therefore, the Z-component in the 125%-scale 'X only' test is supposed to remain zero, which is not the case as shown in Figure 4.8(e-2). The shaking table is controlled by vertical displacement at four points where the vertical actuators are connected. As a result, the vertical acceleration in the middle of the shaking table may not be zero during the horizontal excitation only because of the interaction of the vertical actuators that hold the vertical displacement at zero while balancing the forces due to the overturning moments caused by the horizontal acceleration. These observations for specimen SP1 were also observed for specimen SP2; see Figure 4.9.

4.3.2 Acceleration at the Top of the Column and Mass Blocks

A total of five 3D accelerometers and nine 1D (in the Z-direction) accelerometers were attached to the column and mass blocks. Except for eight 1D accelerometers, they measured the acceleration time history at the top of the column and that at the top of the mass blocks. These are presented and compared to the shaking table acceleration in Figures 4.10 and 4.11. The X-components are presented on the left side,. As discussed above, the shaking table acceleration ('table') is the mean of accelerations measured at the four corners of the table. 'Column-top' denotes the acceleration measured on the top of the column. More precisely, it is obtained below the monolithically RC top block on the east side. 'Mass' denotes the mean of acceleration measured at the four corners on the added concrete blocks. The Z-components are presented on the right side. 'Table' and 'column-top' were obtained at the same locations as the X-components, but 'mass' was obtained at the center of the top surface of the added concrete blocks.

In Figure 4.10(a), (b), and (c), the X- and Z-components in 50%-, 70%-, and 95%-scale tests of SP1 are shown, respectively. Comparing the acceleration time histories to each other, one can make several remarks: (1) the measured X-component had a bigger difference in amplitude from one location to another compared to the Z-component. For example, in case of the 70%-scale test, the PGA_h (i.e., maximum horizontal acceleration) on the shaking table at the top of the column and on the mass blocks were 1.28*g*, 0.94*g*, and 0.30*g*, respectively. Moreover, the dominant frequency of 'mass' was not similar to that of the shaking table acceleration. In contrast, the PGA_v (i.e., maximum vertical acceleration) values were similar to each other and so was the frequency content. Since the column was very stiff axially and more flexible laterally, these differences between PGA_h and PGA_v and their corresponding acceleration time histories were expected. The amplitude of the mass acceleration is discussed further in Section 4.3.3. Another observation is that 'column-top' and 'mass' accelerations in the X-direction did not increase as much as the shaking table acceleration. As the intensity of the input motion increased from 50%- to 95%-scale, the peak acceleration on the shaking table increased from 0.72*g* to 1.82*g* (ratio of 2.53). In contrast, the peak values of 'column-top' and 'mass' changed respectively from 0.72*g* to 1.26*g* (only ratio of 1.75) and from 0.26*g* to 0.33*g* (only ratio of 1.27). This trend continued for the higher intensity level tests, i.e., 125%-scale tests [Figure 4.10(d), (e), and (f)], where the peak acceleration on the mass blocks did not increase higher than 0.38*g* (only a ratio of 1.46 compared with the 0.26*g* for the 50%-scale).

This trend and the capping of the peak acceleration on the mass blocks were expected results since the stiffness of the column decreased with increasing the level of intensity of shaking, and because the base shear capacity of the column was reached [Figure 4.12(a-1)]. This capping was not detected in the Z-components, as shown in Figure 4.12(a-2). The same trends as discussed above for SP1 were observed in 50%- to 125%-scale tests of SP2, as shown in Figures 4.11, 4.12(b-1), and 4.12 (b-2).

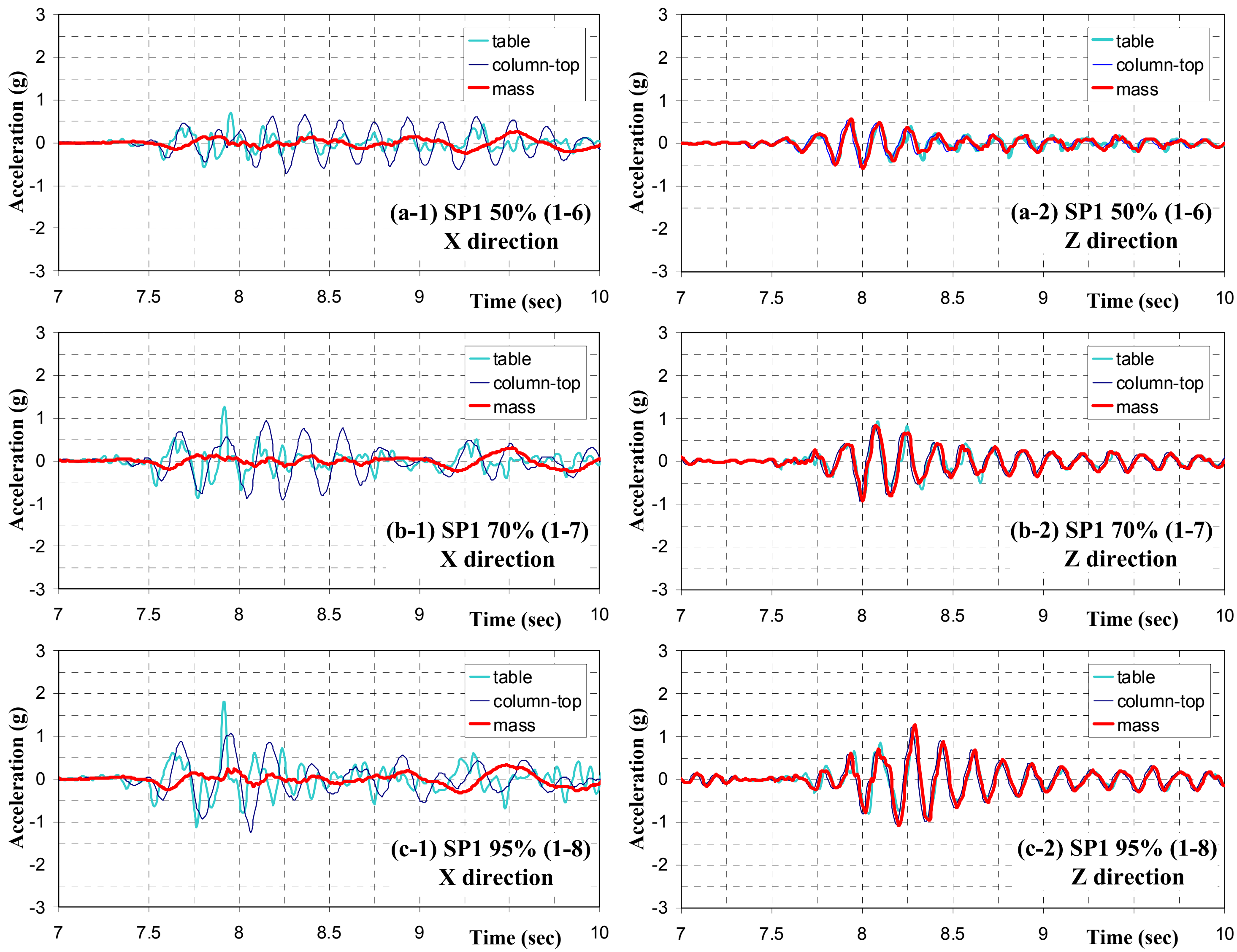

Figure 4.10 Accelerations at the shaking table, top of the column, and top of the mass blocks in SP1 tests.

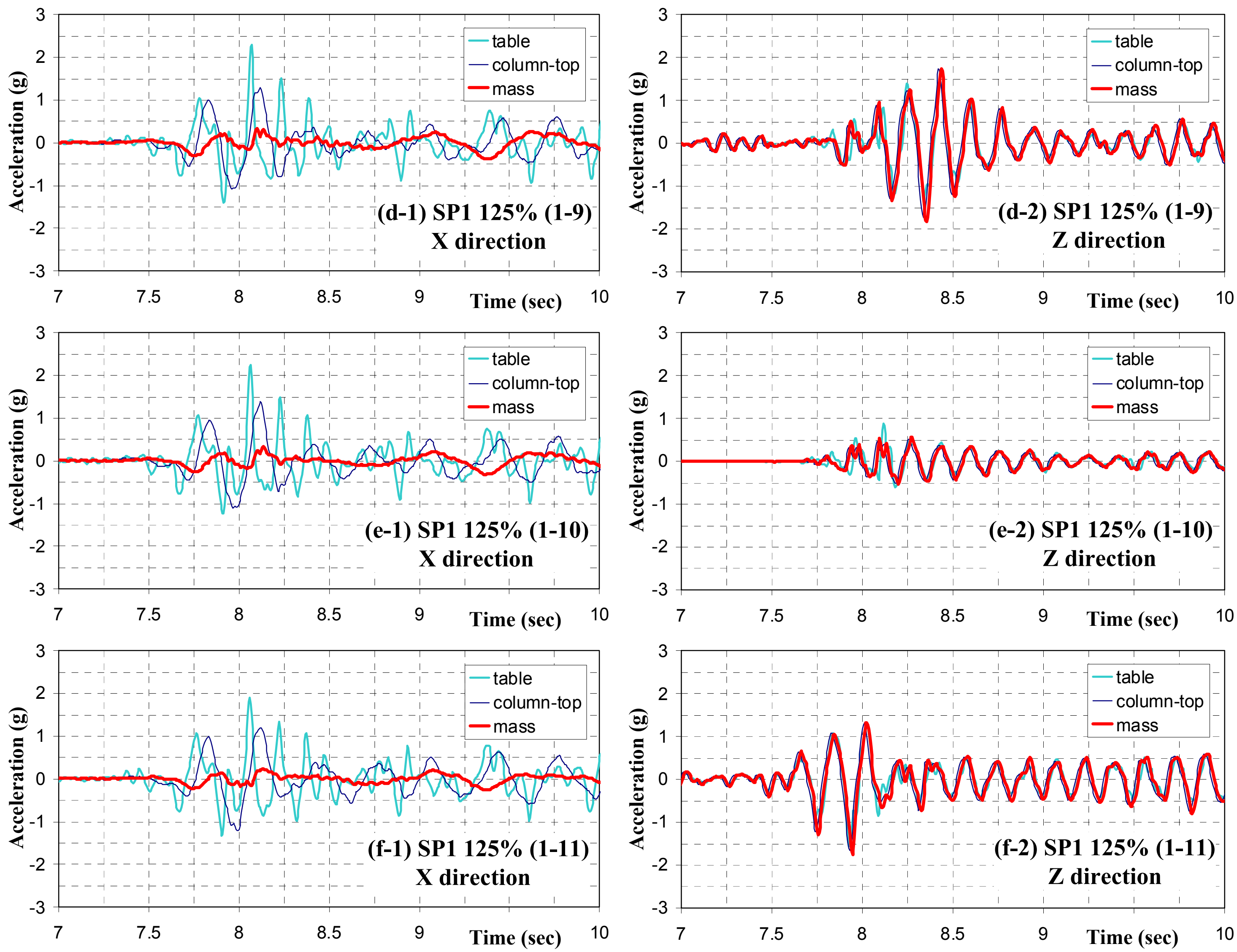

Figure 4.10 Continued.

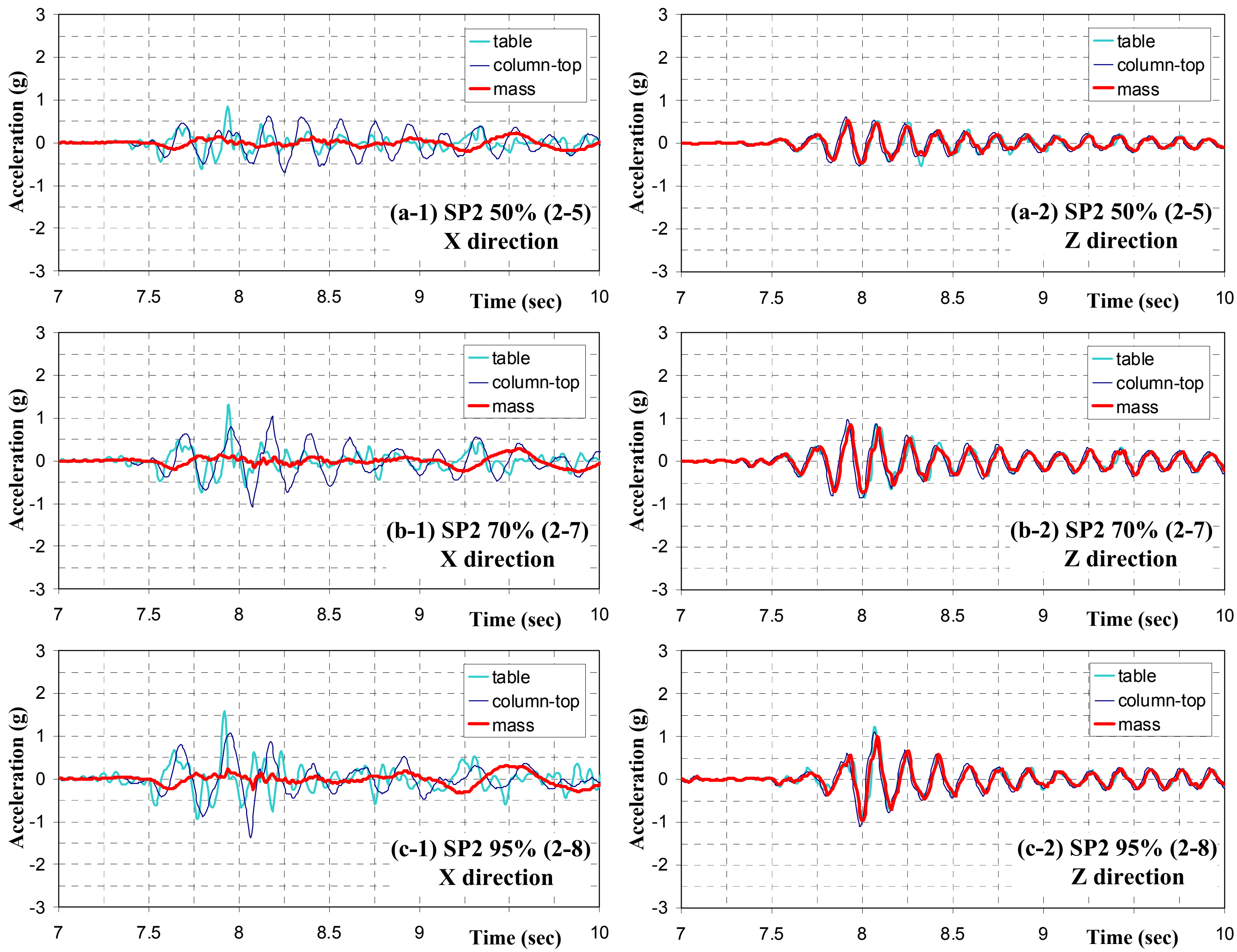

Figure 4.11 Accelerations at the shaking table, top of the column, and top of the mass blocks in SP2 tests.

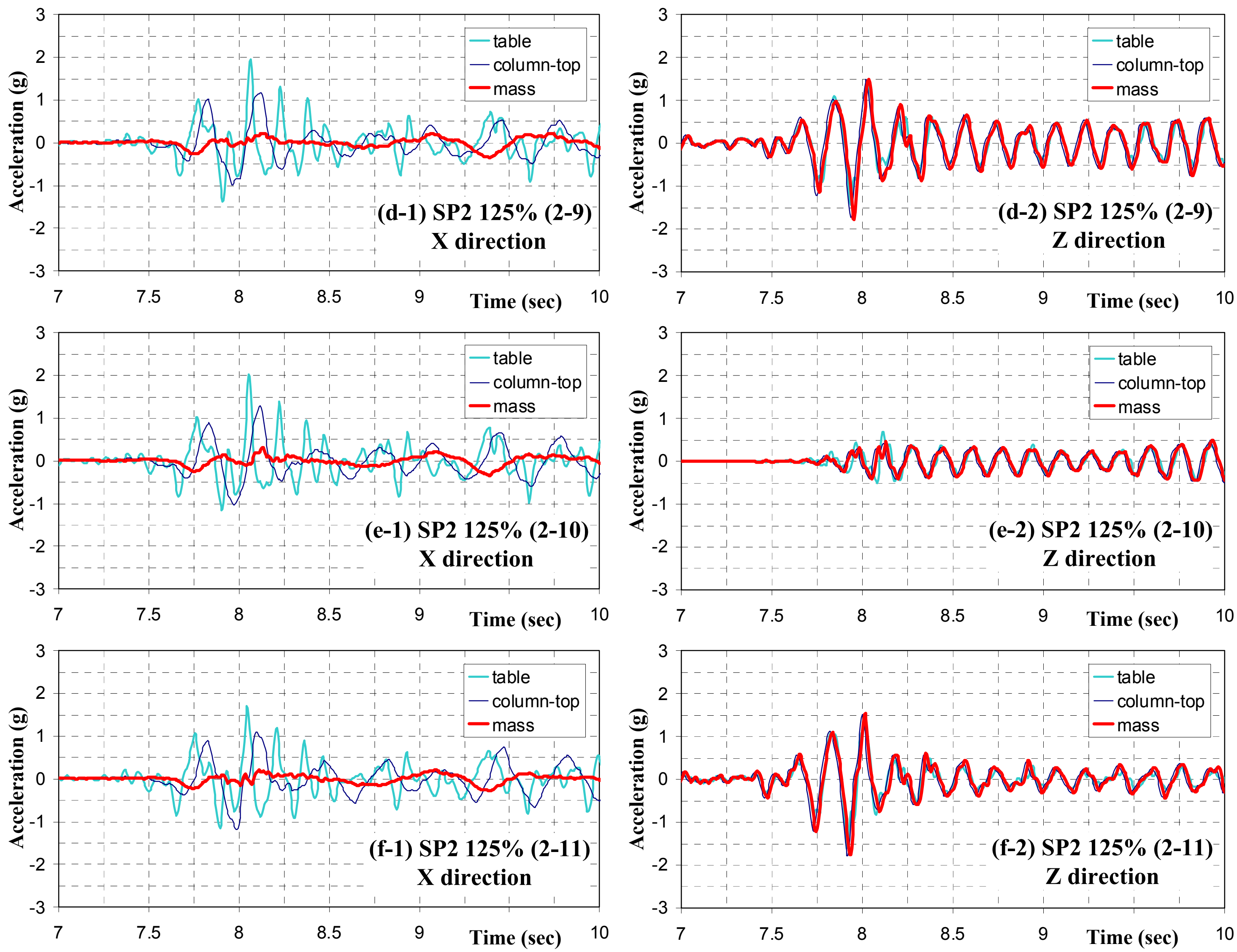

Figure 4.11 Continued.

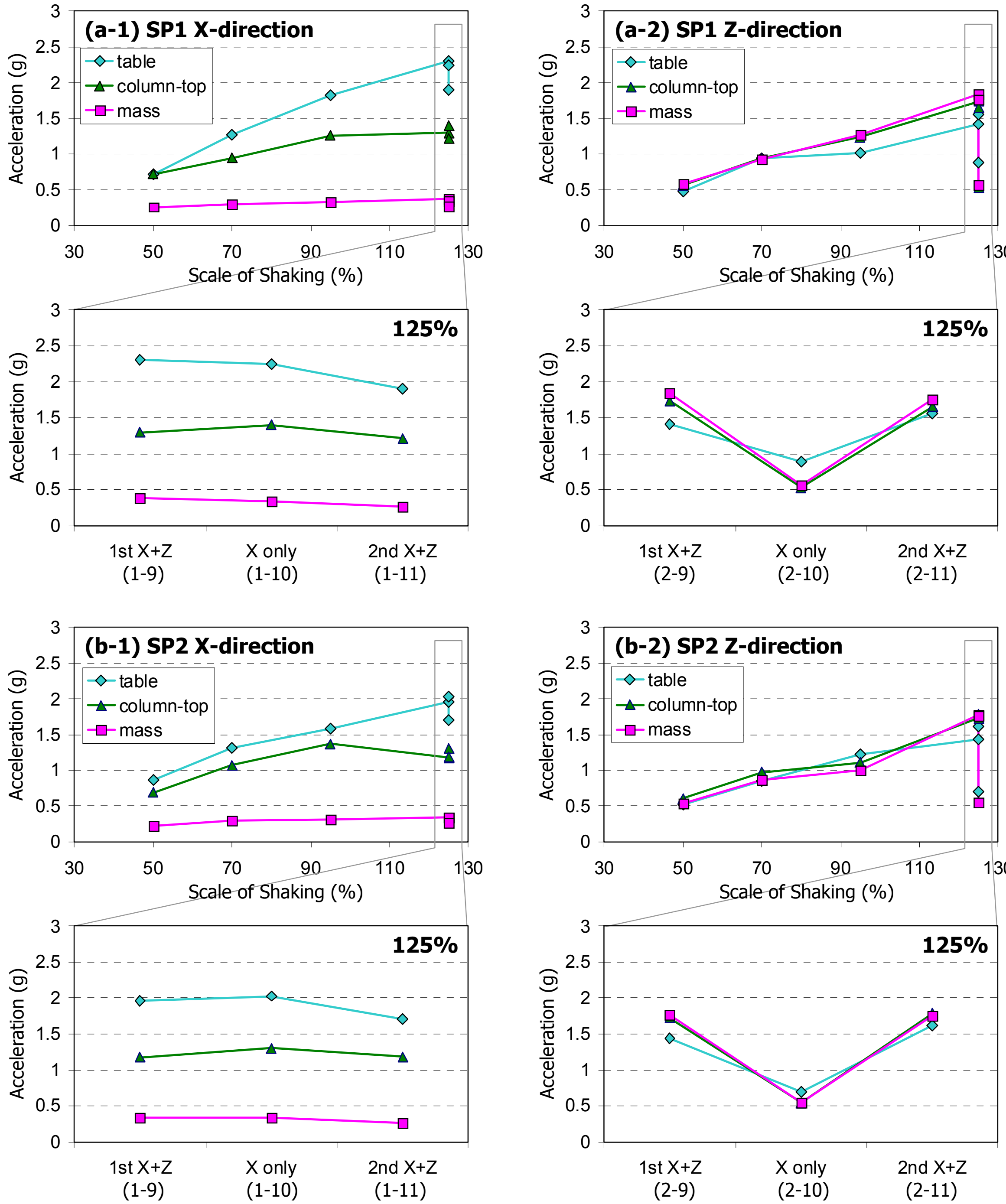

Figure 4.12 Comparison of peak acceleration values.

4.3.3 Rotation of the Mass Blocks

The X-component of the acceleration on the mass blocks was significantly lower than that at the top of the column. This difference was due to the additional translational acceleration due to the rotation of the mass blocks. A quantitative explanation is presented below.

The rotational acceleration is calculated by using the displacement measurements from the wire potentiometers connected to the south side of the mass blocks and the top of the column in X-direction (i.e., direction of the horizontal (north-south) acceleration component). Two wire potentiometers were connected to the south-east and south-west sides of the top concrete blocks. Hence, the mean of these two displacement measurements was calculated to obtain the displacement at point B in Figure 4.13(d). Acceleration at point B was obtained through the double differentiation of the displacement time history at point B. On the other hand, acceleration at the top of the column [point A in Figure 4.13(d)] was obtained from accelerometer measurements. As shown in Figure 4.13(c), the measured accelerations at the top of the column are very similar to the accelerations calculated from the measured displacements by double differentiation, validating the determination of accelerations at point B from the displacements where accelerometers were not present.

The acceleration difference between points B and A divided by the distance between these points [h_{AB} in Figure 4.13(d)] resulted in the rotational accelerations on the mass blocks. Additional acceleration on the mass block due to the rotation was equal to the obtained rotational acceleration multiplied by the distance h_{AT}. Then, acceleration at the top of the mass blocks was calculated with Equation (4.2) by adding the additional acceleration to the measured acceleration at the top of the column.

$$\begin{aligned} a_{derived} &= a_{col-top} + a_{rotation} \\ &= a_{col-top} + \left(\frac{a_{displ(B)} - a_{col-top}}{h_{AB}} \right) \times h_{AT} \\ &= a_{col-top} + \left(a_{displ(B)} - a_{col-top} \right) \times r_h \end{aligned} \tag{4.2}$$

where $a_{col-top}$ is measured acceleration at the top of the column, $a_{displ(B)}$ is the acceleration calculated by differentiation of the mean displacement measured on the south side of the mass blocks, h_{AT} is the vertical distance from the column top to the accelerometers on the mass blocks, and h_{AB} is the vertical distance from the column top to the wire potentiometer targets.

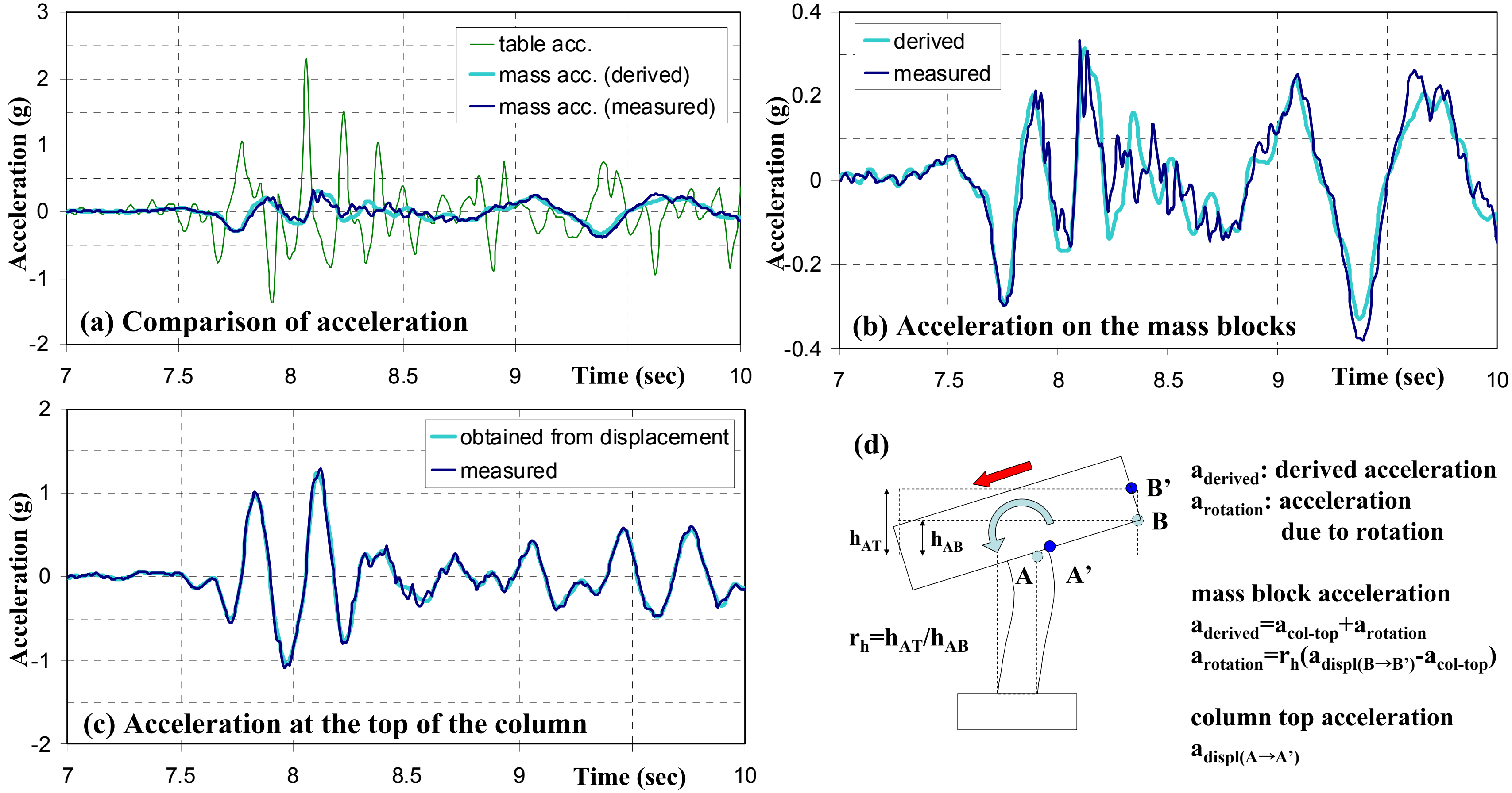

Figure 4.13 Comparison of measured and derived accelerations (specimen SP1, run 1-9).

As shown in Figure 4.13(a) and (b), the derived accelerations calculated with Equation (4.2) matches well with the measured accelerations. This good matching was also observed for the other runs and SP2. This explains the difference observed in Figures 4.10 and 4.11 as being related to the rotation of the mass blocks. In summary, the lateral acceleration was remarkably changed due to the rotation of the added mass. It should be noted that the shear force on the column was accordingly affected by the acceleration of this mass that depended on the rotation mentioned above. This is discussed further in the following section.

4.4 FORCES

4.4.1 Shear and Axial Forces

Figure 4.14 presents the time histories for the axial and shear forces obtained from the load cells for specimens SP1 and SP2 subjected to the 50%, 70%, and 95%-scale Northridge earthquake. The runs for these three levels are denoted as 1-6, 1-7, and 1-8 for SP1 and 2-5, 2-7, and 2-8 for SP2 in Table 4.1 and Figure 4.14(a), (b), and (c), respectively. For the levels of 125%-scale of Northridge earthquake, the corresponding runs are denoted 1-9, 1-10, and 1-11 for SP1 and 2-9, 2-10, and 2-11 for SP2 in Table 4.1 and Figure 4.14 (d), (e), and (f), respectively.

For levels below 125%-scale motion, the axial force was not tension in most cases. SP2 with 95%-scale motion [run 2-8, Figure 4.14(c-2)] experienced very small peak axial tension, only 3.3 kips. As the intensity increased, the peak-to-peak amplitude of the axial force increased significantly. SP1 had peak-to-peak amplitude of 95.9 kips for an axial force under 50%-scale motion, and increased to 141.9 kips and 197.6 kips as the scale increased to 70% and 95%, respectively. Hence, under 95%-scale motion, the axial force amplitude was almost twice as large as that under 50%-scale. However, the increase in the shear force was not as large as that in axial force. The peak-to-peak amplitude of the shear force for SP1 increased from 99.7 kips for 50%-scale to 130.2 kips and 168.5 kips for 70%- and 95%-scales, respectively. Similarly, the peak-to-peak amplitude of SP2 changed as follows: 99.0→156.7→192.7 kips (axial force) and 96.8→132.9→152.5 kips (shear force) for scales of 50%→70%→95%, respectively. This is attributed to the fact that the shear forces in these scales were no longer in the linear range, approaching the shear strength of the test specimens. It was also observed that the minimum axial force, i.e., minimum compression (positive) or maximum tension (negative), took place before the maximum shear force except for the cases of SP1 with 95%-scale and the first 125%-scale motions (runs 1-8, Figure 4.14(c-1) and 1-9, Figure 4.14(d-1), respectively). This observation for the 95%-scale and the first 125%-scale of SP1 is attributed to the somewhat large time lag of the vertical motion between the target and the shaking table, as shown in Figure 4.8(c-2) and (d-2).

A total of three 125%-scale tests were conducted for each specimen. As mentioned, the vertical component was not applied in the second of these three runs for each specimen [runs 1-10, Figure 4.14(e-1), and 2-10, Figure 4.14(e-2)]. As mentioned previously, vertical acceleration was measured on the shaking table even if the vertical component was not applied due to the interaction between the horizontal and vertical actuators. However, the axial force due to such inevitable vertical acceleration had relatively small compression values, with limited effect on the RC column shear capacity.

The peak axial and shear forces for the three runs on 125%-scale changed as follows: 243.9→138.8→193.4 kips (axial force, dark line with triangles in Figure 4.15) and 93.6→95.7→85.1 kips (shear force) for the respective runs 1-9→1-10→1-11 of SP1 and 216.7→134.3→219.8 kips (axial force) and 80.3→84.3→71.6 kips (shear force) for the respective runs 2-9→2-10→2-11 of SP2. It was observed that the peak shear force increased in the 'X only' runs by 2.24% and 4.98% for SP1 and SP2, respectively, which had the smallest peak axial force. For both specimens, the positive and negative shear force peaks changed in the '2nd X+Z' runs, i.e., 1-11, Figure 4.14(f-1) and 2-11, Figure 4.14(f-2), compared to the 'X only' runs, i.e., 1-10, Figure 4.14(e-1), and 2-10, Figure 4.14(e-2), especially the positive peak noticeably decreased after significant tension of approximately 60 kips (55.9 kips for SP1 and 64.0 kips for SP2). The positive shear peak (Figure 4.15, line with squares), i.e., the 3rd shear peak, which is denoted as '3' in Figure 4.14(d-1), decreased from 95.7 kips to 85.1 kips in SP1 and from 84.3kips to 71.6 kips in SP2. Consider that the shear forces were similar prior to significant tension for the 'X only' run, where for SP1 this force was 93.6 kips for run 1-9 and 95.7 kips for run 1-10, and for SP2 it was 80.3 kips for run 2-9 and 84.3 kips for run 2-10. The decrease of the positive peak shear force can be explained partly as a result of the vertical excitation, causing axial tension in the column. The decrease of the positive peak shear force was similar in both specimens (10.5 kips for SP1 and 12.7 kips for SP2). As this was similar for both specimens, it indicates a reduction in the contribution of the concrete to the shear force capacity; however, the transverse reinforcement contribution was different in the two test specimens. In addition, the reduction in the shear force capacity was not asymmetric, considering that the decrease in the absolute shear peak and that in the positive shear peak were not the same.

The positive peak shear force was higher for the 1st X+Z test than the 2nd X+Z test (93.6 kips versus 85.1 kips), since the significant axial tension force (-63.2 kips) took place after this shear peak for SP1. However, for SP2 the positive peak shear force was also higher for the 1st X+Z test than the 2nd X+Z test (80.3 kips versus 71.6 kips), although the significant axial tension force (-61.6 kips) took place before this shear peak. If the three tests together are considered as a continuous test, it can be speculated that the reduction in the shear peak was due to degradation caused by the occurrence of two successive large axial tensile forces. For SP1 the positive peak shear forces after the first axial tensile peak (-63.2 kips in run 1-9) were 93.6 kips (run 1-9) and 95.7 kips (run 1-10); they were reduced to 85.1 kips (run 1-11) after the second axial tensile peak (-56.9 kips in run 1-11). For SP2 the positive peak shear forces after the first axial tensile peak (-61.6 kips in run 2-9) were 80.3 kips (run 2-9) and 84.3 kips (run 2-10); they were reduced to 71.6 kips (run 2-11) after the second axial tensile peak (-64.0 kips in run 2-11). Hence, the positive peak shear force reduced after the second axial tensile peak for both specimens. On the other hand, the peak axial tensile force in the 2nd X+Z tests did not affect the negative peak shear force (85.0 kips in SP1 and 74.6 kips in SP2). This can be explained by the duration of wave propagation in the vertical direction considering that the time between the peak axial tensile force and the negative peak shear force was only about 0.04 sec.

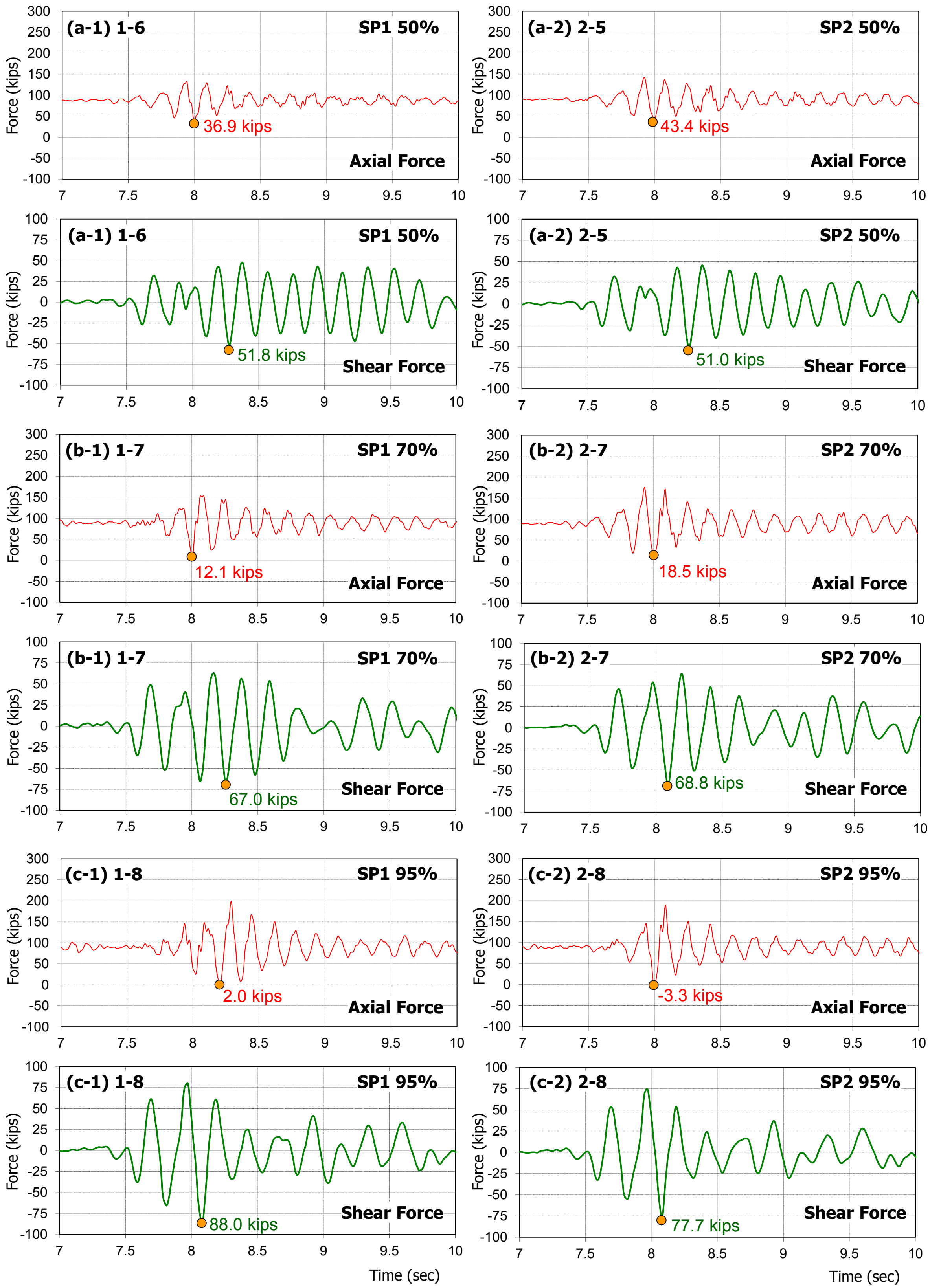

Figure 4.14 Axial force and shear force history.

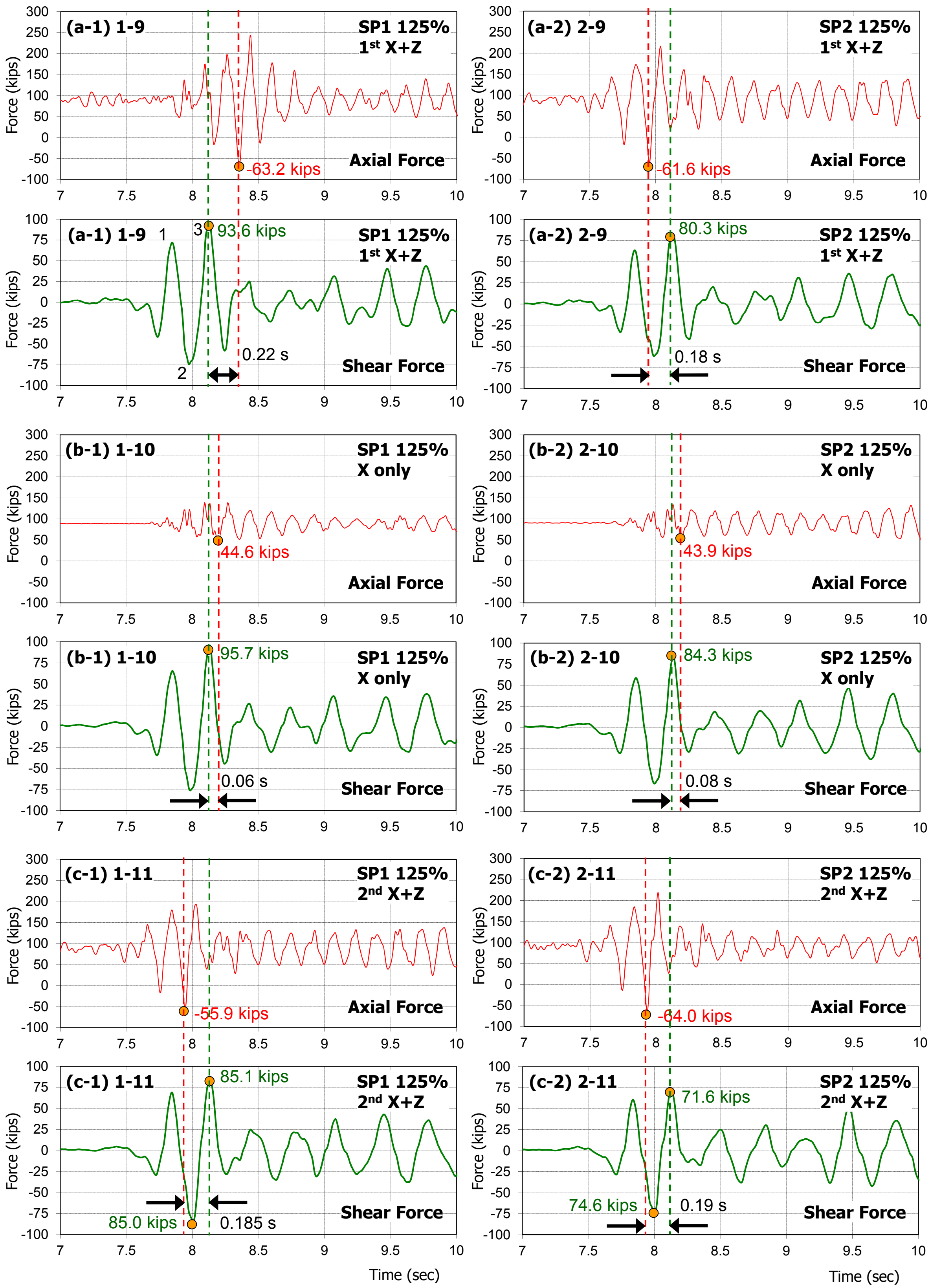

Figure 4.14 Continued.

Table 4.4 compares the axial force at the maximum positive shear force in each test. Even though the decrease of the maximum positive shear force may have partly resulted from the decrease in axial compression, this cannot explain the difference between 'X only' and '2nd X+Z' compared to the difference between 'X only' and '1st X+Z'. In particular, a comparison between runs 2-9 and 2-10 demonstrates that the large difference in the axial force at the maximum positive shear force did not affect the magnitude of the shear force significantly. On the other hand, the maximum tension force and corresponding degradation, as discussed in the previous paragraphs, were more appropriate causes for the shear force difference between 'X only' and 'X+Z' runs.

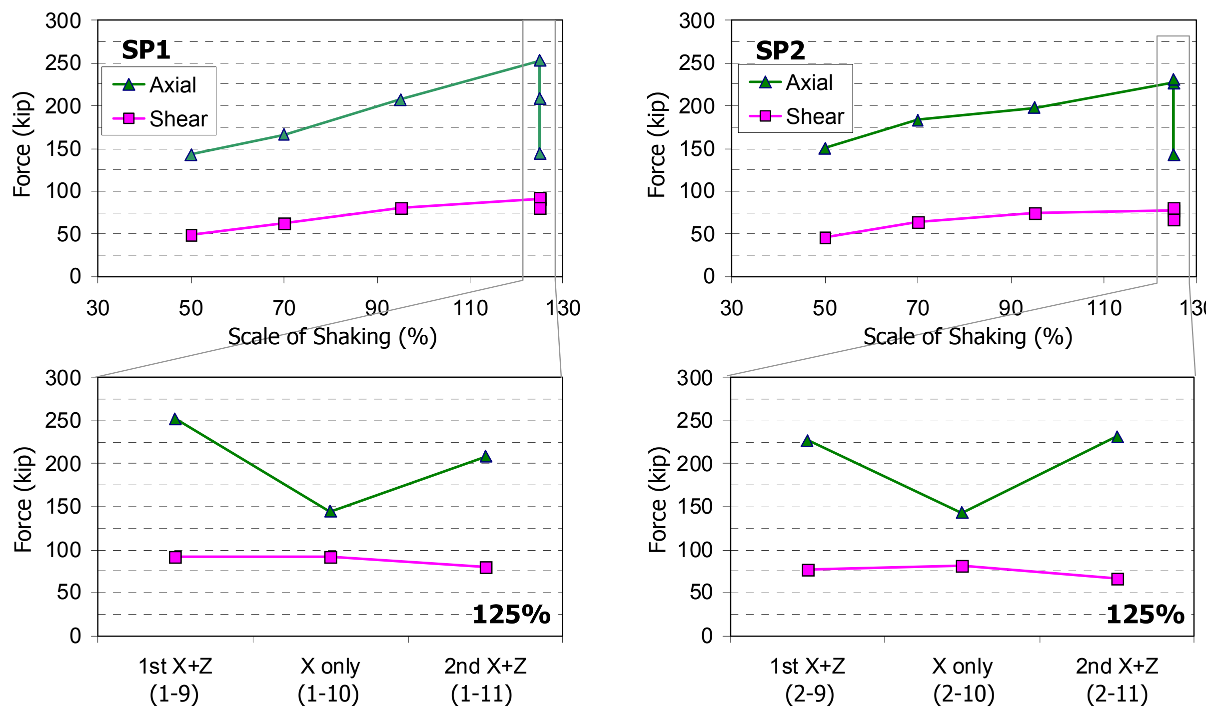

Figure 4.15 Positive peak axial and shear forces with scale of applied shaking table motion.

Table 4.4 Comparison of axial force at the maximum positive shear force.

SP	Run	(a) Axial (kips)	(b) Shear (kips)	(c) Axial ratio compared to 'X only' (%)	(d) Shear ratio compared to 'X only' (%)
1	1st X+Z (1-9)	108.0	93.6	78.8	97.8
	X only (1-10)	137.0	95.7	100.0	100.0
	2nd X+Z (1-11)	68.6	85.1	50.1	88.9
2	1st X+Z (2-9)	43.1	80.3	32.1	95.3
	X only (2-10)	134.2	84.3	100.0	100.0
	2nd X+Z (2-11)	68.6	71.6	51.1	84.9

4.4.2 Bending Moments

Bending moment can be calculated from the axial and shear forces recorded using the load cells installed between the footing and the shaking table. The bending moment at any location of the column can be calculated by using a simple free-body calculation. Figure 4.16(a), (b), and (c) show the bending moment at the base of the column, h = 0 in. and at the top, h = 70 in., subjected to the 50%, 70%, and 95%-scale motions, respectively. Before 10 sec, shear and axial forces were significant. Subsequently, the axial force variation almost ceased after 10 sec, and only the shear force governed the bending moment history. In every case the peak bending moment at the top was larger than that at the base. Moreover, the bending moment at the top and that at the base were out of phase before 9 sec (double curvature). After 10 sec, when the strong part of the horizontal motion ceased, they became in phase (single curvature), and the peak bending moment at the base exceeded that at the top. Therefore, the bending moments at the top and at the base were dominated by the rotational mode before 9 sec but dominated by the translational mode after 9 sec. Figure 4.16(d), (e), and (f) compare the bending moments at the base, h = 0 in., and at the top, h = 70 in, subjected to the 125%-scale motions. Similar to the lower level tests, the bending moment was larger at the top, and the two bending moments were out of phase during the main excitation of the high level tests.

Table 4.5 compares the maximum values obtained in all the test runs. The absolute values are shown in columns (a) and (b), and the relative values compared to M_{max} (3327.5 kip-in for SP and 3300.1 kip-in), which is modified from the value in Table 3.5 due to higher f_y, are shown in columns (c) and (d). The bending moment at the top relative to its M_{max} was at least 30% larger than that at the base in all test runs. The bending moment values for SP1 and SP2 exceeded M_{max} at the top in the 125%-scale. However, the bending moment at the base never exceeded M_{max} for all runs of SP1 and SP2. Note that the base bending moment increased by more than 10% in the 125%-scale 'X only' test compared to the 125%-scale 'X+Z' tests, while there was little difference in the bending moment at the top; see Figure 4.17.

Table 4.5 Comparison of axial force at the maximum positive shear force.

SP	Run	(a) Base (kip-in.)	(b) Top (kip-in).	(c) Base (%)	(d) Top (%)
1	50% (1-6)	2029.62	2712.92	61.00	81.53
	70% (1-7)	1899.07	3531.06	57.07	106.12
	95% (1-8)	2459.33	3551.27	73.91	106.72
	125% ‘1st X+Z’ (1-9)	2910.17	3916.73	87.46	117.71
	125% ‘X only’ (1-10)	3153.47	4110.33	94.77	123.53
	125% ‘2nd X+Z’ (1-11)	2747.91	4046.68	82.58	121.61
2	50% (2-5)	1499.59	2431.99	45.44	73.69
	70% (2-7)	1854.07	3151.16	56.18	95.49
	95% (2-8)	2127.74	3199.51	64.48	96.95
	125% ‘1st X+Z’ (2-9)	2442.27	3627.92	74.01	109.93
	125% ‘X only’ (2-10)	2736.16	3669.18	82.91	111.18
	125% ‘2nd X+Z’ (2-11)	2343.11	3691.44	71.00	111.86

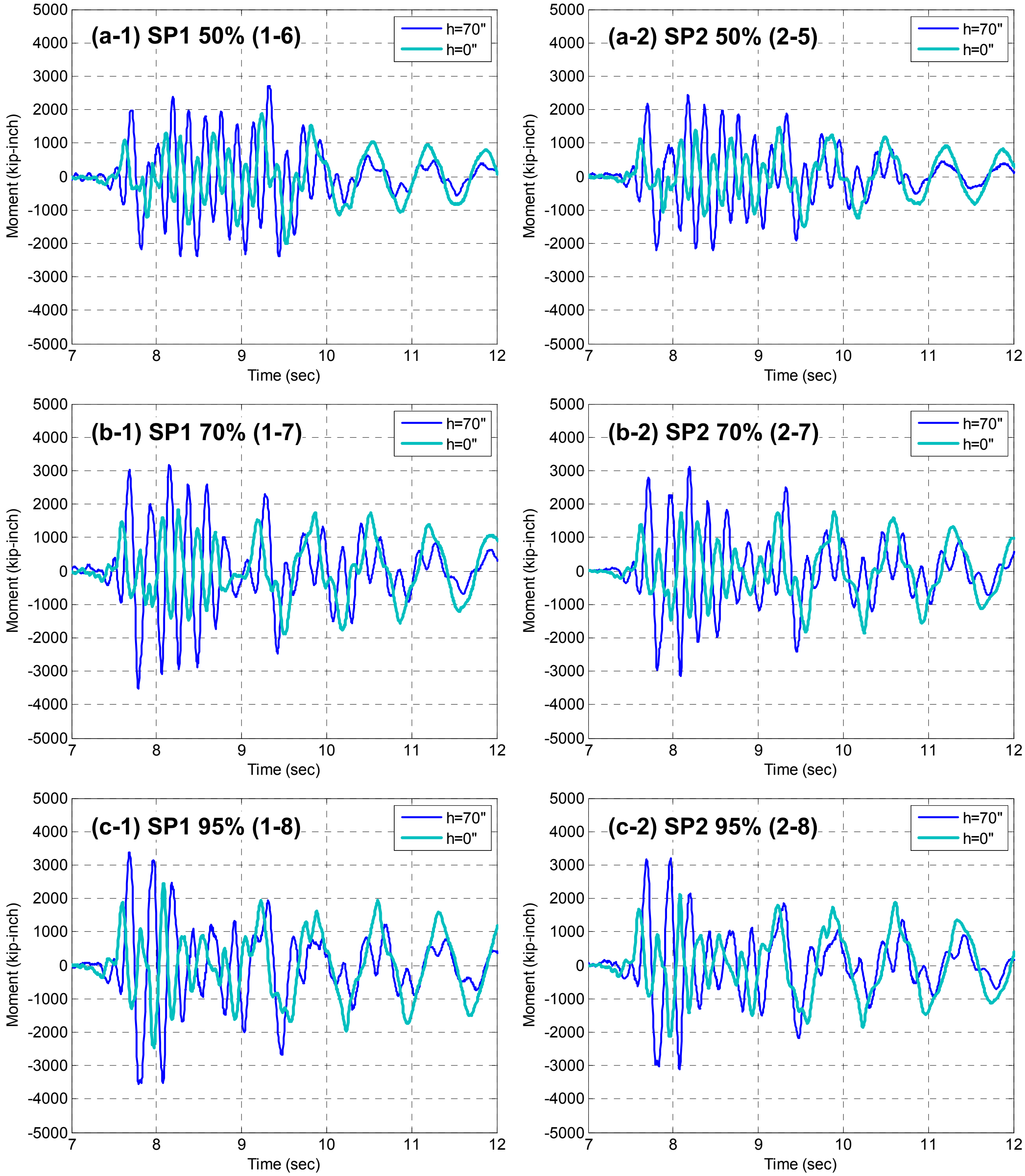

Figure 4.16 Bending moment history at the top and base of the test specimens.

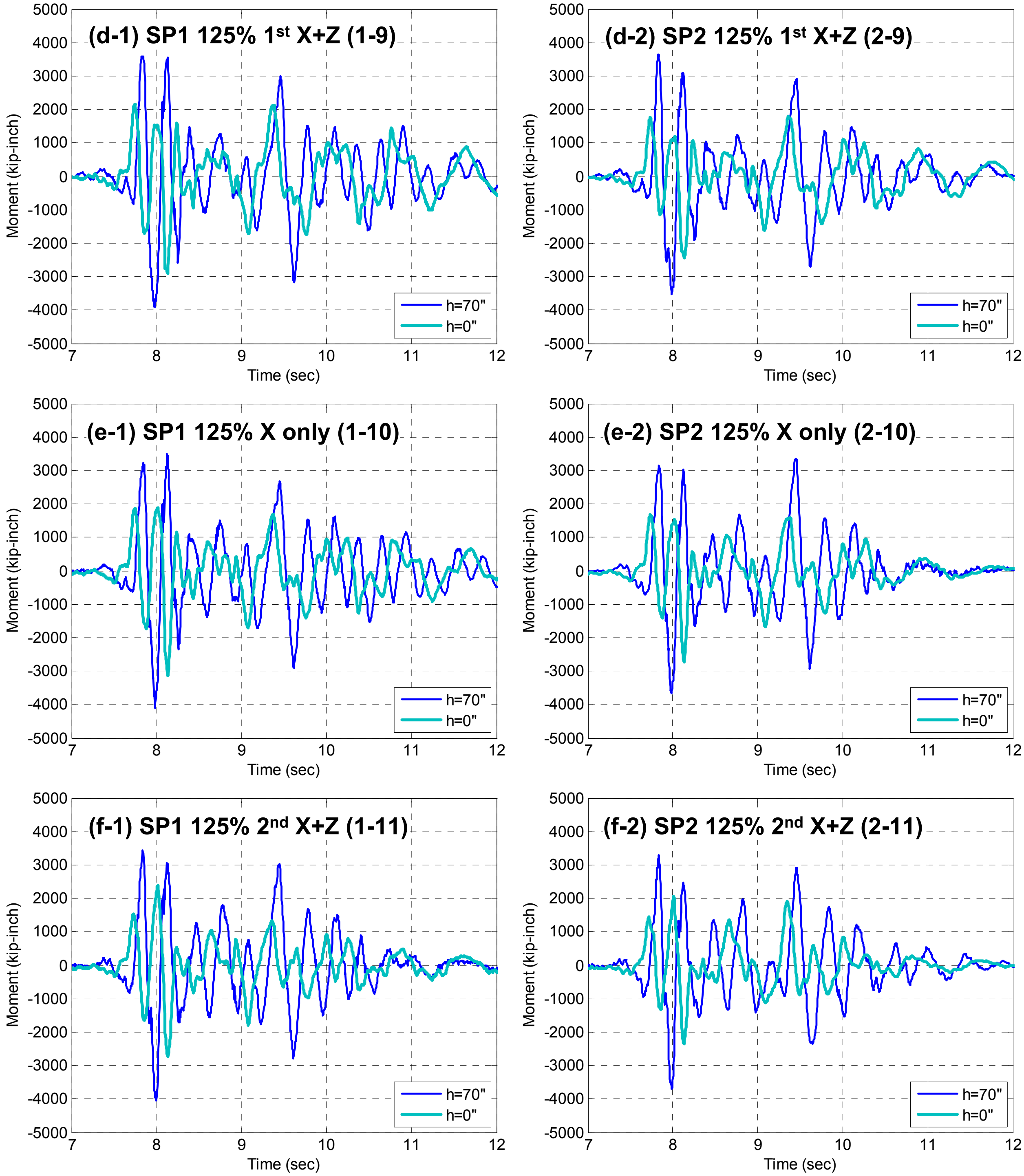

Figure 4.16 Continued.

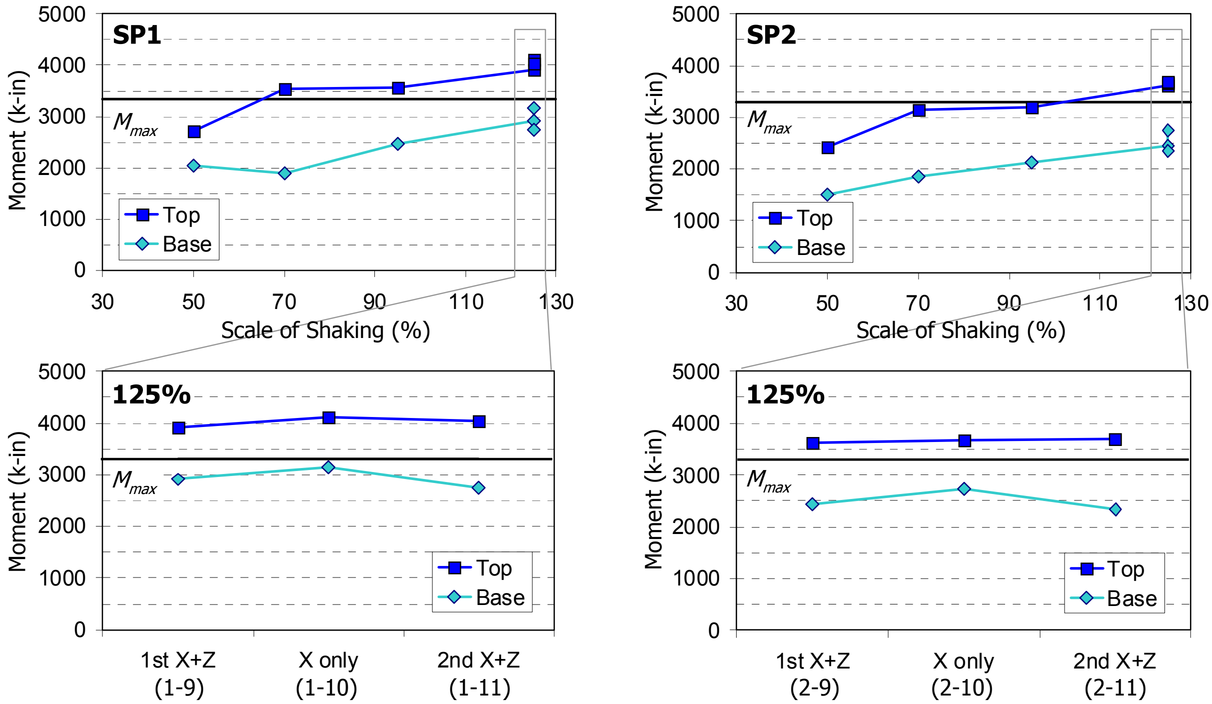

Figure 4.17 Peak bending moments at the top and base of the test specimens.

4.5 DISPLACEMENTS

The lateral and vertical displacement histories were obtained from the wire potentiometers and the DCDTs; see Appendix D for their locations.

4.5.1 Lateral Displacement

The relative lateral displacement in the X-direction is investigated in this section. Since absolute displacement was obtained from the wire potentiometers, each history was modified by subtracting the displacement at the footing to calculate the relative values. All the displacement histories in Figure 4.18 are in the X-direction, in which the horizontal excitation was applied. A total of four wire potentiometers were connected to the south side of the column, and the locations were at h = 15 in., 35 in., 55 in., and 70 in. above the footing top. Hence, the lateral displacement variation along the column height can be examined.

The relative lateral displacement histories subjected to 50%-, 70%-, and 95%-scale motions are shown in Figure 4.18(a), (b), and (c), respectively. As expected, the top displacement was the largest. In 50%- and 70%-scale tests, both specimens experienced peak lateral displacement after 9 sec, i.e., after the main excitation. However, in the 95%-scale test, both specimens experienced peak lateral displacement very slightly before 8 sec.

Figure 4.18(d), (e), and (f) shows the displacement histories for the 125%-scale tests. The top displacement was still the largest in the three runs ‘1st X+Z’, ‘X only’, and ‘2nd X+Z’ tests of both specimens. The peak displacement occurred around 8.14 sec, at which there was a clear 3rd peak of the shear force, see Figure 4.14(d), (e), and (f). Note that the displacement was centered to the positive side, which means the column deflected more toward the north side, where there was residual displacement.

Figure 4.19 compares positive (north) and negative (south) peaks before and after 9 sec. This classification was made since the main excitation ended roughly at 9 sec. Positive and negative values mean the top of the column was deflected to the north and south sides, respectively. The positive peak was larger than the absolute value of the negative peak in most cases, and this difference increased as the intensity of the excitation increased. Except for the case of the 125%-scale '2nd X+Z' test of SP2, the positive peak increased or barely changed for all the 125%-scale runs. The second-order approximation clearly fits well the 'north' peaks in Figure 4.19(a) and (b), but the first-order (linear) approximation is reasonable for the other cases.

The residual displacement increased at the end of every subsequent run. The residual displacement for SP1 was 0.330 in. and 0.220 in. for SP2 at the top after the 125%-scale '2nd X+Z' test. At the other locations, the residual displacement was less than at the top of the column. After the 3rd 125%-scale test, the residual displacement values for SP1 were 0.044, 0.110, and 0.180 in. at h =15 in., 35 in., and 55 in., respectively. The corresponding values for SP2 were -0.005, 0.030, and 0.079 in., respectively.

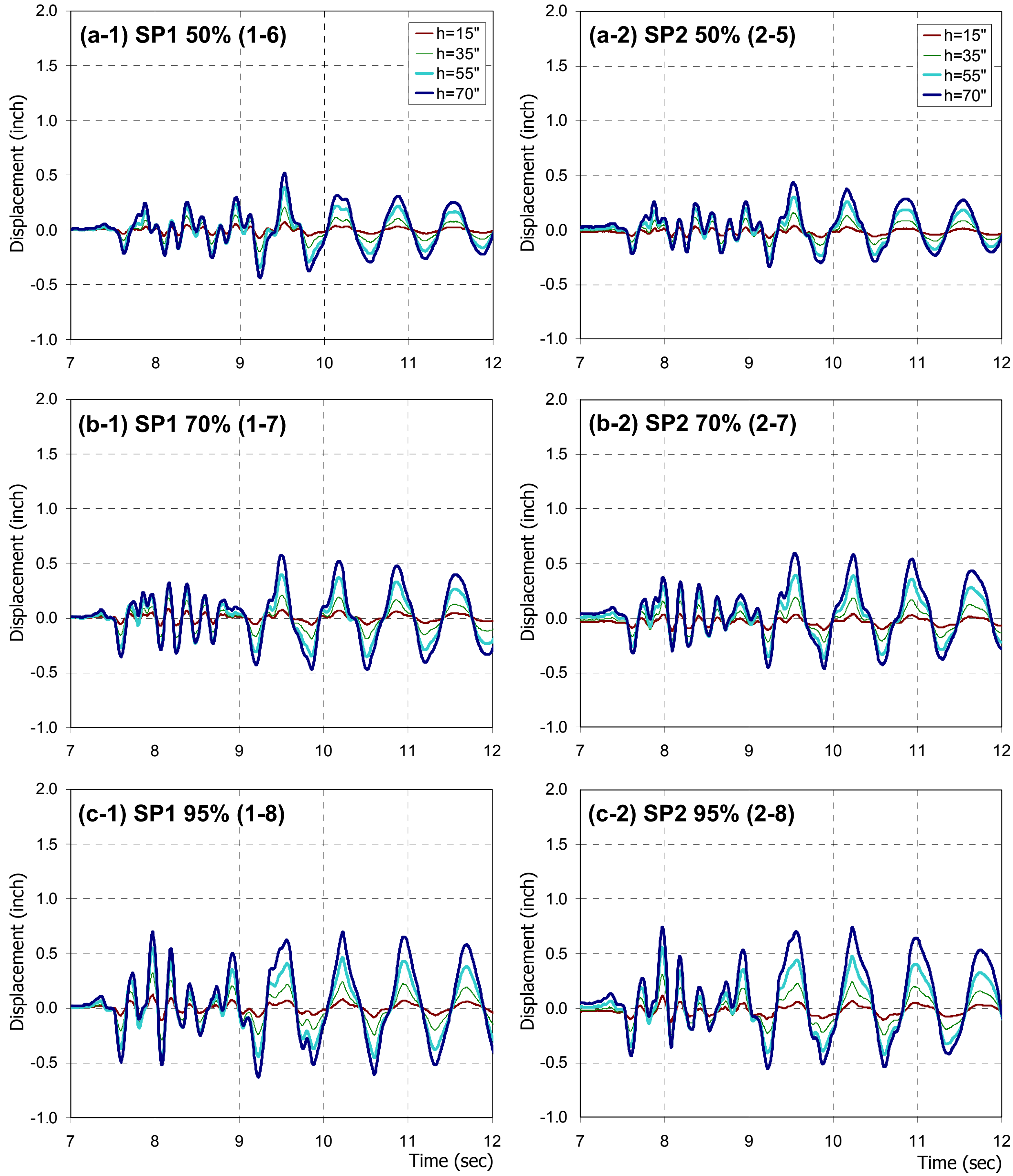

Figure 4.18 **Relative lateral displacement history.**

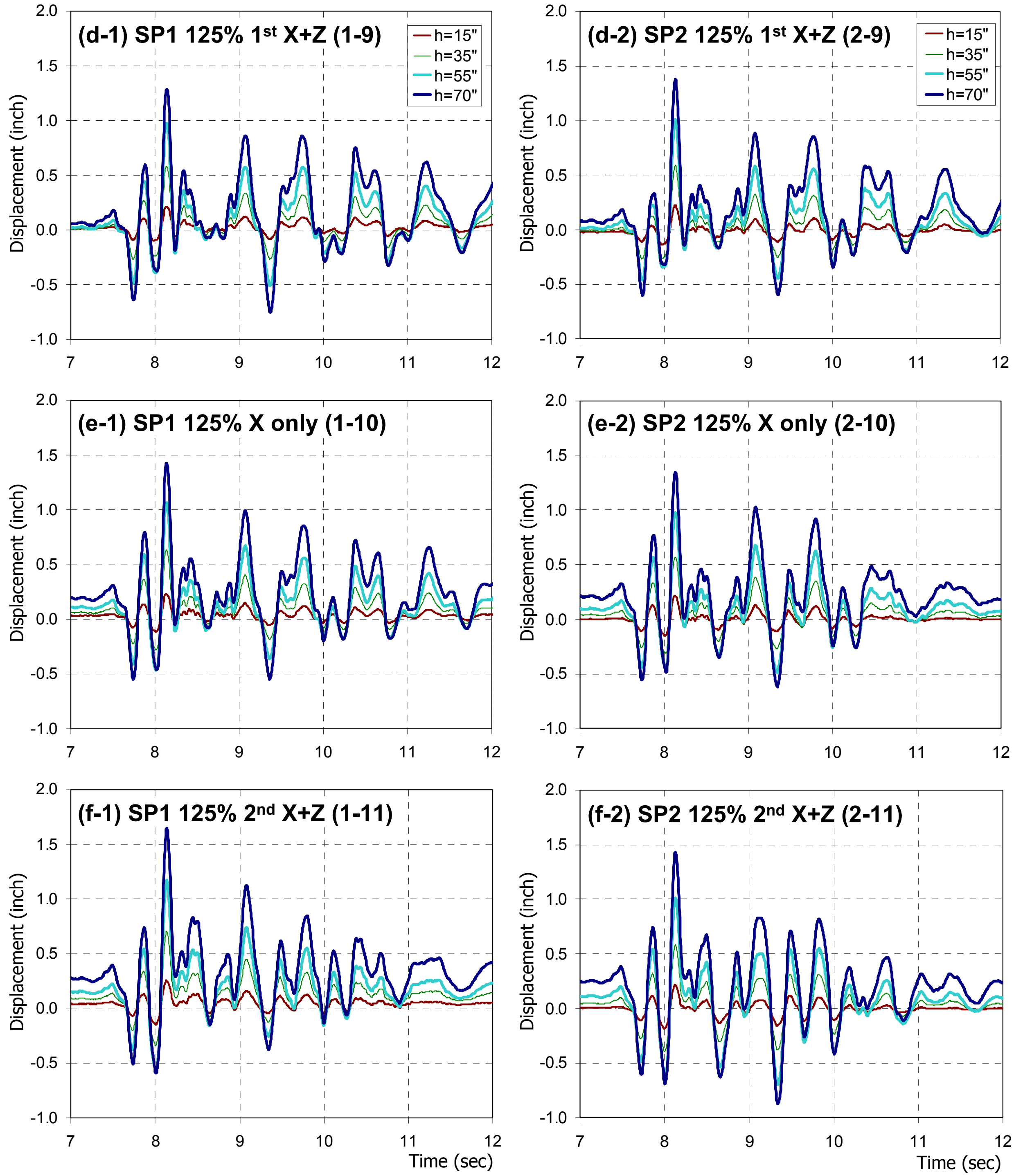

Figure 4.18 Continued.

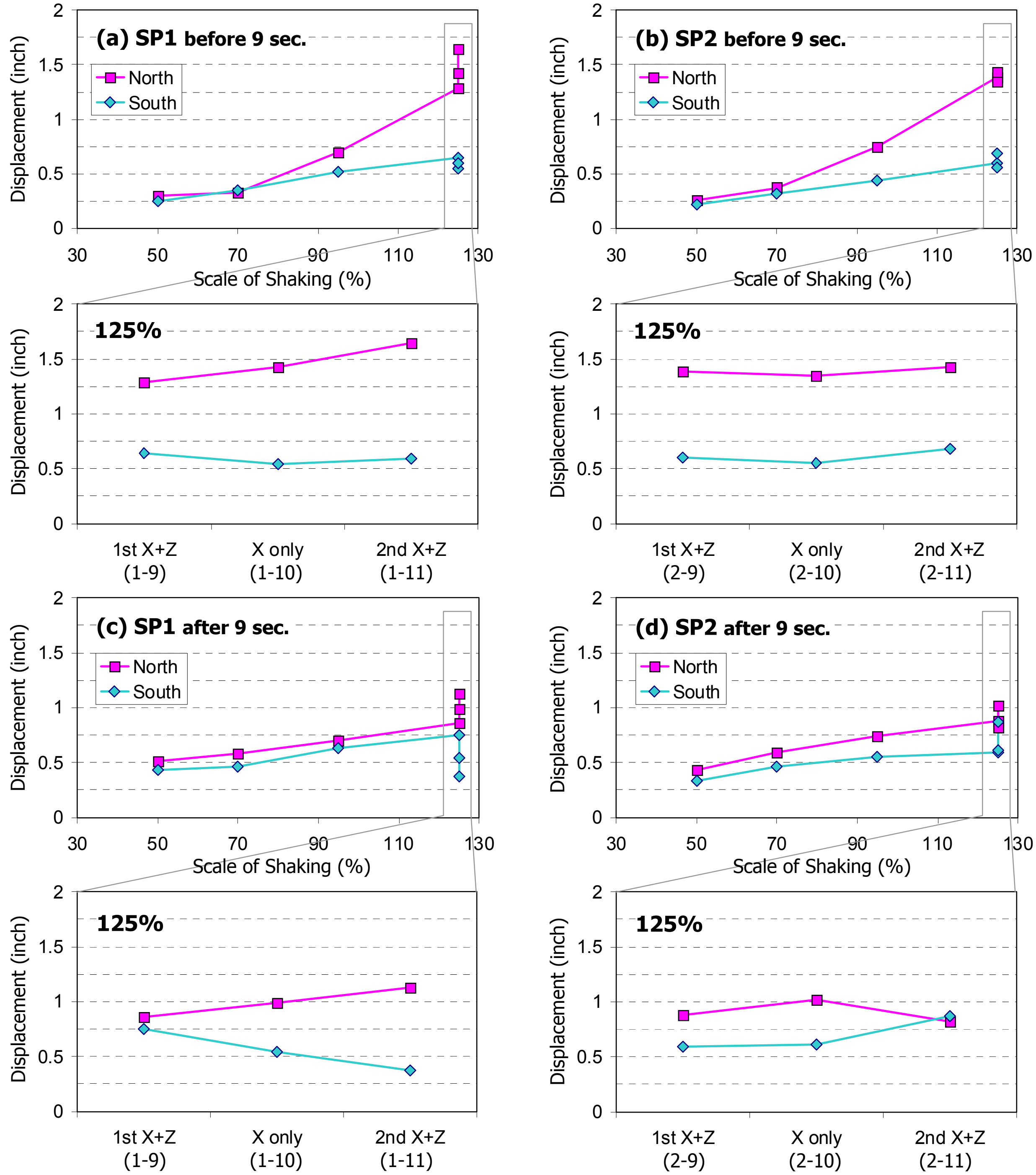

Figure 4.19 Peak relative lateral displacement at the top of the test specimens.

4.5.2 Vertical Displacement

Vertical displacement was measured by wire potentiometers and DCDTs. A total of four wire potentiometers were connected to the bottom of the top concrete blocks. The mean value of the four wire potentiometer measurements is investigated. In addition, two DCDTs were connected to the bottom of the top of the monolithically-cast block on the west and east sides of the column. The mean of the two DCDTs is also discussed in this section.

Figure 4.20(a), (b), and (c) compare the means of the vertical displacement histories from the wire potentiometers and the DCDTs when the specimens were subjected to 50%-, 70%-, and 95%-scale motions, respectively. Worth noting is that the vertical displacement was rarely negative. Since positive displacement was elongation, this observation implies that the centroid of the column cross section had tensile strains most of the time, which is an expected result considering the cross-sectional analysis of a RC column subjected to eccentric axial forces less than the balanced force. The second observation is that the displacement measured by the wire potentiometers was larger than that measured by the DCDT's (up to 17% for the peak positive peaks). Because the wire potentiometers measured displacements of the concrete blocks, it is expected that the displacement history included more oscillations and errors due to the concrete block mass rotations.

Figure 4.20(d), (e), and (f) present vertical displacement histories of the specimens subjected to the 125%-scale motions. The two observations noted above are still valid. In addition, about a 0.05-in. residual displacement was larger than previous cases. Another observation is that the absence of the vertical excitation did not result in a remarkable difference in the vertical displacement. Regarding the peak displacement, there was a decrease in the 125%-scale 'X only' test compared to the '1st X+Z' test. The DCDT measurement of SP1 and SP2 decreased by 3.4% and by 17.7%, respectively; see Figure 4.21. Peak-to-peak amplitude decreased by 14.5% and 29.6% for SP1 and SP2, respectively; see Figure 4.22. The residual vertical displacement increased similar to the case of the residual lateral displacement. Finally, SP1 and SP2 elongated by 0.068 in. and 0.040 in. after the 125%-scale '2nd X+Z' test, respectively.

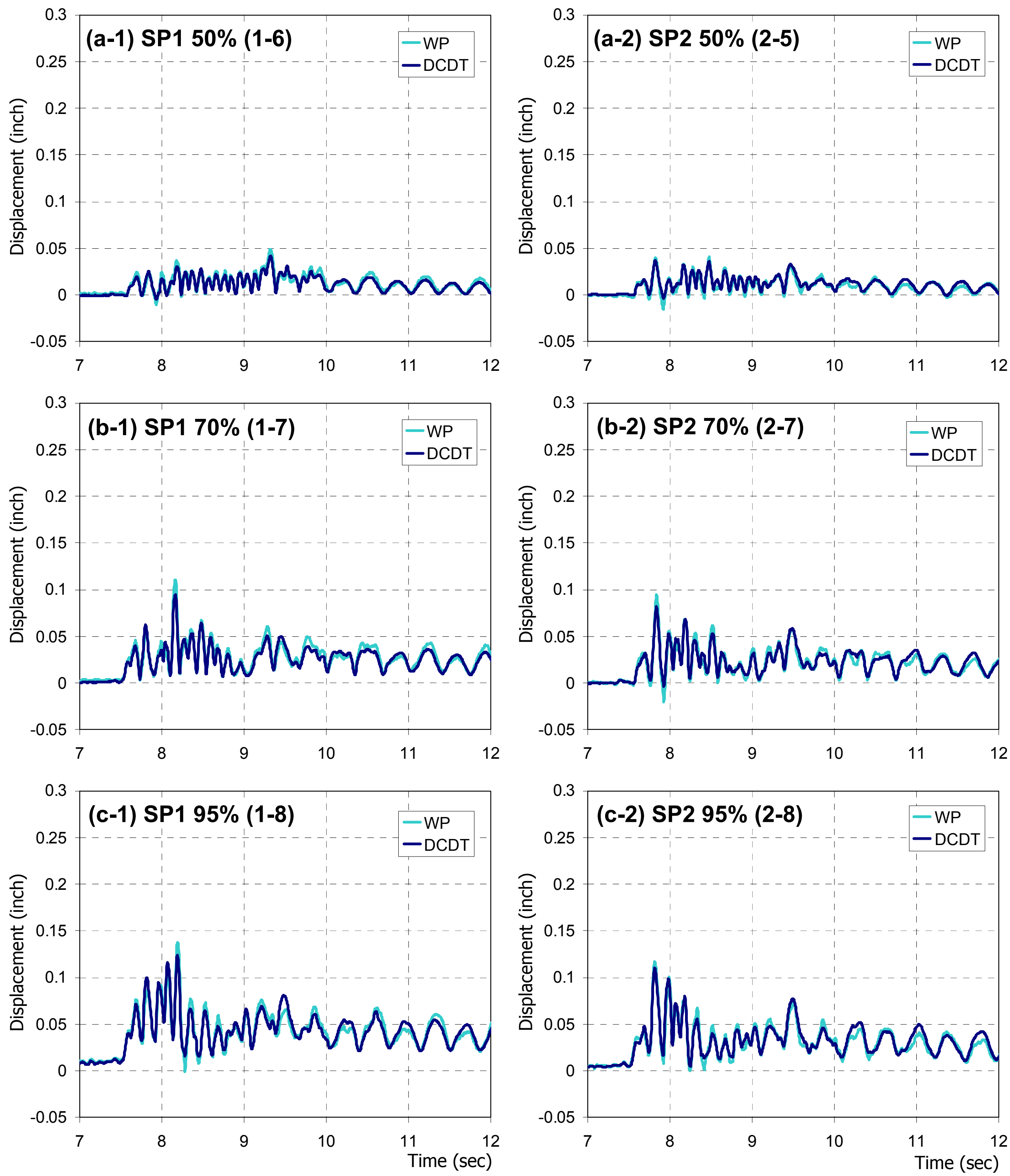

Figure 4.20 **Relative vertical displacement history of the top block and the concrete additional mass blocks.**

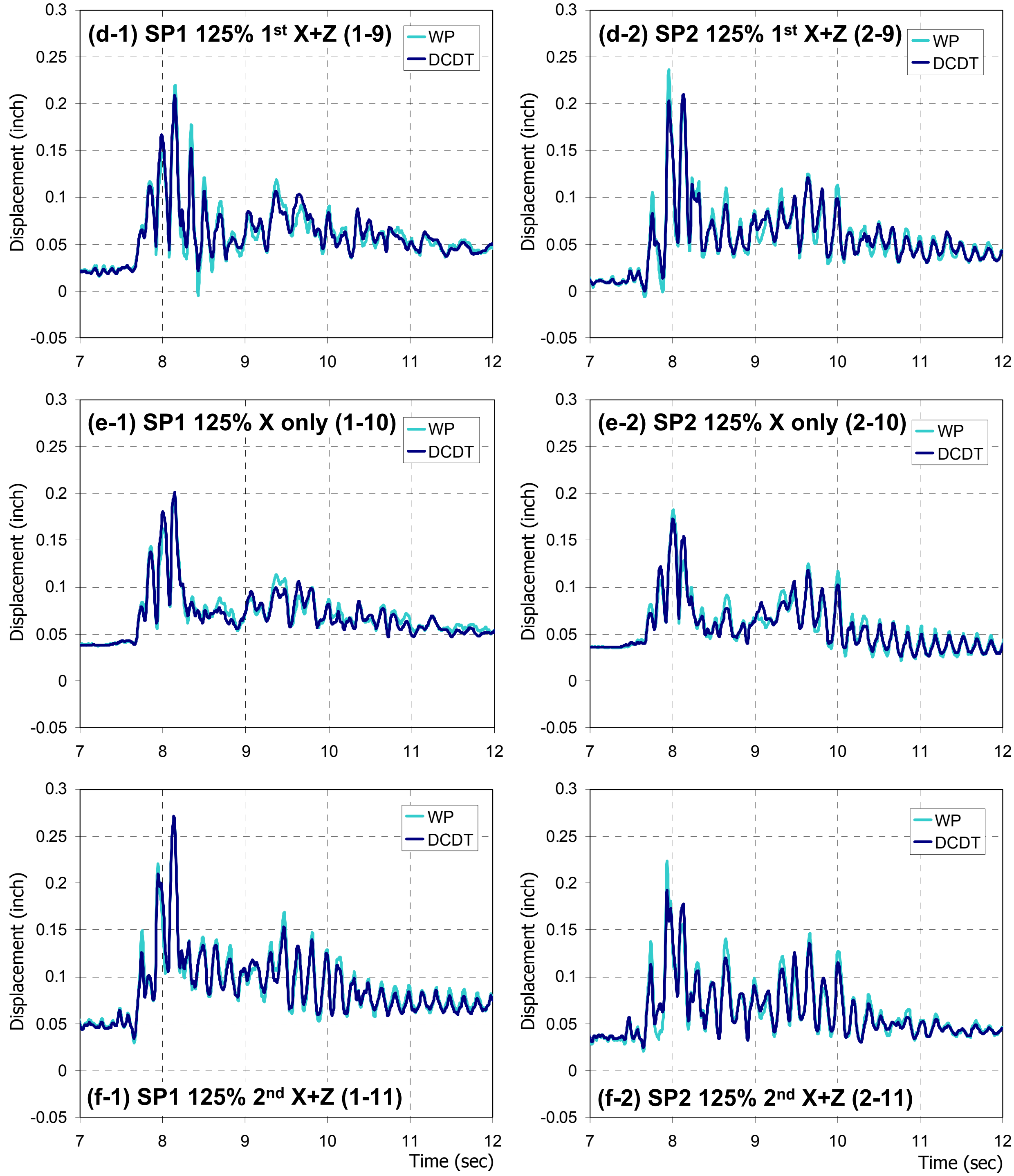

Figure 4.20 Continued.

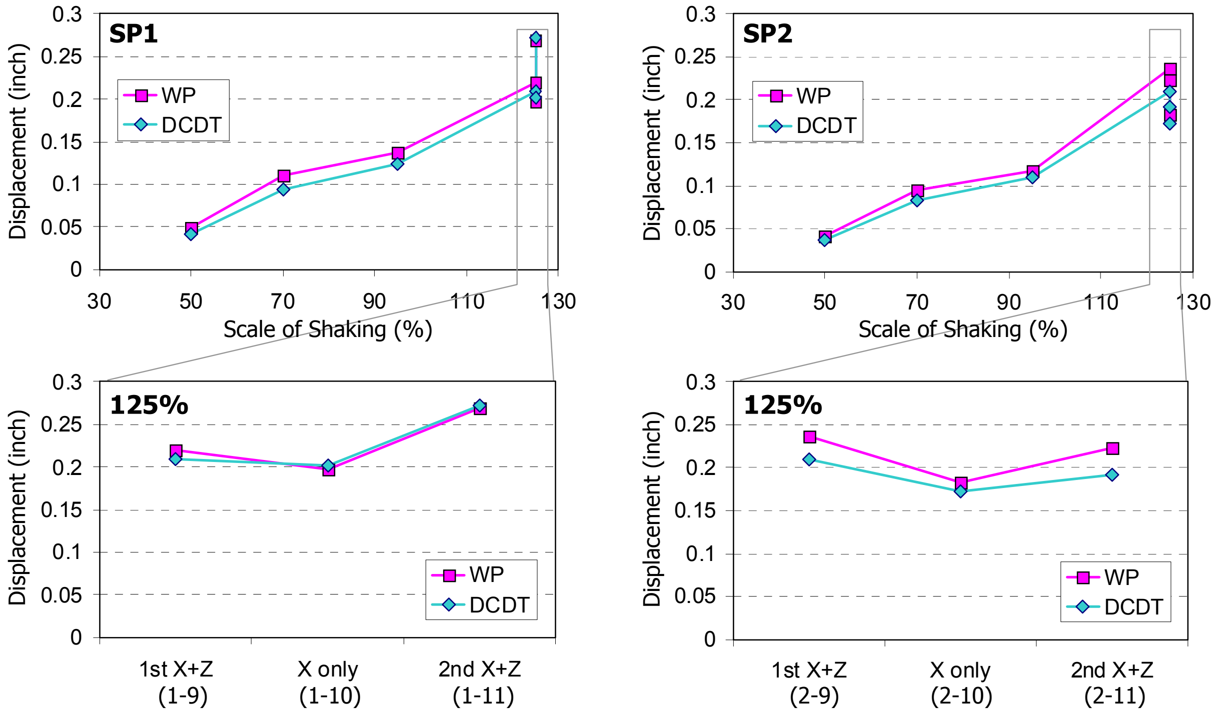

Figure 4.21 Peak vertical displacement of the test specimens.

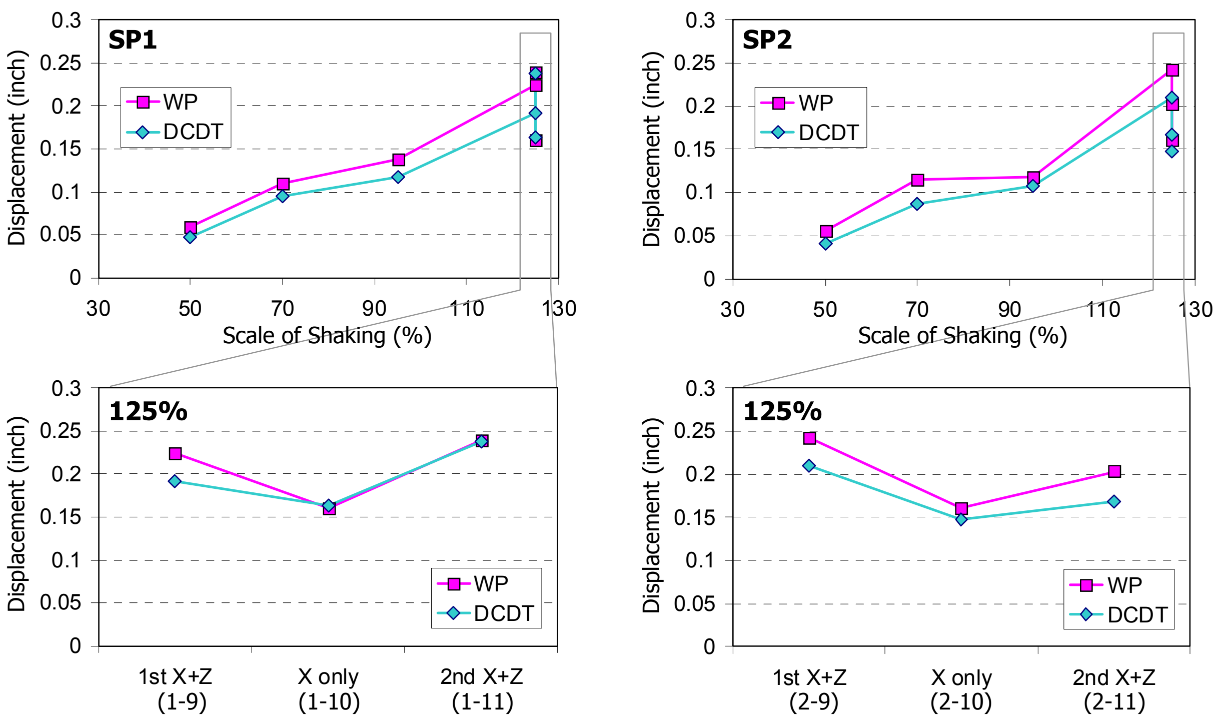

Figure 4.22 Peak-to-peak vertical displacement of the test specimens.

4.6 FORCE-DISPLACEMENT RELATIONSHIPS

Figure 4.32 shows the relationship between the base shear and lateral displacement; Figure 4.24 shows the relationship between the axial force and axial deformation. Note that the axial force is positive in compression and negative in tension, and the axial displacement is positive in elongation and negative in shortening.

Figure 4.23(a), (b), and (c) presents the shear force-lateral displacement relationships of SP1 and SP2 subjected to the respective 50%-, 70%-, and 95%-scale motions (runs 1-7, 1-8, and 1-9 for SP1 and 2-7, 2-8, and 2-9 for SP2). An increased intensity of the ground motion was accompany by a decrease in the lateral stiffness and increasing damage. Figure 4.23(d), (e), and (f) presents the 125%-scale motions (runs 1-10, 1-11, and 1-12 for SP1 and 2-10, 2-11, and 2-12 for SP2), where the lateral stiffness slightly decreased with the increase of runs as the damage in the column increased. In addition, the stiffness in the positive force and displacement side was smaller than that in the negative side, which was a consequence of the pulse in the ground motion resulting in asymmetric displacements and accordingly asymmetric damage distribution. As mentioned previously, the decrease in the maximum positive force in the 125% '2nd X+Z' test with respect to the 125% 'X only' test can be partly attributed to the decrease in shear force capacity due to the presence of axial tension. In addition, it should be noted that the maximum positive and negative shear forces of SP2 (95%- and 125%-scales, respectively, in Figure 4.23) were smaller than those of SP1 since SP2 had lower shear capacity provided by the transverse reinforcement with wider spacing.

Figure 4.24(a), (b), and (c) presents axial force-vertical displacement relationships of SP1 and SP2 subjected to the respective 50%-, 70%-, and 95%-scale motions (runs 1-7, 1-8, and 1-9 for SP1 and 2-7, 2-8, and 2-9 for SP2). This column was not under significant tension before the 125%-scale motion was applied. Note that the gravity load was about 100 kips from the load cells measurements, which represents the origin of the force in the axial force-deformation relationships. The axial elongation was almost eight times the axial shortening due to the opening of the cracks. Figure 4.24(d), (e) and (f) confirms that the vertical component of the 125%-scale motion caused tension and significant compression in the column; see Figure 4.14. The axial force subjected to the excitation with horizontal component only was between 50 and 150 kips, but that subjected to both horizontal and vertical components was between -70 and 250 kips. (The presence of axial force under only horizontal component was due to the presence of vertical acceleration on the shaking table, resulting from the interaction of the vertical and horizontal actuators to balance the overturning moment.) The axial elongation continued to increase for the 125% 'X only' test due to the presence of the cracks.

The straight lines in Figure 4.23 show the lateral stiffness of each test. The stiffness was calculated based on the maximum shear force on the positive and negative sides and the corresponding lateral displacement. Up to 70%-scale test, the stiffness value on the positive side was identical to that on the negative side. However, as the intensity level increased, the stiffness decrease in the positive side was more significant. From 70%- to 95%-scale and from 95%- to the 1st 125%-scale tests, the lateral stiffness on the positive side decreased by about 40%, while that on the negative side decreased by 25% or less. From the 125% '1st X+Z' to the 'X only' and the subsequent tests, the stiffness change was not remarkable on the positive side, but the decrease continued on the negative side. This trend implied that the south side of the column was damaged more first, causing less stiffness on the positive side (positive was previously defined as the direction from south to north). Subsequently, the damage extended to the north side of the column, which caused the following stiffness decrease on the negative side. These observations were consistent with the crack propagation patterns presented in the following section. Note that the stiffness values were different from those obtained from the pullback tests where the column was predominantly deflecting in the first mode, which was the translational mode representing a cantilever column. However, during the ground excitations, the column deflected in a shape that was a combination of translational and rotational modes (presented later in Figure 5.8. Hence, stiffness values calculated from the force-displacement relationships up to 95%-scale tests were on average larger than the lateral stiffness from the pullback test discussed in Section 4.2.1.

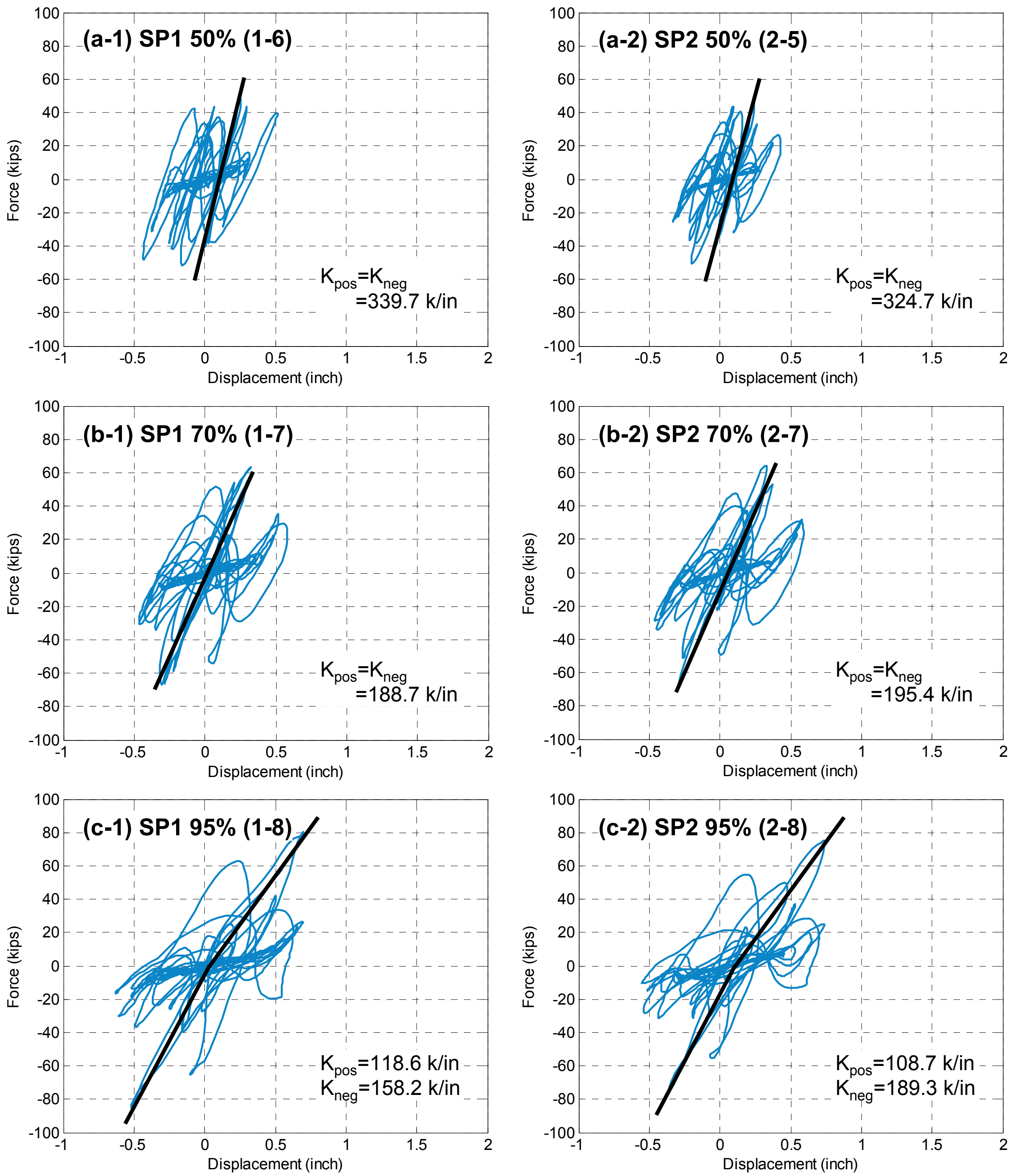

Figure 4.23 Shear force-lateral displacement relationships.

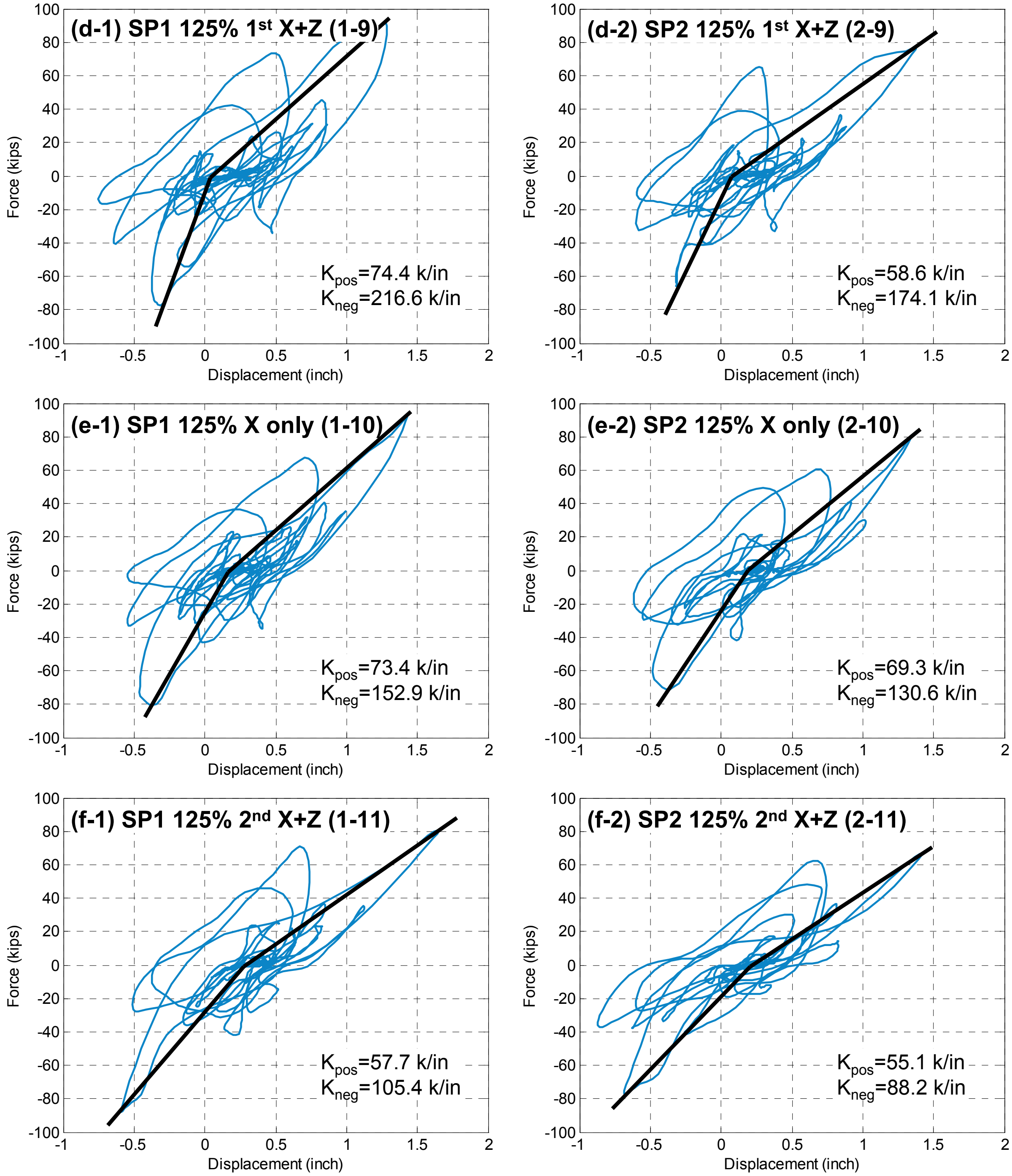

Figure 4.23 Continued.

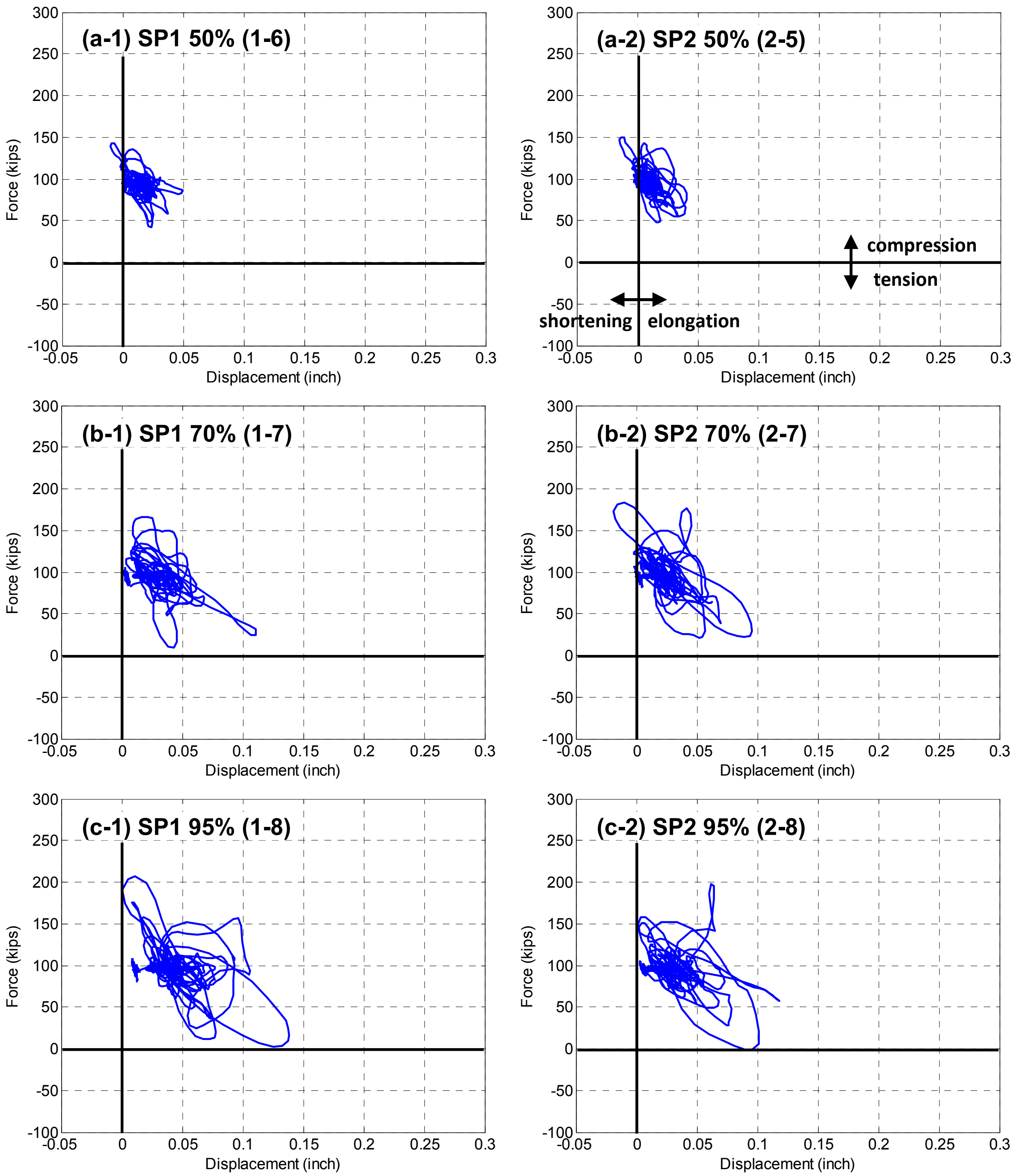

Figure 4.24 Axial force-vertical displacement relationships.

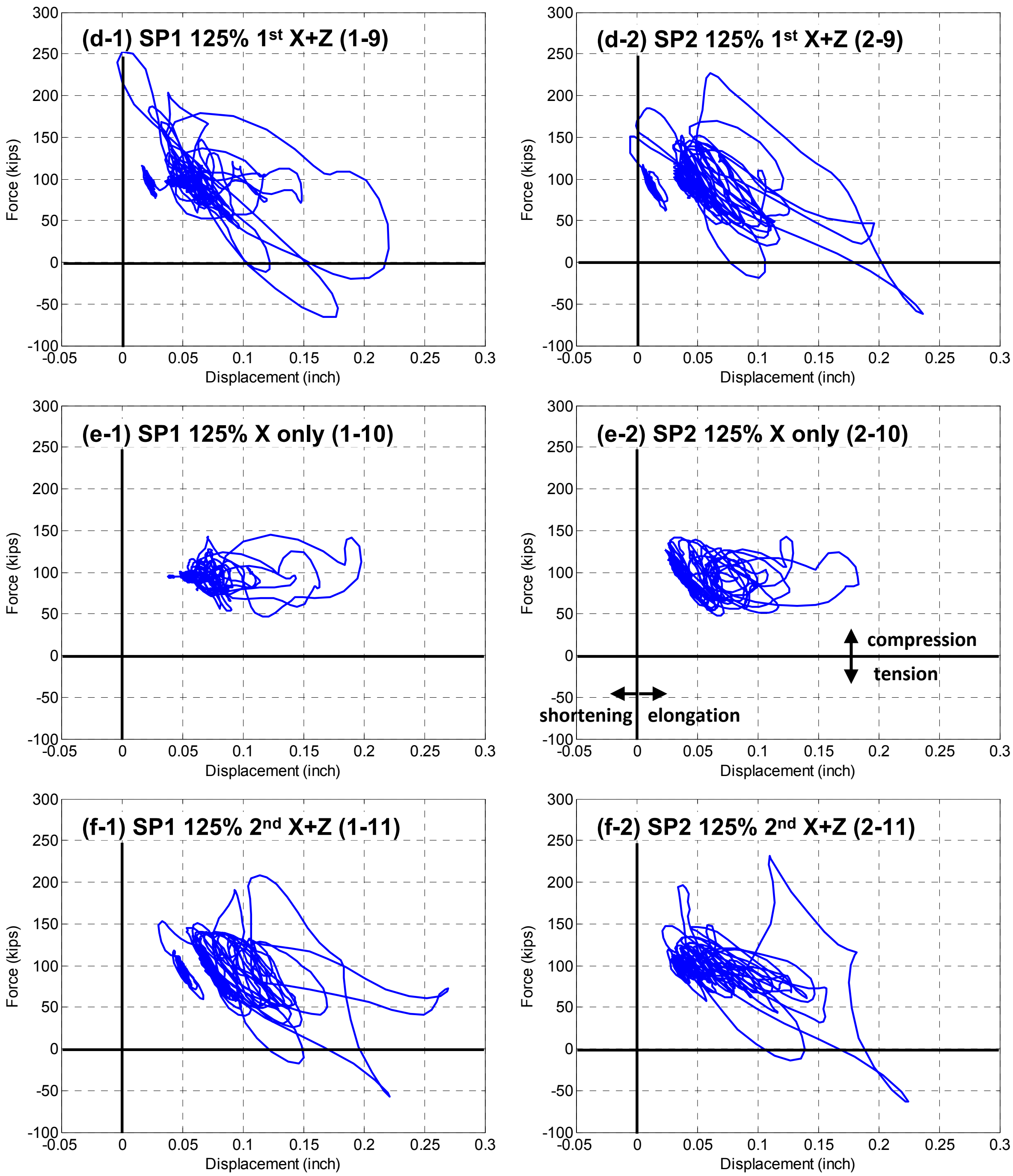

Figure 4.24 Continued.

4.7 CRACK PROPAGATION

Crack initiation and propagation of SP1 and SP2 are shown in Figures 4.25 and 4.26, respectively. Photographs of the damaged specimens SP1 and SP2 are shown in Appendix E. It should be noted that thicker lines represent new cracks that did not exist in the previous runs.

After the 50%-scale test [Figure 4.25(a) for SP1 and Figure 4.26(a) for SP2], only three or four cracks appeared near the top on the south and north sides of SP1; SP2 had more cracks in the upper part of the column, and the first shear crack appeared near h = 60 in.. The lower section of each test specimen experienced less cracks than the upper section. Finally, SP2 had the first vertical crack near h = 40 in. on the north side.

After the 70%-scale test [Figure 4.25(b) for SP1 and Figure 4.26(b) for SP2], several shear cracks appeared near the top on the east and west sides of the columns. In SP1 they were near or above h = 50 in. In SP2 some shear cracks appeared even between h = 35 in. and 50 in. In addition, SP2 had a significant number of vertical cracks above h = 20 in. on the north side.

As shown in Figure 4.25(c) for SP1 and Figure 4.26(c) for SP2, cover spalling started at the top on the north and south sides, and shear cracks appeared near the bottom on the east and west sides after 95%-scale test (runs 1-8 for SP1 and 2-8 for SP2). As a result, there were several shear cracks along the height of the columns, except the regions between h = 25 in. and 35 in. on the east and west sides of SP1 and between h = 20 in. and 35 in, of SP2. SP1 had vertical cracks above h = 30 in. on the north side and above h = 20 in. on the south side. SP2 had similar cracks above h = 10 in. on the north side and between 10 in. and 30 in. on the south side.

As the intensity increased, cracks extended over the columns. In particular, shear cracks were clearly evident in both columns after 125%-scale motions except for the middle of SP1 (h = 30 in. to 40 in., i.e., 1.5D to 2.0D). Compared to the 125%-scale 'X+Z' tests, the 'X only' test produced significantly less shear and vertical cracks [Figure 4.25(e) for SP1 and Figure 4.26(e) for SP2]. This observation is consistent with the reduction of shear strength at '2nd X+Z' test with respect to the 'X only' test (around 12 and 14 kips reduction for SP1 and SP2, respectively); see Section 4.4.1. After the 125%-scale '2nd X+Z' test, the vertical cracks extended over the columns, except for the region between h = 10 in. and 20 in. of SP1. The crack distribution of SP2 was denser than that of SP1 subjected to the same intensity level due to lower shear capacity of SP2 compared to SP1.

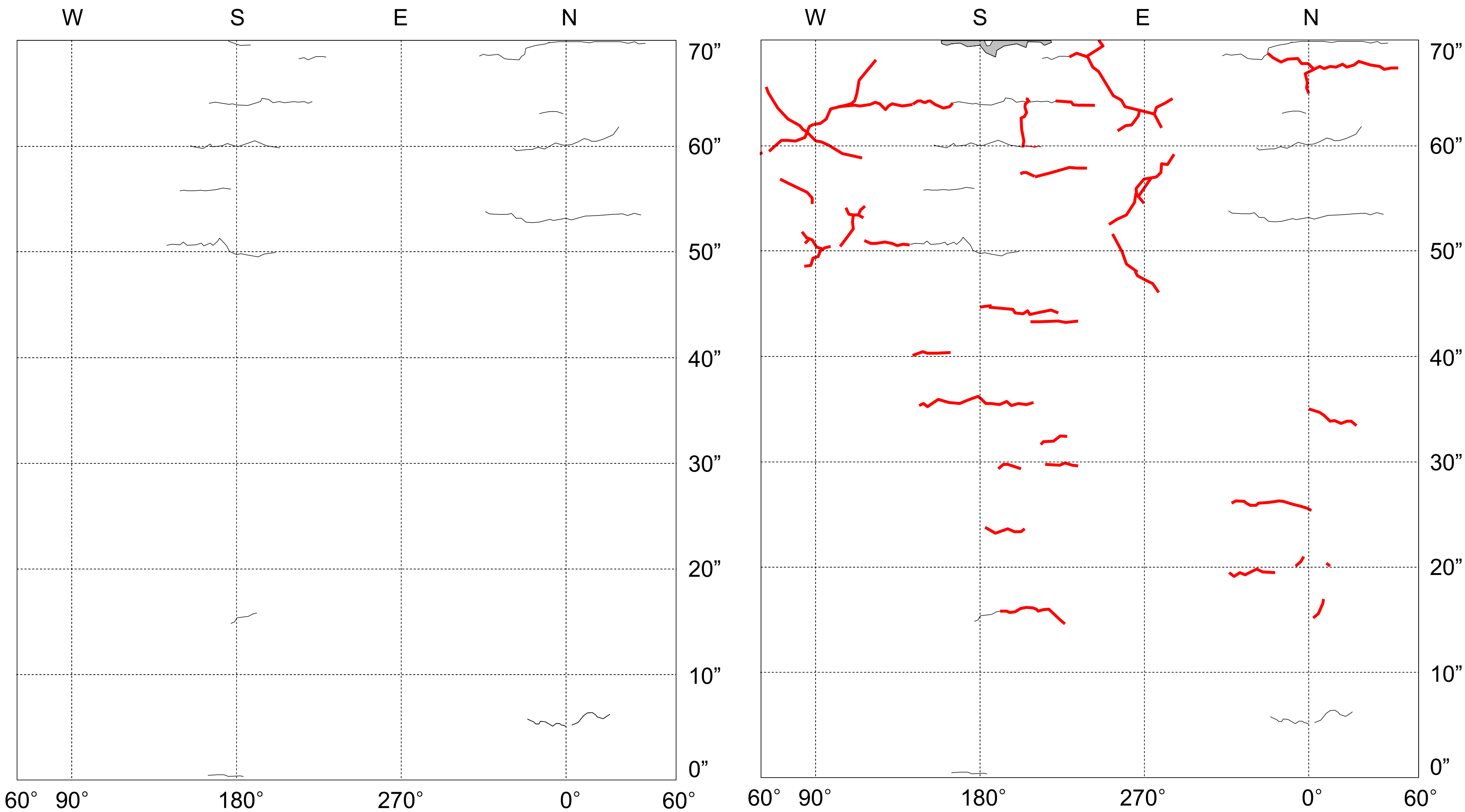

(a) after the 50%-scale run (run 1-6)

(b) after the 70%-scale run (run 1-7)

Figure 4.25 Crack propagation of SP1.

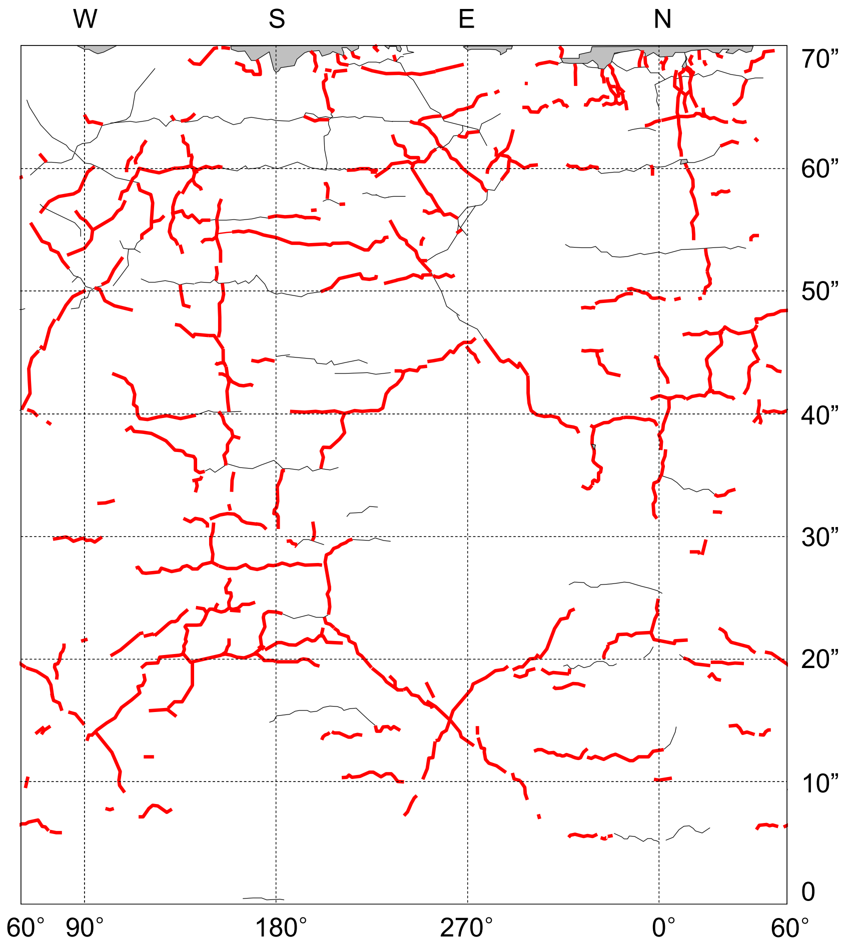

(c) after the 95%-scale run (run 1-8)

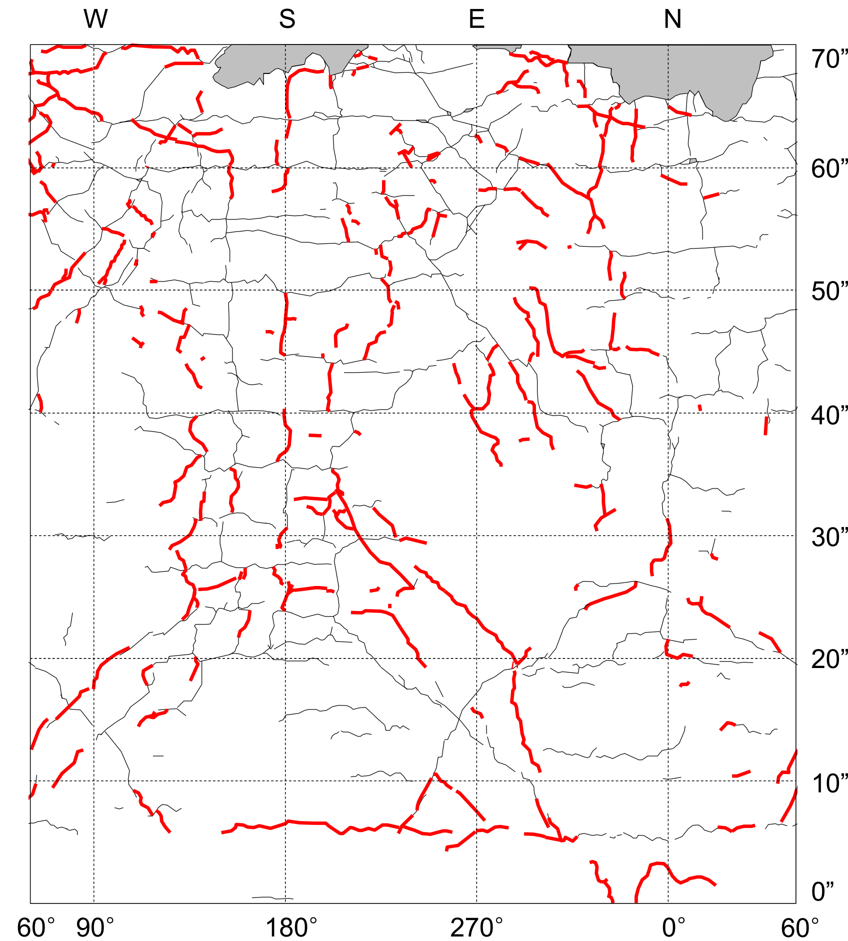

(d) after the 125%-scale '1st X+Z' run (run 1-9)

Figure 4.25 Continued.

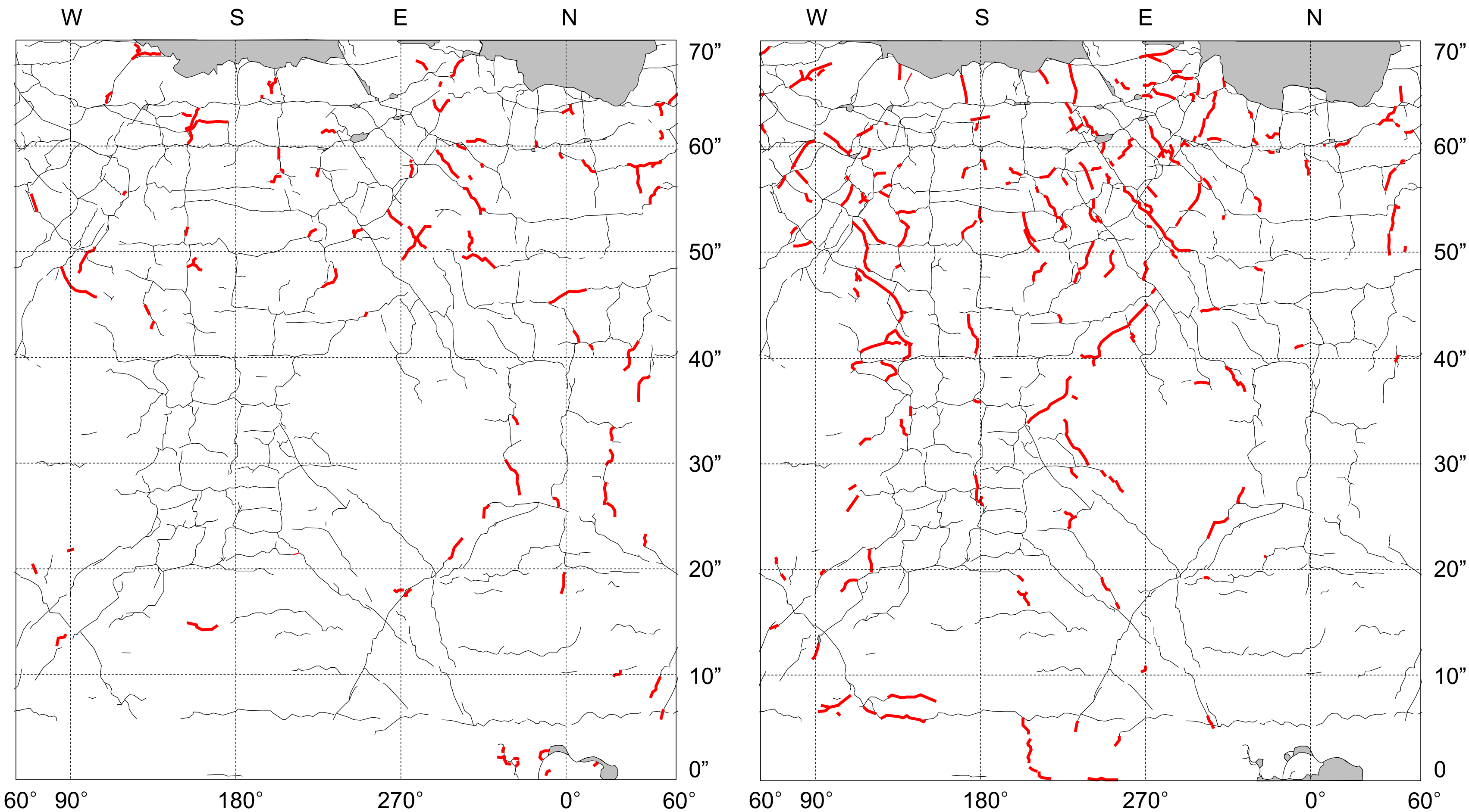

(e) after the 125%-scale ‘X only’ run (run 1-10)

(f) after the 125%-scale ‘2nd X+Z’ run (run 1-11)

Figure 4.25 Continued.

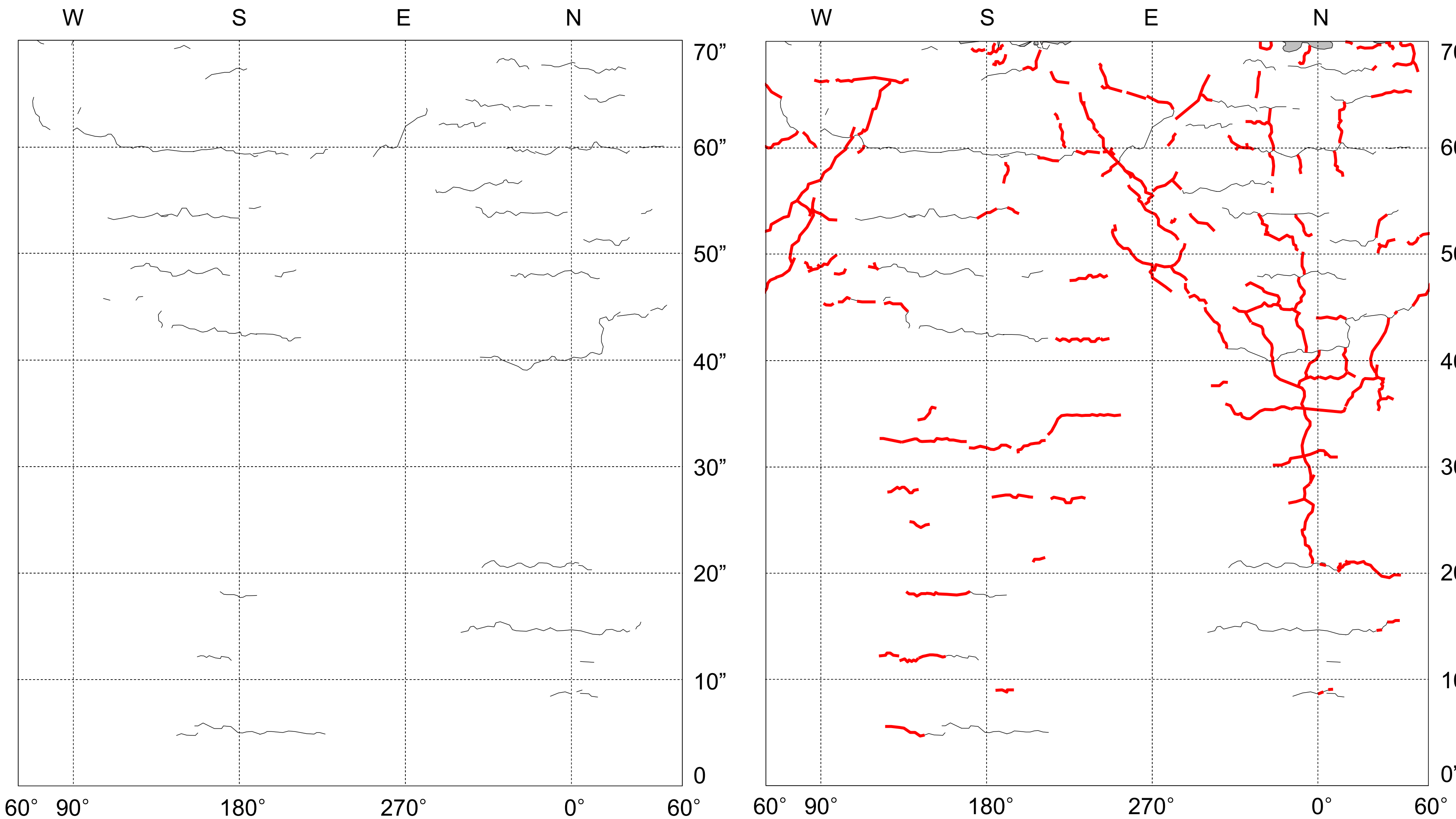

(a) After the 50%-scale run (run 2-6)

(b) After the 70%-scale run (run 2-7)

Figure 4.26 Crack propagation of SP2.

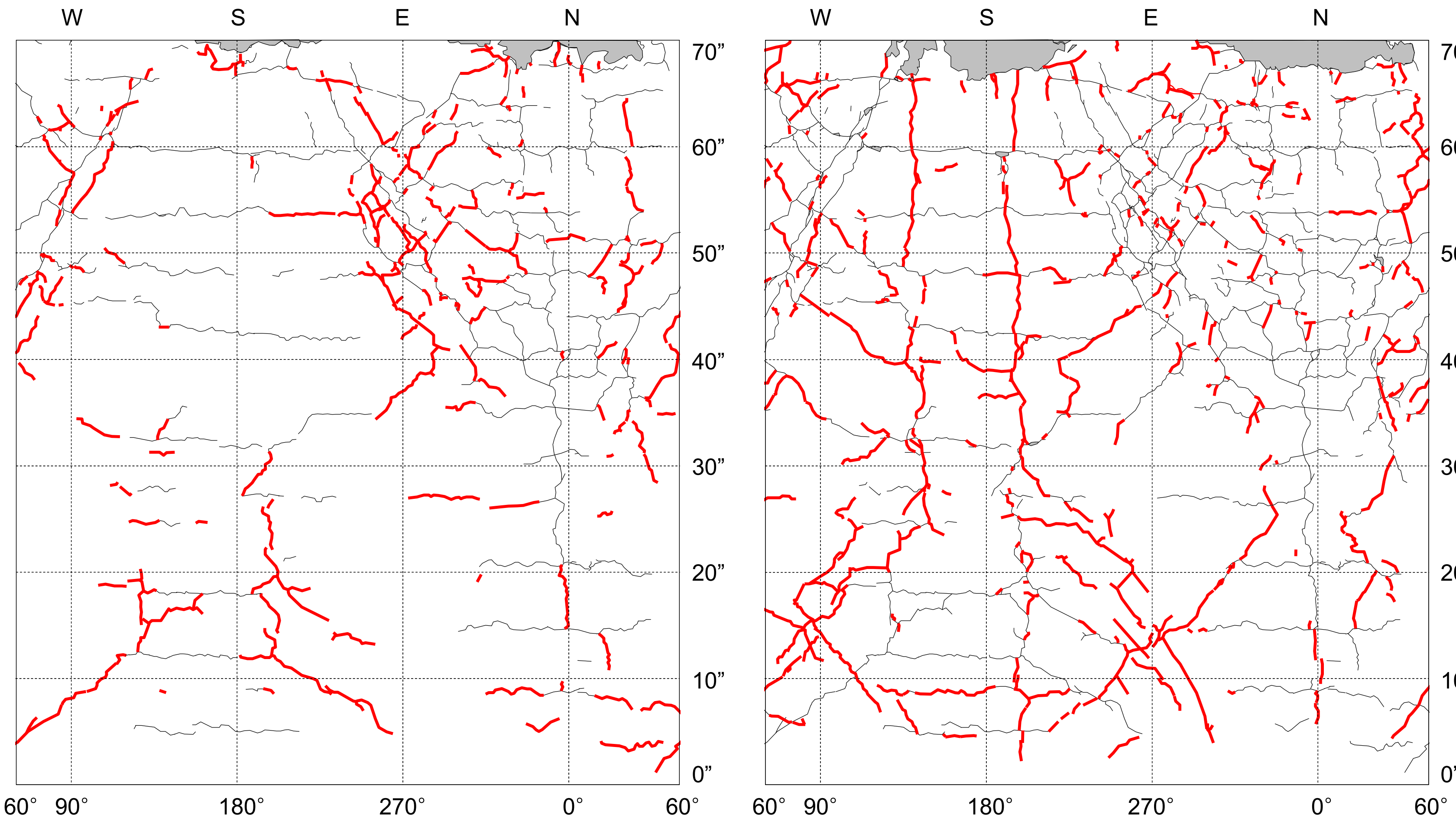

(c) after the 95%-scale run (run 2-8)

(d) after the 125%-scale '1st X+Z' run (run 2-9)

Figure 4.26 Continued.

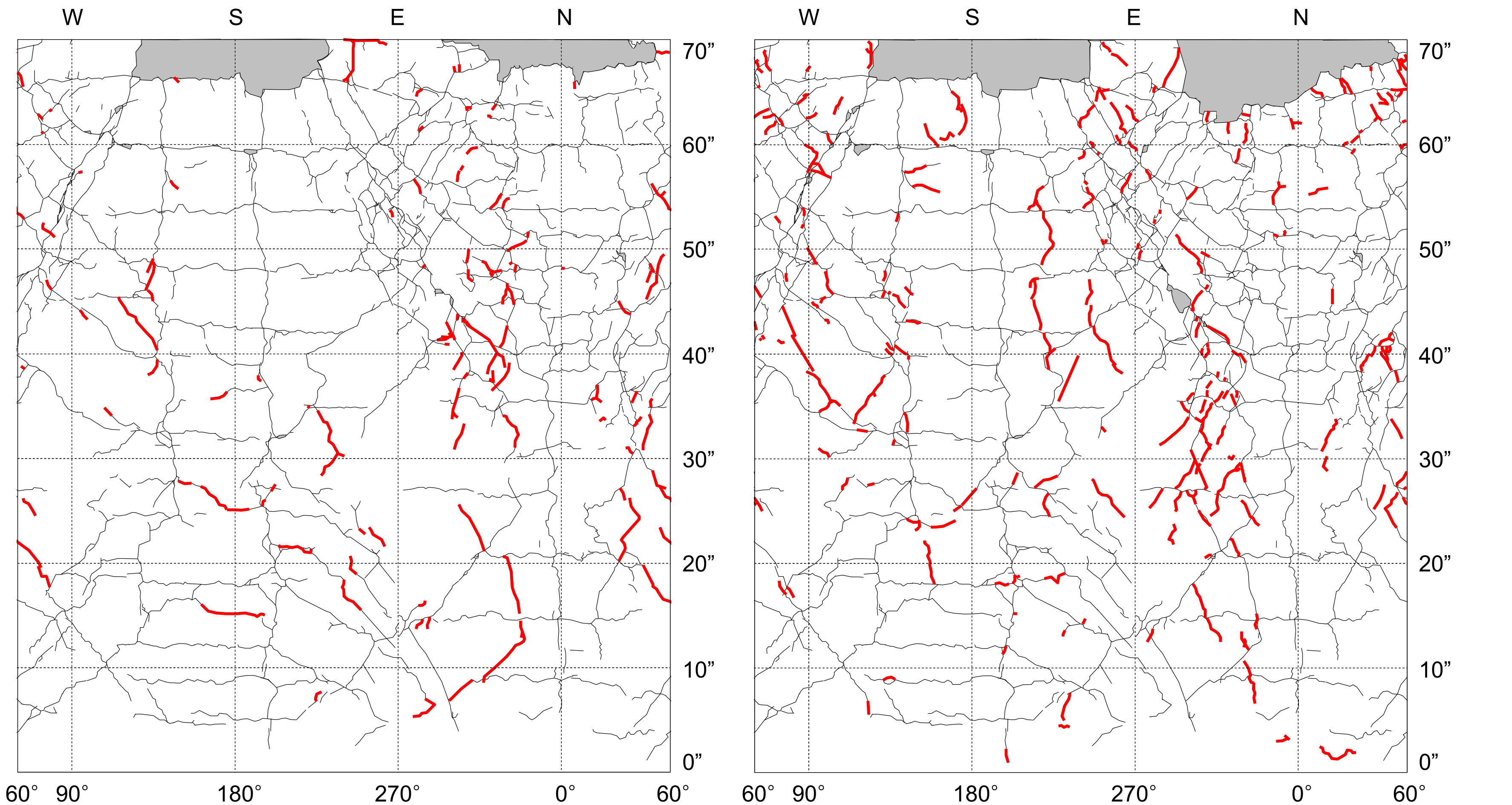

(e) after the 125%-scale ‘X only’ run (run 2-10)

(f) after the 125%-scale ‘2nd X+Z’ run (run 2-11)

Figure 4.26 Continued.

4.8 SUMMARY

Test results regarding global responses were investigated in this chapter. Before the main tests, the pullback and free vibration tests were conducted to determine the initial lateral stiffness and period of each specimen. SP1 was stiffer than SP2 by about 50%, and had a shorter lateral period than SP2 by 8.5%. The rationale for not having the ratio of stiffness equal to the square of the ratio of period was because the tested column represented a 2DOF system in the lateral direction, with coupling between the translational and rotational modes. During the low-intensity excitations, the periods of both specimens became close to each other. Based on this observation, it is speculated that SP2 experienced some cracking before the tests.

Shaking table flexibility had a pronounced effect on the vertical response. The dynamic mode that was introduced by the table stiffness (in the vertical direction) and table mass governed the response in the vertical direction; therefore, response due to the column's dynamic mode was pronounced much less compared to the case of a rigid shaking table.

The acceleration recorded on the mass in the X-direction had a low frequency content and low amplitude compared to that at the top of the column or on the table which was due to the rigid body rotation of mass blocks.

The maximum acceleration at the top of the column or on the mass blocks did not increase linearly with that on the table or the input intensity for two reasons First, the lateral stiffness of the column decreased with increasing level of intensity; second, the base shear capacity of the column was reached at the higher intensity levels. In contrast, the acceleration histories in the Z-direction were almost the same on the table, along the column height, and on top of the mass blocks. The maximum values linearly increased with the input intensity since axial forces were in the linear range and therefore axial stiffness variation was minor.

The force response was essential to the study since it is closely related to shear strength of the column. Similar to the accelerations, the maximum shear force did not increase linearly with the input intensity, but the maximum axial force did. The peak shear force in 125%-scale 'X only' test was larger than 125%-scale 1st or 2nd 'X+Z' test for each specimen, where the peak force was determined by the shear strength at this intensity. Considerable tensile force was induced on the test column due to vertical excitation. Tension in the columns is believed to result in degradation of shear strength, which is mainly due to the degradation of concrete contribution to shear strength.

Comparison of bending moment histories at the base and top of both of the specimens indicated that they were opposite in sign during the strong part of the excitation of all the intensity levels, suggesting that the columns were in double-curvature. Moments at the base and top were similar in sign after the strong part of the excitation ceased for all the tests. Note that three 125%-scale resulted in similar maximum moment values, suggesting that the axial force variation did not affect the bending moment noticeably.

The relative displacement histories captured the horizontal and vertical movement of each specimen. Displacement at the top was the largest in the X-direction at less than 2.0 in. The residual lateral displacement increased with the increased intensity of ground motions. The vertical displacement rarely went to the shortening side, and the residual vertical displacement kept increasing on the elongation side, implying that the column was elongated by the presence of horizontal and diagonal cracks. Damage detection after the tests indicated the presence of cracks consistent with the residual axial displacements. In addition, it was observed that 125%-scale 'X only' motion did not increase the residual vertical displacement.

The change of lateral stiffness is clearly shown in the shear force-lateral displacement relationship. From 95%-scale tests, the decrease in lateral stiffness had a directional difference, implying that the damage was not symmetric on the north and south. In the last 125%-scale test, stiffness in the positive direction was about 17% of that in 50%-scale test. In the axial force-vertical displacement relation, no significant decrease in stiffness was observed.

Flexural damage took place both at the top and base of the column as the scale of the ground motion increased, and flexural damage at the top of the column occurred before that at the base since the moment at the top was larger. This was a result of the large mass moment of inertia at the top of the column. Reduction of the acceleration on the mass block due to the rotations contributed to this situation as well. As a result of flexural yielding both at the top and bottom of the column in double curvature, the shear force reached shear capacity, which would not take place if yielding was occurring at the bottom and the moment at the top was smaller than the yield moment; therefore, shear cracks occurred.

The progress of shear failure was visible in crack patterns. Both specimens started to experience diagonal cracks near h = 50~65 in. on the east and west sides during 70%-scale tests. They spread over the over the east and west sides except h = 25~35 in. Also, there were vertical cracks as well as horizontal cracks on the north and south sides. SP2 had more cracks than SP1, since SP2 had wider hoop spacing. Note that the diagonal cracks did not appear during 125% 'X only' test as many as those in 125% 'X+Z' tests, supporting the observation that the concrete contribution to shear strength was reduced due to the presence of axial tension.

5 Results of Dynamic Tests: Local Responses

5.1 INTRODUCTION

Local responses gathered during the tests by 38 strain gages in each specimen. Locations of these gages are specified in Appendix D. They provide information on the response of each section during the test. The curvatures and longitudinal and transverse strains are presented in this chapter. In addition, the relationships of each response quantity and the force histories discussed in Chapter 4 are investigated.

5.2 CURVATURES

To measure the curvature at certain points on the north and south sides of the column, LVDTs were installed on the instrumentation rods; the locations of these LVDTs are shown in Appendix D. As an alternative to calculating the curvatures using the LVDTs, the longitudinal reinforcement strain data obtained from the strain gages can be used. Theoretically, the curvatures from the LVDTs and from the strain gages should be the same if they were installed at the same height. However, differences exist because of the averaging effect of the LVDTs measurements compared to the point-wise strain gages measurements. Since the strains obtained from the gages were less noisy, and were not affected by averaging, the curvatures in this section were computed using the strain measurements along the longitudinal reinforcing bars. Sign convention for curvature is such that it is positive when $\left(\varepsilon_{SL} - \varepsilon_{NL}\right)$ is positive, where ε_{NL} and ε_{SL} are the longitudinal strain on the north and south bars, respectively. This convention results in consistent signs for displacements and curvatures, i.e., when displacement is positive, curvature is also positive.

Figure 5.1 shows the curvature histories at h = 10 in. and 60 in. Up to 70%-scale motion [Figure 5.1(a) and (b)], both specimens had similar curvature time histories. Also, the curvatures of both specimens remained within $\pm 0.5 \times 10^{-3}$ in.$^{-1}$, and no residual curvature was detected. The curvature histories at h = 10 in. had an opposite sign to that at h = 60 in. between 8~9 sec (double curvature), during the strong motion part of the excitation applied in X- and Z-directions' however, both cross sections had the same curvature sign and consistent lateral displacements, i.e., single curvature, after 9.5 sec. The first noticeable difference of the magnitude of curvatures for the two cross sections (top and bottom) appeared during the 95%-scale motion. Between 7.5

and 8.5 sec, the curvature at h = 60 in. had two negative peaks, implying that the north side elongated more than the south side. After these two peaks, the curvature at h = 60 in. had residual curvatures of -0.41×10^{-3} and -0.28×10^{-3} in.$^{-1}$ for SP1 and SP2, respectively. Under the same motion, there was no residual curvature at the cross-section at h = 10 in. Due to the residual curvature at h = 60 in., the column was in double curvature even after the strong motion part of the excitation. Note that the curvature of the cross section near the top of the column was influenced more by the higher modes of vibration than that of the cross section near the bottom of the column. This was manifested in the form of superposed small amplitude high-frequency oscillations in the curvature time history of the cross section near the top of the column due to the effect of the rotational mode of vibration.

In the 125%-scale tests, see Figure 5.1(d), (e) and (f), SP1 and SP2 experienced different curvature results. In these figures, three blue dashed lines indicate the time of the shear peaks, and a red solid line indicates the time of the axial tension peak (which is over 50 kips). The main shear peaks, i.e., two positive and one negative shear peaks, appeared between 7.8 and 8.2 sec of each test, as discussed in Section 4.4.1. First, the cross section at h = 10 in. did not experience any residual curvature in SP1 but it did in SP2, with the amount of approximately -0.25×10^{-3} in.$^{-1}$ at the end of the 2nd X+Z test. Second, the curvature at h = 60 in. increased as the 125%-scale runs were repeated with the residual curvature approaching zero, from -0.31×10^{-3} in^{-1} (run 1-9) to -0.14×10^{-3} in.$^{-1}$ (run 1-10) to -0.08×10^{-3} in.$^{-1}$ (run 1-11). In addition, the peak-to-peak amplitudes in SP1 increased significantly as the 125%-scale runs were repeated, but they did not in SP2; refer to Table 5.1 and Figure 5.2. In similar to smaller scale runs, the column was in double curvature during the strong motion part of the excitation between 7.5 and 8.5 sec, and large curvature peaks occurred at the shear peaks. However, unlike the small scale runs, after 9.5 sec the column experienced complex curvature pattern due to the large curvature peaks and concentration of damage at h = 60 in. In general, the curvature at the top cross section of the column was at least three times higher than that at the bottom cross-section at shear peaks when tensile strain occurred at the top.

Figure 5.2 presents the change of the maximum peak-to-peak amplitude (see Table 5.1). It increased until the 125%-scale '1st X+Z' test. The increase of the maximum peak-to-peak amplitude at h = 60 in. was most significant between 70% and 95%-scale tests.

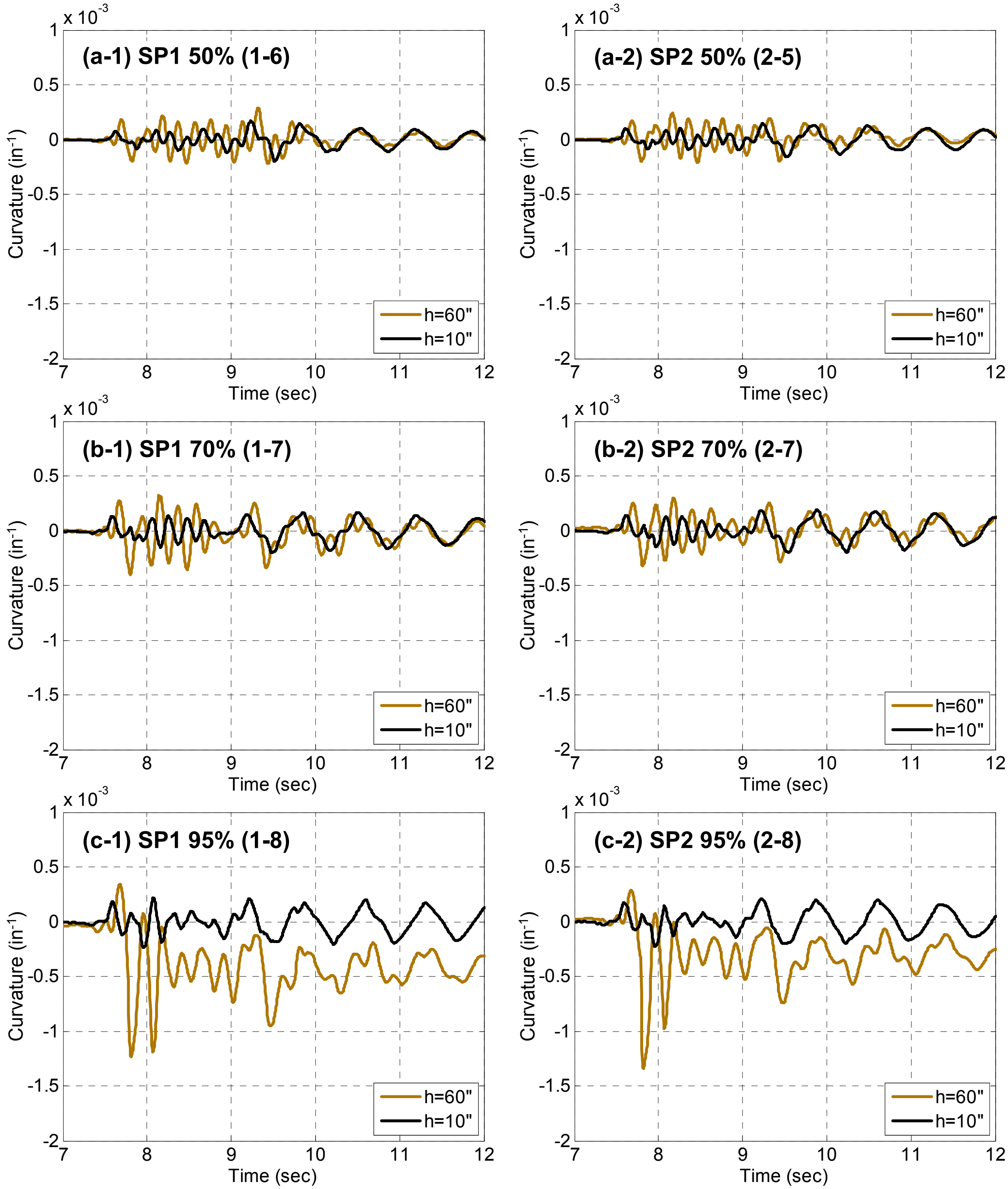

Figure 5.1 Comparison of curvature histories at *h* = 10 in. and 60 in.

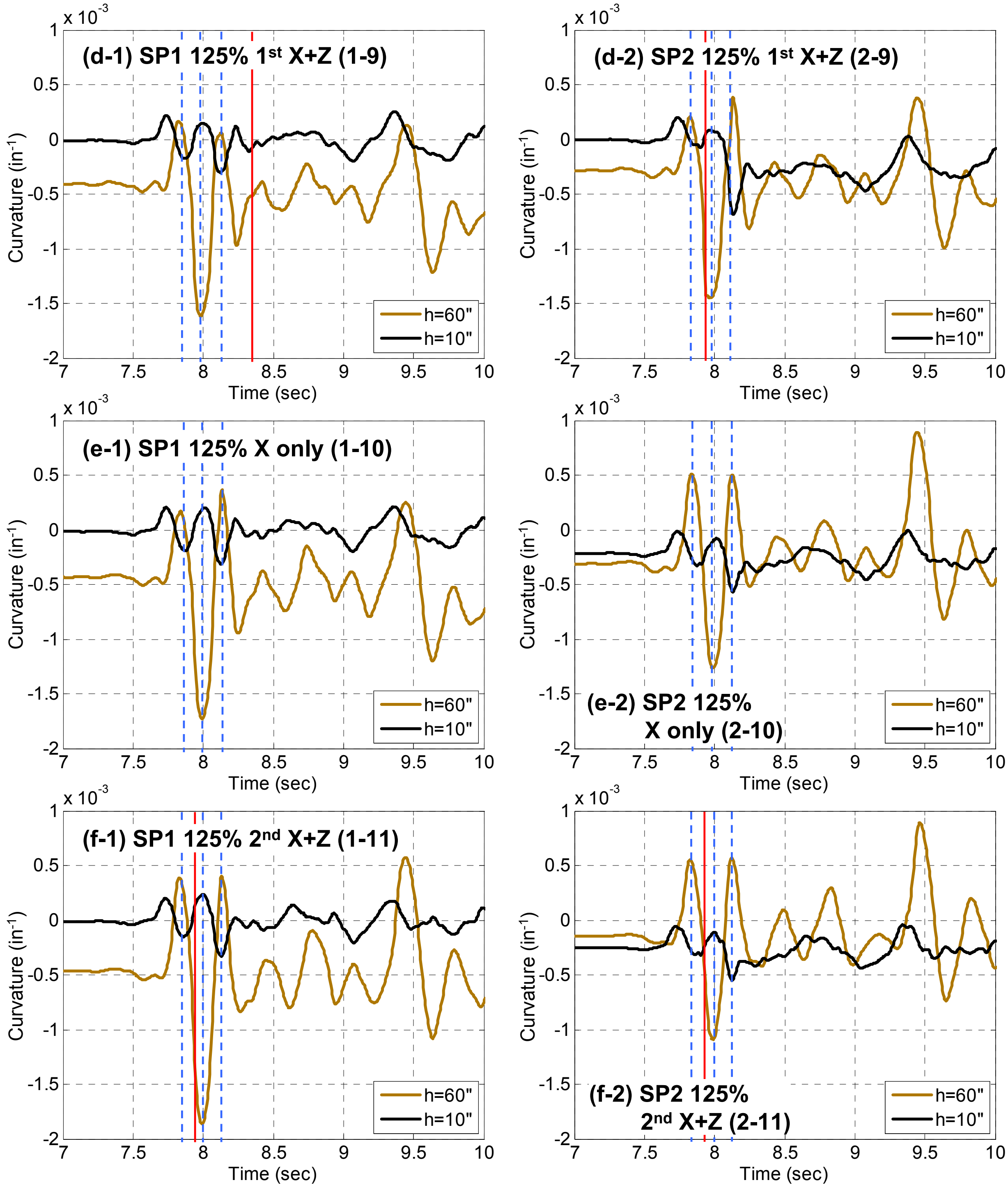

Figure 5.1 Continued.

Table 5.1 Peak curvatures.

SP	Run	Negative and positive peaks		Peak to peak	
		(a) *h* = 10 in. (10^{-3} in.$^{-1}$)	(b) *h* = 60 in. (10^{-3} in.$^{-1}$)	(c) *h* = 10 in. (10^{-3} in.$^{-1}$)	(d) *h* = 60 in. (10^{-3} in.$^{-1}$)
1	50% (1-6)	-0.20, 0.17	-0.22, 0.29	0.37	0.51
	70% (1-7)	-0.20, 0.17	-0.41, 0.32	0.37	0.73
	95% (1-8)	-0.24, 0.22	-1.23, 0.34	0.45	1.57
	125% ‘1st X+Z’ (1-9)	-0.30, 0.26	-1.62, 0.16	0.56	1.78
	125% ‘X only’ (1-10)	-0.32, 0.21	-1.73, 0.37	0.53	2.10
	125% ‘2nd X+Z’ (1-11)	-0.33, 0.57	-1.86, 0.58	0.57	2.44
2	50% (2-5)	-0.16, 0.14	-0.21, 0.24	0.30	0.45
	70% (2-7)	-0.20, 0.19	-0.32, 0.29	0.39	0.61
	95% (2-8)	-0.22, 0.21	-1.34, 0.29	0.43	1.63
	125% ‘1st X+Z’ (2-9)	-0.69, 0.20	-1.45, 0.39	0.89	1.83
	125% ‘X only’ (2-10)	-0.57, -0.01	-1.26, 0.89	0.56	2.15
	125% ‘2nd X+Z’ (2-11)	-0.55, -0.04	-1.09, 0.89	0.51	1.98

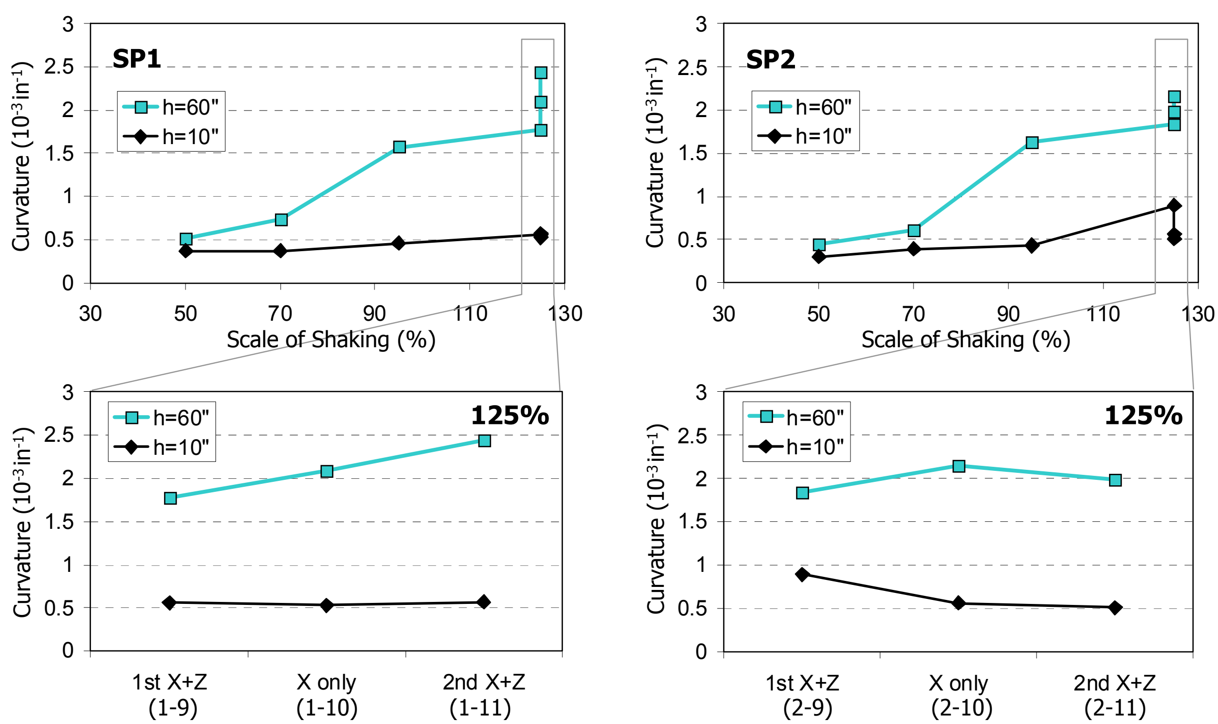

Figure 5.2 Peak-to-peak curvatures of the specimens.

5.3 MOMENT-CURVATURE RELATIONSHIPS

Figure 5.3 presents the moment-curvature relationships under 50%-, 70%-, 95%-, and 125%-scale motions, comparing *h* = 10 in. and 60 in. As discussed in Section 4.4.2, the bending moment at the top was larger than that at the base. This was consistent in all the tests, and the moment peaks at 60 in. were larger than the peaks at 10 in. by up to 90%.

In 50%- and 70%-scale tests, each specimen had an almost linear moment-curvature relationship. Under the 95%-scale motion, it was no longer linear at *h* = 60 in. The curvature at the top cross section of the column shifted to the negative $0.3 \sim 0.4 \times 10^{-5}$ in.$^{-1}$ and continued to oscillate around it. However, the moment-curvature relationship remained linear at *h* = 10 in., and the maximum values were similar to those in the smaller intensity level tests. In addition, during the 95%-scale test the tangent of the moment-curvature relationship at *h* = 60 in. started to degrade and became different from that at *h* = 10 in. for both specimens.

In 125%-scale tests, the two specimens had different moment-curvature relationships. First, due to different residual curvature, the relationships at the same height, *h* = 10 in. or *h* = 60 in. did not have the same origin. For example, the residual curvature of SP1 cross section at *h* = 10 in. remained zero for all tests; that of SP2 became roughly -3.0×10^{-5} in^{-1} after the 125%-scale '1st X+Z' test, i.e., SP2 was more damaged at *h* = 10 in. than SP1. Second, at *h* = 60 in., the area of the hysteresis loops (indicative of the dissipated energy due to material damage) of SP1 was larger than that of SP2. SP1 with hoops with closer spacing was able to dissipate more energy in flexure, while SP2 with larger spaced hoops, dissipated less energy in flexure due to the existence of brittle shear damage. Moreover, the hysteresis loops of each specimen became flatter (less stiff) due to larger curvature beyond that corresponding to the maximum bending moment. The initial tangent of the moment-curvature relationship at *h* = 60 in. of both specimens, as shown by the superposed straight lines in Figure 5.3(d), (e), and (f), decreased by about 17% in 'X only' test compared to '1st X+Z' test (4800 kip-in^2 to 4000 kip-in^2), but remained almost the same in the '2nd X+Z test'. Finally, due to less damage of the column bottom cross section compared to that of the column top cross-section, the reduction of the initial tangent at *h* = 10 in. was not noticeable compared to that at *h* = 60 in.

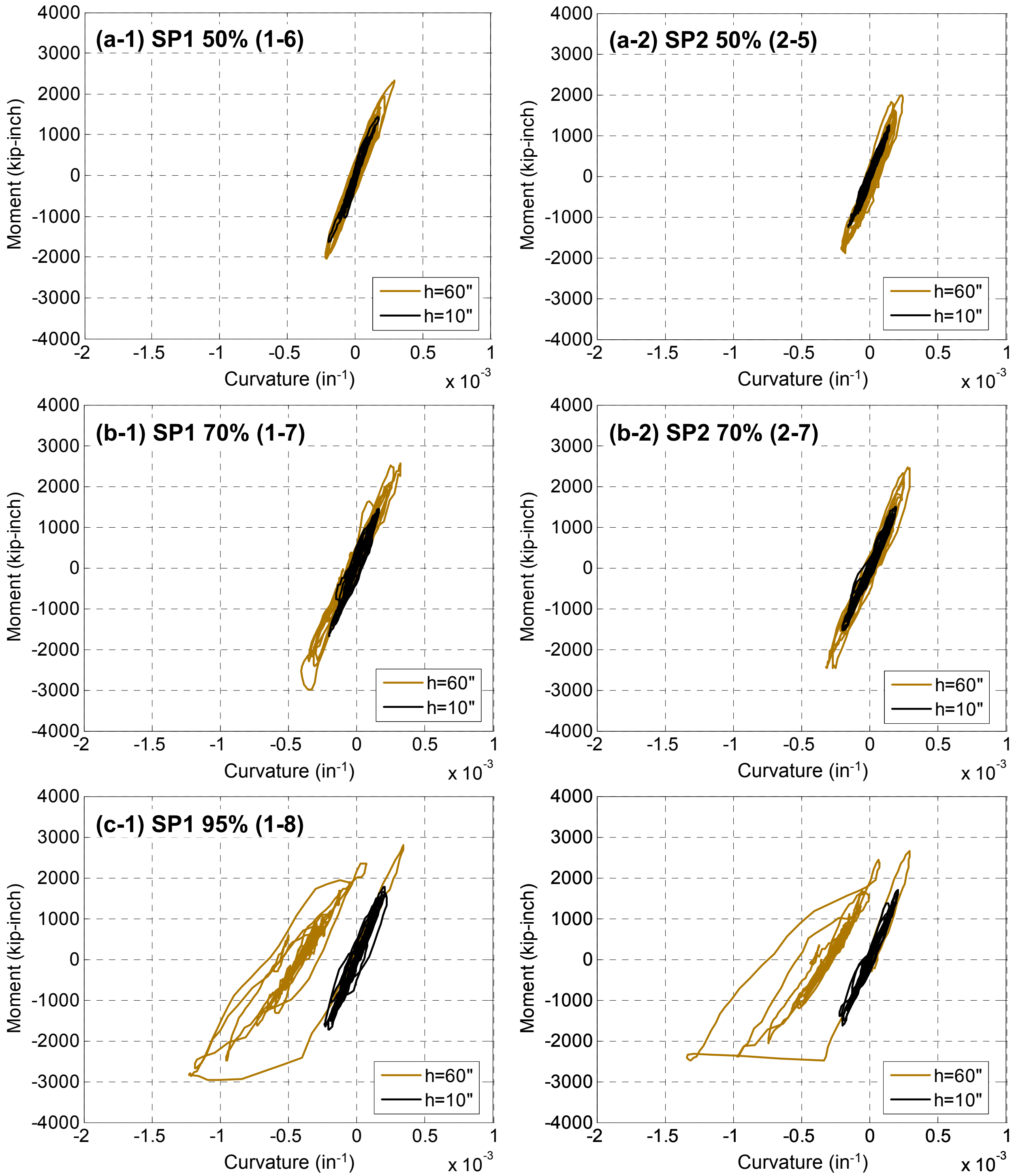

Figure 5.3 **Moment-curvature relationships at *h* = 10 in. and 60 in.**

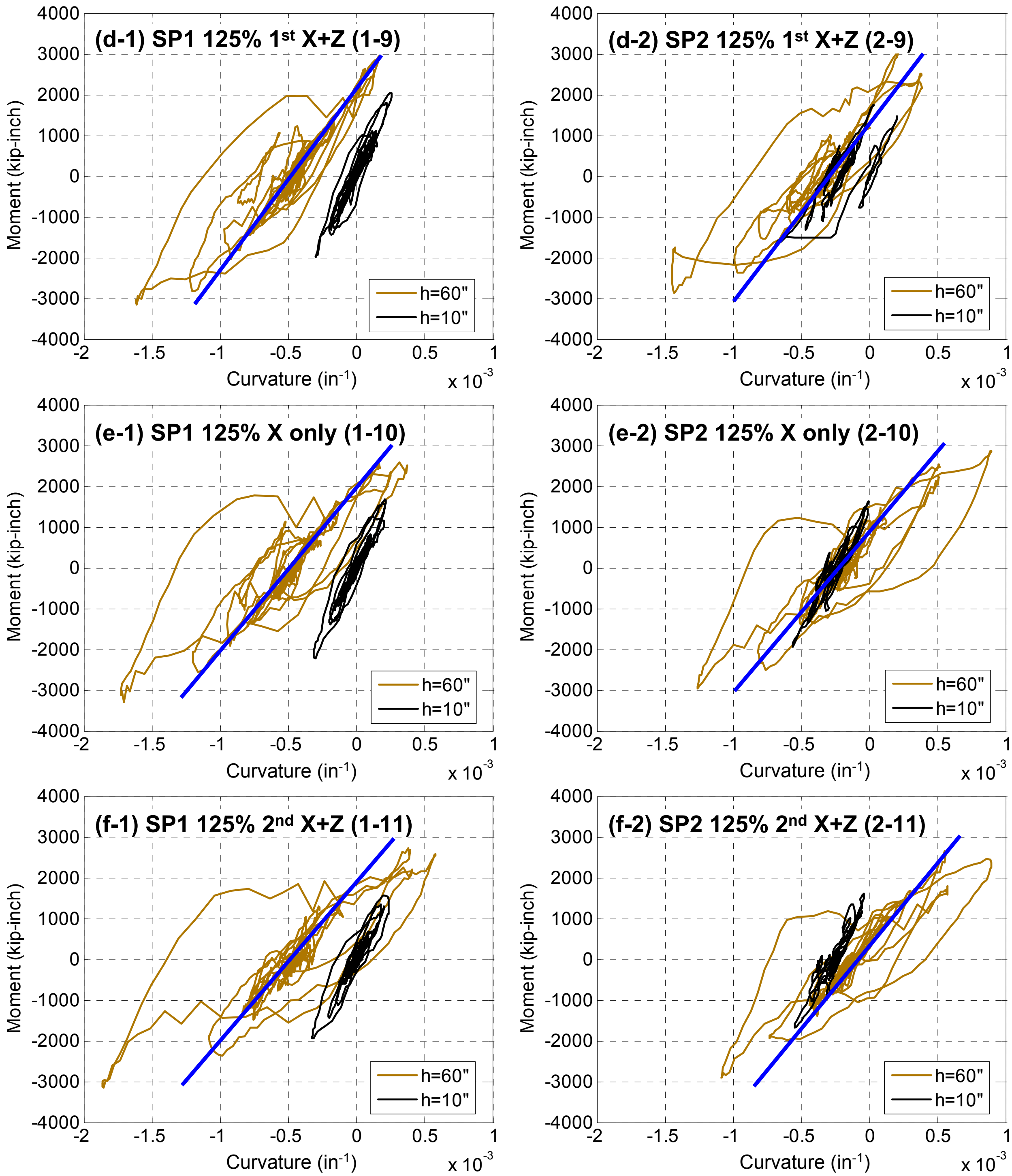

Figure 5.3 Continued.

5.4 LONGITUDINAL STRAINS

5.4.1 Longitudinal Strains on the North and South (X direction)

This section compares the longitudinal strains of the two specimens during the three 125%-scale tests. Figure 5.4 shows the strain history of longitudinal reinforcing bars on the north and south sides of SP1, that for SP2 is shown in Figure 5.5. In these two figures, NL and SL indicate measurements on the north and south sides, respectively. Each of these designations is followed by a number pointing to the height where the strain gages are located according to the key shown in the figures. For example, 'NL3' stands for the longitudinal strain at h = 30 in. on the north side. Since there are six gages on each bar on the north and south sides, the responses at six cross sections were obtained Note that positive strain indicates shortening (compression) and negative strain indicates elongation (tension). To observe the response at the times of the axial tension and shear peaks, one solid line (for axial tension) and three dashed lines (for shear) are superposed on the time histories.

Figure 5.4(a) shows the strains under 125%-scale '1st X+Z' motion for SP1 where the tension peak took place after the shear peaks. In summary:

1. There was a remarkable difference in the strain history along the height. For example, NL1 was shortened at the first shear peak, but the strain became tensile as the height increased, and NL6 showed a tensile strain peak at that point. This behavior was observed at other shear peaks and on the south side as well, implying that the test specimen was in double curvature as evidenced by the bending moments and curvatures discussed earlier.
2. A strain peak was noticeable at the tension peak after the main shear peaks. This was particularly the case at h = 60 in. on the north side (NL6) and at h = 10 in. on the south side (SL1).
3. The south side (SL6) was about 6 times more elongated than the north side (NL6) due to the large negative moment peak measured at around 8 sec.

For SP1, the 125%-scale 'X only' motion was applied [Figure 5.4(b)] after the '1st X+Z' run. The response was very similar to the previous case except for the tension peak effect and the strain measurements at NL6, which showed larger tensile strain peaks. The maximum tensile strain was almost three times larger than that of the '1st X+Z', and it occurred at the third shear peak. Also, the tensile strain due to rocking of the mass blocks after the shear peaks was almost 2.5 times larger than that of the '1st X+Z' run. However, SL6 was similar to that of the '1st X+Z' run, implying that the damage at the column top propagated from the south side to the north side as expected because the horizontal acceleration was not symmetric. Leaning toward the positive side (Figure 4.8) as does the shear force does (Figure 4.14)., it causes large tension on the south side first, i.e., damaging the south side first.

Figure 5.4(c) shows the response when 125%-scale '2nd X+Z' motion was applied to SP1. Strains on the north side, NL1 to NL3, changed abruptly from the compression side (positive) to the tension side (negative) at the tension peak. Other gages had similar results compared to '1st

X+Z' and 'X only', but NL6 and SL6 did not. First, as tests were repeated, their residual strain increased. Second, the difference between the 1st and 3rd shear peaks also increased. However, the longitudinal strain on the south side was larger than that on the north side. As mentioned in Section 5.2, the specimen was in double curvature at the shear peaks.

Figure 5.5 shows the strain history plots on the north and south sides of SP2 under the 125%-scale runs; the response was similar to SP1, but the peak values were larger. Note that SL1 had 3 to 4 times larger tensile strain values than those of SP1. This was particularly the case for the elongation under the '1st X+Z' run; see Figure 5.5(a). Moreover, NL6 for SP2, obtained from the '1st X+Z' run, experienced larger strain than that of SP1. This resulted from the damage at the top of SP2, which was more severe than that of SP1 for the different runs.

Figures 5.6 and 5.7 present the peak-to-peak amplitude and the maximum (in an absolute sense) tensile strain on the north and south sides. Note that the tensile strain is negative, but the absolute values are used in these plots. Since the strain can stay negative from the beginning to the end of a run, it is possible that the maximum tensile strain is larger than the corresponding peak-to-peak amplitude. For example, the maximum tensile peak of SL6 of SP1 was larger than the corresponding peak-to-peak amplitude for the same run. In summary:

1. The longitudinal strain near the top had the largest tensile value in most runs. The only exception was NL6 of SP1, especially in the '1st X+Z' test run. There was no significant difference between NL6 and NL1 or NL3 in this particular test.
2. In SP1, the elongation measured by SL6 was the largest and increased as the runs were repeated. Compared to SL1, the strains from SL6 were about 5 times larger in peak-to-peak amplitude and 7 times larger in the maximum tensile strain. NL6 of SP1 also increased with repeated runs; it was 4 times larger than other locations for the '2nd X+Z' test. NL1 was slightly larger than NL3 in most cases, but the difference was not significant compared to NL6.
3. In case of SP2, NL6 and SL6 remained the largest on each side, but they did not increase with repeated runs. The decrease of SL6 in the 'X only' test compared to the '1st X+Z' run was remarkable, where the peak-to-peak amplitude and the maximum tensile strain decreased by 26% and 9.3%, respectively. In the '2nd X+Z' run, these values remained almost the same, with a slight decrease of 3.6% and slight increase by 0.8%, respectively. SL1 showed a similar trend; it was slightly less than half of SL6 but its maximum tensile value for SP2 was about twice as large as that of SP1. Finally, NL1 and NL3 remained less than 25% of NL6.

Figure 5.8 shows schematics of the deflected shapes of the test specimens. As discussed above, the strain responses near the top and the base were different at each shear peak and the observed anti-phase during the main excitation. This is expected because as shown in Figure 4.16, the bending moment histories at the top and the base also show anti-phase. This implies double curvature, if the residual elongation due to tension at the top is ignored. At the first shear peak, the top on the north side elongated and the base on the north side shortened. On the other hand, the top on the south side shortened and the base on the south side elongated. These directions (signs) of the straining actions were reversed at the second peak but where the same at the third shear peak.

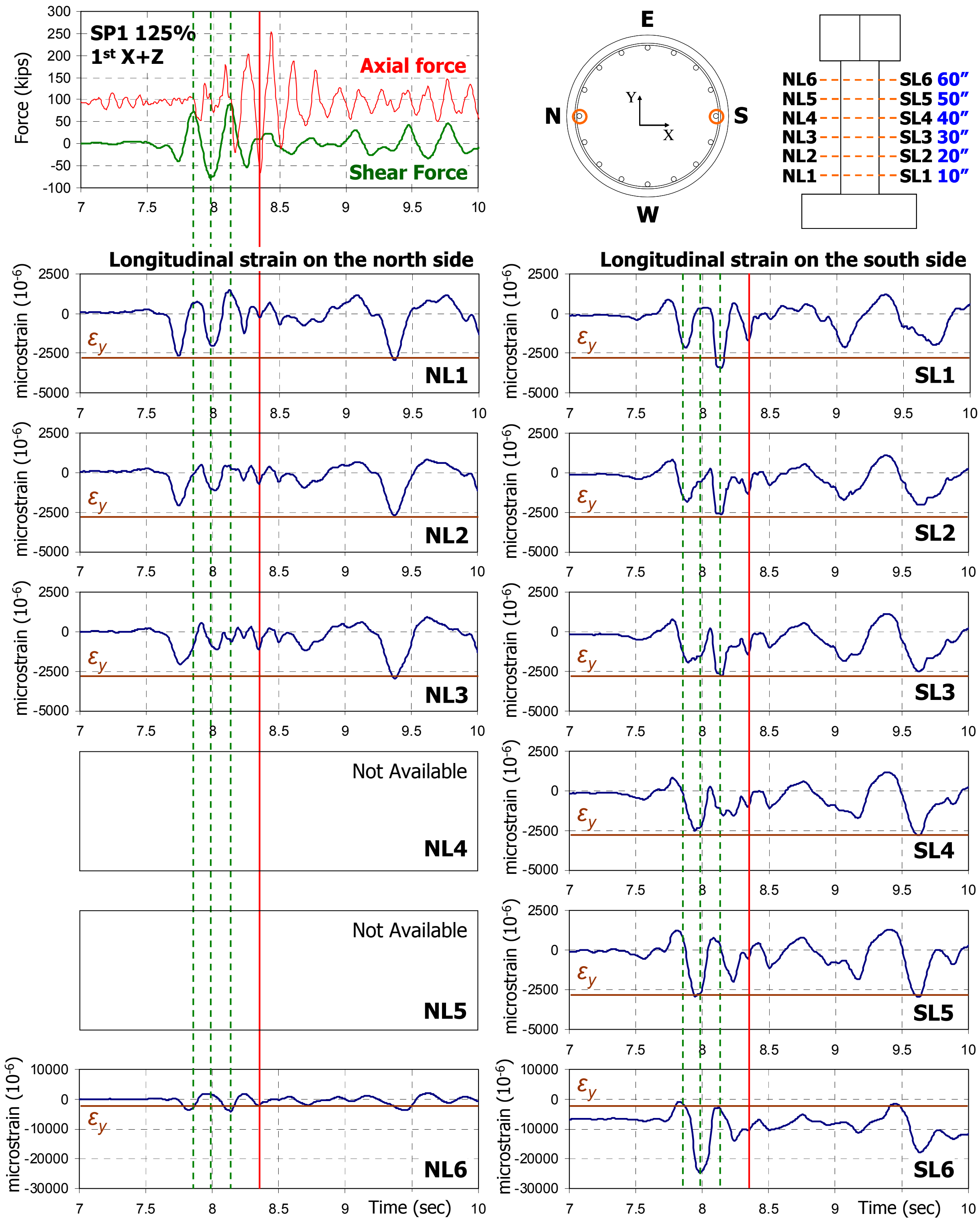

(a) SP1 125% 1st X+Z

Figure 5.4 Longitudinal strains on the north and south sides of SP1 in the 125%-scale runs.

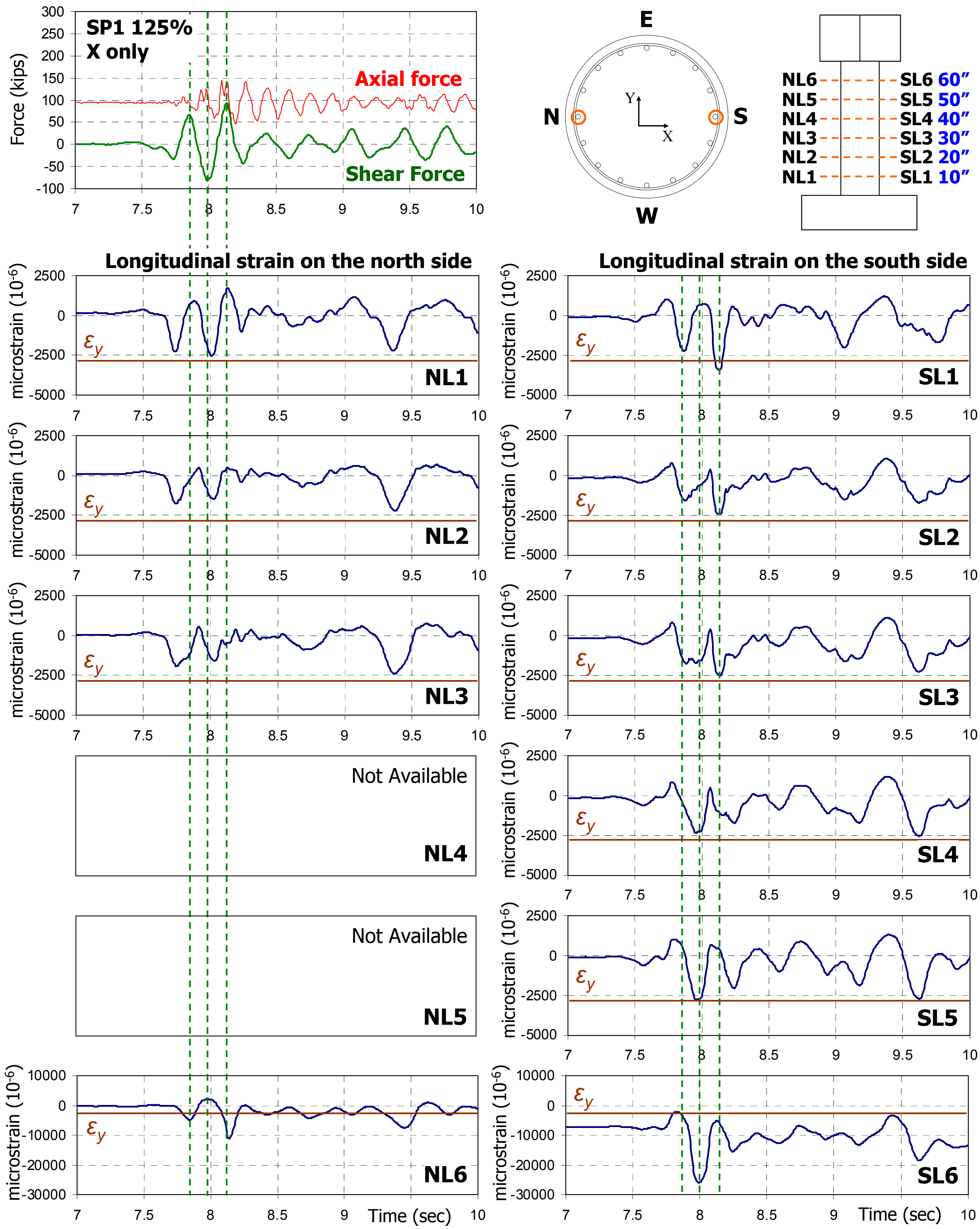

(b) SP1 125% X only

Figure 5.4 Continued.

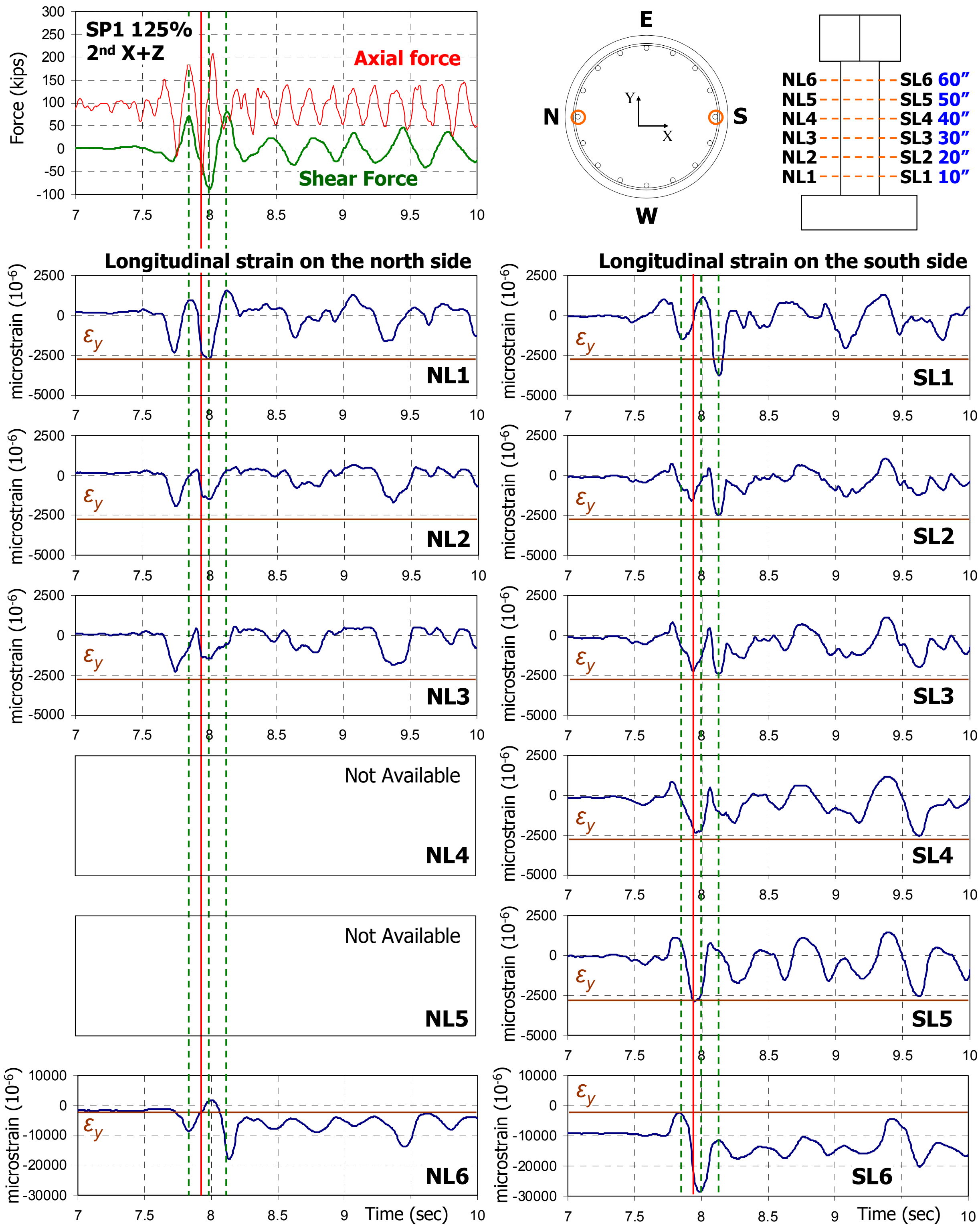

(c) SP1 125% 2nd X+Z

Figure 5.4 Continued.

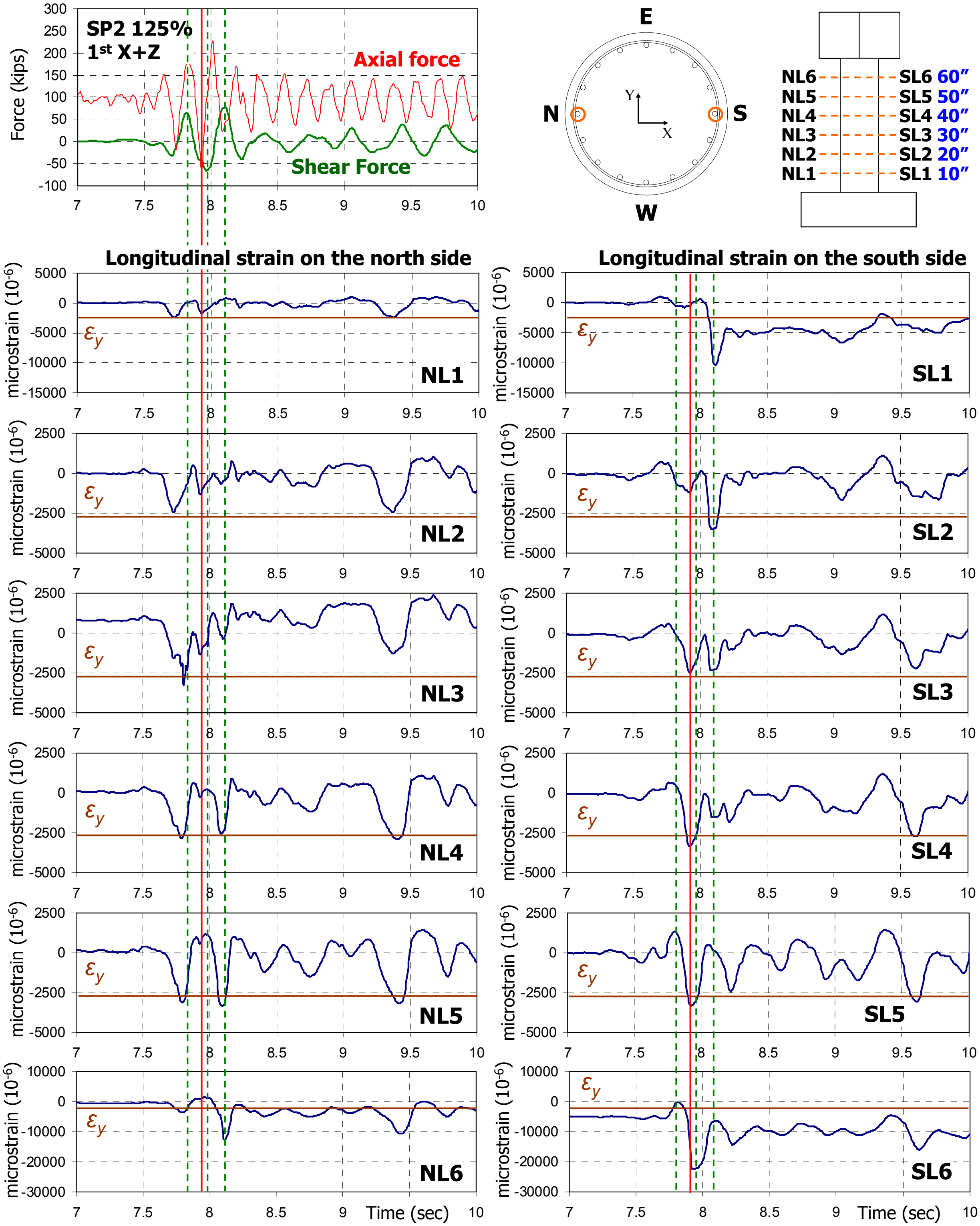

(a) SP2 125% 1st X+Z

Figure 5.5 Longitudinal strains on the north and south sides of SP2 in the 125%-scale runs.

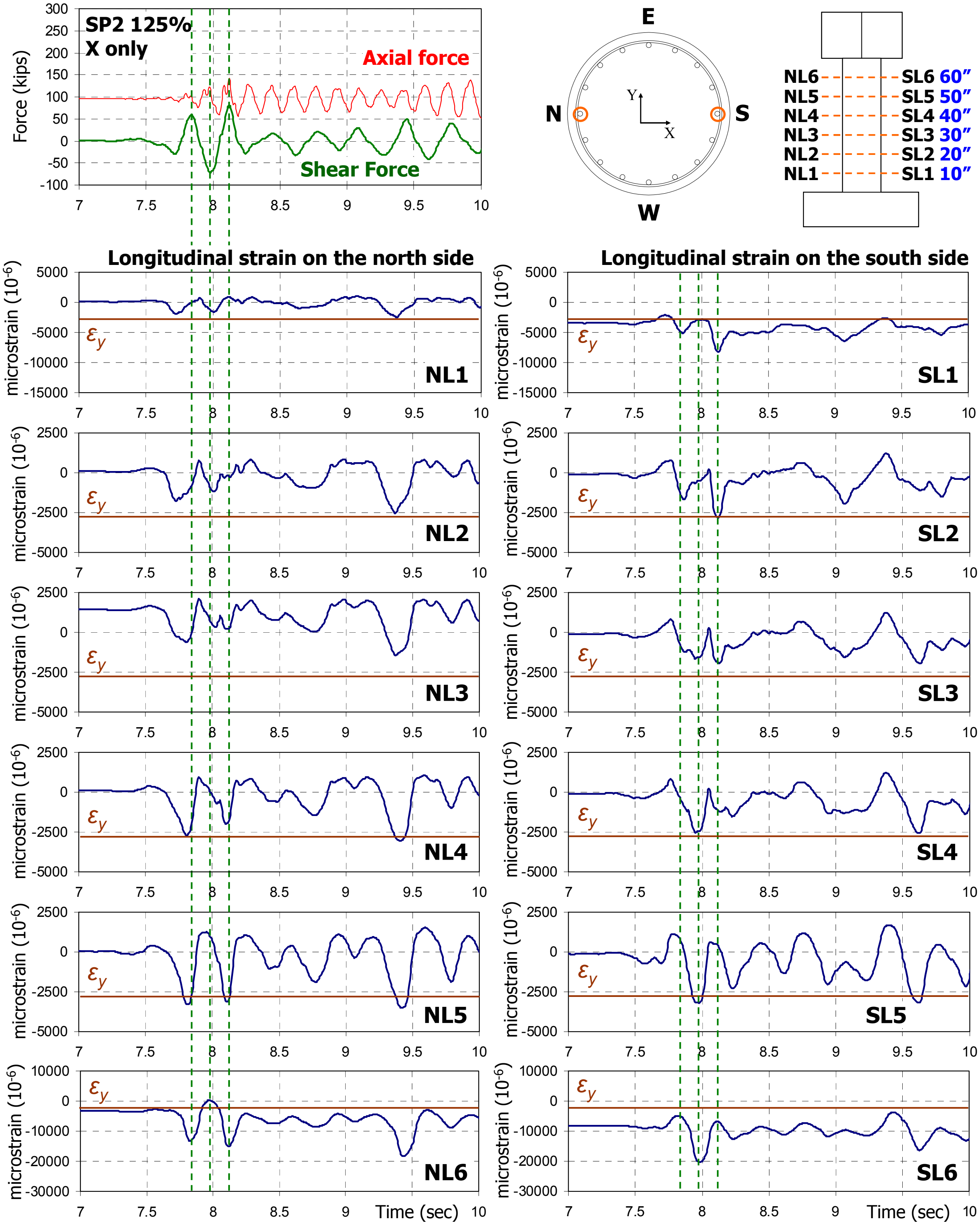

(b) SP2 125% X only

Figure 5.5 Continued.

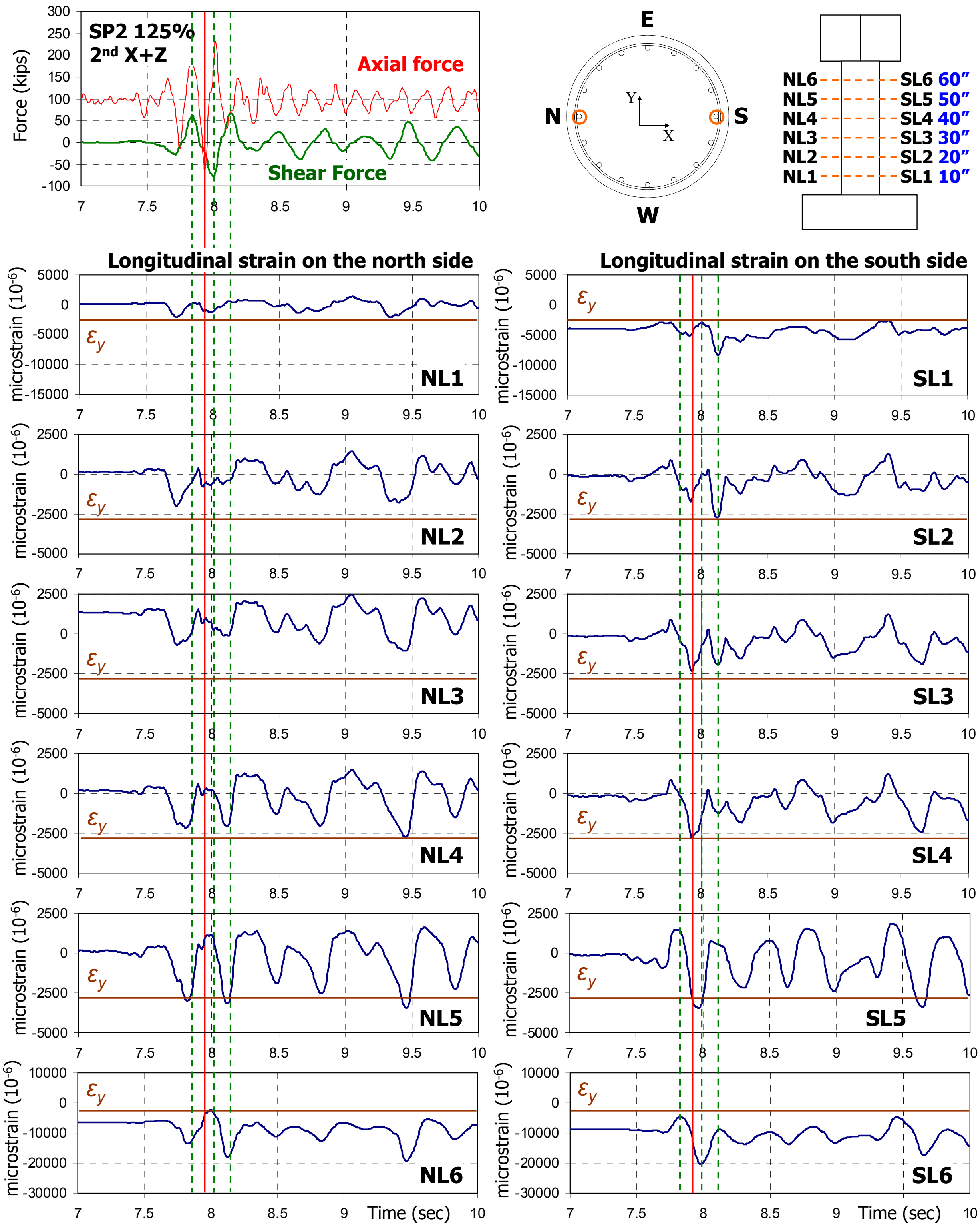

(c) SP2 125% 2nd X+Z

Figure 5.5 Continued.

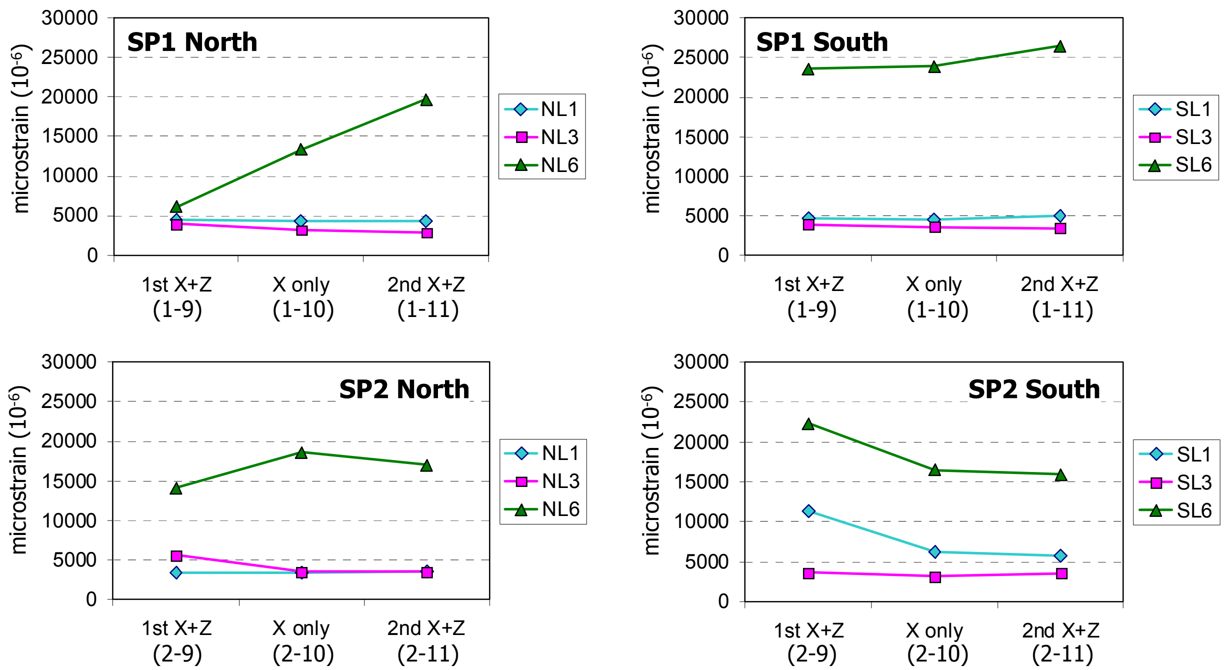

Figure 5.6 Peak-to-peak strain amplitudes of NL and SL in the 125%-scale runs.

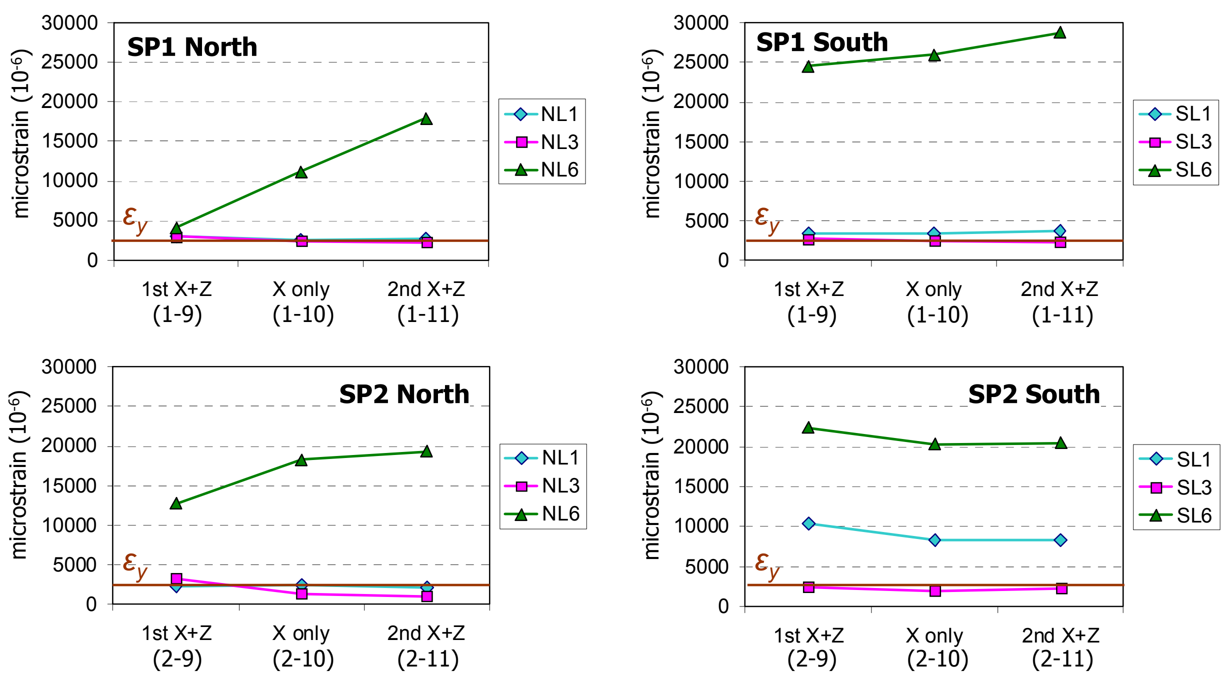

Figure 5.7 Peak tensile strains of NL and SL in the 125%-scale runs.

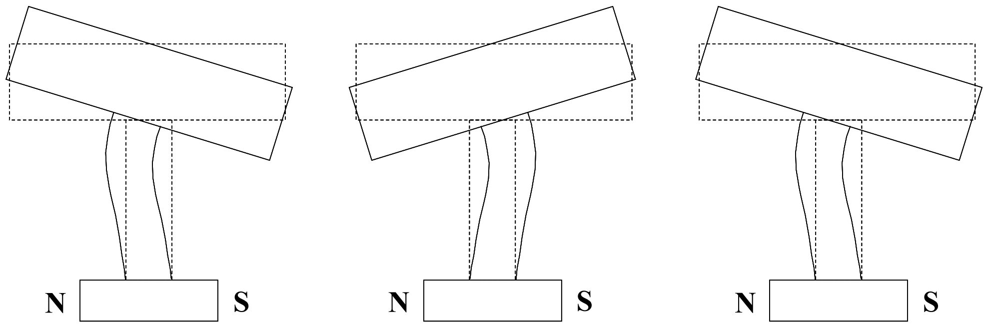

(a) first shear peak (b) second shear peak (c) third shear peak

Figure 5.8 Schematic deflected shapes of the test specimens at shear peaks

5.4.2 Longitudinal Strains on the East and West (Y-Direction)

Similar to the X-direction, Figure 5.9 presents the longitudinal strains on the east and west (Y-direction) sides of SP1; Figure 5.10 presents those of SP2. Since three gages were installed on each bar on the east and west sides, only the response at these three sections were obtained.

In Figure 5.9(a), the strain at each section of SP1 under 125%-scale '1st X+Z' motion is shown. 'EL' and 'WL' designations imply the longitudinal strain on the east and west sides, respectively. Similar to the north and south sides, the number following these designations indicates the section height. For example, 'EL1' indicates the longitudinal strain at the first instrumented section, i.e., h = 20 in, on the east side. The following remarks can be made:

- All the strain values were less than those on the north and south sides. Maximum tensile strain at WL1 was less than 80% of that at NL2, both of which were at the same height.
- The strain at h = 35 in. was less affected by the shear peaks than that at h = 20 in. or 50 in. Moreover, the west side was very slightly affected by the tension peak.
- The strain remained negative, i.e., tensile, in most locations and runs except at EL3, partly due to the initial strain of EL3. This implies that the force distribution was not uniform on the east and west sides, suggesting the presence of biaxial bending with a small component in the transverse direction. This was confirmed by the difference between EL and WL at the same height, where WL was more elongated than EL. Similar to the north and south sides, the strains below h = 35 in. (EL1 and WL1) had distinct peaks before the three main shear peaks.

Figure 5.9(b) shows the strain under 'X only' run. In this case, EL1 and WL1 had more similar responses than the previous run. In addition, the strain values decreased slightly in most runs. The strain results from the '2nd X+Z' run for SP1 are shown in Figure 5.9(c). The following remarks can be made:

- WL1 showed larger tensile strain than EL1, especially at the tension peak and the third shear peak.

- The tension peak occurred between the first and second shear peaks and the strain peak, which was once observed at the second shear peak was not obvious in this run.
- The strain peak at the tension peak was clear in all runs.
- Compared to the strains at the first and second shear peaks, that at the third shear peak increased more in the ‘2nd X+Z’ run. In the ‘1st X+Z’ and ‘X only’ runs, the strain at the third peak was similar to first and second shear peaks, but larger tensile strain was observed. In particular, the increase in EL3 and WL3 was significant. The only difference was the presence of the tension peak between the first and the second shear peaks. The ‘1st X+Z’ run also had the tensile peak at over 50 kips, but it occurred after the third shear peak. This implies that the tension and the arrival time interval may affect the tensile strain in the upper part of the column.

In Figure 5.10(a), the strain at each section of SP2 under 125%-scale ‘1st X+Z’ motion is shown. The following remarks can be made:

- Similar to the ‘2nd X+Z’ run of SP1, the tension peak was observed between the first and second shear peaks, corresponding to a strain peak at the tension peak rather than at the second shear peak. In case of SP1, the third shear peak had the largest strain peak at almost all gages; this was not the case for SP2.
- EL2 and EL3 had the largest strain peaks at the tension peak; this was observed in the ‘2nd X+Z’ run.

For the ‘X only’ run [Figure 5.10(b)], EL2 and EL3 had their peak strains at the second shear peak. In Figure 5.10(c), WL2 and WL3 were not significantly affected at the second shear peak. Clearly, the top mass rocking between the east and west sides affected the strain of the upper part of the column. The following are observations on the peak-to-peak amplitude (Figure 5.11) and the maximum tensile strain (Figure 5.12) on the east and west sides of SP2:

- The variation noted in Figure 5.11 for SP2 was wider than that of SP1. For example, the peak-to-peak amplitude of WL3 (in micro-strains) changed for the three 125%-scale runs as follows: from 2172 to 1996 to 2639 for SP1 and 3994 to 3841 to 4186 for SP2. The amplitude decreased in the second run and increased in the third run and in most locations. The only exception was WL2 of SP2, which increased gradually; however, the difference between the first and the second runs was about 10%, i.e., significantly smaller than that between the second and third runs, which was 33%.
- The maximum tensile strain for SP2 had a similar trend (Figure 5.12) as that of SP1. Another interesting feature of the strain peak was that the measured strain location exhibited a certain order in the amplitude value, which was found to be consistent in most runs. On the west side, WL3 was the largest, WL1 was the second largest, and WL2 was the smallest (i.e., WL3 > WL1 > WL2). On the east side, the same trend (i.e., EL3 > EL1 > EL2) was observed except for the maximum tensile strain of SP2. Note that the variation of EL1 was not as remarkable as those of the other gages.

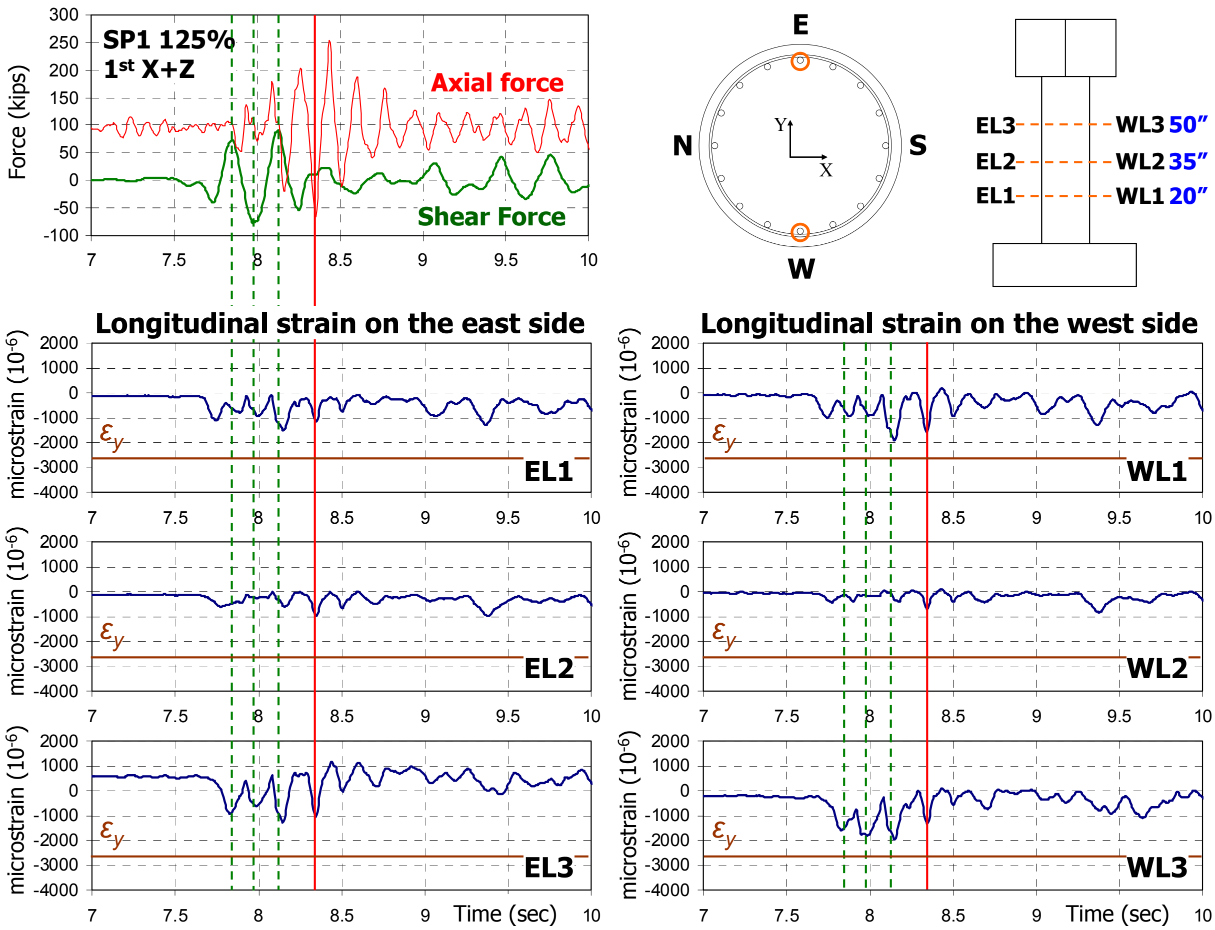

(a) SP1 125% 1st X+Z

Figure 5.9 Longitudinal strains on the east and west sides of SP1 in the 125%-scale runs.

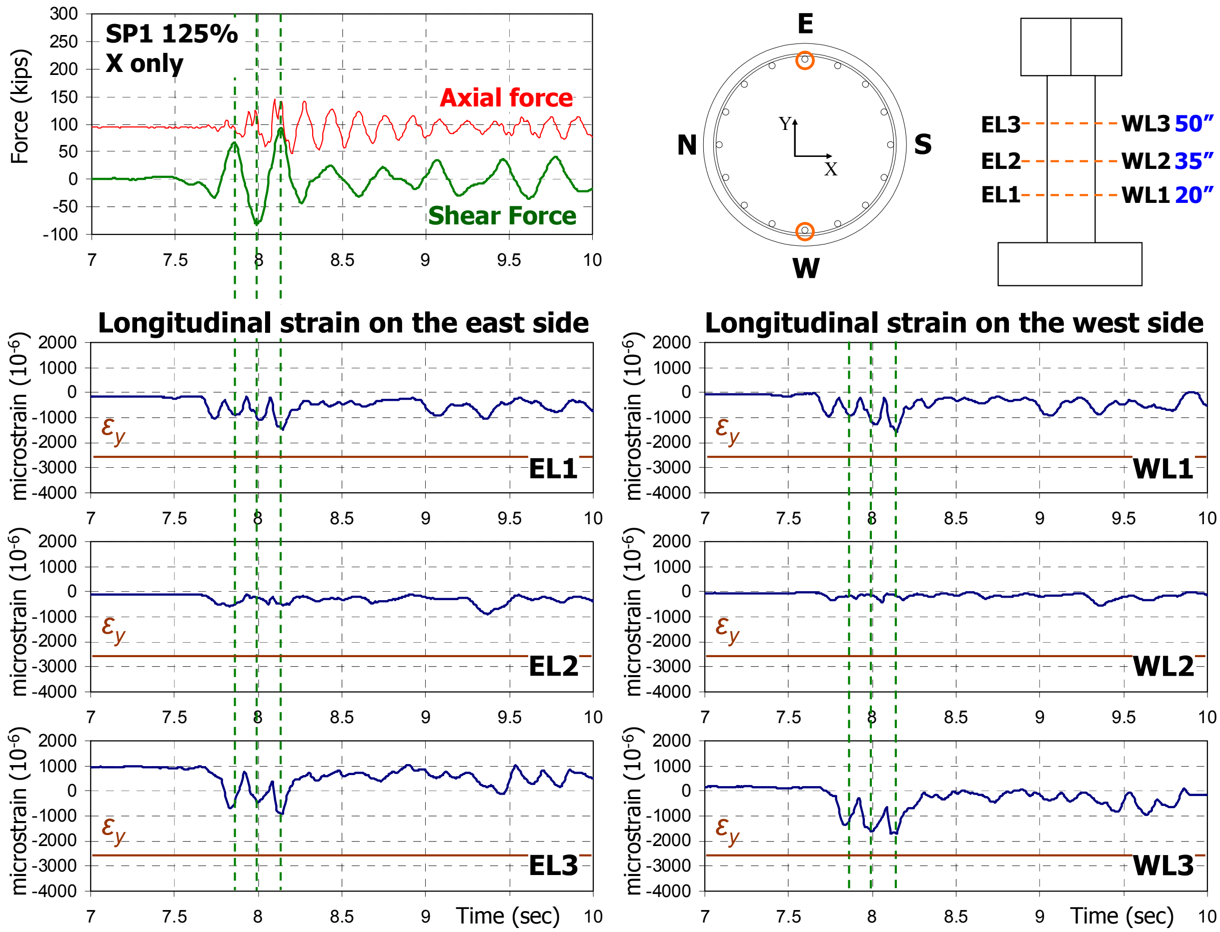

(b) SP1 125% X only

Figure 5.9 Continued.

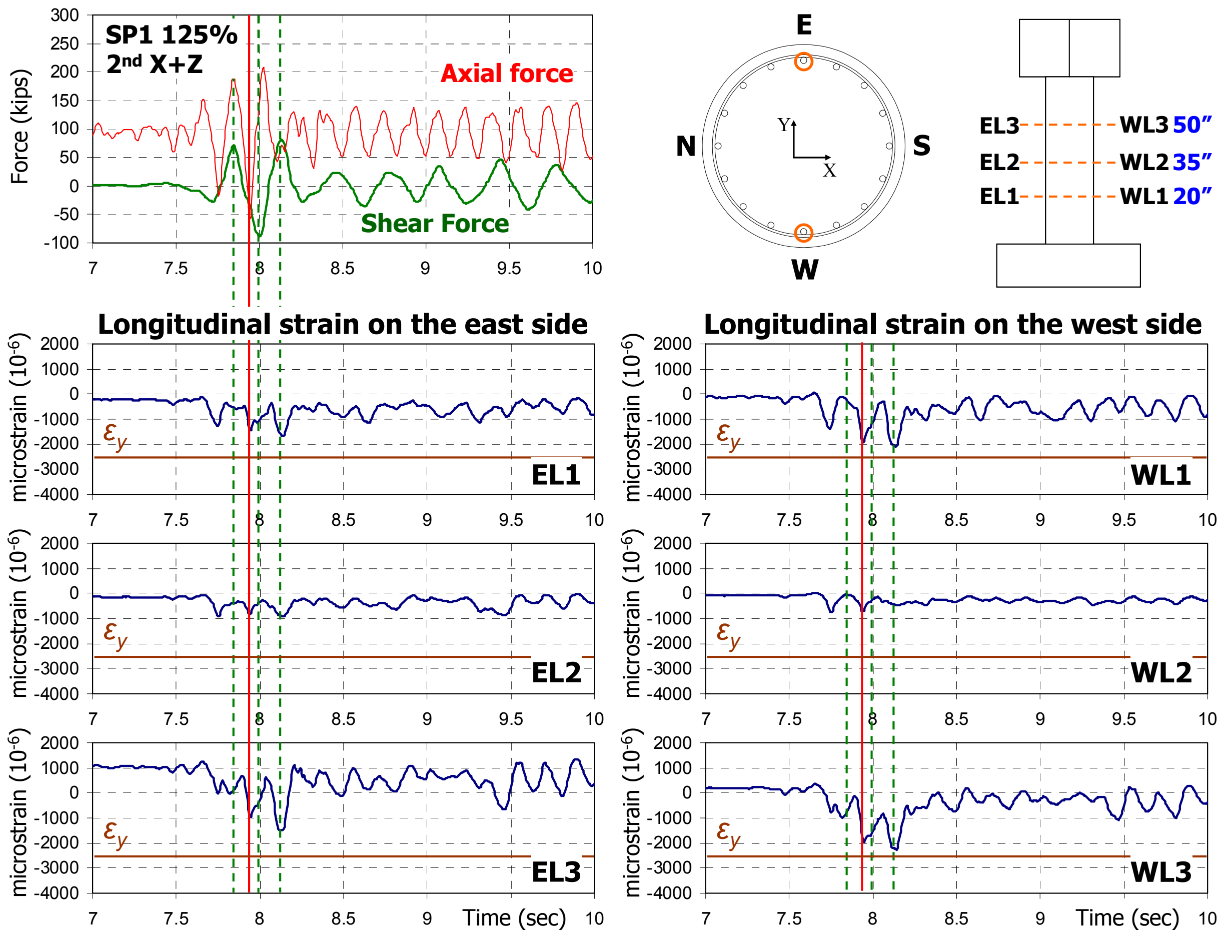

(c) SP1 125% 2nd X+Z

Figure 5.9 Continued.

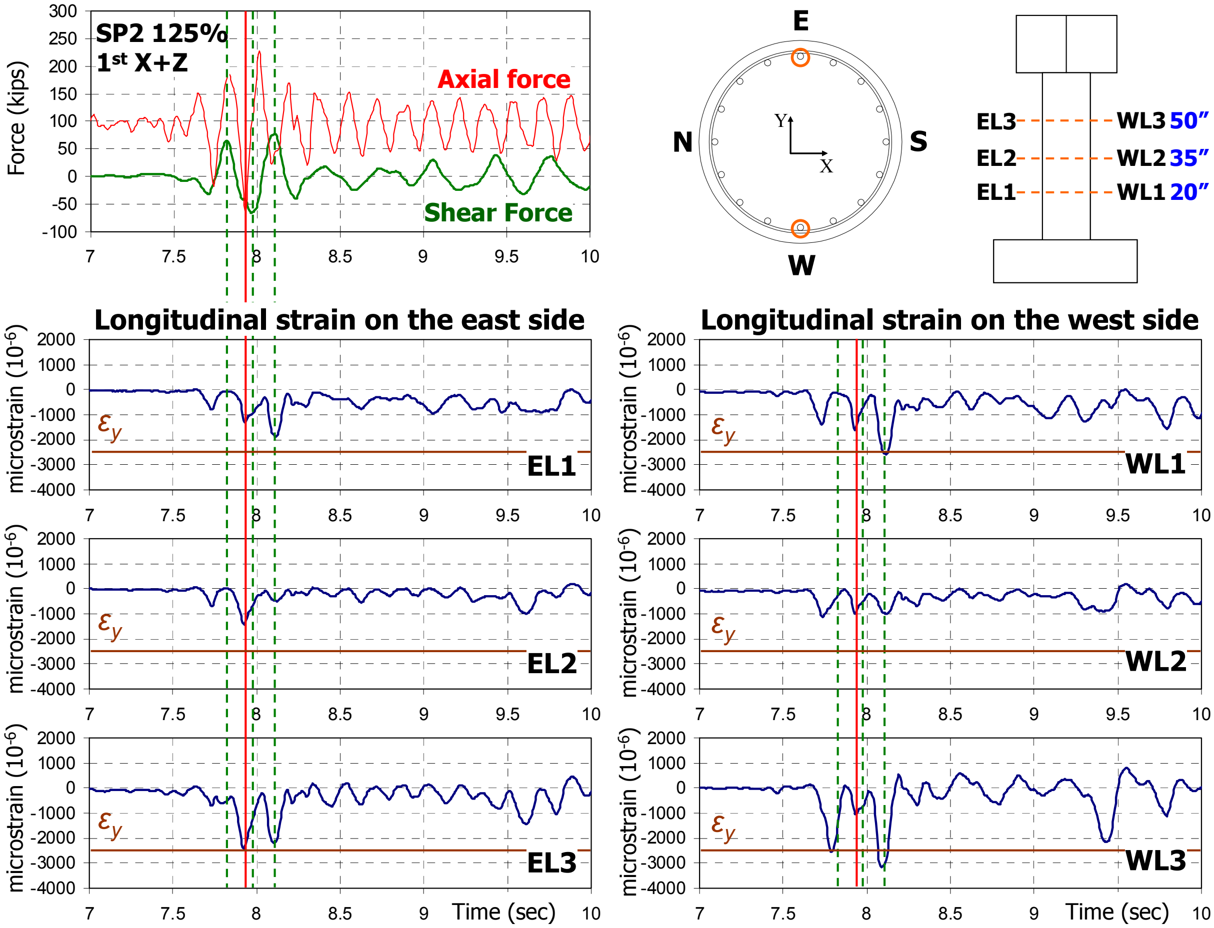

(a) SP2 125% 1st X+Z

Figure 5.10 Longitudinal strains on the east and west sides of SP2 in the 125%-scale runs.

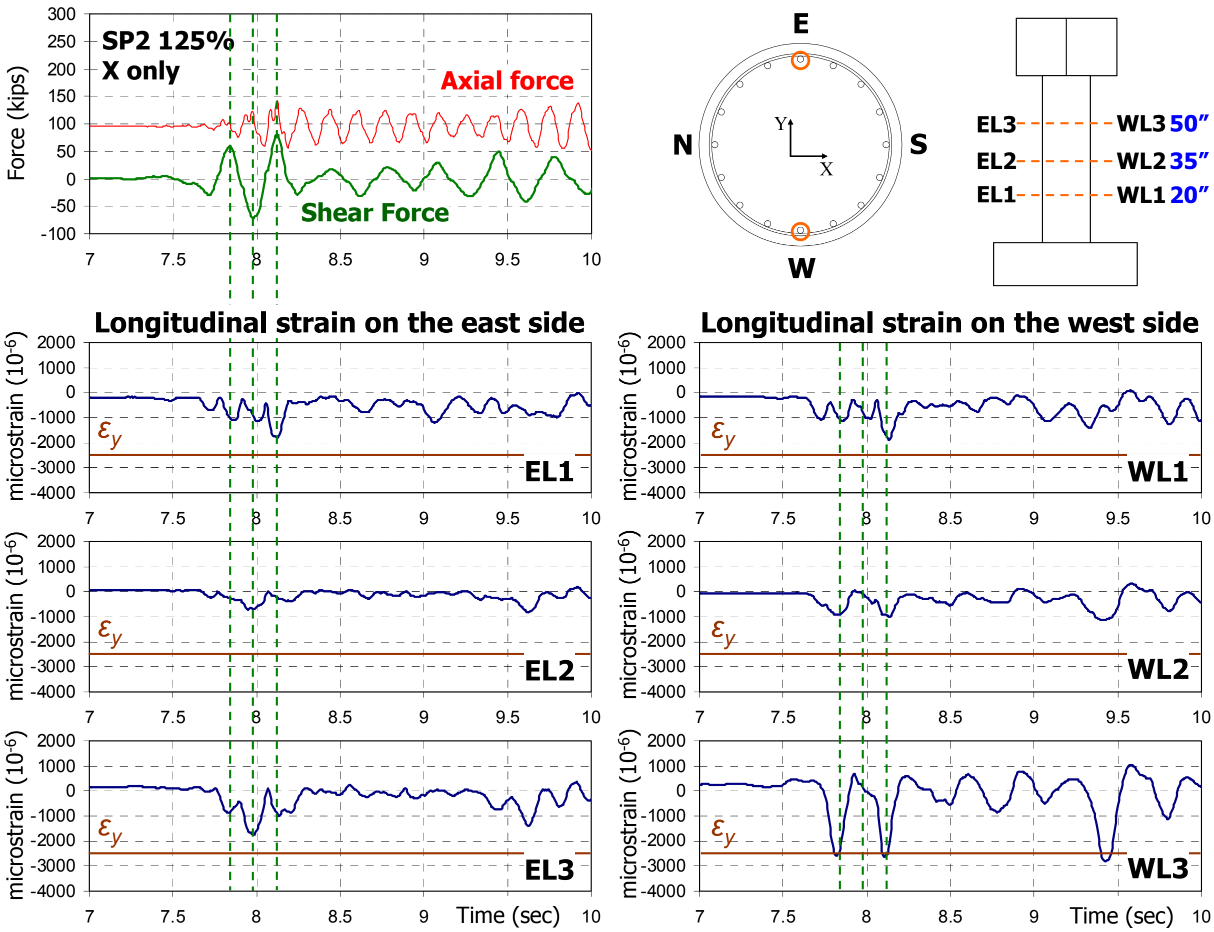

(b) SP2 125% X only

Figure 5.10 Continued.

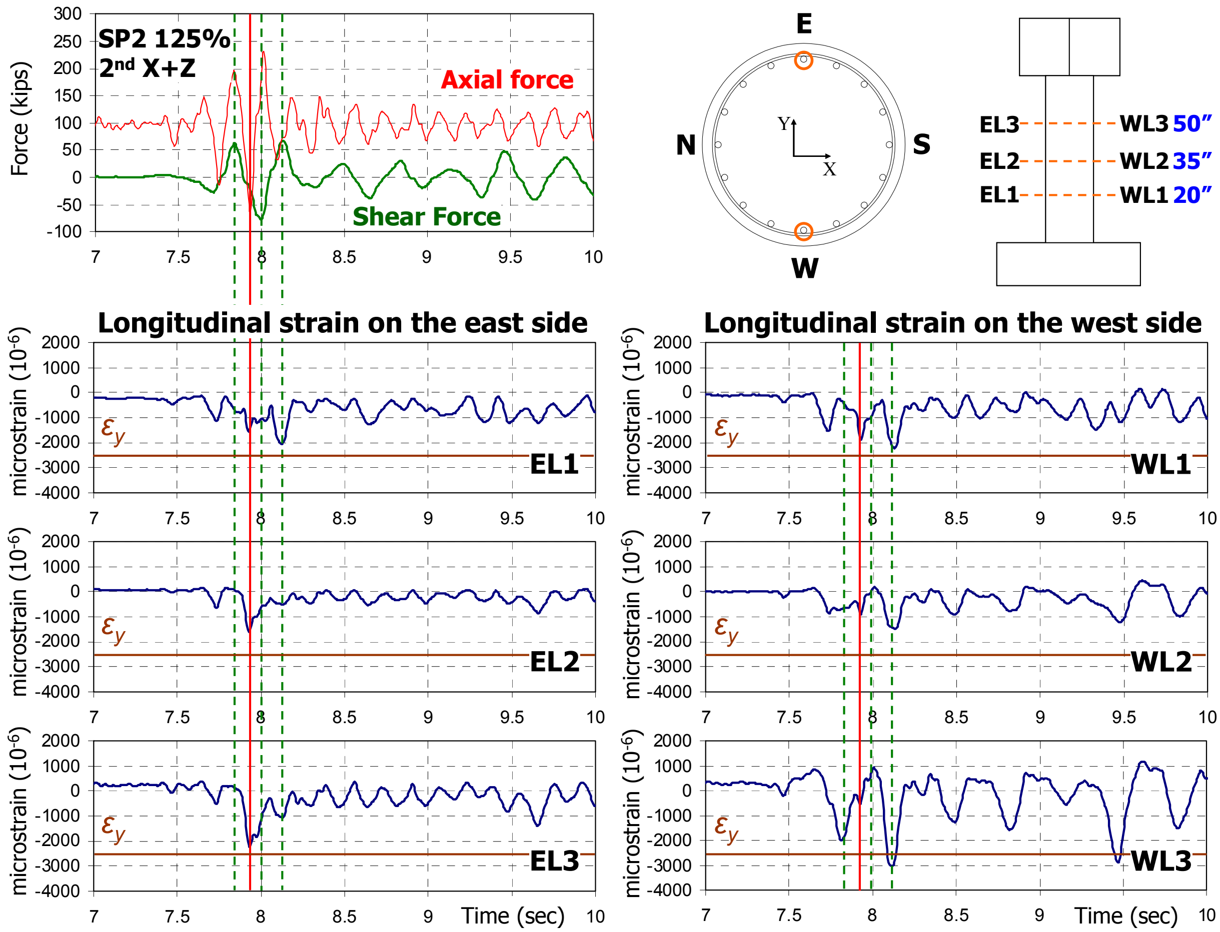

(c) SP2 125% 2nd X+Z

Figure 5.10 Continued.

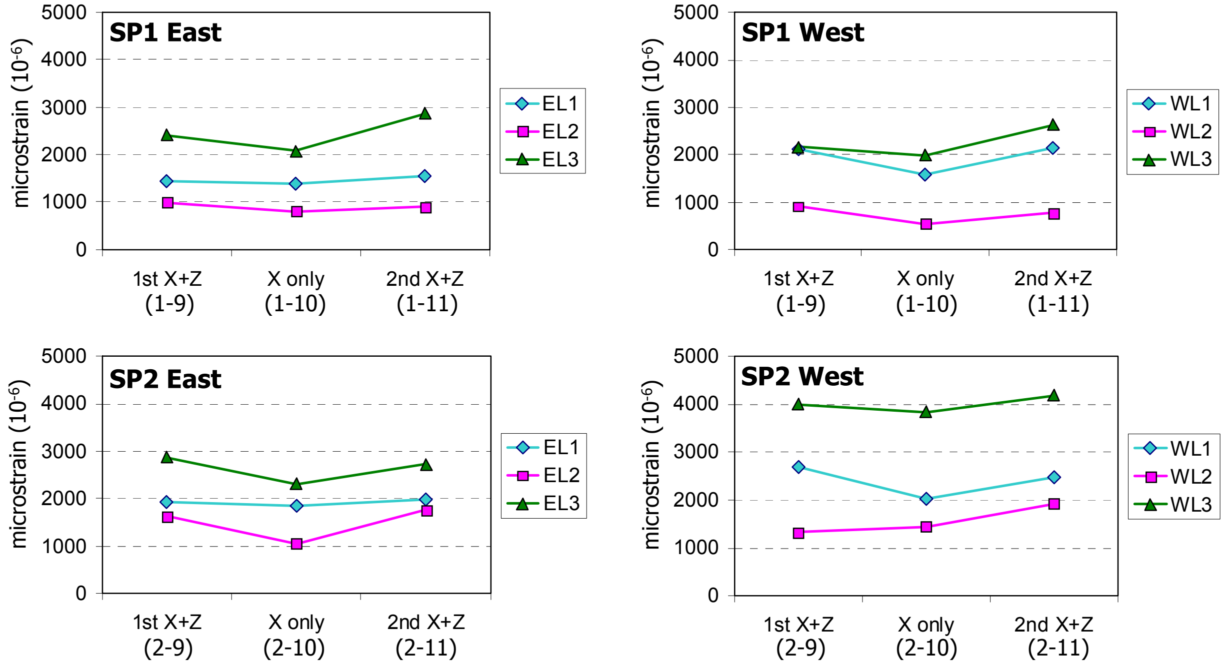

Figure 5.11 Peak-to-peak strain amplitudes of EL and WL in the 125%-scale runs.

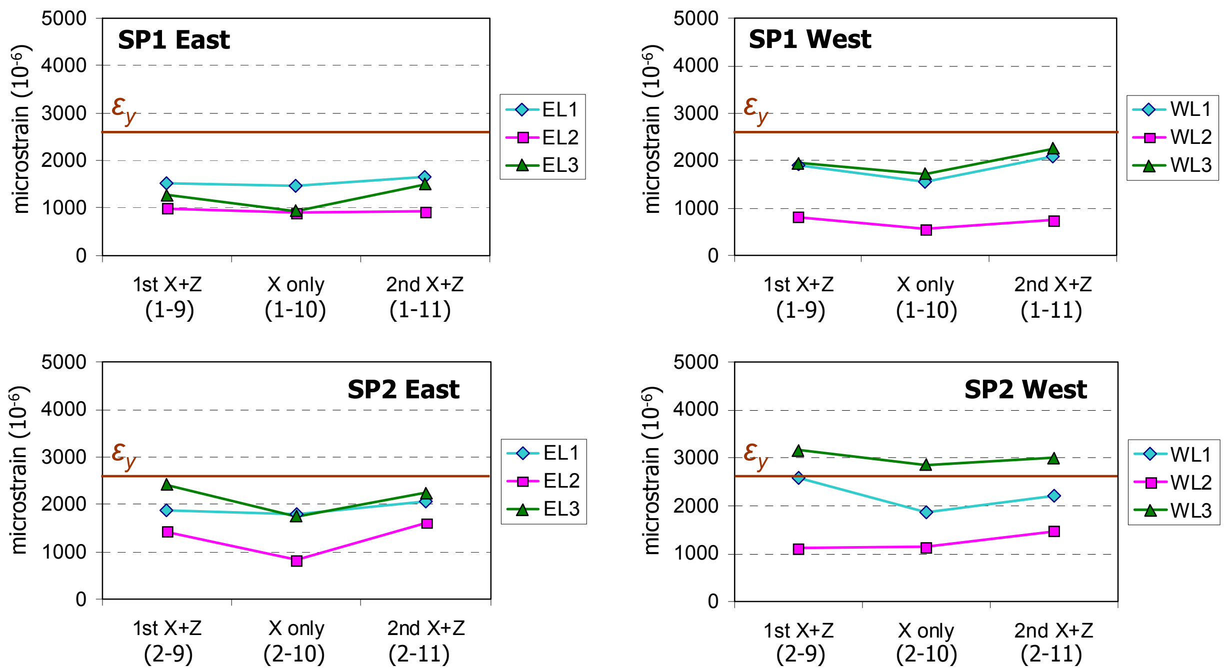

Figure 5.12 Peak tensile strains of EL and WL in the 125%-scale runs.

5.5 TRANSVERSE STRAINS

5.5.1 Transverse Strains on the North and South (X-Direction)

A total of 14 strain gages were installed on the hoops on the north and south sides of the columns. Each side had seven gages. Six gages were uniformly distributed with spacing of 10 in. and one gage was placed at the middle of the column at h = 35 in.. Figure 5.13 shows the results of the hoop strains of SP1. Figure 5.14 shows the results from strain gages of SP2. Similar to the previous designations, "NH" and "SH" stand for the hoop strains on the north and south, respectively. The following number (ranging from 1 to 7) following these designations indicates the height of section where the gage is installed, corresponding to h = 10 in., 20 in., 30 in., 35 in. (mid-height), 40 in., 50 in., and 60 in., respectively.

In Figure 5.13(a), the hoop strain at each section of SP1 under 125%-scale '1st X+Z' motion is shown. These observations can be made:

- Similar to the longitudinal strain, the transverse strain had peaks at the shear peaks and the tension peak.
- The lower and upper parts of the column were different in terms of the strain peak amplitudes. For example, NH2 and NH3 were smaller than NH4, NH5, and NH6. On the south side, SH1, SH3, SH4, and SH5 were relatively small, implying confinement variation the higher the section location, and an increase in the corresponding hoop tensile strain near the column top (i.e., at NH5, NH6, SH6, and SH7). This was expected since the compressive uniaxial stresses and accordingly the lateral strains and stresses were larger at the top due to the presence of larger bending moments.
- SH2 had the largest tensile peak at the first and third shear peaks and the tension peak; there was no significant peak at the maximum tension in any of the other strain gages.
- Some gages, such as NH2, SH1, and SH4, measured larger tensile strain at the second shear peak rather than the first and third shear peaks. These peaks were small because of the tension-compression reversal caused by the double-curvature behavior.

Under 'X only' run [Figure 5.13(b)], the response was very similar to the '1st X+Z' run, but the hoop strain increased. NH3 had the largest peak at the second shear peak compared to NH2, SH1, and SH4. Note that SH4 remained almost the same and relatively small. In Figure 5.13(c), the vertical component was added; it had a tension peak between the first and second shear peaks. The hoop strain continued to increase in this run as clearly evident in Figures 5.15 and 5.16.

Figure 5.14(a) shows the hoop strain of SP2 subjected to the '1st X+Z' run. The following remarks can be inferred:

- Most gages on the south side had no noticeable peak before the third shear peak; this was also observed in NH1. However, the tensile peak of SH7 increased gradually at every shear peak.

- Different from the south side, the north-side gages had two tensile peaks at the first and third shear peaks except for NH2 and NH7, where the peak tensile strain occurred at the third shear peak, which increased as the height increased.
- Even without vertical component [Figure 5.14(b)], the overall strain increased similar to SP1. The strain peaks at the first and second shear peaks were noticeable; however, the third peak was still the largest in most runs and strain gage locations.

Figure 5.14(c) shown the results from the '2nd X+Z' run where it is observed that the hoop strain continued to increase; NH6 had a relatively large and sharp peak at the second shear peak.

Based on the peak-to-peak amplitude (Figure 5.15) and the maximum tensile strain (Figure 5.16) at h = 10 in., 40 in., and 60 in. in each run, the following remarks can be made:

- In SP1, three different sections had similar peak-to-peak amplitude and tension peak values on the north side, but they differed on the south side. In particular, SH6 was about three times larger than SH1 and SH4.
- In every run, the hoop strain peak increased as the runs progressed among the six shown in Figure 5.16, except for NH1 and NH4.
- In SP2, five gages among the six (except for NH1) had larger values than those of SP1.
- The strain increased as the location of the hoop got higher. The only exception was NH4, where its tensile strain peak decreased by 19.6% in the '2nd X+Z' test. Other than that, the strain increased as runs progressed.

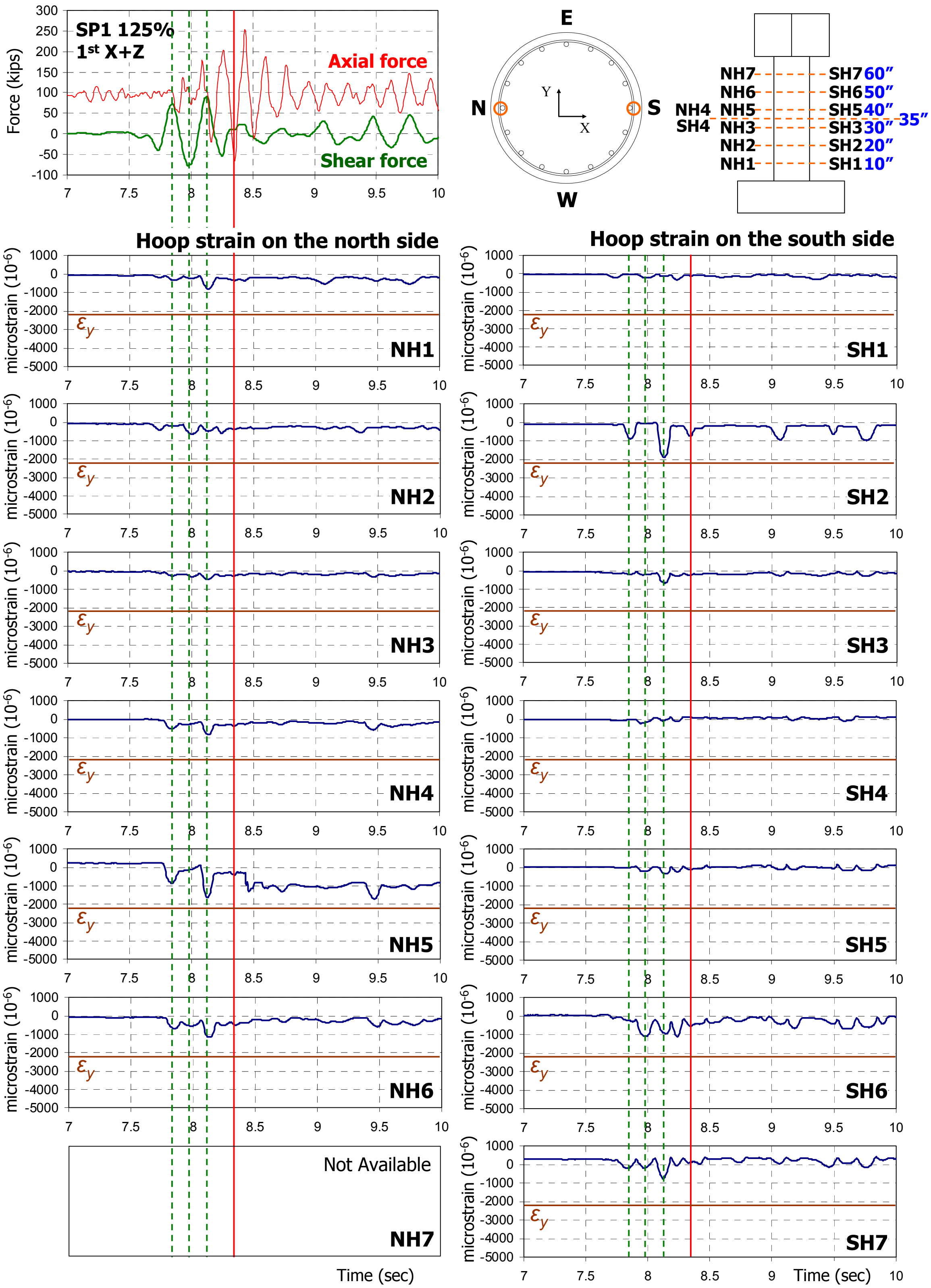

(a) SP1 125% 1st X+Z

Figure 5.13 Hoop strains on the north and south sides of SP1 in the 125%-scale runs.

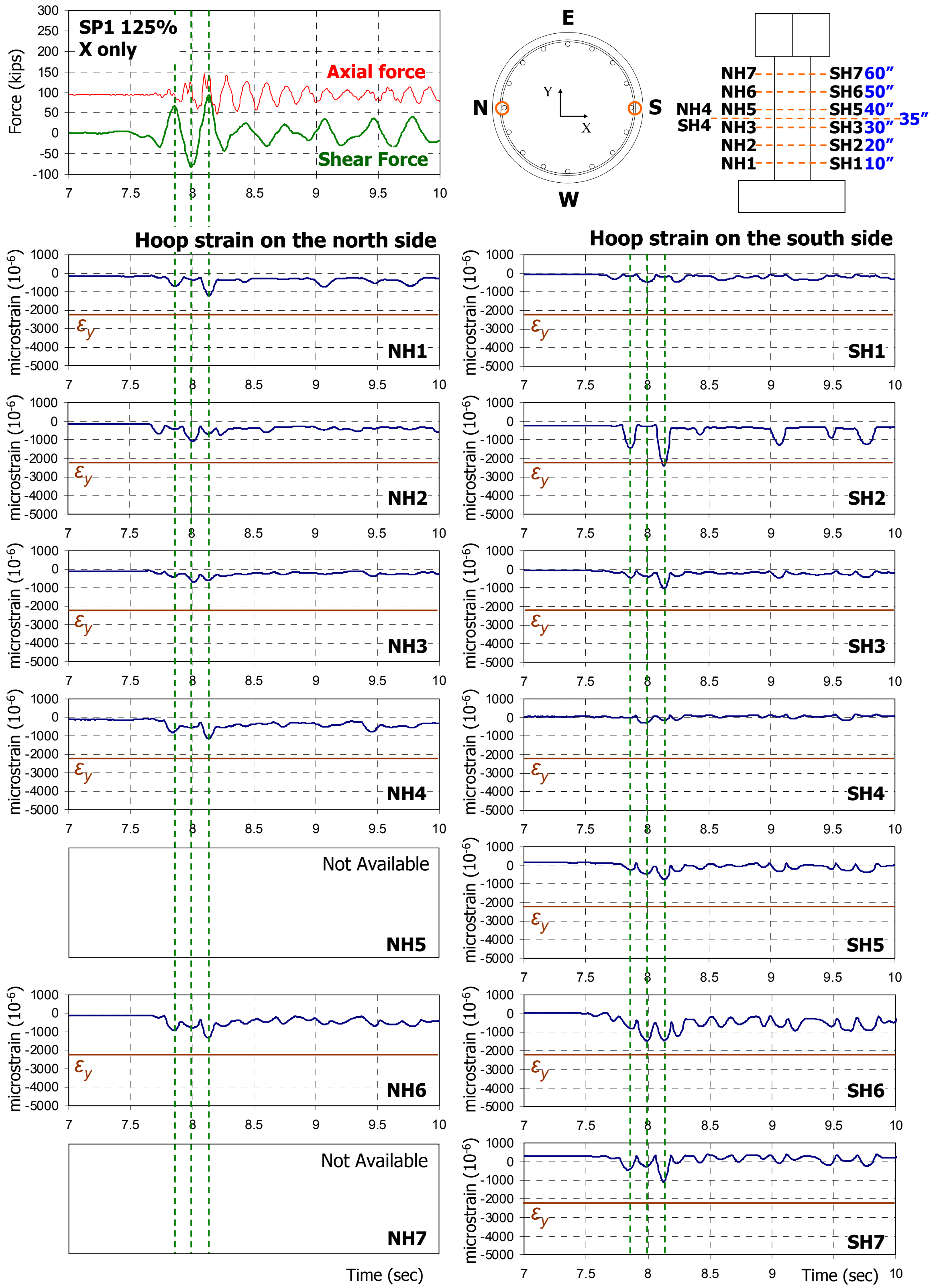

(b) SP1 125% X only

Figure 5.13 Continued.

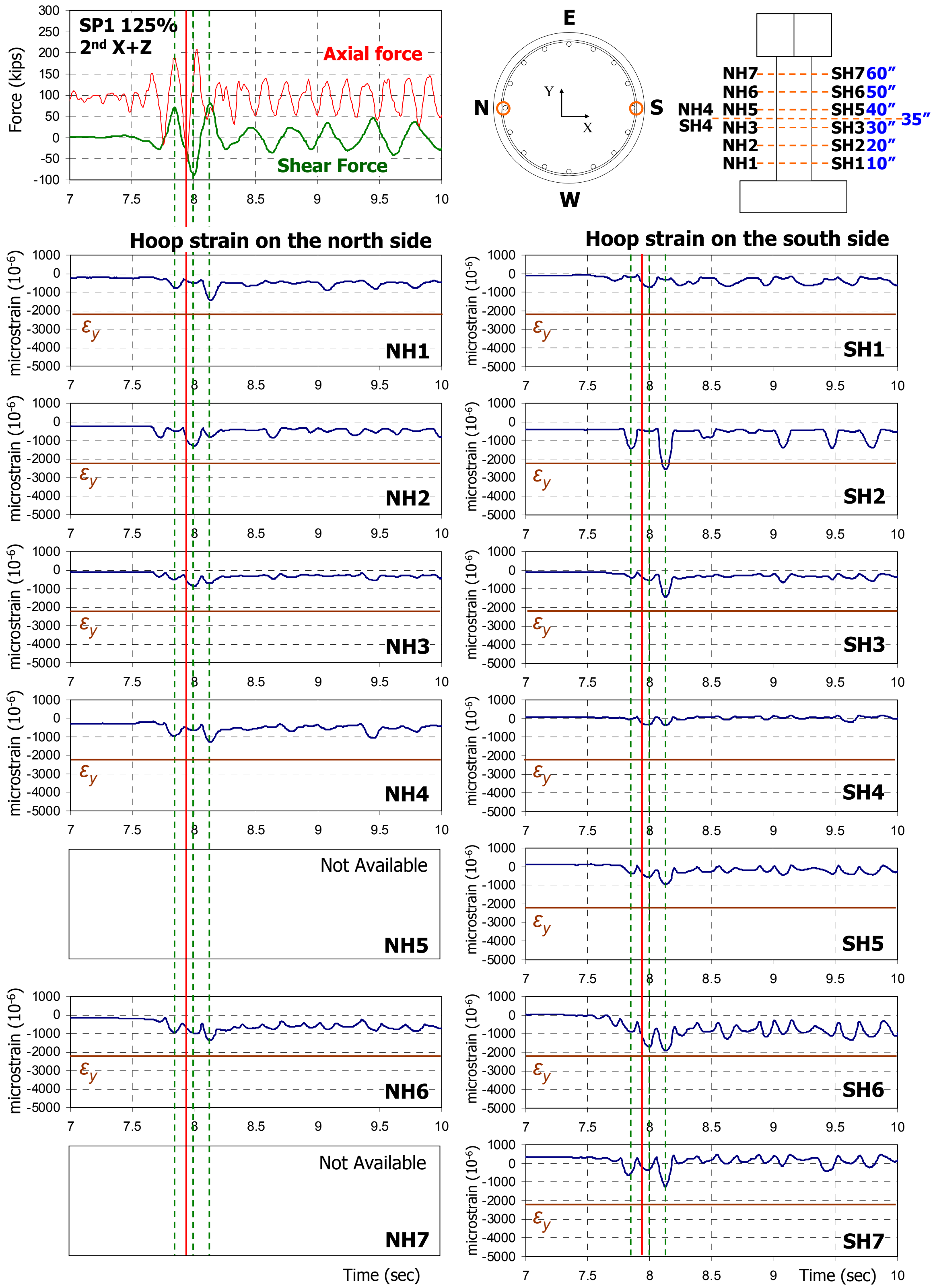

(c) SP1 125% 2nd X+Z

Figure 5.13 Continued.

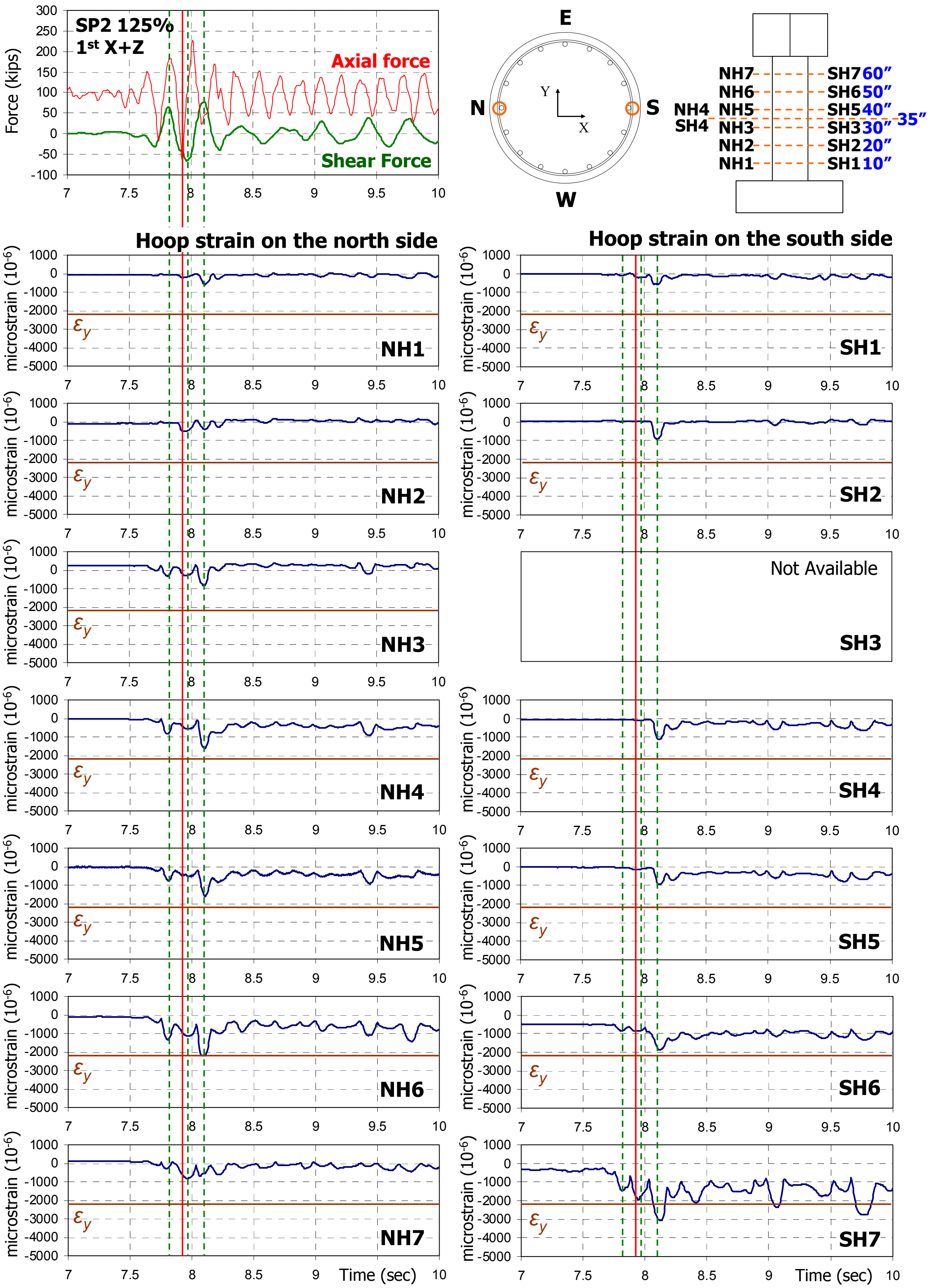

(a) SP2 125% 1st X+Z

Figure 5.14 Hoop strains on the north and south sides of SP2 in the 125%-scale runs.

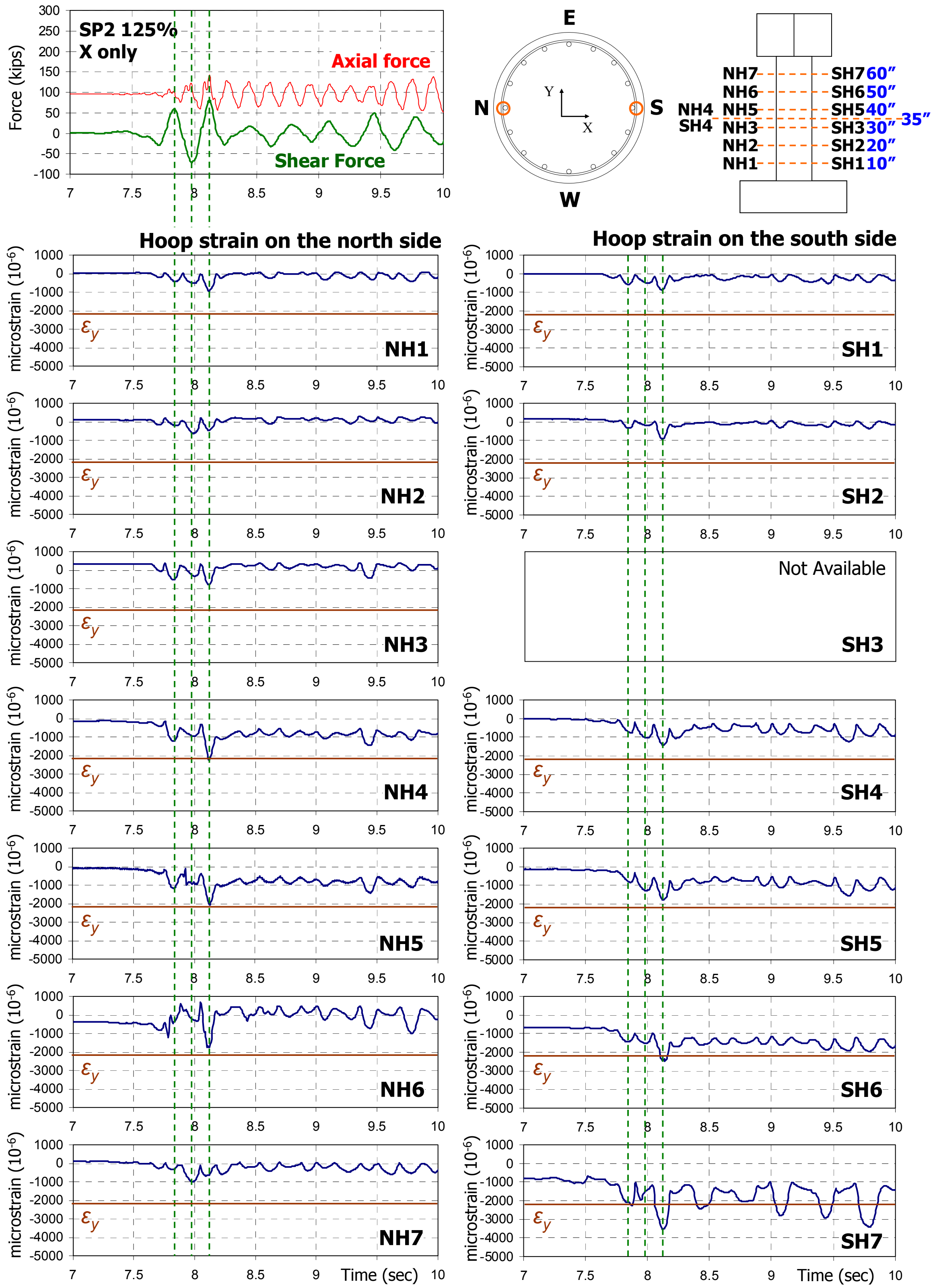

(b) SP2 125% X only

Figure 5.14 Continued.

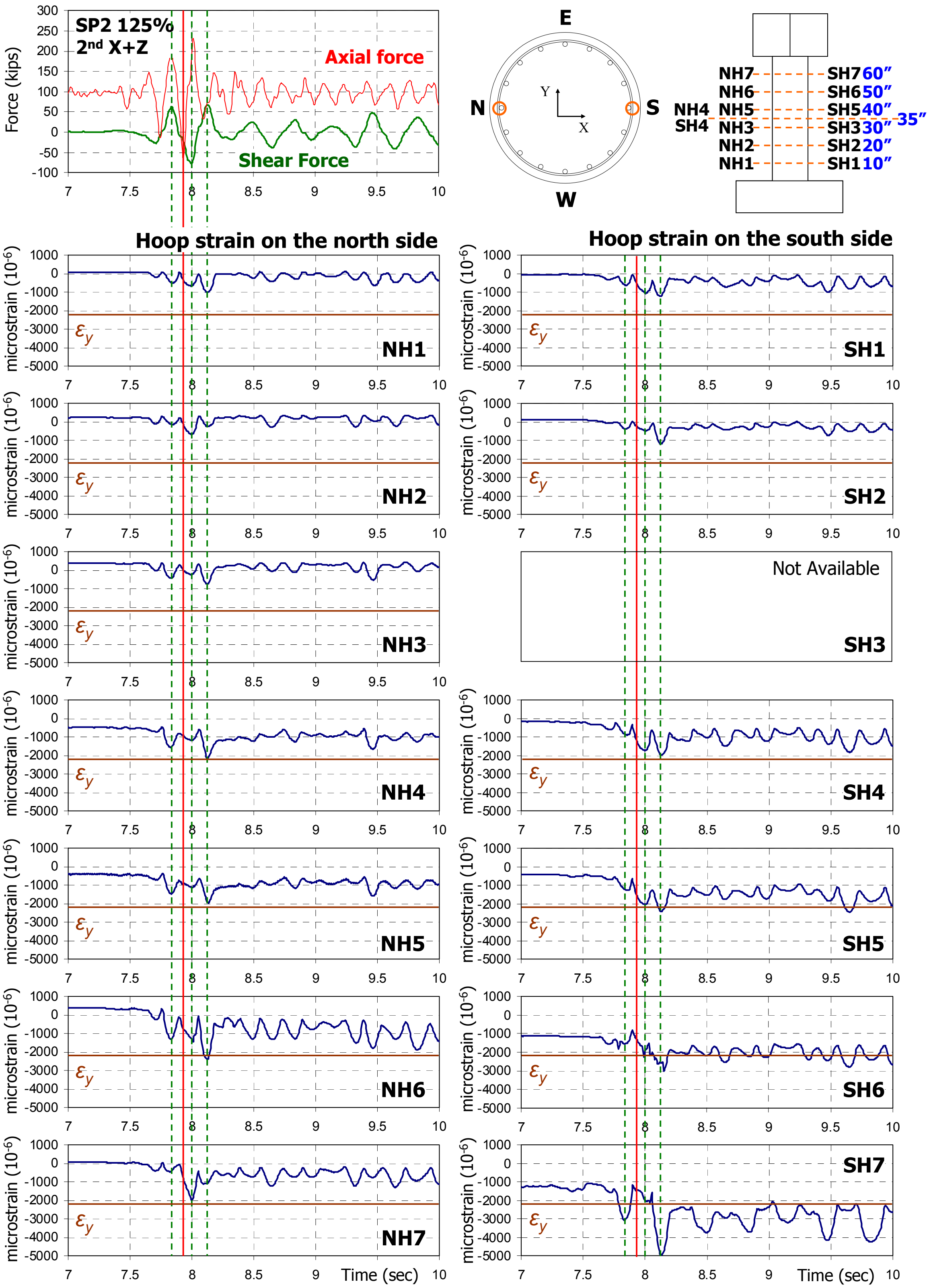

(c) SP2 125% 2nd X+Z

Figure 5.14 Continued.

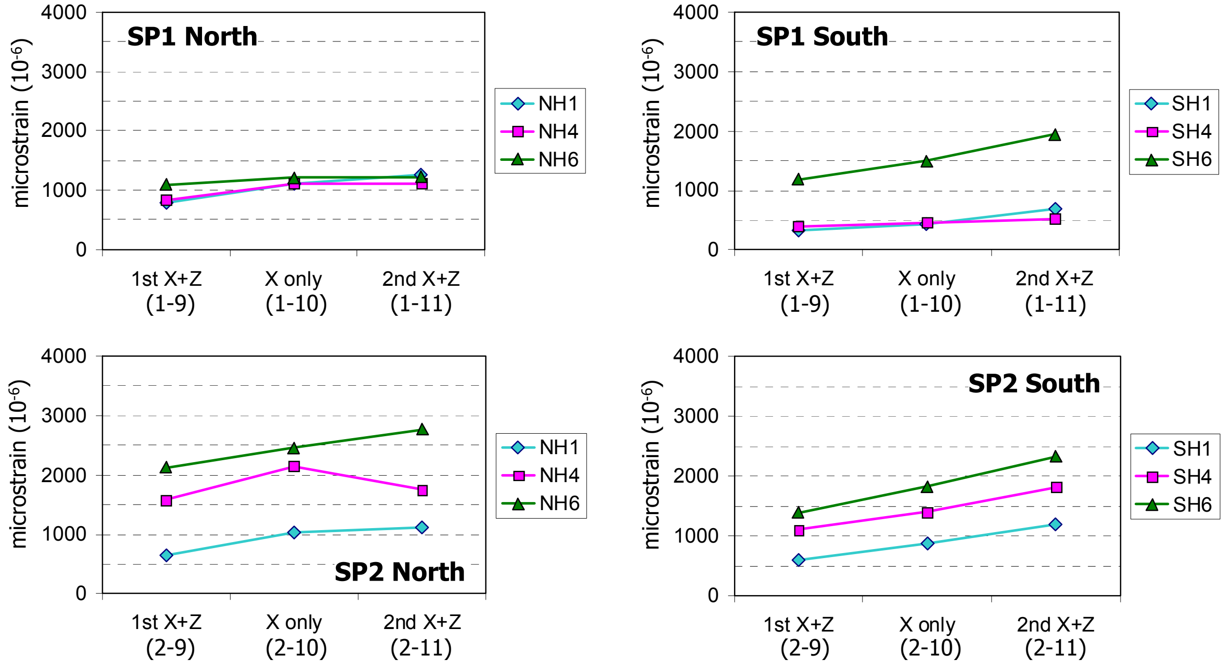

Figure 5.15 Peak-to-peak amplitudes of NH and SH in the 125%-scale runs.

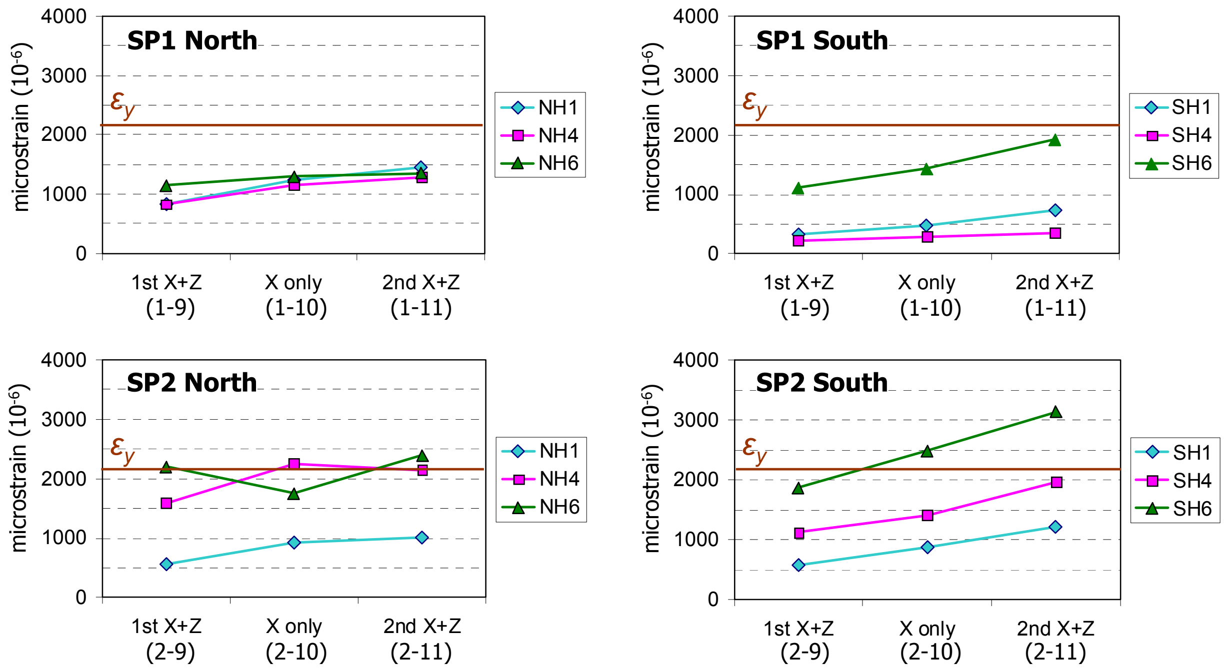

Figure 5.16 Peak tensile strains of NH and SH in the 125%-scale runs.

5.5.2 Transverse Strains at *h* =10 in. and 35 in.

A total of 10 gages were attached to two hoops to capture transverse strain in different directions along the hoop circumference. For the hoop at *h* = 10 in., six gages were used; the central angle between two adjacent gages was 60°. Among the six gages, gages NH1 and SH1, discussed in Section 5.5.1, were compared to other gages on the same hoop in this section. For the hoop at *h* = 35 in., four gages were installed; the central angle between two adjacent gages was 90°. The hoop strains around these two cross sections of SP1 are shown in Figure 5.17 and those of SP2 are shown in Figure 5.18.

Figure 5.17(a) presents the strain response when '1st X+Z' was applied to SP1. The following remarks can be made:

- At *h* = 10 in, most gages had the maximum tensile strain at the third shear peak. Among the six gages, NEH1 and NWH1 had noticeable peak and residual strains.
- At *h* = 35 in., the response measured by NH4 was the largest; it had the maximum tensile peak at the third shear peak. Other than for the gages on the north side, the hoop strain at *h* = 10 in. was larger than that at *h* = 35 in.

Figure 5.17(b) presents the strain response when the 'X only' motion was applied to SP1. The following remarks can be made:

- All the peak values at *h* = 10 in. increased by at least 20% compared with those in the '1st X+Z' test. The trend of this increase was also detected in the peak-to-peak amplitude. Due to residual strain after the '1st X+Z' run, the peak-to-peak amplitude of NWH1 did not significantly grow (5%), but the maximum tensile peak increased by almost 30%.
- The hoop strain on the south side had its maximum tensile peak at the second shear peak even though it was relatively small.

Figure 5.17(c) presents the strain response when '2nd X+Z' motion was applied to SP1. The following remarks can be made:

- The peaks were larger than the previous runs, except for the peak-to-peak amplitude of NEH1 and WH4. The strain of WH4 at *h* = 35 in. was more on the compression side as runs progressed.
- The peak-to-peak amplitude at *h* = 10 in. on the south side increased by 30% or more; this was larger than that on the north side.
- The maximum tensile peak on the south side occurred at the second shear peak; it became more distinct than the run of 'X only' motion.

For SP2 (Figure 5.18), the following observations can be made:

- Under the '1st X+Z' motion [Figure 5.18(a)], most gages had large peaks at the third shear peak, but EH4 and WH4 had their peaks at the tensile peak. The elongation in SP2 was larger than SP1 in most runs and gage locations. In particular, the tensile strain at *h* = 35 in. was more than 188% of that measured from SP1. However, the decrease in the amplitude was detected at NWH1 and NH1, where NWH1 was almost two-thirds of that measured in SP1. This trend was consistent in the peak-to-peak amplitude and the maximum tensile strain values.

- The peak at the first shear peak observed in SP1 was not as defined as that for SP2. The larger hoop strain observed in SP2 compared to SP1 at h = 35 in., where the effect of bending moment was not significant, was the due to the greater shear damage in SP2. The smaller strain in SP2 than SP1 at h = 10 in., where the effect of bending moment was considerable, was due to the smaller moments and corresponding smaller axial compressive stresses and lateral pressure in SP2.
- The response under 'X only' motion [Figure 5.18(b)] was similar to that of SP1. The strain peak increased by 15% or more compared to the previous run. In addition, the strain peaks at the first shear peak were observed.
- Under the '2nd X+Z' run [Figure 5.18(c)], the peaks increased; this trend was significant on the south side regardless of the cross-section location. Except for SWH1, EH4, and WH4, the maximum strain peaks appeared at the third shear peak. Note that the strains from WH4 of SP2 were very different from those of SP2. They had the smallest peak in SP1, but they were comparable to SH4 in SP2.

Figures 5.19 and 5.20 present the peak-to-peak amplitudes and maximum tensile strains of the hoop at h = 10 in. Similarly, those for h = 35 in. are shown in Figure 5.21. From these plots, the following observations can be made:

- The north and south difference at h = 10 in. was noticeable in SP1.
- The gages that were not along the X axis (N-S) of each cross-section had larger values than those on the NH or SH located along the X-axis. In case of the cross section at h = 35 in., a discrepancy between the north and other directions was observed, and it was more marked in SP1 than SP2.
- Most strain peaks increased as runs progressed.

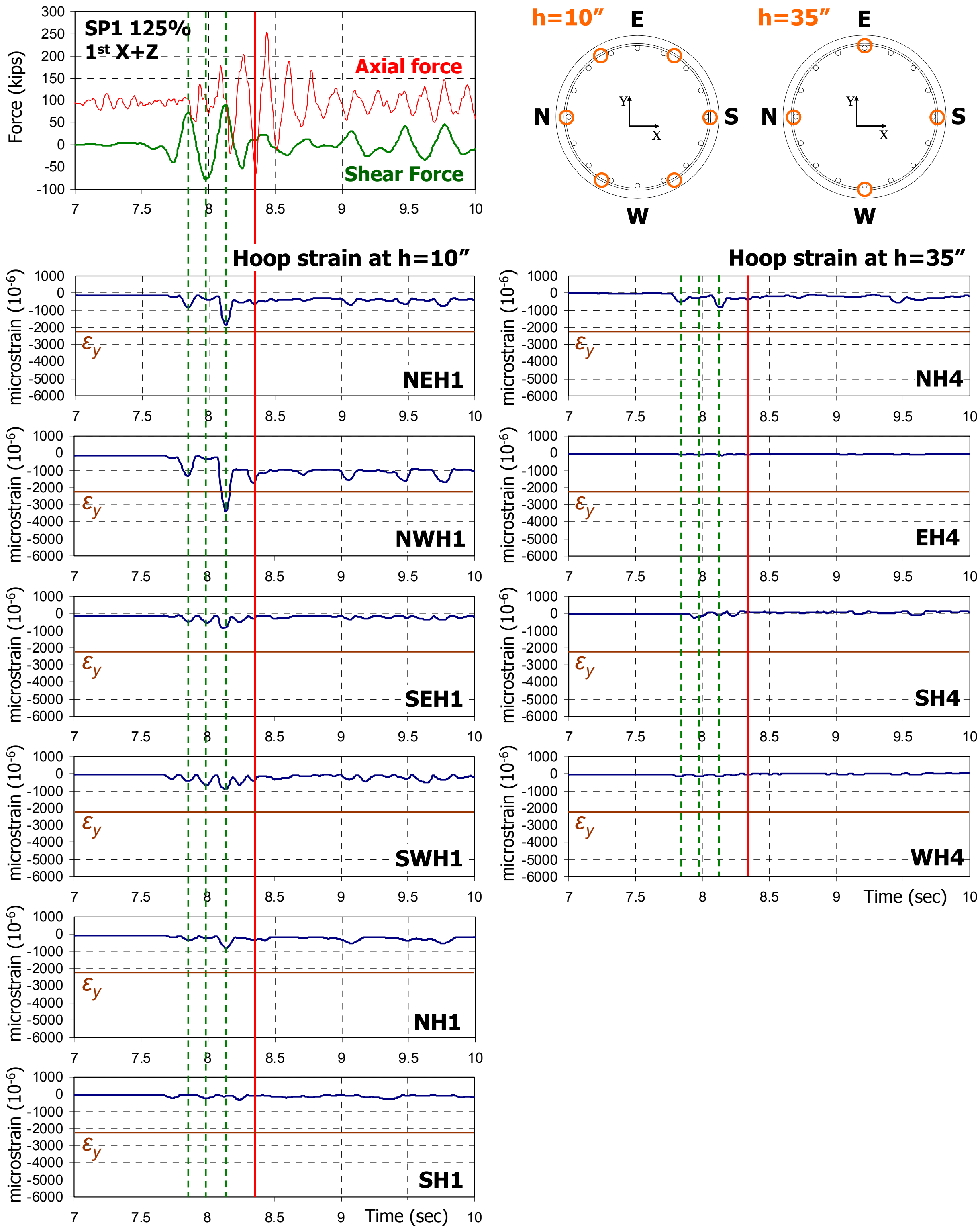

(a) SP1 125% 1st X+Z

Figure 5.17 Hoop strains at two cross-sections of SP1 in the 125%-scale runs.

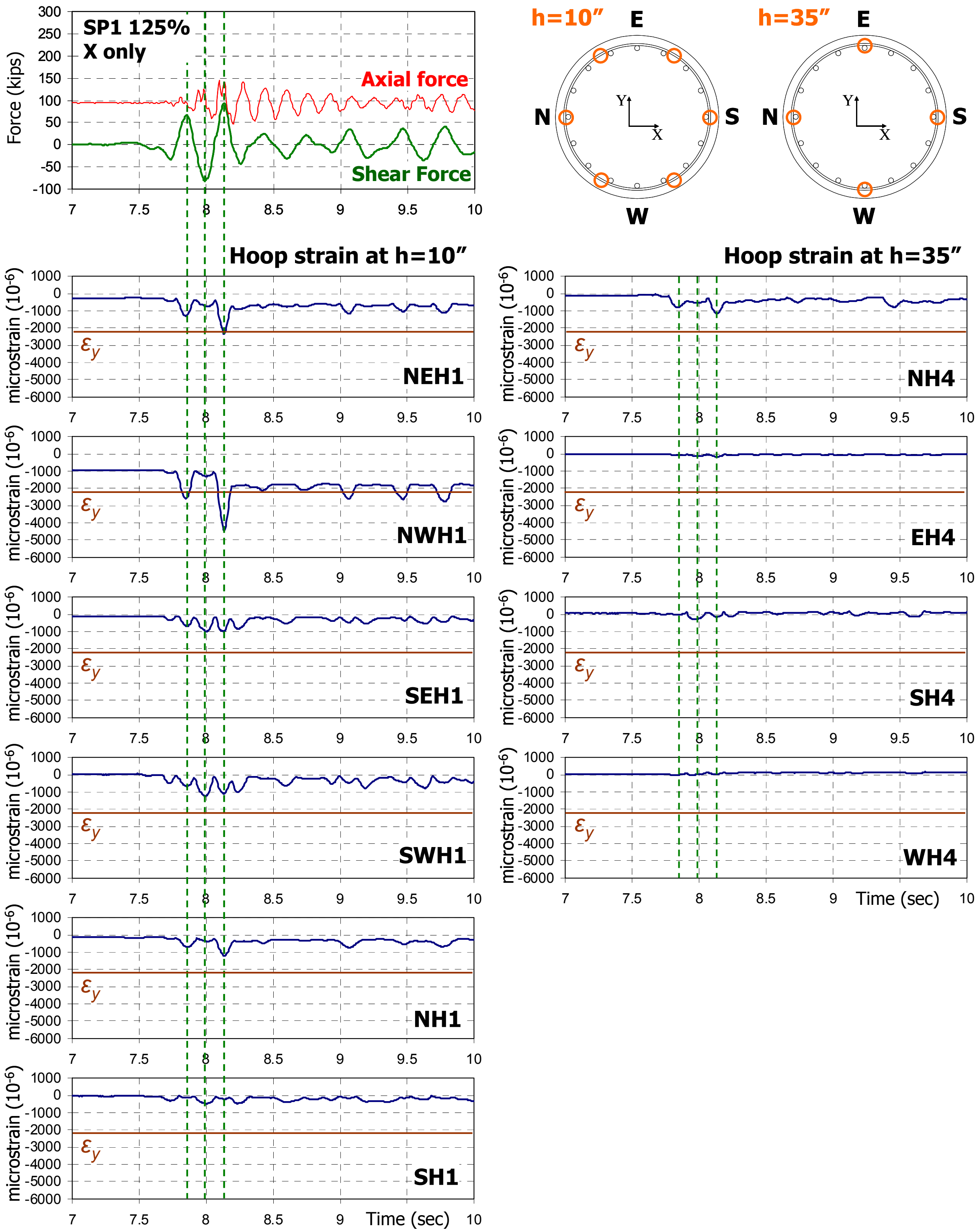

(b) SP1 125% X only

Figure 5.17 Continued.

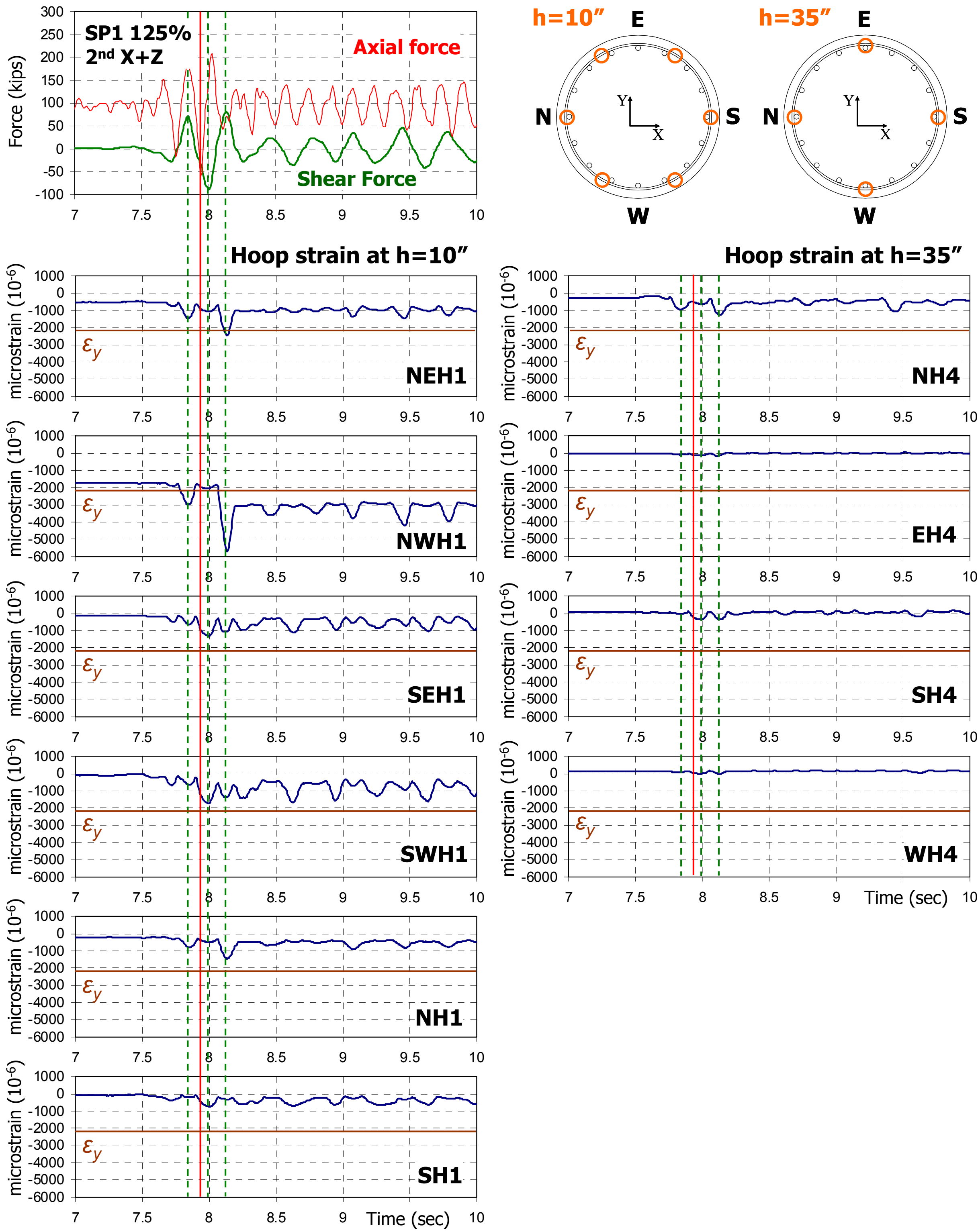

(c) SP1 125% 2nd X+Z

Figure 5.17 Continued.

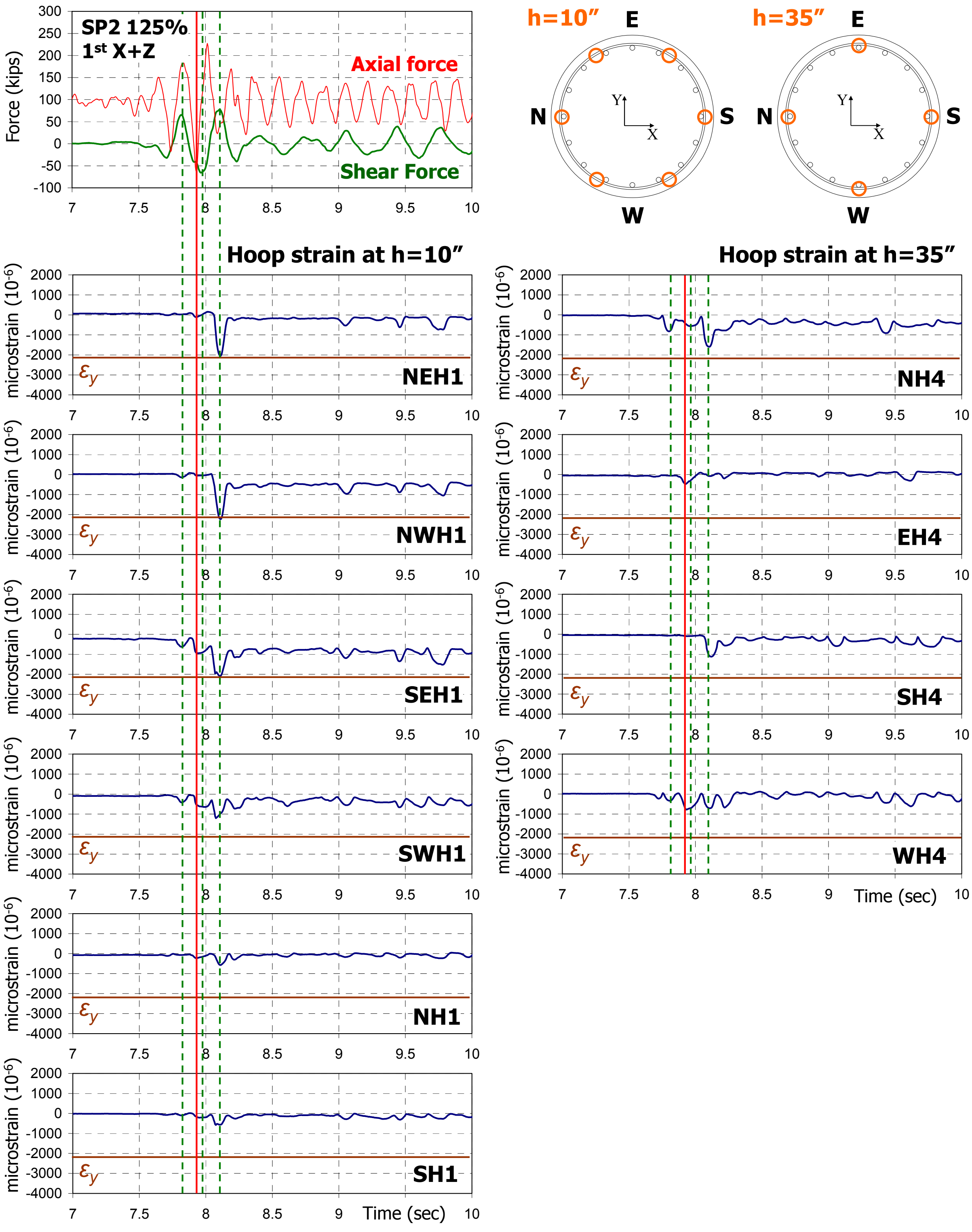

(a) SP2 125% 1st X+Z

Figure 5.18 Hoop strains at two cross-sections of SP2 in the 125%-scale runs.

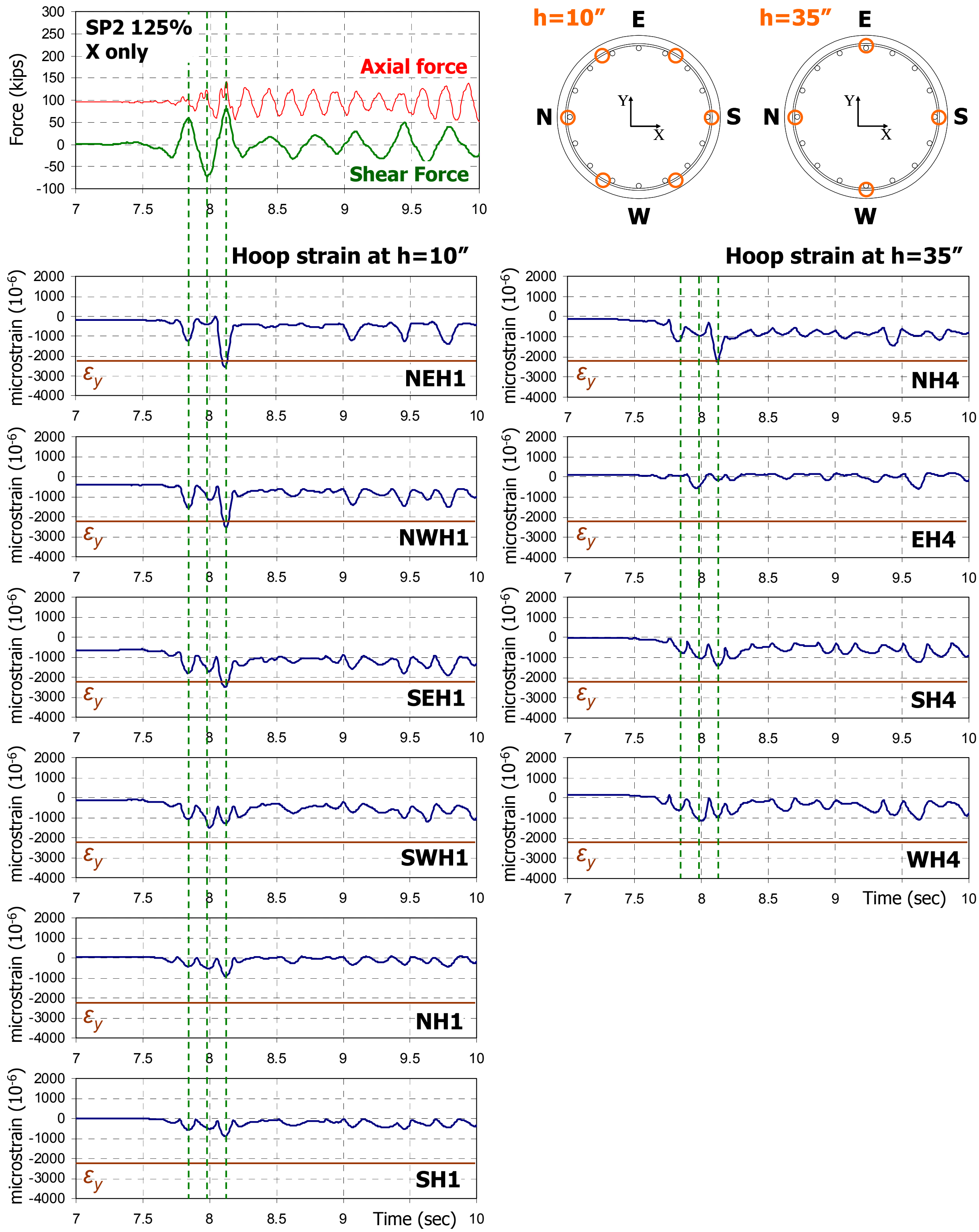

(b) SP2 125% X only

Figure 5.18 Continued.

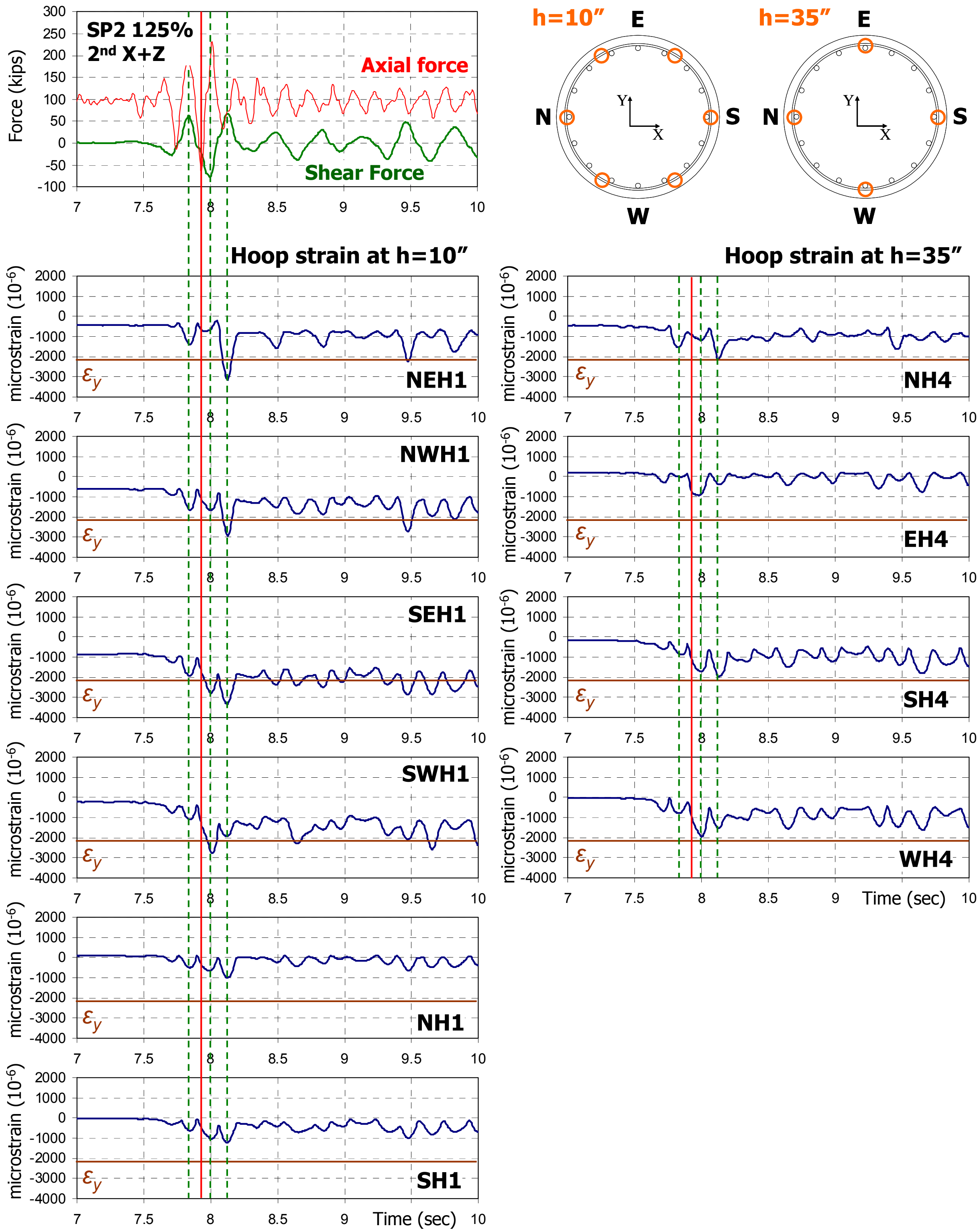

(c) SP2 125% 2nd X+Z

Figure 5.18 Continued.

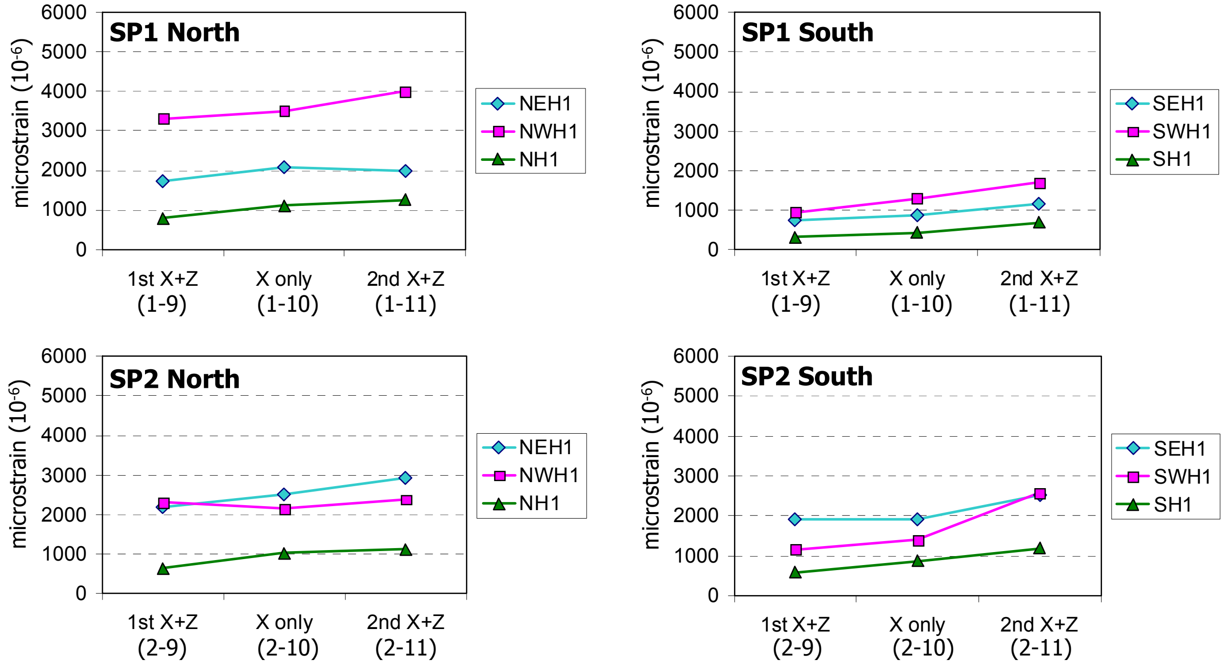

Figure 5.19 Peak-to-peak amplitudes of hoop strain at *h* = 10 in. in the 125%-scale runs.

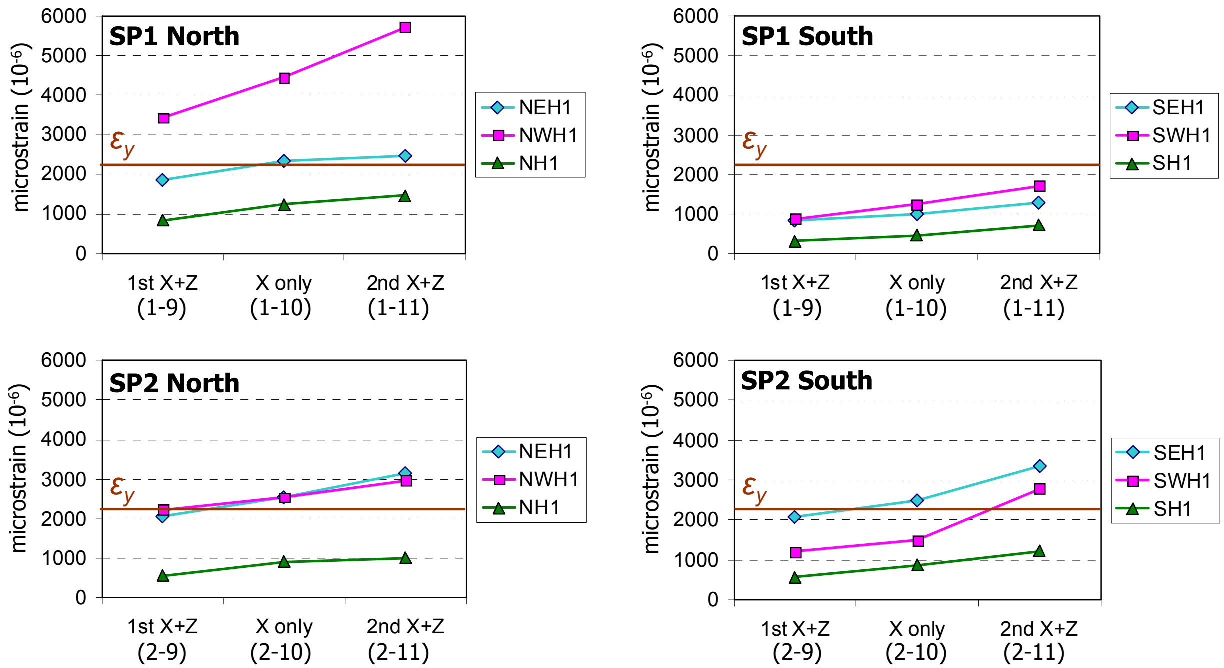

Figure 5.20 Peak tensile strains of the hoop at *h* = 10 in. in the 125%-scale runs.

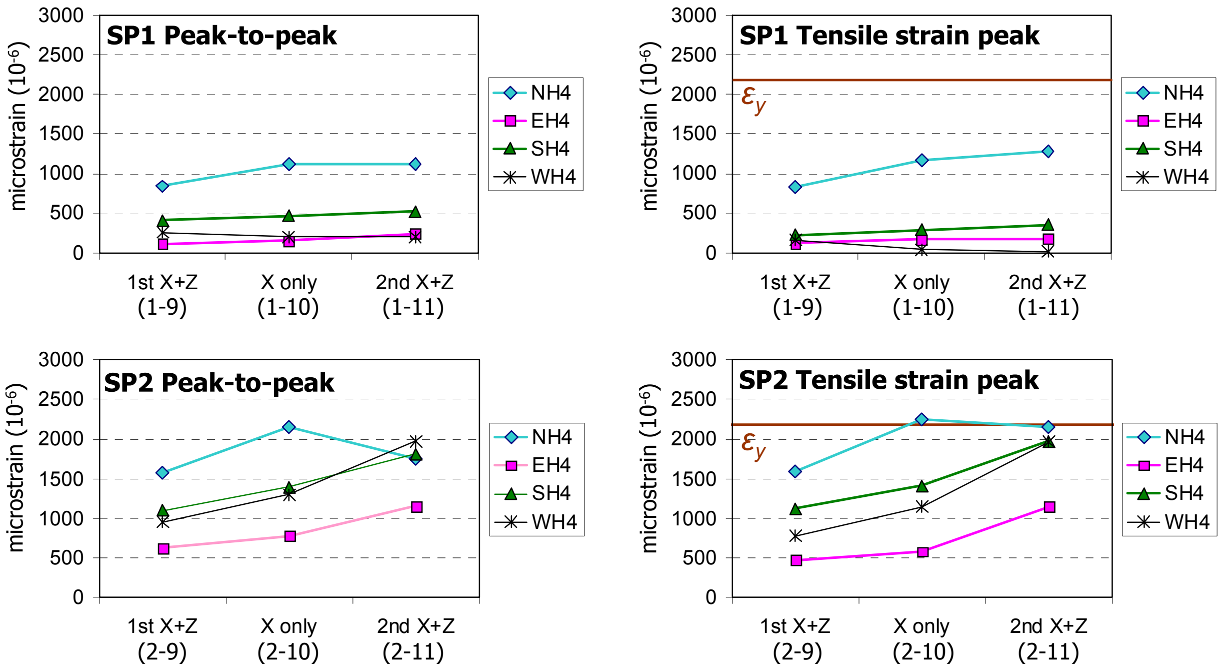

Figure 5.21 Peak-to-peak amplitudes and peak tensile strains at *h* = 35 in. in the 125%-scale runs.

5.6 SUMMARY

Local responses were presented and discussed in this chapter. The curvature histories were calculated from the longitudinal strains on the north and south sides. The closest cross-sections to the base and the top were at h = 10 in. and 60 in., respectively. The comparison suggests that the column was in double curvature during the main excitation. The peak curvature at h = 60 in. was up to five times larger than that at h = 10 in. The initial tangent in moment-curvature relationship (M-φ) decreased as the intensity increased, especially at h = 60 in. In contrast, the initial tangent at h = 10 in. did not change significantly.

The longitudinal strain response was measured at the four reinforcing bars on the north, south, east, and west sides. A total of six cross sections were instrumented for the north and south direction, and three cross sections were instrumented for the east and west direction. As observed in the curvature responses, double-curvature was confirmed by the longitudinal strain on the north and south sides (since the phase angle between the time histories of the strain measurements was shifted along the height during the main excitation). The largest longitudinal strain was detected near the top of the column. This was followed by the value near the base. Finally the middle of the column had the smallest strain value. The effect of the 125%-scale 'X only' motion was not remarkably different from that of the '1st X+Z' or '2nd X+Z' runs. For the east and west sides, the abrupt change in tensile strain due to axial tension was remarkable. It was more significant than that on the north and south sides. The axial force significantly affected the strain histories on the east and west, and one of the peaks in each history appeared at the tension peak. The maximum tensile strain under 125%-scale motion decreased when the vertical (Z) component was not applied. A phase angle shift was also detected on the east and west sides.

The transverse strains on the north and south were measured at seven cross sections. Moreover, two cross sections at columns heights from the base of h = 10 in. and 35 in. had six and four gages around the hoop, respectively. The maximum transverse strain increased with repeated runs for most gages. Therefore, the effect of vertical excitation on transverse strains was not significant. Effect of shear was dominant on strains at h = 35 in., whereas bending moment-induced axial stresses and corresponding lateral stresses affected the strains more at h = 10 in.

6 Development and Evaluation of Computational Models

6.1 INTRODUCTION

This chapter presents the computational models developed in order to predict the response of the tested bridge columns. In addition to the conventional modeling of RC columns, a new shear spring was developed and implemented in the utilized computational platform, OpenSees [2000], in order to incorporate shear strength estimation based on ACI-318-11 [2011] or Caltrans SDC [2013] equations. Various response quantities obtained from the different models were compared with the test results to evaluate the developed computational models.

6.2 DEVELOPMENT OF OPENSEES ELEMENTS

OpenSees [2000], a software framework for developing applications to simulate the performance of structural systems, provides a considerable number of material models. However, none of the existing models can be directly employed to model the variation of the shear capacity as a function of the axial force or the ductility as implied by the code equations such as ACI-318-11 or the Caltrans SDC. In this section, existing material models are discussed and a new material model for SDC or ACI-based shear springs is proposed.

6.2.1 Existing Material and Element Objects in OpenSees

6.2.1.1 Flexure-Shear Interaction Displacement-Based Beam-Column Element

Massone et al. [2006] proposed and developed a beam-column element model that includes flexure and shear interaction in OpenSees. They modified the displacement-based element that already included linear curvature and constant axial strain distributions to include shear deformation. Element formulation (fiber element), sectional analysis, and fiber modeling were modified.

Based on linear interpolation of the curvature and constant axial strain, a third strain component was included to account for shear flexibility. The fiber discretization no longer leads to just uniaxial behavior but rather a bidirectional response by incorporating a membrane material model based on simple uniaxial stress-strain relationships for concrete and steel.

Although the material models can be cyclic, the element model formulation has been implemented and verified initially for monotonic static analysis. Details of the formulation can be found in Massone et al. [2006]. The compatibility equations to relate nodal displacements and internal strains are defined only in 2D. Therefore, 3D analysis is not possible using this element. In addition, only a specific geometric transformation called "*LinearInt*", which is based on the traditional geometric linear transformation, can be used.

The proposed modeling approach in Massone et al. [2006] involves incorporating RC panel behavior into a macroscopic fiber-based model. Results obtained with the analytical model were compared to test results for a slender wall and four short wall specimens [Massone et al. 2006]. A reasonably good lateral load-displacement response prediction was obtained for the slender wall. Although the model underestimated the inelastic shear deformations experienced by the wall, shear yielding and coupled nonlinear shear-flexure behavior were successfully represented in the analysis results. Unfortunately, the above-mentioned code equations (ACI or Caltrans SDC) cannot be represented with this element since it does not consider the effect of axial force in the shear strength estimation.

6.2.1.2 Limit State Uniaxial Material

Elwood and Moehle [2003] developed "*Limit State*" material models based on the existing hysteretic material in OpenSees. Each *Limit State* material model can be interpreted as a spring in series with the nonlinear beam-column element. It captures the additional deformations—either shear or axial—that take place after detection of failure. The *Limit State* material uses a drift capacity model to determine the point of shear or axial failure for a column (see Figure 6.1) and subsequently controls the post-failure response of the element resulting in strength degradation. In this *Limit State* material, empirical drift capacity models at shear failure are proposed [Equations (6.1) and (6.2)], where the influence of axial load (*P*) on the drift ratio is taken into consideration only for columns with transverse reinforcement ratio, ρ_S .

$$\frac{\Delta_S}{L} = \frac{1}{30} + 5\rho_S - \frac{4}{1000}\frac{v}{\sqrt{f_c'}} \geq \frac{1}{100} \quad \text{(psi)}$$
$$\frac{\Delta_S}{L} = \frac{1}{30} + 5\rho_S - \frac{1}{3010}\frac{v}{\sqrt{f_c'}} \geq \frac{1}{100} \quad \text{(MPa)} \qquad \text{for } \rho_S > 0.4\% \qquad (6.1)$$

Incorporating the influence of axial load on the drift ratio,

$$\frac{\Delta_S}{L} = \frac{3}{100} + 4\rho_S - \frac{1}{500}\frac{v}{\sqrt{f_c'}} - \frac{1}{40}\frac{P}{A_g f_c'} \geq \frac{1}{100} \quad \text{(psi)}$$
$$\frac{\Delta_S}{L} = \frac{3}{100} + 4\rho_S - \frac{1}{6020}\frac{v}{\sqrt{f_c'}} - \frac{1}{40}\frac{P}{A_g f_c'} \geq \frac{1}{100} \quad \text{(MPa)} \qquad \text{for } \rho_S < 0.4\% \qquad (6.2)$$

where Δ_S/L is the drift ratio of the column at shear failure, f_c' is the concrete compressive strength, v is the maximum experienced shear stress, *P* is the axial load, and A_g is the gross cross-sectional area. Note that *P* is positive for compression.

Equations (6.1) and (6.2) were proposed to be used in modeling shear-critical columns only, i.e., if the shear capacity defined by an appropriate shear strength model is exceeded by the shear demand calculated according to accepted analytical procedures. The axial failure model was also derived by Elwood and Moehle [2003] to determine how much axial load must be transferred to neighboring elements after a column shear failure and to aid in quantifying the ability of a structural system to resist collapse; the results of this collapse analysis are beyond the scope of this research. Moreover, the data used for calibration of the shear and axial limit curve equations are derived from column experiments conducted mostly under compressive axial loads and none under tensile loads, the relevant topic for the test specimens discussed herein. For an interested reader in the topic of progressive collapse analysis, refer to Talaat and Mosalam [2008].

The proposed drift capacity model defined by Equations (6.1) and (6.2) (and schematically demonstrated with Figures 6.1 and 6.2) represents the shear failure modeling and estimation in an alternative approach compared to the code equations, in the sense of defining a drift ratio corresponding to shear failure rather than defining the shear failure in terms of shear strength and reducing the shear strength as a function of ductility or axial tensile force. The use of this drift capacity model is not applicable in this study since Equation (6.2) is derived from a database of tests with only axial compression; it does not represent the investigated axial tension effects caused by including the vertical acceleration component of the ground motion.

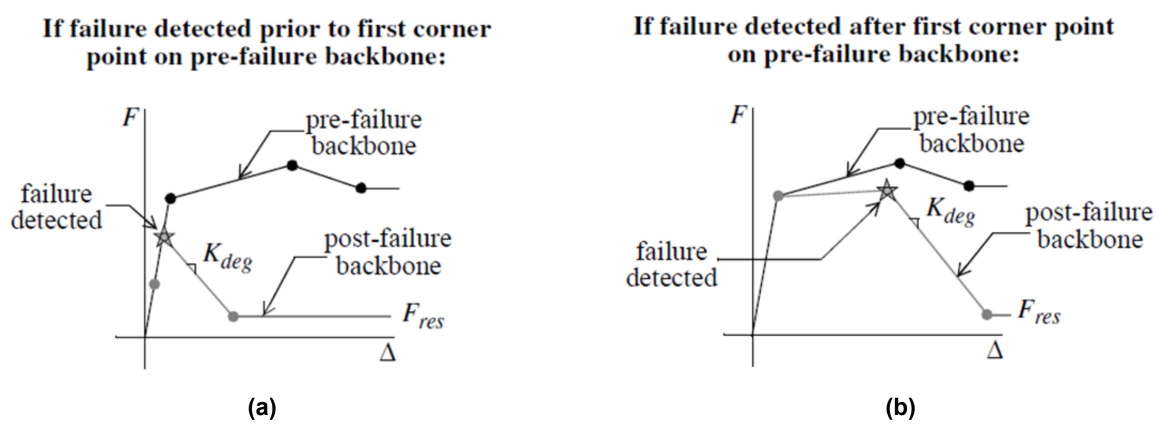

Figure 6.1 **Post-failure backbone curves using the Limit State uniaxial material [Elwood and Moehle 2003].**

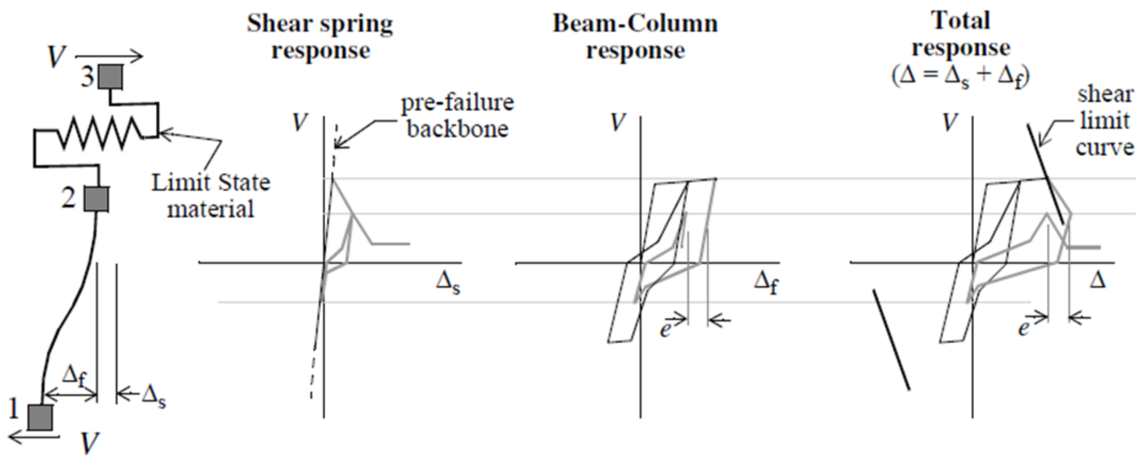

Figure 6.2 **Shear spring model in series using the Limit State uniaxial material [Elwood and Moehle 2003].**

The proposed drift capacity model defined by Equations (6.1) and (6.2) (and schematically demonstrated with Figures 6.1 and 6.2) represents the shear failure modeling and estimation in an alternative approach compared to the code equations, in the sense of defining a drift ratio corresponding to shear failure rather than defining the shear failure in terms of shear strength and reducing the shear strength as a function of ductility or axial tensile force. The use of this drift capacity model is not applicable in this study since Equation (6.2) is derived from a database of tests with only axial compression; it does not represent the investigated axial tension effects caused by including the vertical acceleration component of the ground motion.

6.2.2 Proposed Shear Spring Model

Incorporation of ACI and SDC code equations for shear capacity into OpenSees is achieved by proposing a new material and implementing it into OpenSees' source code. Although, a common and intended use of this new material for a zero-length element connected to a beam-column element, it can be directly employed within a beam column element by aggregating the material into a section. The former approach is followed in the analyses conducted within this study. Considered cases are designated as 'ACI shear spring' and 'SDC shear spring' in order to represent ACI and SDC equations, respectively. The force-displacement relationship of the proposed spring material model is shown in Figure 3.1. This relationship is based on a bilinear envelope (for simplicity), which is defined by the initial stiffness ($K_{elastic}$), the yield force (V_y), and the hardening ratio for post-yield stiffness (r). Initial stiffness is the shear stiffness calculated as GA/L, where G is the shear modulus, A is shear area, and L is the length of the column. Before yielding, the yield force is updated at each integration time step with Equations (1.1) to (1.6) for ACI shear spring using the axial force at that time step in Equations (1.5) and (1.6), and with Equations (1.32) to (1.38) for Caltrans SDC shear spring using the displacement ductility and axial force at that time step in Equations (1.34) to (1.37). The displacement ductility is calculated as the displacement at a specified node (the node at the top of the column in the analyses presented here) normalized by the yield displacement, both of which (the node number and the yield displacement) are input parameters to the new material model in OpenSees.

At the time step where the demand reaches capacity, yielding takes place and the force-displacement relationship follows post-yield behavior. The yield force is not updated and kept constant afterwards unless the column is subjected to any value of axial tension (in the case of the Caltrans SDC spring) and a predetermined value of tension (specified as an input parameter) in the case of the ACI spring. The yield force is kept constant after this final modification. The basis of this second modification is the significant change of the yield force as a result of axial tension. In the case of ACI spring, if the predetermined tension value takes place before any yielding, the yield force is not updated after reaching this predefined tension value. This option permits investigating yielding dynamics in the close vicinity of the maximum axial tension. For example, if the maximum axial tension, which produces significant reduction in shear strength, takes place before a shear peak with a small time interval in between, and the demand does not reach the capacity, a potential yielding may not be captured unless the yield force is kept constant in this small interval. The yielding would take place if the axial and shear peaks were closer. In addition, as mentioned in Chapter 5, it was observed that the shear strength degradation was due to the existence of previous tensile peaks during the tests. Such an option was not required for the SDC shear spring since the shear force is explicitly kept constant in the SDC equation in the mentioned small interval (because the contribution of concrete to the shear strength is zero under any value of tension).

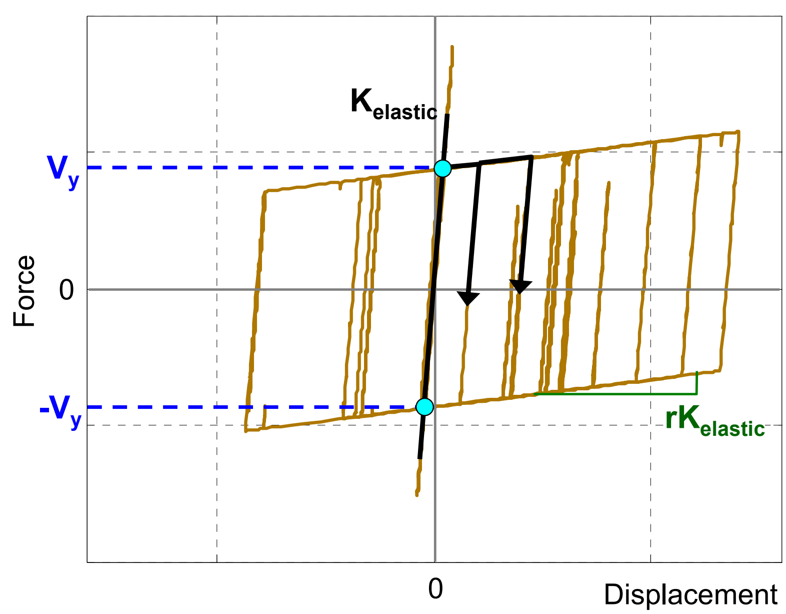

Figure 6.3 Hysteresis of the proposed shear spring material model.

6.3 COMPUTATIONAL MODELING

This section discusses the analytical modeling of the test specimens. First, the structural model including a column, a footing, mass, and springs for the load cells is discussed and the force-based beam-column elements used in the modeling, namely "*Beam With Hinges*" and "*Nonlinear Beam Column*" elements are described. Second, the material models for concrete and reinforcing bars are presented. Third, the fiber section modeling to capture the nonlinear behavior is presented. Finally, the computational results are compared with the test results reported earlier.

6.3.1 Modeling of the Single Reinforced Concrete Column

The specimen consists of a footing, a column, and a top block. Steel beams and mass blocks are placed on top of the test specimen and four load cells connect the specimen to the table below the footing. These features are expected to affect the dynamic and nonlinear responses of the test column. Hence, the whole set-up above the table is modeled in this computational investigation.

6.3.1.1 Models Using "Beam With Hinges" Elements: A-1 and A-2

A "*Beam With Hinges*" (*BWH*) element is a commonly used force-based element to examine the nonlinear response of frame structures. Figure 6.4 shows the composition of a *BWH* element. It has localized plasticity at the ends, i.e., hinges, and the remaining part is kept linearly elastic. The length of each hinge is defined by the user.

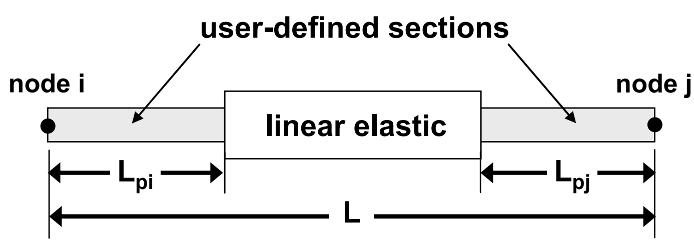

Figure 6.4 OpenSees "*Beam With Hinges*" element [2000].

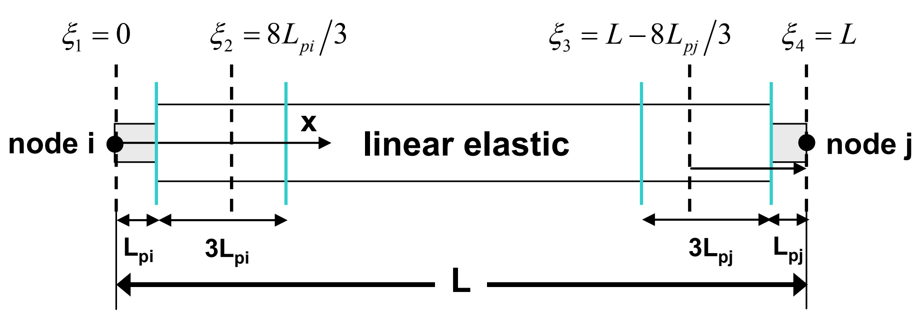

Figure 6.5 OpenSees modified Gauss-Radau integration [Scott and Fenves 2006].

To reduce computational cost, a modified Gauss-Radau integration [Scott and Fenves 2006] is implemented in "*BWH 1*" instead of the conventional integration method that uses two integration points per hinge. Scott and Fenves [2006] developed the modified Gauss-Radau integration to evaluate the integration over a length of $4L_p$ instead of L_p. As a result, the integration points are at 0, $8L_{pi}/3$, $L-8L_{pj}/3$, and L; see Figure 6.5. Nonlinear behavior is confined to the integration points at the ends, and the largest bending moment at the ends are captured.

Since the second and third sections are in the linear elastic part, they are not applicable to record the strain and stress histories that are necessary for comparison to the test data. A "*Beam With Hinges 2*" (*BWH 2*) element is an alternative, because it adopts the original Gauss-Radau integration with integration points at 0, $2L_{pi}/3$, $L-2L_{pj}/3$, and L, where all four sections are in the plastic hinge zones. Therefore, instead of using the *BWH 1*, a *BWH 2* element can be utilized for more refined local responses.

Figure 6.6(a) presents the test specimen models using *BWH* elements to represent the column. Two rigid elements at the top and the base are used for the top block and the footing, respectively. The nodal mass above the top rigid element has three translational and three rotational degrees of freedom, associated with the mass and mass moment of inertia of the mass assembly consisting of the top block, steel beams, lead blocks, and additional concrete blocks. A rotational spring is added below the rigid element at the base, because the specimen was placed on four load cells that were connected to the shaking table and they are not perfectly rigid. As shown in Figure 6.6(a), the difference between Models A-1 and A-2 is the existence of a shear spring in Model A-2. Comparison of the results from these two models leads to the investigation of the effect of the code-based shear spring on the response. The ACI and SDC code equations are implemented in the spring and are designated as Model A-2-ACI and Model A-2-SDC, respectively. Note that the hardening ratio in the shear springs is set as $r = 0.01$.

The hinge length is defined by Caltrans SDC 7.6.2. Based on Paulay and Priestley [1992], it specifies the plastic hinge length of RC columns as follows:

$$L_p = \begin{cases} 0.08L + 0.15 f_{ye} d_{bl} \geq 0.3 f_{ye} d_{bl} & (\text{in., ksi}) \\ 0.08L + 0.022 f_{ye} d_{bl} \geq 0.044 f_{ye} d_{bl} & (\text{mm, MPa}) \end{cases} \tag{6.3}$$

where f_{ye} and d_{bl} are the expected yield stress and the nominal bar diameter of the column longitudinal reinforcing bars, respectively. Because the column with diameter D was in double curvature and had damage due to flexure at the base and the top, the same hinge length was assumed at both ends, i.e., $L_{pi} = L_{pj} = L_p$. The calculated L_p based on the SDC is 14.5 in. (368 mm), corresponding to $0.725D$, where D is the diameter of the column.

6.3.1.2 Models Using "Nonlinear Beam Column" Elements: B-1 and B-2

Unlike *BWH* elements, the "*Nonlinear Beam Column*" (*NLBC*) elements in OpenSees consider the spread of plasticity along the element. The user defines the number of integration points. Figure 6.6(b) shows the specimen model with four *NLBC* elements. Elements at the ends are 15 in. long; seven integration points are employed in each element. Elements in the middle are 20 in. long, five integration points are used. Other components of the NLBC model are identical to those of the BWH Models A. Similar to Models A, the shear spring makes a distinction between Models B-1 and B-2. The ACI and SDC shear springs are included; the models are designated as Model B-2-ACI and Model B-2-SDC, respectively. Similar to A-2-ACI and A-2-SDC, the hardening ratio is specified as $r = 0.01$ in the shear springs.

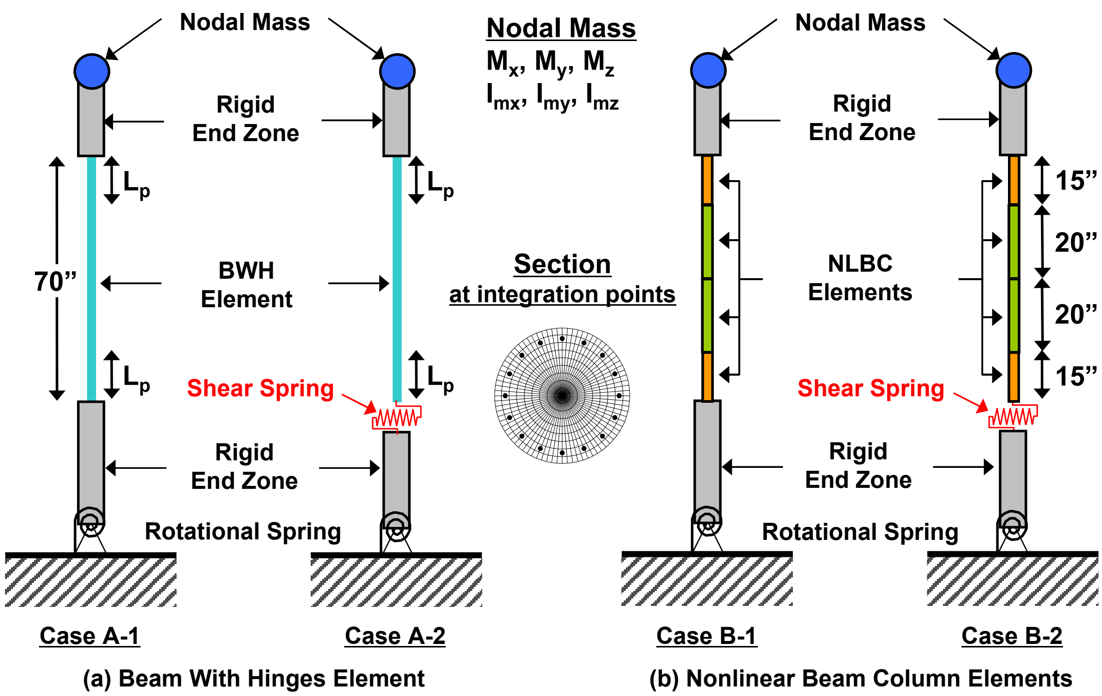

Figure 6.6 Specimen modeling.

6.3.2 Material Modeling

6.3.2.1 Concrete Modeling

For the core and cover concrete, the "*Concrete02*" model is utilized. It is a uniaxial concrete material model with tensile strength and linear tension softening. The parameters which define this model are as follows:

- \$fpc: compressive strength
- \$epsc0: strain at compressive strength
- \$fpcu: crushing strength
- \$epsu: strain at crushing strength
- \$ft: tensile strength
- \$Ets: absolute value of tension softening stiffness
- \$lambda: ratio between unloading slope at \$epsu and initial slope. The initial slope for this model is $2\$fpc/\$epsc0$.

Figure 6.7 presents the stress-strain relationship of *Concrete02* material, where negative and positive stresses (and strains) represent compression and tension, respectively. Table 3.1 summarizes the parameters utilized for this concrete model in this study. Cover concrete properties are based on the material tests presented in Chapter 3. For core concrete of Model A, compressive strength and strain properties are calculated based on Mander [Mander et al. 1988], using the confinement provided by the hoops (which have 2 in. (SP1) or 3 in. (SP2) spacing). For core concrete of Model B (which has *NLBC* elements), the compressive strength is the same as that of Model A. However, the strain corresponding to the compressive strength ($epsc0) is modified to match the initial stiffness calculated as 2$fpc/$epsc0 to the tangent modulus of elasticity obtained from the material tests. This modification was necessary for Model B since the stiffness of the column was obtained by integrating the response of the sections along the column height. This was not significant for Model A, where the initial stiffness of the column was mostly dominated by the middle elastic part where the elastic modulus is specified separately.

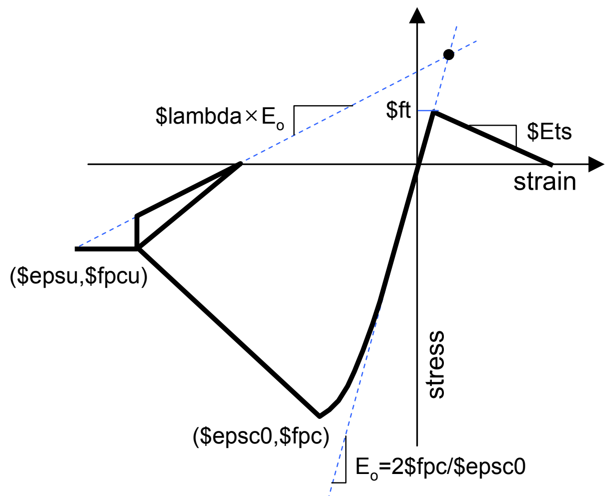

Figure 6.7 OpenSees *Concrete02* model: material parameters [2000].

Table 6.1 Concrete model parameters for computational models.

Parameter	Units	Cover Concrete	Core Concrete	
			Hoops @ 2 in.	Hoops @ 3 in.
$fpc	(ksi) (MPa)	-4.1 (-28.0)	-5.12 (-35.3)	-4.77 (-32.9)
$epsc0 (A)	N/A	-0.003	-0.0069	-0.0056
$epsc0 (B)	N/A	-0.003	-0.0085	-0.0094
$fpcu	(ksi) (MPa)	-0.41 (-2.80)	-2.28 (-15.7)	-0.0 (-0.0)
$epsu	N/A	-0.006	-0.0126	-0.0097
$ft	(ksi) (MPa)	0.41 (2.80)		
$lambda	N/A	0.8		

6.3.2.2 *Steel Modeling*

For reinforcing bars, the "*Steel02*" model is used, which is a uniaxial Giuffre-Menegotto-Pinto [Menegotto and Pinto 1973] steel material with isotropic strain hardening. The model accounts for the Bauschinger effect, which contributes to the gradual stiffness degradation of the reinforced concrete members under cyclic response. This model has an isotropic hardening option for tension and compression portions of the hysteresis. Despite its simplicity, this bilinear model predicts the basic material responses accurately over most of the strain range; however, it does not account for the initial yield plateau of the reinforcing steel or the degradation of the steel strength. For this model, the following parameters need to be defined:

- $\$F_y$: yield strength
- $E: initial elastic tangent modulus
- $b: strain-hardening ratio (ratio between post-yield tangent and initial elastic tangent)
- $R0, $cR1, $cR2: parameters that control the transition from elastic to plastic branches
- $a1, $a2, $a3, $a4: isotropic hardening parameters

Table 6.2 summarizes the parameters utilized for this steel model in this study. Longitudinal and transverse reinforcing steel bars have properties specified in columns (a) and (b), respectively. Figure 6.8 presents the stress-strain relationship of *Steel02* material. Note that E_p is defined by multiplying two parameters, $E and $b. Based on the properties in Table 6.2, the E_p for longitudinal and transverse reinforcement are 455.42 ksi (3140 MPa) and 580.15 ksi (4000 MPa), respectively.

Table 6.2 Steel model parameters for computational models.

Parameter	Units	(a) Longitudinal	(b) Transverse
$\$F_y$	(ksi) (MPa)	77.5 (534.3)	63.0 (435.3)
$E	(ksi) (MPa)	29007.5 (200000)	
$b	N/A	0.0157	0.0200
$R0, $cR1, $cR2	N/A	Default	
$a1, $a2, $a3, $a4	N/A	Default (no isotropic hardening)	

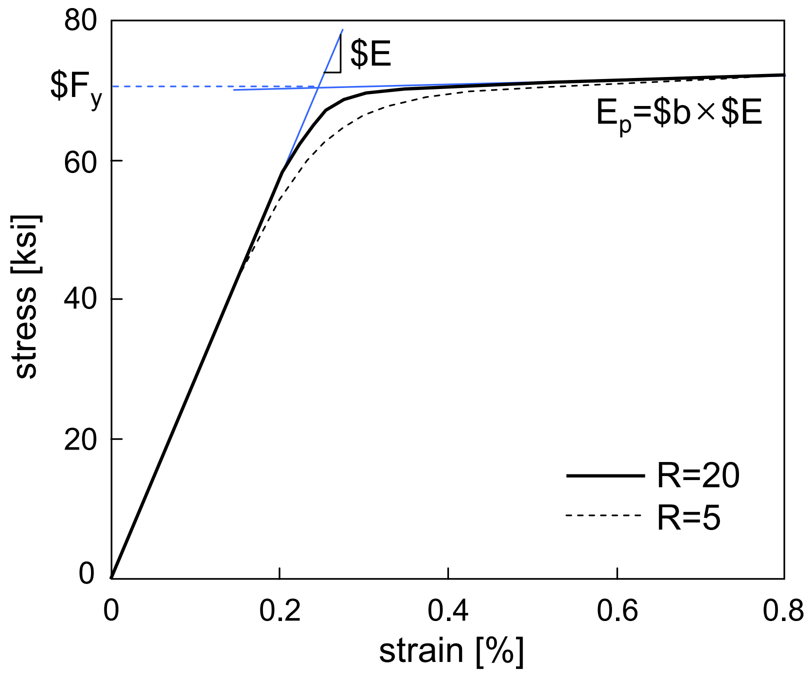

Figure 6.8 OpenSees *Steel02* model: material parameters [2000].

6.3.3 Fiber Section Modeling

Fiber section modeling, which consists of subdividing a cross section into discretized fibers with a finite area and uniaxial force-deformation relationship of the material associated with the fiber, is capable of representing the flexural behavior and its interaction with the axial force in beam-column elements. Therefore, this type of modeling is widely used in structural analysis applications. There are various commands in OpenSees to divide a section into regular fibers. Amongst these commands, the "*Circular Patch*" command is useful to define the fibers of a circular cross section. For the sections of the analyzed columns, the core that is confined by hoops consists of 80 subdivisions in the circumferential direction and 80 subdivisions in the radial direction, as shown in Figure 6.9. The cover is similarly divided by the same command and has 80 and 10 subdivisions in the circumferential and radial directions, respectively. Moreover, "*Circular Layer*" command is utilized to construct a circular layer of reinforcing bars. Sixteen longitudinal bars are uniformly distributed along the circumference for the considered cross section, as shown in Figure 6.9.

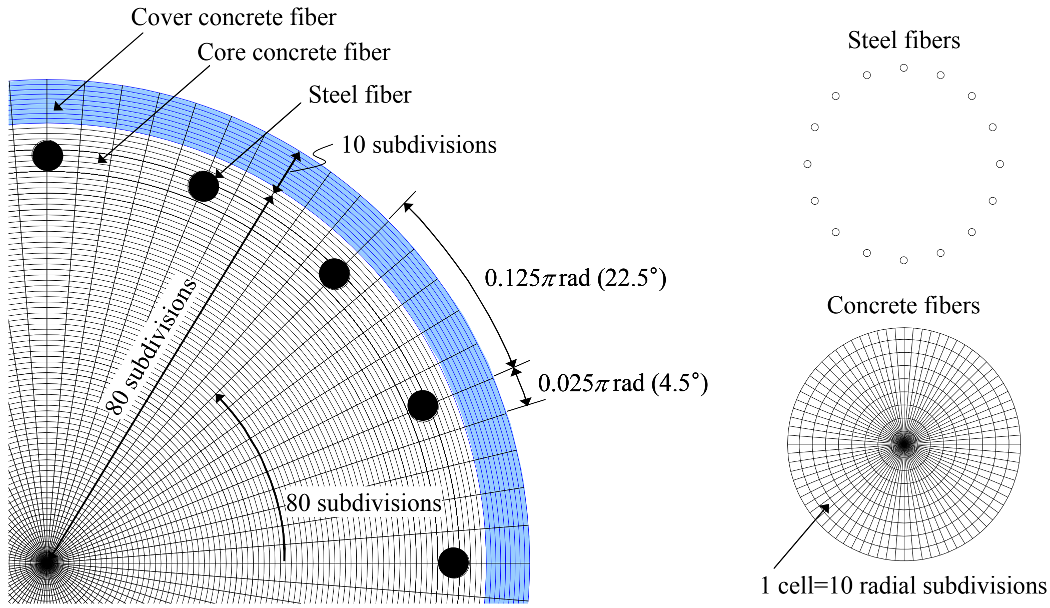

Figure 6.9 Fiber section modeling.

6.3.4 Modeling of Damping

The damping matrix cannot be determined directly from the structural dimensions and the damping properties of the materials. In most of the structural engineering applications, classical damping is utilized, which is an adequate idealization if similar damping mechanisms are distributed throughout the structure. The Rayleigh damping matrix, $[C]$, one of the common types of classical damping, is computed as a linear combination of the mass and stiffness matrices, $[M]$ and $[K]$, respectively. It is considered as a practical method because it provides a banded damping matrix even for large systems.

For the analysis of the tested columns, mass-and-tangential stiffness proportional Rayleigh damping is used with constants calculated based on the first mode (translation in X) frequency (ω_i) of the computational model and the vertical (translation in Z) frequency of the specimen ($\omega_{vertical}$). The reason for not choosing vertical frequency of the computational model is discussed in Section 6.3.5. As a result, the coefficients for Rayleigh damping (assuming a damping ratio ζ) are calculated as follows:

$$a_0 = \zeta \frac{2\omega_i \omega_{vertical}}{\omega_i + \omega_{vertical}} \quad a_1 = \zeta \frac{2}{\omega_i + \omega_{vertical}} \qquad \text{where } i = 1 \tag{6.4}$$

$$[C] = a_0[M] + a_1[K] \tag{6.5}$$

Damping in RC structures, which does not include the hysteretic damping due to yielding and damage, varies based on the level of cracking and other internal mechanisms of the concrete material. Accordingly, the conducted tests are classified into three groups (see Table 6.3), where each group is assigned a different damping ratio (ζ) based on the measured data. The damping ratio for the dynamic tests is calculated from the FFT of the horizontal acceleration measured on the top of the mass blocks using the half-power bandwidth method [Chopra 2006]. Two scale levels of tests are used for this purpose, as shown in Table 6.3. The damping ratio in the free vibration tests is estimated from the absolute lateral displacement history in the X-direction, however. Since the calculated damping ratios of SP1 and SP2 are similar, same damping values are used in analysis of both of the specimens, as listed in Table 6.3.

Table 6.3 Damping ratio.

Test	Damping ratio, ζ (%)
Free Vibration	2.0
5%-scale or 12.5%-scale	2.5
25%-scale or above	4.0

6.3.5 Model Adjustment due to Shaking Table Effect

As mentioned in Section 4.2.3, the shaking table is not perfectly rigid. Its flexibility affects the response of the test specimen, especially in the vertical direction. Given that the vertical natural period of the column is much shorter than that of the shaking table, and the vertical period of the shaking table is dominant in the whole system (combined test specimen and shaking table as one system), this situation is similar to the case of a stiff structure supported on a soft foundation. If the shaking table effect is ignored, and the vertical acceleration recorded on the shaking table is directly used as the input to the analytical model, an acceleration history with higher frequencies is obtained at the top of the column. However, these high frequencies are not present in the test data (Figure 6.10) because of the dominance of the shaking table period in the vertical response of the system.

In order to demonstrate the shaking table effect on the vertical response, elastic dynamic analysis is conducted for the 2DOF system presented in Figure 6.11(b), where $\mathbf{u_1}$ and $\mathbf{u_2}$ represent the vertical displacements of the shaking table and the test specimen, respectively, and $\mathbf{\ddot{u}_g}$ represents the input target acceleration denoted as 'target' in Chapter 4. Since the effective mass and stiffness of the shaking table [$\mathbf{m_t}$ and $\mathbf{k_t}$ in Figure 6.11(b)] are not known accurately, they are varied as input parameters to match the vertical periods identified from the FFT plots of the measured acceleration. Based on the results of the analysis conducted with the ground motion in Figure 4.1, Figure 6.11 demonstrates that the acceleration histories at the shaking table level and at the top of the column are very similar: this is in agreement with the test data. Therefore, the flexibility of the shaking table not only results in the modification of the target accelerations (i.e., difference between input to the shaking table and its output in terms of accelerations) but also governs the test specimen response in the vertical Z-direction.

Based on these findings, it can be concluded that not only the test specimen but the whole system—including the shaking table—should be modeled, and that the target input should be used as the input to the analytical model instead of the measured accelerations on the shaking table. That said, this approach is not feasible since the shaking table effective stiffness varies from test to test and even within a test. Considering that one of the main goals of the investigation in this study is the evaluation of the effect of axial tension (caused by the vertical acceleration of the ground shaking) on the shear capacity and the development of the corresponding analytical modeling, imposing the measured forces directly in the analytical model agrees more with these goals rather than modeling a complex table response with several sources of uncertainties and gross assumptions. Therefore, the recorded axial force history (from the load cells installed underneath the test specimen footing and above the shaking table) is directly applied to the column as an external force excitation in the conducted analyses. In order to equate the restoring forces to the external forces, the model mass in the vertical direction is set to almost zero, corresponding to 2.5×10^{-4} of the original mass.

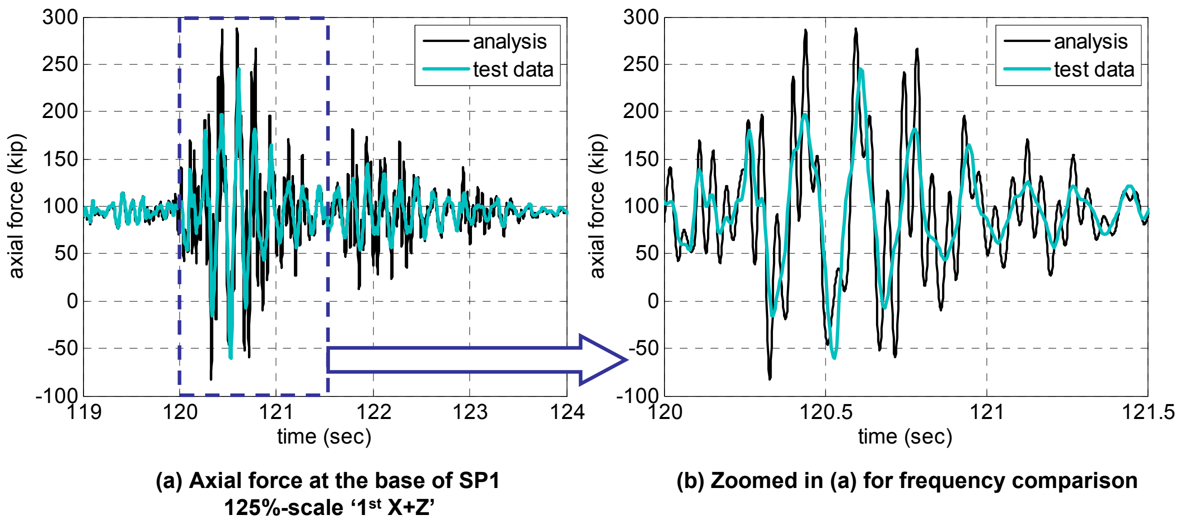

Figure 6.10 **Axial force difference between the analytical result and test data measured at the base of SP1 under the 125%-scale '1st X+Z' motion.**

6.3.6 Input Acceleration

Average of the accelerations recorded near the four load cells on the base plate underneath the test specimen is used as an input motion in the X- and Y-directions. The recorded accelerations are low-pass filtered with a cutoff frequency of 40 Hz. In the vertical direction, the recorded axial force time history filtered with a cutoff frequency of 30 Hz is used as external force excitation as discussed above. In order to capture the correct accumulation of nonlinearity, such as the residual displacements, input for the different scale tests are combined into a single long acceleration record.

6.3.7 Other Parameters for Dynamic Analysis

As explained above, a damping ratio of 4% is used in these analyses. Considering that the test specimen experienced some undetermined shrinkage cracking even before any shaking, 63.8% of E_c obtained from the cylinder tests is used to match the natural periods in the 50%-scale test, which were 0.63 sec for SP1 and 0.65 sec for SP2. The Newmark integration with integration parameters γ = 0.5 and β = 0.25 is used for time integration using a time step of 0.0012 sec, corresponding to only 4% of the vertical period of SP1 and SP2, which was determined as 0.03 sec. This small time step is chosen for accuracy. Also, the Newton-Raphson method with line search is used as the nonlinear solution algorithm.

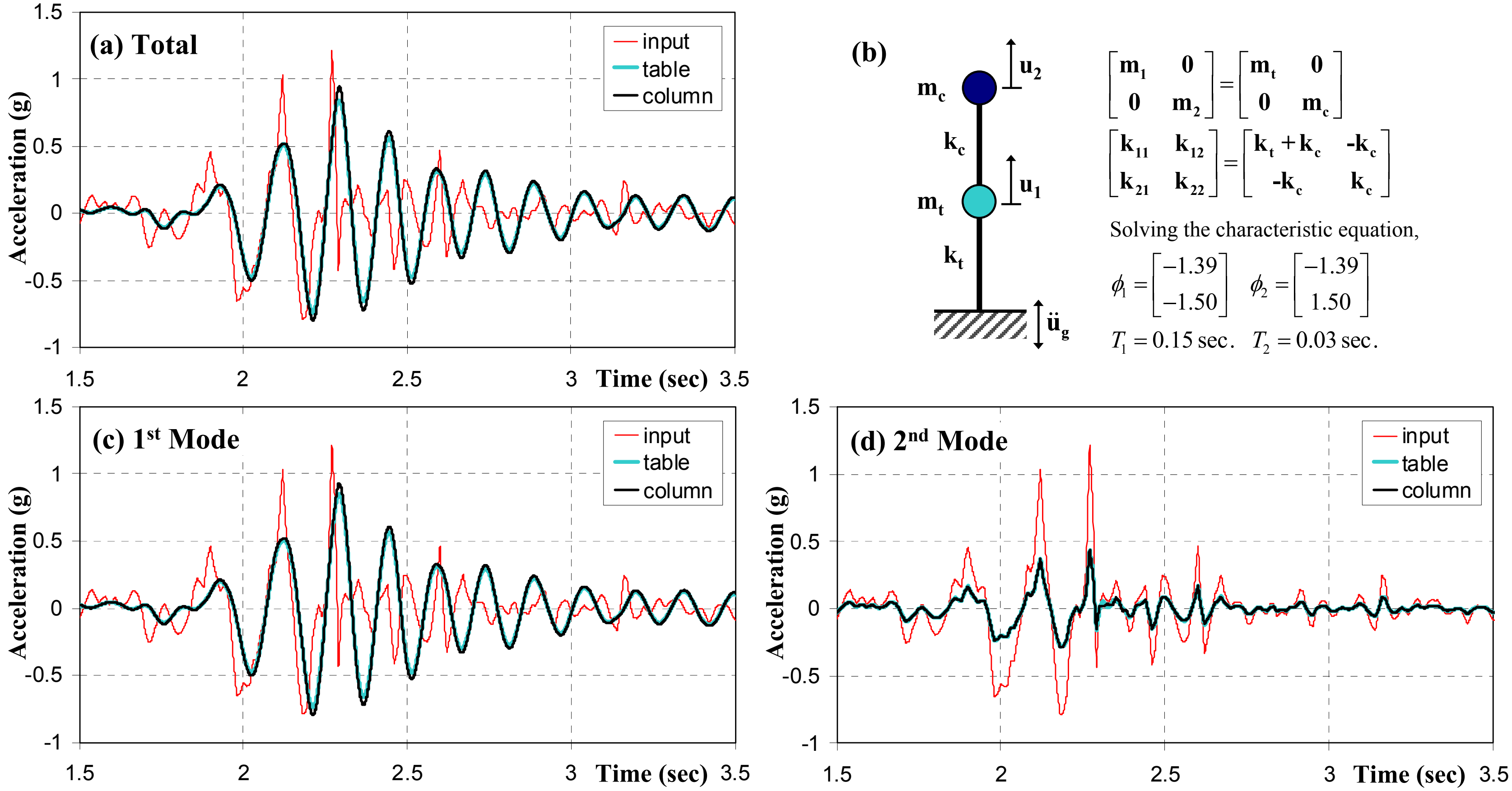

Figure 6.11 Two-DOF analysis for the shaking table and test specimen responses

6.4 COMPARISON OF COMPUTATIONAL AND EXPERIMENTAL RESULTS

6.4.1 Stiffness and Free Vibration Tests

The stiffness and free vibration test results are simulated with sufficient accuracy by the analytical model described above. For this purpose, the stiffness of each model is first matched to that obtained in the stiffness test. Thereafter, the lateral displacement history from the analysis is compared to the test results. Figure 6.12 shows the lateral displacement of both specimens from the free vibration tests. Absolute displacement histories are compared since the analytical model involves a rotational spring at the base representing the shaking table flexibility.

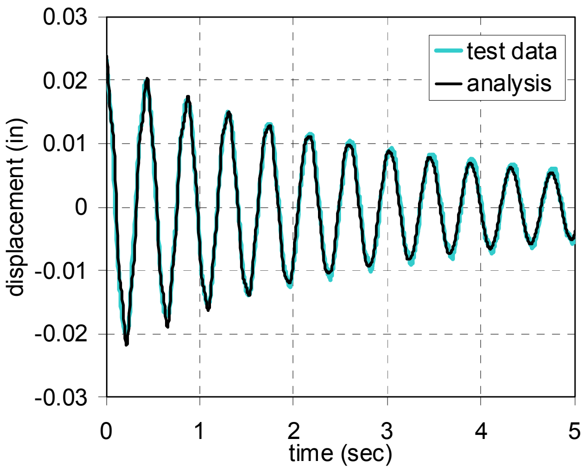

(a) SP1: Absolute displacement 1st trial

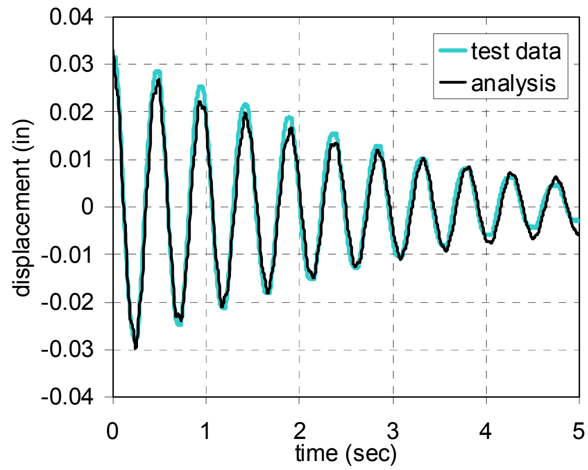

(b) SP2: Absolute displacement 2nd trial

Figure 6.12 Comparison of the free vibration test data and the analysis results (model A-1).

6.4.2 Global Responses

As discussed in Chapter 4, the specimens were not significantly damaged in the tests up to 25%-scale intensity level. In addition, the shear spring affects the response only for high-intensity level motions. Therefore, the behavior of the tested specimens are compared with the analytical investigation results for the tests with scales greater than 50% to examine the effect of vertical component of the ground motion. The global responses of Models A-1, A-2, B-1, and B-2 are compared. As mentioned, Models ‘A’ and ‘B’ incorporate *BWH* and *NLBC* elements, respectively; “1” and “2 “represent the cases with and without the shear spring, respectively. Two springs, i.e., ACI and SDC springs, are utilized in Models A-2 and B-2. They are designated as A-2-ACI or B-2-ACI and A-2-SDC or B-2-SDC, respectively.

6.4.2.1 Shear Force

Before investigating the computational results, the code-based shear strength estimation is discussed. Figures 6.13 and 6.14 compare the shear strength estimation of ACI and SDC equations with the absolute value of the shear force histories obtained from the test results. As already mentioned in Chapter 1, both the ACI and SDC equations have terms for the effect of the axial force on the shear capacity. Note that the axial forces and displacements gathered from the test results are used in these shear strength estimations. The two code equations provide similar estimations under compression, but they differ under tension, which is clearly shown in Figure 6.13(b) for 95%-scale run applied to specimen SP2. Up to 70%-scale, SDC and ACI have similar shear capacity estimation and the shear force is less than the shear capacity. In the 95%-scale run of SP2, the first sudden decrease in shear strength takes place using the SDC estimation due to a small axial tension of 1.4 kips (6.2 kN). SDC and ACI estimations are considerably different under the 125%-scale motions as shown in Figure 6.14. Since there is significant axial tension in the 1st and 3rd runs (Runs 1-9 and 1-11 for SP1 and Runs 2-9 and 2-11 for SP2), SDC estimation reduces down to V_s (shear strength provided by the hoops) only, i.e., 43.8 kips (194.8 kN) for SP1 and 27.5 kips (122.3 kN) for SP2, which correspond to 57.3% and 66.8% reduction compared to the initial full shear capacity, i.e., V_s+V_c where V_c is the shear strength provided by the concrete with no axial tension. Moreover, there are noticeable decreases in SDC estimation due to large ductility. As a result, SDC equation provides a more conservative estimation than ACI equation due to tension or large ductility. Accordingly, the shear demands of SP1 and SP2 exceed the shear capacity estimated by SDC in all the 125%-scale tests, consistent with the observed shear damage described in Chapter 4. However, although SDC equation predicts the presence of shear damage, it does so in a rather conservative manner as it can be observed from the comparison of the shear strength equation prediction of SDC with the shear force. The SDC shear capacity prediction is sometimes smaller than half of the shear force, as in runs 1-11 and 2-11. Noting that the shear forces are obtained from the test data, they should be bounded by the shear capacity values, signifying the underestimation of the shear strength by the SDC equation.

Similar observations can be made by examining the computational results. Figures 6.15 and 6.16 compare the shear force responses obtained from Models A-1, A-2-ACI, A-2-SDC, B-1, B-2-ACI, and B-2-SDC to those obtained from the SP1 tests. Figure 6.15 presents the shear force histories from models A-1, B-1, and the test data of SP1 subjected to 50%, 70%, and 95%-scale excitations. (Because the shear springs did not yield at these levels, models A-2 and B-2 including the shear springs produced very similar results to models A-1 and B-1l therefore, they are not presented.) Note that small differences are expected because the additional flexibility introduced by the finite stiffness of the shear spring can cause slight changes in the dynamic response. It can be observed that there is a close resemblance in shear force responses obtained from models A-1 and B-1 and these responses are comparable to the shear force history from the test data. An exception is the presence of high frequency, which is more noticeable in the analysis results. In particular, the high frequency content is notable in the response of A-1 under the 50%-scale motion. It seems that the free vibration occurs between 12.5 and 14.5 sec.

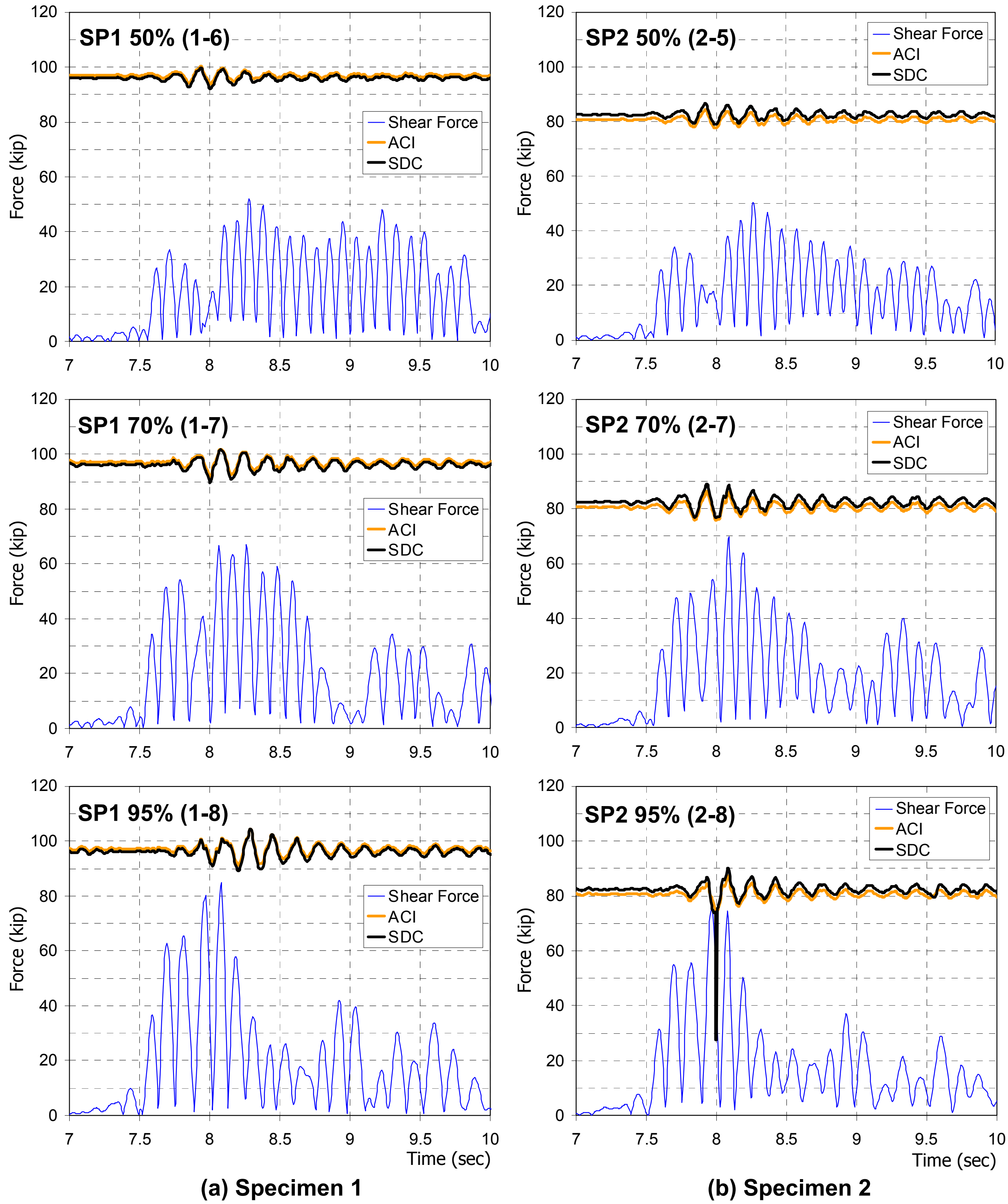

Figure 6.13 Comparison of shear force and shear strength estimation of ACI and SDC based on the data from 50%-, 70%-, and 95%-scale runs.

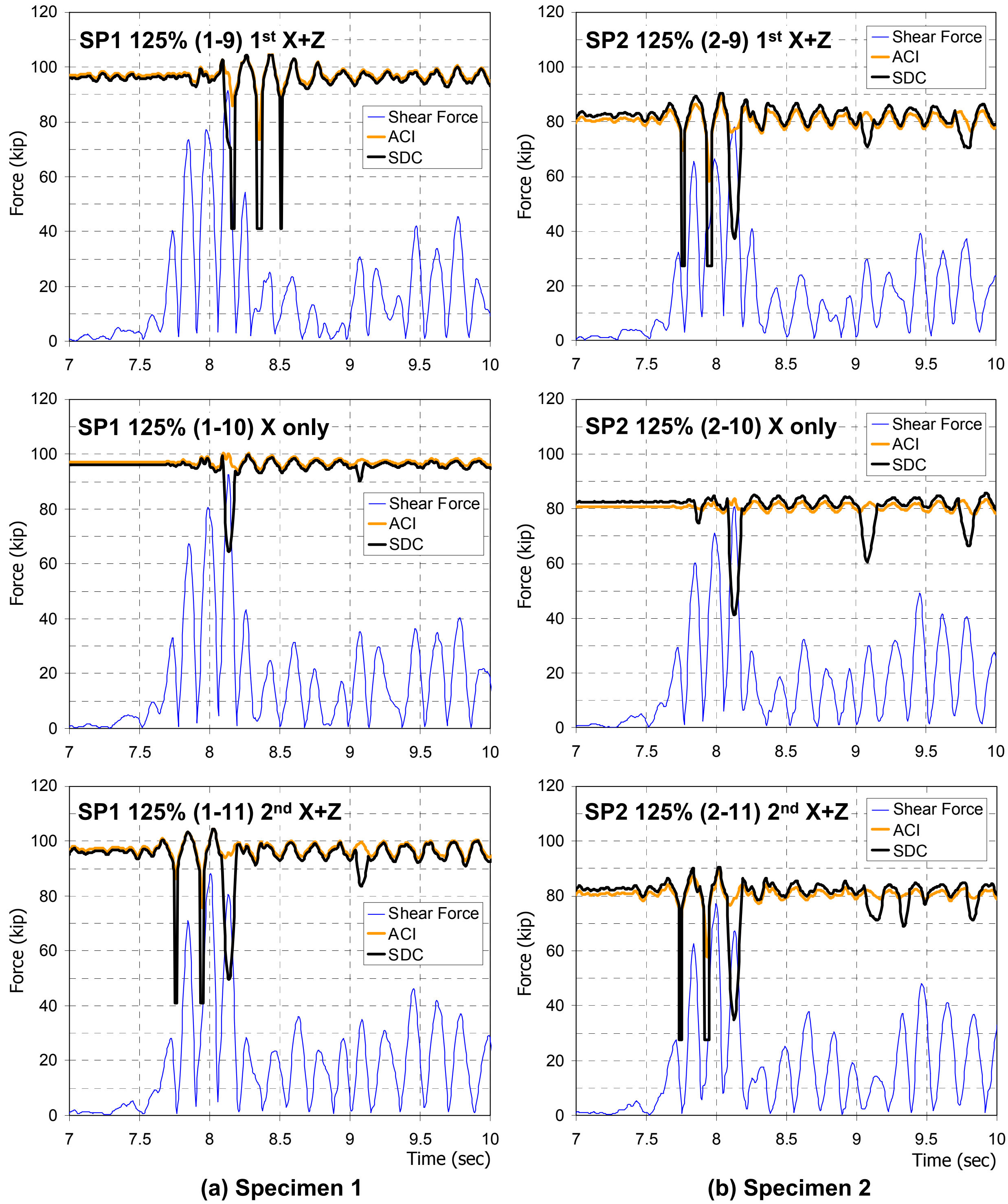

Figure 6.14 Comparison of shear force and shear strength estimation of ACI and SDC based on the data from 125%-scale runs.

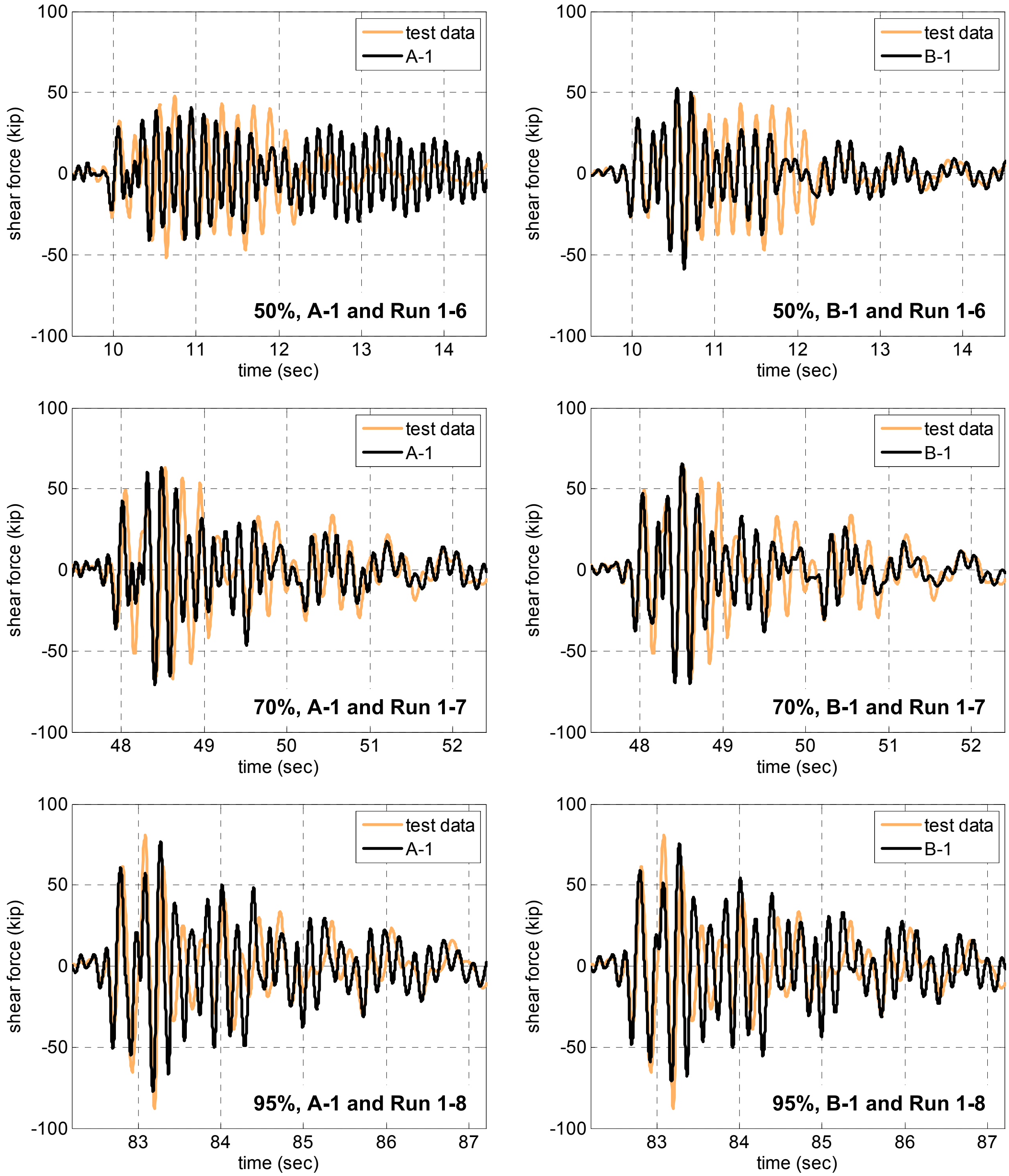

Figure 6.15 Comparison of shear force histories of SP1 subjected to 50%-, 70%-, and 95%-scale motions.

Figure 6.16 compares the shear force histories obtained from the analysis of each model and from the 125%-scale runs of SP1. Figure 6.16(a), (b), and (c) presents comparisons for the '1st X+Z', 'X only', and '2nd X+Z', respectively. Figure 6.16(a) demonstrates that the six models produced similar results. All of them were successful in matching the maximum shear forces at the peaks designated as 1, 2, and 3. At the third peak (indicated as '3'), which corresponds to the time of maximum shear force in test data, shear force of models A-1 and B-1 were equal to 90.6% and 91.3% of the experimental results, respectively. Models A-2 and B-2 were slightly more successful than models A-1 or B-1 in detecting the maximum because the period was slightly changed due to the presence of the shear spring (which further affects the global responses). However, these differences were not due to the inelastic response (i.e., yielding) in the shear spring. The only remarkable difference regarding the inelastic response of the shear spring was the peak value of model A-2-SDC for the peak designated '4'. Compared to other models, it had smaller shear force, -54.63 kips, which was close to the test response, -58.4 kips, which was caused by the unique features of the SDC estimation; the fourth shear peak appeared after tension (8.175 sec in Figure 6.14 and 120.33 sec in Figure 6.17). Therefore, the shear strength was reduced to only the contribution of the transverse steel reinforcement (hoops) at that time and was kept at this value afterwards. However, this tension did not result in yielding of the ACI shear spring because the shear demand was still smaller than the strength calculated in the spring, and the tension was smaller than the specified limit. Note that the tension limit in the analysis is set to be close to the maximum tension, see discussion in Section 6.2.2. As a result, the two code springs provided different shear force values at the fourth peak at 120.4 sec, as shown in Figure 6.16(a).

In contrast to the successful prediction of the shear force at the fourth shear peak by model A-2-SDC, model B-2-SDC did not capture the fourth peak. The reason for this difference can be better understood by comparing the spring responses in Figure 6.17 for Models A-2-SDC and B-2-SDC. Figure 6.17(a) presents the axial force applied to the shear spring, whereas Figure 6.17(b) and (c) plot the deformation and shear force histories recorded at the SDC springs. Dashed vertical lines indicate the start and end points of the axial tension interval. Some observations regarding these figures are as follows:

- The two SDC springs had different deformation and force histories after the first tension.
- Significant deformation began at different times, corresponding to the first tension for A-2-SDC and the second tension for B-2-SDC, suggesting that the two springs yielded at different times.
- The two models had the same axial force histories [Figure 6.17(a) and (d)] but the shear force during the first tension was not the same [Figure 6.17(e)]. Model A-2-SDC had a slightly larger force, exceeding the code-based strength under tension. However, the force in model B-2-SDC was slightly under the limit, V_y, which is equal to V_s due to tension. Therefore, yielding took place in model A-2-SDC, but not in model B-2-SDC. This demonstrates the dependence of the analytical model

prediction on slight changes, and the corresponding difficulties that can arise during the prediction of the observed response with analytical modeling.

The different yielding patterns of the springs in the two models are evident in the hysteresis plots [e.g., Figure 6.18(a-2) versus Figure 6.19(a-2)], where the horizontal axis represents the deformation of the spring. The shear spring in model B-2-SDC model yielded at the time corresponding to the second tension and the shear strength decreased by the SDC code equation.

Figure 6.16(b) shows the shear responses under the 125%-scale ‘X only’ motion. As the previous run, the responses of models A-1 and B-1 are still comparable to the test data, with peak shear force estimations equal to 93.3% and 91.3% of the test response, respectively. The shear springs in the two SDC models (A-2-SDC and B-2-SDC) have 35.8% or less lower shear peaks compared to the other models because of the yield shear force consisting of only the transverse steel reinforcement (hoops) contribution. Another noticeable observation is the decreased peaks of the ACI models. As shown in Figure 6.18(b-1) and Figure 6.19(b-1), yielding takes place in the shear springs of the two ACI models. However, except for the third and fourth peaks, the shear force histories remain similar to those of models A-1 and B-1 since the shear strength of the ACI spring is larger than that of the SDC spring. Finally, Figure 6.16(c) presents the shear responses under the 125%-scale ‘2^{nd} X+Z’ motion. The shear force obtained from models A-1 and B-1 are equal to 98.7% and 101.7% of the maximum test response at the third peak. In general, the analysis results are comparable to the test data for this run.

The differences in analytical compared to the experimental response ratios under repeated runs for the 125%-scale is interesting. The ratio of the shear force obtained from the analytical models to the shear force obtained from test results at the third shear peak, denoted as ‘Response ratio’ in the Y-axis, is presented in Figure 6.20 for the 125%-scale runs. The analytical models without the shear spring (models A-1 and B-1) tend to improve their predictions with repeated runs. Predictions of the models with the shear springs are comparatively less successful for the ‘X only’ run. Considering that the goal of incorporating the shear springs is to capture accurately the effect of the axial force on the shear strength, it can be concluded that the ACI shear spring is successful in achieving this goal for models A and B. Successful prediction of the shear strength for the ‘2^{nd} X+Z’ motion, which is the strength reduced due to degradation of concrete contribution, leads to this conclusion. Although the predictions for models A-1 and B-1 for this motion are more accurate, the slight conservativeness of the code spring is desirable. This is observed more clearly for SP2.

Another important observation is that models A-1 and B-1 are deficient in reflecting the shear degradation even though they are good in predicting the peak values under the ‘2^{nd} X+Z’. The peaks under the ‘1^{st} X+Z’ and ‘2^{nd} X+Z’ did not significantly change (A-1: 84.82→84.10 kips, B-1: 85.47→86.71 kips), but these peaks decreased more in the tests. This explains why A-1 and B-1 become better in their predictions under the ‘2^{nd} X+Z’. If the model provided a better prediction under ‘1^{st} X+Z’, its overestimation under the last motion, i.e., the ‘2^{nd} X+Z’, could be significant. In addition, the increase in ratio from ‘X only’ to ‘2^{nd} X+Z’ is bigger than that from ‘1^{st} X+Z’ to ‘X only’, shown clearly in Figure 6.20. This observation implies that the models without the shear springs do not accurately take into account the damage of the column due to vertical excitation. As discussed later, this is observed more clearly for SP2. This increase of the ratio between the model prediction and the experimental finding is not the case for the A-2-ACI and B-2-ACI and clearly not the case for A-2-SDC and B-2-SDC, where the SDC spring is more sensitive to the damage accumulation than the ACI spring.

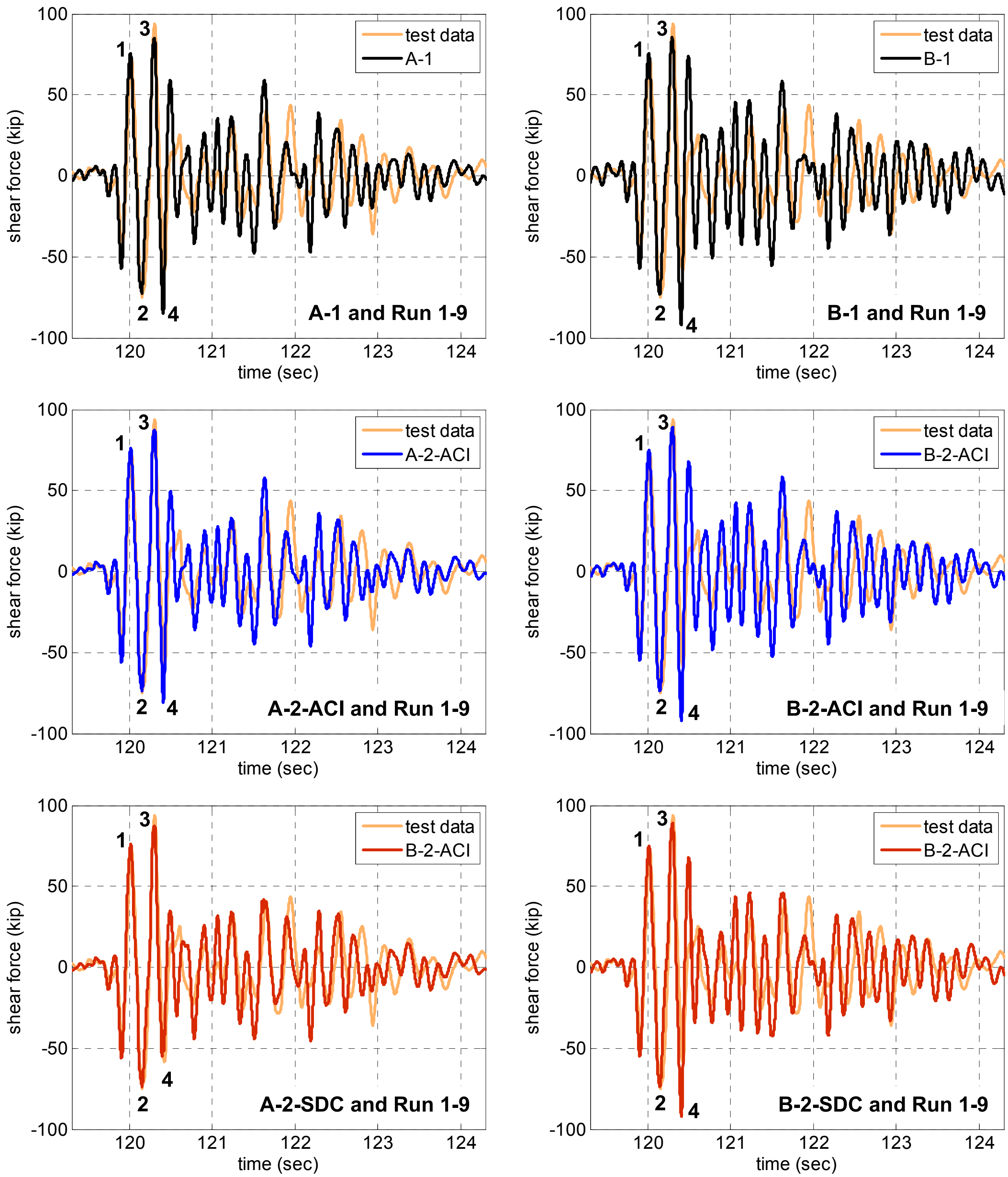

(a) 125% 1st X+Z

Figure 6.16 Comparison of shear force histories of SP1 subjected to 125%-scale motions.

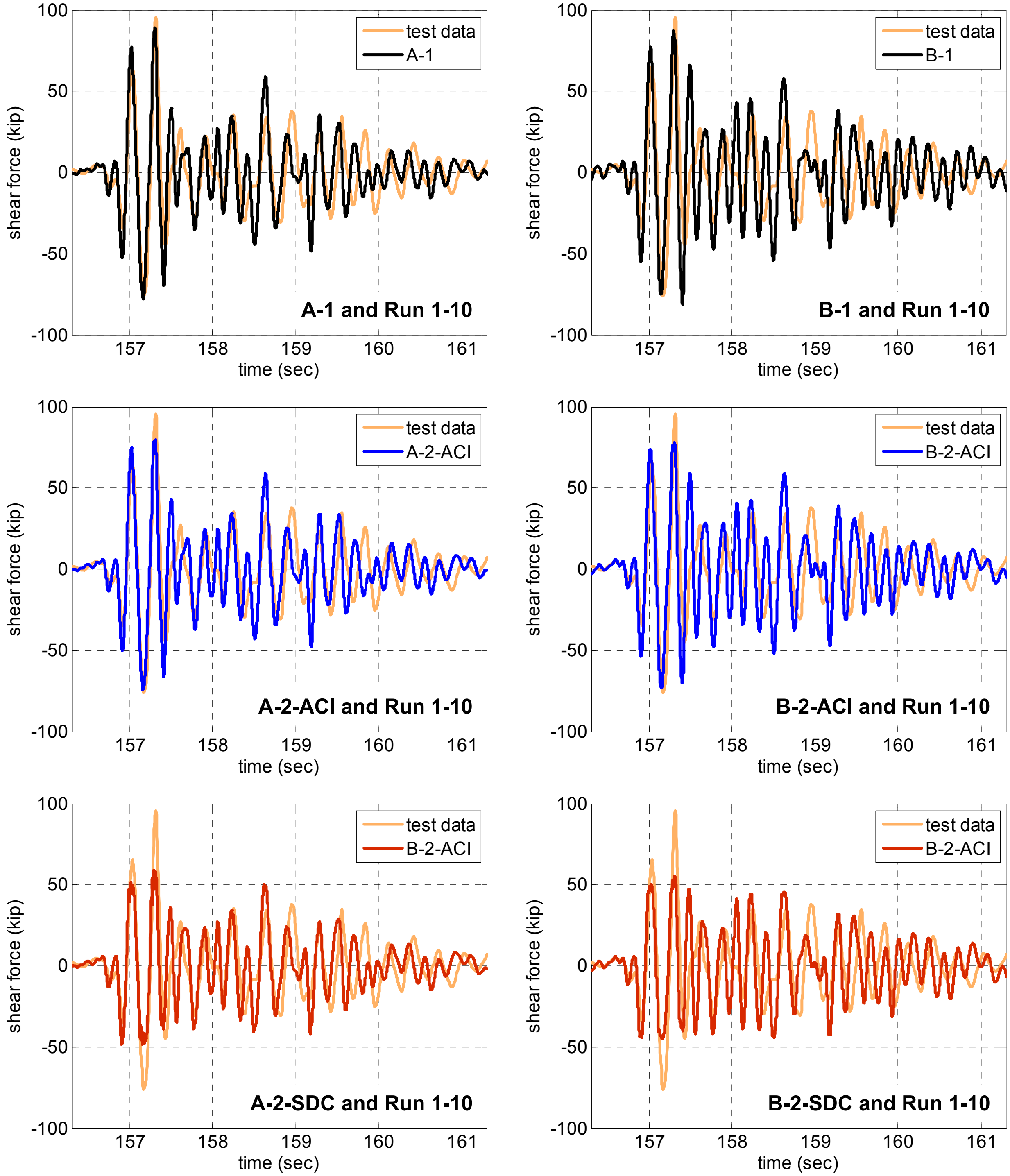

(b) 125% X only

Figure 6.16 Continued.

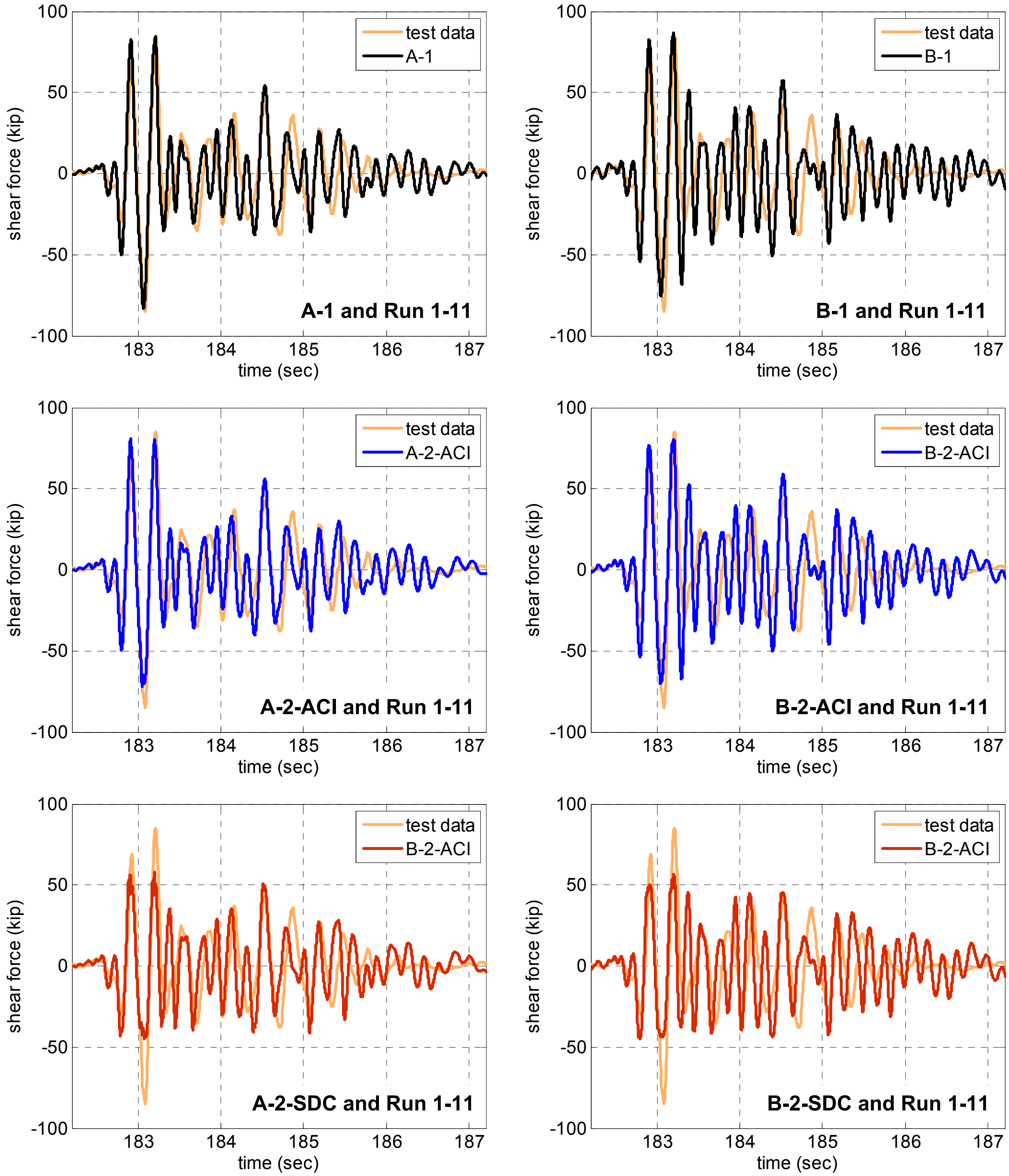

(c) 125% 2nd X+Z

Figure 6.16 Continued.

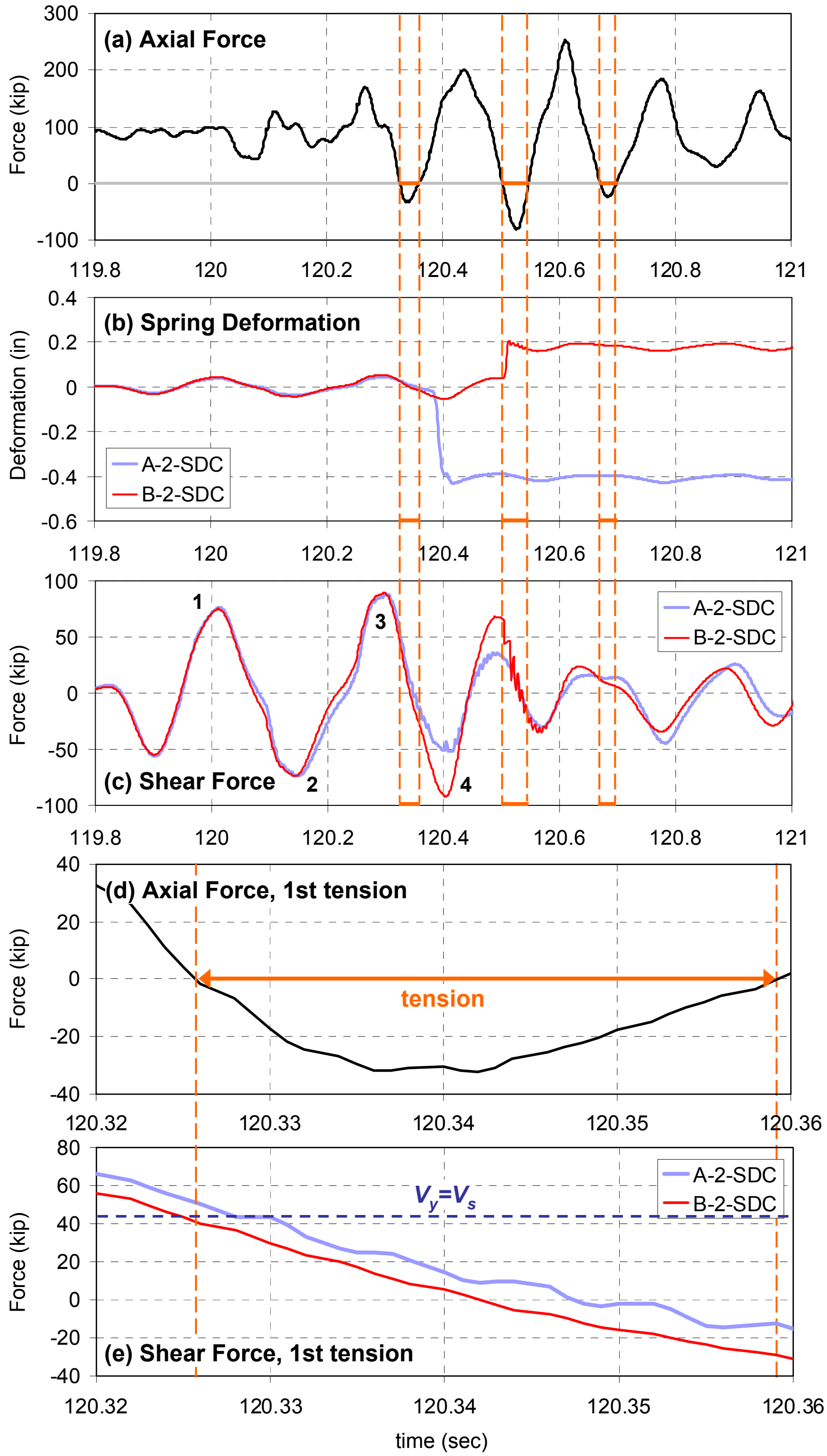

Figure 6.17 **Comparison of the shear spring responses of SP1 A-2-SDC and B-2-SDC models subjected to 125%-scale '1st X+Z' motion.**

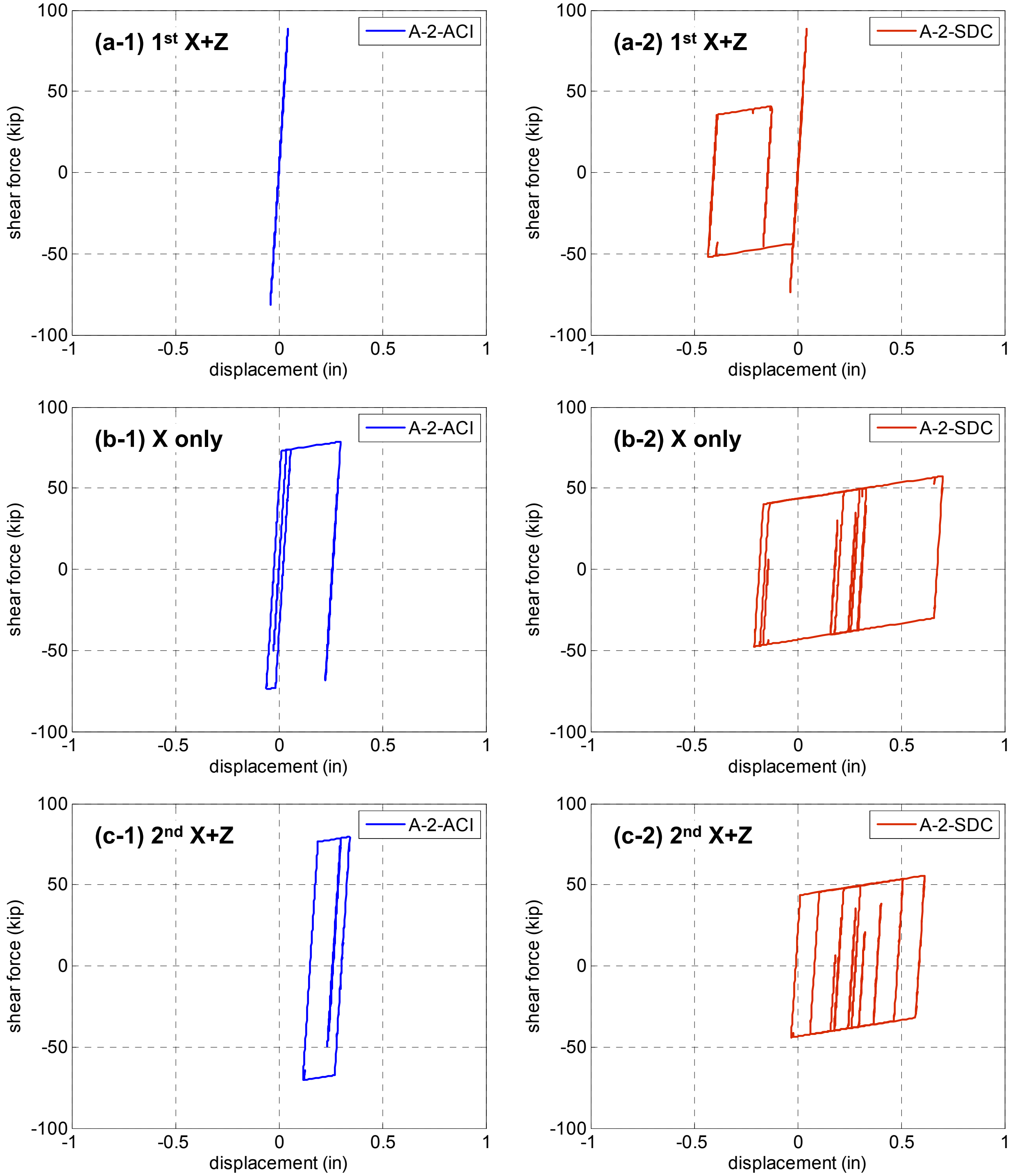

Figure 6.18 Shear spring hysteresis of SP1 A-2 models subjected to 125%-scale motions.

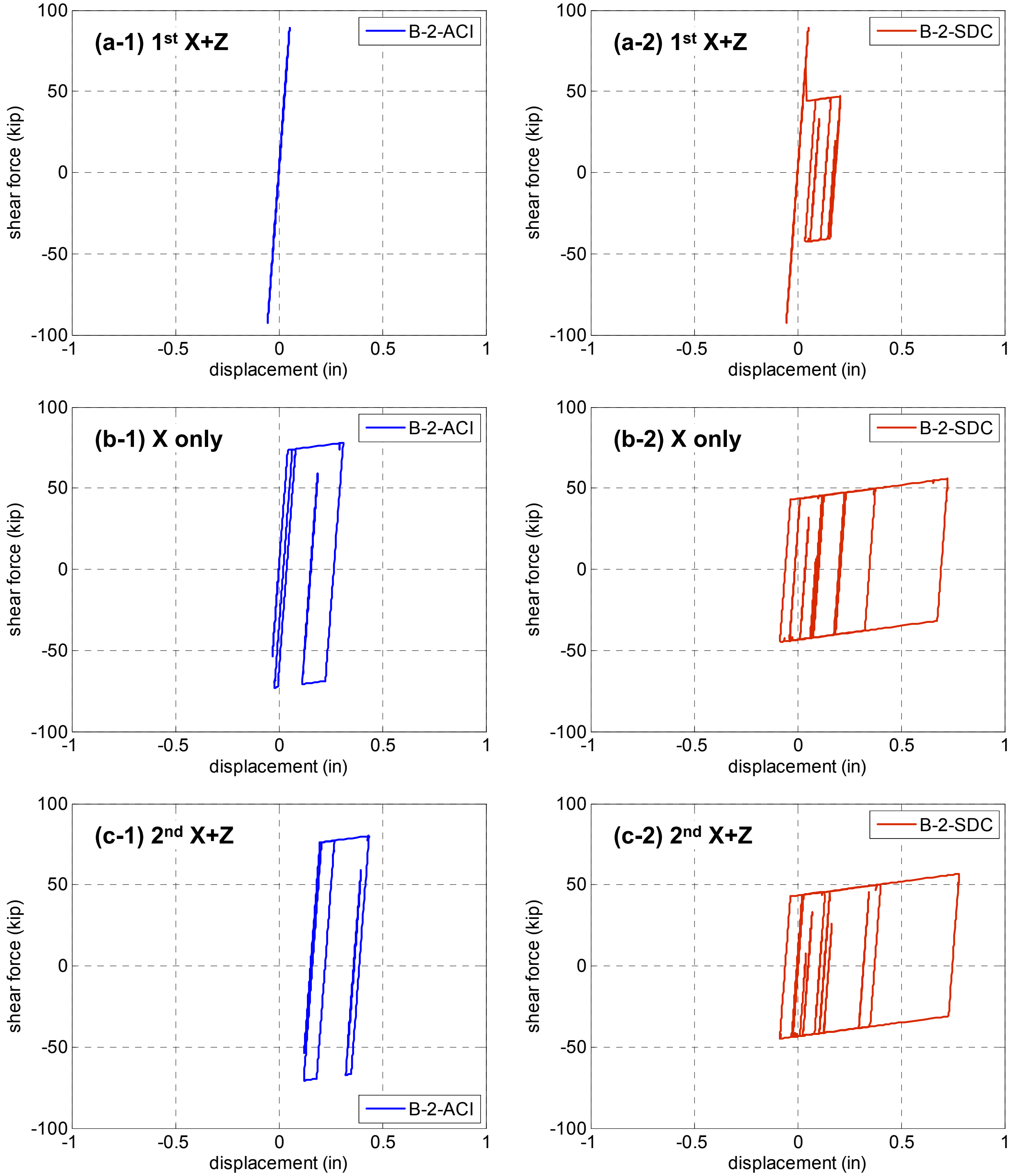

Figure 6.19 Shear spring hysteresis of SP1 B-2 models subjected to 125%-scale motions.

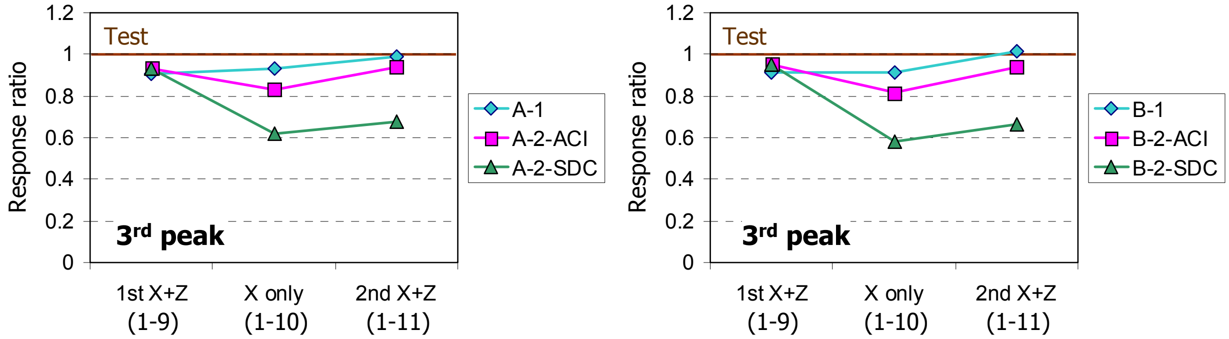

Figure 6.20 Comparison of the third peak ratios obtained from SP1 A and B models to the test data under the 125%-scale motions.

Similar to the previous discussion related to SP1, the shear force responses under 50% to 125%-scale motions are presented in the following figures for SP2. Figure 6.21 compares the responses from models A-1 and B-1 to SP2 test data under 50%, 70%, and 95%-scale motions. Although models A-1 and B-1 provided different shear responses, they are comparable to the test data with varying degrees of matching at different points in time. Figure 6.22 (a), (b), and (c) presented the results under 125%-scale '1st X+Z', 'X only,' and '2nd X+Z' motions, respectively. Similar to SP1 results, the maximum value of the test data is observed at the third peak for all runs. Both models A-2 and B-2 models had smaller values than the test data at this peak in every run, which is basically dictated by the value of the shear strength and the time when it takes place. In case of SP1, the shear strength (yield shear, V_y) of the ACI spring was determined by the tension peak that occurred after the main shear peaks under the '1st X+Z' ground motion. Because of the predefined tension limit, the yielding took place later as it was caused by the demand under the 'X only' motion. However, for SP2, the shear demand reached V_y of the ACI spring at the instant of the tension peak, which occurred between the first and second shear peaks during the '1st X+Z' motion. As a result, yielding took place during this motion and the remaining shear history was affected by this value of V_y. This observation is also confirmed by an examination of the hysteresis relationships in Figures 6.23 and 6.24, where the yielding initially took place in the '1st X+Z' motion for both models with ACI and SDC springs. In addition, V_y values for both springs in SP2 were smaller than those for the springs of SP1, as shown in Figures 6.18 and 6.19. For SP2, the V_y for the ACI and SDC springs were 54.39 kips and 29.01 kips (compared to 73.0 kips and 43.8 kips for SP1), which decreased by 25.5% and 33.8%, respectively. This reduction is due to the lower contribution provided by steel hoops (V_s) caused by the lower transverse reinforcement ratio.

Figure 6.25 presents the ratios between the computational results and the test data at the third peak. Although similar to those of SP1 (Figure 6.20) in that the results for models A-1 and B-1 are comparable to the test data, they overestimated the shear force response of SP2 subjected to the '2nd X+Z' motion. Model A-1 and B-1 reached 106.3% and 112.5% of the maximum from the test data, respectively. Models with the ACI shear springs (A-2-ACI and B-2-ACI) were deemed successful in predicting the '2nd X+Z' motion in the sense that they captured the shear strength degradation accurately enough [while being on the desirable conservative (underestimation) side]. Conservative estimates of the SDC shear spring for SP2 lacked accuracy as was in the case of SP1. Similar to SP1 models, A-1 and B-1 have a deficiency in reflecting the shear degradation. The peaks of models A-1 and B-1 under the ‘1st X+Z’ and the ‘2nd X+Z’ runs changed as follows: 78.64→81.38 kips (A-1), 84.27→86.13 kips (B-1). In addition, the increase in these response ratios from ‘X only’ run to ‘2nd X+Z’ run was bigger than the previous change from ‘1st X+Z’ run to ‘X only’ run.

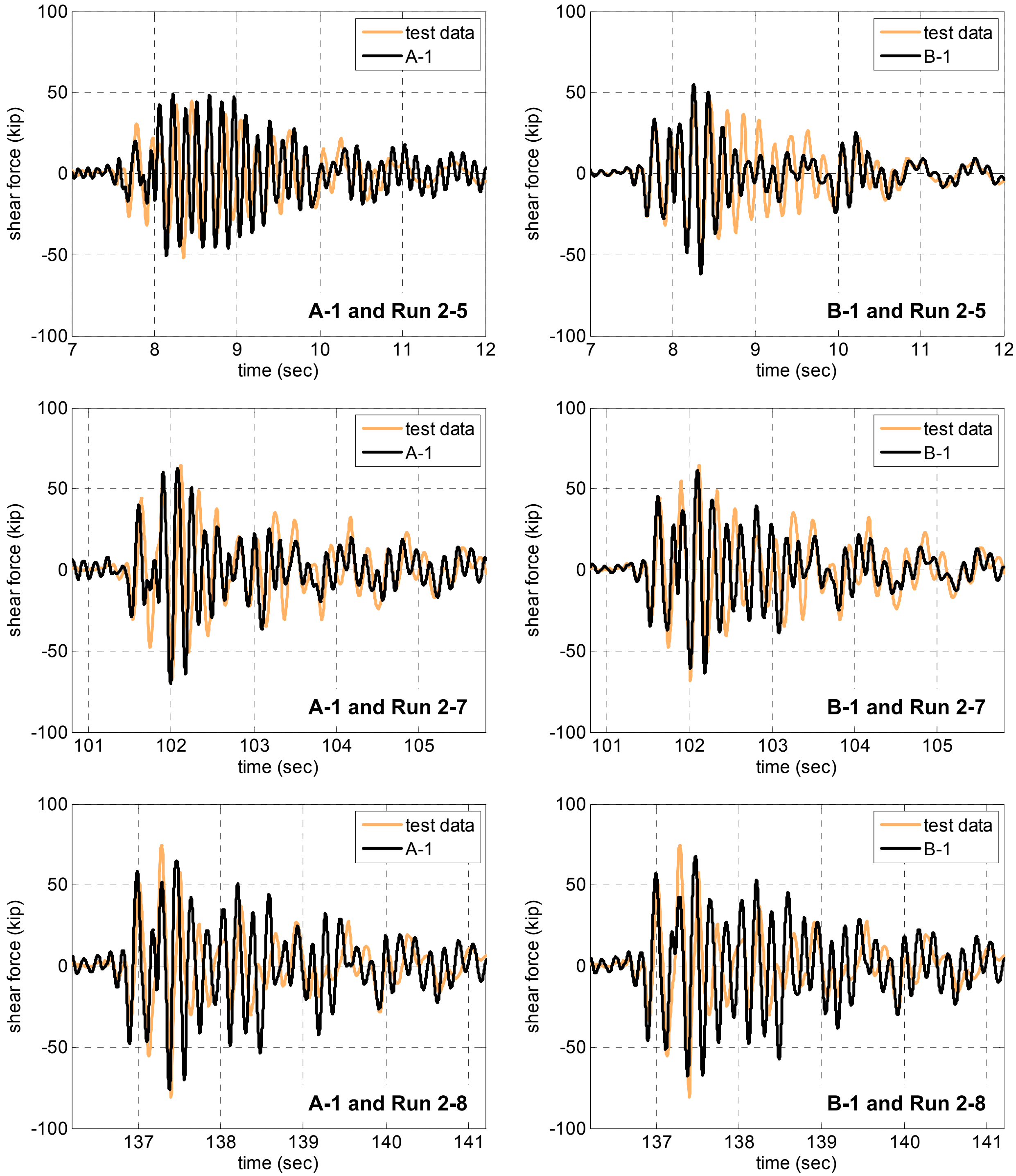

Figure 6.21 **Comparison of shear force histories of SP2 subjected to 50%-, 70%-, and 95%-scale motions.**

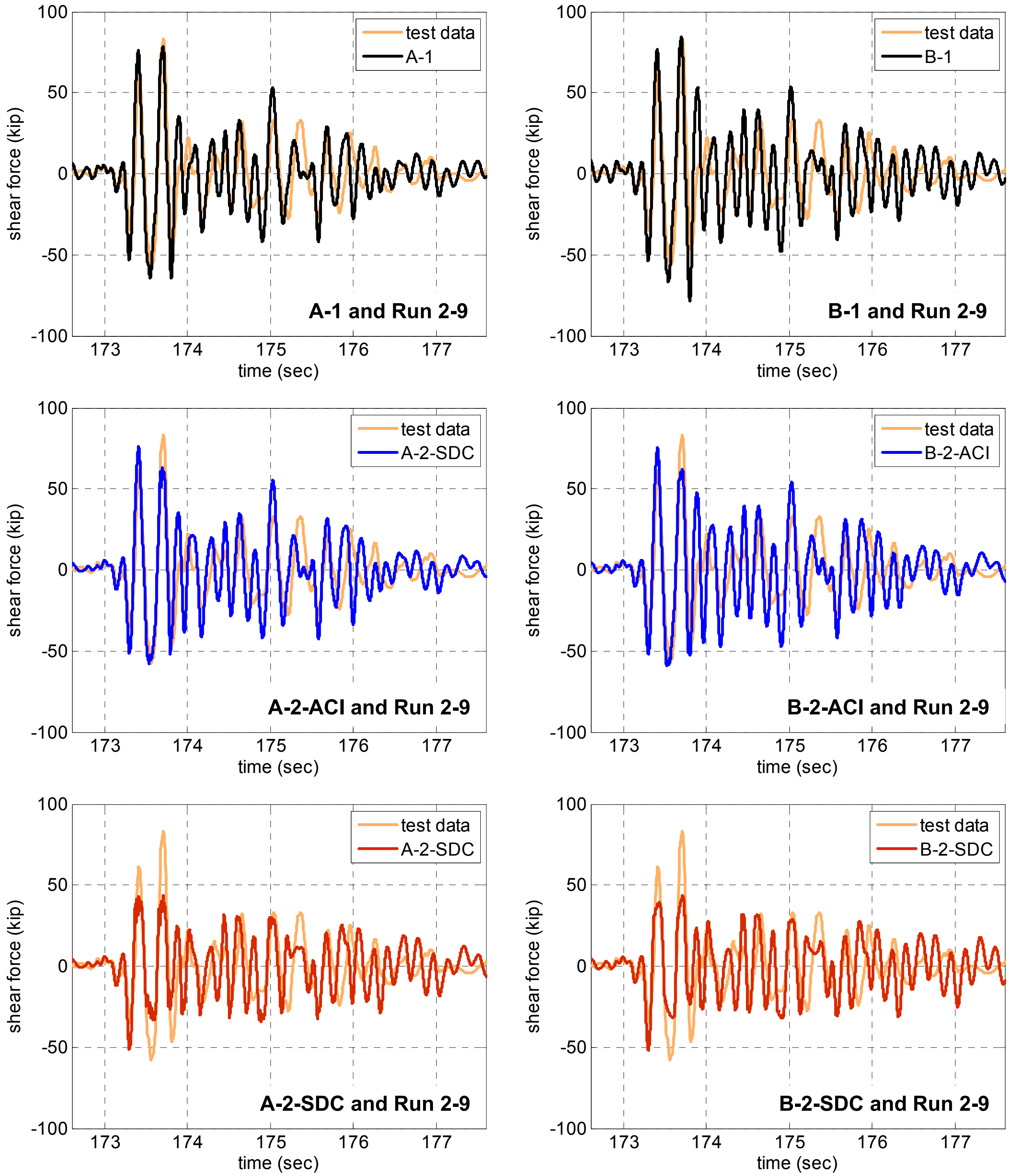

(a) 125% 1st X+Z

Figure 6.22 Comparison of shear force histories of SP2 subjected to 125%-scale motions.

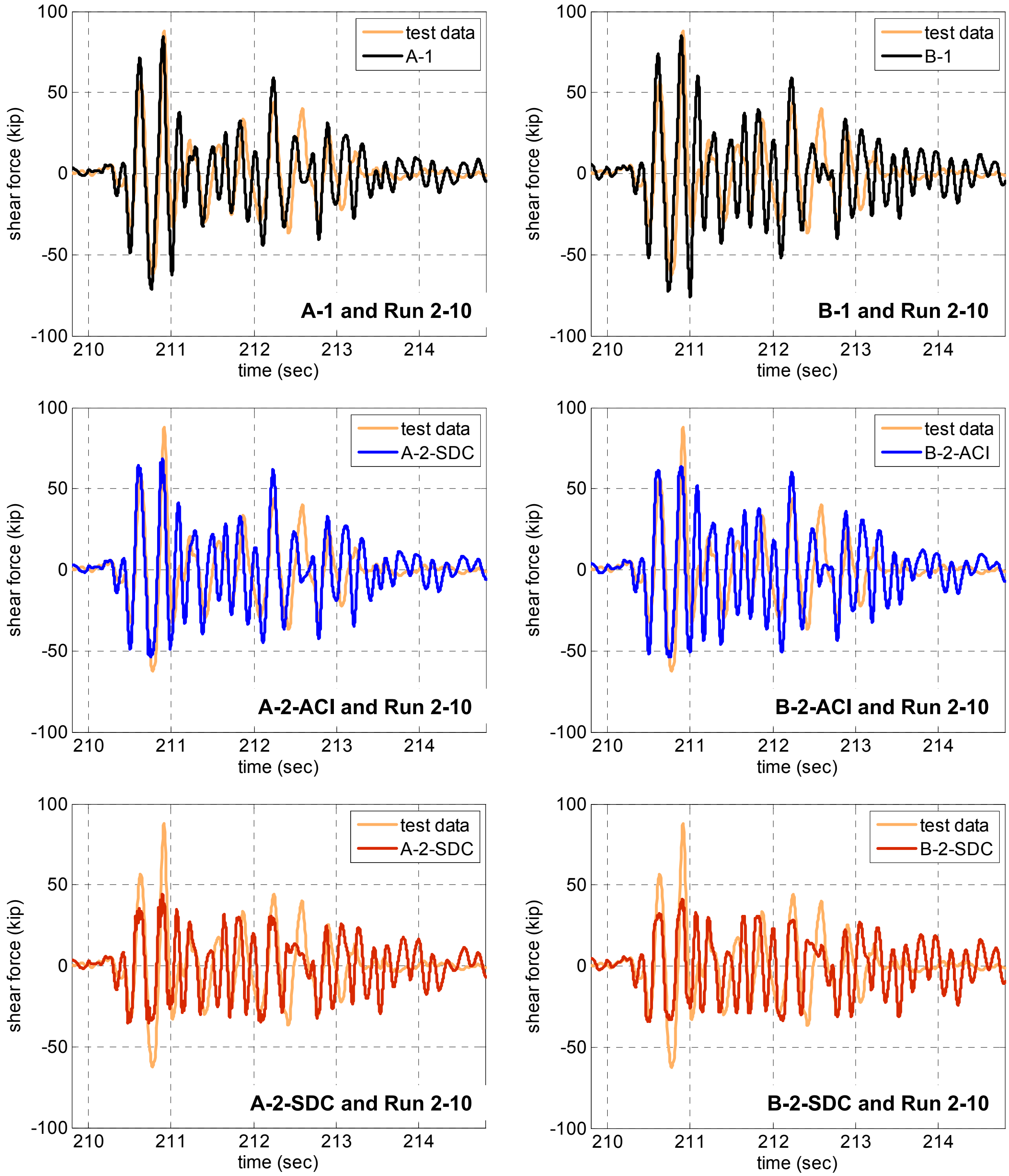

(b) 125% X only

Figure 6.22 Continued.

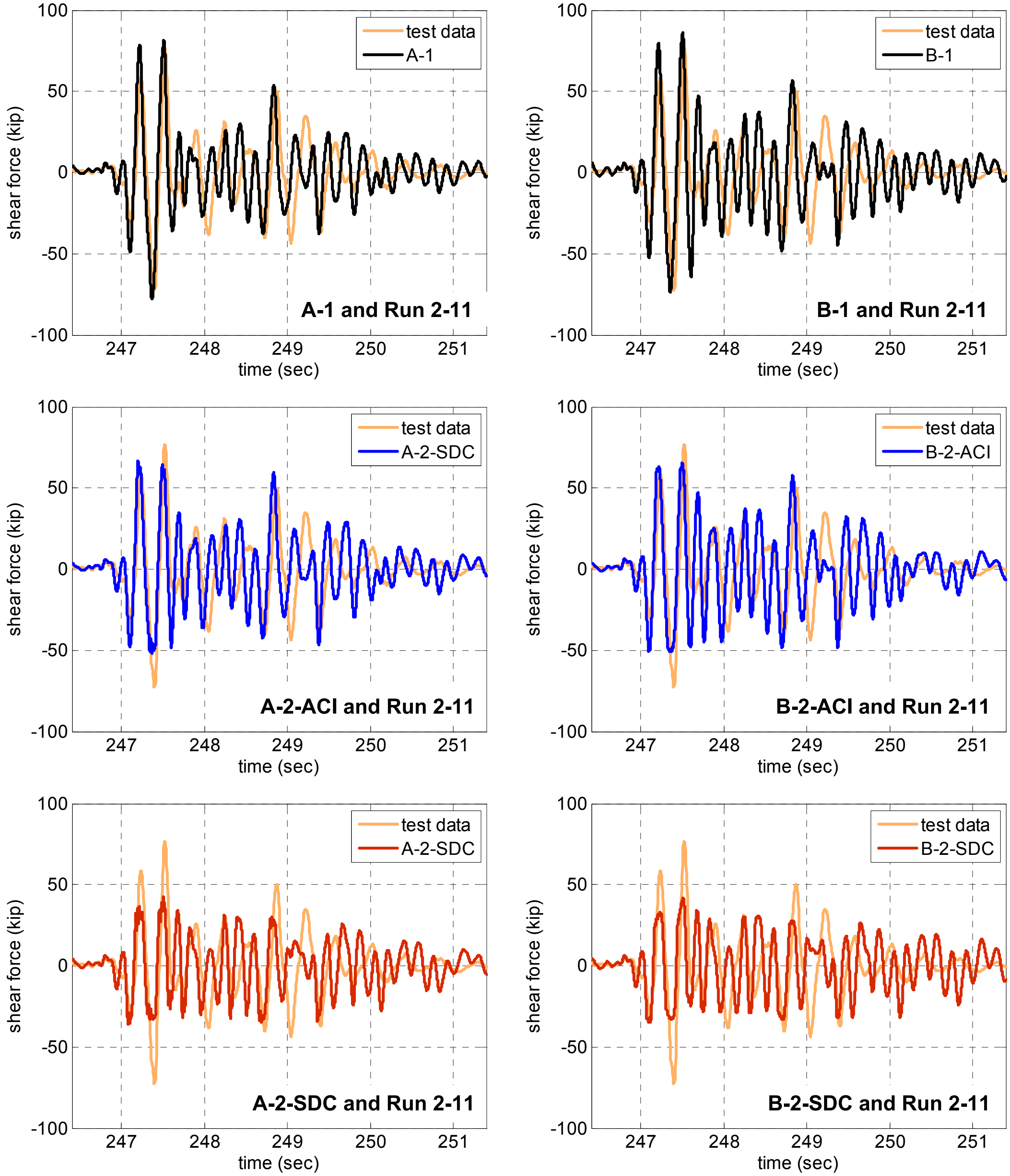

(c) 125% 2nd X+Z

Figure 6.22 Continued.

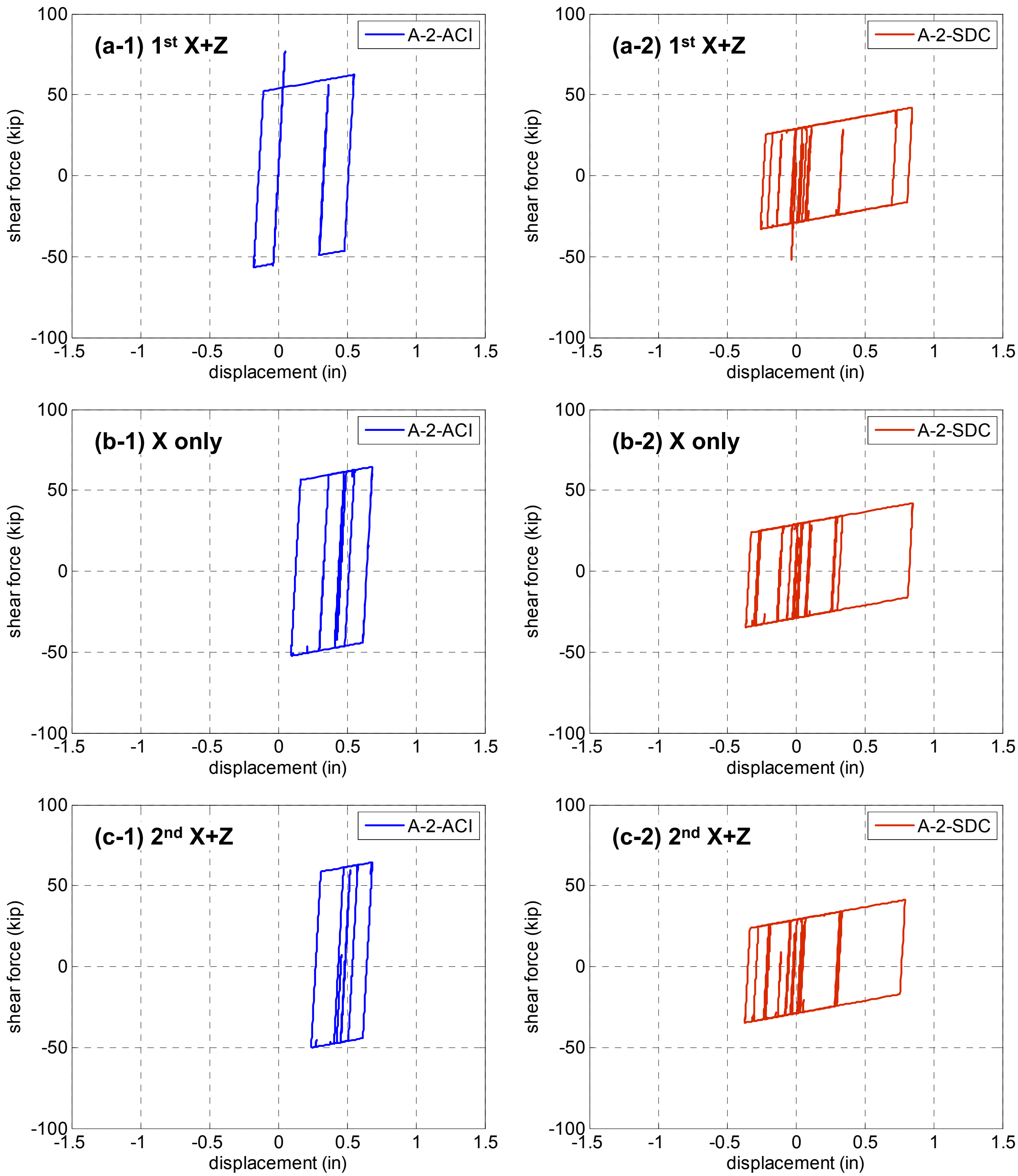

Figure 6.23 Shear spring hysteresis of SP2 A-2 models subjected to 125%-scale motions.

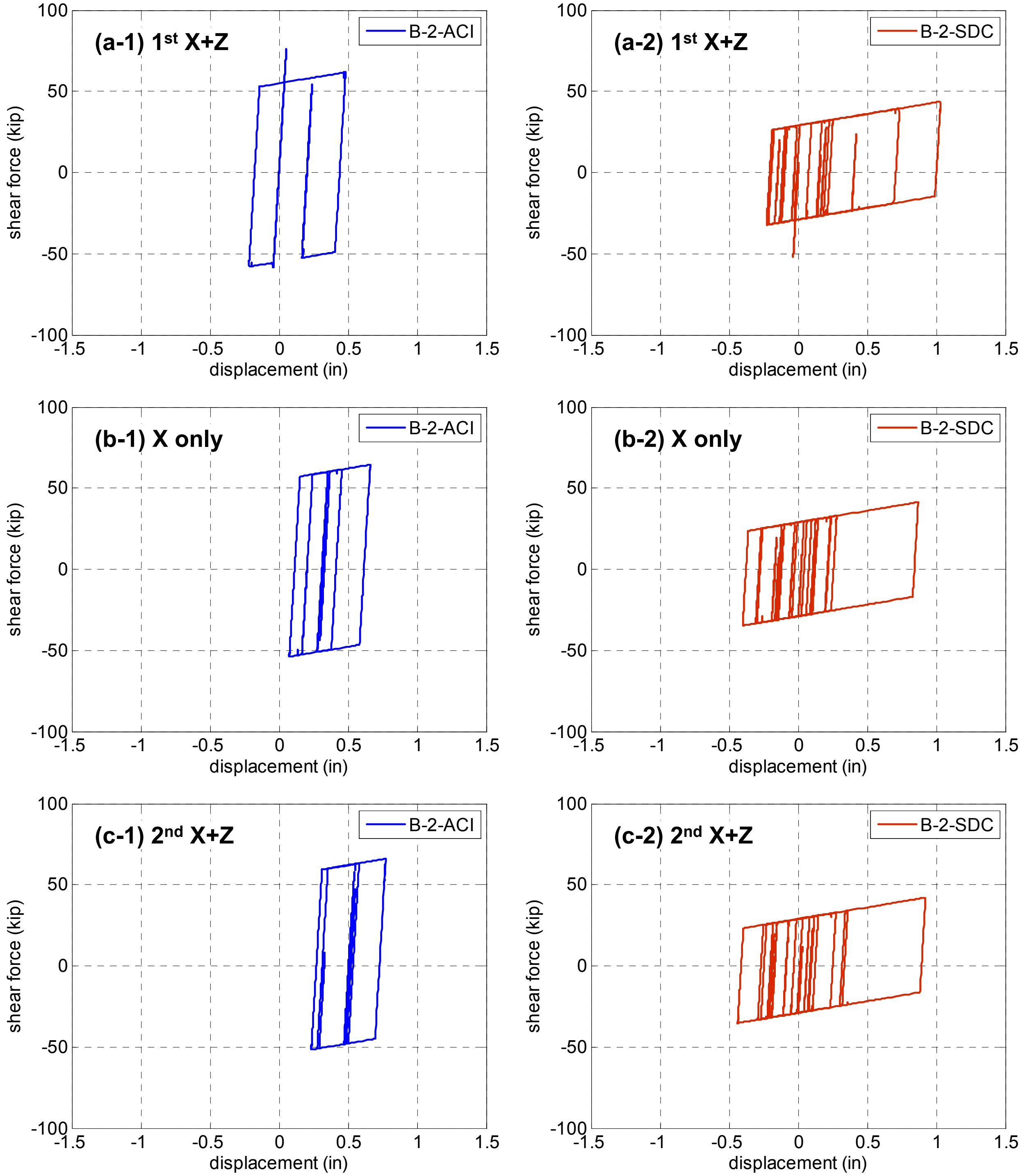

Figure 6.24 Shear spring hysteresis of SP2 B-2 models subjected to 125%-scale motions.

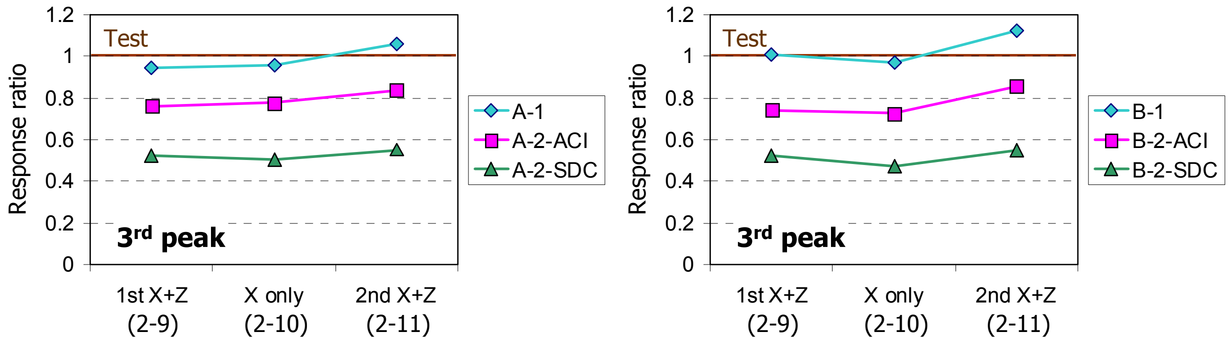

Figure 6.25 Comparison of the third peak ratios obtained from SP2 A and B models to the test data subjected to 125%-scale motions.

6.4.2.2 Bending Moment at the Base

The bending moment at the base of the column is evaluated by examining the time histories and maximum values. Figure 6.26 compares the bending moment histories of SP1 obtained from models A-1 and B-1 with the test data under 50%, 70%, and 95%-scale motions. Models A-1 and B-1 produced similar responses sufficiently close to the test data, except for the presence of high-frequency contents in the analytical results of models A-2 and B-2. The results of Models A-2 and B-2 models are not presented here as their responses were similar to models A-1 and B-1.

Figure 6.27 compares the moment at the base obtained from the analytical models with the test results for the 125%-scale motions. Under the '1st X+Z' motion, all six models provided very similar results. The fourth peak, indicated as '4', had the maximum base moment in all cases. Test results are well matched by the analytical models in this case. The only observed discrepancy is that the frequency of the base moment time history caused by the top mass rotation after 122 sec is not well captured. Considering the fact that these periods are matched under the lower-intensity level motions, it can be concluded that the periods of each model are not elongated to the same extent. This observation is valid for the following two 125%-scale runs, as shown in Figure 6.27(b) and (c). Similar to the shear force time histories, the ACI and SDC springs decreased the amplitude of the main peaks under 'X only' motion, which is remarkable especially at the fourth peak. Note that the fourth peak of the base moment coincided with the third peak of the shear force.

Figures 6.28 and 6.29 present are the base moment responses of SP2. Similar to the shear force, the ACI spring affected the amplitude of the peaks from the 125%-scale 'X only' motion, but the SDC spring initially yields under '1st X+Z' motion. Both models had smaller peaks than those for SP1, which is due to wider hoop spacing, i.e., lower V_y. In addition, SP2 had a greater change in the frequency after the main excitation than SP1 did, which is expected because SP2 was more damaged than SP1 even before the 125%-scale runs.

Figure 6.30 presents the ratio between the maximum bending moment values from the computational models and the test data under 125%-scale motions at the fourth peak, which corresponds to the maximum of the test data. Models A-1 and B-1 overestimated the base moment responses in most of the cases, with the overestimation being larger for the runs with vertical excitation compared to the ‘X only’ case. Similar to the case of maximum shear values, models A-2 and B-2 with the shear springs were successful in reducing these ratios, with accurate estimations of ACI spring model while the SDC spring, produced inaccurate, overly conservative results.

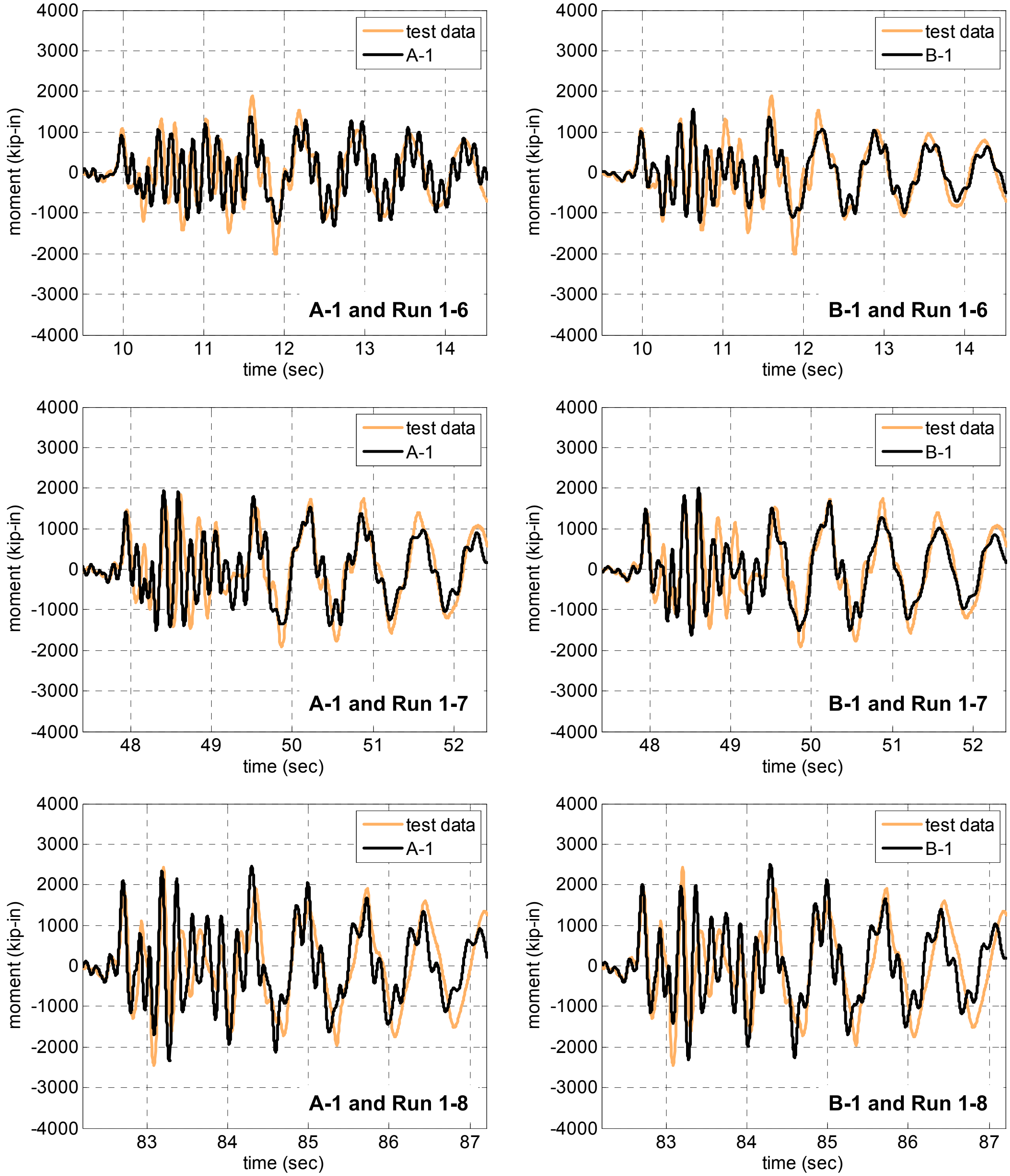

Figure 6.26 Comparison of bending moment histories at the base of SP1 subjected to 50%-, 70%-, and 95%-scale motions.

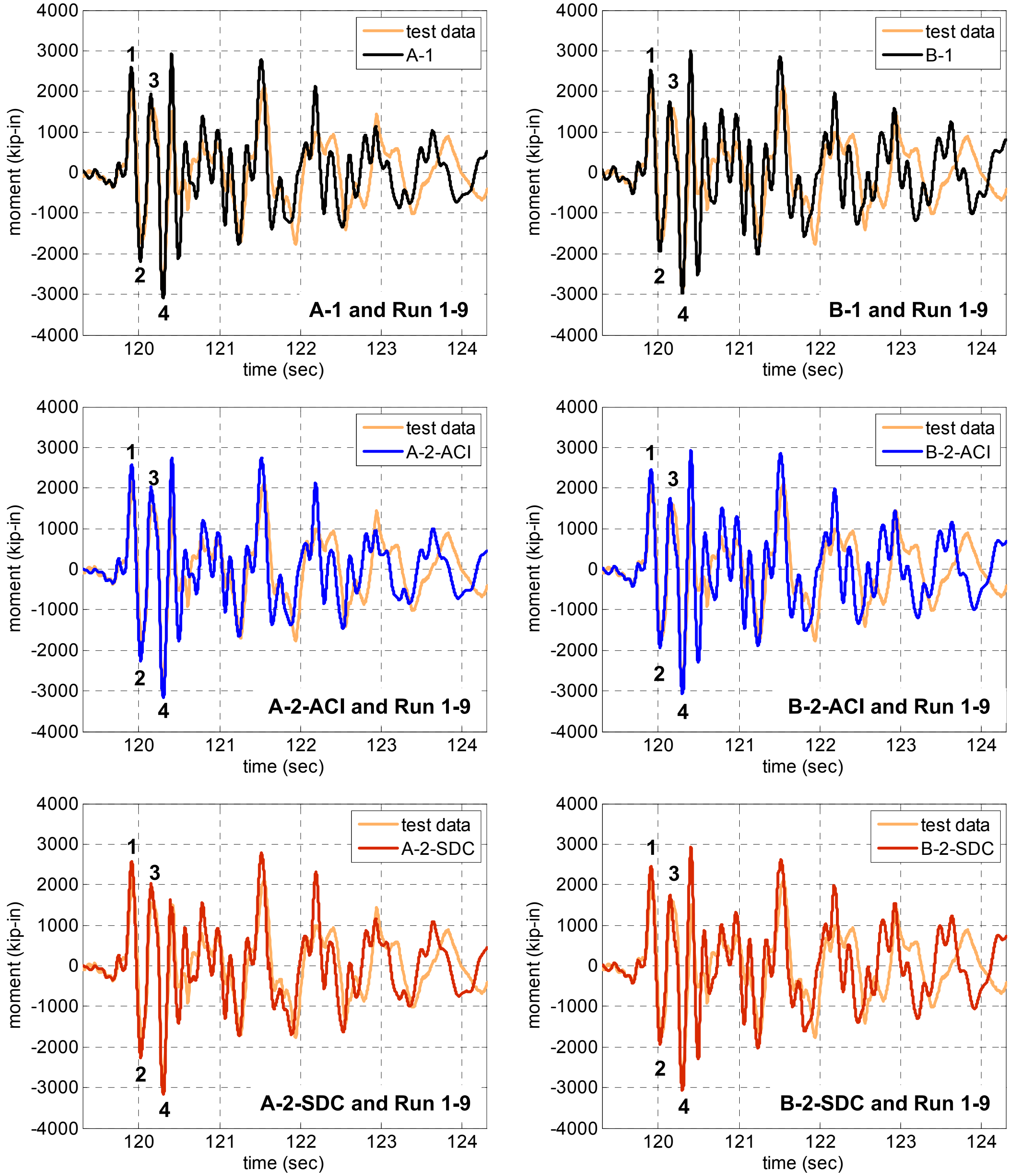

(a) 125% 1st X+Z

Figure 6.27 **Comparison of bending moment histories at the base of SP1 subjected to 125%-scale motions.**

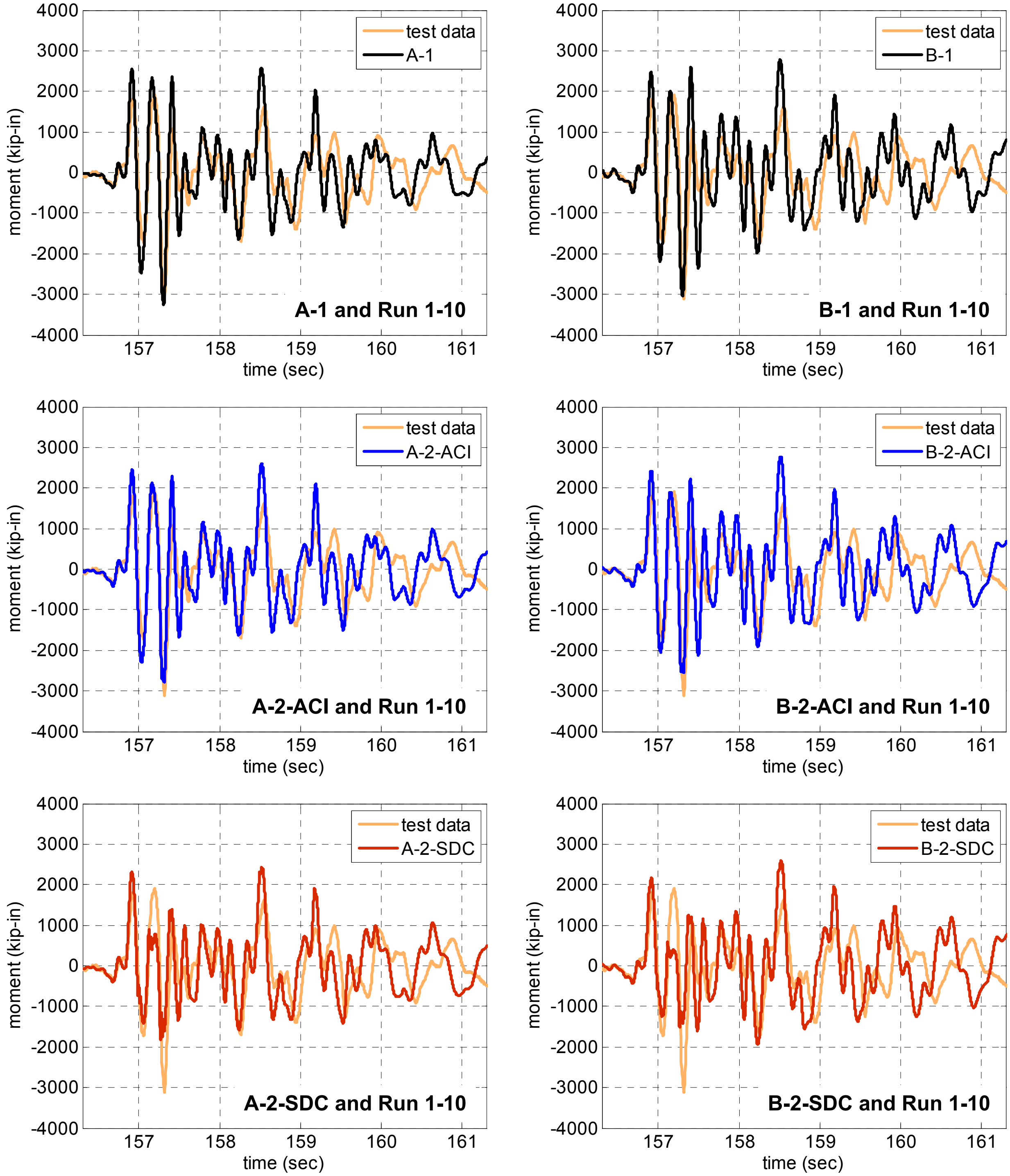

(b) 125% X only

Figure 6.27 Continued.

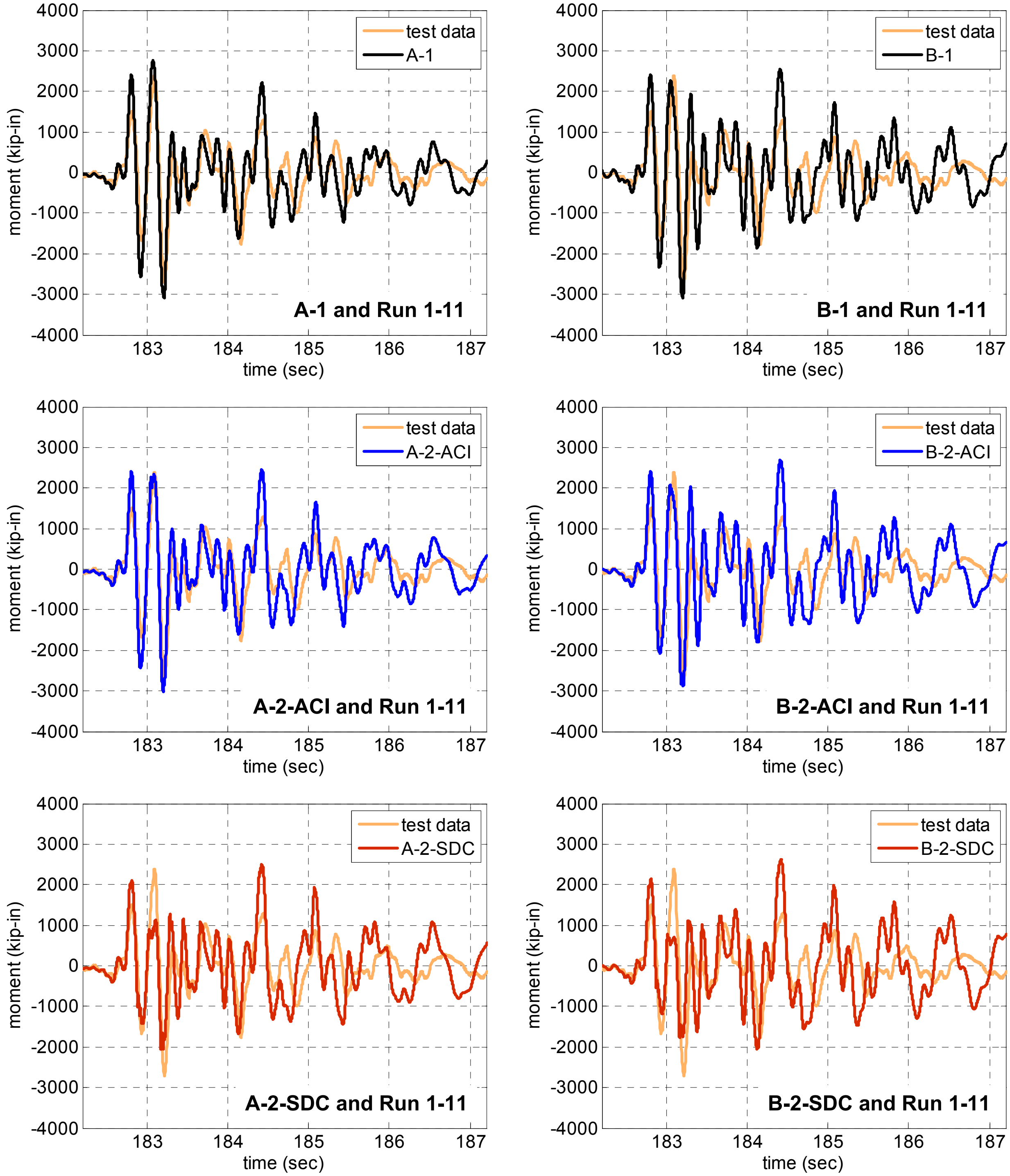

(c) 125% 2nd X+Z

Figure 6.27 Continued.

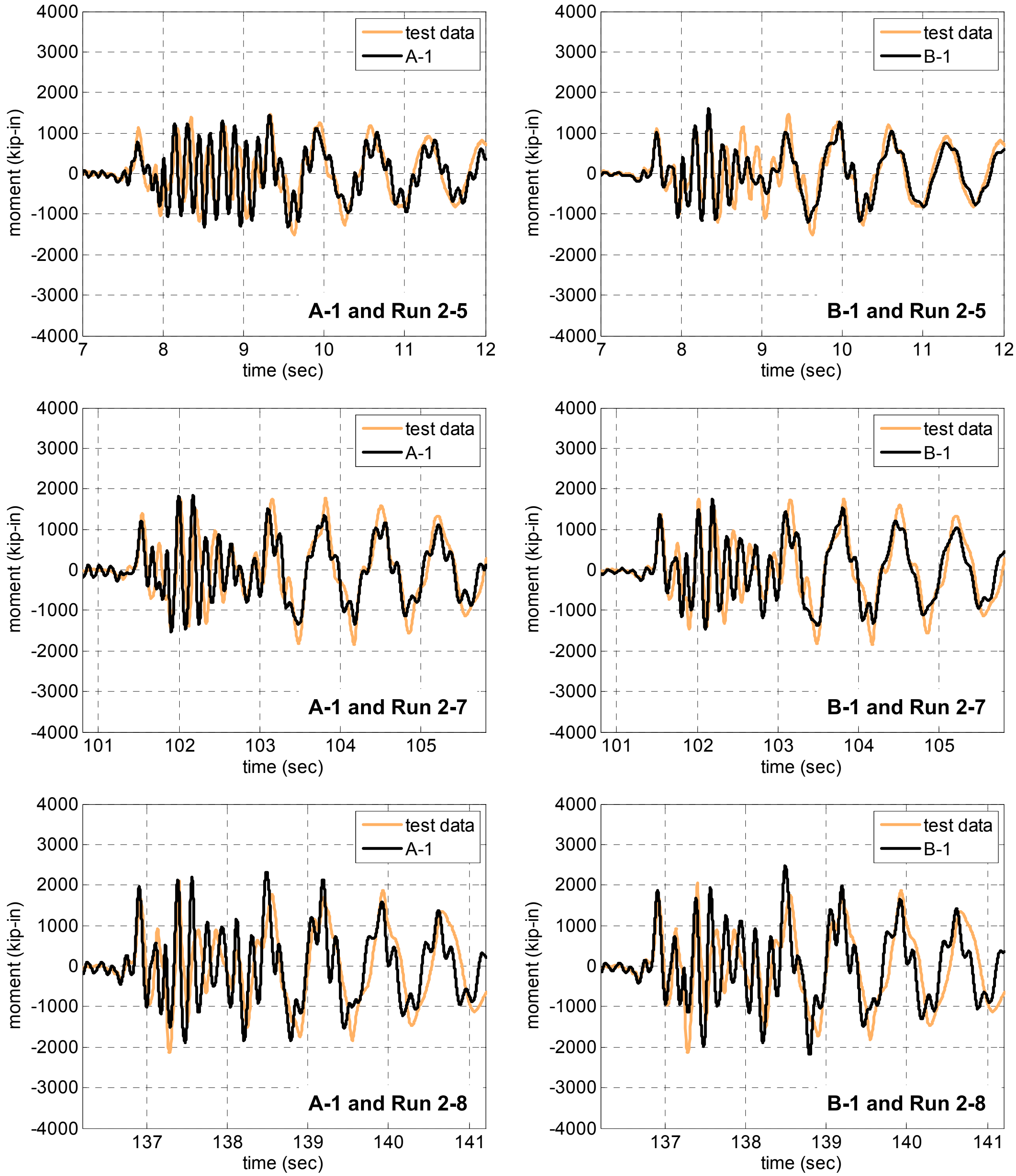

Figure 6.28 Comparison of bending moment histories at the base of SP2 subjected to 50%-, 70%-, and 95%-scale motions.

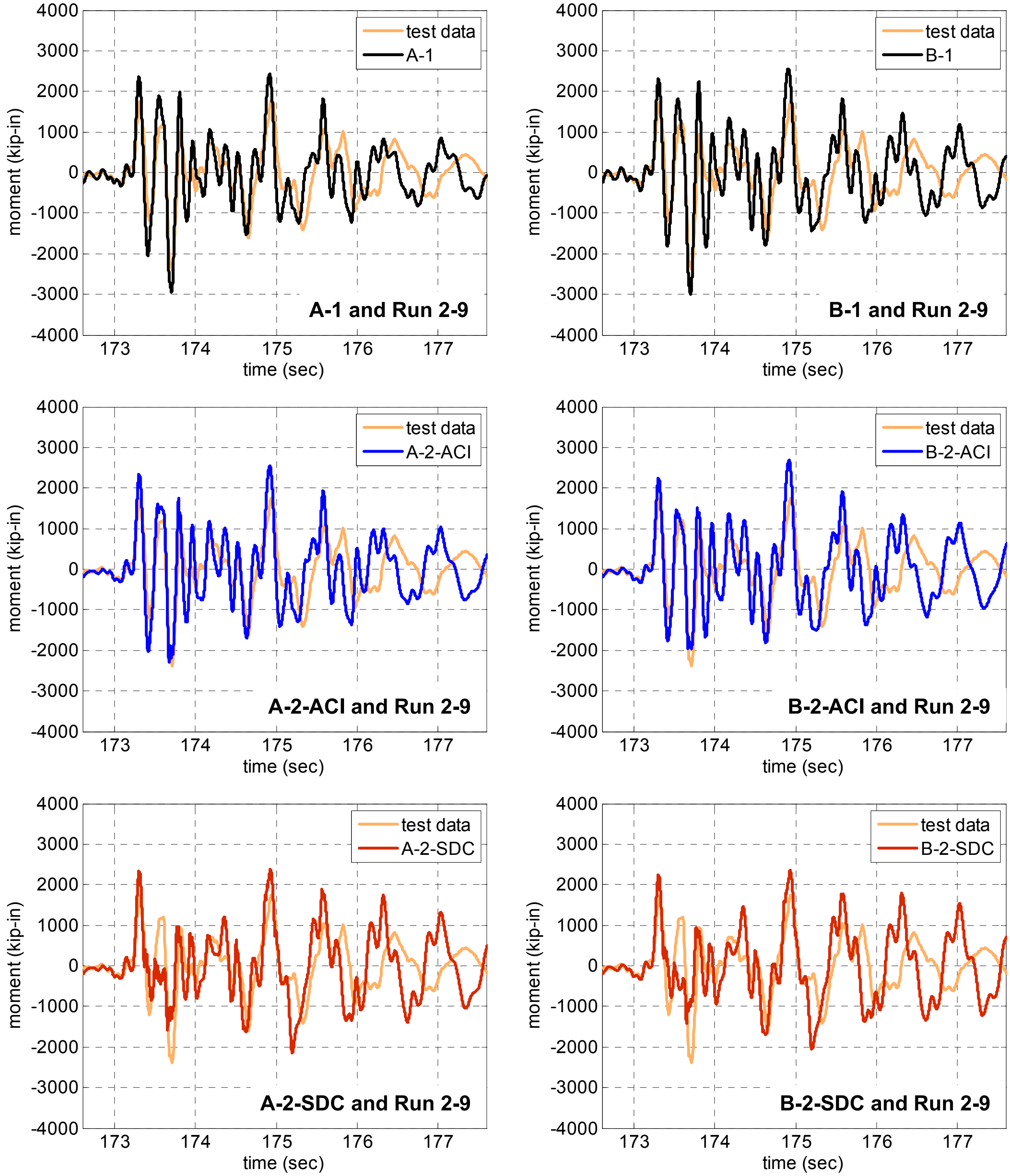

(a) 125% 1st X+Z

Figure 6.29 **Comparison of bending moment histories at the base of SP2 subjected to 125%-scale motions.**

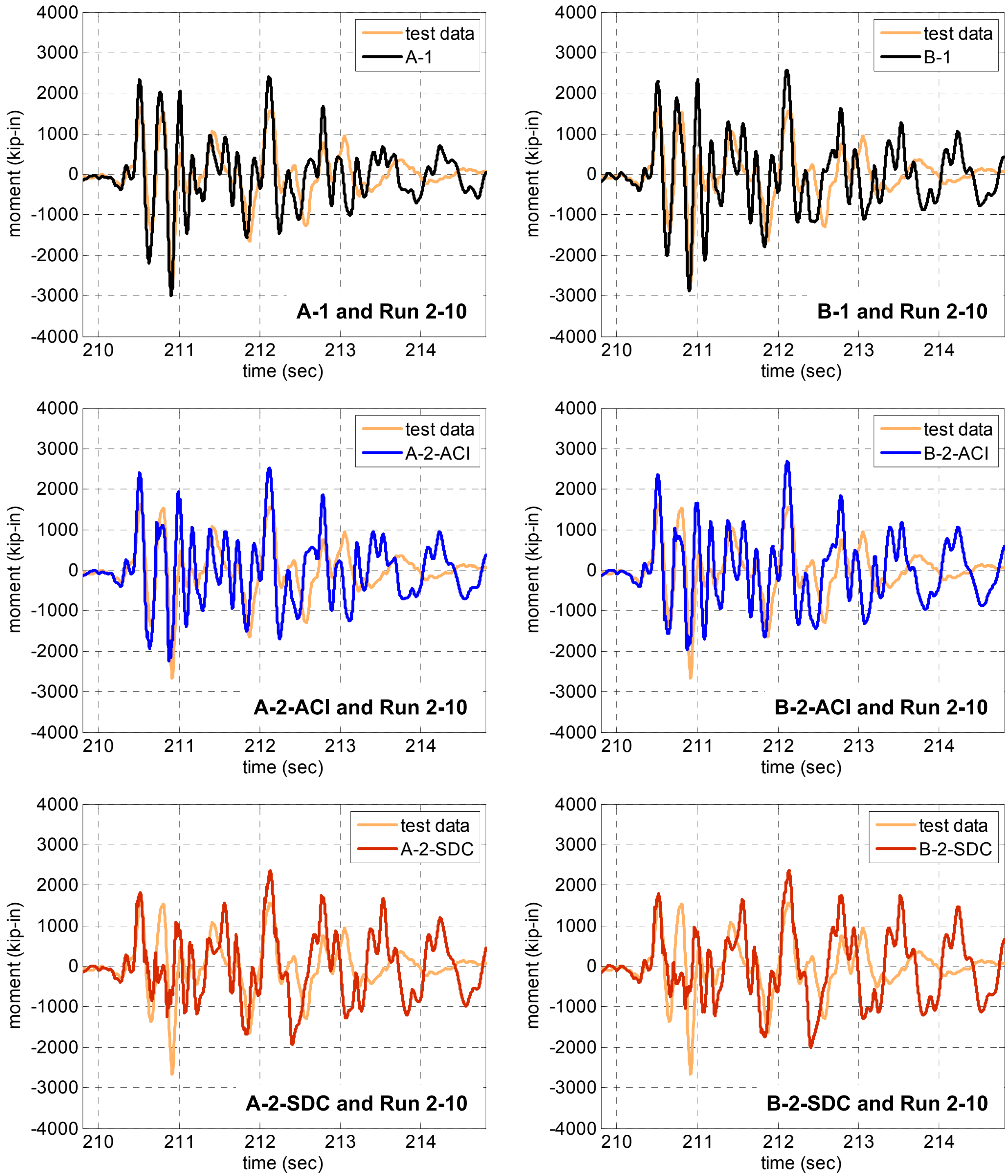

(b) 125% X only

Figure 6.29 Continued.

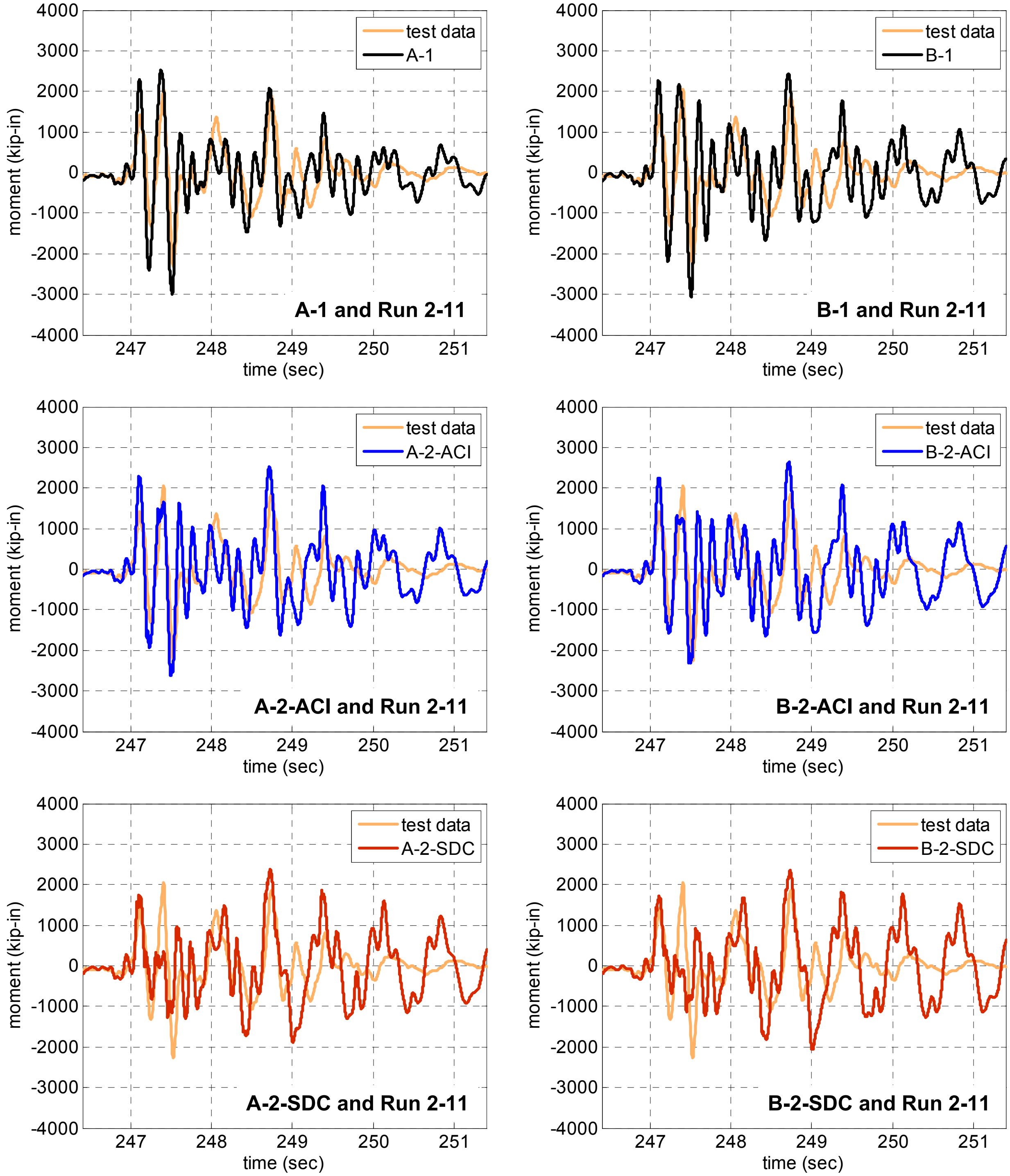

(c) 125% 2nd X+Z

Figure 6.29 Continued.

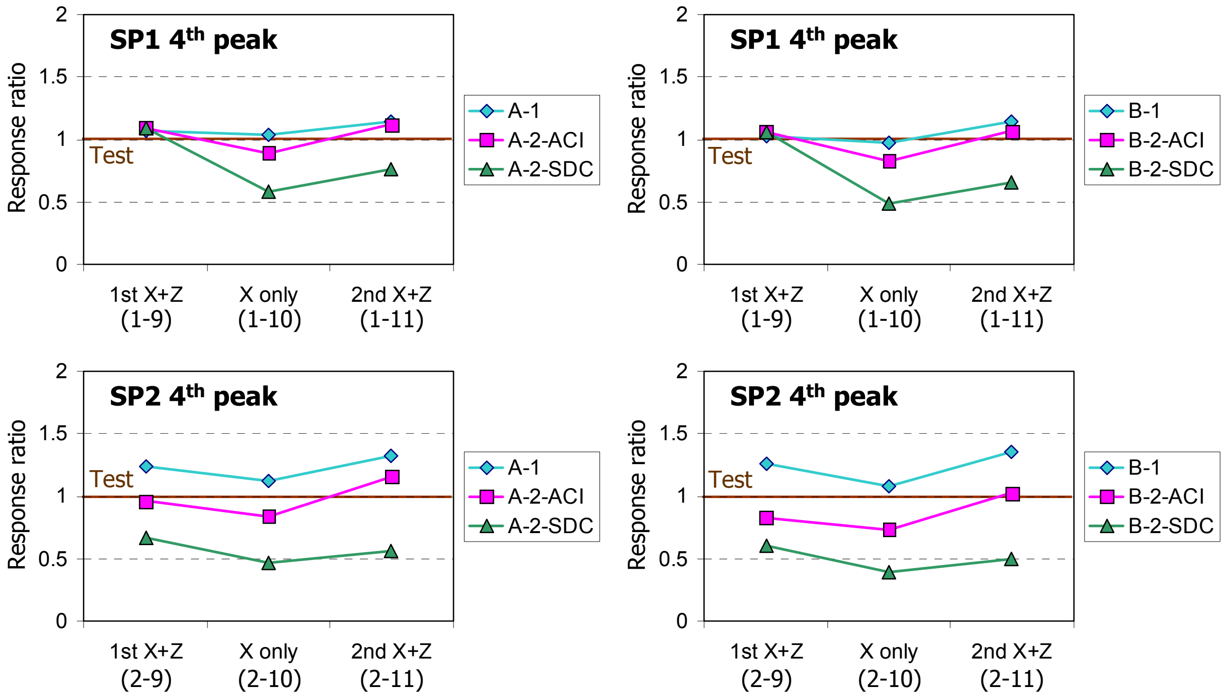

Figure 6.30 **Comparison of base moment ratios between the computational models to the test data at the fourth peak under the 125%-scale motions.**

6.4.2.3 Bending Moment at the Top

This section discusses the bending moment at the top of the column. Figure 6.31 compares the test results and the top moment responses obtained from Models A-1 and B-1. Compared to the base moment responses, the top moment has noticeable high-frequency content, which is due to the effect of the top mass rotational mode of vibration on the bending moment at the top of the column. In general, the analytical models are successful in the incorporation of this effect.

Figure 6.32 presents the top moment responses of each model subjected to 125%-scale motions. In Figure 6.32(a), the responses under '1st X+Z' are compared to the test data. The third peak, denoted as '3', is the maximum, coinciding with the time of maximum shear force. Although the models underestimate the bending moment at this peak, they captured the variation of the bending moment with time very well. Figure 6.35 compares the response ratios of each model to the test data at peak '3'. Similar to the previous cases, the order of these ratios is as follows: A-1 > A-2-ACI > A-2-SDC (or B-1 > B-2-ACI > B-2-SDC) in most cases.

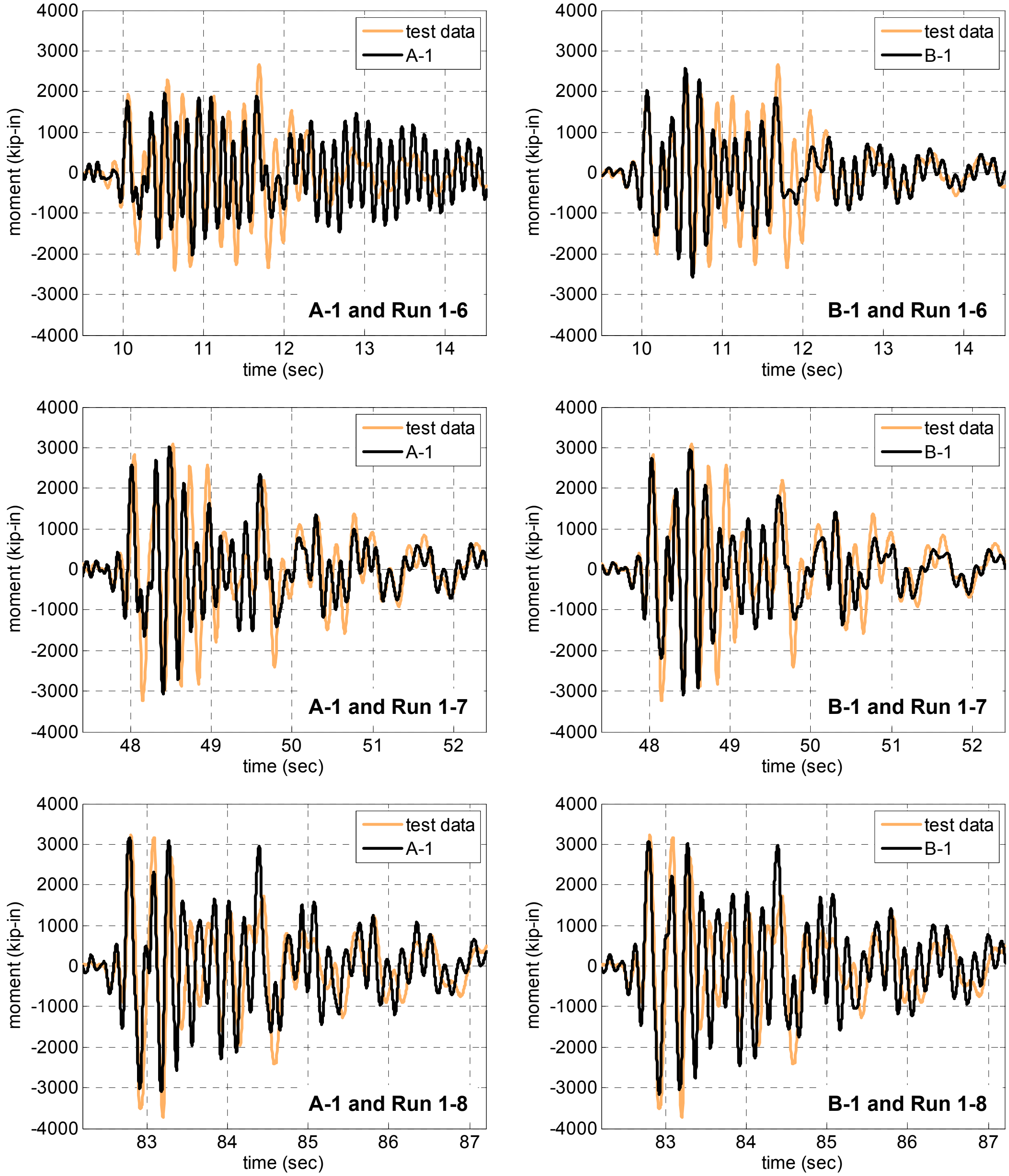

Figure 6.31 Comparison of bending moment histories at the top of SP1 subjected to 50%-, 70%-, and 95%-scale motions.

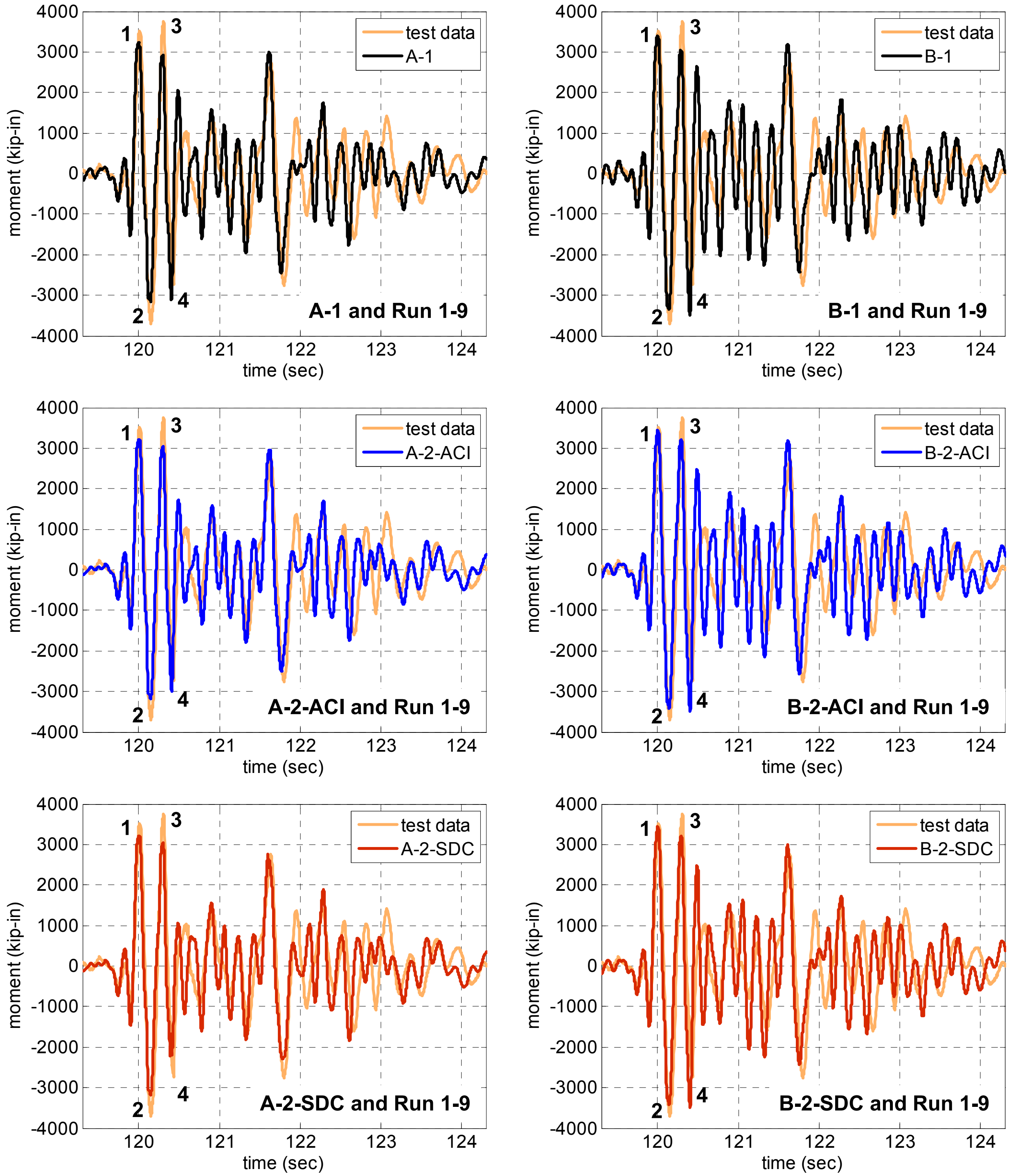

(a) 125% 1st X+Z

Figure 6.32 Comparison of bending moment histories at the top of SP1 subjected to 125%-scale motions.

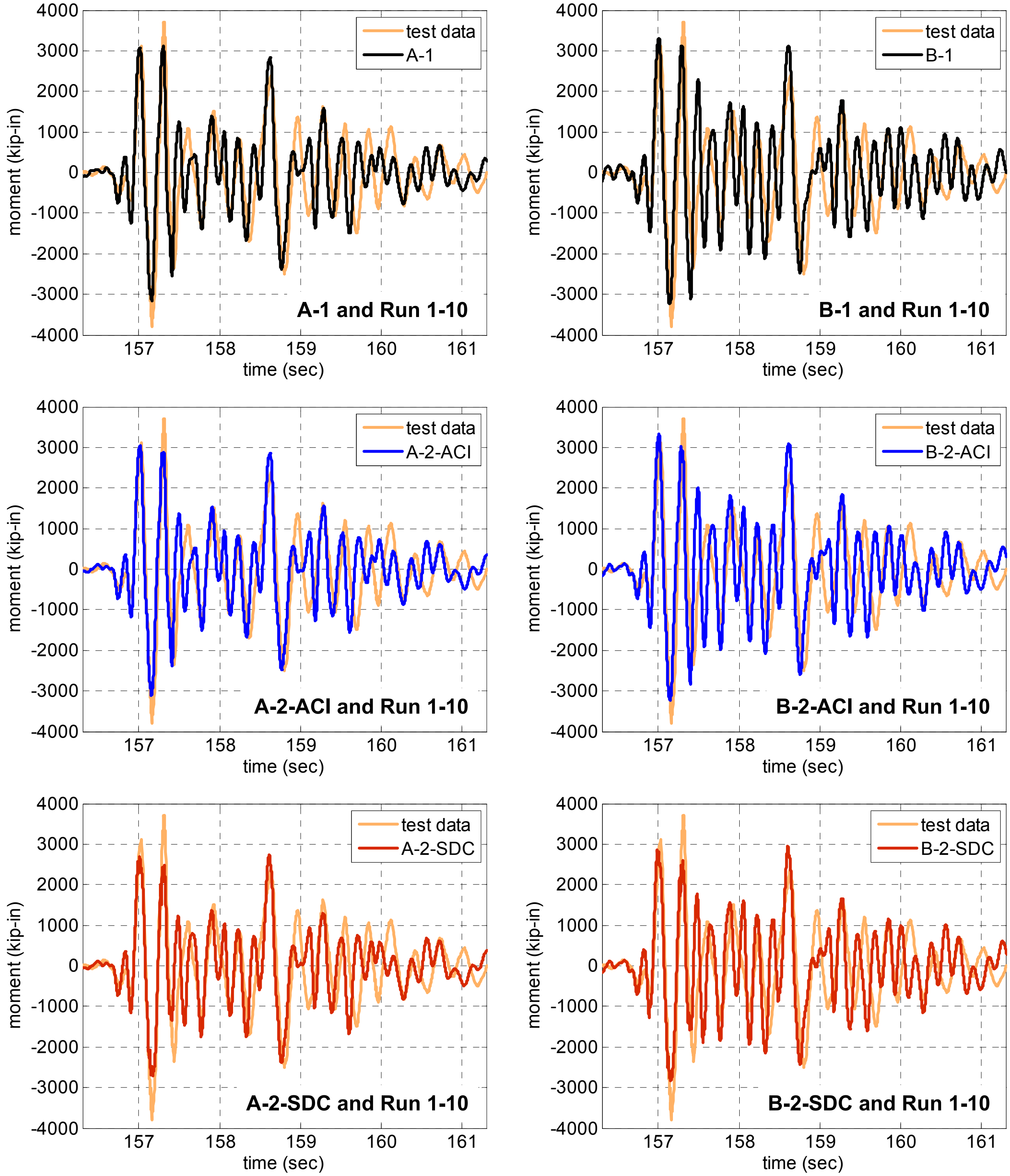

(b) 125% X only

Figure 6.32 Continued.

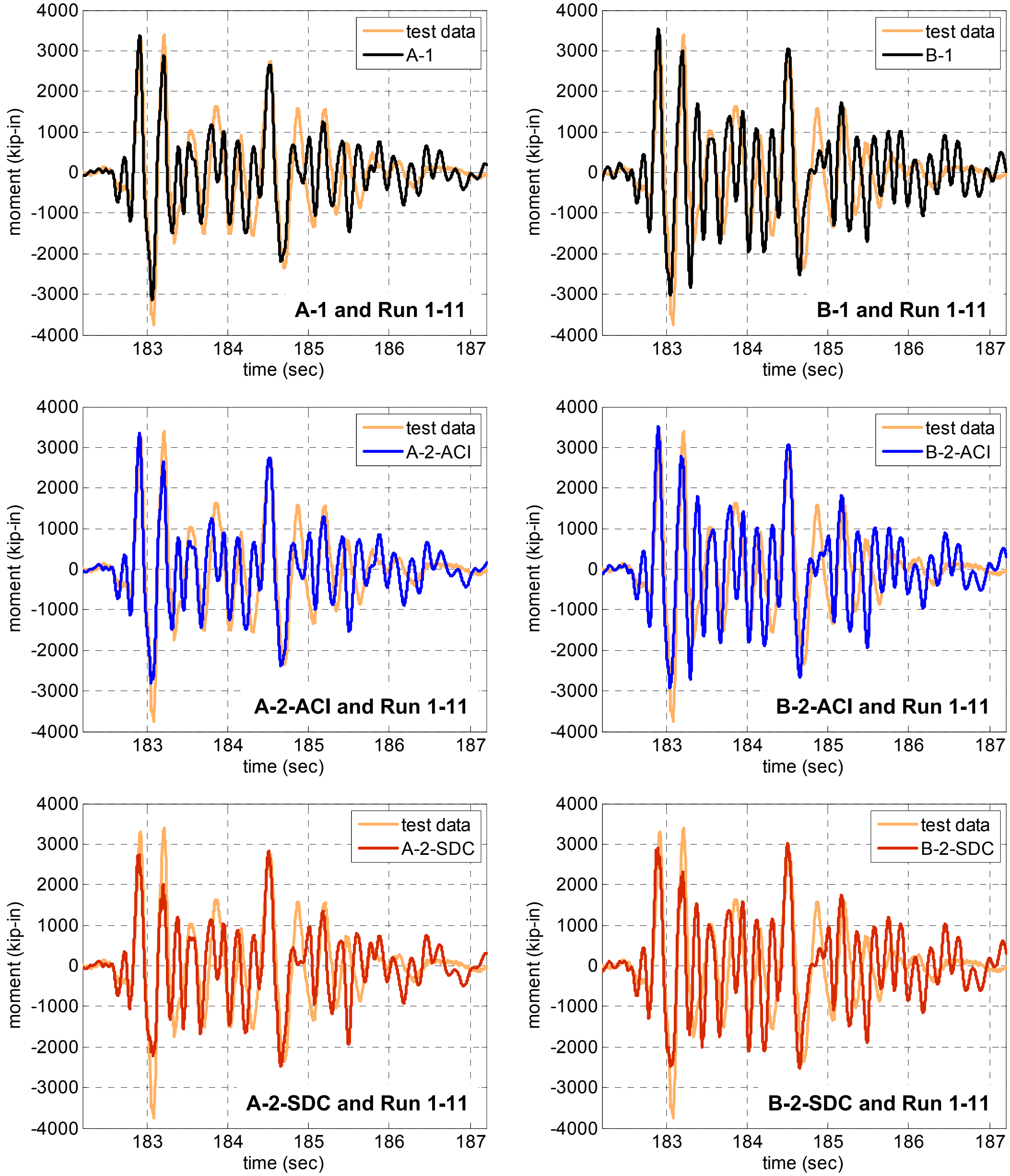

(c) 125% 2nd X+Z

Figure 6.32 Continued.

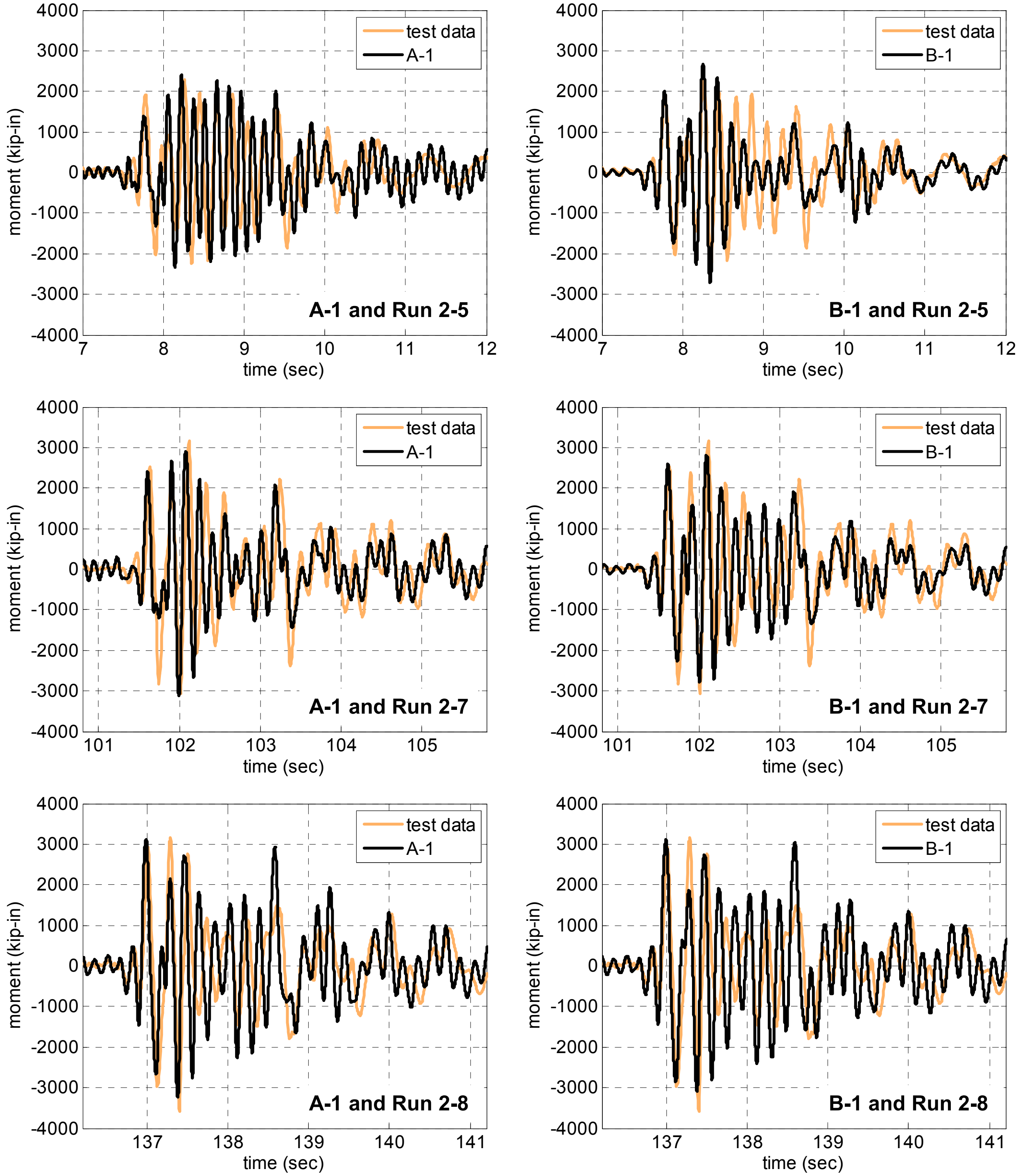

Figure 6.33 Comparison of bending moment histories at the top of SP2 subjected to 50%-, 70%-, and 95%-scale motions.

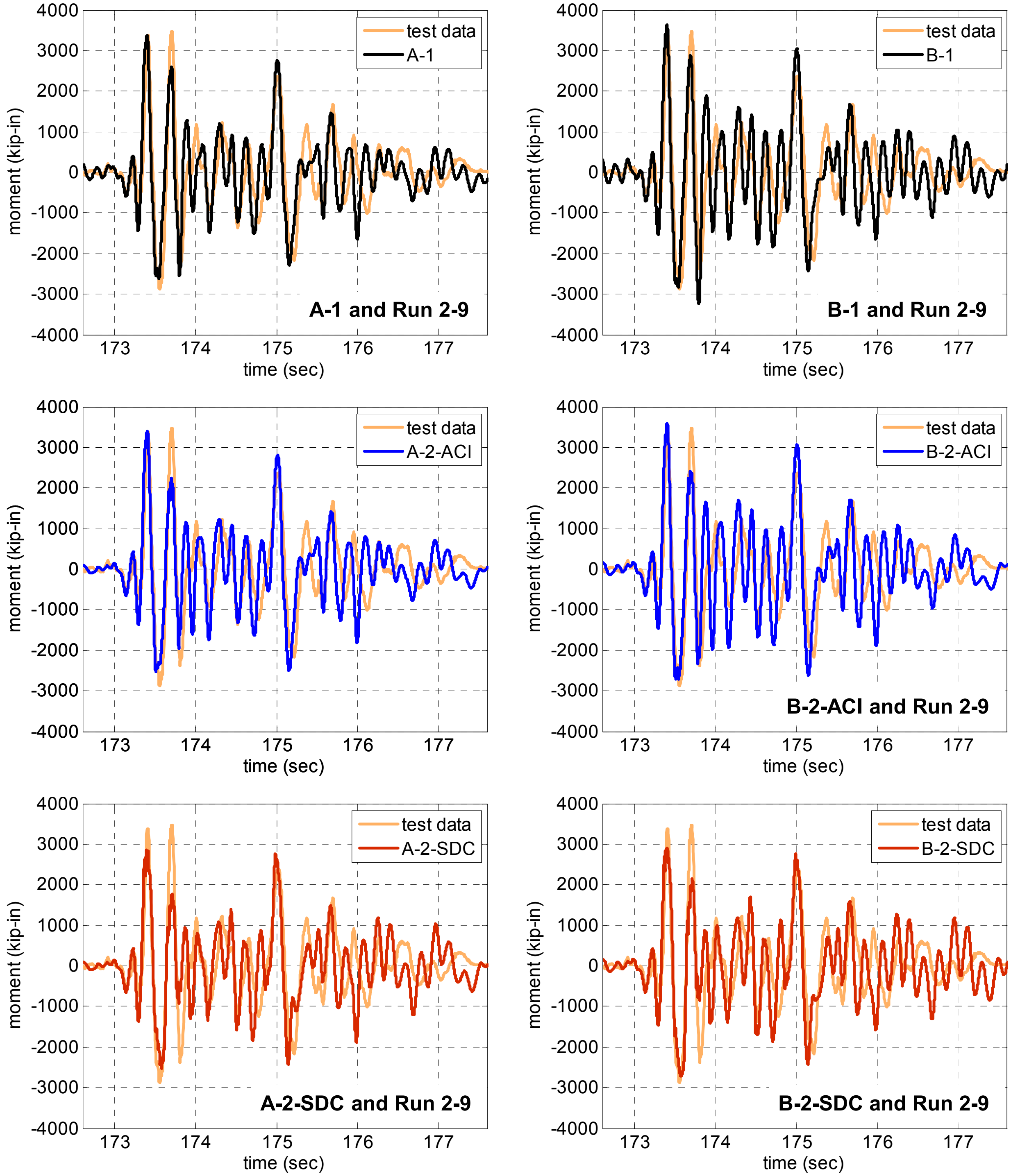

(a) 125% 1st X+Z

Figure 6.34 Comparison of bending moment histories at the top of SP2 subjected to 125%-scale motions.

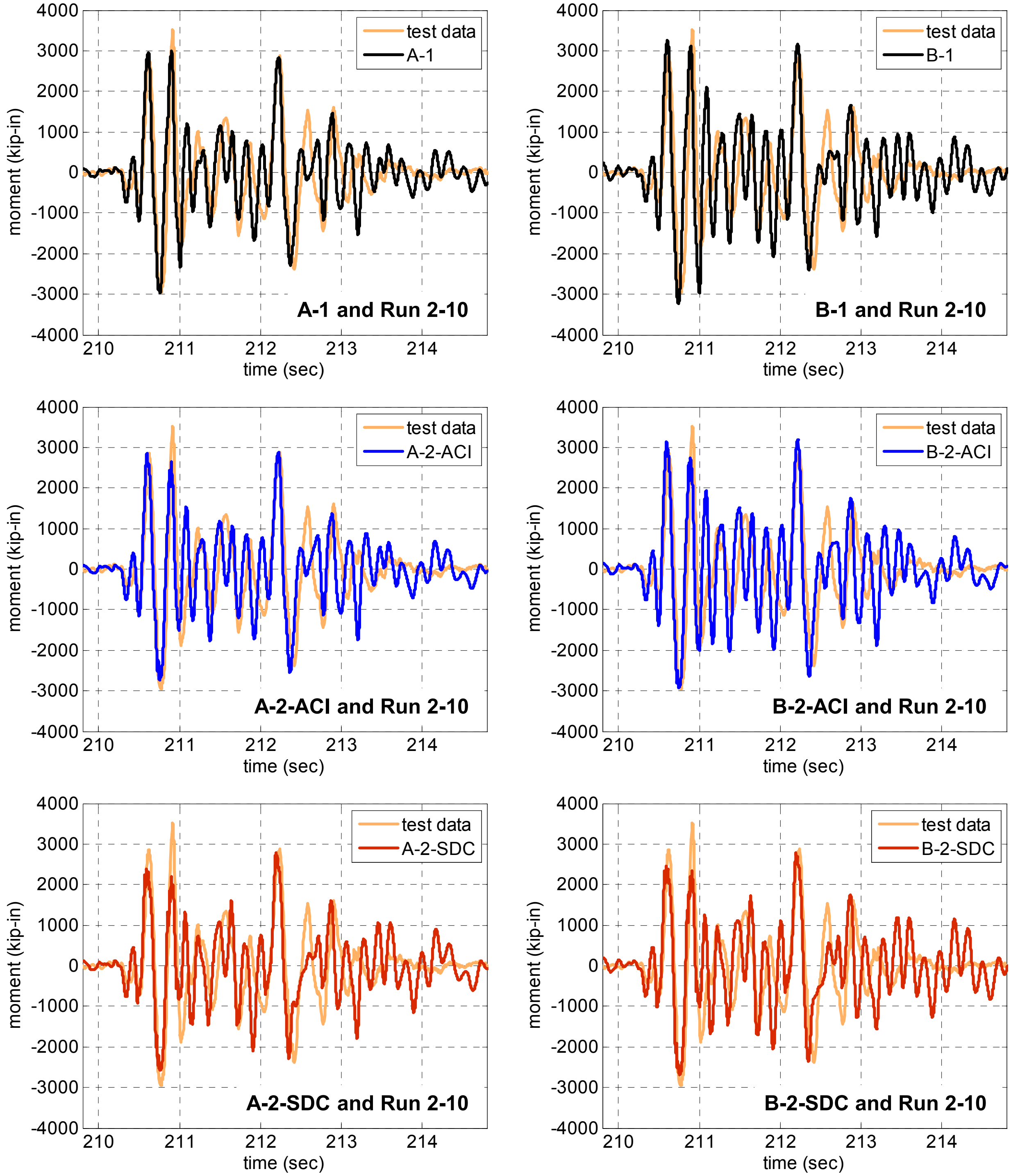

(b) 125% X only

Figure 6.34 Continued.

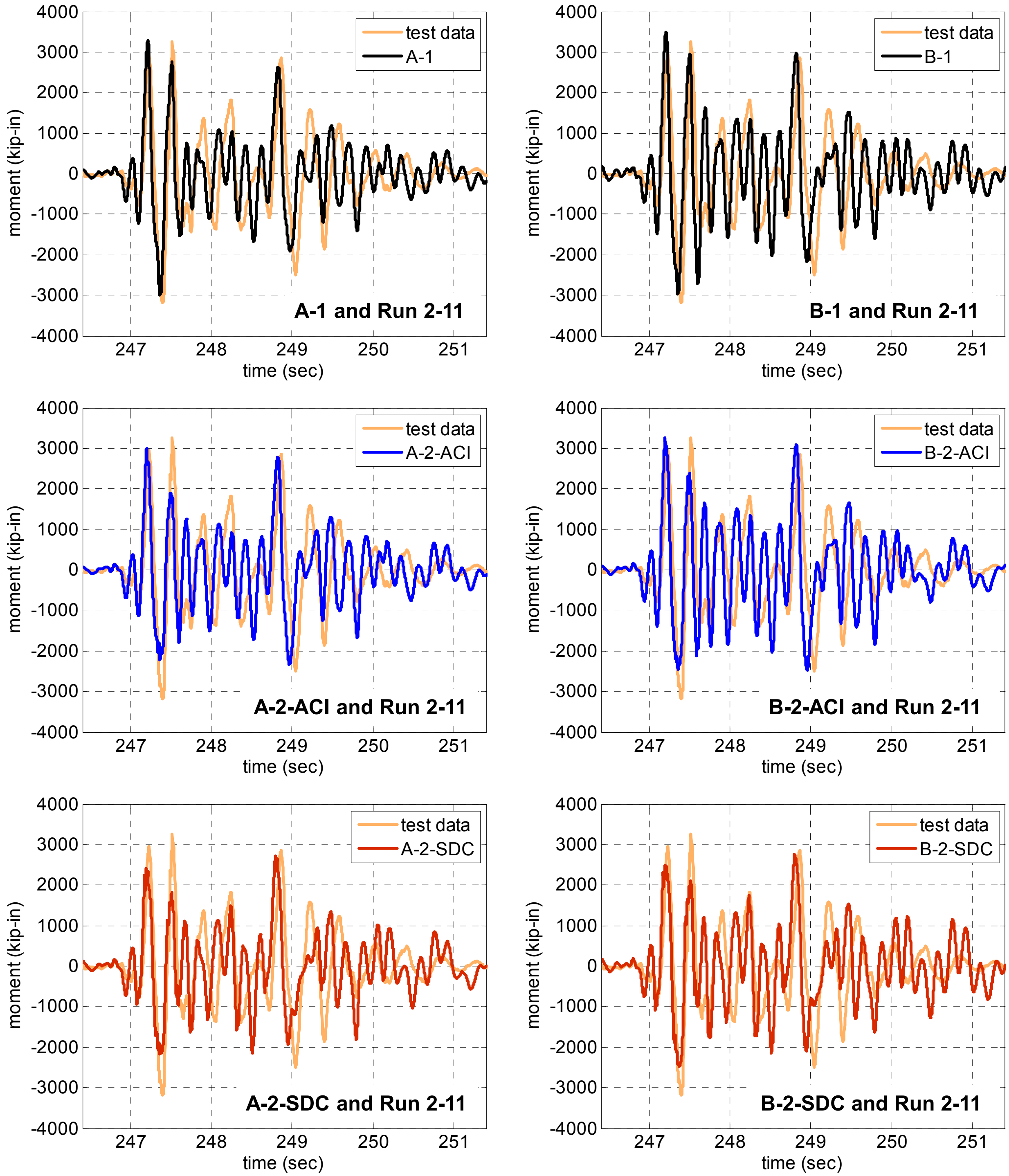

(c) 125% 2nd X+Z

Figure 6.34 Continued.

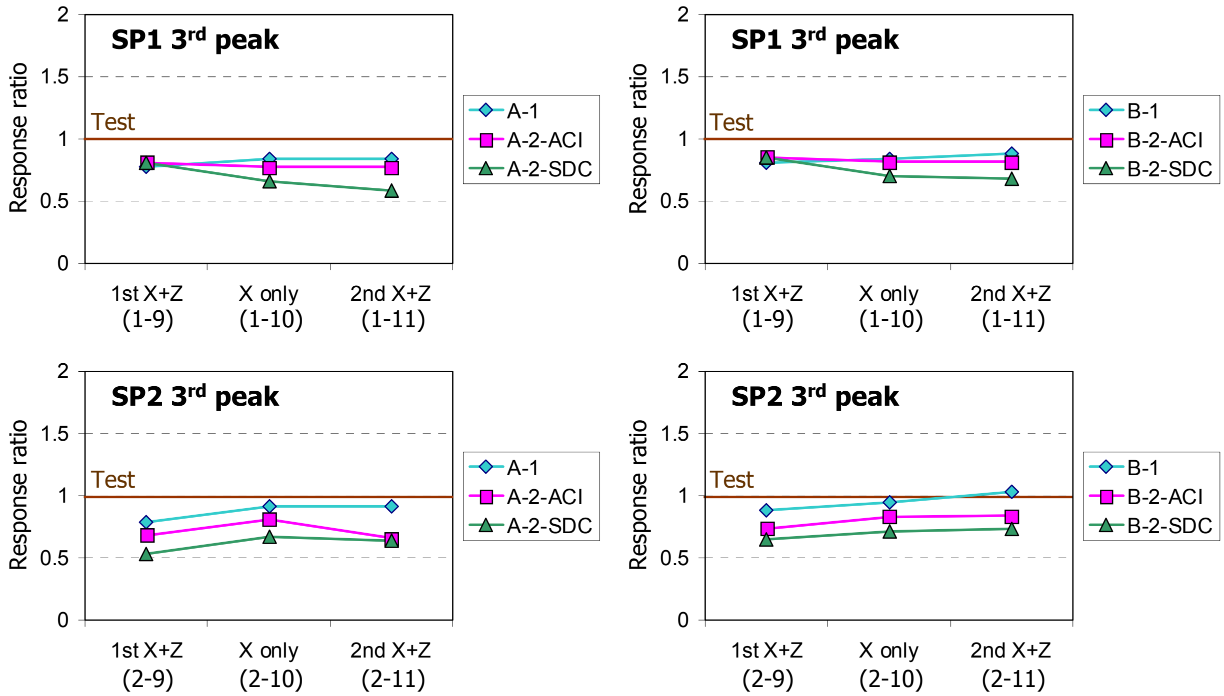

Figure 6.35 Comparison of top moment ratios between the computational models to the test data at the third peak under the 125%-scale motions.

6.4.2.4 Lateral Displacement at the Top

This section compares the top displacement histories in the X-direction obtained from the computational models to those measured during the tests. Figure 6.36 presents the lateral displacement histories of SP1 subjected to 50%, 70%, and 95%-scale motions. Figure 6.37 presents the displacement histories for the 125%-scale motions. Despite the slight frequency shifts at the second half of motions 1-8 and 1-9 and some difference in the negative peak displacement of motion 1-9, Models A-1, B-1, A-2-ACI, and B-2-ACI estimate displacements with sufficient accuracy. Differences between the test data and Models A-2-SDC and B-2-SDC are more significant for motion 1-9. Presence of a shear spring improved the results considerably for motion 1-10. Both of the models with ACI and SDC springs provided displacement histories close to the test data, with the A-2-ACI model providing in the best predictions. A similar observation can be stated for motion 1-11. Note that although model A-2-ACI, which provided the best predictions for motions 1-10 and 1-11, captured the positive displacements with very good accuracy, it underestimated the negative displacements. Overall, displacement predictions provided by the analytical models can be regarded as sufficiently accurate with the presence of a shear spring, resulting in an improvement in the predictions.

Similar to SP1, model predictions of SP2 for motions 2-5 to 2-9 are accurate as shown in Figure 6.38 and Figure 6.39(a). However, for ground motions 2-10 and 2-11, the presence of a shear spring was not sufficient to improve the predictions where the responses obtained from the analytical models are different from the test results; see Figure 6.38(b) and (c).

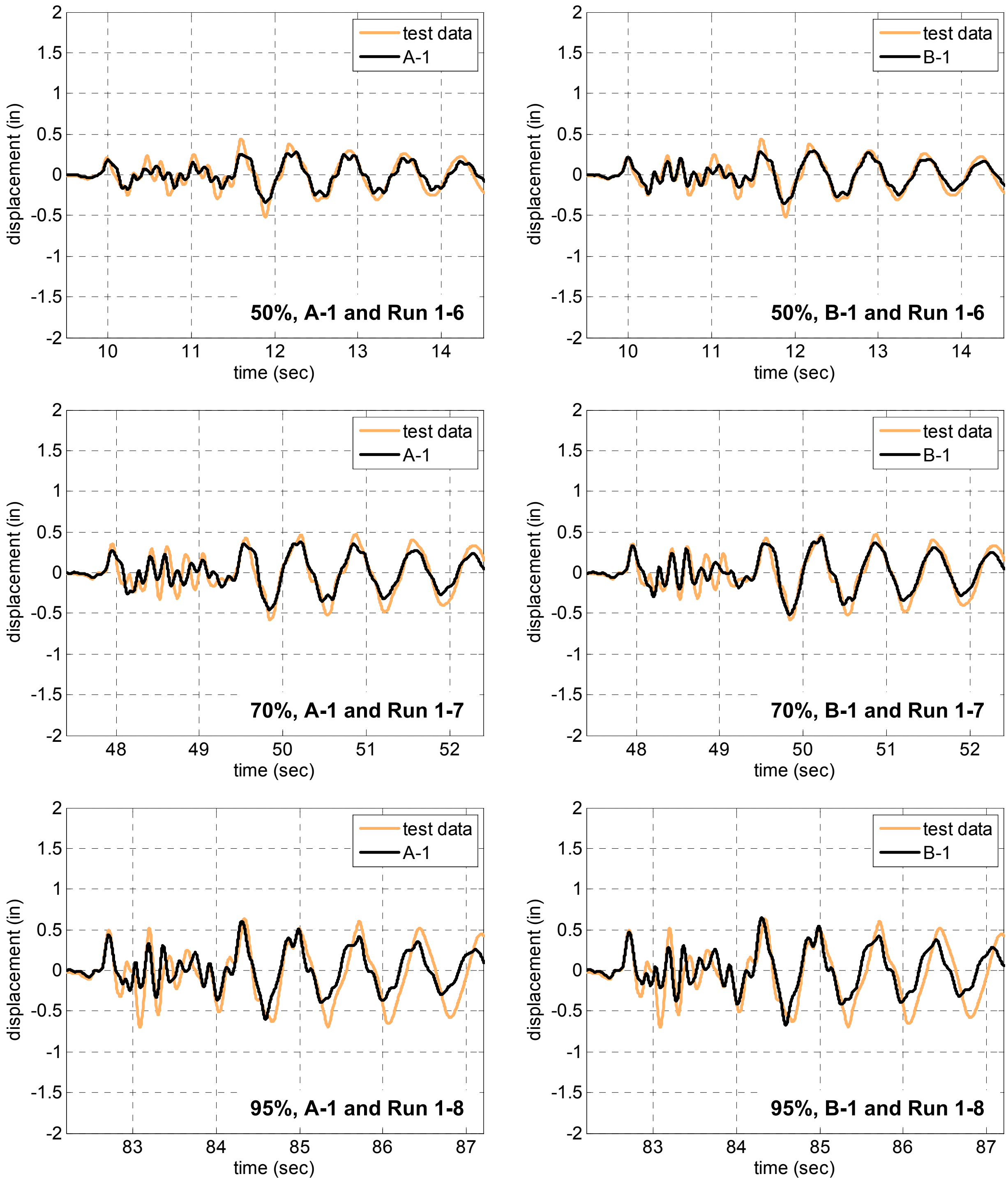

Figure 6.36 Comparison of lateral displacement histories of SP1 subjected to 50%-, 70%-, and 95%-scale motions.

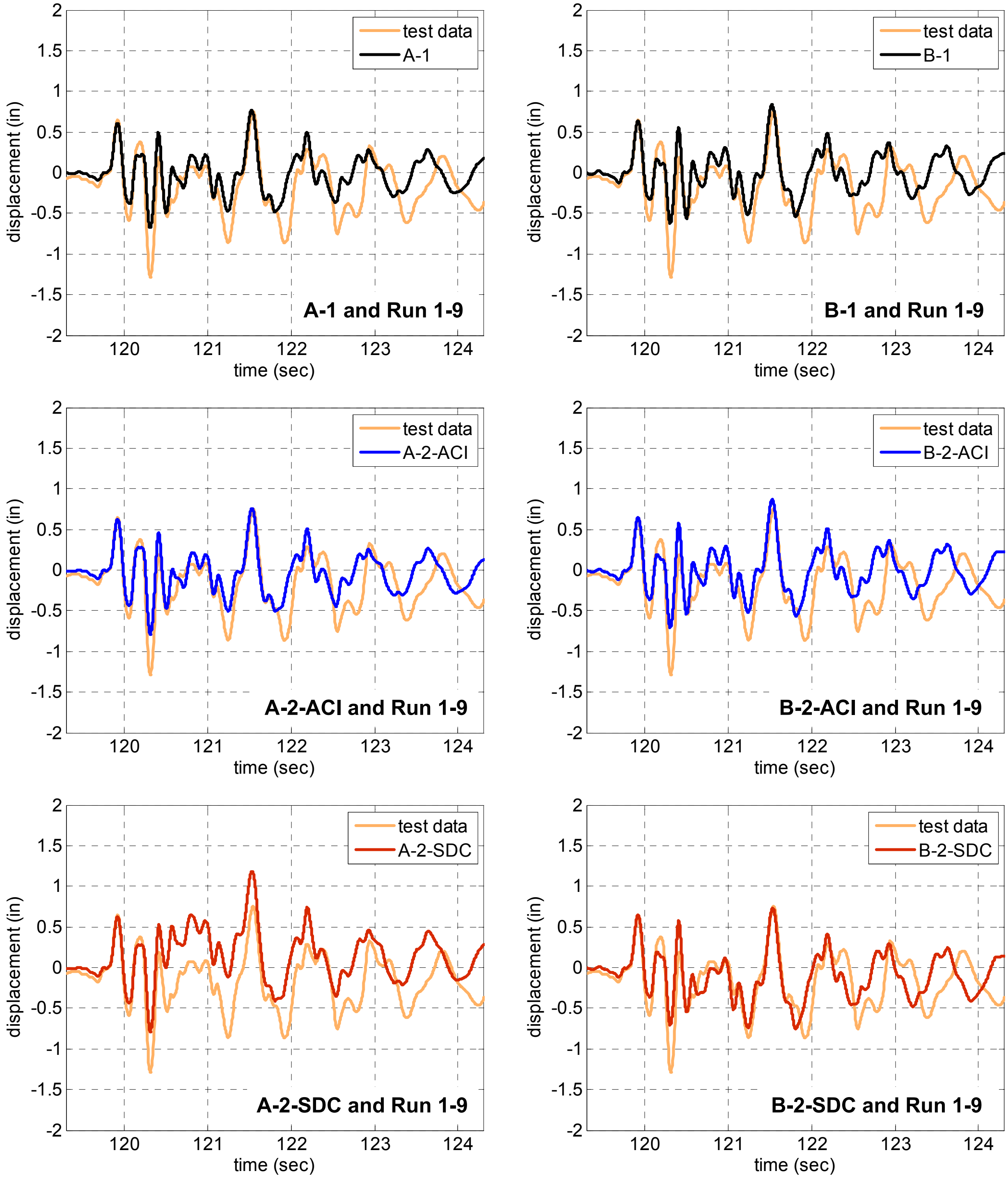

(a) 125% 1st X+Z

Figure 6.37 Comparison of lateral displacement histories of SP1 subjected to 125%-scale motions.

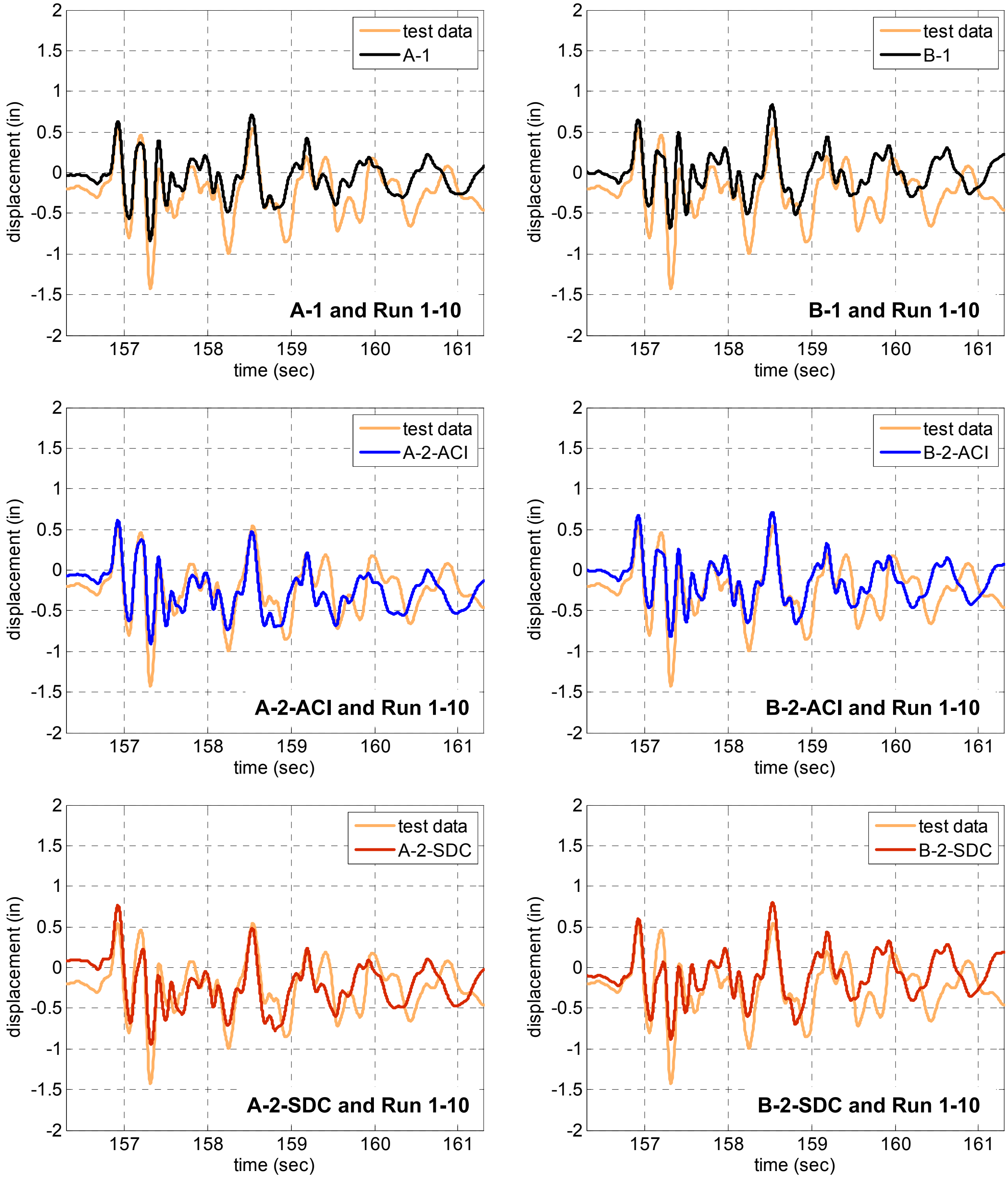

(b) 125% X only

Figure 6.37 Continued.

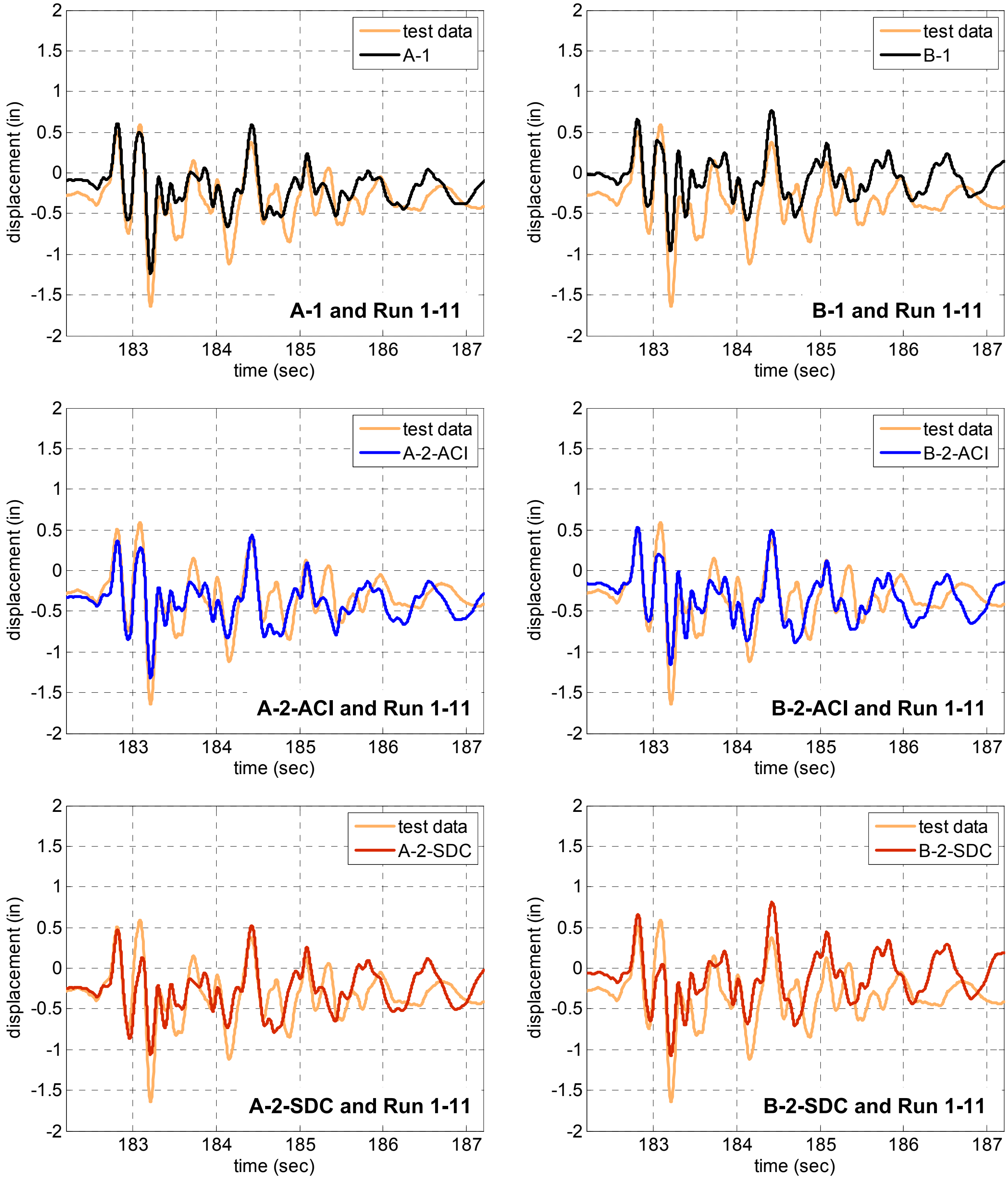

(c) 125% 2nd X+Z

Figure 6.37 Continued.

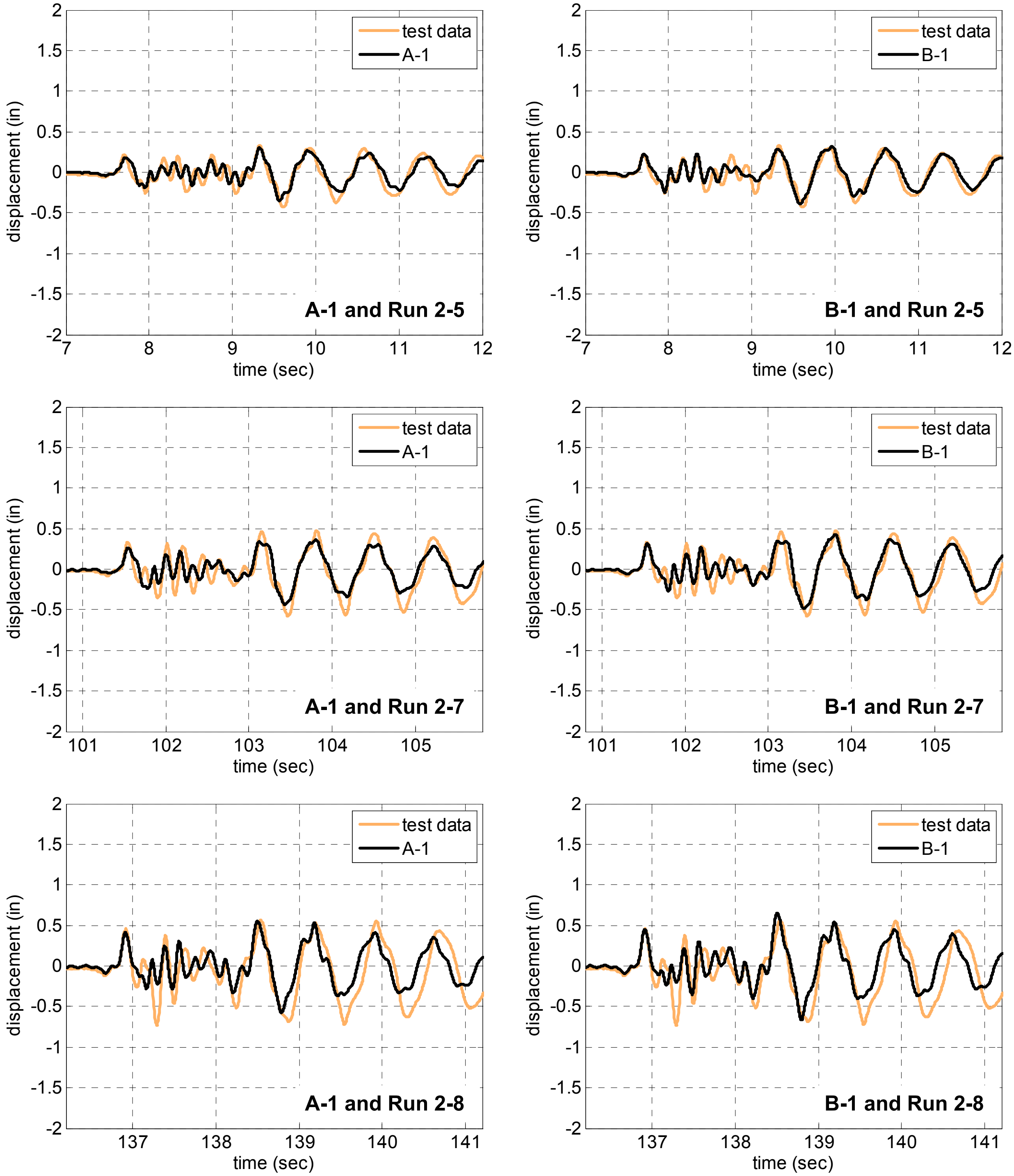

Figure 6.38 Comparison of lateral displacement histories of SP2 subjected to 50%-, 70%-, and 95%-scale motions.

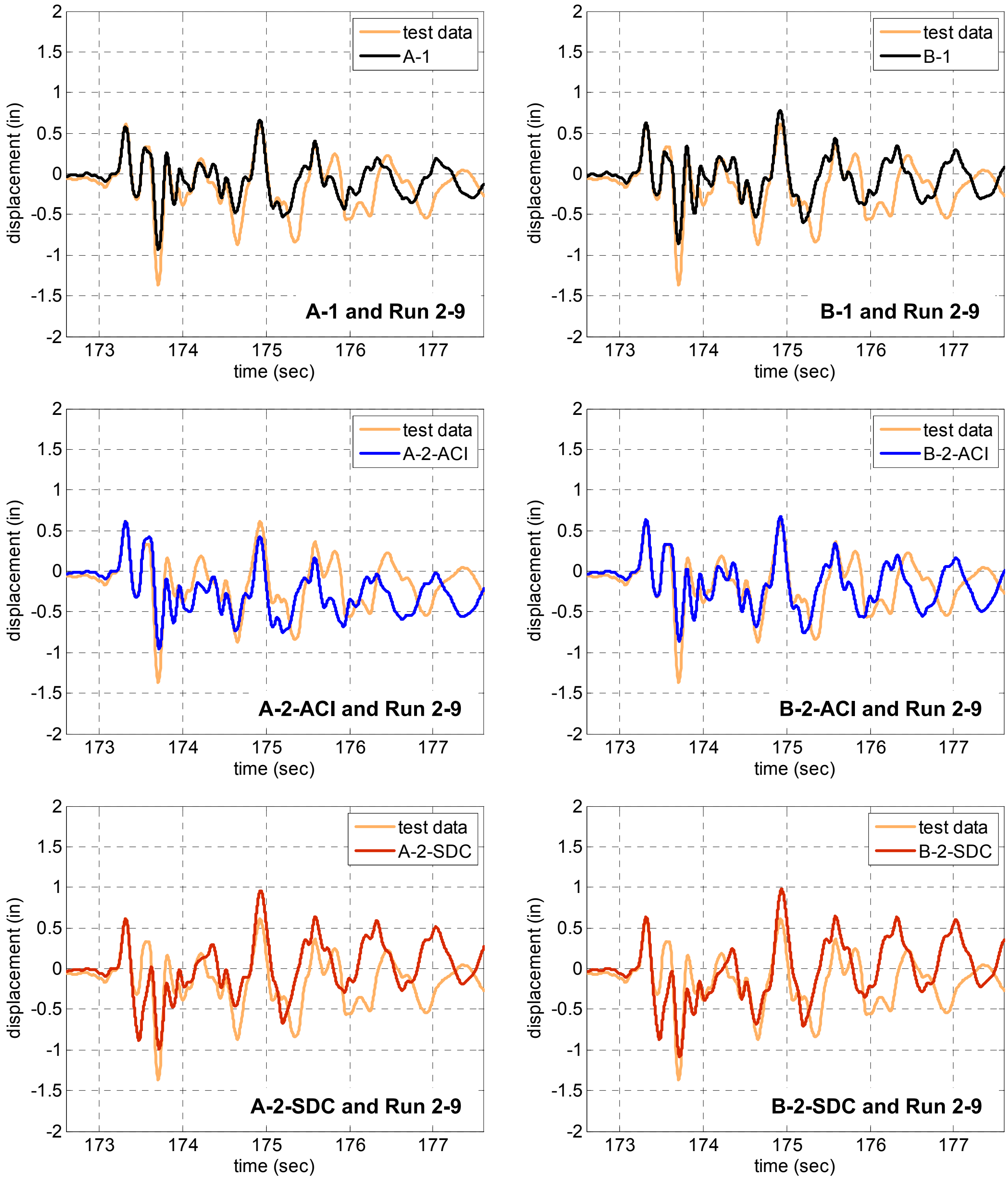

(a) 125% 1st X+Z

Figure 6.39 Comparison of lateral displacement histories of SP2 subjected to 125%-scale motions.

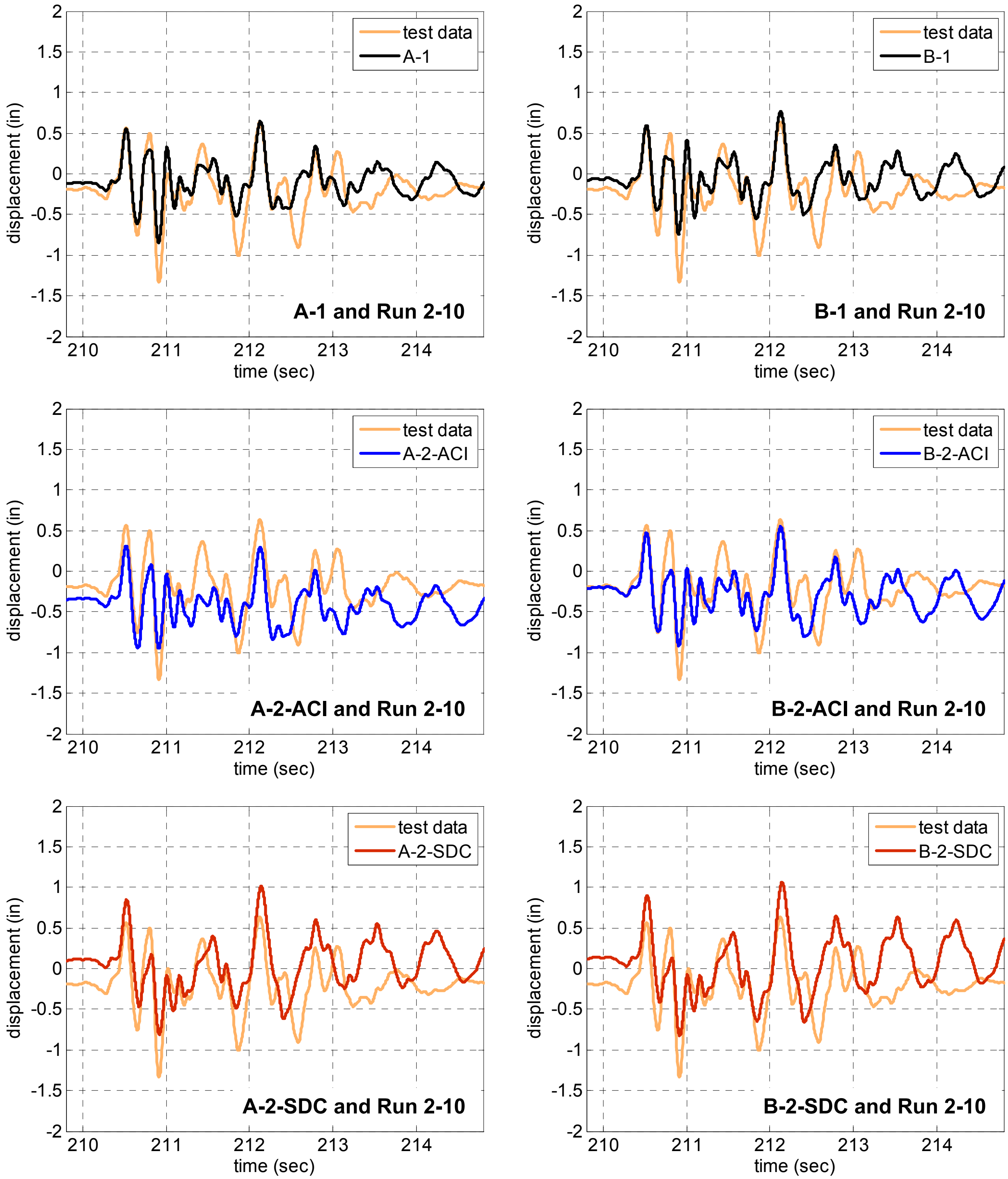

(b) 125% X only

Figure 6.39 Continued.

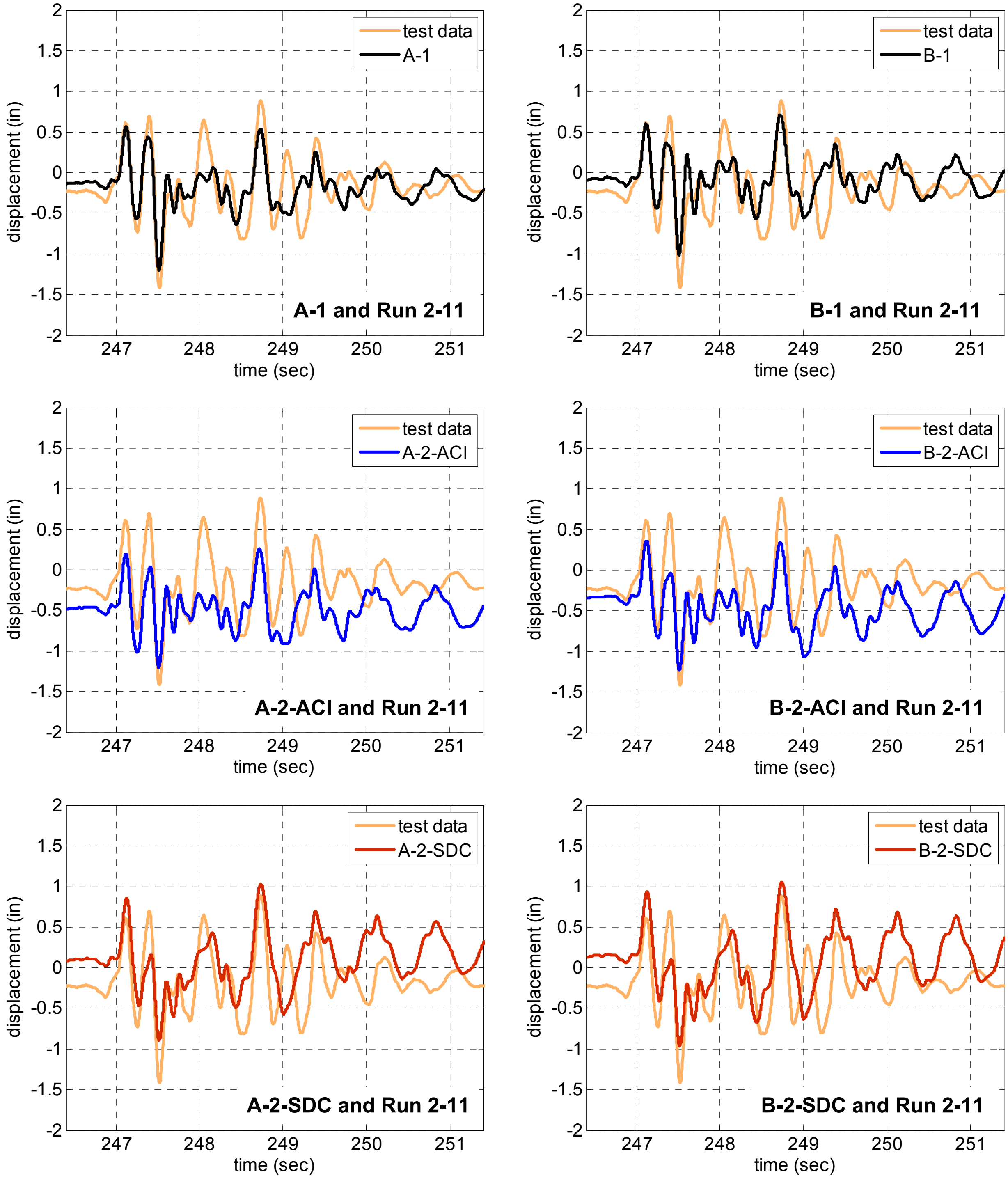

(c) 125% 2nd X+Z

Figure 6.39 Continued.

6.4.2.5 Vertical Displacement at the Top

The vertical displacement responses from the computational models are compared to the test data in this section. Model A-1 or B-1 for SP1 did not even come close to estimating the vertical displacement measured in the 50%, 70%, and 95%-scale tests (Figure 6.40), since crack openings (especially the shear cracks on the east and west sides) were not adequately modeled in a fiber-section analysis. This trend continued for the higher-intensity tests. Figure 6.41 shows the computational results for SP1 under the 125%-scale motions. Under '1st X+Z' motion, all six models had similar responses. It is interesting to note that all the analytical models not only predicted smaller elongation compared to the test data but also indicate shortening for a duration of time that is not observed in the test data. This is mainly due to the lack of explicit consideration of the shear cracks and their openings in the analytical model. These observations are also valid for SP2, as shown in Figure 6.42 and Figure 6.43.

Errors in the vertical displacement prediction do not introduce significant problems regarding the main aim of the study, which is to investigate the effect of axial tension on the shear capacity. Therefore, further improvement of the vertical displacement predictions using modifications in the model is not considered, since these additional modifications would be beyond the scope of fiber modeling and would require more detailed finite element models.

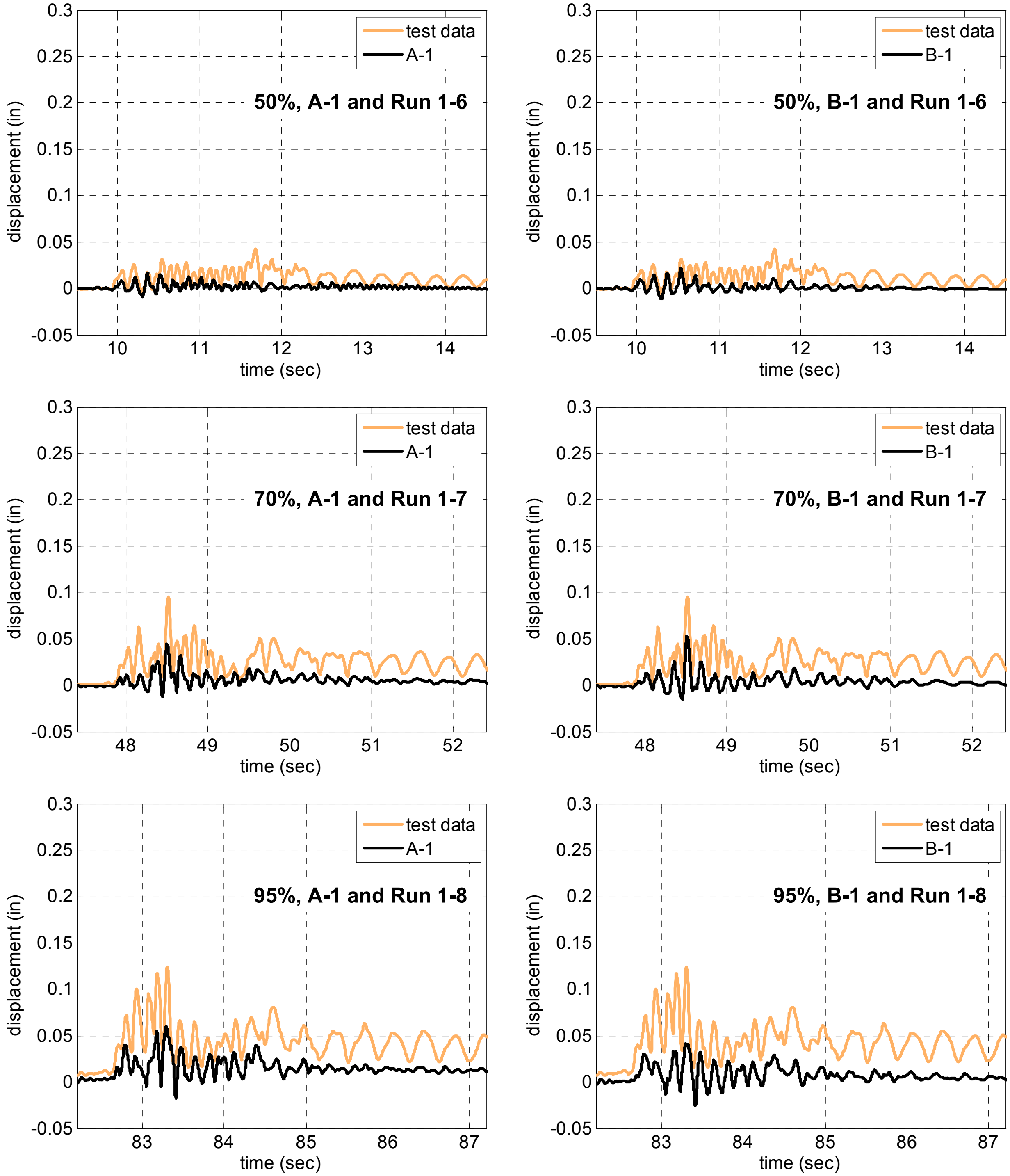

Figure 6.40 Comparison of vertical displacement histories of SP1 subjected to 50%-, 70%-, and 95%-scale motions.

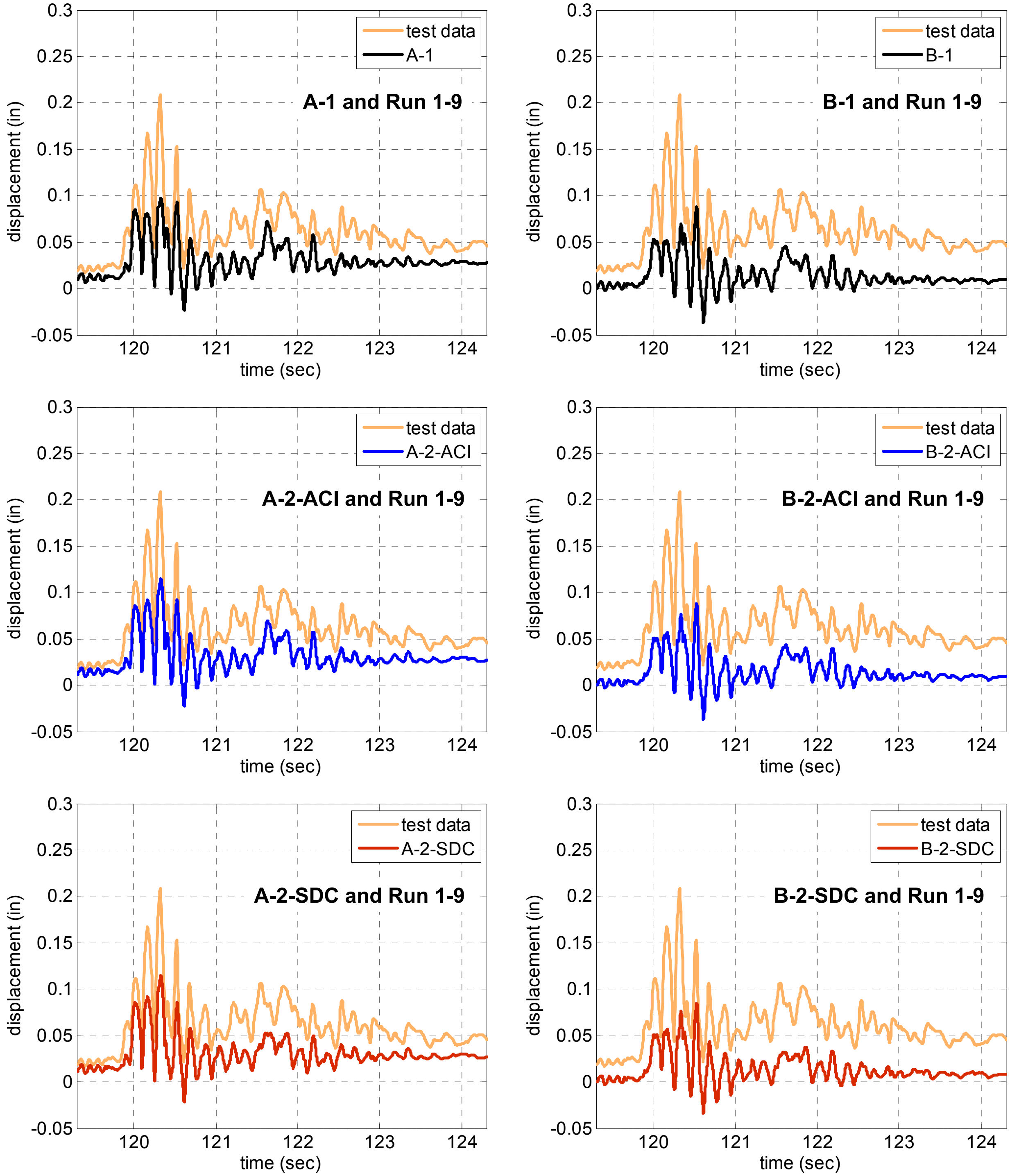

(a) 125% 1st X+Z

Figure 6.41 Comparison of vertical displacement histories of SP1 subjected to 125%-scale motions.

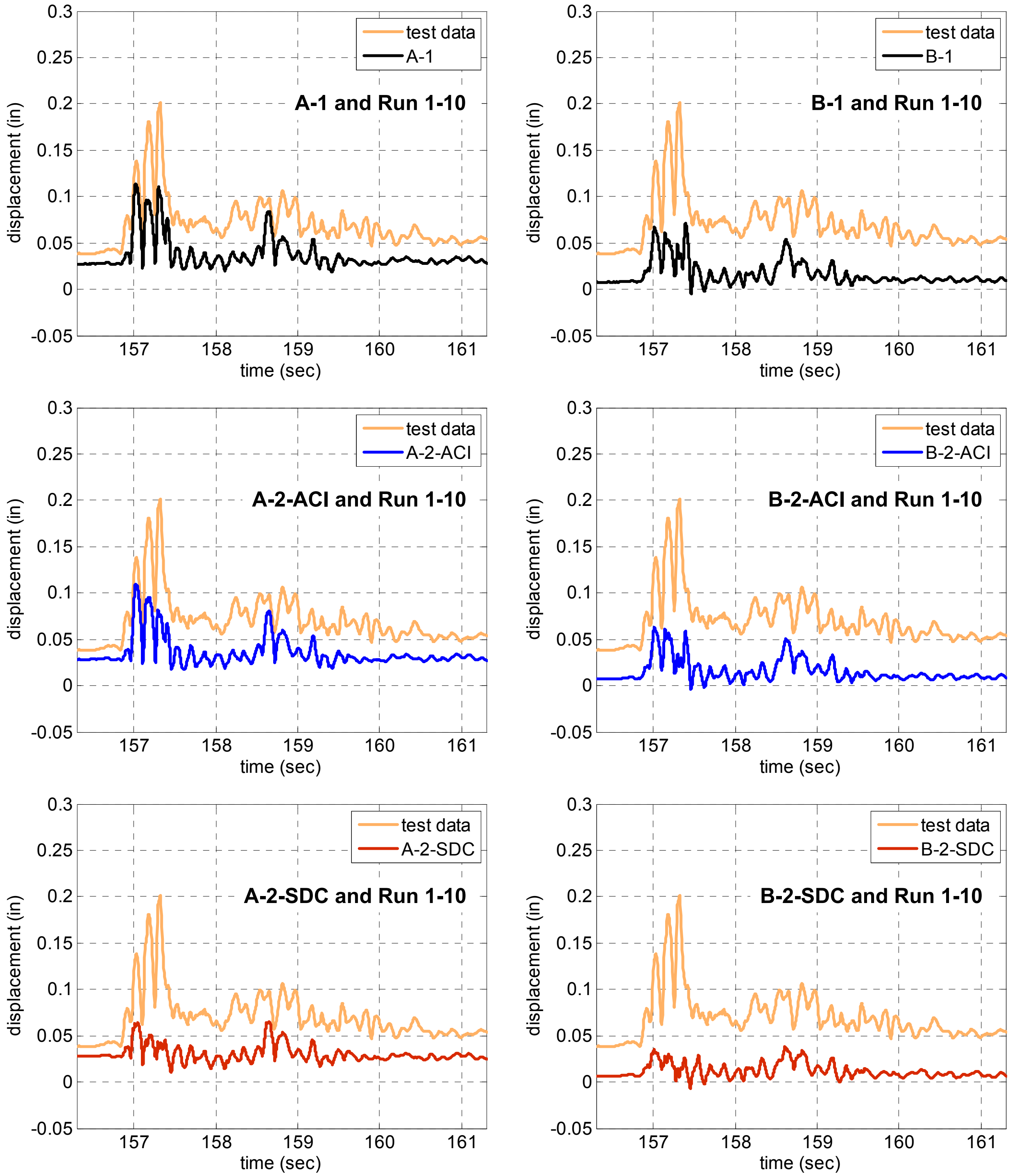

(b) 125% X only

Figure 6.41 Continued.

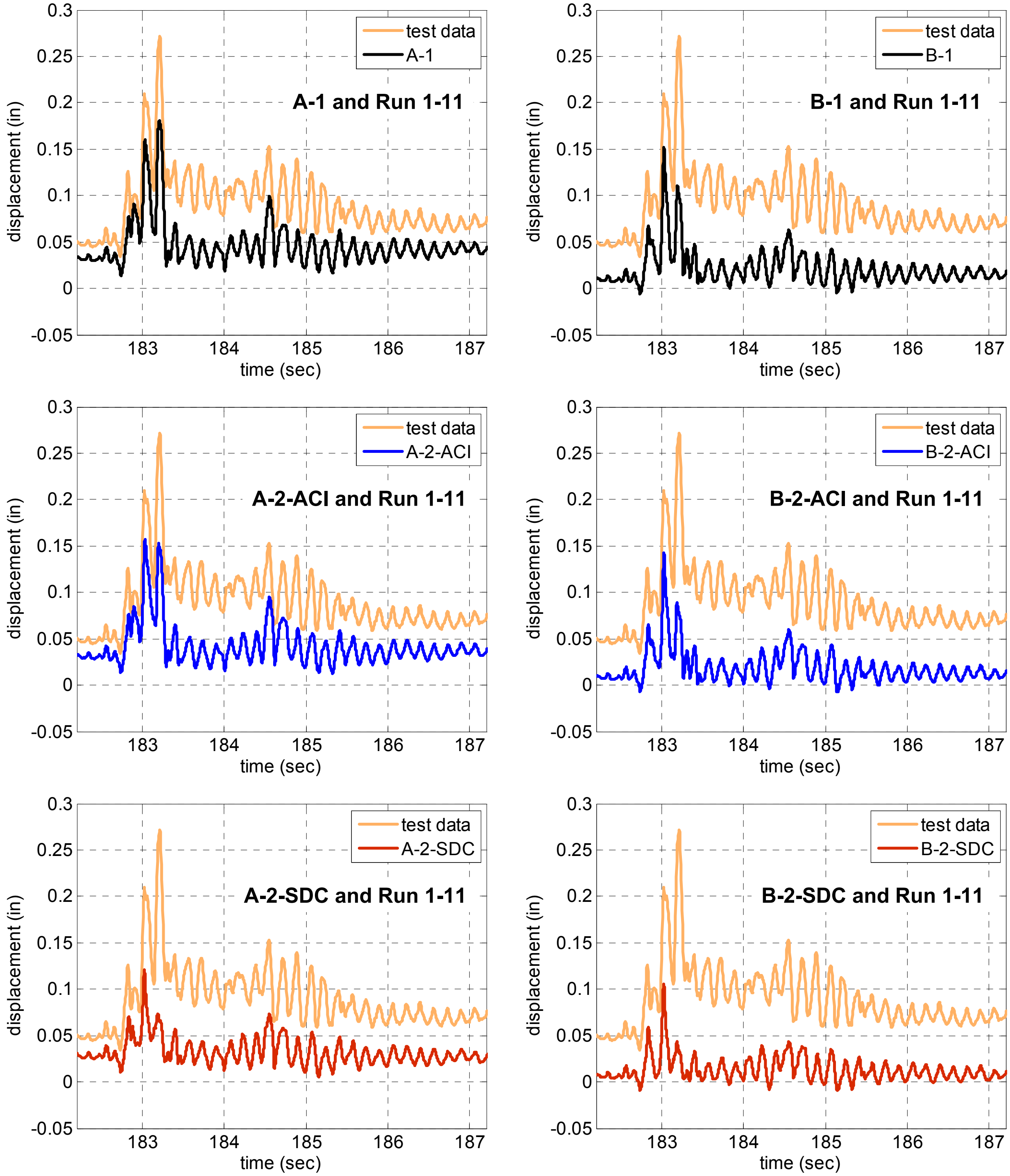

(c) 125% 2nd X+Z

Figure 6.41 Continued.

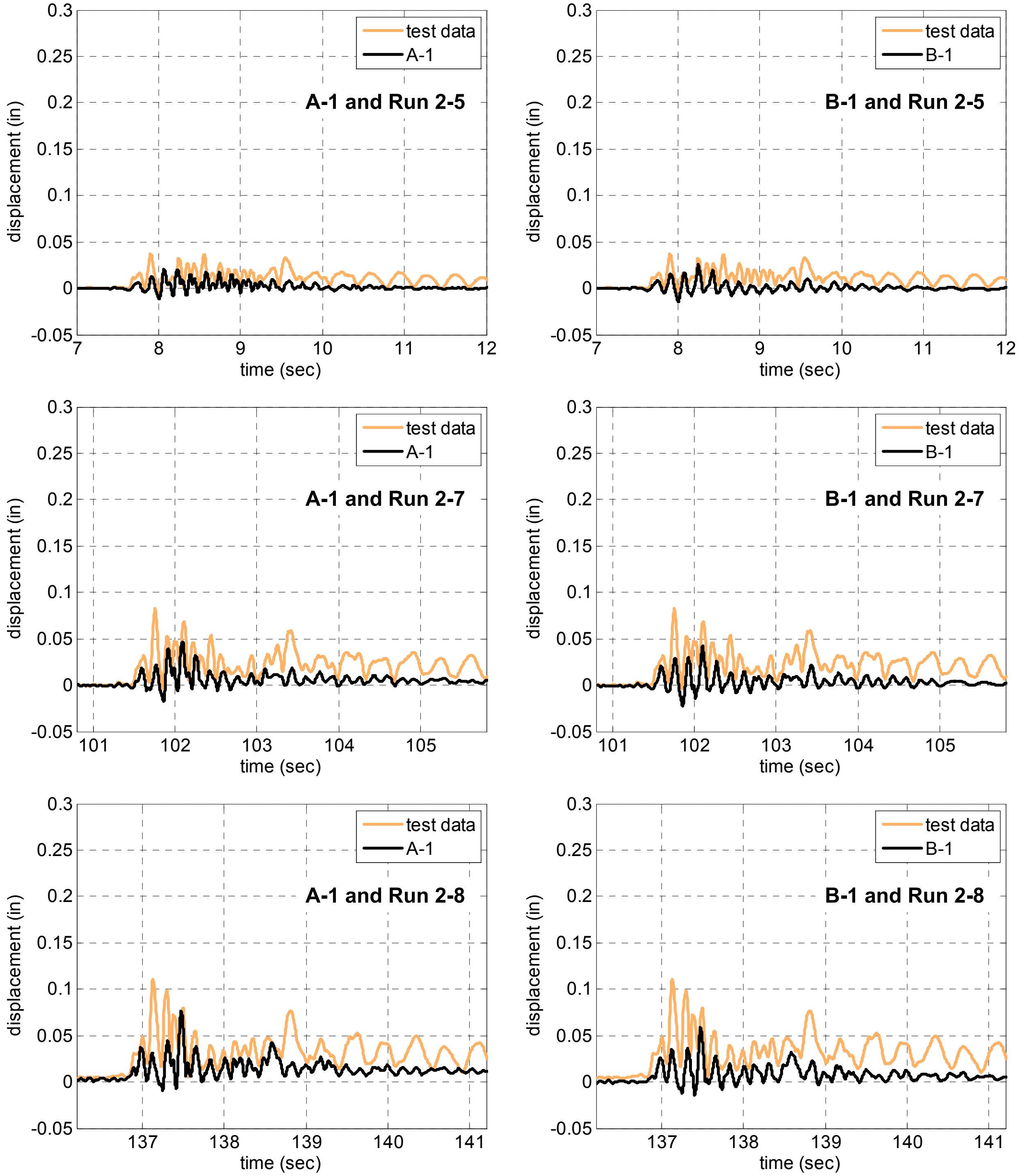

Figure 6.42 Comparison of vertical displacement histories of SP2 subjected to 50%-, 70%-, and 95%-scale motions.

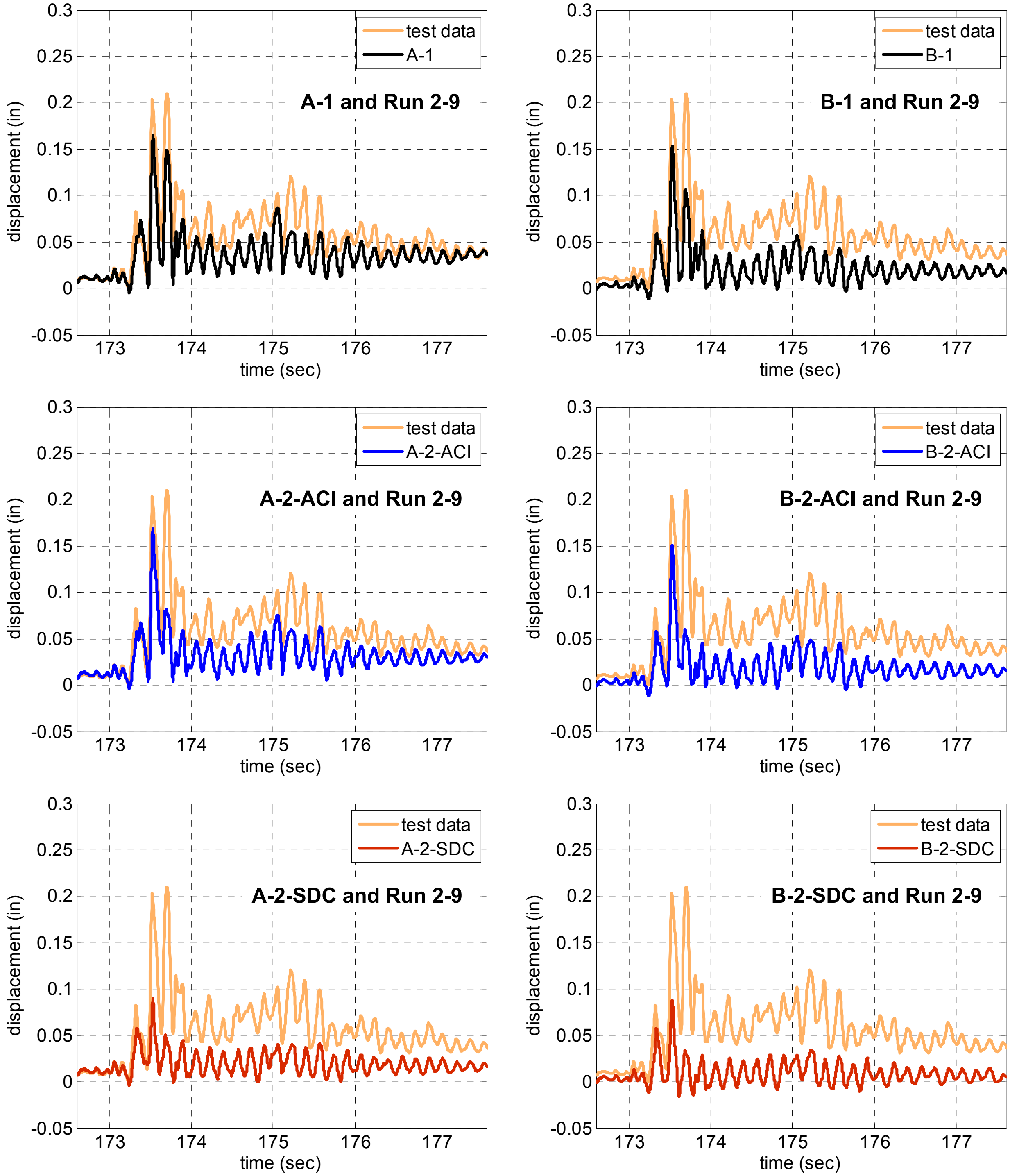

(a) 125% 1st X+Z

Figure 6.43 Comparison of vertical displacement histories of SP2 subjected to 125%-scale motions.

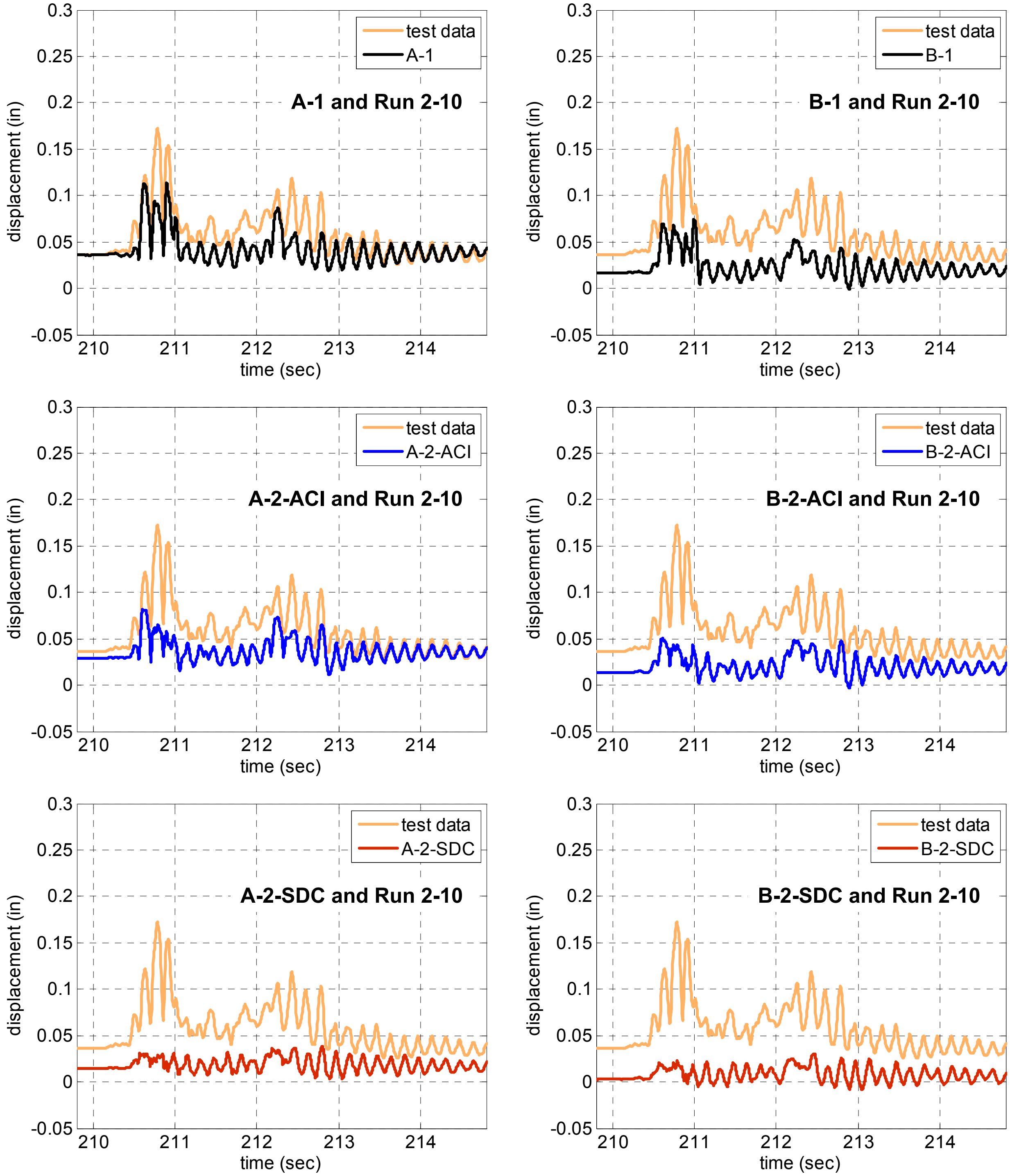

(b) 125% X only

Figure 6.43 Continued

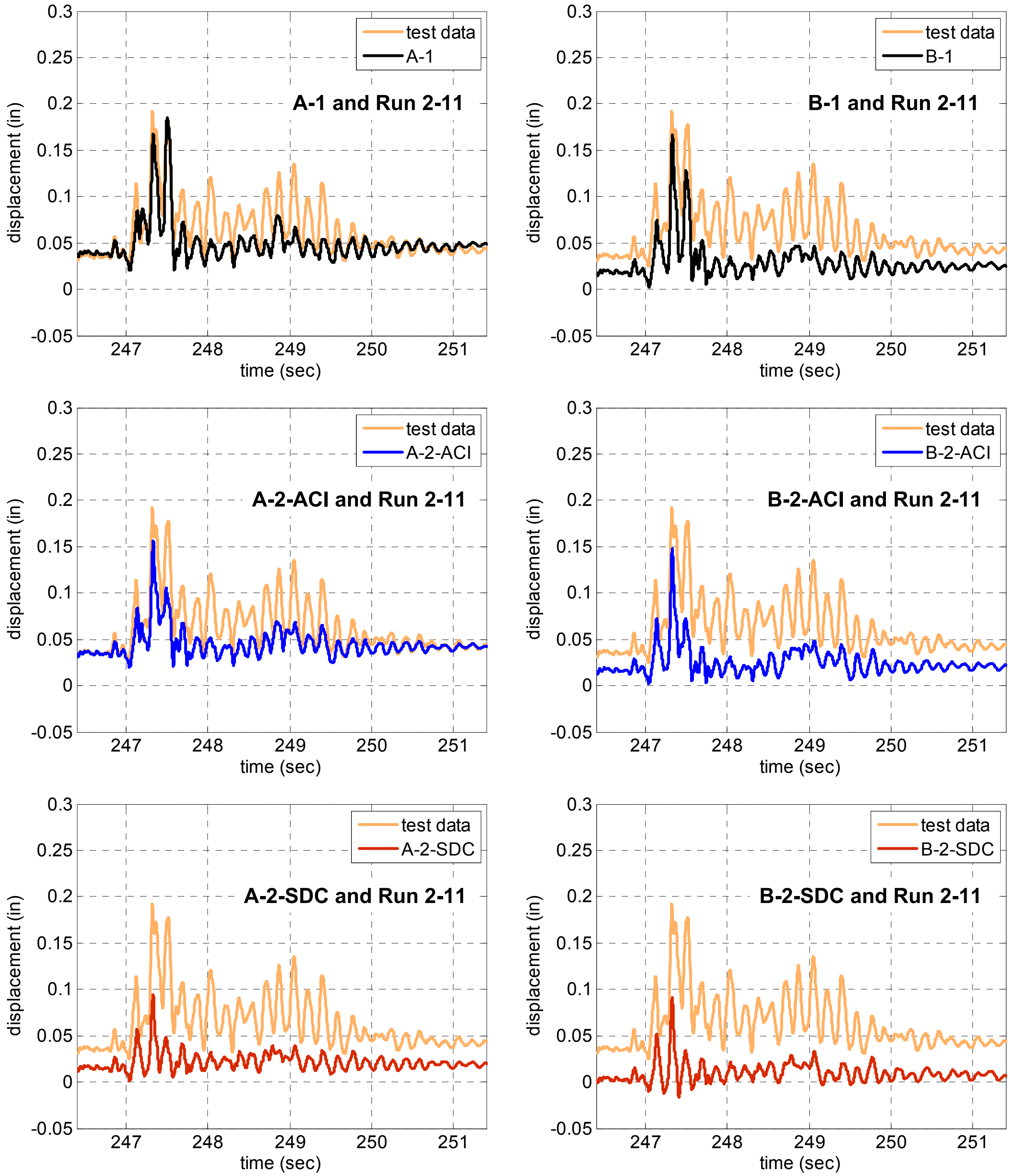

(c) 125% 2nd X+Z

Figure 6.43 Continued.

6.4.2.6 Force-Displacement Relationships

Figures 6.44 and 6.54 present the force-displacement relationship comparisons for SP1 and SP2, respectively, subjected to the 125%-scale motions. The effect of the shear spring in reducing the shear forces is once again observed in these figures. As indicated before, the ACI spring model achieves this reduction in a more accurate manner compared to the SDC spring model, with both springs remaining on the conservative side. The flatness of the top and bottom parts of the relationships for the models with springs indicates the presence of more hardening However, since the shear spring dictates the response in the 125%-scale runs, strain hardening in flexural response becomes ineffective in changing this behavior.

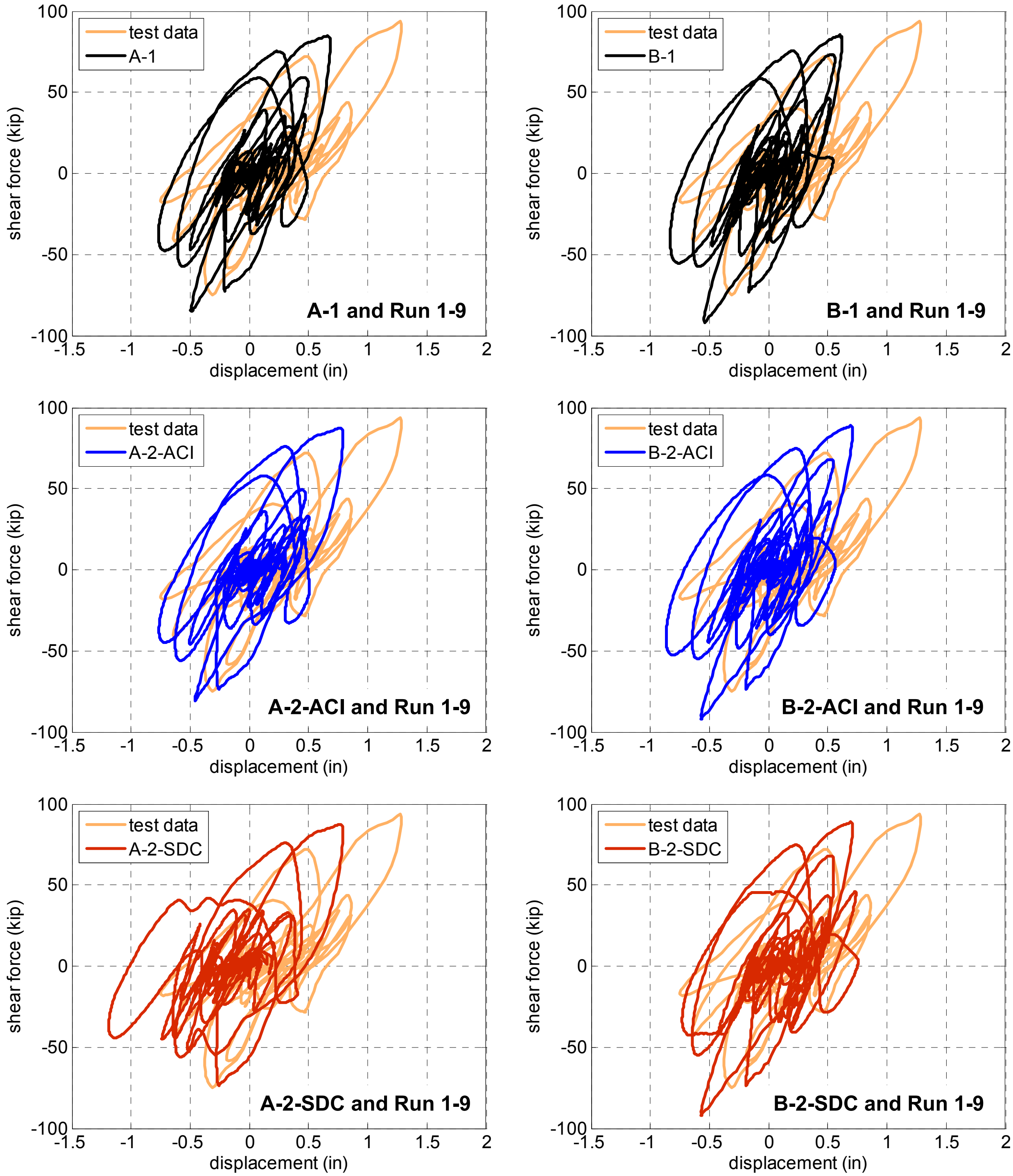

(a) 125% 1st X+Z

Figure 6.44 Comparison of shear force-lateral displacement relationships of SP1 subjected to 125%-scale motions.

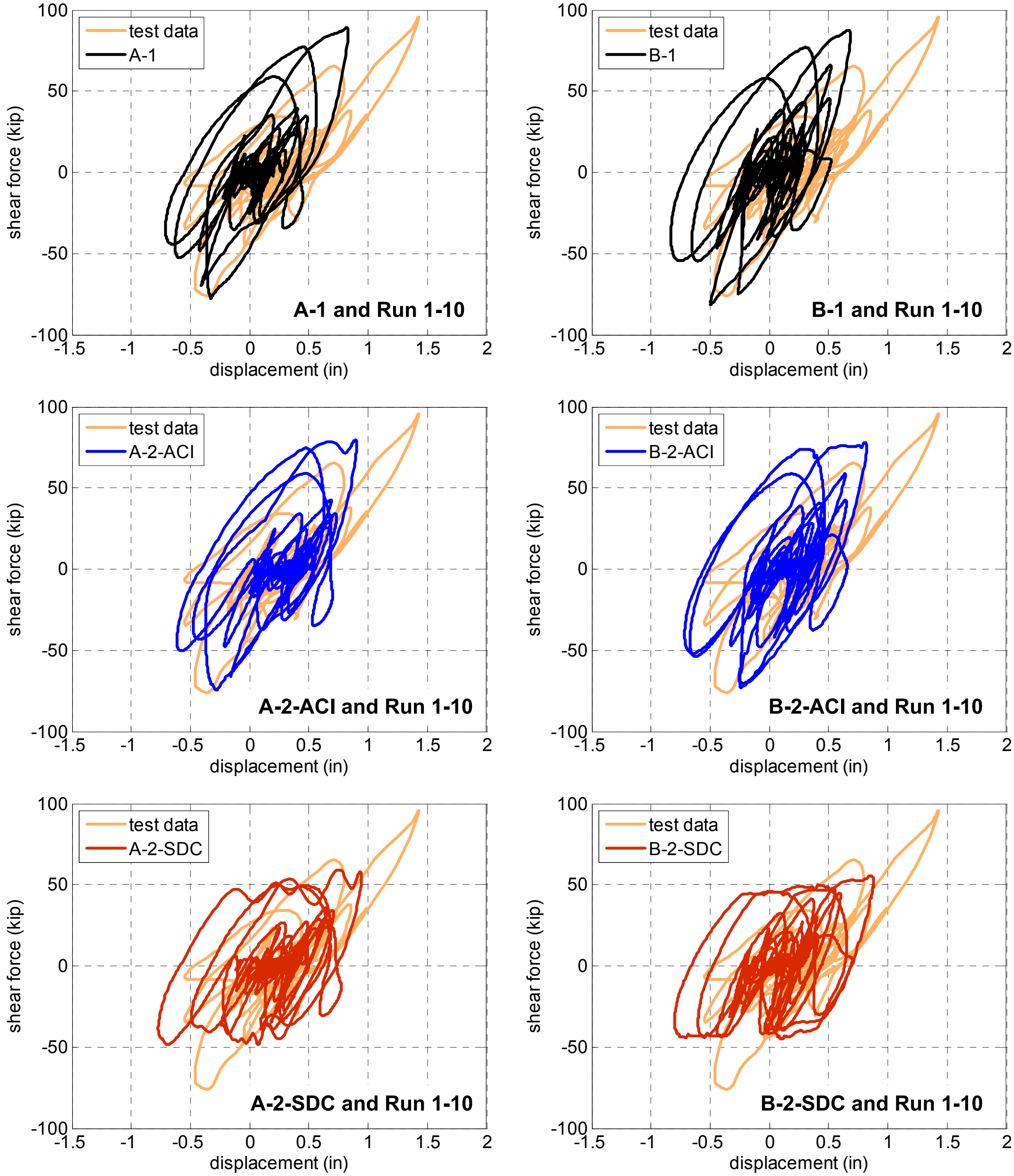

(b) 125% X only

Figure 6.44 Continued.

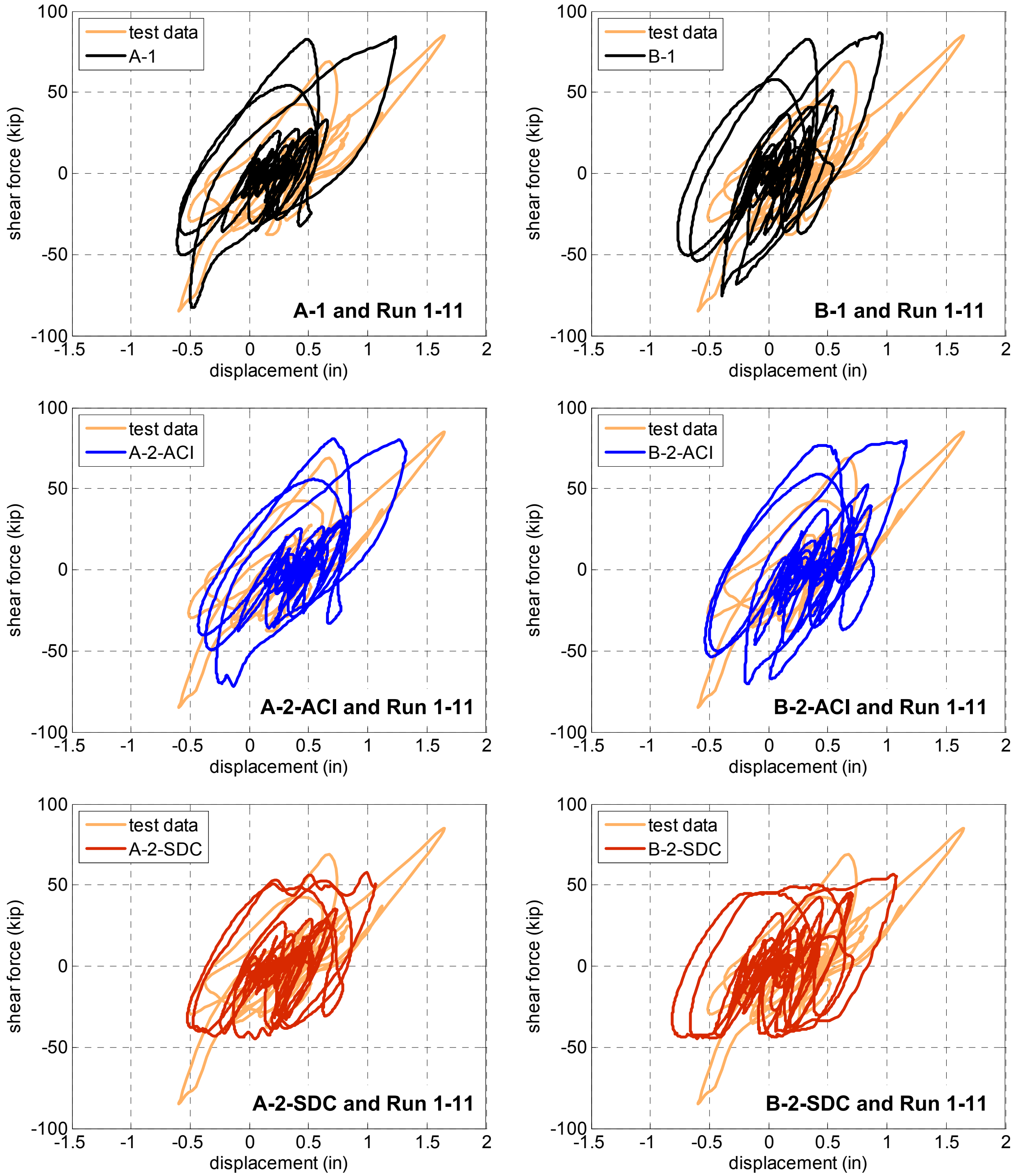

(c) 125% 2nd X+Z

Figure 6.44 Continued.

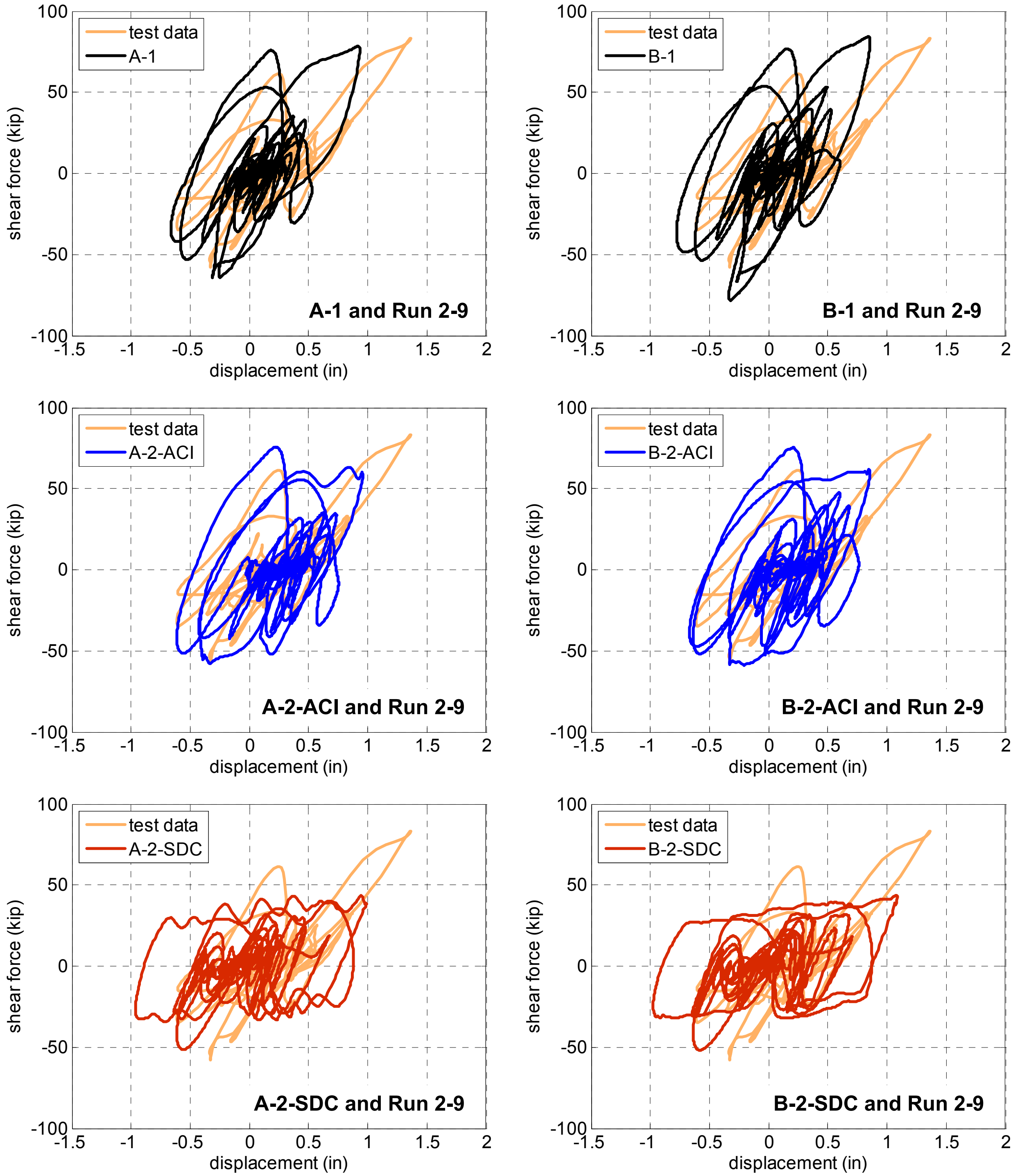

(a) 125% 1st X+Z

Figure 6.45 **Comparison of shear force-lateral displacement relationships of SP2 subjected to 125%-scale motions.**

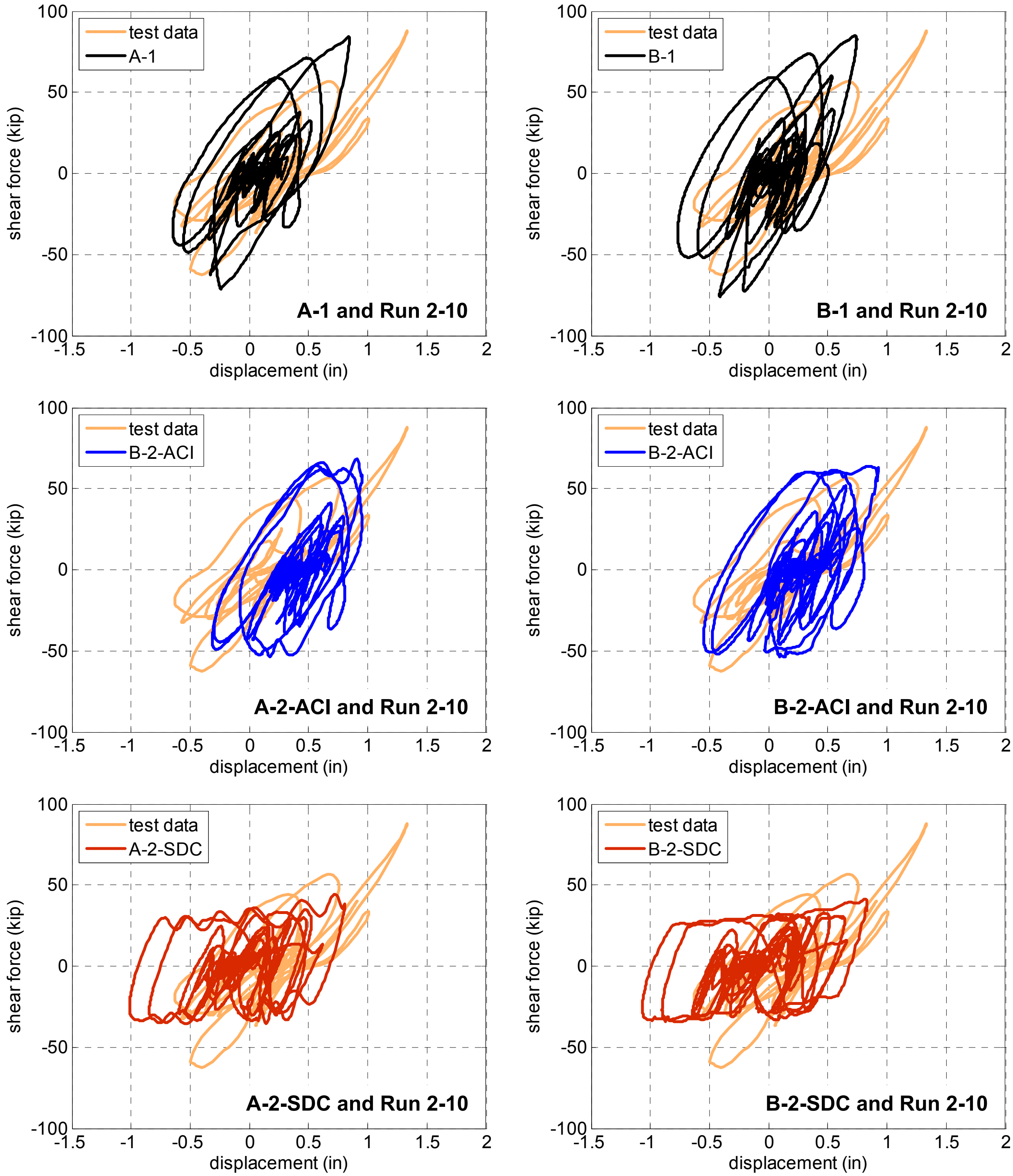

(b) 125% X only

Figure 6.45 Continued.

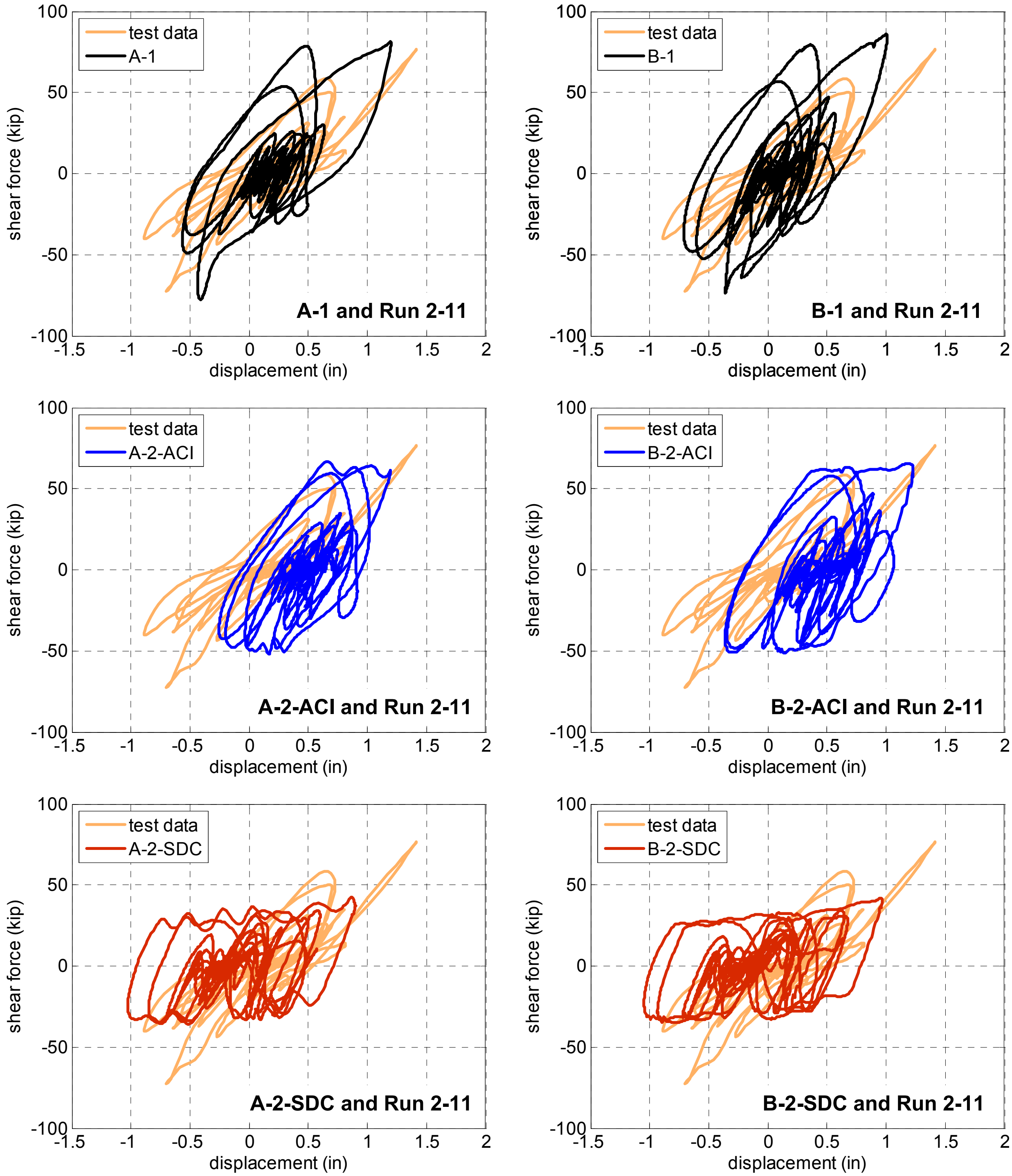

(c) 125% 2nd X+Z

Figure 6.45 Continued.

6.4.3 Local Responses

Local responses were obtained from the predefined sections in Model B with *NLBC* elements. As mentioned in Section 6.3.1.1, two middle sections in a *BWH 1* element were in the elastic range. Instead, *BWH 2* was utilized for local responses; they were similar to the results obtained from Model B. Compared to the test data reported in Appendix F, the curvatures and strains close to the column base reasonably match the experimental data. However, errors are particularly significant for the strains close to the column top. As sample results, the bending moment-curvature relationships of SP1 at h = 60 in. and 10 in. are shown in Figure 6.46. The relationships under 50%- to 125%-scale motions were estimated by B-1, B-2-ACI, and B-2-SDC. All the models provided similar moment-curvature relationships at h = 10 in. or 60 in., and similarly decent results were obtained in estimating the relationships at h = 10 in. The results for the section at h = 60 in., however, did not estimate the response well at all compared to the test data. In particular, the models failed to capture large negative curvatures. Figure 6.47 presents the bending moment-curvature relationships of SP2 at h = 60 in. and 10 in. Like the SP1 cases, the models did not provide a good prediction of large curvature. Since the section at h = 10 in. of SP2 experienced larger curvature than that of SP1, the computational result is not as accurate as that for SP1. However, it is still an improvement over the prediction for the section at h = 60 in.

6.5 SUMMARY

Since existing elements in OpenSees are not suitable to incorporate the code-based shear strength estimation, two shear springs, which adopt the shear strength predictions by the ACI and SDC equations, were developed. The force-displacement relationship of the proposed springs is based on a bilinear envelope, which is defined by the initial stiffness, the yield force, and the hardening ratio for post-yield stiffness. Before yielding, the yield force is updated at each integration time step using the axial force and displacement ductility at that time step. At the time step where the demand reaches the capacity, yielding takes place and the force-displacement relationship follows the post-yield behavior. The yield force is not updated and kept constant afterwards unless the column is subjected to any value of axial tension in the case of the Caltrans SDC spring and a predetermined value of tension fin the case of the ACI spring. The yield force is kept constant after this final modification. Due to some unique features of the SDC equation, its shear strength is estimated as V_s, i.e., the shear resistance of concrete is completely ignored under axial tension.

Two types of computational models were utilized. Model A has a *BWH* element, and Model B had *NLBC* elements for the column. Each model considered columns without shear springs (A-1 and B-1) and with shear springs, designated as A-2-ACI, A-2-SDC, B-2-ACI, and B-2-SDC. For the input motion in X- and Y-directions, the acceleration histories recorded on the shaking table during 50% to 125%-scale tests were used. For the Z-direction, because of the flexibility of the shaking table, the axial force recorded by the load cells (after summation of all four values) was used instead of vertical acceleration. To maintain the dynamic equilibrium, negligible nodal mass was utilized for the Z-direction. The computational results were compared with those obtained from the tests.

The computational models containing *BWH* and *NLBC* elements provided similar results Both models were successful in capturing the shear force and lateral displacement history measured during the tests. They captured the rotational mode effect on the moment at the column top accurately. In shear force and bending moment, the amplitude of each response is generally in the following order: A-1>A-2-ACI>A-2-SDC (or B-1>B-2-ACI>B-2-SDC). The models without the shear springs did not capture the shear strength degradation accurately, whereas the models including ACI and SDC shear springs captured the shear strength degradation due to axial tension. Although both of the models incorporating springs provided results on the conservative side, the ACI shear spring predictions would safely be considered as accurate and SDC shear spring predictions as highly conservative. Note that all the models investigated in this chapter provided reasonable estimations for the lateral displacement response, but they did not for the vertical displacement response. As a result, local responses estimated by each model did not even come close to matching those obtained from the test results.

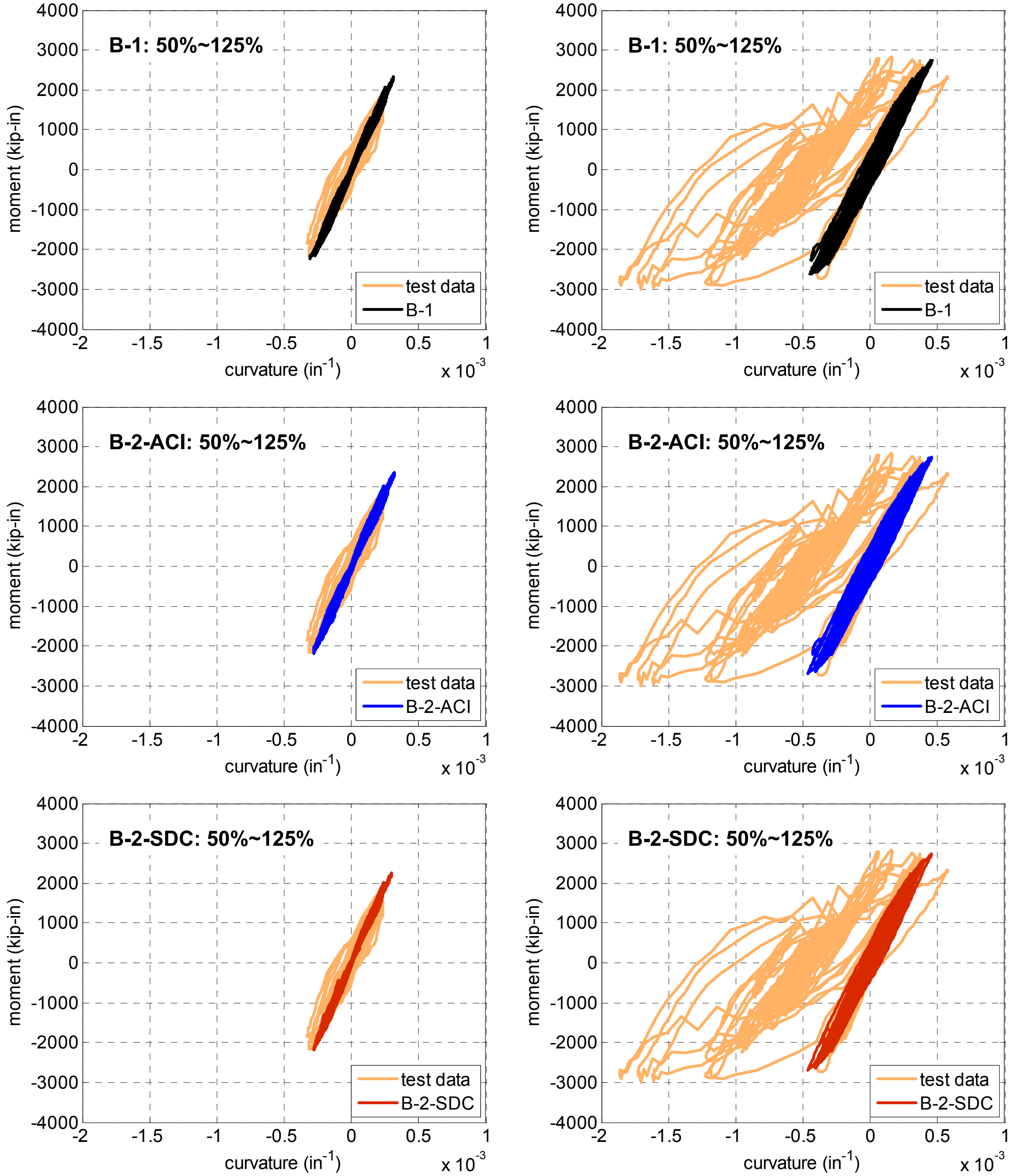

(a) *h*=10”

(b) *h*=60”

Figure 6.46 Comparison of bending moment-curvature relationships at *h* = 10 in. and 60 in. of SP1 under 50%- to 125%-scale motions.

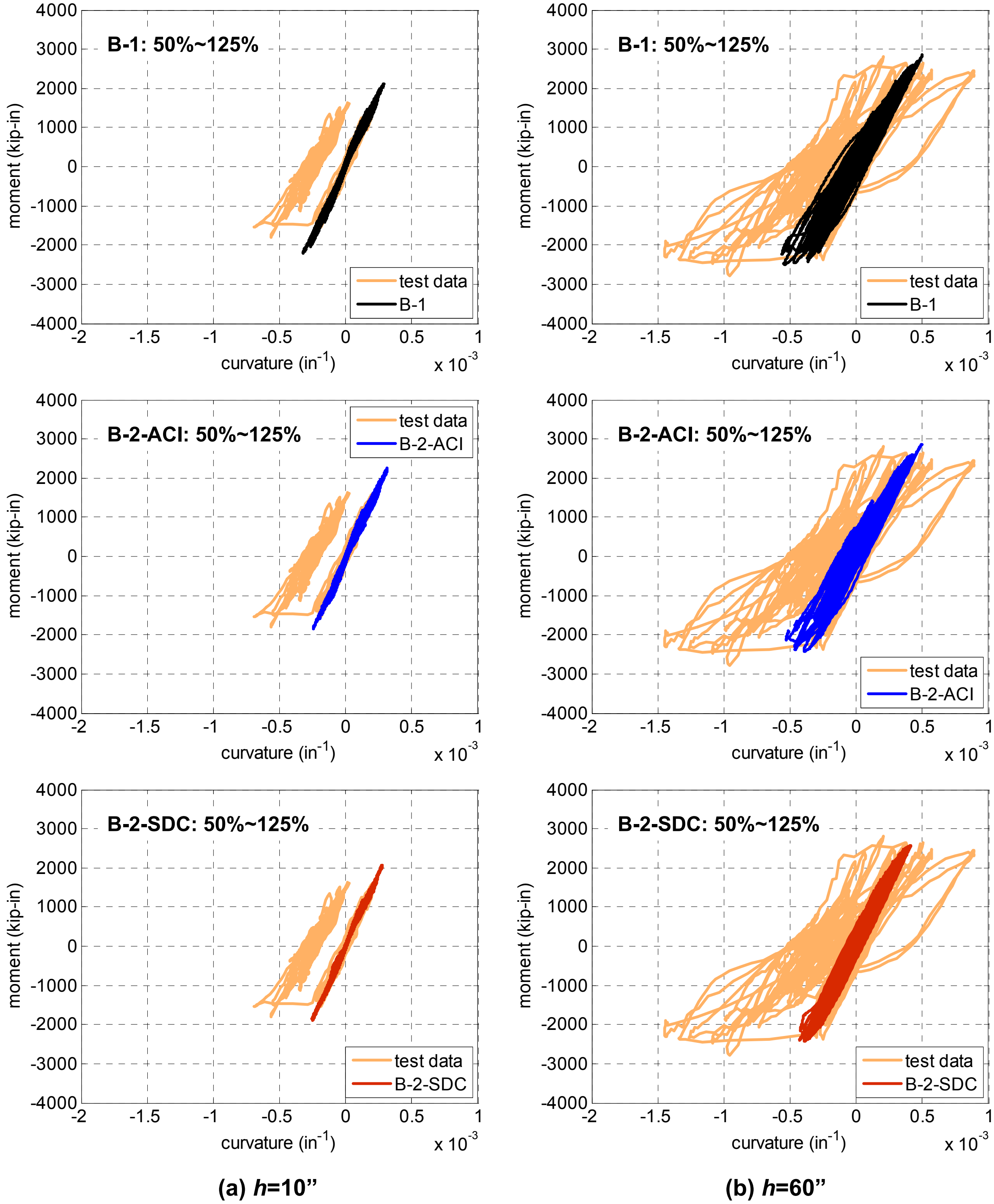

Figure 6.47 Comparison of bending moment-curvature relationships at *h* = 10 in. and 60 in. of SP2 under 50%- to 125%-scale motions.

7 Development and Evaluation of Computational Models

7.1 MAIN CONTRIBUTIONS OF REPORT

Various research projects have been conducted to examine the effect of vertical excitation on reinforced concrete (RC) bridge columns. Field evidence, analytical studies, and static or hybrid simulations suggested that excessive axial tension or tensile strain of the column may lead to shear degradation and that vertical excitation can be the cause of shear failure. However, due to the limitation of current test facilities, the published literature does not report dynamic experiments to investigate the effect of vertical excitation on the shear strength of RC bridge columns. This report provides the experimental and analytical results that confirm that vertical acceleration can result in shear strength degradation of RC structural elements.

Two1/4-geometrical scale specimens (referred to as SP1 and SP2) were constructed and tested on the UC-Berkeley shaking table located at the Richmond Field Station. The two specimens had different transverse reinforcement ratio. Only SP1 satisfied the requirement of Caltrans Bridge Design Specifications. As a result of an extensive analytical investigation and preliminary fidelity tests, 1994 Northridge earthquake acceleration recorded at the Pacoima Dam was selected as an input motion among 3551 earthquake acceleration records in the PEER NGA database. The chosen ground motion was applied to the test specimens at various levels ranging from 5% to 125%. The specimens were subjected to a combination of a vertical component and a single horizontal component in most of the cases. A single horizontal component was also applied in some of the cases (25%-, 50%-, and 125%-scales) to make a direct evaluation of the effect of the vertical excitation.

As part of the computational modeling, a new shear spring model was developed and implemented in the utilized computational platform, OpenSees [2000]. The model was developed in order to incorporate shear strength estimations based on ACI-318-11 or Caltrans SDC equations to address the effect of column axial load and displacement ductility on these estimates according to these two codes provisions.

7.2 MAIN CONCLUSIONS

The conclusions are grouped into two sets. The first set of findings reports on results from the from the experimental investigations. The second set of findings compares the experimental results with the results the analytical modeling.

7.2.1 Global Responses

- The horizontal component of the acceleration on the mass blocks was significantly lower than that recorded at the top of the column. This is a result of the rigid body rotation of the mass blocks due to the rotation at the top of the column. Reduction of the horizontal acceleration increased the bending moment at the top of the column relative to the bending moment at the base.
- The shaking table flexibility had a pronounced effect on the vertical response. The dynamic mode, which was introduced by the shaking table stiffness (in the vertical direction) and its mass, governed the response in the vertical direction. Therefore, the response due to the column's axial mode was reduced compared to the case of a rigid shaking table. However, it should be notes that the flexibility of the shaking table did not affect the current investigation because the mode introduced by the shaking table flexibility had a significantly larger period compared to the column's vertical period. As a matter of fact, the effect of the shaking table flexibility is analogous to the effect of bridge girders in elongating the period of the bridge system compared to the period of a single bridge column.
- Considerable tensile force was induced on the test column due to vertical excitation.
- Tension in the columns resulted in degradation of shear strength, which was mainly due to the degradation of the concrete contribution to shear strength.
- Reduction in the concrete strength was also evidenced by the comparison of shear cracks in the 125%-scale horizontal only and horizontal and vertical tests.
- Flexural damage at the top of the column took place before the flexural damage at the base since the bending moment at the top was larger. This is a result of the large mass moment of inertia at the top of the column. Reduction of the acceleration on the mass block due to the rotations contributed to this situation as well.
- Flexural damage occurred and propagated both at the top and base of the column as the scale of the ground motion increased.
- As a result of flexural yielding both at the top and base of the column bending in double curvature, shear force reached shear capacity, which would not have occurred if yielding had happened at the base and the bending moment at the top was smaller than the yielding bending moment. Shear cracks occurred as a result.
- Tensile force due to vertical excitation reduced the shear strength and increased shear cracks.

7.2.2 Analytical Results

- Developed computational models were successful in capturing the shear force and displacement histories measured during the tests. They captured accurately the rotational mode effect on the bending moment at the column top.
- Investigated computational models, namely "*Beam with Hinges*" (Model A) and "*Nonlinear Beam-Column*" (Model B) provided similar results.
- The dominance of the shaking table flexibility on the vertical response was demonstrated by an elastic dynamic analysis of a two-degrees-of-freedom system that modeled the column and the shaking table together as a structural system.
- Due to the difficulty in modeling the shaking table stiffness, which varies during a test as well as between different intensity tests, measured axial force was directly applied to the computational models. This approach addressed the main purpose of this investigation to evaluate axial tension on the shear capacity and the development of a corresponding computational modeling approach.
- Accurate representation of the vertical displacement response required a more detailed finite element model so that cracking could be modeled. However, because vertical displacement produced by the axial force was the end result of this investigation, which does not change the interaction of axial and shear response; such a detailed finite element model was not considered.
- Both the ACI-218-11 and SDC equations captured the shear strength degradation due to axial force. Both of the equations provided results on the conservative side; the ACI equation predictions could be considered as accurate and SDC equation predictions as highly conservative. (Elimination of the concrete contribution to shear strength under tension was the primary reason for the highly conservative predictions of SDC equation). Strength reduction caused by ductility was not as significant as that by tension.
- The developed shear springs element implemented in OpenSees fulfilled the objectives of the computational modeling for simulating the effect of the axial force on the shear strength.

7.3 SUGGESTED FUTURE EXTENSIONS

The experimental and computational investigation conducted in this study revealed that considerable axial tension can be induced in bridge columns, resulting in degradation in the shear strength. Based on the obtained results, suggestions for future research are:

- Hybrid simulation of an entire bridge system where the column is tested and the rest of the system is computationally modeled is a viable option for the evaluation of axial tension in bridge columns. This approach has three advantages. First, the elongated vertical period due to presence of the bridge deck can be considered. Second, the elimination of a possible shaking table effect on the vertical response can be achieved. Third, modeling the complicated mass assembly in the computer is now possible. The hybrid simulation test can be conducted by using three actuators, where one horizontal actuator is dedicated to the lateral degree-of-freedom and two vertical actuators are dedicated to the lateral and rotational degrees-of-freedom at the top of the column.

- The development of shear springs elements that adopt the ACI and SDC equations based on a bilinear hysteresis relationship. It is recommended to modify the hysteresis model to include strength and stiffness degradation as well as pinching.
- Further investigation of the response of the tested and computationally-modeled columns with a suite of ground motions, e.g., using the PEER NGA database is recommendation. It is possible to generate fragility curves based on three cases: namely, (a) no shear spring: (b) ACI-based shear spring, and (c) SDC-based shear spring.
- Generalization of the developed shear spring can be conducted where coupling between the fiber discretization and the shear behavior can be addressed on a more fundamental level, e.g., using the modified compression field theory (MCFT) [Vecchio and Collins 1986].

REFERENCES

AASHTO (2012). *LRFD Bridge Design Specifications*, 6th Edition, 2010 Interim Revisions, American Association of State and Highway Transportation Officials, Washington, D.C.

ACI Committee 318 (2011). Building Code Requirements for Structural Concrete and Commentary, ACI 318-11, American Concrete Institute, Farmington Hills, MI.

Alves S.W. (2005). *Nonlinear Analysis of Pacoima Dam with Spatially Nonuniform Ground Motion*, PhD Dissertation, California Institute of Technology, Pasadena, CA.

Amirbekian R.V., Bolt B.A. (1998). Spectral comparison of vertical and horizontal seismic strong ground motions in alluvial basins, *Earthq. Spectra*, 14: 573−595.

ASTM (2009). *Standard Test Methods for Tension Testing of Metallic Materials*, ASTM Standard E8/E8M, ASTM International, West Conshohocken, PA.

ASTM (2010). *Standard Practice for Making and Curing Concrete Test Specimens in the Field*, ASTM Standard C31/C31M ,ASTM International, West Conshohocken, PA.

ASTM (2010). *Standard Practice for Sampling Freshly Mixed Concrete*, ASTM Standard C172/C172M, ASTM International, West Conshohocken, PA.

Bentz E.C., Vecchio F.J., Collins M.P. (2006). "Simplified modified compression field theory for calculating shear strength of reinforced concrete elements, *ACI Structural Journal*, 103(4) 614−624.

Bozorgnia Y., Campbell K.W. (2004). The vertical-to-horizontal response spectral ratio and tentative procedures for developing simplified v/h and vertical design spectra, *J. Earthq. Eng.*, 8(2): 175−207.

Bozorgnia Y., Mahin S.A., Brady A.G. (1998). Vertical Response of Twelve Structures Recorded during the Northridge Earthquake, *Earthquake Spectra*, 14(3): 411-432.

Bozorgnia Y., Niazi M. (1993). Distance Scaling of Vertical and Horizontal Response Spectra of the Loma Prieta Earthquake, *Earthq. Eng. Struct. Dyn.*, 22: 695-707.

Caltrans (2013). *Seismic Design Criteria*, SDC-2013, California Department of Transportation, Sacramento, CA.

CEN (1992). *Design of Concrete Structures, Part 1*, European Committee for Standardization, European Standard ENV 1992-1-1, Brussels.

Chopra A.K. (2006). *Dynamics of Structures, Theory and Applications to Earthquake Engineering*, Pearson Prentice Hall, 3rd Edition, Upper Saddle River, NJ.

Collier C.J., Elnashai A.S. (2001). A procedure for combining vertical and horizontal seismic action effects, *J. Earthq. Eng.*, 5(4): 521−539.

Computers and Engineering, Inc. (2006). *SAP2000 Manuals*, Version 11, Berkeley, CA.

CSA (2004). *Design of Concrete Structures (CSA-A23.3-04),* Canadian Standards Association, Rexdale, ON.

Elgamal A., He L. (2004). Vertical earthquake ground motion records: An overview, *J. Earthq. Eng.*, 8(5): 663−697.

Elnashai A.S. (1997). Seismic design with vertical earthquake motion, in: *Seismic Design for the Next Generation of Codes*, P. Fajfar, P. and H. Krawinkler (eds.), Balkema, Rotterdam, pp. 91−100.

Elnashai A.S., Papazoglou A.J. (1997). Procedure and spectra for analysis of RC structures subjected to strong vertical earthquake loads, *J. Earthq. Eng.*, 1(1): 121−155.

Elwood K., Moehle J. (2003). Shake table tests and analytical studies on the gravity load collapse of reinforced concrete frames, *PEER Report 2003/01*, Pacific Earthquake Engineering Research Center, University of California, Berkeley, CA.

FEMA (2000). *Prestandard and Commentary for the Seismic Rehabilitation of Buildings, Report FEMA-356,* Federal Emergency Management Agency, Washington, D.C.

Fenves G.L., Mojtahedi S. (1995). Effect of contraction joint opening on Pacoima Dam in the 1994 Northridge earthquake, *Proceedings, SMIP95 Seminar on Seismological and Engineering Implications of Recent Strong-Motion Data*, pp. 57–68.

Jeong H., Mahin S.A., Sasaki T., Kawashima K. (2008). *Progress Report: Large-scale Tests of a US Bridge Column Using the E-Defense Shaking*, April 2008.

Kawase H., Aki K. (1990). Topography effect at the critical sv-wave incidence: possible explanation of damage pattern by the Whittier Narrows, California, Earthquake of 1 October 1987, *Bull. Seismol. Soc. Am.*, 80: 1–30.

Kawashima K., Ukon H., Kajiwara K. (2007). Bridge seismic response experiment Program using E-Defense, *Proceedings of 39th UJNR Panel on Wind and Seismic Effect*, Technical Memorandum, Public Works Research Institute, Tsukuba Science City, Japan, No. 4075, pp. 57–66.

Kim S.J., Elnashai A.S. (2008). Seismic assessment of RC structures considering vertical ground motion, *MAE Center Report No. 08–03*, Mid-America Earthquake Center, University of Illinois, Urbana-Champagne, IL.

Kunnath S.K., Abrahamson N.A., Chai Y.H., Erduran E., Yilmaz Z. (2008). Development of guidelines for incorporation of vertical ground motion effects in seismic design of highway bridges, *Technical Report*, Contract No. CA/UCD-SESM-08-01, California Department of Transportation, Sacramento, CA.

Mander J.B., Priestley M.J.N., Park R. (1988). Theoretical stress–strain model for confined concrete, ASCE, *J. Struct. Div.,* 114: 1804–1826.

Massone L.M., Orakcal K., Wallace J.W. (2006). Shear-flexure interaction for structural walls, *ACI Special Publication*, 236: 127–150.

Menegotto M., Pinto P. (1973). Method of analysis for cyclically loaded reinforced concrete plane frames including changes in geometry and non-elastic behavior of elements under combined normal force and bending, *Proceedings. IABSE Symposium on Resistance and Ultimate Deformability of Structures Acted on by Well-Defined Repeated Loads*, Final Report, Lisbon, Portugal.

Newmark N.M., Blume J.A., Kapur K.K. (1973). Seismic design spectra for nuclear power plants, ASCE, *J. Power Div.*, 99: 287–303.

Newmark N.M., Hall W.J. (1982). *Earthquake Spectra and Design*, Earthquake Engineering Research Institute, Berkeley, CA.

McKenna F., Fenves G.L., Scott M.H., Jeremic B. (2000). *Open System for Earthquake Engineering Simulation* (*OpenSees*), Pacific Earthquake Engineering Research Center, University of California, Berkeley, CA, http://opensees.berkeley.edu/.

Niazi M., Bozorgnia Y. (1992). Behavior of Near-Source Vertical and Horizontal Response Spectra at SMART-1 Array, Taiwan, *Earthq. Eng. Struct. Dyn.*, 21: 37-50.

Papazoglou A.J., Elnashai A.S. (1996). Analytical and field evidence of the damaging effect of vertical earthquake ground motion, *Earthq. Eng. Struct. Dyn.*, 25: 1109–1137.

Paulay T., Priestley M.J.N. (1992). *Seismic Design of Reinforced Concrete and Masonry Buildings*, John Wiley and Sons, New York.

PEER (2013). PEER-NGA Database**,** Pacific Earthquake Engineering Research Center, University of California, Berkeley, CA,http://peer.berkeley.edu/nga/.

Priestley M.J.N., Benzoti G., Ohtaki T., Seible F. (1996). Seismic performance of circular reinforced concrete columns under varying axial load, *Report-SSRP-96/04*, Division of Structural Engineering, University of California, San Diego, CA.

Priestley M.J.N., Verma R., Xiao Y. (1994). Seismic shear strength of reinforced concrete columns, ASCE, *J. Struct. Eng*., 120(8): 2310–2329.

Sakai J., Unjoh S. (2007). Shake table experiment on circular reinforced concrete bridge column under multidirectional seismic excitation, ASCE, *Proceedings, Structural Engineering Research Frontiers*, pp. 1–12, doi: 10.1061/40944(249)37.

Scott M.H., Fenves G.L. (2006). Plastic hinge integration methods for force of structural engineering, ASCE, *J. Struct. Eng*., 132(2): 244–252.

Silva W. (1997). Characteristics of vertical strong ground motions for applications to engineering design, *Technical Report NCEER-97-0010*, National Center for Earthquake Engineering Research, SUNY, Buffalo, New York.

Talaat M.M., Mosalam K.M. (2008). Computational modeling of progressive collapse in reinforced concrete frame structures, *PEER Report 2007/10*, Pacific Earthquake Engineering Research Center, University of California, Berkeley, CA.

Vecchio F.J., Collins M.P. (1986). The modified compression-field theory for reinforced concrete elements subjected to shear, *ACI Journal*, 83(2): 219–231.

Walraven J.C. (1981). Fundamental analysis of aggregate interlock, *Proceedings*, ASCE, 107(ST11): 2245–2270.

Appendix A: Selected Ground Motions

Table A.1 presents the list of 61 ground motions selected in Section 2.1. It provides the record sequence number, earthquake ID, earthquake name, record date, station name, and peak acceleration values of the three components of each ground motion.

Table A.1 Selected ground motions.

No.	RSN	EQID	Earthquake name	YYYYMMDD	Station name	PGA, unit=*g*		
						H1	H2	V
1	495	0097	Nahanni, Canada	19851223	Site 1	0.9778	1.0957	2.0865
2	181	0050	Imperial Valley-06	19791015	El Centro Array #6	0.4105	0.4390	1.6550
3	126	0041	Gazli, USSR	19760517	Karakyr	0.6083	0.7175	1.2639
4	1051	0127	Northridge-01	19940117	Pacoima Dam (upper left)	1.5849	1.2852	1.2291
5	779	0118	Loma Prieta	19891018	LGPC	0.9663	0.5872	0.8860
6	319	0073	Westmorland	19810426	Westmorland Fire Sta	0.3682	0.4963	0.8380
7	1063	0127	Northridge-01	19940117	Rinaldi Receiving Sta	0.8252	0.4865	0.8343
8	982	0127	Northridge-01	19940117	Jensen Filter Plant	0.5706	1.0239	0.8249
9	879	0125	Landers	19920628	Lucerne	0.7268	0.7892	0.8185
10	825	0123	Cape Mendocino	19920425	Cape Mendocino	1.4973	1.0395	0.7536
11	585	0110	Baja California	19870207	Cerro Prieto	1.3883	0.8904	0.5896
12	3474	0175	Chi-Chi, Taiwan-06	19990925	TCU079	0.6224	0.7743	0.5807
13	407	0080	Coalinga-05	19830722	Oil City	0.8663	0.4471	0.5683
14	949	0127	Northridge-01	19940117	Arleta - Nordhoff Fire Sta	0.3440	0.3081	0.5523
15	752	0118	Loma Prieta	19891018	Capitola	0.5285	0.4433	0.5411
16	1633	0144	Manjil, Iran	19900620	Abbar	0.5146	0.4964	0.5378
17	706	0113	Whittier Narrows-01	19871001	Whittier Narrows Dam upstream	0.2294	0.3160	0.5050
18	959	0127	Northridge-01	19940117	Canoga Park - Topanga Can	0.3558	0.4203	0.4888
19	3475	0175	Chi-Chi, Taiwan-06	19990925	TCU080	0.5376	0.4688	0.4800
20	540	0101	N. Palm Springs	19860708	Whitewater Trout Farm	0.4922	0.6121	0.4712
21	1507	0137	Chi-Chi, Taiwan	19990920	TCU071	0.5669	0.6548	0.4487
22	459	0090	Morgan Hill	19840424	Gilroy Array #6	0.2222	0.2920	0.4050
23	802	0118	Loma Prieta	19891018	Saratoga - Aloha Ave	0.5125	0.3242	0.3893
24	230	0056	Mammoth Lakes-01	19800525	Convict Creek	0.4165	0.4416	0.3881
25	149	0048	Coyote Lake	19790806	Gilroy Array #4	0.2481	0.2710	0.3873
26	189	0050	Imperial Valley-06	19791015	SAHOP Casa Flores	0.2874	0.5060	0.3793
27	95	0031	Managua, Nicaragua-01	19721223	Managua, ESSO	0.4213	0.3373	0.3766
28	1085	0127	Northridge-01	19940117	Sylmar - Converter Sta East	0.8283	0.4930	0.3765
29	810	0118	Loma Prieta	19891018	UCSC Lick Observatory	0.4502	0.3946	0.3673
30	619	0113	Whittier Narrows-01	19871001	Garvey Res. - Control Bldg	0.3836	0.4568	0.3619
31	418	0082	Coalinga-07	19830725	Coalinga-14th & Elm (Old CHP)	0.4311	0.7325	0.3324
32	412	0080	Coalinga-05	19830722	Pleasant Valley P.P. - yard	0.6020	0.3268	0.3165
33	952	0127	Northridge-01	19940117	Beverly Hills - 12520 Mulhol	0.6169	0.4444	0.3142
34	265	0064	Victoria, Mexico	19800609	Cerro Prieto	0.6212	0.5873	0.3043
35	1042	0127	Northridge-01	19940117	N Hollywood - Coldwater Can	0.2982	0.2707	0.2894
36	1006	0127	Northridge-01	19940117	LA - UCLA Grounds	0.2779	0.4738	0.2650
37	235	0057	Mammoth Lakes-02	19800525	Mammoth Lakes H. S.	0.4407	0.3895	0.2644
38	1620	0138	Duzce, Turkey	19991112	Sakarya	0.0160	0.3764	0.2590
39	232	0056	Mammoth Lakes-01	19800525	Mammoth Lakes H. S.	0.3211	0.2392	0.2527
40	372	0077	Coalinga-02	19830509	Anticline Ridge Free-Field	0.5763	0.6733	0.2496
41	1645	0145	Sierra Madre	19910628	Mt Wilson - CIT Seis Sta	0.2760	0.2001	0.2372
42	185	0050	Imperial Valley-06	19791015	Holtville Post Office	0.2526	0.2208	0.2301
43	1642	0145	Sierra Madre	19910628	Cogswell Dam - Right	0.3020	0.2641	0.2275

No.	RSN	EQID	Earthquake name	YYYYMMDD	Station name	PGA, unit=*g*		
						H1	H2	V
					Abutment			
44	809	0118	Loma Prieta	19891018	UCSC	0.3112	0.3862	0.2266
45	1520	0137	Chi-Chi, Taiwan	19990920	TCU088	0.5223	0.5084	0.2224
46	398	0079	Coalinga-04	19830709	Oil City	0.3868	0.3705	0.2103
47	1617	0138	Duzce, Turkey	19991112	Lamont 375	0.9701	0.5137	0.1934
48	589	0113	Whittier Narrows-01	19871001	Alhambra - Fremont School	0.3327	0.4137	0.1899
49	248	0061	Mammoth Lakes-06	19800527	Convict Creek	0.2658	0.3156	0.1884
50	264	0063	Mammoth Lakes-08	19800531	USC McGee Creek Inn	0.5316	0.1840	0.1795
51	1623	0139	Stone Canyon	19720904	Melendy Ranch	0.4798	0.5153	0.1734
52	71	0030	San Fernando	19710209	Lake Hughes #12	0.3658	0.2828	0.1673
53	1009	0127	Northridge-01	19940117	LA - Wadsworth VA Hospital North	0.2526	0.2536	0.1630
54	2622	0172	Chi-Chi, Taiwan-03	19990920	TCU071	0.3803	0.1945	0.1425
55	395	0079	Coalinga-04	19830709	Anticline Ridge Pad	0.3775	0.2611	0.1370
56	708	0114	Whittier Narrows-02	19871004	Altadena - Eaton Canyon	0.2644	0.1990	0.1217
57	394	0079	Coalinga-04	19830709	Anticline Ridge Free-Field	0.3300	0.2746	0.1146
58	683	0113	Whittier Narrows-01	19871001	Pasadena - Old House Rd	0.2314	0.2576	0.1019
59	2942	0174	Chi-Chi, Taiwan-05	19990922	CHY024	0.2626	0.2391	0.1003
60	714	0114	Whittier Narrows-02	19871004	LA - Obregon Park	0.3741	0.2606	0.0985
61	380	0077	Coalinga-02	19830509	Oil Fields - Skunk Hollow	0.3129	0.3428	0.0822

Appendix B: Construction Photographs and Specimen Installation

B.1 CONSTRUCTION PROCEDURES

Two specimens were constructed from July 8 to July 28, 2010 at the Richmond Field Station. Table B.1 summarizes the sequence of construction. The photographs taken at each step are shown in Figures B.1 to B.4.

First, forms for footings were made [Figure B.1(a)] and the steel cages were woven. In the main, top, bottom, and transverse reinforcement formed the cage [Figure B.1(b)]. Because the longitudinal reinforcing bars and hoops of the column were embedded into the footing, they were also included in the construction of the cages [Figure B.1(c) and (d)]. Eighteen strain gages per specimen were installed on the longitudinal reinforcing bars prior to constructing the cages. Second, the formwork for footings was completed [Figure B.2(a)], and the concrete mix specified in Section 3.4.3.1 was placed into the forms [Figure B.2(b)]. After leveling the footing surface [Figure B.2(c)], the footings were watered and covered by plastic. Third, hoops were placed around the column longitudinal reinforcing bars. SP1 had 2 in. spacing and SP2 had 3 in. spacing. The strain gages on the longitudinal reinforcing bars were attached inward to avoid damage that might occur when placing the hoops. Subsequently, gages for transverse strain were installed on the hoops [Figure B.3(a)].

Table B.1 Construction process.

Date	Items
July 8~10	Strain gages on longitudinal reinforcing bars installed
July 15~16	Footing reinforcing bars completed
July 20	Footing concrete mix placed
July 21	Hoops in-place
July 21~22	Strain gages on hoops installed
July 23	Sonotube, top block forms in-place
July 27	Top block rebars completed
July 28	Column concrete mix placed

(a) bottom reinforcement

(b) top and transverse reinforcement

(c) column hoops

(d) longitudinal reinforcement of the column

Figure B.1 Footing construction: reinforcement.

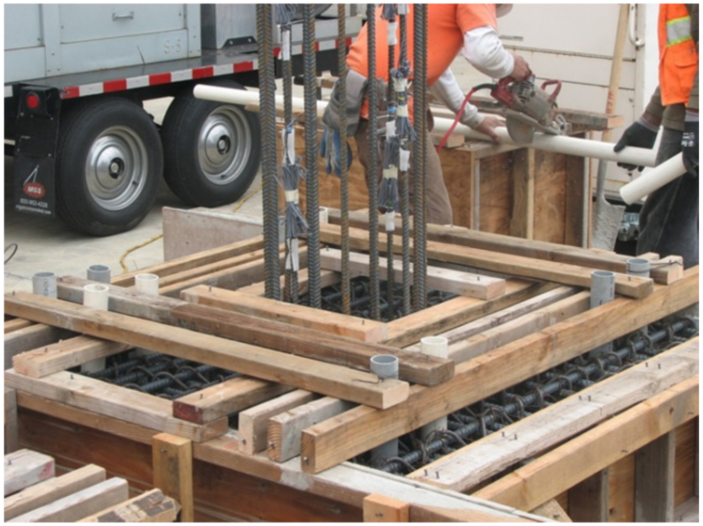

(a) finishing formwork

(b) placing concrete mix

(c) leveling footing surface

(d) finished footing surface

Figure B.2 Footing construction: placing concrete.

(a) strain gages on column reinforcement

(b) formwork for top block

(c) top block form

(d) top block reinforcement

Figure B.3 Column and top block construction: reinforcement.

(a) placing concrete mix

(b) leveling top block surface

(c) finished top block surface

(d) test cylinders

Figure B.4 Column and top block construction: placing concrete.

B.2 SET-UP PROCEDURES

To hold the test specimen and the mass blocks on the shaking table, a base plate and four steel beams were added to the test setup. The specimen cannot be held at the center of the shaking table with the existing system unless the footing size is increased. If the specimen is off the center, an erroneous result is expected with high probability. If the footing size is increased, it causes overweight on the shaking table and lowers the maximum applicable intensity of an input motion. A thick steel plate is an alternative to put the specimen at the center without adding significant weight on the table. Figure B.5(a) shows the base plate fixed to the shaking table. Four load cells were attached to the plate and the specimen was supported on them [Figure B.5(b)]. Load cells between the plate and the specimen capture the force below the specimen. The steel beams shown in Figure B.5(c) and (d) were connected to the specimen by prestressing rods. They supported the concrete blocks and lead blocks.

In Figure B.6, the procedure of hanging the lead blocks and putting the concrete blocks on the specimen is presented. As shown in Figure B.6, total of three bundles of lead blocks were hung from each beam. Each bundle had different numbers of lead blocks as discussed in Section 3.5.1.4. The closest bundle to the specimen has 4, the middle one had 6, and the farthest has 8 blocks. Each bundle was assembled outside of the shaking table and moved by the overhead crane. Finally, it was hung by four prestressing rods at the tip of 6×4 tubes. After hanging the lead blocks, two concrete blocks were placed on the specimen. The prestressing rods through the beams and the concrete blocks provided fixation of these concrete blocks during the test. To ensure integration and avoid the damage of the concrete blocks, grout was applied between the beams and the bottom concrete block, and between the concrete blocks themselves [Figure B.6(c)]. Finally, another concrete block was added as shown in Figure B.6(d), and the prestressing rods were tightened.

(a) connecting base plate to the table

(b) installing load cells and the specimen on the base plate

Figure B.5 Test set-up before adding mass blocks.

(a) hanging lead blocks

(b) installing the first concrete block on the specimen

(c) grouting between the beam and the concrete block

(d) installing the second concrete block

Figure B.6 Adding mass blocks to the test set-up.

Appendix C: Design Drawings and Details

C.1 SPECIMEN DRAWINGS

Drawings for the test set-up and specimens are presented here. Figure C.1 shows the schematic drawing of the test set-up. Height of the setup height was about 13 ft, from the base plate to the concrete blocks. The specimen height was 9 ft 4 in, including its footing and top block. As shown in Figure C.2, the two specimens were identical except for the hoop spacing. The top block was 45° off compared to the footing, and the steel beams shown in Figure C.6 were connected to this top block by prestressing rods. Figures C.3 and C.4 present the details of the reinforcement for the top block and footing.

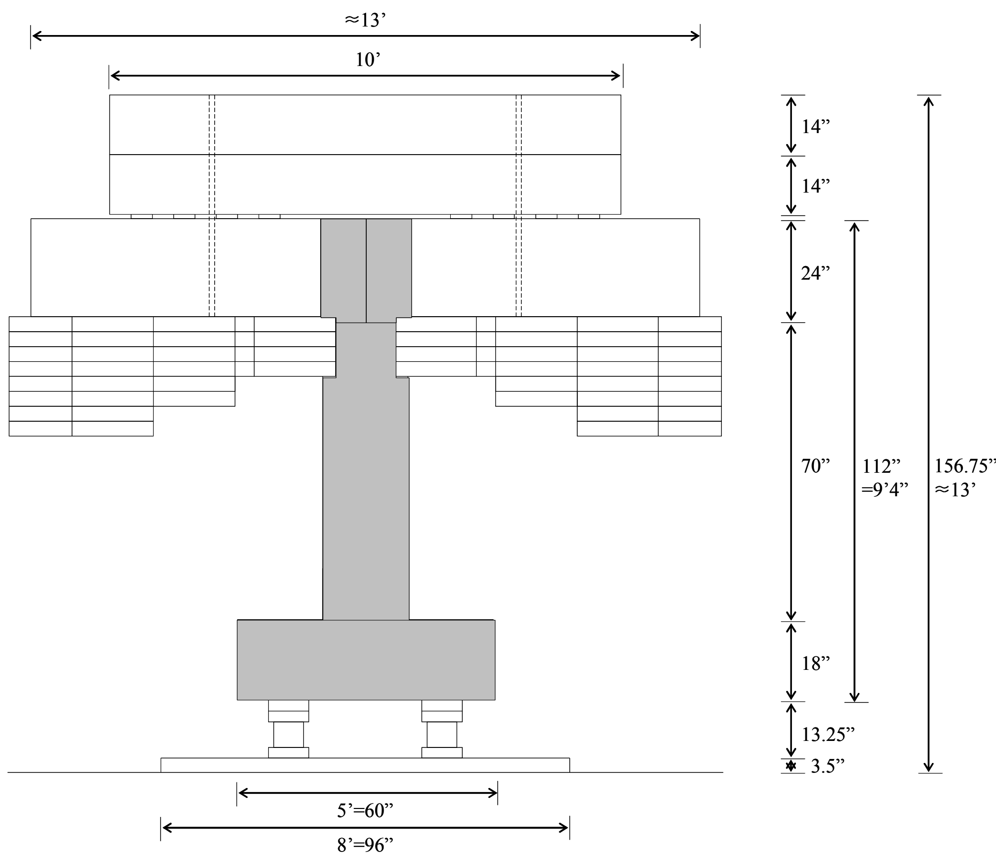

Figure C.1 Schematic drawing of test set-up.

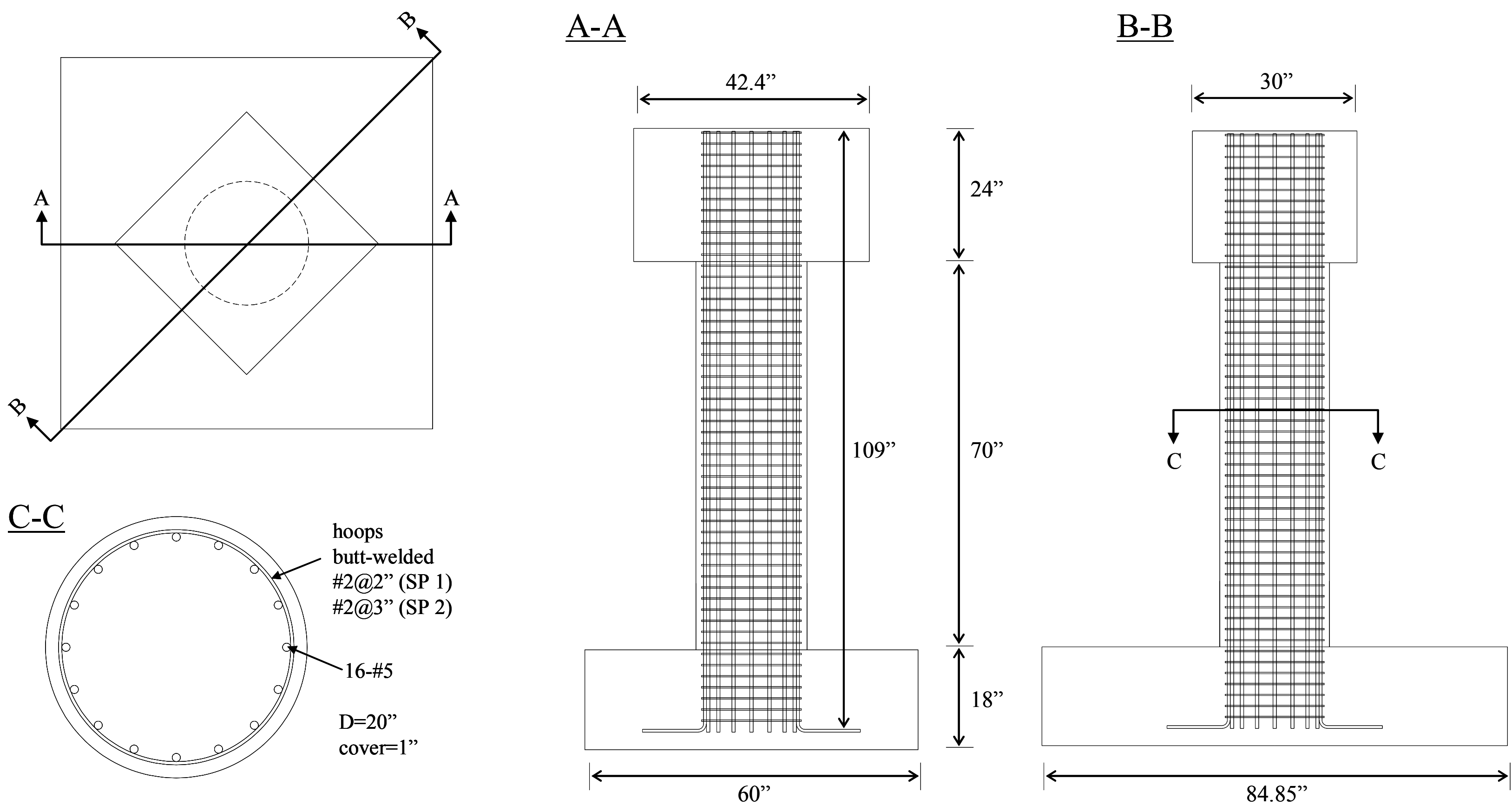

Figure C.2 Column cross section and reinforcement.

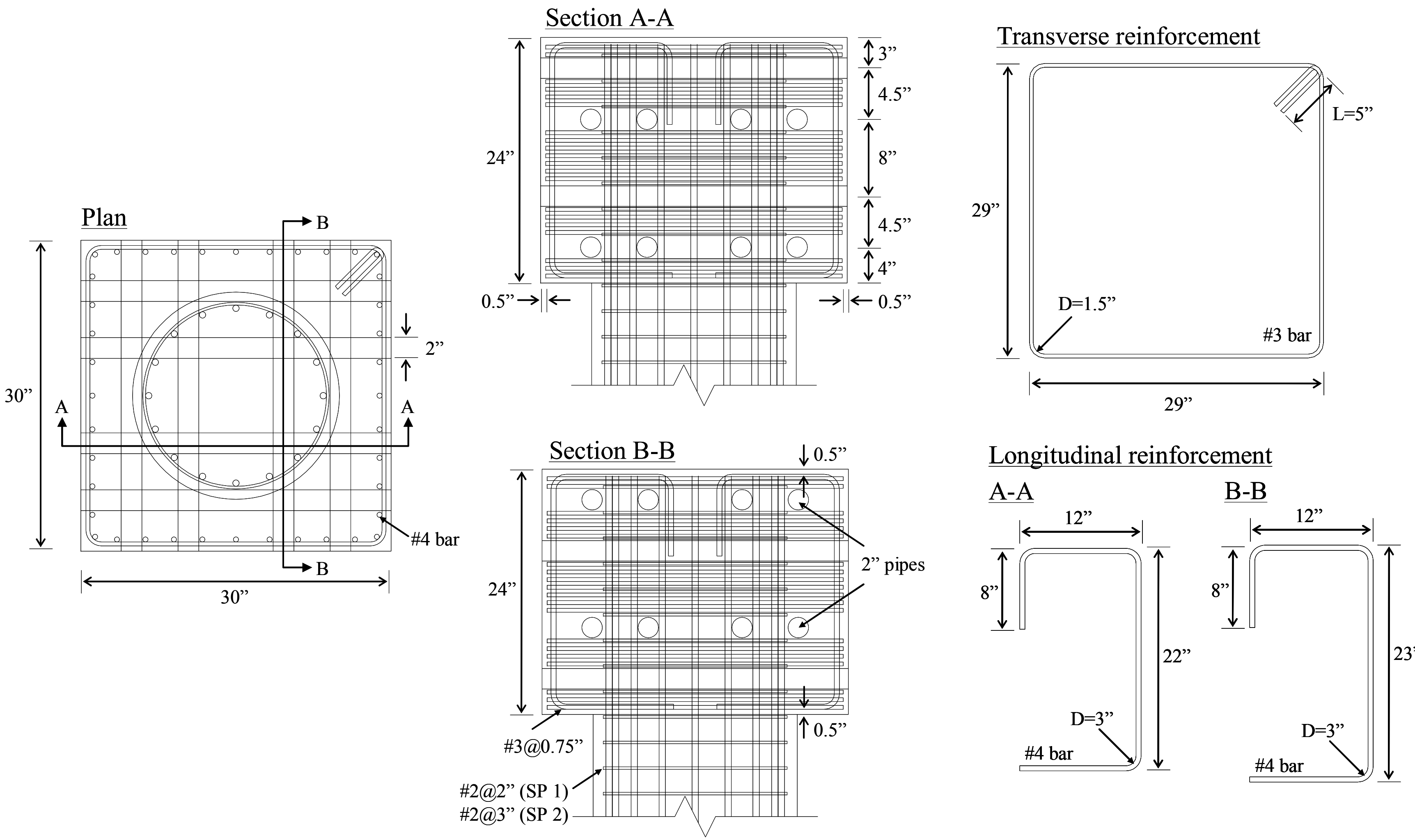

Figure C.3 Top block plan, cross sections, and reinforcement.

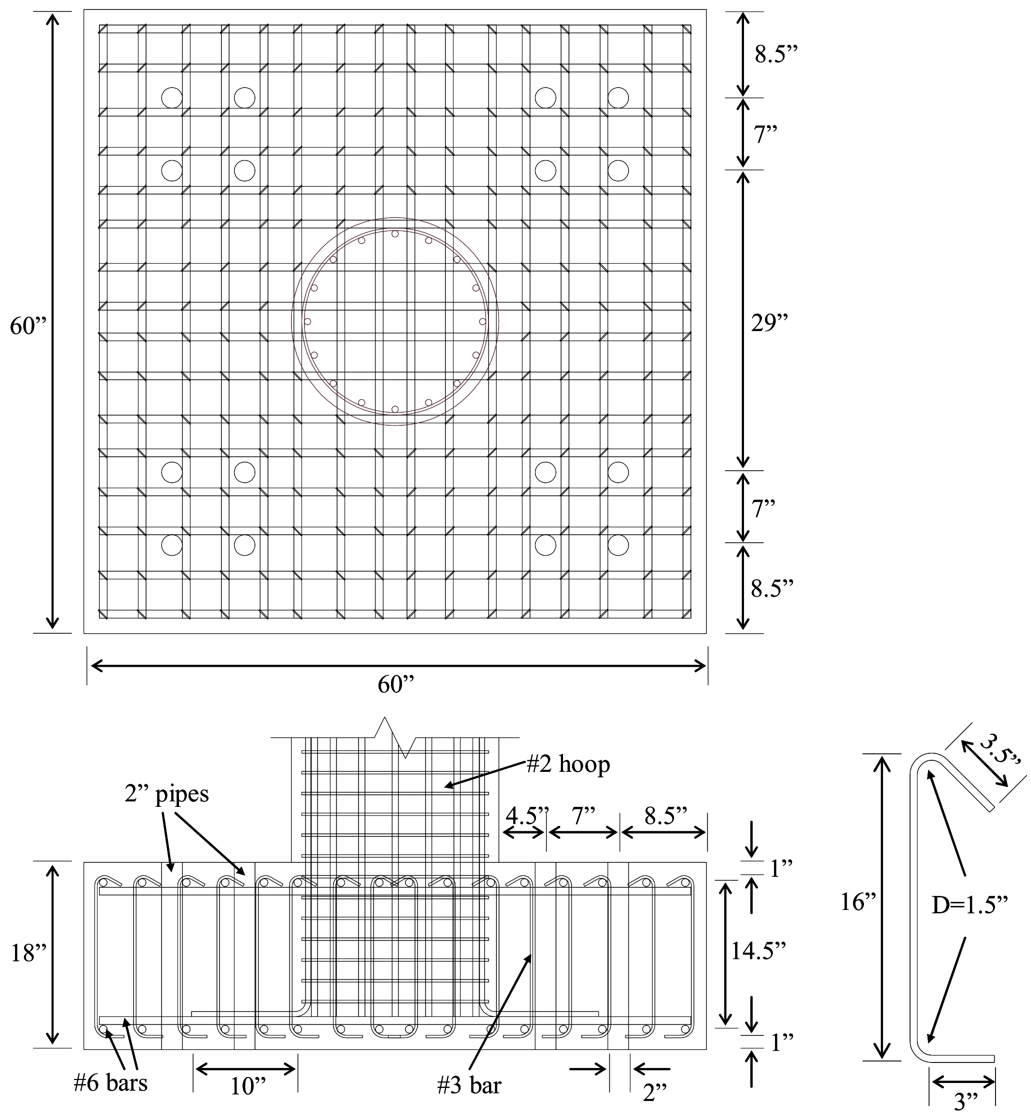

Figure C.4 Footing plan, cross section, and reinforcement.

C.2 DESIGN OF BASE PLATE AND TOP STEEL BEAMS

A base plate was designed to seat the test specimen at the center of the shaking table. Nine 2.5-in. holes and sixteen 7/8 in. tap holes were drilled on an 8 ft×8 ft×3.35 in. steel plate consisting of ASTM A36 steel. Figure C.5 specifies the location of these holes. Nine 2.5-in. holes connected the plate to the shaking table and sixteen 7/8 in. tab holes connected the load cells to the plate, centering the specimen on the shaking table.

A total of four steel beams were designed to support the concrete blocks and to hang the lead blocks, as shown in Figure C.6. Six hangers, HSS6×4×1/2 tubes, were welded to the beam, a HSS12×20×1/2 tube. Four thick plates were welded to the hangers to fill the gap between concrete blocks and hangers. The beam length was 8 ft. and its depth was about 27 in from the top plate to the bottom of the HSS12×20. In the middle of the big tube, there was a 3-in. hole for the prestressing rod, which held the concrete blocks in place during excitation. Because the beams were connected by horizontal steel rods through the top block of the test specimen, the beams in the opposite sides should include holes at the same location. For this reason, NE and SW beams were identical (as were the NW and SE beams). The weight per one beam was about 2.36 kips.

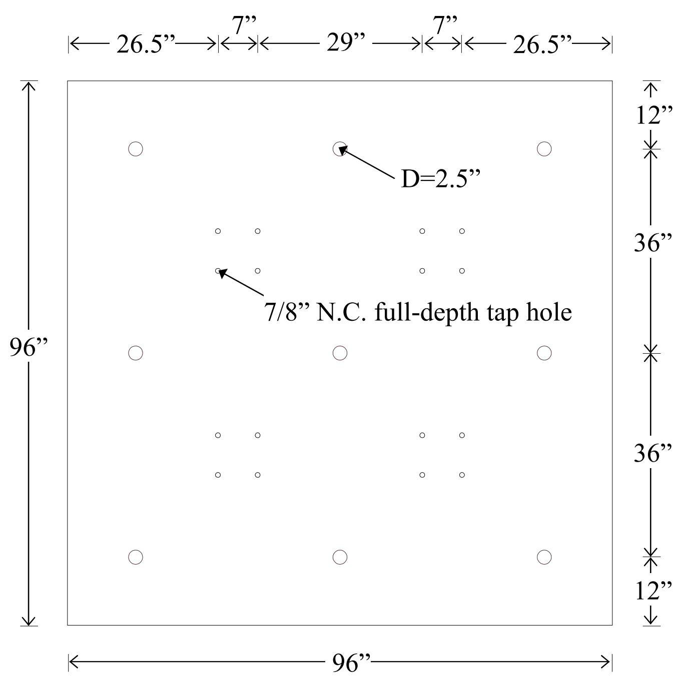

Figure C.5 Base plate plan.

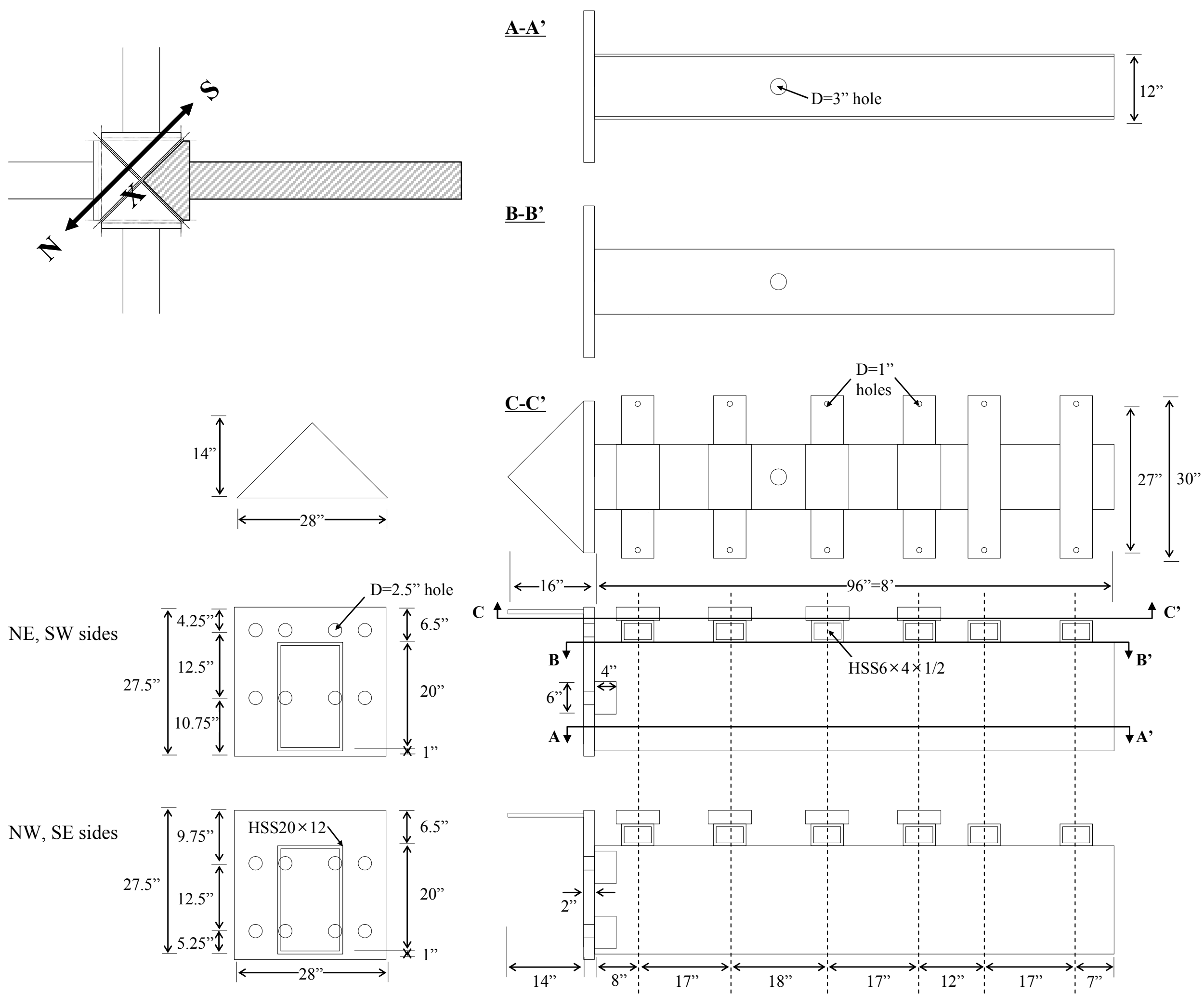

Figure C.6 Top steel beam plan, elevations, and cross sections.

Appendix D: Instrumentation Details and Location

This section describes the channels and measuring instruments used in a series of tests. A total of 137 channels were used, including 16 default channels for the actuators under the shaking table. Other channels were used to obtain strains, forces, accelerations, and displacements over the specimen and set-up. Section D.1 provides the list of all channels and specifies the channel name, type of measurement, location, etc. Section D.2 presents the removed channels during the tests. Section D.3 provides drawings that show the location of each measuring instrument.

D.1 CHANNEL LIST

The channels used in the tests are summarized in Table D.1.

Table D.1 Channel description.

No.	Name	Type	Location	Note
1	H1O	Default measurement below the table (displacement)	South side actuator	displacement (Y-dir)
2	H2O		East side actuator	displacement (X-dir)
3	H3O		North side actuator	displacement (Y-dir)
4	H4O		West side actuator	displacement (X-dir)
5	V1O		SE corner actuator	displacement (Z-dir)
6	V2O		NE corner actuator	
7	V3O		NW corner actuator	
8	V4O		SW corner actuator	
9	H1-2	Default measurement below the table (acceleration)	East side actuator	acceleration (Y-dir)
10	H3-4		West side actuator	acceleration (X-dir)
11	H4-1		South side actuator	acceleration (Y-dir)
12	H2-3		North side actuator	acceleration (X-dir)
13	V1ACC		SE corner actuator	acceleration (Z-dir)
14	V2ACC		NE corner actuator	
15	V3ACC		NW corner actuator	
16	V4ACC		SW corner actuator	
17	SE LC1SX	Load cell	SE corner below the footing	shear force (X-dir)
18	SE LC1SY			shear force (Y-dir)
19	SE LC1Ax			axial force (Z-dir)
20	NE LC2SX		NE corner below the footing	shear force (X-dir)
21	NE LC2SY			shear force (Y-dir)
22	NE LC2Ax			axial force (Z-dir)
23	NW LC3SX		NW corner below the footing	shear force (X-dir)
24	NW LC3SY			shear force (Y-dir)
25	NW LC3Ax			axial force (Z-dir)
26	SW LC4SX		SW corner below the footing	shear force (X-dir)
27	SW LC4SY			shear force (Y-dir)
28	SW LC4Ax			axial force (Z-dir)
29	Accel1X	3D Accelerometer	SE corner on the base plate	acceleration (X-dir)
30	Accel1Y			acceleration (Y-dir)
31	Accel1Z			acceleration (Z-dir)
32	Accel2X		NE corner on the base plate	acceleration (X-dir)
33	Accel2Y			acceleration (Y-dir)
34	Accel2Z			acceleration (Z-dir)
35	Accel3X		NW corner on the base plate	acceleration (X-dir)
36	Accel3Y			acceleration (Y-dir)
37	Accel3Z			acceleration (Z-dir)
38	Accel4X		SW corner on the base plate	acceleration (X-dir)
39	Accel4Y			acceleration (Y-dir)

No.	Name	Type	Location	Note
40	Accel4Z			acceleration (Z-dir)
41	Accel5X		SE corner on the mass blocks	acceleration (X-dir)
42	Accel5Y			acceleration (Y-dir)
43	Accel5Z			acceleration (Z-dir)
44	Accel6X		NE corner on the mass blocks	acceleration (X-dir)
45	Accel6Y			acceleration (Y-dir)
46	Accel6Z			acceleration (Z-dir)
47	Accel7X		NW corner on the mass blocks	acceleration (X-dir)
48	Accel7Y			acceleration (Y-dir)
49	Accel7Z			acceleration (Z-dir)
50	Accel8X		SW corner on the mass blocks	acceleration (X-dir)
51	Accel8Y			acceleration (Y-dir)
52	Accel8Z			acceleration (Z-dir)
53	Accel9Z	1D Accelerometer	North side, *h* = 0 in.	acceleration (Z-dir)
54	Accel10Z		North side, *h* = 5 in.	
55	Accel11Z		North side, *h* = 15 in.	
56	Accel12Z		North side, *h* = 25 in.	
57	Accel13Z		Center on the mass blocks	
58	Accel14Z		North side, *h* = 45 in.	
59	Accel15Z		North side, *h* = 55 in.	
60	Accel16Z		North side, *h* = 65 in.	
61	NovoT1	Novotechnik	North side, *h* = 0~5 in.	displacement (Z-dir)
62	NovoT2		North side, *h* = 5~15 in.	
63	NovoT3		North side, *h* = 15~25 in.	
64	NovoT4		North side, *h* = 25~35 in.	
65	NovoT5		North side, *h* = 35~55 in.	
66	NovoT6		North side, *h* = 55~65 in.	
67	NovoT7		North side, *h* = 65~70 in.	
68	NovoT8		South side, *h* = 0~5 in.	
69	NovoT9		South side, *h* = 5~15 in.	
70	NovoT10		South side, *h* = 15~25 in.	
71	NovoT11		South side, *h* = 25~35 in.	
72	NovoT12		South side, *h* = 55~65 in.	
73	NovoT13		South side, *h* = 65~70 in.	
74~ 111	SG1~38	Strain gage	Longitudinal re-bars and hoops	
112	NovoT14	Novotechnik	South side, *h* = 35~55 in.	displacement (Z-dir)
113	W Vrt.DCDT	DCDT	West side, *h* = 70 in.	displacement (Z-dir)
114	WP1	Wire potentiometer	North, below the mass blocks	displacement (Z-dir)
115	WP2		South, below the mass blocks	
116	WP3		East, below the mass blocks	
117	WP4		West, below the mass blocks	
118	WP5		South, footing, *h* = 0 in.	displacement (X-dir)

No.	Name	Type	Location	Note
119	WP6		South, footing, h = 0 in.	
120	WP7		South, column, h = 15 in.	
121	WP8		South, column, h = 35 in.	
122	WP9		South, column, h = 55 in.	displacement (X-dir)
123	WP10		South, column, h = 70 in.	
124	WP11		South, mass block	
125	WP12		South, mass block	
126	WP13		Northwest, column, h = 35 in.	displacement (diagonal)
127	WP14		Northwest, column, h = 70 in.	
128	WP15		Southwest, column, h = 35 in.	
129	WP16		Southwest, column, h = 70 in.	
130	WP17		West, footing, h = 0 in.	displacement (Y-dir)
131	WP18		West, mass block	
132	WP19		West, mass block	
133	Accel17X	3D Accelerometer	East side, h = 70 in.	acceleration (X-dir)
134	Accel17Y			acceleration (Y-dir)
135	Accel17Z			acceleration (Z-dir)
136	E Vrt.DCDT	DCDT	East side, h = 70 in.	displacement (Z-dir)
137	Accel18Z	1D Accelerometer	North side, h = 70 in.	acceleration (Z-dir)

D.2 DATA REDUCTION

Not all data could be used in the analysis. In particular, strain gages are vulnerable to damage. During a series of tests, only several channels for strain gages had erroneous readings. Table D.2 lists the channels removed in each test.

Table D.2 Removed channels.

SP	Channel name	Location
1	NL4	Longitudinal rebar on the north side, h = 40 in.
	NL5	Longitudinal rebar on the north side, h = 50 in.
	NH5	Hoop on the north side, h = 40 in.
	NH7	Hoop on the north side, h = 60 in.
2	SH3	Hoop on the south side, h = 30 in.

D.3 INSTRUMENTATION DRAWINGS

Figure D.1 presents the location of strain gages in each cross section. Small rectangles represent the gages on the hoop and the longitudinal reinforcing bars at each cross section. Figure D.1(a) is for h = 30 in., 40 in., and 60 in., Figure D.1(b) is for h = 10 in., Figure D.1(c) is for h = 20 in. and 50 in., and Figure D.1(d) for h = 35 in.

Figures D.2 and D.3 present elevations and plans of the set-up with external measuring instruments, respectively. The locations of the Novotechniks, wire potentiometers, and accelerometers are indicated. Six threaded rods go through the column at h = 5 in., 15 in., 25 in., 35 in., 55 in., and 65 in. in the X-direction. They were unbonded from the surrounding concrete except near the center of the column. The length of the bonded part was roughly 14 in. A total of fourteen Novotechniks were mounted on the north and south sides [Figure D.2(a) and (b)]. Each Novotechnik's location was specified in Table D.1. For example, 'NovoT1' was attached to the rod at h = 5 in. and measured the Z-directional displacement between h = 0 in. and 5 in. on the north side of the column. 'NovoT8' is at the same position on the opposite side. As a result, the curvature at h = 2.5 in. can be obtained with these instruments. Similarly, the curvature histories at h = 10 in., 20 in., 30 in., 45 in., 60 in., and 67.5 in. were obtained; see Figure D.4. The curvature history from the Novotechniks can be compared to that from the strain gages on the longitudinal reinforcing bars at h = 10 in., 20 in., 30 in., and 60 in.

Wire potentiometers were connected to the south and west sides of the set- up [Figure D.2(b) and (c)]. On the south side [Figure D.2(b)], two wire potentiometers were connected to the footing (h = 0 in.), and the average of both measurements was used to calculate relative displacement of the column. Four wire potentiometers were connected to the column at h = 15 in., 35 in., 55 in. and 70 in., and two wire potentiometers were connected to the top concrete block. On the west side, one perpendicular wire potentiometer was connected to the footing, and four diagonal wire potentiometers were connected to the column [Figure D.3(b)], i.e., two at h = 35 in. and two at h = 70 in. Two wire potentiometers on the concrete blocks captured the Y-directional displacement. Four wire potentiometers were connected to the bottom of the concrete block, as shown in Figure D.3(d); they measured vertical displacement of the block from the base plate.

Two DCDTs measured the vertical displacement of the column on the east and west sides. The average of the DCDTs was considered as a more reliable measurement rather than the average of two wire potentiometers on the east and west sides. This is due to fluctuations of the concrete blocks. These two different measurements are compared in Figure 4.20.

Nine 3D accelerometers were attached to the set-up. Four at the corners of the base plate [Figure D.3(a)], four at the corners of the top concrete block [Figure D.3(c)] and one below the top block captured the acceleration in X-, Y- and Z-directions. Nine 1D accelerometers were used on the north side of the column and their locations are specified in Table D.1.

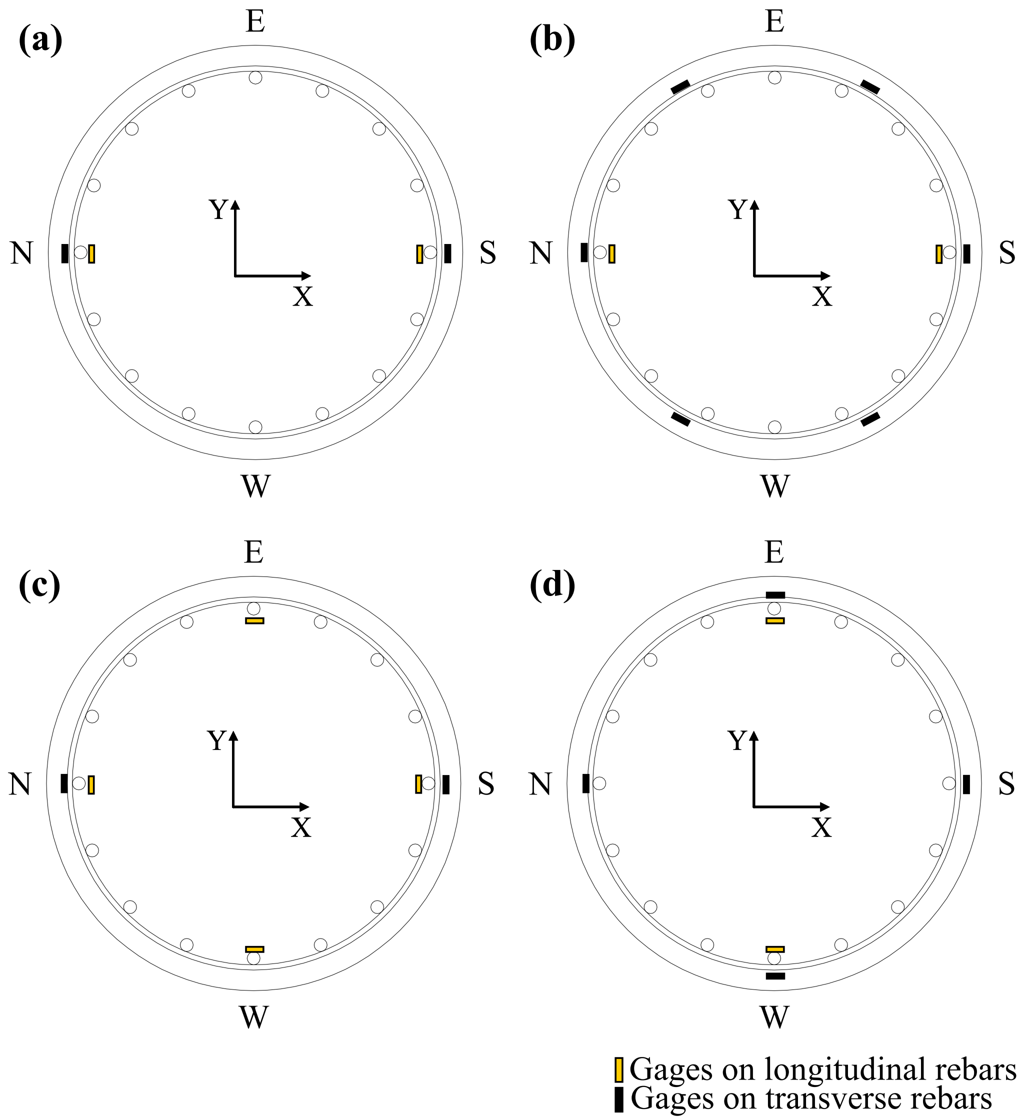

Figure D.1 Strain gages.

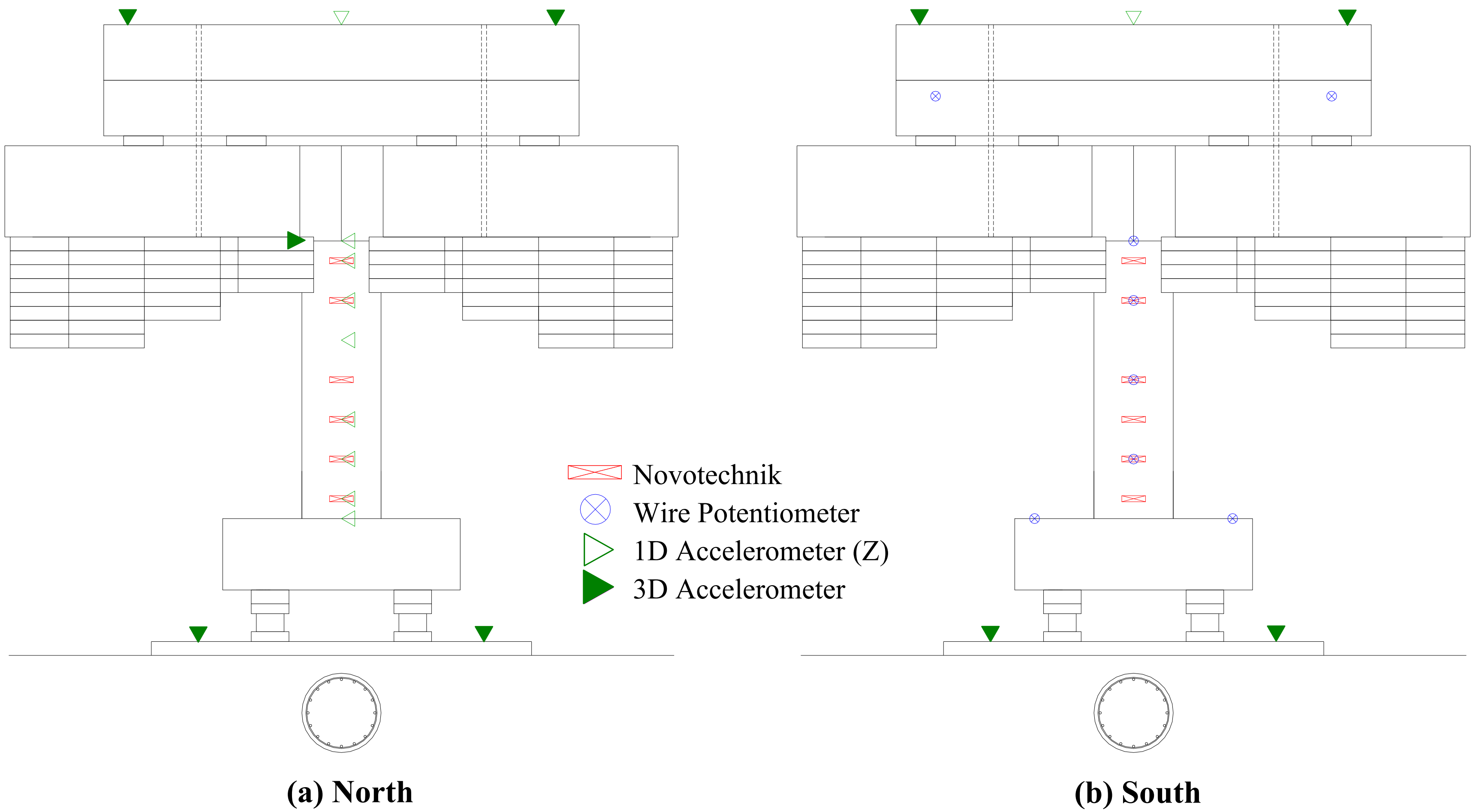

Figure D.2 External measurement: elevation.

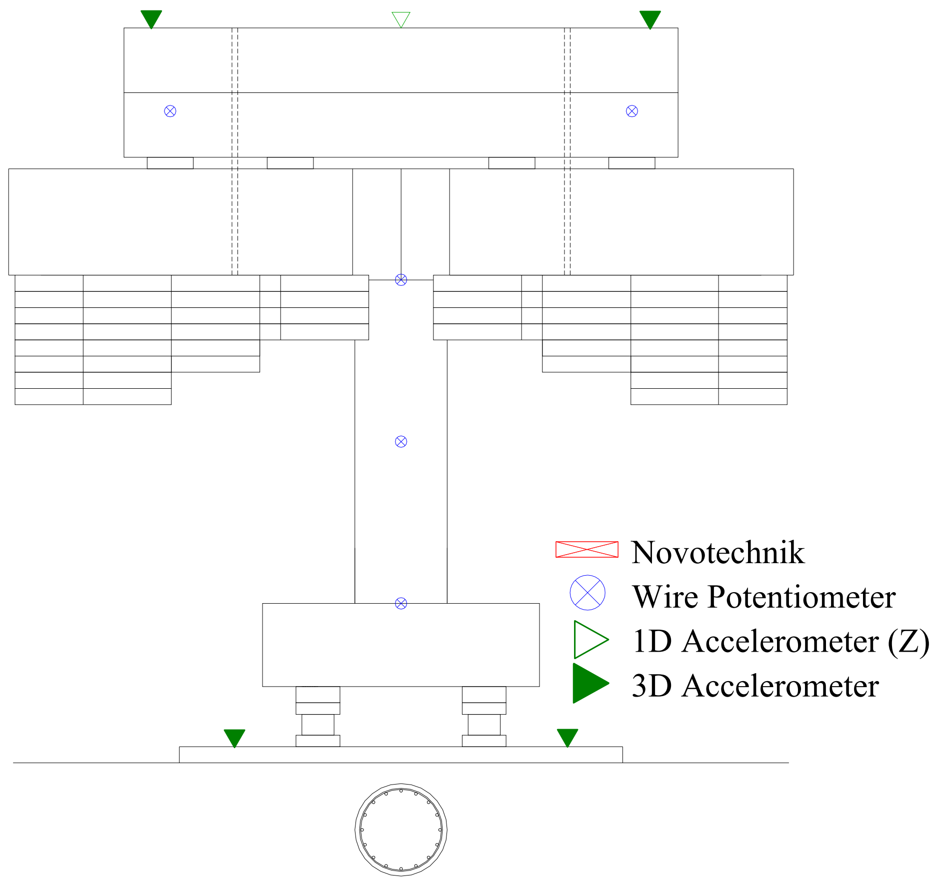

(c) West

Figure D.2 Continued.

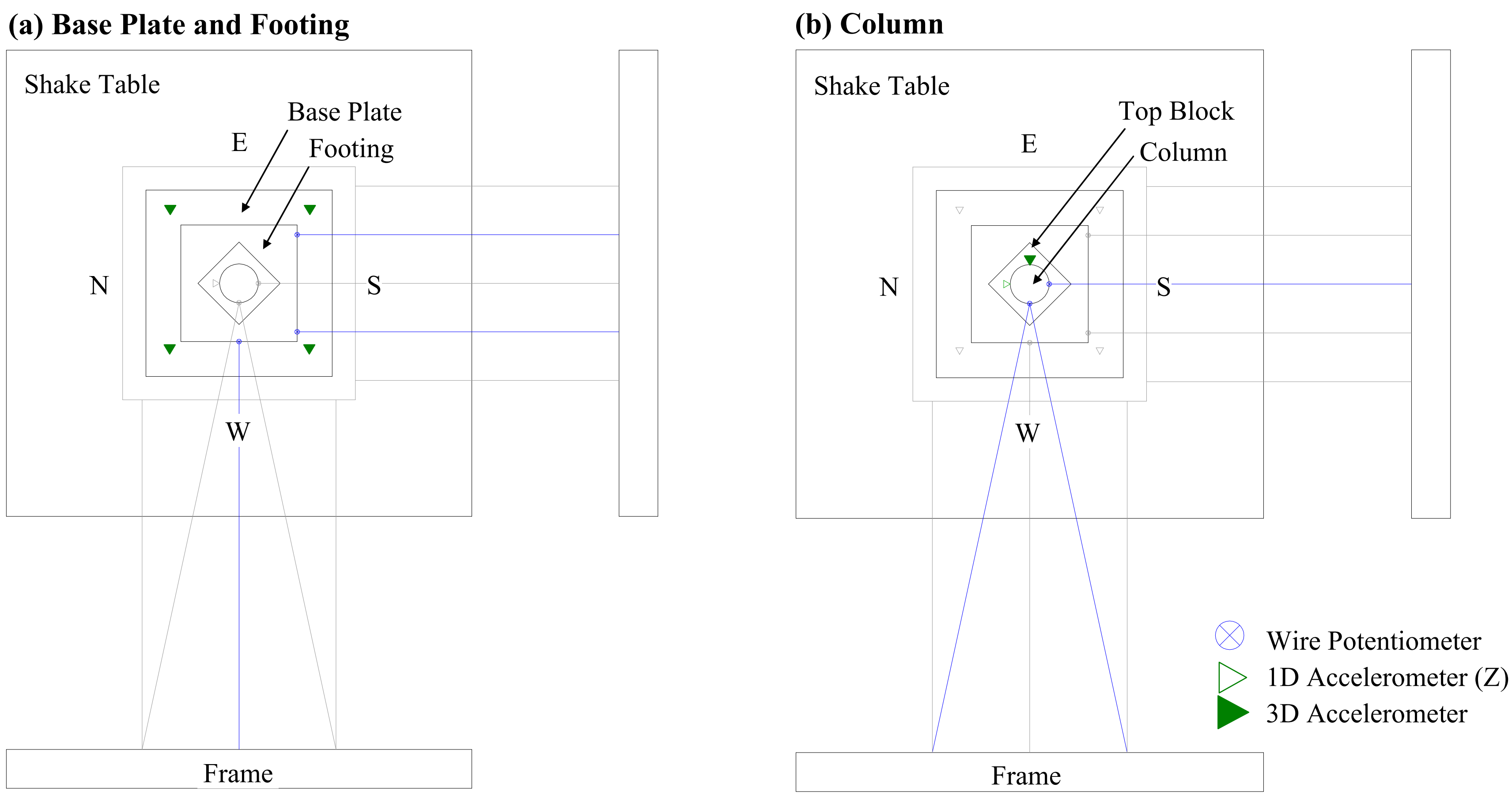

Figure D.3 External measurement: plan.

(c) Concrete Blocks

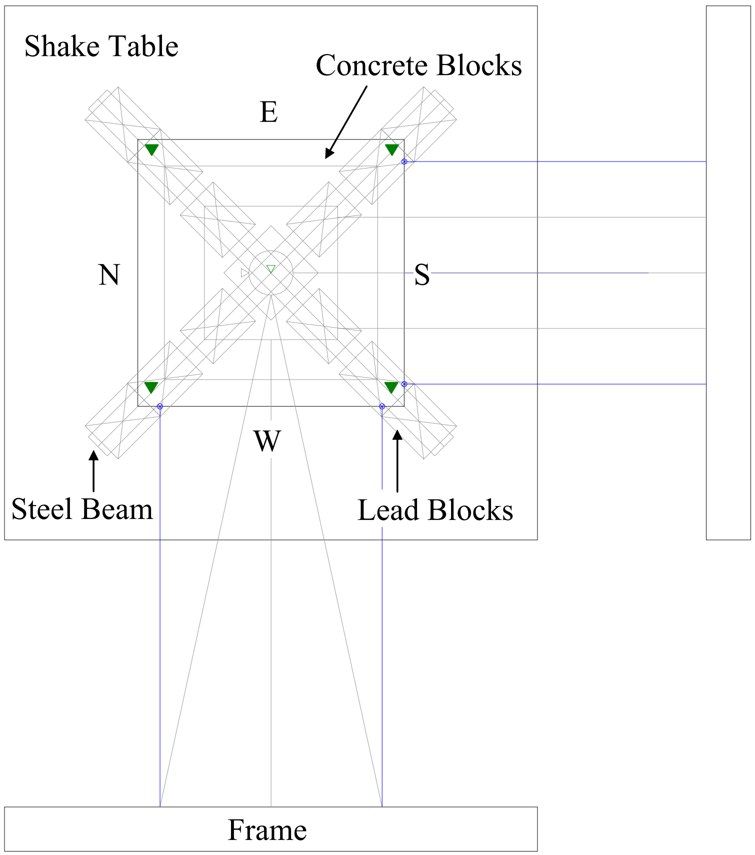

(d) Vertical Measurements below Mass Blocks

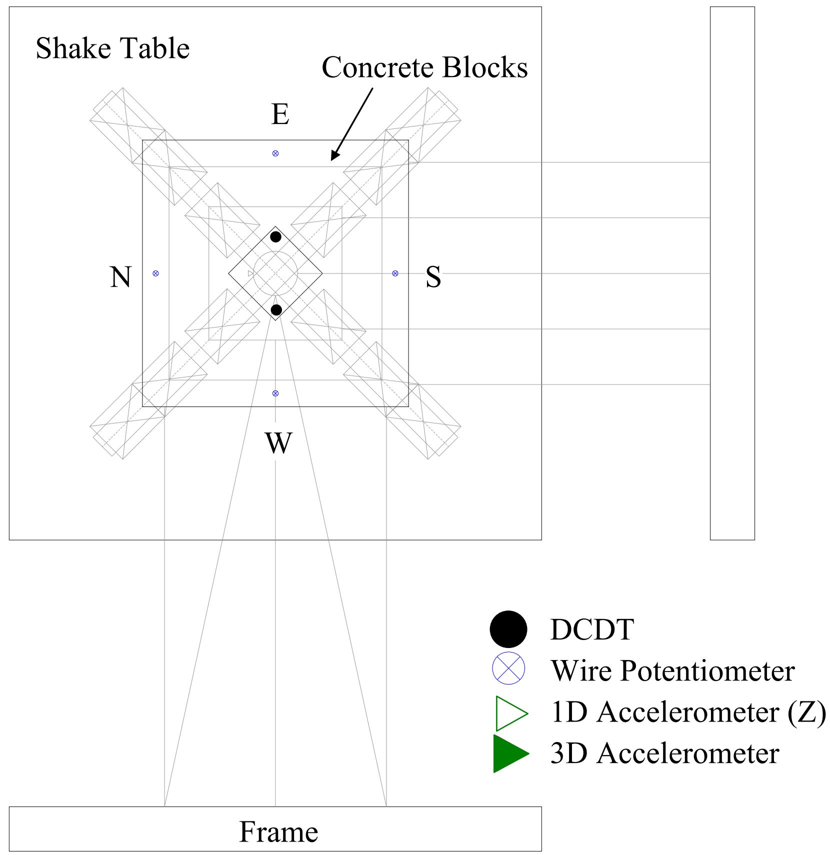

Figure D.3 Continued.

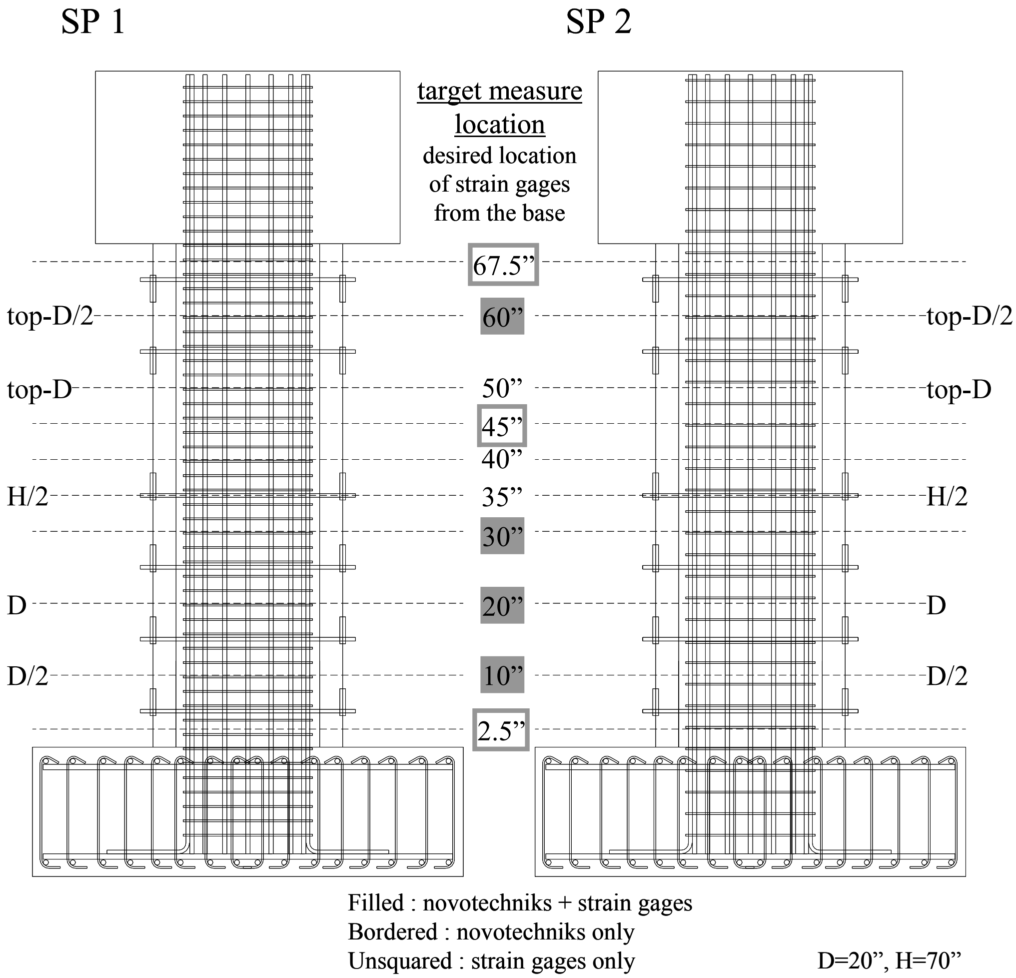

Figure D.4 **Target measure location of the Novotechniks and strain gages.**

Appendix E: Test Photographs

The photographs of test specimens were taken on the north, west, south, and east sides of the specimen. Figure E.1 shows damage at the top and the base of both specimens after a series of tests, i.e., the third 125%-scale test. Photographs of SP1 after 70%, 95% and the third 125%-scale runs are presented in Figures E.2, E.3, and E.4. Those of SP2 are shown in Figures E.5, E.6, and E.7.

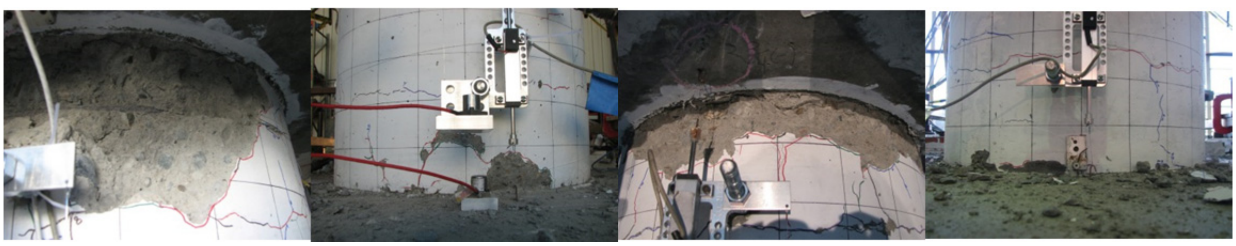

(a) SP1 top on the north | **(b) SP1 base on the north** | **(c) SP1 top on the south** | **(d) SP1 base on the south**

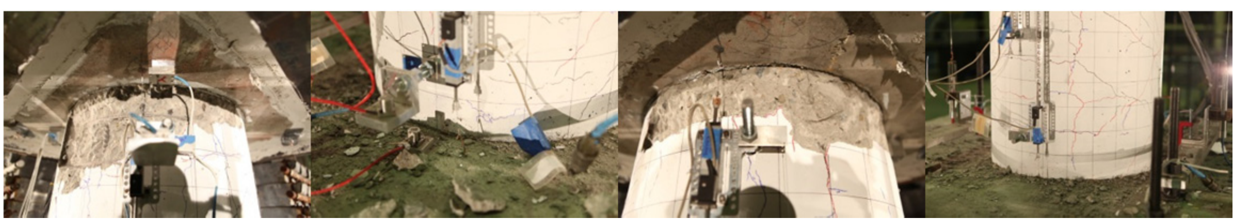

(e) SP2 top on the north | **(e) SP2 base on the north** | **(f) SP2 top on the south** | **(g) SP2 base on the south**

Figure E.1 Test photographs of the top and base after 125%-scale runs (runs 1-11, 2-11).

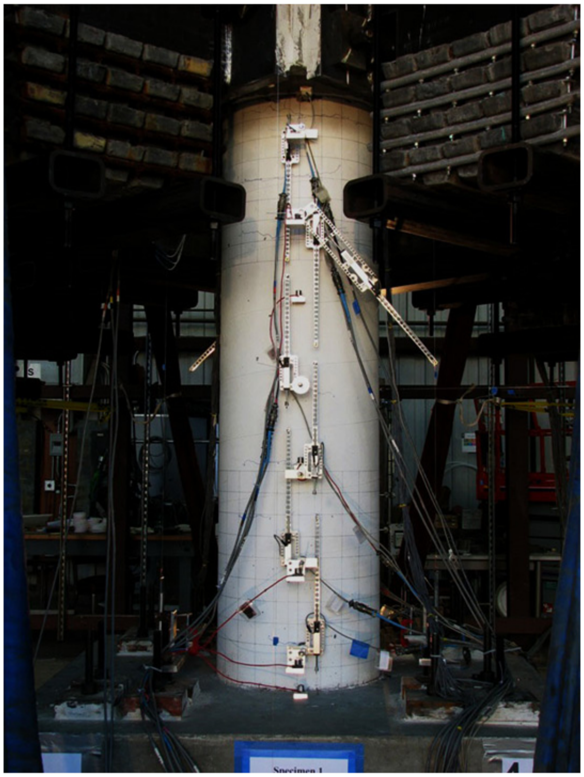

(a) north

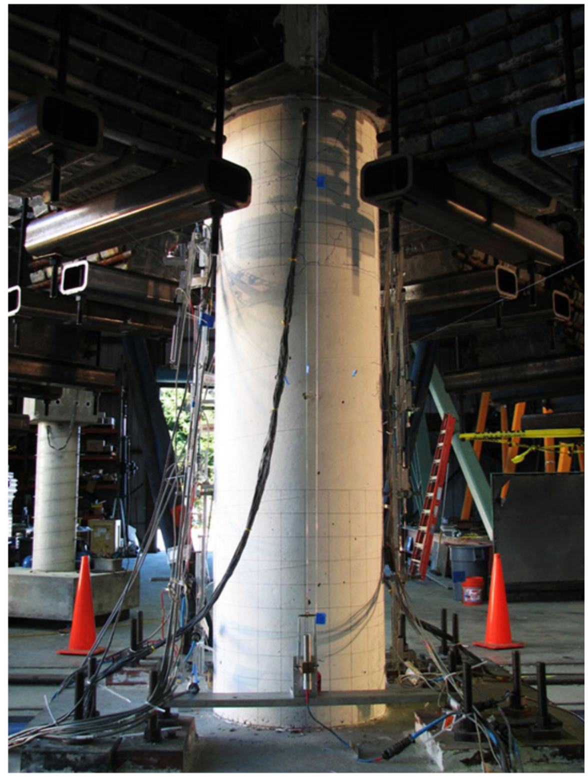

(b) west

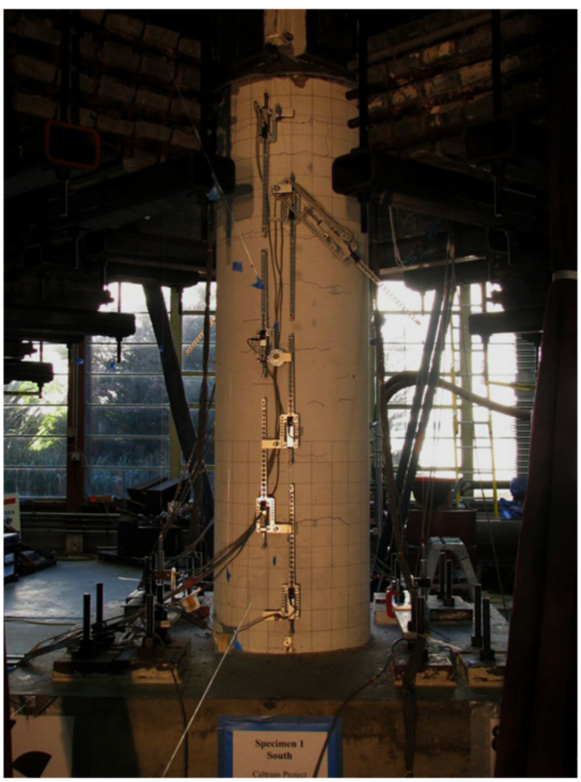

(c) South

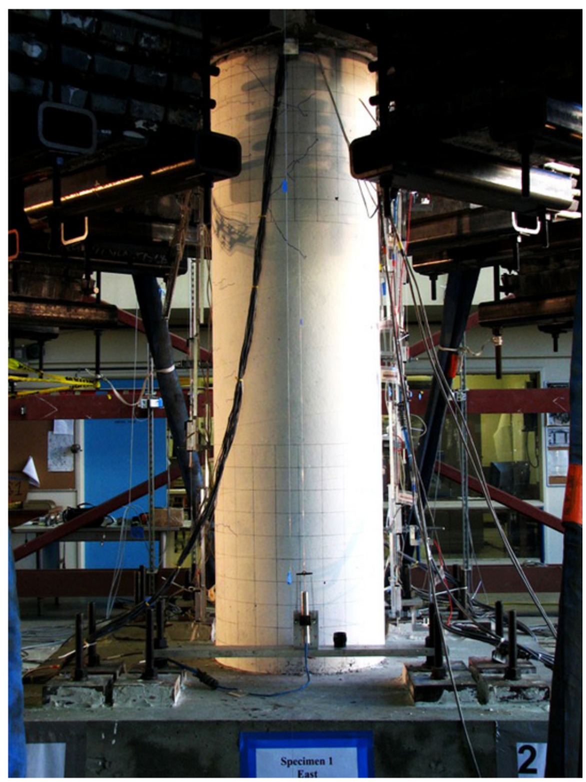

(d) East

Figure E.2 Test photographs of SP1 after the 70%-scale run (run 1-7).

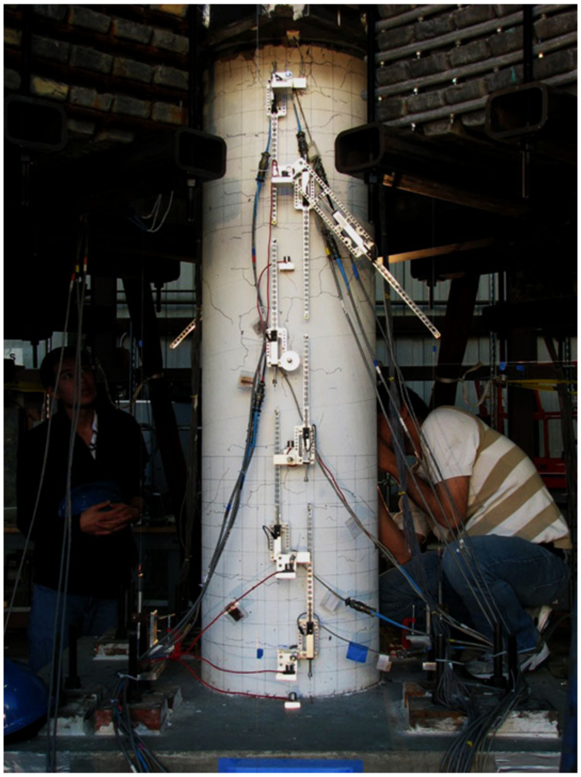

(a) north

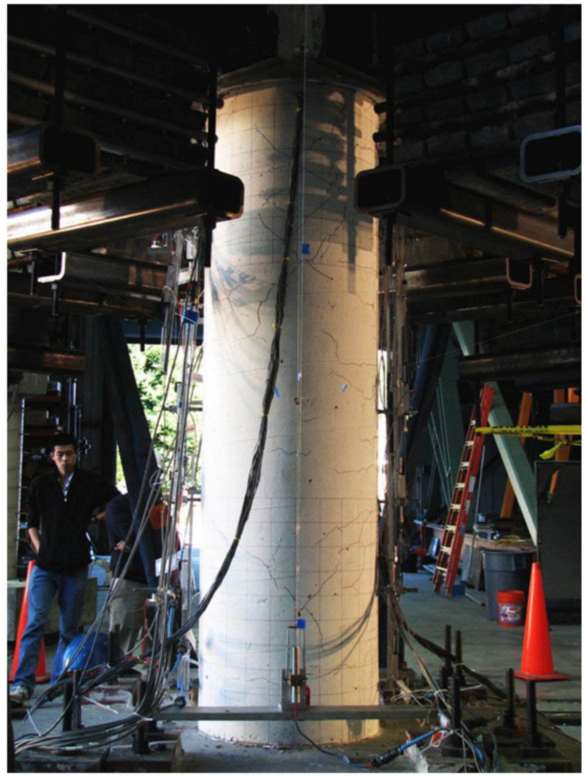

(b) west

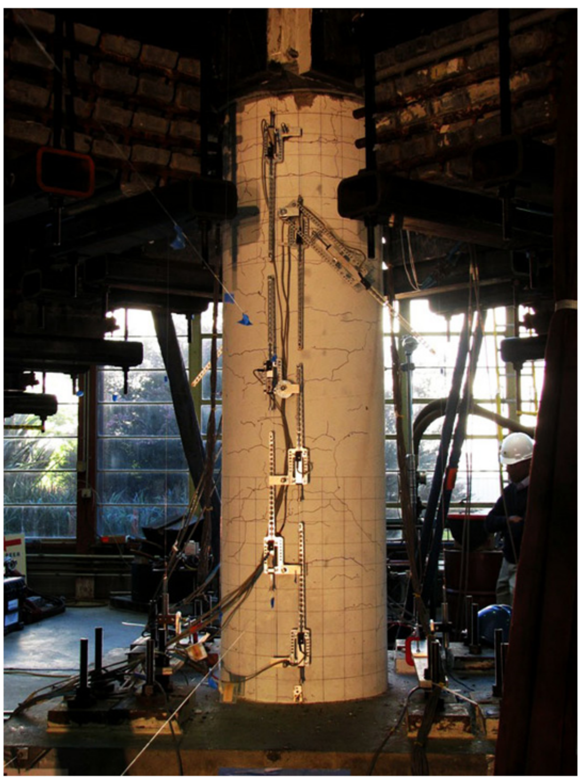

(c) south

(d) east

Figure E.3 Test photographs of SP1 after the 95%-scale run (run 1-8).

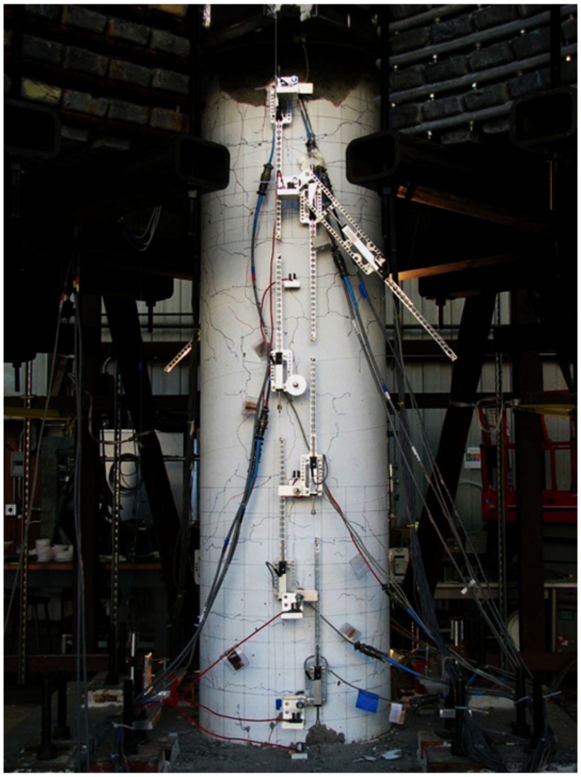

(a) north

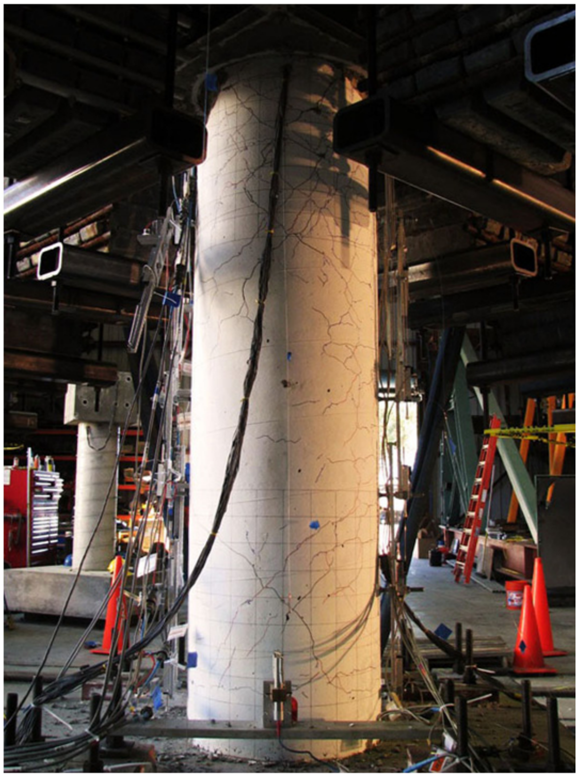

(b) west

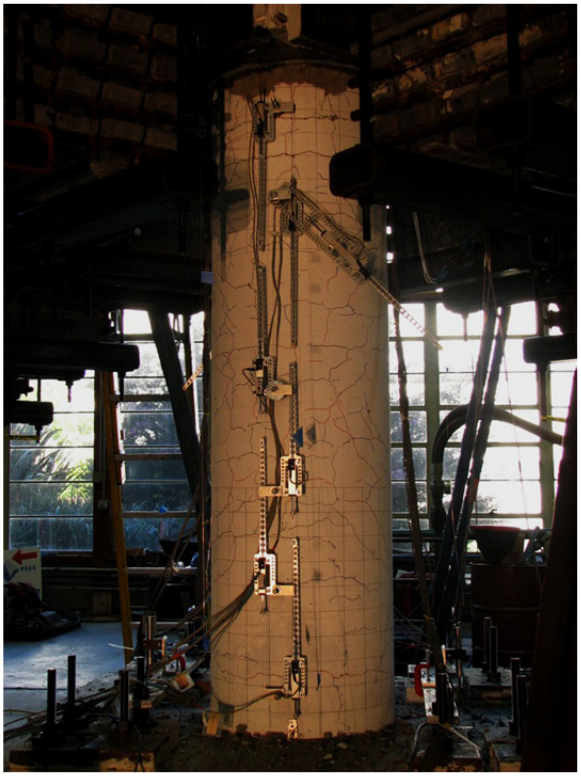

(c) south

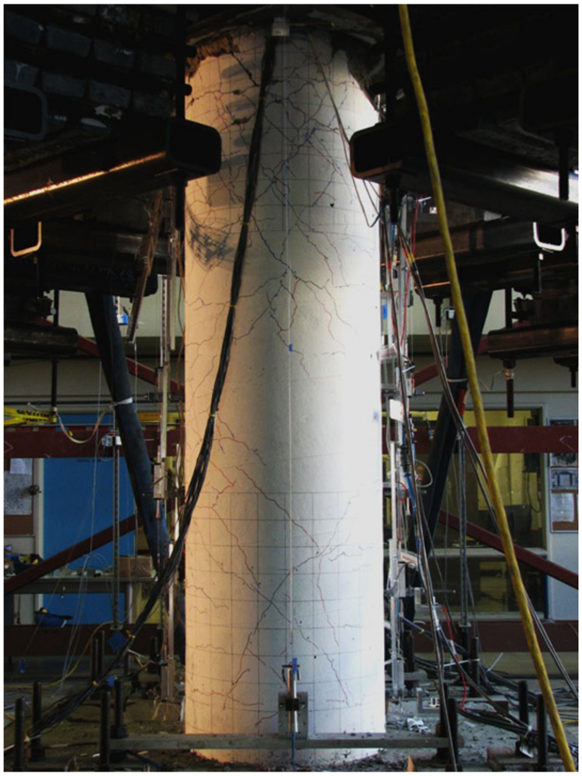

(d) east

Figure E.4 Test photographs of SP1 after the 125%-scale run (run 1-11).

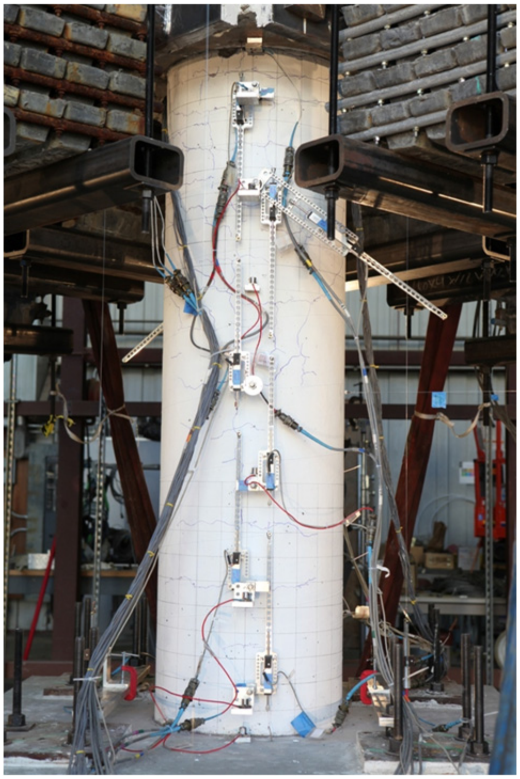

(a) north

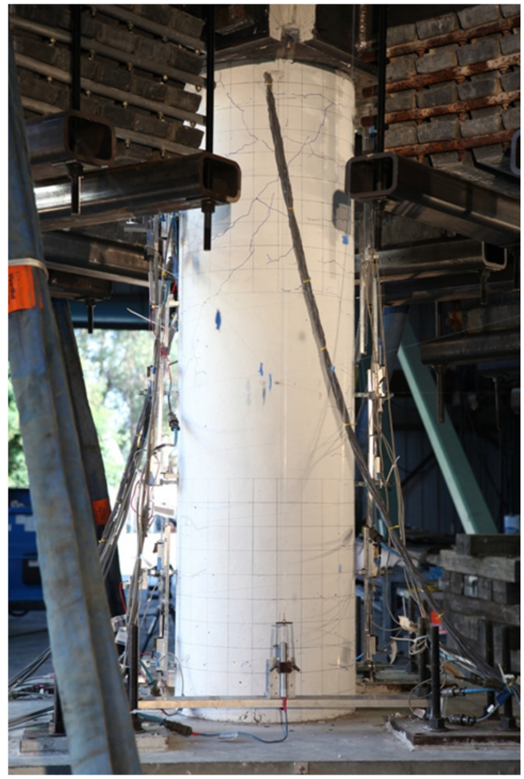

(b) west

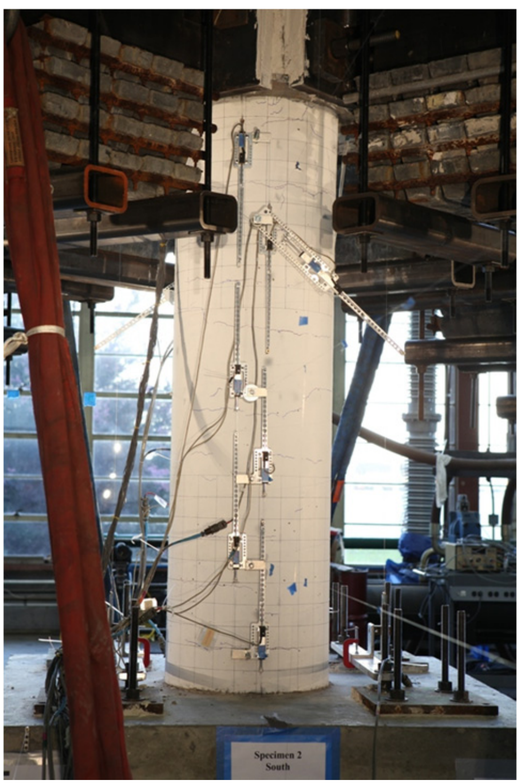

(c) south

(d) east

Figure E.5 Test photographs of SP2 after the 70%-scale run (run 2-7).

(a) north

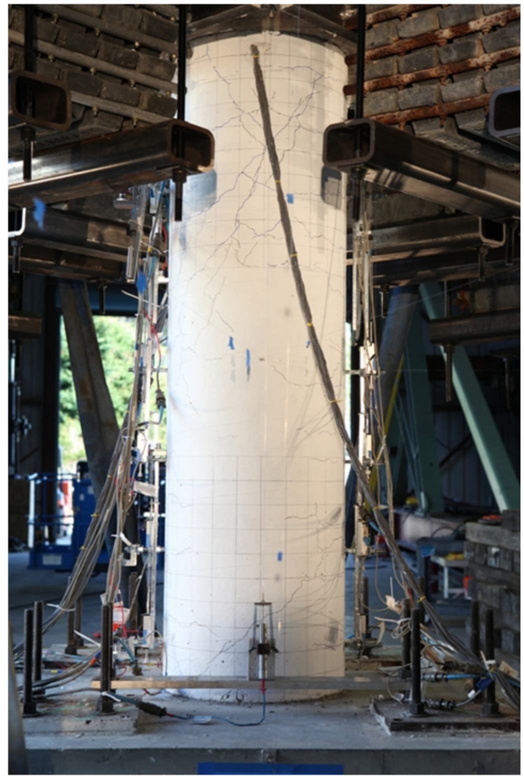

(b) west

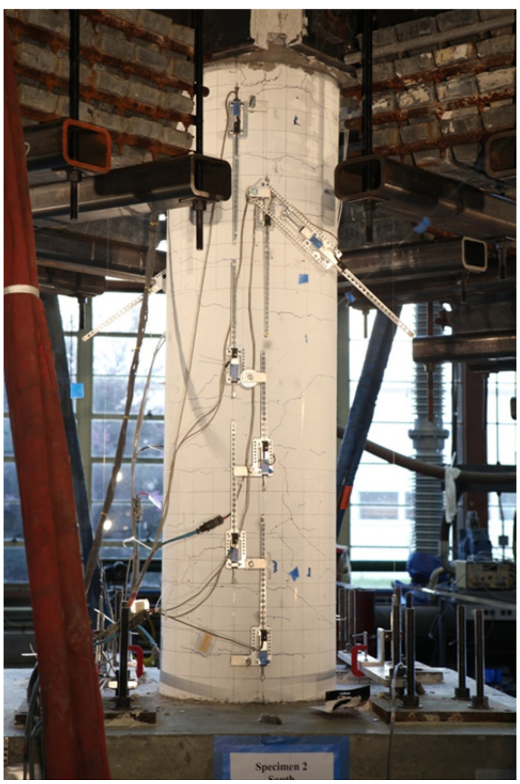

(c) south

(d) east

Figure E.6 Test photographs of SP2 after the 95%-scale run (run 2-8).

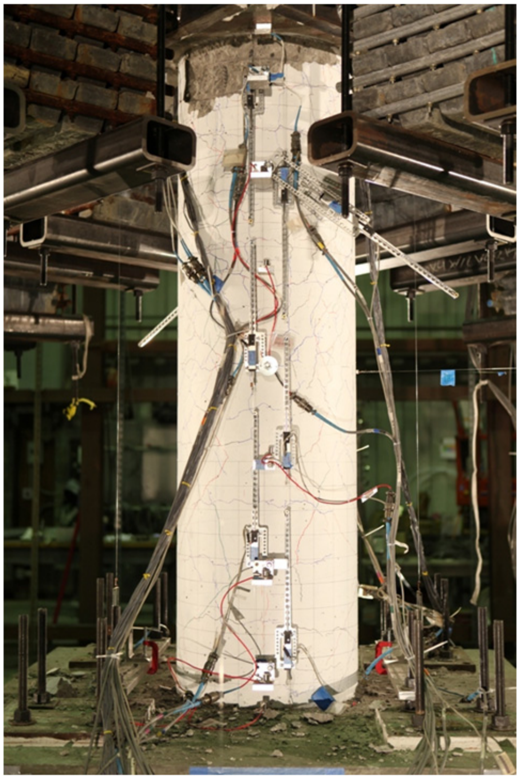

(a) north

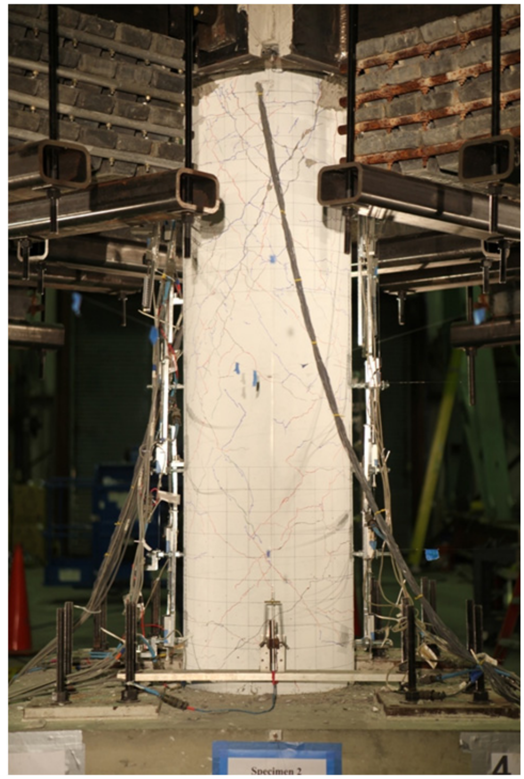

(b) west

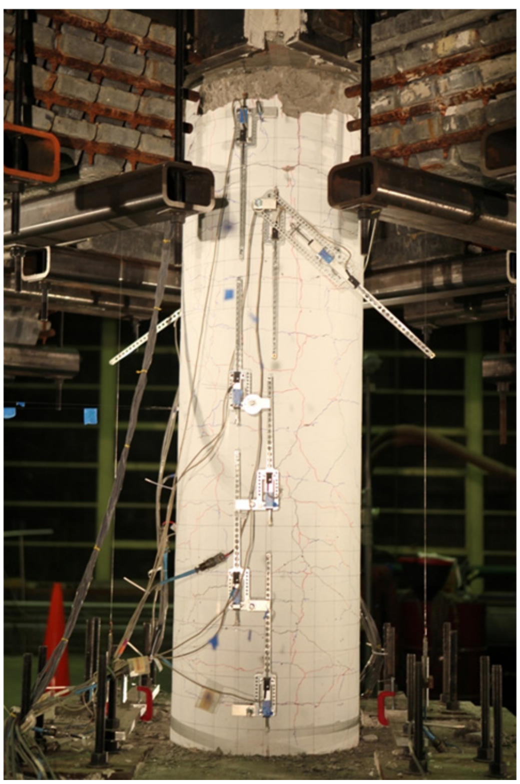

(c) south

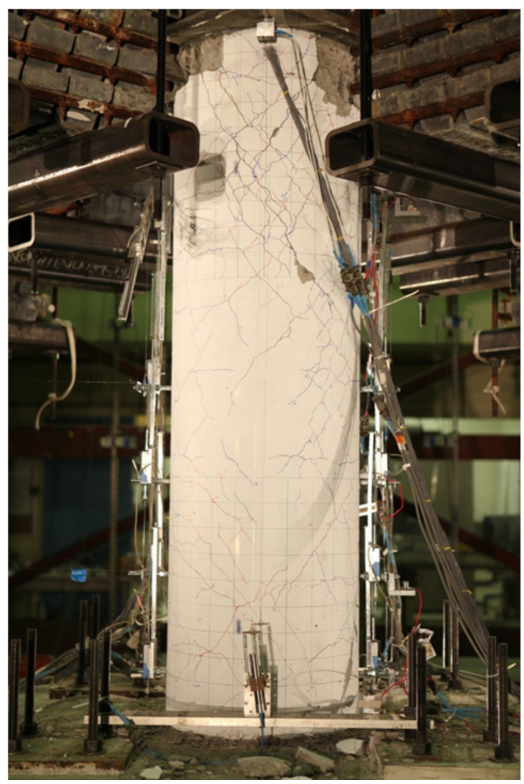

(d) east

Figure E.7 Test photographs of SP2 after the 125%-scale run (run 2-11).

Appendix F: Local Responses of Computational Models

The local responses of the computational model B-1 are discussed below. Only the results from B-1 are presented, since B-1, B-2-ACI and B-2-SDC provide similar local responses and those of A-1, A-2-ACI and A-2-SDC with a *BWH2* element are also similar.

F.1 CURVATURES

Figures F.1 and F.2 compare curvature histories from the computational model B-1 to the test data obtained of SP1. Both model B-1 and SP1 have the steel reinforcing bars on the north and south sides, and the curvatures in the X-direction (N-S) were calculated from those longitudinal strains at h = 10 in. and 60 in. The following are observations on the curvature histories of SP1:

- The curvature history at h = 60 in. was larger than that at h = 10 in. The results from model B-1 agree with this trend qualitatively.
- Model B-1 was accurate in predicting the curvature history at h = 10 in., which is between -3.1×10^{-4} and 3.1×10^{-4} in.$^{-1}$.
- Model B-1 was also accurate in predicting the curvature history at h = 60 in. subjected to 50%- and 70%-scale motions. The minimum and maximum values from Model B-1 were -3.2×10^{-4} and 3.6×10^{-4} in^{-1}, respectively.
- From 95%-scale, the difference between the curvatures of model B-1 and SP1 increased significant. In particular, B-1 did not capture the negative peaks and negative residual curvatures. Comparing the minimum values under each motion, model B-1 reached 32.1%, 27.6%, 25.2%, and 23.6% of the test data subjected to 95% and the three 125%-scale motions. Even in the peak-to-peak amplitude, i.e., fluctuation, the results from model B-1 are not comparable to the test data.

The trend in the difference between curvatures from the computational model and the test specimen is still valid for SP2 with some qualifications. Note that the section of SP2 at 10 in. had a large curvature history, but model B-1 did not capture its peaks after 95%-scale motion; see Figures F.3 and F.4.

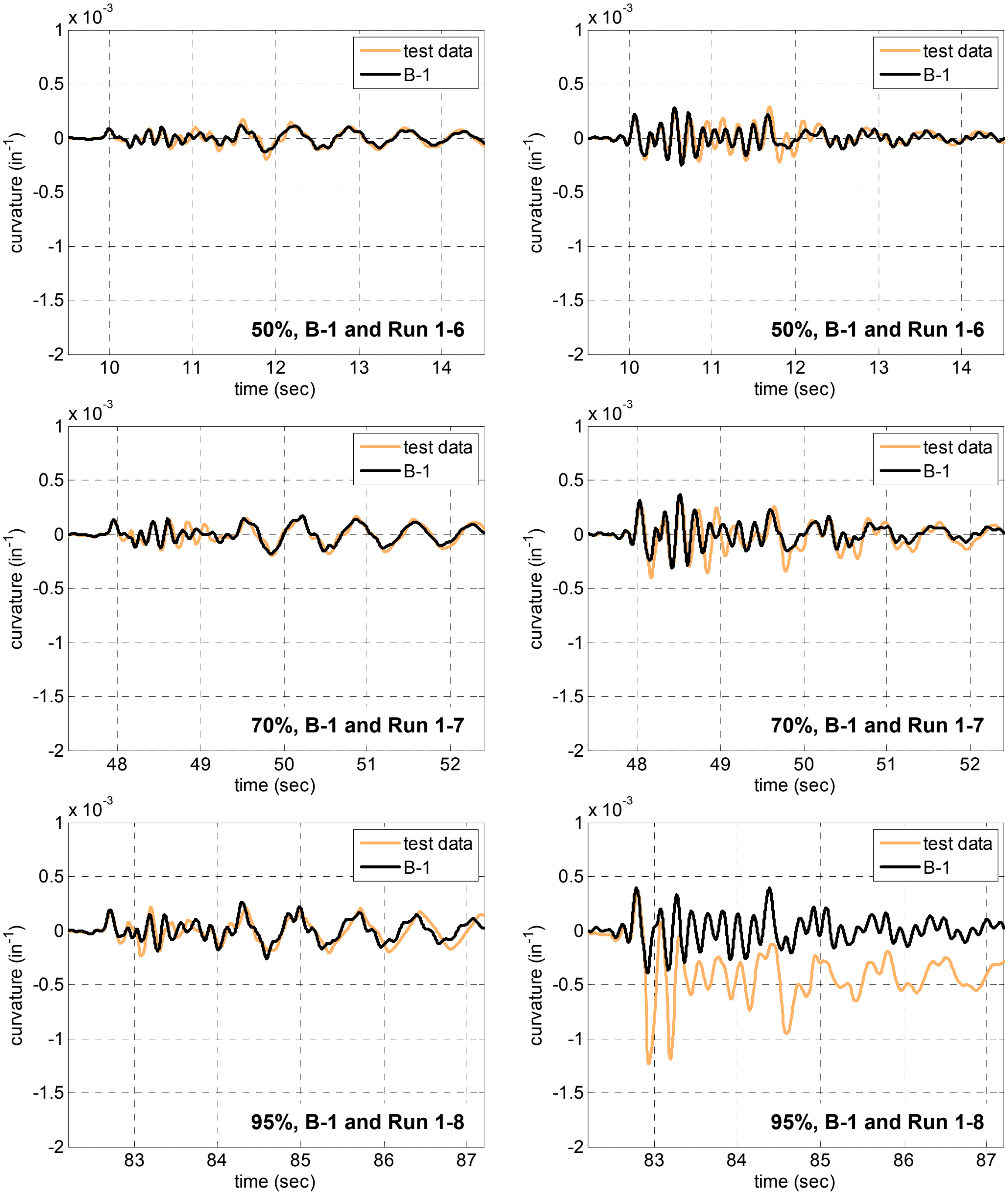

(a) *h*=10”

(b) *h*=60”

Figure F.1 Comparison of curvature histories at *h* = 10 in. and 60 in. of SP1 subjected to 50%-, 70%-, and 95%-scale motions.

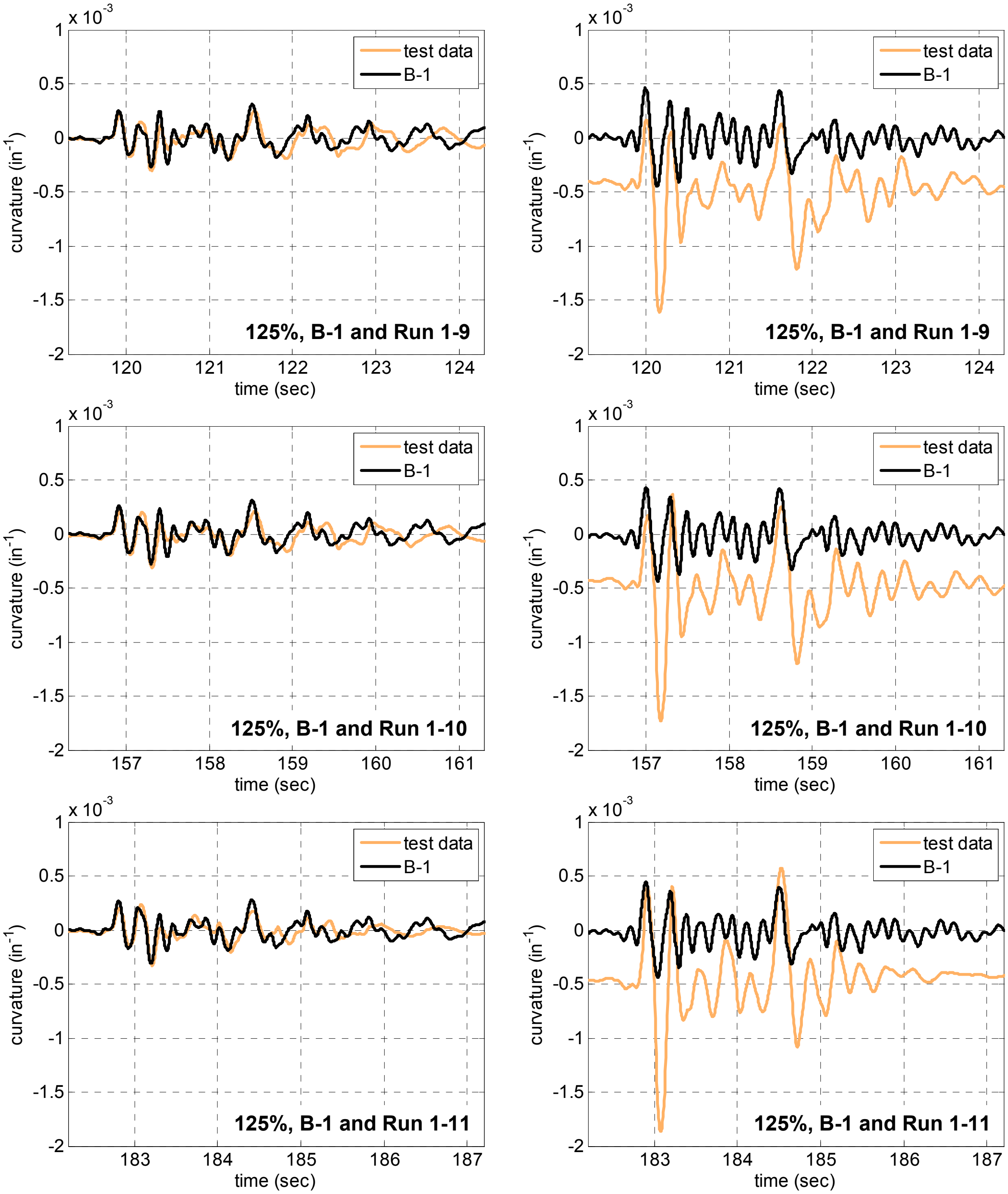

(a) ***h*=10”** **(b)** ***h*=60”**

Figure F.2 Comparison of curvature histories at *h* = 10 in. and 60 in. of SP1 subjected to 125%-scale motions.

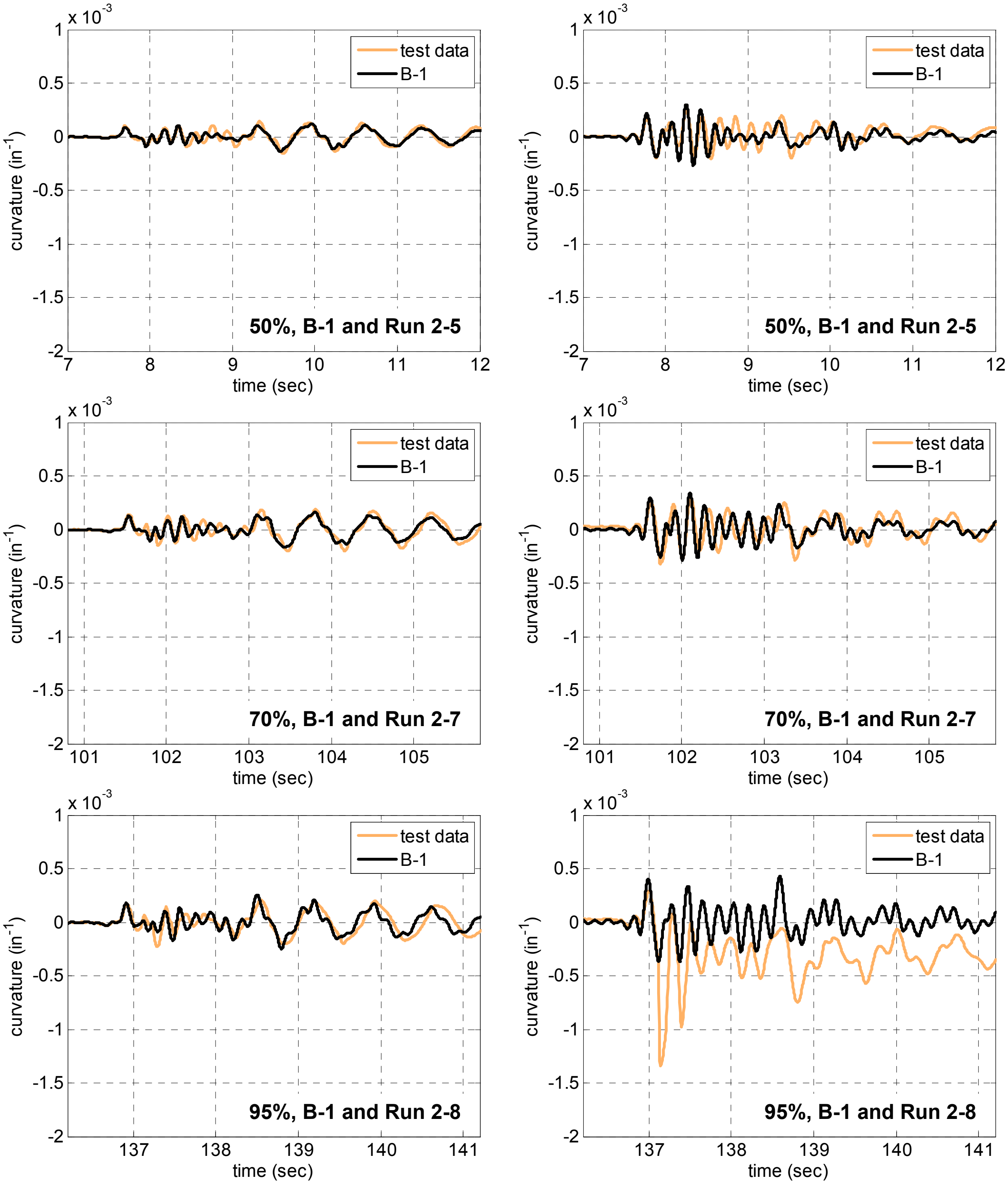

(a) *h*=10” **(b) *h*=60”**

Figure F.3 Comparison of curvature histories at *h* = 10 in. and 60 in. of SP2 subjected to 50%-, 70%-, and 95%-scale motions.

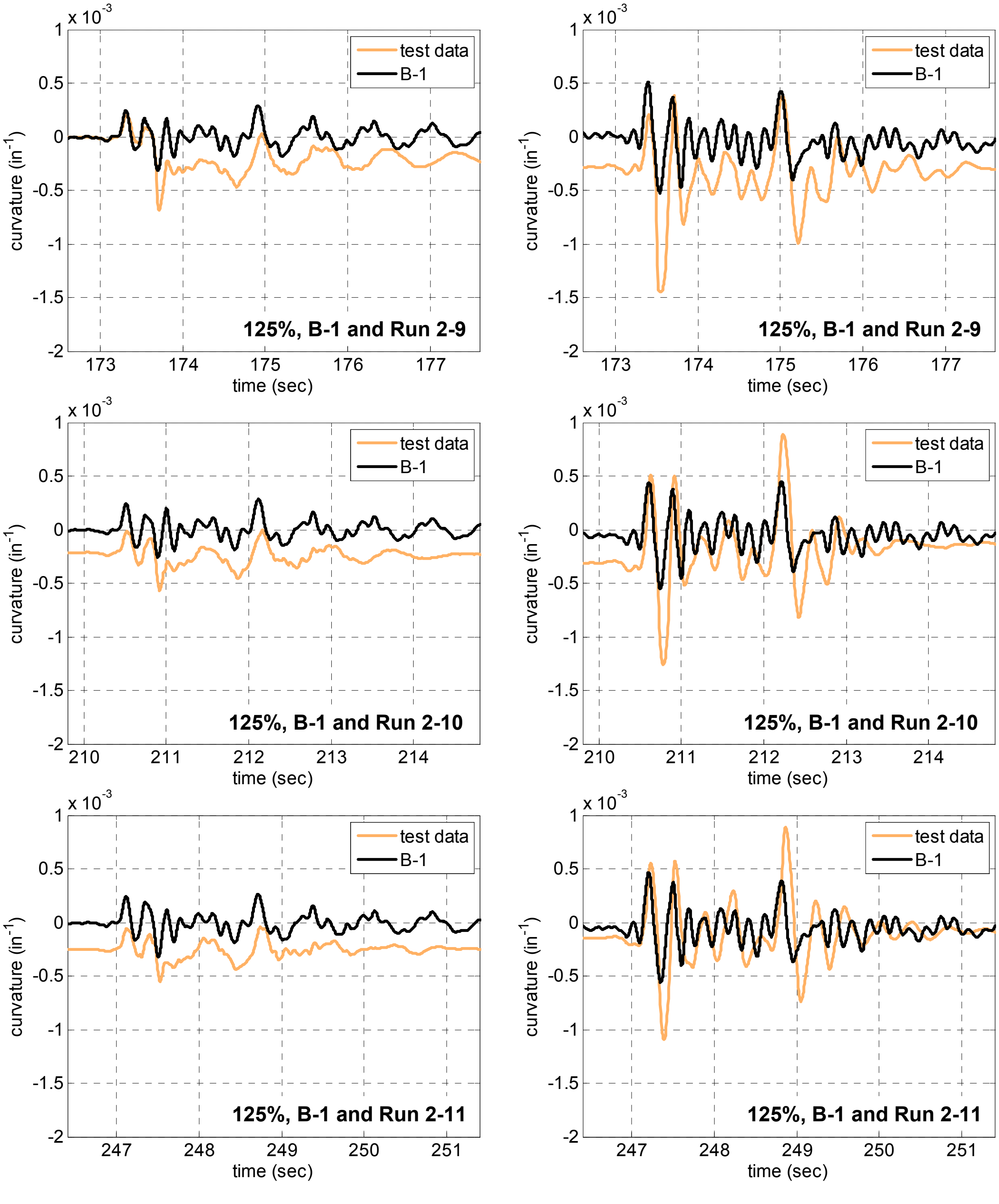

(a) *h*=10" **(b) *h*=60"**

Figure F.4 Comparison of curvature histories at *h* = 10 in. and 60 in. of SP2 subjected to 125%-scale motions.

F.2 MOMENT-CURVATURE RELATIONSHIPS

The bending moment-curvature relationships obtained from the sections at h = 10 in. and 60 in. were compared to the test data in Figure F.5. The results were obtained from model B-1. As mentioned in Section F.1, model B-1 did not capture the amplitude of the curvature, especially at h = 60 in. under 125%-scale motions.

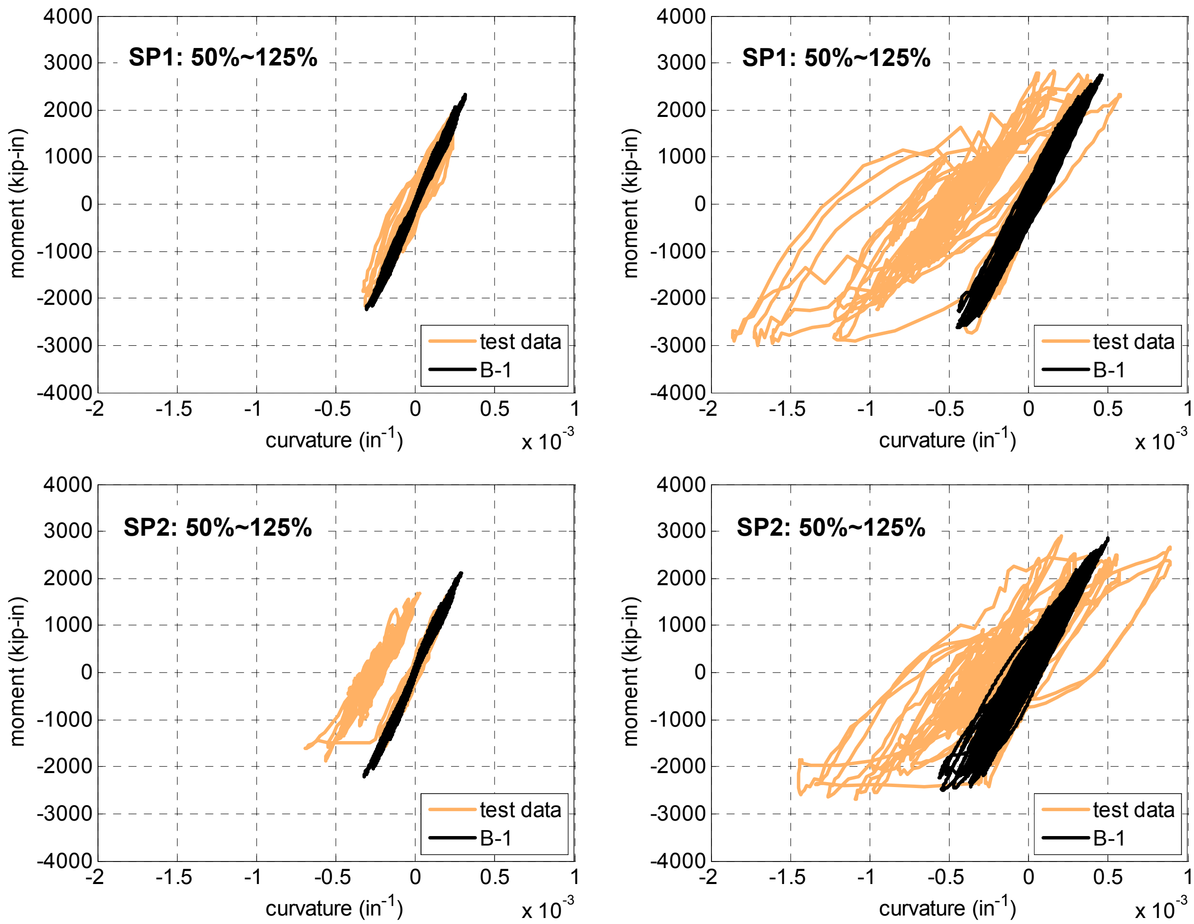

(a) *h*=10” **(b) *h*=60”**

Figure F.5 Comparison of bending moment-curvature relationships at *h* = 10 in. and 60 in. of SP1 and SP2 under 50% to 125%-scale motions.

F.3 LONGITUDINAL STRAINS

Since the curvatures were calculated based on the longitudinal strains on the north and south, the difference between computational and experimental data resulted from the strain histories obtained from model B-1. Figures F.6 to F.11 compare the longitudinal strain histories on the north, south, east, and west of model B-1 to the test data obtained from SP1. Figures F.6 and F.7

show the longitudinal strain histories on the north and south sides at h = 10 in. from 50%-scale motion. Figures F.8 and F.9 present those on the north and south sides at h = 60 in. from 50%-scale motion. The strains on the east and west sides at h = 35 in. subjected to the same motions are shown in Figures F.10 and F.11. The observations on the longitudinal strains of SP1 are as follows:

- The longitudinal strains on the north and south at h = 10 in. obtained from model B-1 are comparable to the test data, even though the peak values were somewhat different.
- Model B-1 was not accurate in predicting the longitudinal strains on the north and south at h = 60 in. It provided good estimation for the strains on the north before 125%-scale ‘X only’ motion and for the strains on the south before 95%-scale motion. It did not capture the significant difference in longitudinal strain between north and south sides.
- Model B-1 captured the peak strains on the east and west sides at h = 35 in. with accuracy, except for the response under 125%-scale ‘X only’ motion. It underestimated the tensile strain. In addition, positive strain, i.e., shortening, caused by fluctuation of axial force was detected in all computational results from model B-1, but it was not observed in the tests.

Similar to the curvatures, analogues observations to SP1 could be made for the computational results of SP2. To avoid repetition, only the results for SP1 are shown in this appendix.

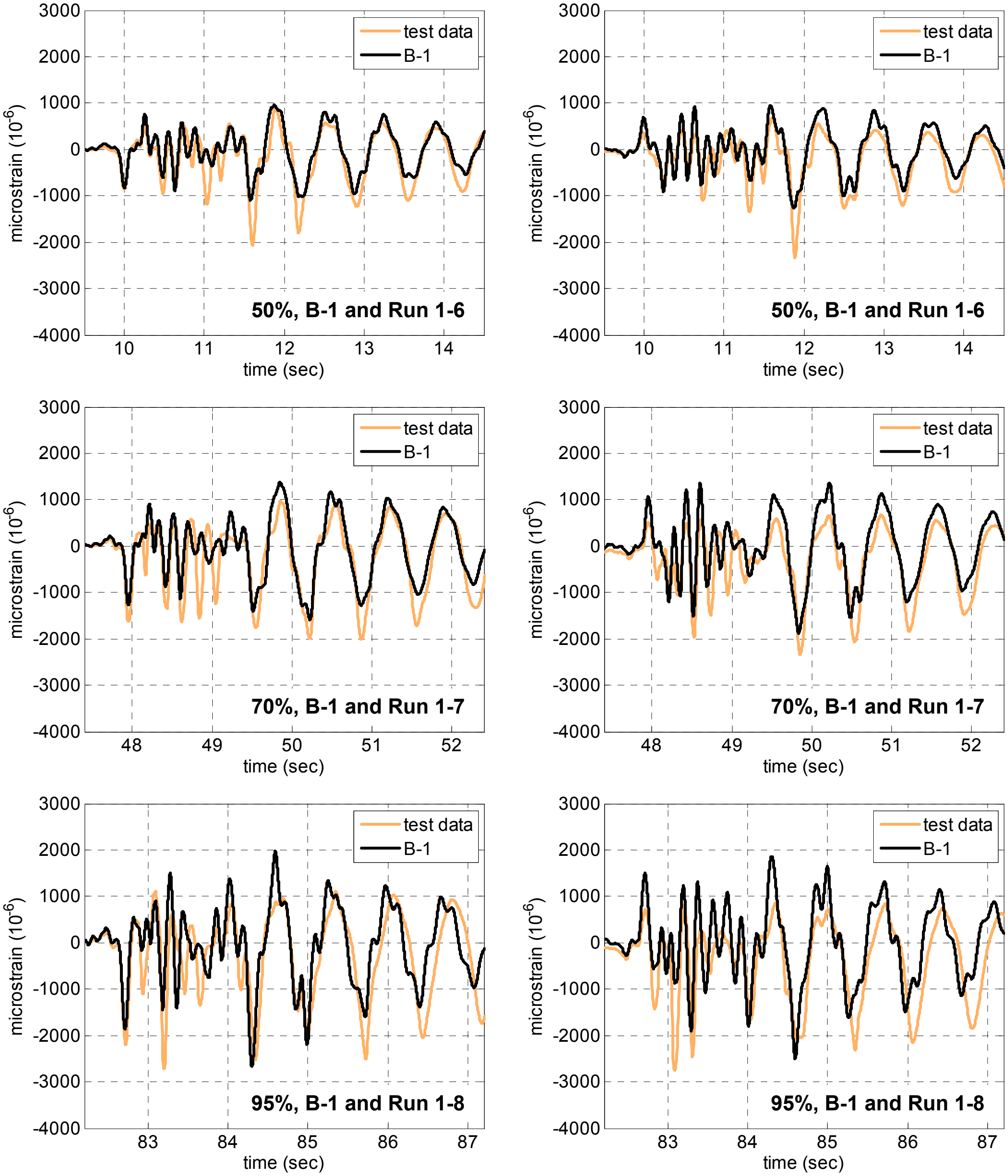

(a) north

(b) south

Figure F.6 **Comparison of longitudinal strain histories at *h* = 10 in. on the north and south of SP1 subjected to 50%-, 70%-, and 95%-scale motions.**

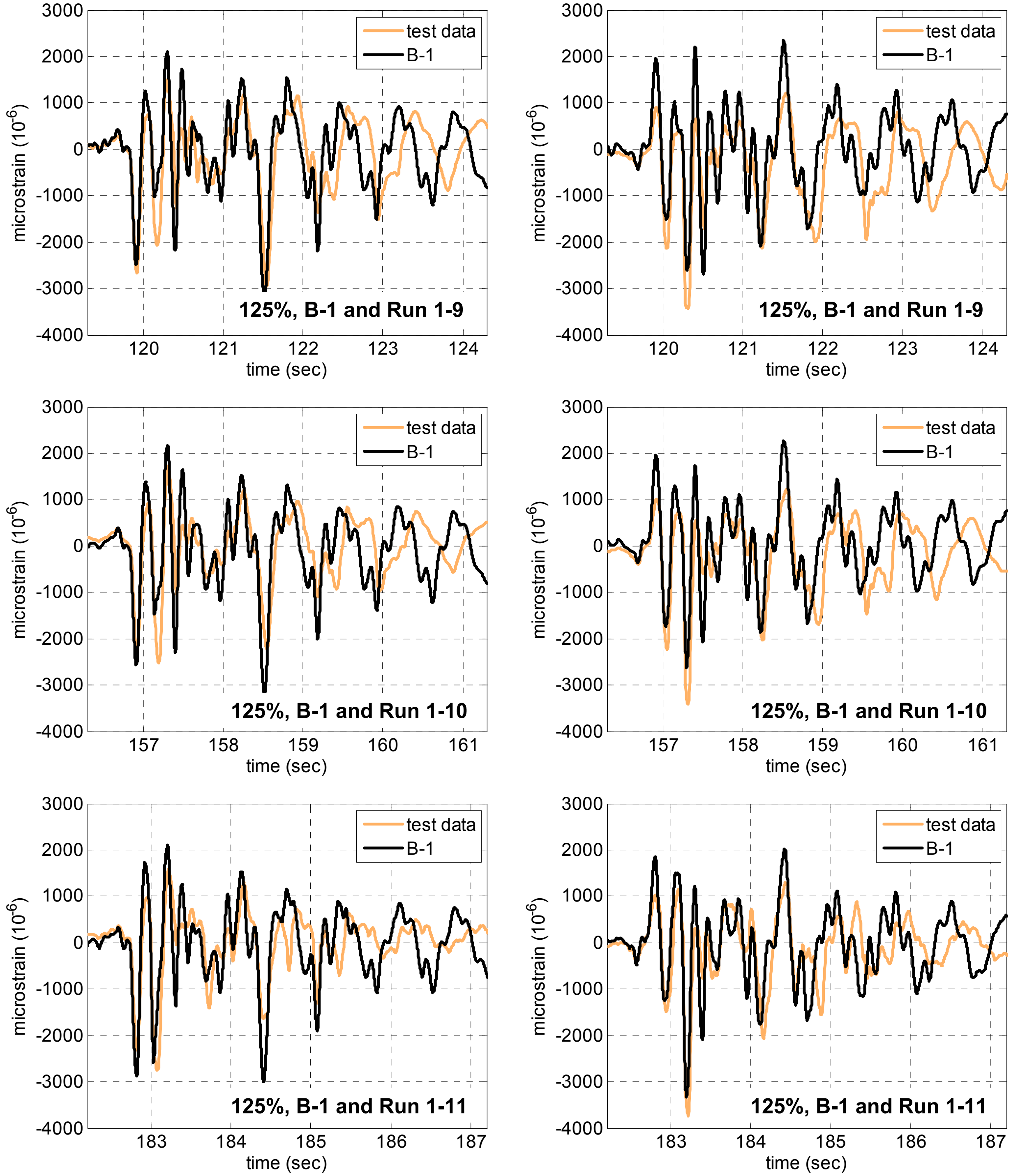

(a) north **(b) south**

Figure F.7 Comparison of longitudinal strain histories at *h* = 10 in. on the north and south of SP1 subjected to 125%-scale motions.

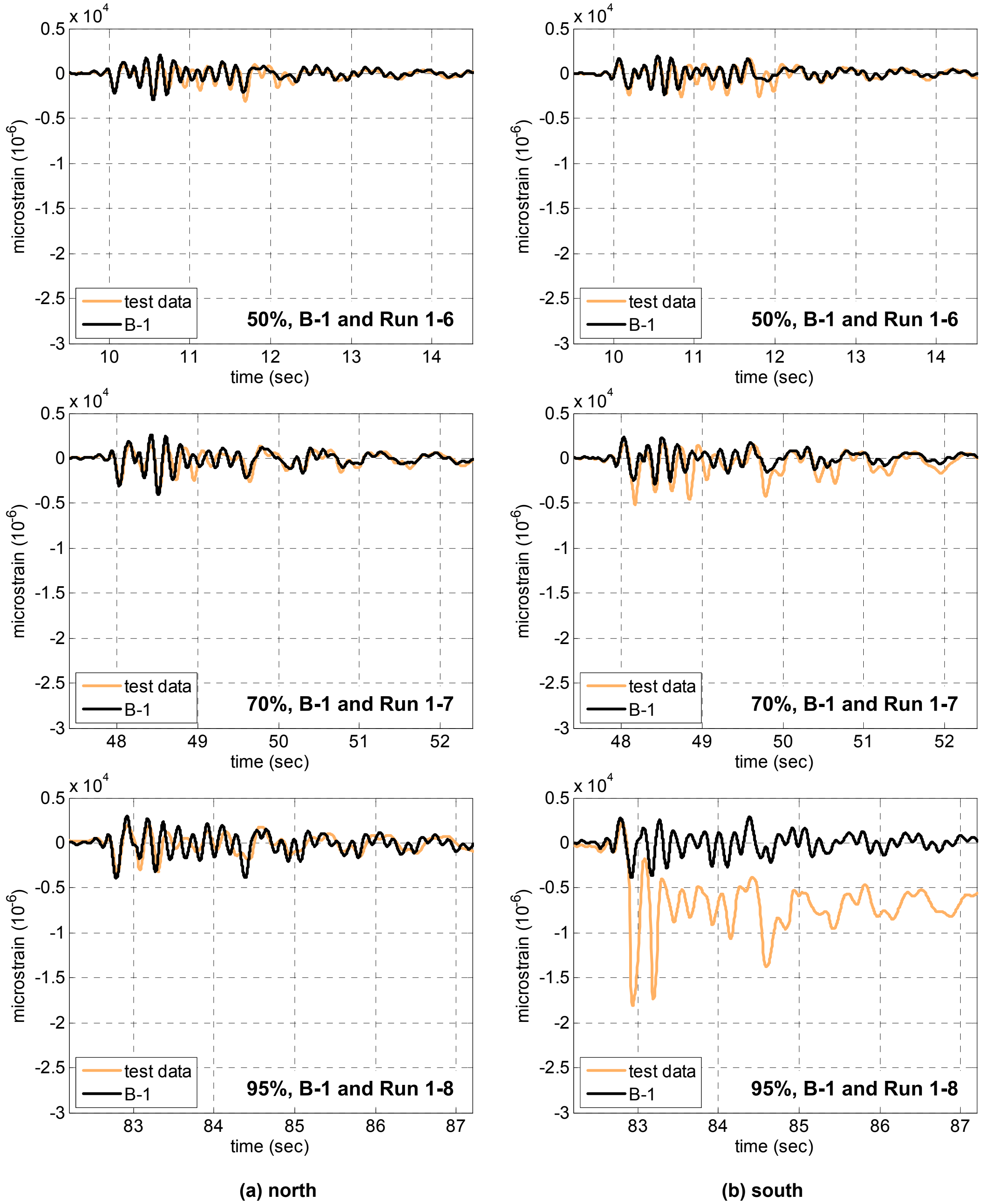

Figure F.8 **Comparison of longitudinal strain histories at *h* = 60 in. on the north and south of SP1 subjected to 50%-, 70%-, and 95%-scale motions.**

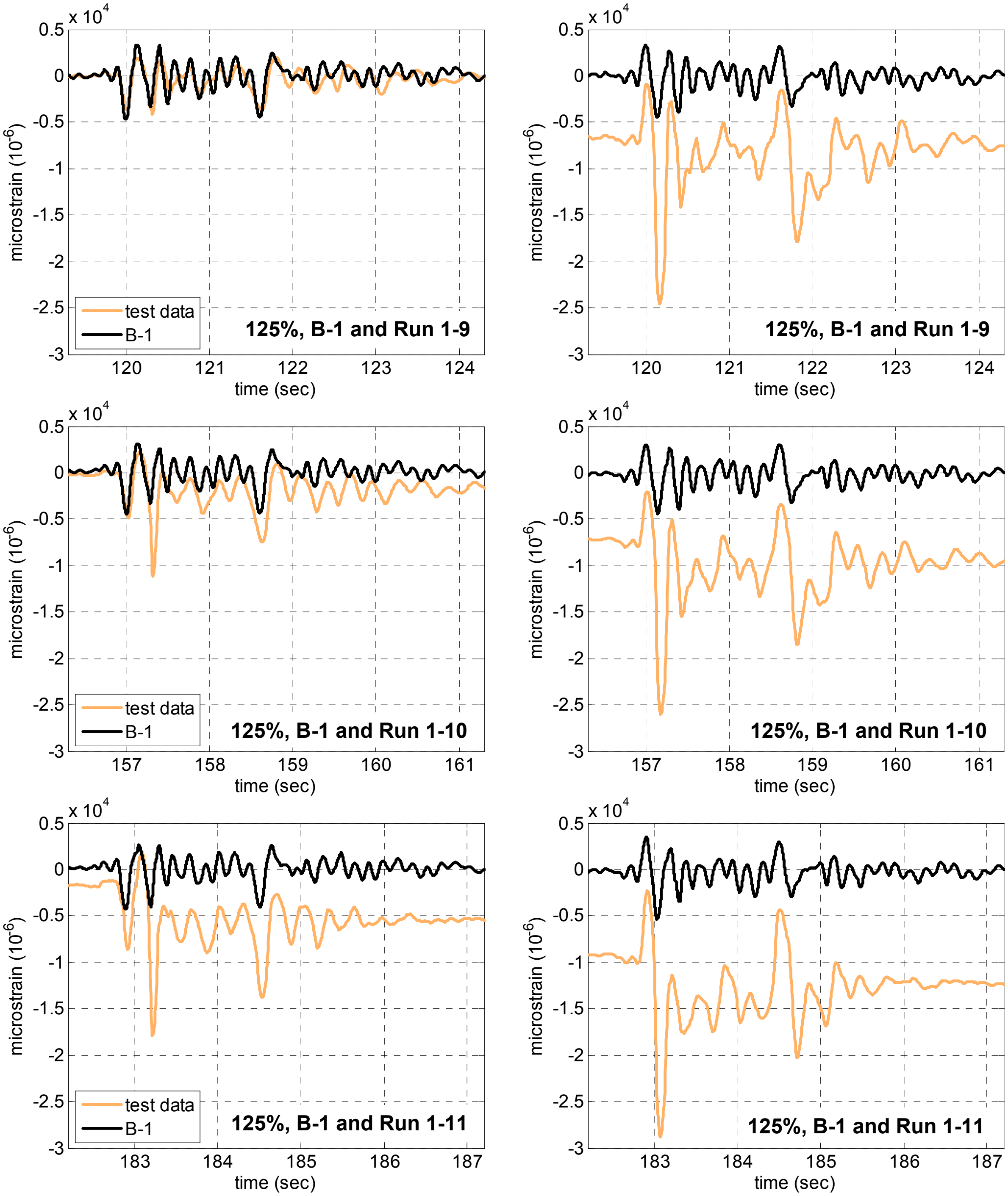

(a) north

(b) south

Figure F.9 **Comparison of longitudinal strain histories at *h* = 60 in. on the north and south of SP1 subjected to 125%-scale motions.**

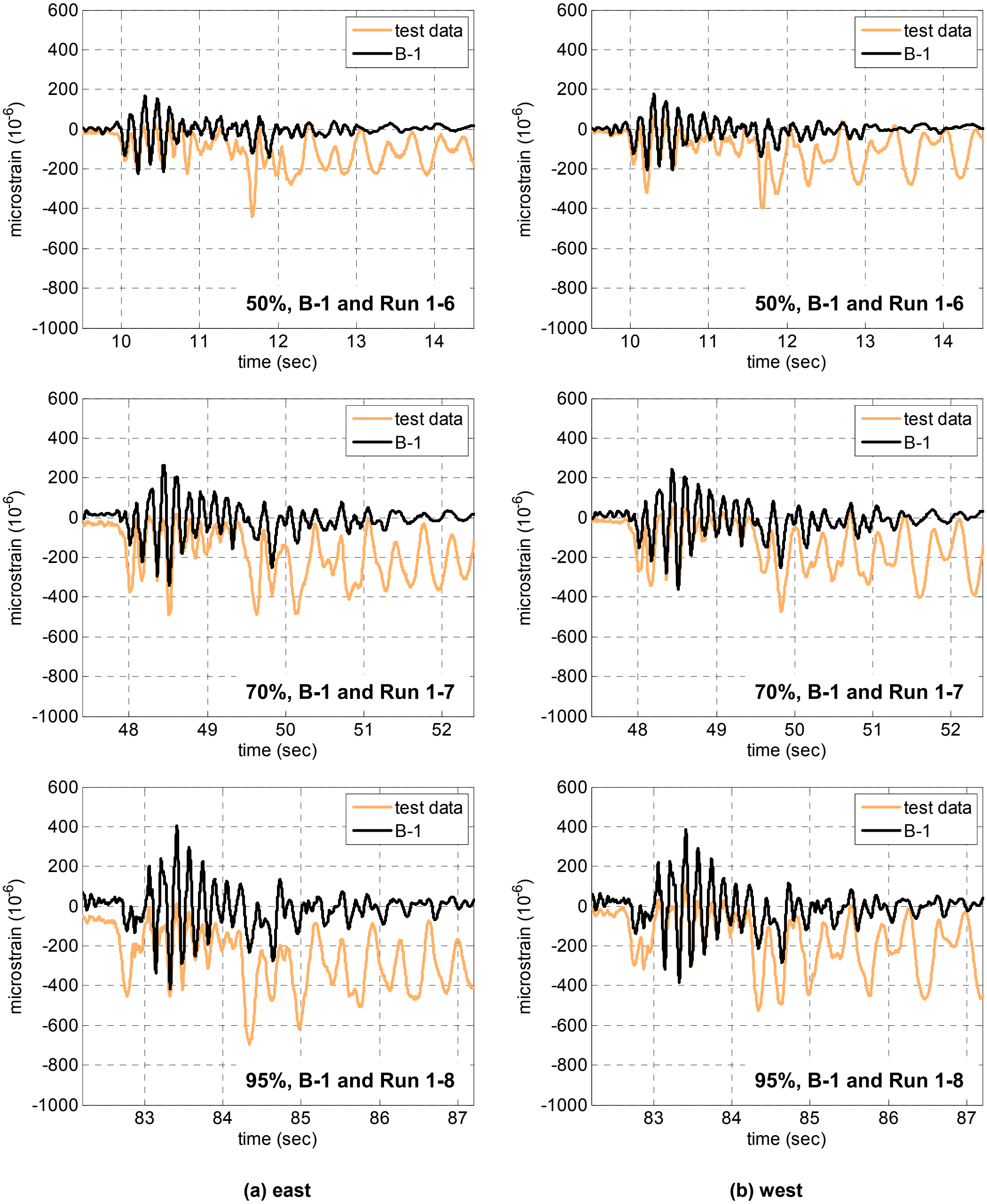

Figure F.10 Comparison of longitudinal strain histories at *h* = 35 in. on the east and west of SP1 subjected to 50%-, 70%-, and 95%-scale motions.

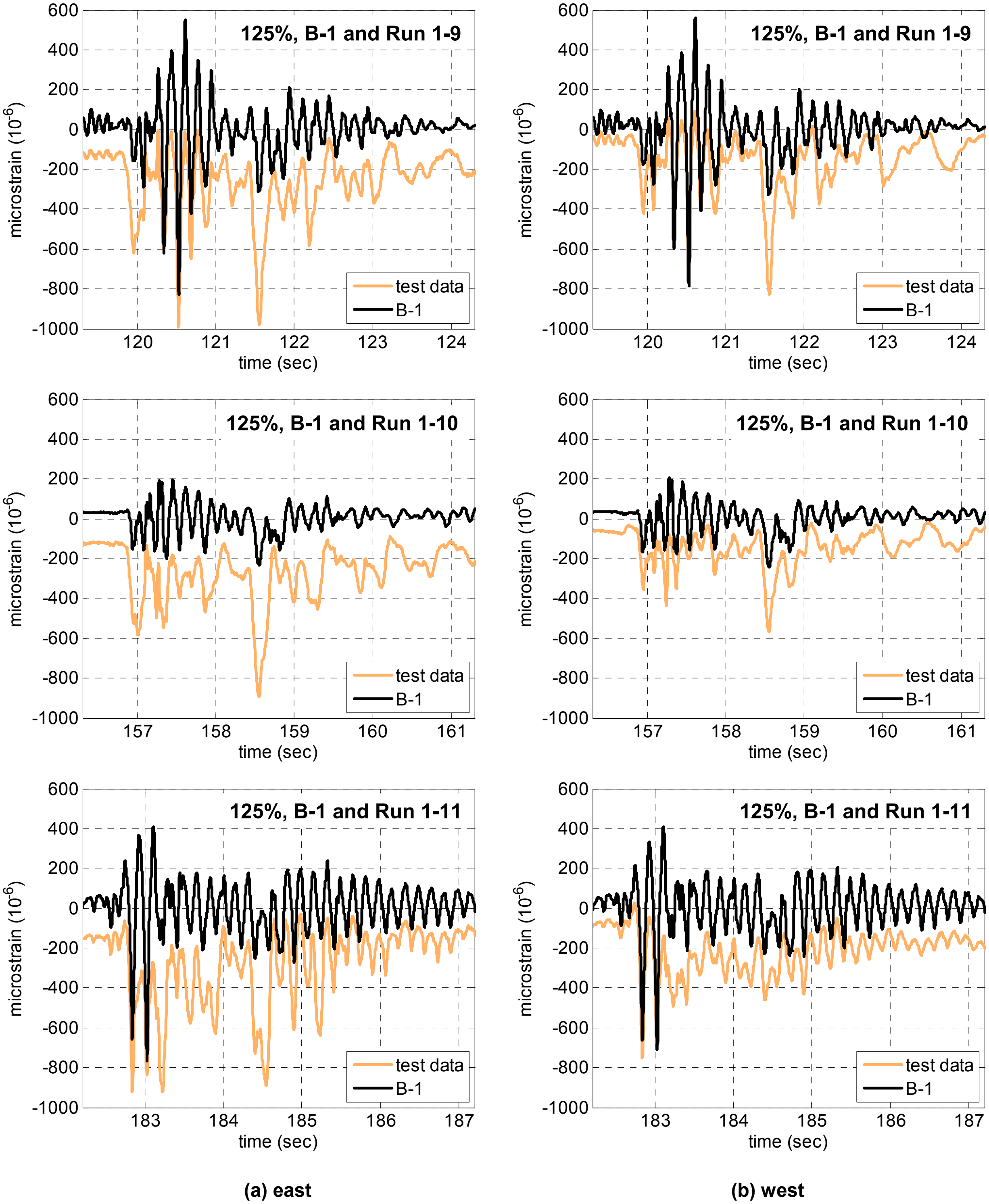

Figure F.11 **Comparison of longitudinal strain histories at *h* = 35 in. on the east and west of SP1 subjected to 125%-scale motions.**

PEER REPORTS

PEER reports are available as a free PDF download from http://peer.berkeley.edu/publications/peer_reports_complete.html. Printed hard copies of PEER reports can be ordered directly from our printer by following the instructions at http://peer.berkeley.edu/publications/peer_reports.html. For other related questions about the PEER Report Series, contact the Pacific Earthquake Engineering Research Center, 325 Davis Hall mail code 1792, Berkeley, CA 94720. Tel.: (510) 642-3437; Fax: (510) 665-1655; Email: peer_editor@berkeley.edu

PEER 2014/04 *Effect of Vertical Acceleration on Shear Strength of Reinforced Concrete Columns.* Hyerin Lee and Khalid M. Mosalam. April 2014.

PEER 2014/03 *Retest of Thirty-Year-Old Neoprene Isolation Bearings.* James M. Kelly and Niel C. Van Engelen. March 2014.

PEER 2014/02 *Theoretical Development of Hybrid Simulation Applied to Plate Structures.* Ahmed A. Bakhaty, Khalid M. Mosalam, and Sanjay Govindjee. January 2014.

PEER 2014/01 *Performance-Based Seismic Assessment of Skewed Bridges.* Peyman Kaviani, Farzin Zareian, and Ertugrul Taciroglu. January 2014.

PEER 2013/25 *Earthquake Engineering for Resilient Communities: 2013 PEER Internship Program Research Report Collection.* Heidi Tremayne (Editor), Stephen A. Mahin (Editor), Jorge Archbold Monterossa, Matt Brosman, Shelly Dean, Katherine deLaveaga, Curtis Fong, Donovan Holder, Rakeeb Khan, Elizabeth Jachens, David Lam, Daniela Martinez Lopez, Mara Minner, Geffen Oren, Julia Pavicic, Melissa Quinonez, Lorena Rodriguez, Sean Salazar, Kelli Slaven, Vivian Steyert, Jenny Taing, and Salvador Tena. December 2013.

PEER 2013/24 *NGA-West2 Ground Motion Prediction Equations for Vertical Ground Motions.* September 2013.

PEER 2013/23 *Coordinated Planning and Preparedness for Fire Following Major Earthquakes.* Charles Scawthorn. November 2013.

PEER 2013/22 *GEM-PEER Task 3 Project: Selection of a Global Set of Ground Motion Prediction Equations.* Jonathan P. Stewart, John Douglas, Mohammad B. Javanbarg, Carola Di Alessandro, Yousef Bozorgnia, Norman A. Abrahamson, David M. Boore, Kenneth W. Campbell, Elise Delavaud, Mustafa Erdik and Peter J. Stafford. December 2013.

PEER 2013/21 *Seismic Design and Performance of Bridges with Columns on Rocking Foundations.* Grigorios Antonellis and Marios Panagiotou. September 2013.

PEER 2013/20 *Experimental and Analytical Studies on the Seismic Behavior of Conventional and Hybrid Braced Frames.* Jiun-Wei Lai and Stephen A. Mahin. September 2013.

PEER 2013/19 *Toward Resilient Communities: A Performance-Based Engineering Framework for Design and Evaluation of the Built Environment.* Michael William Mieler, Bozidar Stojadinovic, Robert J. Budnitz, Stephen A. Mahin and Mary C. Comerio. September 2013.

PEER 2013/18 *Identification of Site Parameters that Improve Predictions of Site Amplification.* Ellen M. Rathje and Sara Navidi. July 2013.

PEER 2013/17 *Response Spectrum Analysis of Concrete Gravity Dams Including Dam-Water-Foundation Interaction.* Arnkjell Løkke and Anil K. Chopra. July 2013.

PEER 2013/16 *Effect of hoop reinforcement spacing on the cyclic response of large reinforced concrete special moment frame beams.* Marios Panagiotou, Tea Visnjic, Grigorios Antonellis, Panagiotis Galanis, and Jack P. Moehle. June 2013.

PEER 2013/15 *A Probabilistic Framework to Include the Effects of Near-Fault Directivity in Seismic Hazard Assessment.* Shrey Kumar Shahi, Jack W. Baker. October 2013.

PEER 2013/14 *Hanging-Wall Scaling using Finite-Fault Simulations.* Jennifer L. Donahue and Norman A. Abrahamson. September 2013.

PEER 2013/13 *Semi-Empirical Nonlinear Site Amplification and its Application in NEHRP Site Factors.* Jonathan P. Stewart and Emel Seyhan. November 2013.

PEER 2013/12 *Nonlinear Horizontal Site Response for the NGA-West2 Project.* Ronnie Kamai, Norman A. Abramson, Walter J. Silva. May 2013.

PEER 2013/11 *Epistemic Uncertainty for NGA-West2 Models.* Linda Al Atik and Robert R. Youngs. May 2013.

PEER 2013/10 *NGA-West 2 Models for Ground-Motion Directionality.* Shrey K. Shahi and Jack W. Baker. May 2013.

PEER 2013/09 *Final Report of the NGA-West2 Directivity Working Group.* Paul Spudich, Jeffrey R. Bayless, Jack W. Baker, Brian S.J. Chiou, Badie Rowshandel, Shrey Shahi, and Paul Somerville. May 2013.

PEER 2013/08 *NGA-West2 Model for Estimating Average Horizontal Values of Pseudo-Absolute Spectral Accelerations Generated by Crustal Earthquakes.* I. M. Idriss. May 2013.

PEER 2013/07 *Update of the Chiou and Youngs NGA Ground Motion Model for Average Horizontal Component of Peak Ground Motion and Response Spectra.* Brian Chiou and Robert Youngs. May 2013.

PEER 2013/06 *NGA-West2 Campbell-Bozorgnia Ground Motion Model for the Horizontal Components of PGA, PGV, and 5%-Damped Elastic Pseudo-Acceleration Response Spectra for Periods Ranging from 0.01 to 10 sec.* Kenneth W. Campbell and Yousef Bozorgnia. May 2013.

PEER 2013/05 *NGA-West 2 Equations for Predicting Response Spectral Accelerations for Shallow Crustal Earthquakes.* David M. Boore, Jonathan P. Stewart, Emel Seyhan, Gail M. Atkinson. May 2013.

PEER 2013/04 *Update of the AS08 Ground-Motion Prediction Equations Based on the NGA-West2 Data Set.* Norman Abrahamson, Walter Silva, and Ronnie Kamai. May 2013.

PEER 2013/03 *PEER NGA-West2 Database.* Timothy D. Ancheta, Robert B. Darragh, Jonathan P. Stewart, Emel Seyhan, Walter J. Silva, Brian S.J. Chiou, Katie E. Wooddell, Robert W. Graves, Albert R. Kottke, David M. Boore, Tadahiro Kishida, and Jennifer L. Donahue. May 2013.

PEER 2013/02 *Hybrid Simulation of the Seismic Response of Squat Reinforced Concrete Shear Walls.* Catherine A. Whyte and Bozidar Stojadinovic. May 2013.

PEER 2013/01 *Housing Recovery in Chile: A Qualitative Mid-program Review.* Mary C. Comerio. February 2013.

PEER 2012/08 *Guidelines for Estimation of Shear Wave Velocity.* Bernard R. Wair, Jason T. DeJong, and Thomas Shantz. December 2012.

PEER 2012/07 *Earthquake Engineering for Resilient Communities: 2012 PEER Internship Program Research Report Collection.* Heidi Tremayne (Editor), Stephen A. Mahin (Editor), Collin Anderson, Dustin Cook, Michael Erceg, Carlos Esparza, Jose Jimenez, Dorian Krausz, Andrew Lo, Stephanie Lopez, Nicole McCurdy, Paul Shipman, Alexander Strum, Eduardo Vega. December 2012.

PEER 2012/06 *Fragilities for Precarious Rocks at Yucca Mountain.* Matthew D. Purvance, Rasool Anooshehpoor, and James N. Brune. December 2012.

PEER 2012/05 *Development of Simplified Analysis Procedure for Piles in Laterally Spreading Layered Soils.* Christopher R. McGann, Pedro Arduino, and Peter Mackenzie–Helnwein. December 2012.

PEER 2012/04 *Unbonded Pre-Tensioned Columns for Bridges in Seismic Regions.* Phillip M. Davis, Todd M. Janes, Marc O. Eberhard, and John F. Stanton. December 2012.

PEER 2012/03 *Experimental and Analytical Studies on Reinforced Concrete Buildings with Seismically Vulnerable Beam-Column Joints.* Sangjoon Park and Khalid M. Mosalam. October 2012.

PEER 2012/02 *Seismic Performance of Reinforced Concrete Bridges Allowed to Uplift during Multi-Directional Excitation.* Andres Oscar Espinoza and Stephen A. Mahin. July 2012.

PEER 2012/01 *Spectral Damping Scaling Factors for Shallow Crustal Earthquakes in Active Tectonic Regions.* Sanaz Rezaeian, Yousef Bozorgnia, I. M. Idriss, Kenneth Campbell, Norman Abrahamson, and Walter Silva. July 2012.

PEER 2011/10 *Earthquake Engineering for Resilient Communities: 2011 PEER Internship Program Research Report Collection.* Eds. Heidi Faison and Stephen A. Mahin. December 2011.

PEER 2011/09 *Calibration of Semi-Stochastic Procedure for Simulating High-Frequency Ground Motions.* Jonathan P. Stewart, Emel Seyhan, and Robert W. Graves. December 2011.

PEER 2011/08 *Water Supply in regard to Fire Following Earthquake.* Charles Scawthorn. November 2011.

PEER 2011/07 *Seismic Risk Management in Urban Areas. Proceedings of a U.S.-Iran-Turkey Seismic Workshop.* September 2011.

PEER 2011/06 *The Use of Base Isolation Systems to Achieve Complex Seismic Performance Objectives.* Troy A. Morgan and Stephen A. Mahin. July 2011.

PEER 2011/05 *Case Studies of the Seismic Performance of Tall Buildings Designed by Alternative Means.* Task 12 Report for the Tall Buildings Initiative. Jack Moehle, Yousef Bozorgnia, Nirmal Jayaram, Pierson Jones, Mohsen Rahnama, Nilesh Shome, Zeynep Tuna, John Wallace, Tony Yang, and Farzin Zareian. July 2011.

PEER 2011/04 *Recommended Design Practice for Pile Foundations in Laterally Spreading Ground.* Scott A. Ashford, Ross W. Boulanger, and Scott J. Brandenberg. June 2011.

PEER 2011/03 *New Ground Motion Selection Procedures and Selected Motions for the PEER Transportation Research Program.* Jack W. Baker, Ting Lin, Shrey K. Shahi, and Nirmal Jayaram. March 2011.

PEER 2011/02 *A Bayesian Network Methodology for Infrastructure Seismic Risk Assessment and Decision Support.* Michelle T. Bensi, Armen Der Kiureghian, and Daniel Straub. March 2011.

PEER 2011/01 *Demand Fragility Surfaces for Bridges in Liquefied and Laterally Spreading Ground.* Scott J. Brandenberg, Jian Zhang, Pirooz Kashighandi, Yili Huo, and Minxing Zhao. March 2011.

PEER 2010/05 *Guidelines for Performance-Based Seismic Design of Tall Buildings.* Developed by the Tall Buildings Initiative. November 2010.

PEER 2010/04 *Application Guide for the Design of Flexible and Rigid Bus Connections between Substation Equipment Subjected to Earthquakes.* Jean-Bernard Dastous and Armen Der Kiureghian. September 2010.

PEER 2010/03 *Shear Wave Velocity as a Statistical Function of Standard Penetration Test Resistance and Vertical Effective Stress at Caltrans Bridge Sites.* Scott J. Brandenberg, Naresh Bellana, and Thomas Shantz. June 2010.

PEER 2010/02 *Stochastic Modeling and Simulation of Ground Motions for Performance-Based Earthquake Engineering.* Sanaz Rezaeian and Armen Der Kiureghian. June 2010.

PEER 2010/01 *Structural Response and Cost Characterization of Bridge Construction Using Seismic Performance Enhancement Strategies.* Ady Aviram, Božidar Stojadinović, Gustavo J. Parra-Montesinos, and Kevin R. Mackie. March 2010.

PEER 2009/03 *The Integration of Experimental and Simulation Data in the Study of Reinforced Concrete Bridge Systems Including Soil-Foundation-Structure Interaction.* Matthew Dryden and Gregory L. Fenves. November 2009.

PEER 2009/02 *Improving Earthquake Mitigation through Innovations and Applications in Seismic Science, Engineering, Communication, and Response. Proceedings of a U.S.-Iran Seismic Workshop.* October 2009.

PEER 2009/01 *Evaluation of Ground Motion Selection and Modification Methods: Predicting Median Interstory Drift Response of Buildings.* Curt B. Haselton, Ed. June 2009.

PEER 2008/10 *Technical Manual for Strata.* Albert R. Kottke and Ellen M. Rathje. February 2009.

PEER 2008/09 *NGA Model for Average Horizontal Component of Peak Ground Motion and Response Spectra.* Brian S.-J. Chiou and Robert R. Youngs. November 2008.

PEER 2008/08 *Toward Earthquake-Resistant Design of Concentrically Braced Steel Structures.* Patxi Uriz and Stephen A. Mahin. November 2008.

PEER 2008/07 *Using OpenSees for Performance-Based Evaluation of Bridges on Liquefiable Soils.* Stephen L. Kramer, Pedro Arduino, and HyungSuk Shin. November 2008.

PEER 2008/06 *Shaking Table Tests and Numerical Investigation of Self-Centering Reinforced Concrete Bridge Columns.* Hyung IL Jeong, Junichi Sakai, and Stephen A. Mahin. September 2008.

PEER 2008/05 *Performance-Based Earthquake Engineering Design Evaluation Procedure for Bridge Foundations Undergoing Liquefaction-Induced Lateral Ground Displacement.* Christian A. Ledezma and Jonathan D. Bray. August 2008.

PEER 2008/04 *Benchmarking of Nonlinear Geotechnical Ground Response Analysis Procedures.* Jonathan P. Stewart, Annie On-Lei Kwok, Yousseff M. A. Hashash, Neven Matasovic, Robert Pyke, Zhiliang Wang, and Zhaohui Yang. August 2008.

PEER 2008/03 *Guidelines for Nonlinear Analysis of Bridge Structures in California.* Ady Aviram, Kevin R. Mackie, and Božidar Stojadinović. August 2008.

PEER 2008/02 *Treatment of Uncertainties in Seismic-Risk Analysis of Transportation Systems.* Evangelos Stergiou and Anne S. Kiremidjian. July 2008.

PEER 2008/01 *Seismic Performance Objectives for Tall Buildings.* William T. Holmes, Charles Kircher, William Petak, and Nabih Youssef. August 2008.

PEER 2007/12 *An Assessment to Benchmark the Seismic Performance of a Code-Conforming Reinforced Concrete Moment-Frame Building.* Curt Haselton, Christine A. Goulet, Judith Mitrani-Reiser, James L. Beck, Gregory G. Deierlein, Keith A. Porter, Jonathan P. Stewart, and Ertugrul Taciroglu. August 2008.

PEER 2007/11 *Bar Buckling in Reinforced Concrete Bridge Columns.* Wayne A. Brown, Dawn E. Lehman, and John F. Stanton. February 2008.

PEER 2007/10 *Computational Modeling of Progressive Collapse in Reinforced Concrete Frame Structures.* Mohamed M. Talaat and Khalid M. Mosalam. May 2008.

PEER 2007/09 *Integrated Probabilistic Performance-Based Evaluation of Benchmark Reinforced Concrete Bridges.* Kevin R. Mackie, John-Michael Wong, and Božidar Stojadinović. January 2008.

PEER 2007/08 *Assessing Seismic Collapse Safety of Modern Reinforced Concrete Moment-Frame Buildings.* Curt B. Haselton and Gregory G. Deierlein. February 2008.

PEER 2007/07 *Performance Modeling Strategies for Modern Reinforced Concrete Bridge Columns.* Michael P. Berry and Marc O. Eberhard. April 2008.

PEER 2007/06 *Development of Improved Procedures for Seismic Design of Buried and Partially Buried Structures.* Linda Al Atik and Nicholas Sitar. June 2007.

PEER 2007/05 *Uncertainty and Correlation in Seismic Risk Assessment of Transportation Systems.* Renee G. Lee and Anne S. Kiremidjian. July 2007.

PEER 2007/04 *Numerical Models for Analysis and Performance-Based Design of Shallow Foundations Subjected to Seismic Loading.* Sivapalan Gajan, Tara C. Hutchinson, Bruce L. Kutter, Prishati Raychowdhury, José A. Ugalde, and Jonathan P. Stewart. May 2008.

PEER 2007/03 *Beam-Column Element Model Calibrated for Predicting Flexural Response Leading to Global Collapse of RC Frame Buildings.* Curt B. Haselton, Abbie B. Liel, Sarah Taylor Lange, and Gregory G. Deierlein. May 2008.

PEER 2007/02 *Campbell-Bozorgnia NGA Ground Motion Relations for the Geometric Mean Horizontal Component of Peak and Spectral Ground Motion Parameters.* Kenneth W. Campbell and Yousef Bozorgnia. May 2007.

PEER 2007/01 *Boore-Atkinson NGA Ground Motion Relations for the Geometric Mean Horizontal Component of Peak and Spectral Ground Motion Parameters.* David M. Boore and Gail M. Atkinson. May. May 2007.

PEER 2006/12 *Societal Implications of Performance-Based Earthquake Engineering.* Peter J. May. May 2007.

PEER 2006/11 *Probabilistic Seismic Demand Analysis Using Advanced Ground Motion Intensity Measures, Attenuation Relationships, and Near-Fault Effects.* Polsak Tothong and C. Allin Cornell. March 2007.

PEER 2006/10 *Application of the PEER PBEE Methodology to the I-880 Viaduct.* Sashi Kunnath. February 2007.

PEER 2006/09 *Quantifying Economic Losses from Travel Forgone Following a Large Metropolitan Earthquake.* James Moore, Sungbin Cho, Yue Yue Fan, and Stuart Werner. November 2006.

PEER 2006/08 *Vector-Valued Ground Motion Intensity Measures for Probabilistic Seismic Demand Analysis.* Jack W. Baker and C. Allin Cornell. October 2006.

PEER 2006/07 *Analytical Modeling of Reinforced Concrete Walls for Predicting Flexural and Coupled–Shear-Flexural Responses.* Kutay Orakcal, Leonardo M. Massone, and John W. Wallace. October 2006.

PEER 2006/06 *Nonlinear Analysis of a Soil-Drilled Pier System under Static and Dynamic Axial Loading.* Gang Wang and Nicholas Sitar. November 2006.

PEER 2006/05 *Advanced Seismic Assessment Guidelines.* Paolo Bazzurro, C. Allin Cornell, Charles Menun, Maziar Motahari, and Nicolas Luco. September 2006.

PEER 2006/04 *Probabilistic Seismic Evaluation of Reinforced Concrete Structural Components and Systems.* Tae Hyung Lee and Khalid M. Mosalam. August 2006.

PEER 2006/03 *Performance of Lifelines Subjected to Lateral Spreading.* Scott A. Ashford and Teerawut Juirnarongrit. July 2006.

PEER 2006/02 *Pacific Earthquake Engineering Research Center Highway Demonstration Project.* Anne Kiremidjian, James Moore, Yue Yue Fan, Nesrin Basoz, Ozgur Yazali, and Meredith Williams. April 2006.

PEER 2006/01 *Bracing Berkeley. A Guide to Seismic Safety on the UC Berkeley Campus.* Mary C. Comerio, Stephen Tobriner, and Ariane Fehrenkamp. January 2006.

PEER 2005/16 *Seismic Response and Reliability of Electrical Substation Equipment and Systems.* Junho Song, Armen Der Kiureghian, and Jerome L. Sackman. April 2006.

PEER 2005/15 *CPT-Based Probabilistic Assessment of Seismic Soil Liquefaction Initiation.* R. E. S. Moss, R. B. Seed, R. E. Kayen, J. P. Stewart, and A. Der Kiureghian. April 2006.

PEER 2005/14 *Workshop on Modeling of Nonlinear Cyclic Load-Deformation Behavior of Shallow Foundations.* Bruce L. Kutter, Geoffrey Martin, Tara Hutchinson, Chad Harden, Sivapalan Gajan, and Justin Phalen. March 2006.

PEER 2005/13 *Stochastic Characterization and Decision Bases under Time-Dependent Aftershock Risk in Performance-Based Earthquake Engineering.* Gee Liek Yeo and C. Allin Cornell. July 2005.

PEER 2005/12 *PEER Testbed Study on a Laboratory Building: Exercising Seismic Performance Assessment.* Mary C. Comerio, editor. November 2005.

PEER 2005/11 *Van Nuys Hotel Building Testbed Report: Exercising Seismic Performance Assessment.* Helmut Krawinkler, editor. October 2005.

PEER 2005/10 *First NEES/E-Defense Workshop on Collapse Simulation of Reinforced Concrete Building Structures.* September 2005.

PEER 2005/09 *Test Applications of Advanced Seismic Assessment Guidelines.* Joe Maffei, Karl Telleen, Danya Mohr, William Holmes, and Yuki Nakayama. August 2006.

PEER 2005/08 *Damage Accumulation in Lightly Confined Reinforced Concrete Bridge Columns.* R. Tyler Ranf, Jared M. Nelson, Zach Price, Marc O. Eberhard, and John F. Stanton. April 2006.

PEER 2005/07 *Experimental and Analytical Studies on the Seismic Response of Freestanding and Anchored Laboratory Equipment.* Dimitrios Konstantinidis and Nicos Makris. January 2005.

PEER 2005/06 *Global Collapse of Frame Structures under Seismic Excitations.* Luis F. Ibarra and Helmut Krawinkler. September 2005.

PEER 2005//05 *Performance Characterization of Bench- and Shelf-Mounted Equipment.* Samit Ray Chaudhuri and Tara C. Hutchinson. May 2006.

PEER 2005/04 *Numerical Modeling of the Nonlinear Cyclic Response of Shallow Foundations.* Chad Harden, Tara Hutchinson, Geoffrey R. Martin, and Bruce L. Kutter. August 2005.

PEER 2005/03 *A Taxonomy of Building Components for Performance-Based Earthquake Engineering.* Keith A. Porter. September 2005.

PEER 2005/02 *Fragility Basis for California Highway Overpass Bridge Seismic Decision Making.* Kevin R. Mackie and Božidar Stojadinović. June 2005.

PEER 2005/01 *Empirical Characterization of Site Conditions on Strong Ground Motion.* Jonathan P. Stewart, Yoojoong Choi, and Robert W. Graves. June 2005.

PEER 2004/09 *Electrical Substation Equipment Interaction: Experimental Rigid Conductor Studies.* Christopher Stearns and André Filiatrault. February 2005.

PEER 2004/08 *Seismic Qualification and Fragility Testing of Line Break 550-kV Disconnect Switches.* Shakhzod M. Takhirov, Gregory L. Fenves, and Eric Fujisaki. January 2005.

PEER 2004/07 *Ground Motions for Earthquake Simulator Qualification of Electrical Substation Equipment.* Shakhzod M. Takhirov, Gregory L. Fenves, Eric Fujisaki, and Don Clyde. January 2005.

PEER 2004/06 *Performance-Based Regulation and Regulatory Regimes.* Peter J. May and Chris Koski. September 2004.

PEER 2004/05 *Performance-Based Seismic Design Concepts and Implementation: Proceedings of an International Workshop.* Peter Fajfar and Helmut Krawinkler, editors. September 2004.

PEER 2004/04 *Seismic Performance of an Instrumented Tilt-up Wall Building.* James C. Anderson and Vitelmo V. Bertero. July 2004.

PEER 2004/03 *Evaluation and Application of Concrete Tilt-up Assessment Methodologies.* Timothy Graf and James O. Malley. October 2004.

PEER 2004/02 *Analytical Investigations of New Methods for Reducing Residual Displacements of Reinforced Concrete Bridge Columns.* Junichi Sakai and Stephen A. Mahin. August 2004.

PEER 2004/01 *Seismic Performance of Masonry Buildings and Design Implications.* Kerri Anne Taeko Tokoro, James C. Anderson, and Vitelmo V. Bertero. February 2004.

PEER 2003/18 *Performance Models for Flexural Damage in Reinforced Concrete Columns.* Michael Berry and Marc Eberhard. August 2003.

PEER 2003/17 *Predicting Earthquake Damage in Older Reinforced Concrete Beam-Column Joints.* Catherine Pagni and Laura Lowes. October 2004.

PEER 2003/16 *Seismic Demands for Performance-Based Design of Bridges.* Kevin Mackie and Božidar Stojadinović. August 2003.

PEER 2003/15 *Seismic Demands for Nondeteriorating Frame Structures and Their Dependence on Ground Motions.* Ricardo Antonio Medina and Helmut Krawinkler. May 2004.

PEER 2003/14 *Finite Element Reliability and Sensitivity Methods for Performance-Based Earthquake Engineering.* Terje Haukaas and Armen Der Kiureghian. April 2004.

PEER 2003/13 *Effects of Connection Hysteretic Degradation on the Seismic Behavior of Steel Moment-Resisting Frames.* Janise E. Rodgers and Stephen A. Mahin. March 2004.

PEER 2003/12 *Implementation Manual for the Seismic Protection of Laboratory Contents: Format and Case Studies.* William T. Holmes and Mary C. Comerio. October 2003.

PEER 2003/11 *Fifth U.S.-Japan Workshop on Performance-Based Earthquake Engineering Methodology for Reinforced Concrete Building Structures.* February 2004.

PEER 2003/10 *A Beam-Column Joint Model for Simulating the Earthquake Response of Reinforced Concrete Frames.* Laura N. Lowes, Nilanjan Mitra, and Arash Altoontash. February 2004.

PEER 2003/09 *Sequencing Repairs after an Earthquake: An Economic Approach.* Marco Casari and Simon J. Wilkie. April 2004.

PEER 2003/08 *A Technical Framework for Probability-Based Demand and Capacity Factor Design (DCFD) Seismic Formats*. Fatemeh Jalayer and C. Allin Cornell. November 2003.

PEER 2003/07 *Uncertainty Specification and Propagation for Loss Estimation Using FOSM Methods.* Jack W. Baker and C. Allin Cornell. September 2003.

PEER 2003/06 *Performance of Circular Reinforced Concrete Bridge Columns under Bidirectional Earthquake Loading*. Mahmoud M. Hachem, Stephen A. Mahin, and Jack P. Moehle. February 2003.

PEER 2003/05 *Response Assessment for Building-Specific Loss Estimation.* Eduardo Miranda and Shahram Taghavi. September 2003.

PEER 2003/04 *Experimental Assessment of Columns with Short Lap Splices Subjected to Cyclic Loads*. Murat Melek, John W. Wallace, and Joel Conte. April 2003.

PEER 2003/03 *Probabilistic Response Assessment for Building-Specific Loss Estimation.* Eduardo Miranda and Hesameddin Aslani. September 2003.

PEER 2003/02 *Software Framework for Collaborative Development of Nonlinear Dynamic Analysis Program.* Jun Peng and Kincho H. Law. September 2003.

PEER 2003/01 *Shake Table Tests and Analytical Studies on the Gravity Load Collapse of Reinforced Concrete Frames.* Kenneth John Elwood and Jack P. Moehle. November 2003.

PEER 2002/24 *Performance of Beam to Column Bridge Joints Subjected to a Large Velocity Pulse.* Natalie Gibson, André Filiatrault, and Scott A. Ashford. April 2002.

PEER 2002/23 *Effects of Large Velocity Pulses on Reinforced Concrete Bridge Columns.* Greg L. Orozco and Scott A. Ashford. April 2002.

PEER 2002/22 *Characterization of Large Velocity Pulses for Laboratory Testing*. Kenneth E. Cox and Scott A. Ashford. April 2002.

PEER 2002/21 *Fourth U.S.-Japan Workshop on Performance-Based Earthquake Engineering Methodology for Reinforced Concrete Building Structures*. December 2002.

PEER 2002/20 *Barriers to Adoption and Implementation of PBEE Innovations.* Peter J. May. August 2002.

PEER 2002/19 *Economic-Engineered Integrated Models for Earthquakes: Socioeconomic Impacts.* Peter Gordon, James E. Moore II, and Harry W. Richardson. July 2002.

PEER 2002/18 *Assessment of Reinforced Concrete Building Exterior Joints with Substandard Details.* Chris P. Pantelides, Jon Hansen, Justin Nadauld, and Lawrence D. Reaveley. May 2002.

PEER 2002/17 *Structural Characterization and Seismic Response Analysis of a Highway Overcrossing Equipped with Elastomeric Bearings and Fluid Dampers: A Case Study.* Nicos Makris and Jian Zhang. November 2002.

PEER 2002/16 *Estimation of Uncertainty in Geotechnical Properties for Performance-Based Earthquake Engineering.* Allen L. Jones, Steven L. Kramer, and Pedro Arduino. December 2002.

PEER 2002/15 *Seismic Behavior of Bridge Columns Subjected to Various Loading Patterns.* Asadollah Esmaeily-Gh. and Yan Xiao. December 2002.

PEER 2002/14 *Inelastic Seismic Response of Extended Pile Shaft Supported Bridge Structures.* T.C. Hutchinson, R.W. Boulanger, Y.H. Chai, and I.M. Idriss. December 2002.

PEER 2002/13 *Probabilistic Models and Fragility Estimates for Bridge Components and Systems.* Paolo Gardoni, Armen Der Kiureghian, and Khalid M. Mosalam. June 2002.

PEER 2002/12 *Effects of Fault Dip and Slip Rake on Near-Source Ground Motions: Why Chi-Chi Was a Relatively Mild M7.6 Earthquake.* Brad T. Aagaard, John F. Hall, and Thomas H. Heaton. December 2002.

PEER 2002/11 *Analytical and Experimental Study of Fiber-Reinforced Strip Isolators*. James M. Kelly and Shakhzod M. Takhirov. September 2002.

PEER 2002/10 *Centrifuge Modeling of Settlement and Lateral Spreading with Comparisons to Numerical Analyses***.** Sivapalan Gajan and Bruce L. Kutter. January 2003.

PEER 2002/09 *Documentation and Analysis of Field Case Histories of Seismic Compression during the 1994 Northridge, California, Earthquake.* Jonathan P. Stewart, Patrick M. Smith, Daniel H. Whang, and Jonathan D. Bray. October 2002.

PEER 2002/08 *Component Testing, Stability Analysis and Characterization of Buckling-Restrained Unbonded Braces™.* Cameron Black, Nicos Makris, and Ian Aiken. September 2002.

PEER 2002/07 *Seismic Performance of Pile-Wharf Connections.* Charles W. Roeder, Robert Graff, Jennifer Soderstrom, and Jun Han Yoo. December 2001.

PEER 2002/06 *The Use of Benefit-Cost Analysis for Evaluation of Performance-Based Earthquake Engineering Decisions.* Richard O. Zerbe and Anthony Falit-Baiamonte. September 2001.

PEER 2002/05 *Guidelines, Specifications, and Seismic Performance Characterization of Nonstructural Building Components and Equipment*. André Filiatrault, Constantin Christopoulos, and Christopher Stearns. September 2001.

PEER 2002/04 *Consortium of Organizations for Strong-Motion Observation Systems and the Pacific Earthquake Engineering Research Center Lifelines Program: Invited Workshop on Archiving and Web Dissemination of Geotechnical Data, 4–5 October 2001.* September 2002.

PEER 2002/03 *Investigation of Sensitivity of Building Loss Estimates to Major Uncertain Variables for the Van Nuys Testbed.* Keith A. Porter, James L. Beck, and Rustem V. Shaikhutdinov. August 2002.

PEER 2002/02 *The Third U.S.-Japan Workshop on Performance-Based Earthquake Engineering Methodology for Reinforced Concrete Building Structures*. July 2002.

PEER 2002/01 *Nonstructural Loss Estimation: The UC Berkeley Case Study.* Mary C. Comerio and John C. Stallmeyer. December 2001.

PEER 2001/16 *Statistics of SDF-System Estimate of Roof Displacement for Pushover Analysis of Buildings.* Anil K. Chopra, Rakesh K. Goel, and Chatpan Chintanapakdee. December 2001.

PEER 2001/15 *Damage to Bridges during the 2001 Nisqually Earthquake.* R. Tyler Ranf, Marc O. Eberhard, and Michael P. Berry. November 2001.

PEER 2001/14 *Rocking Response of Equipment Anchored to a Base Foundation.* Nicos Makris and Cameron J. Black. September 2001.

PEER 2001/13 *Modeling Soil Liquefaction Hazards for Performance-Based Earthquake Engineering.* Steven L. Kramer and Ahmed-W. Elgamal. February 2001.

PEER 2001/12 *Development of Geotechnical Capabilities in OpenSees*. Boris Jeremić. September 2001.

PEER 2001/11 *Analytical and Experimental Study of Fiber-Reinforced Elastomeric Isolators*. James M. Kelly and Shakhzod M. Takhirov. September 2001.

PEER 2001/10 *Amplification Factors for Spectral Acceleration in Active Regions*. Jonathan P. Stewart, Andrew H. Liu, Yoojoong Choi, and Mehmet B. Baturay. December 2001.

PEER 2001/09 *Ground Motion Evaluation Procedures for Performance-Based Design.* Jonathan P. Stewart, Shyh-Jeng Chiou, Jonathan D. Bray, Robert W. Graves, Paul G. Somerville, and Norman A. Abrahamson. September 2001.

PEER 2001/08 *Experimental and Computational Evaluation of Reinforced Concrete Bridge Beam-Column Connections for Seismic Performance*. Clay J. Naito, Jack P. Moehle, and Khalid M. Mosalam. November 2001.

PEER 2001/07 *The Rocking Spectrum and the Shortcomings of Design Guidelines.* Nicos Makris and Dimitrios Konstantinidis. August 2001.

PEER 2001/06 *Development of an Electrical Substation Equipment Performance Database for Evaluation of Equipment Fragilities.* Thalia Agnanos. April 1999.

PEER 2001/05 *Stiffness Analysis of Fiber-Reinforced Elastomeric Isolators.* Hsiang-Chuan Tsai and James M. Kelly. May 2001.

PEER 2001/04 *Organizational and Societal Considerations for Performance-Based Earthquake Engineering.* Peter J. May. April 2001.

PEER 2001/03 *A Modal Pushover Analysis Procedure to Estimate Seismic Demands for Buildings: Theory and Preliminary Evaluation.* Anil K. Chopra and Rakesh K. Goel. January 2001.

PEER 2001/02 *Seismic Response Analysis of Highway Overcrossings Including Soil-Structure Interaction.* Jian Zhang and Nicos Makris. March 2001.

PEER 2001/01 *Experimental Study of Large Seismic Steel Beam-to-Column Connections.* Egor P. Popov and Shakhzod M. Takhirov. November 2000.

PEER 2000/10 *The Second U.S.-Japan Workshop on Performance-Based Earthquake Engineering Methodology for Reinforced Concrete Building Structures.* March 2000.

PEER 2000/09 *Structural Engineering Reconnaissance of the August 17, 1999 Earthquake: Kocaeli (Izmit), Turkey.* Halil Sezen, Kenneth J. Elwood, Andrew S. Whittaker, Khalid Mosalam, John J. Wallace, and John F. Stanton. December 2000.

PEER 2000/08 *Behavior of Reinforced Concrete Bridge Columns Having Varying Aspect Ratios and Varying Lengths of Confinement.* Anthony J. Calderone, Dawn E. Lehman, and Jack P. Moehle. January 2001.

PEER 2000/07 *Cover-Plate and Flange-Plate Reinforced Steel Moment-Resisting Connections.* Taejin Kim, Andrew S. Whittaker, Amir S. Gilani, Vitelmo V. Bertero, and Shakhzod M. Takhirov. September 2000.

PEER 2000/06 *Seismic Evaluation and Analysis of 230-kV Disconnect Switches.* Amir S. J. Gilani, Andrew S. Whittaker, Gregory L. Fenves, Chun-Hao Chen, Henry Ho, and Eric Fujisaki. July 2000.

PEER 2000/05 *Performance-Based Evaluation of Exterior Reinforced Concrete Building Joints for Seismic Excitation.* Chandra Clyde, Chris P. Pantelides, and Lawrence D. Reaveley. July 2000.

PEER 2000/04 *An Evaluation of Seismic Energy Demand: An Attenuation Approach.* Chung-Che Chou and Chia-Ming Uang. July 1999.

PEER 2000/03 *Framing Earthquake Retrofitting Decisions: The Case of Hillside Homes in Los Angeles.* Detlof von Winterfeldt, Nels Roselund, and Alicia Kitsuse. March 2000.

PEER 2000/02 *U.S.-Japan Workshop on the Effects of Near-Field Earthquake Shaking.* Andrew Whittaker, ed. July 2000.

PEER 2000/01 *Further Studies on Seismic Interaction in Interconnected Electrical Substation Equipment.* Armen Der Kiureghian, Kee-Jeung Hong, and Jerome L. Sackman. November 1999.

PEER 1999/14 *Seismic Evaluation and Retrofit of 230-kV Porcelain Transformer Bushings*. Amir S. Gilani, Andrew S. Whittaker, Gregory L. Fenves, and Eric Fujisaki. December 1999.

PEER 1999/13 *Building Vulnerability Studies: Modeling and Evaluation of Tilt-up and Steel Reinforced Concrete Buildings.* John W. Wallace, Jonathan P. Stewart, and Andrew S. Whittaker, editors. December 1999.

PEER 1999/12 *Rehabilitation of Nonductile RC Frame Building Using Encasement Plates and Energy-Dissipating Devices.* Mehrdad Sasani, Vitelmo V. Bertero, James C. Anderson. December 1999.

PEER 1999/11 *Performance Evaluation Database for Concrete Bridge Components and Systems under Simulated Seismic Loads.* Yael D. Hose and Frieder Seible. November 1999.

PEER 1999/10 *U.S.-Japan Workshop on Performance-Based Earthquake Engineering Methodology for Reinforced Concrete Building Structures.* December 1999.

PEER 1999/09 *Performance Improvement of Long Period Building Structures Subjected to Severe Pulse-Type Ground Motions*. James C. Anderson, Vitelmo V. Bertero, and Raul Bertero. October 1999.

PEER 1999/08 *Envelopes for Seismic Response Vectors.* Charles Menun and Armen Der Kiureghian. July 1999.

PEER 1999/07 *Documentation of Strengths and Weaknesses of Current Computer Analysis Methods for Seismic Performance of Reinforced Concrete Members.* William F. Cofer. November 1999.

PEER 1999/06 *Rocking Response and Overturning of Anchored Equipment under Seismic Excitations.* Nicos Makris and Jian Zhang. November 1999.

PEER 1999/05 *Seismic Evaluation of 550 kV Porcelain Transformer Bushings.* Amir S. Gilani, Andrew S. Whittaker, Gregory L. Fenves, and Eric Fujisaki. October 1999.

PEER 1999/04 *Adoption and Enforcement of Earthquake Risk-Reduction Measures.* Peter J. May, Raymond J. Burby, T. Jens Feeley, and Robert Wood.

PEER 1999/03 *Task 3 Characterization of Site Response General Site Categories*. Adrian Rodriguez-Marek, Jonathan D. Bray, and Norman Abrahamson. February 1999.

PEER 1999/02 *Capacity-Demand-Diagram Methods for Estimating Seismic Deformation of Inelastic Structures: SDF Systems*. Anil K. Chopra and Rakesh Goel. April 1999.

PEER 1999/01 *Interaction in Interconnected Electrical Substation Equipment Subjected to Earthquake Ground Motions.* Armen Der Kiureghian, Jerome L. Sackman, and Kee-Jeung Hong. February 1999.

PEER 1998/08 *Behavior and Failure Analysis of a Multiple-Frame Highway Bridge in the 1994 Northridge Earthquake.* Gregory L. Fenves and Michael Ellery. December 1998.

PEER 1998/07 *Empirical Evaluation of Inertial Soil-Structure Interaction Effects.* Jonathan P. Stewart, Raymond B. Seed, and Gregory L. Fenves. November 1998.

PEER 1998/06 *Effect of Damping Mechanisms on the Response of Seismic Isolated Structures.* Nicos Makris and Shih-Po Chang. November 1998.

PEER 1998/05 *Rocking Response and Overturning of Equipment under Horizontal Pulse-Type Motions.* Nicos Makris and Yiannis Roussos. October 1998.

PEER 1998/04 *Pacific Earthquake Engineering Research Invitational Workshop Proceedings, May 14–15, 1998: Defining the Links between Planning, Policy Analysis, Economics and Earthquake Engineering.* Mary Comerio and Peter Gordon. September 1998.

PEER 1998/03 *Repair/Upgrade Procedures for Welded Beam to Column Connections.* James C. Anderson and Xiaojing Duan. May 1998.

PEER 1998/02 *Seismic Evaluation of 196 kV Porcelain Transformer Bushings.* Amir S. Gilani, Juan W. Chavez, Gregory L. Fenves, and Andrew S. Whittaker. May 1998.

PEER 1998/01 *Seismic Performance of Well-Confined Concrete Bridge Columns.* Dawn E. Lehman and Jack P. Moehle. December 2000.

ONLINE PEER REPORTS

The following PEER reports are available by Internet only at http://peer.berkeley.edu/publications/peer_reports_complete.html.

PEER 2012/103 *Performance-Based Seismic Demand Assessment of Concentrically Braced Steel Frame Buildings.* Chui-Hsin Chen and Stephen A. Mahin. December 2012.

PEER 2012/102 *Procedure to Restart an Interrupted Hybrid Simulation: Addendum to PEER Report 2010/103.* Vesna Terzic and Bozidar Stojadinovic. October 2012.

PEER 2012/101 *Mechanics of Fiber Reinforced Bearings.* James M. Kelly and Andrea Calabrese. February 2012.

PEER 2011/107 *Nonlinear Site Response and Seismic Compression at Vertical Array Strongly Shaken by 2007 Niigata-ken Chuetsu-oki Earthquake.* Eric Yee, Jonathan P. Stewart, and Kohji Tokimatsu. December 2011.

PEER 2011/106 *Self Compacting Hybrid Fiber Reinforced Concrete Composites for Bridge Columns.* Pardeep Kumar, Gabriel Jen, William Trono, Marios Panagiotou, and Claudia Ostertag. September 2011.

PEER 2011/105 *Stochastic Dynamic Analysis of Bridges Subjected to Spacially Varying Ground Motions.* Katerina Konakli and Armen Der Kiureghian. August 2011.

PEER 2011/104 *Design and Instrumentation of the 2010 E-Defense Four-Story Reinforced Concrete and Post-Tensioned Concrete Buildings.* Takuya Nagae, Kenichi Tahara, Taizo Matsumori, Hitoshi Shiohara, Toshimi Kabeyasawa, Susumu Kono, Minehiro Nishiyama (Japanese Research Team) and John Wallace, Wassim Ghannoum, Jack Moehle, Richard Sause, Wesley Keller, Zeynep Tuna (U.S. Research Team). June 2011.

PEER 2011/103 *In-Situ Monitoring of the Force Output of Fluid Dampers: Experimental Investigation.* Dimitrios Konstantinidis, James M. Kelly, and Nicos Makris. April 2011.

PEER 2011/102 *Ground-motion prediction equations 1964 - 2010.* John Douglas. April 2011.

PEER 2011/101 *Report of the Eighth Planning Meeting of NEES/E-Defense Collaborative Research on Earthquake Engineering.* Convened by the Hyogo Earthquake Engineering Research Center (NIED), NEES Consortium, Inc. February 2011.

PEER 2010/111 *Modeling and Acceptance Criteria for Seismic Design and Analysis of Tall Buildings.* Task 7 Report for the Tall Buildings Initiative - Published jointly by the Applied Technology Council. October 2010.

PEER 2010/110 *Seismic Performance Assessment and Probabilistic Repair Cost Analysis of Precast Concrete Cladding Systems for Multistory Buildlings.* Jeffrey P. Hunt and Božidar Stojadinovic. November 2010.

PEER 2010/109 *Report of the Seventh Joint Planning Meeting of NEES/E-Defense Collaboration on Earthquake Engineering. Held at the E-Defense, Miki, and Shin-Kobe, Japan, September 18–19, 2009.* August 2010.

PEER 2010/108 *Probabilistic Tsunami Hazard in California.* Hong Kie Thio, Paul Somerville, and Jascha Polet, preparers. October 2010.

PEER 2010/107 *Performance and Reliability of Exposed Column Base Plate Connections for Steel Moment-Resisting Frames.* Ady Aviram, Božidar Stojadinovic, and Armen Der Kiureghian. August 2010.

PEER 2010/106 *Verification of Probabilistic Seismic Hazard Analysis Computer Programs.* Patricia Thomas, Ivan Wong, and Norman Abrahamson. May 2010.

PEER 2010/105 *Structural Engineering Reconnaissance of the April 6, 2009, Abruzzo, Italy, Earthquake, and Lessons Learned.* M. Selim Günay and Khalid M. Mosalam. April 2010.

PEER 2010/104 *Simulating the Inelastic Seismic Behavior of Steel Braced Frames, Including the Effects of Low-Cycle Fatigue.* Yuli Huang and Stephen A. Mahin. April 2010.

PEER 2010/103 *Post-Earthquake Traffic Capacity of Modern Bridges in California.* Vesna Terzic and Božidar Stojadinović. March 2010.

PEER 2010/102 *Analysis of Cumulative Absolute Velocity (CAV) and JMA Instrumental Seismic Intensity (I_{JMA}) Using the PEER–NGA Strong Motion Database.* Kenneth W. Campbell and Yousef Bozorgnia. February 2010.

PEER 2010/101 *Rocking Response of Bridges on Shallow Foundations.* Jose A. Ugalde, Bruce L. Kutter, and Boris Jeremic. April 2010.

PEER 2009/109 *Simulation and Performance-Based Earthquake Engineering Assessment of Self-Centering Post-Tensioned Concrete Bridge Systems.* Won K. Lee and Sarah L. Billington. December 2009.

PEER 2009/108 *PEER Lifelines Geotechnical Virtual Data Center.* J. Carl Stepp, Daniel J. Ponti, Loren L. Turner, Jennifer N. Swift, Sean Devlin, Yang Zhu, Jean Benoit, and John Bobbitt. September 2009.

PEER 2009/107 *Experimental and Computational Evaluation of Current and Innovative In-Span Hinge Details in Reinforced Concrete Box-Girder Bridges: Part 2: Post-Test Analysis and Design Recommendations.* Matias A. Hube and Khalid M. Mosalam. December 2009.

PEER 2009/106 *Shear Strength Models of Exterior Beam-Column Joints without Transverse Reinforcement.* Sangjoon Park and Khalid M. Mosalam. November 2009.

PEER 2009/105 *Reduced Uncertainty of Ground Motion Prediction Equations through Bayesian Variance Analysis.* Robb Eric S. Moss. November 2009.

PEER 2009/104 *Advanced Implementation of Hybrid Simulation.* Andreas H. Schellenberg, Stephen A. Mahin, Gregory L. Fenves. November 2009.

PEER 2009/103 *Performance Evaluation of Innovative Steel Braced Frames.* T. Y. Yang, Jack P. Moehle, and Božidar Stojadinovic. August 2009.

PEER 2009/102 *Reinvestigation of Liquefaction and Nonliquefaction Case Histories from the 1976 Tangshan Earthquake.* Robb Eric Moss, Robert E. Kayen, Liyuan Tong, Songyu Liu, Guojun Cai, and Jiaer Wu. August 2009.

PEER 2009/101 *Report of the First Joint Planning Meeting for the Second Phase of NEES/E-Defense Collaborative Research on Earthquake Engineering.* Stephen A. Mahin et al. July 2009.

PEER 2008/104 *Experimental and Analytical Study of the Seismic Performance of Retaining Structures.* Linda Al Atik and Nicholas Sitar. January 2009.

PEER 2008/103 *Experimental and Computational Evaluation of Current and Innovative In-Span Hinge Details in Reinforced Concrete Box-Girder Bridges. Part 1: Experimental Findings and Pre-Test Analysis.* Matias A. Hube and Khalid M. Mosalam. January 2009.

PEER 2008/102 *Modeling of Unreinforced Masonry Infill Walls Considering In-Plane and Out-of-Plane Interaction.* Stephen Kadysiewski and Khalid M. Mosalam. January 2009.

PEER 2008/101 *Seismic Performance Objectives for Tall Buildings.* William T. Holmes, Charles Kircher, William Petak, and Nabih Youssef. August 2008.

PEER 2007/101 *Generalized Hybrid Simulation Framework for Structural Systems Subjected to Seismic Loading.* Tarek Elkhoraibi and Khalid M. Mosalam. July 2007.

PEER 2007/100 *Seismic Evaluation of Reinforced Concrete Buildings Including Effects of Masonry Infill Walls.* Alidad Hashemi and Khalid M. Mosalam. July 2007.

The Pacific Earthquake Engineering Research Center (PEER) is a multi-institutional research and education center with headquarters at the University of California, Berkeley. Investigators from over 20 universities, several consulting companies, and researchers at various state and federal government agencies contribute to research programs focused on performance-based earthquake engineering.

These research programs aim to identify and reduce the risks from major earthquakes to life safety and to the economy by including research in a wide variety of disciplines including structural and geotechnical engineering, geology/seismology, lifelines, transportation, architecture, economics, risk management, and public policy.

PEER is supported by federal, state, local, and regional agencies, together with industry partners.

PEER Core Institutions:
University of California, Berkeley (Lead Institution)
California Institute of Technology
Oregon State University
Stanford University
University of California, Davis
University of California, Irvine
University of California, Los Angeles
University of California, San Diego
University of Southern California
University of Washington

PEER reports can be ordered at http://peer.berkeley.edu/publications/peer_reports.html or by contacting

Pacific Earthquake Engineering Research Center
University of California, Berkeley
325 Davis Hall, mail code 1792
Berkeley, CA 94720-1792
Tel: 510-642-3437
Fax: 510-642-1655
Email: peer_editor@berkeley.edu

ISSN 1547-0587X